

Electron Momentum Distributions from Strong-Field-Induced Ionization of Atoms and Molecules

Von der Fakultät für Mathematik und Physik
der Gottfried Wilhelm Leibniz Universität Hannover

zur Erlangung des akademischen Grades
Doktor der Naturwissenschaften
Dr. rer. nat.

genehmigte Dissertation von

M.Sc. Simon Brennecke

2023

Referent: Prof. Dr. Manfred Lein
Leibniz Universität Hannover, Deutschland

Korreferent: Prof. Dr. Reinhard Dörner
Johann Wolfgang Goethe-Universität Frankfurt, Deutschland

Korreferent: Prof. Dr. Lars Bojer Madsen
Universität Aarhus, Dänemark

Tag der Promotion: 05.05.2023

Abstract

High-intensity femtosecond laser pulses in the visible or infrared range can induce electron emission. This single-ionization process may be interpreted as a sequence of (nonadiabatic) tunnel ionization and subsequent acceleration of the electron by the external oscillating field in the presence of the electrostatic force between electron and parent ion. Based on the analysis of photoelectron momentum distributions from the numerical solution of the time-dependent Schrödinger equation, this thesis theoretically studies a variety of phenomena taking place in atoms as well as in molecules in strong fields. The underlying physical mechanisms are revealed by simplified models which take the nonperturbative character of the ionization process into account.

The simulation results for several settings are directly compared to measurements, offering the possibility to benchmark state-of-the-art theory and experiment against each other. One example of this is an investigation of the nonadiabatic strong-field ionization of atomic hydrogen in an attoclock setting. More generally, the deflection of the photoelectrons is analyzed in different attoclock configurations to explore the initial conditions of electrons at the tunnel exit—the position where the electron appears after tunneling. When a molecule is ionized, its orbital structure influences the liberated electron wave packet. The orbital imprint on the momentum-space phase of the wave packet, which encodes spatial information, is demonstrated and an interferometric approach to access these phases is evaluated. A characterization of the freed wave packet is crucial as it influences subsequent processes.

Such secondary processes are induced when the electron is driven back to the parent ion and scatters off. Similar to focusing of light by a lens, the Coulomb attraction forces scattered electron wave packets through focal points, causing a shift of their phase. Due to the interference of outgoing waves, these phases become visible in electron momentum distributions. For a faithful description, these focal-point effects must be included in a prefactor of the exponentiated action in semiclassical models. Furthermore, the control of electron scattering dynamics is demonstrated for low-energy electrons close to the continuum threshold by means of near-single-cycle terahertz pulses. The temporally-localized preparation of the electron wave packet by a femtosecond laser pulse at a well-defined time within the terahertz field enables a switching between different regimes of dynamics, ranging from recollision-free acceleration to extensive scattering phenomena.

In contrast to most studies in the electric dipole approximation that consider only the temporal evolution of the external electric field, various beyond-dipole effects in strong-field ionization are explored in the present work. The microscopic mechanisms of nondipole modifications are thoroughly analyzed. There, the effects of the spatially-varying electric field and of the magnetic field as well as their fingerprints on the geometry of the momentum distributions are identified. Furthermore, the subcycle time resolution of the light-induced momentum transfer in an attoclock-like setup is explored theoretically. Electron recollisions entirely change the observed nondipole effects and render the observations sensitive to the electronic target structure. The high-order above-threshold ionization caused by large-angle scattering is investigated both for exemplary atoms and for diatomic molecules through examination of nondipole shifts of the lateral momentum distribution. The phases of the electron wave packets are also altered by beyond-dipole effects. It is shown that this results in a displacement of ring-link structures known as above-threshold ionization rings that are caused by intercycle interference. In addition, the holographic structures arising from the subcycle interference of scattered and nonscattered electrons are modified.

Keywords: strong-field ionization, time-dependent Schrödinger equation, nondipole effects

Contents

Abstract	iii
Contents	v
1 Introduction	1
2 Introduction to Basic Concepts in Strong-Field Physics	7
2.1 Basic ideas in strong-field ionization	7
2.1.1 The simple man’s model	9
2.1.2 Nondipole effects	11
2.2 The time-dependent Schrödinger equation	13
2.2.1 Minimal-coupling Hamiltonian	14
2.2.2 Unitary transformation to “natural gauge”	15
2.2.3 Gordon-Volkov states	15
2.3 Strong-field approximation	16
2.3.1 Saddle-point analysis and the appearance of quantum orbits	17
2.4 Semiclassical two-step model	19
2.5 Analytical R-matrix theory	21
3 Gouy’s Phase Anomaly in Electron Waves Produced by Strong-Field Ionization	23
3.1 Introduction	23
3.2 Anatomy of momentum distributions for linear polarization	25
3.2.1 Computational details	25
3.2.2 Comparison of TDSE results in 2D and 3D	27
3.3 Semiclassical model	28
3.3.1 Semiclassical approximation	28
3.3.2 Approximation of the under-the-barrier dynamics	30
3.3.3 Inversion problem	32
3.3.4 Explicit scheme of the simulation	33
3.3.5 Symmetry considerations for linearly-polarized fields	33
3.4 Results and discussion	35
3.4.1 Observing Gouy’s phase anomaly in photoelectron holography	37
3.4.2 Intracycle interference	40
3.4.3 Interference of high-energy electrons	42
3.4.4 Interference in bicircular counter-rotating fields	43
3.5 Conclusion	46

4	Control of Electron Wave Packets Close to the Continuum Threshold Using THz Waveforms	49
4.1	Introduction	49
4.2	Computational details	50
4.3	THz-field-free distributions	51
4.4	Streaking of ATI peaks	53
4.5	Dynamics of low-energy electrons	55
4.5.1	Classical model	56
4.5.2	Discussion	57
4.6	Dynamics of zero-energy electrons	62
4.7	Conclusion	65
5	Momentum-Resolved Attoclock	67
5.1	Introduction	67
5.2	Attoclock using close-to-circularly-polarized fields	70
5.2.1	Geometry of the electron wave packets	72
5.2.2	The influence of the Coulomb potential	73
5.2.3	Nonadiabatic ionization of atomic hydrogen	75
5.2.4	Classical backpropagation	80
5.3	Bicircular attoclock	87
5.3.1	Classical adiabatic model	90
5.3.2	Scaling towards the adiabatic limit	93
5.3.3	Advanced models based on probability distributions	96
5.4	Conclusion	99
6	Position Offsets in Strong-field Ionization of Small Molecules	101
6.1	Introduction	101
6.2	Ab-initio calculation of position offsets	103
6.2.1	Motivation based on the PFT model	103
6.2.2	Computational details	106
6.2.3	Results and discussion	107
6.3	Holographic angular streaking of electrons	115
6.3.1	Co-rotating two-color fields	115
6.3.2	Quantum-orbit model	117
6.3.3	Results for a short-range potential	122
6.3.4	Results for a long-range potential	125
6.4	Conclusion	127
7	Nondipole Modification of the AC Stark Effect in Above-Threshold Ionization	129
7.1	Introduction	129
7.2	Ponderomotive shift of ATI rings	130
7.2.1	The (classical) ponderomotive energy	131
7.2.2	Multiphoton picture using the ac Stark effect	132
7.2.3	Time-domain picture	133
7.3	TDSE results	134
7.3.1	Computational details	134
7.3.2	Nondipole shift of the ATI rings	134
7.3.3	AC Stark shift of the ground state	137
7.4	Conclusion	138

8	Microscopic Study of Nondipole Effects in Recollision-Free Ionization	139
8.1	Introduction	139
8.2	The influence of Coulomb and nonadiabatic effects	142
8.2.1	Computational details	142
8.2.2	Angle-resolved nondipole shifts for elliptical polarization	143
8.2.3	Coulomb effects during the continuum motion	144
8.2.4	The influence of nonadiabaticity on the momentum transfer	147
8.2.5	Momentum transfer during the under-the-barrier motion	149
8.3	Disentanglement of magnetic and electric nondipole effects	151
8.3.1	Simple man's model	151
8.3.2	Results for quasilinear fields	155
8.3.3	Results for circularly-polarized fields	156
8.4	Conclusion	163
9	High-Order Above-Threshold Ionization Beyond the Electric Dipole Approximation	165
9.1	Introduction	165
9.2	Anatomy of nondipole effects in HATI	166
9.2.1	Computational details	166
9.2.2	TDSE results for the hydrogen molecular ion	168
9.3	Simple man's model beyond the dipole approximation	169
9.4	Low-frequency approximation model	173
9.5	Hydrogen molecular ion	176
9.6	Xenon	181
9.7	Conclusion	187
10	Strong-Field Photoelectron Holography Beyond the Dipole Approximation	189
10.1	Introduction	189
10.2	Anatomy of nondipole effects in photoelectron holography	190
10.2.1	Computational details for helium	193
10.3	Semiclassical model beyond the electric dipole approximation	193
10.4	Simple man's model beyond the dipole approximation	196
10.5	Results and discussion	197
10.5.1	The central holographic fringe without Coulomb focusing	197
10.5.2	Higher-order holographic fringes	200
10.5.3	The central holographic fringe including Coulomb focusing	202
10.6	Conclusion	208
11	Summary and Conclusion	209
A	Methods	213
A.1	Introduction to scattering theory	213
A.1.1	Calculation of scattering states for rotationally-symmetric systems	215
A.2	Numerical solution of the time-dependent Schrödinger equation	216
A.2.1	Generalized pseudospectral method in spherical coordinates	216
A.2.2	Cartesian split-operator method	221
A.2.3	Choice of the potential	226
A.2.4	Focal-volume averaging	228
A.3	Strong-field approximation beyond the dipole approximation	229
A.3.1	Adiabatic expansion of the saddle-point times	230
A.3.2	Adiabatic expansion of the wave packet	231
A.4	Analytic approximations for tunnel-exit positions	232

A.4.1	Adiabatic expansion of the tunnel-exit position in the SFA	232
A.4.2	Tunnel-exit positions from the analytical R-matrix theory	232
A.5	Low-frequency approximation beyond the dipole approximation	234
Bibliography		237
List of Abbreviations		265
Curriculum Vitae		267
List of Publications		269

Chapter 1

Introduction

Light-matter interaction—the absorption and emission of light by electrons in atoms, molecules and solids—plays a crucial role in science as well as in technology and is the foundation of numerous applications. Examples reach from lasers and spectroscopy techniques over light-emitting diodes and solar cells to the definition of time standards and quantum computing. One of the earliest manifestations of quantum mechanics in light-matter interaction is the photoelectric effect where the absorption of one photon leads to the ejection of an initially-bound electron [1]. However, with increasing intensity of the radiation, not only one, but multiple photons can be absorbed [2–4]. Photoionization is even induced with photon energies smaller than the ionization potential. Thus, atoms and molecules can be ionized by light fields in the visible or infrared range (with wavelengths between about 400 nm and 3 μm). The detection of the released electrons results in photoelectron energy spectra with multiple peaks that are separated by the photon energy. Since more photons than necessary to overcome the ionization threshold are absorbed, this process is known as above-threshold ionization (ATI) [5].

A revolution in photoionization was initiated by the temporal confinement of radiation energy into short, but very intense laser pulses with only tens of femtosecond duration (in excess of 10^{13} W/cm² intensity) [6]. This led to the discovery of numerous fascinating phenomena and established strong-field physics—a new domain in light-matter interaction. In this regime, the strength of the forces due to the external electromagnetic fields are comparable with the electrostatic Coulomb attraction between ion and outer-shell electrons. Hence, the physical mechanisms in strong-field ionization are fundamentally different compared to single-photon ionization and are usually not adequately represented by perturbation theory in the interaction.

Instead, the physics behind many strong-field phenomena is often well described by the following sequence of steps [7–10]: In a first release or ionization step, an electron wave packet is created in the continuum. In a second step, the electron wave packet is accelerated by the electromagnetic field. Depending on the shape of the driving field, the wave packet can return to its parent ion. In a third step, recollisions may induce different processes such as efficient extreme ultraviolet (XUV) photon emission in high-harmonic generation (HHG) [11, 12], the release of a second electron in nonsequential double ionization (NSDI) [13–15] or the elastic scattering resulting in high-order above-threshold ionization (HATI) [16–18]. Due to the temporal localization of the stages on the scale of an optical cycle, the physical mechanism is susceptible to the subcycle variation of the driving fields. Hence, even though the periods of the external fields are on a femtosecond time scale, the long standing dream of observing and controlling of electron dynamics in atoms and molecules on their much shorter natural time scale (attoseconds) became possible [19–21].

In many ultrafast imaging methods, the structure and dynamics of the targets are probed by using the recolliding electrons [22]. For example, in high-harmonic generation spectroscopy [23–27] structural information is contained in the emitted radiation whereas in strong-field photoelectron holography [28–32] or in laser-induced electron diffraction (LIED) [33–35] the target structure is reflected in the electron momentum distribution. Due to the large kinetic energies and therefore small wavelengths of the return-

ing electron waves in strong infrared fields, the target can be imaged with high spatial resolution [22]. Since large-angle scattering forms the physical foundation of LIED, the differential scattering cross section of the target dominates the shape of the momentum distributions [36–38]. In molecules, the electron wave scatters off the various atomic centers, creating a multi-slit diffraction pattern [33, 39] that encodes information on the molecular structure and its dynamics [40–42].

The application of high-harmonic generation as a table-top source for coherent attosecond XUV pulses and the achievements in high-harmonic spectroscopy were one of the earliest driving forces in strong-field physics [19–21]. However, the measurement of full three-dimensional photoelectron momentum distributions (PMDs) from single ionization of atoms and molecules became possible by developing and improving the velocity-map imaging (VMI) technique [43] in combination with tomography techniques [44–47] and the cold target recoil ion momentum spectroscopy (COLTRIMS) systems (also known as reaction microscopes) [48–51]. In COLTRIMS, static electric and magnetic fields (usually) guide photoelectrons and ions to position-sensitive detectors. Measuring their times of flight as well as positions of impact in coincidence allows the retrieval of the three-dimensional momenta of the electrons for each detected event. In contrast to high-harmonic generation, the investigation of electron momentum distributions has several advantages: It offers the opportunity to study recollision-free processes, it does not rely on recombination of the electron and it is not affected by coherent phase-matching effects. For these reasons, the analysis of momentum distributions may allow deeper insights into the created continuum wave packets and into the ionization process itself.

The physics in strong fields is usually located on the boundary between quantum mechanics and classical physics. Depending on the particular observables, both the particle properties and the wave properties of electrons become visible. Hence, strong-field ionization provides a simple environment to study fundamental quantum-mechanical effects of matter waves such as tunneling, focusing, or interference. For example, electron tunneling through a time-dependent potential barrier often describes the ionization step well. The exact description of this quantum-mechanical process raises some questions such as: Is the tunneling probability susceptible to the time dependence of the barrier? What influence does the structure of the initial quantum state of the atom or the molecule have on the photoelectron wave packet? Do the tunneling characteristics depend on the velocity of the released electron? Is it possible to resolve the ionization process in time? One important concept that provides answers to these and other arising questions is the “attoclock” method that studies tunnel ionization on an attosecond time scale in an interference-free and recollision-free setting [52–54]. There, a two-dimensional polarization form such as a circularly-polarized field is applied that ionizes an atom or a molecule and afterward governs the dynamics, leading to a mapping of the ionization time and the velocity of the released electron to its final momentum. The main observable is the peak of the photoelectron momentum distribution, containing information on the ionization process in the presence of the Coulomb attraction of the parent ion (see for example the reviews [55, 56]).

When ionizing molecules, their structure leaves an imprint on the outgoing electron wave packet. For example in molecular imaging with circular polarization, the time-to-momentum mapping of the attoclock is considered to attribute the measured photoelectron angular distribution to the orientation-dependent ionization probability of the molecular orbital (see for example Refs. [57–61]). Hence, an “image” of the orbital from which ionization takes place can be generated and the complexity of recollisions as in other techniques such as LIED is avoided. Typically, in such recollision-free strong-field experiments with molecules, the probability density is observed and the phase of the electron wave function in momentum space is not considered. In single-photon ionization, the variation of the phase is related to the Wigner time delay [62] and can be characterized by the attosecond streaking technique [63, 64] or reconstruction of attosecond harmonic beating by interference of two-photon transitions (RABBITT) technique [65–68]. However, the influence of the molecular structure on the phases of the momentum-space wave function is nearly unexplored in strong-field ionization. Even though these phases cannot be directly measured, the analysis of interference structures in electron momentum distributions can be considered for their investigation [69]. A characterization of the liberated electron wave packet is important as it influences secondary processes such as HHG or LIED (see for example [25, 29, 70]).

Different types of double-slit-like interference scenarios are already well-known from strong-field ionization with linear polarization [71–76]. Thus, the electron momentum distribution can act as a “phasometer”, measuring the phase difference between waves. When electrons are driven back to the vicinity of the parent ion, their motion is influenced by electron-ion scattering in the presence of the external electromagnetic field. The scattered electron waves are focused in long-range potentials similar to focusing of a light wave by a lens. This so-called Coulomb focusing [77] results in an enhancement of the yield in the photoelectron momentum distribution [78, 79]. In addition, a phase change of the wave while passing a focal point is also expected for electrons analogous to the Gouy phase shift in optics [80]. So far, it was not considered whether these focal-point phases modify the interference structures in momentum distributions.

A plethora of different scattering phenomena appears in strong fields reaching from large-angle scattering [16–18] to soft recollisions in the Coulomb field, leading to low-energy structures [81–86]. Whereas head-on collisions of high-energy electrons can be described as single light-field-free scattering events, the interplay between the electromagnetic field and the long-range Coulomb force acting between the electron and the parent ion is crucial at low energies. The control and modification of the recollision processes of electrons with energies in the eV range was demonstrated either by tailoring the driving laser pulses [87–93] or by using two pulse schemes [94–100]. The dynamics of weakly-bound Rydberg states [101, 102] and also the dynamics of low-energy continuum electrons in the meV range [103] can be manipulated on a picosecond timescale by pump-probe schemes based on the ionization with terahertz pulses [104, 105]. The question arises whether it is possible to deliberately switch electron-ion collisions on and off and adjust their properties for electron wave packets at energies close to the continuum threshold.

From a theoretical perspective, a remarkable trait of strong-field physics is that many effects can be intuitively described by means of classical trajectories, i.e., by only considering the particle properties of the electron. The simple man’s model [7, 8] is the most famous example, considering only classical particles in the external electromagnetic field without invoking electron-ion interaction at all. This intuitive model creates the opportunity to explain complex physical mechanism on a simple basis. However, the retrieval of information from the highly nonlinear harmonic signal or from photoelectron momentum distributions is a theoretical challenge, requiring more elaborate models that should be as simple, but at the same time as accurate as possible. An effective quantum-mechanical treatment of recollision-free ionization is offered by the strong-field approximation (SFA) [106–108] and its generalization to describe recollisions [18, 109]. Its further approximation employing a saddle-point method results in a simplified analytical model where the probability amplitude is given by a coherent superposition of a finite number of quantum orbits, i.e., Newtonian trajectories evolving in complex time [110–112]. This quantum-orbit model contains the notion of a trajectory-based description to interpret momentum distribution, but nevertheless considers the ionization process on a quantum-mechanical basis. To enhance the quality of the modeling, several refined methods were developed that consider the electron-ion interaction more accurately, for example the analytical R-matrix (ARM) theory [113, 114]. To preserve the clarity of classical mechanics, the semiclassical description adds “(quantum-mechanical) wave flesh on classical bones” [115] by associating a semiclassical phase with each trajectory. This resulted in a variety of models such as the trajectory-based Coulomb-corrected strong-field approximation (TCSFA) [116–119], the quantum-trajectory Monte Carlo (QTMC) model [120], the Coulomb quantum-orbit strong-field approximation (CQSFA) [121], or the semiclassical two-step (SCTS) model [122].

Intuitive models allow a simple interpretation of phenomena. However, their reliability and accuracy should be benchmarked against either experimental results or more sophisticated theoretical approaches. Usually, in strong-field physics, the electromagnetic field can be treated classically. Hence, a nonrelativistic description of the electron dynamics in atoms or simple molecules requires the numerical solution of the time-dependent Schrödinger equation (TDSE). In this thesis, almost all observed effects are confirmed by TDSE simulations in the single-active-electron (SAE) approximation. In the SAE approximation, the motion of one active electron is governed by the influence of the external electromagnetic field and an effective potential representing the forces from the nuclei and other electrons. This

approach usually works very well for single ionization. However, a number of effects involving nuclear motion (see for example Refs. [123, 124]) or multielectron physics (see for example Refs. [54, 125, 126]) were identified, i.e., their treatment requires many-particle approaches as in Refs. [123, 127–133].

Already more than 400 years ago, the deflection of comet tails observed by Kepler indicated that radiation also applies a pressure on matter, acting in the light-propagation direction. This facet of light-matter interaction is related to the transfer of linear photon momentum as it is well-known from Compton scattering of quasi-free electrons [134]. As of now, effects of photon momentum transfer impact a broad range of scientific fields ranging from astrophysics [135, 136] over plasma physics [137] and the optical tweezers [138, 139] to laser cooling [140–143]. Nevertheless, strong-field ionization is mostly discussed in the electric dipole approximation, neglecting the effect of the photon momentum. In a wave picture, the dipole approximation only considers a spatially homogeneous, time-dependent external electric field and furthermore neglects the magnetic field of the light wave. For laser parameters in the so-called “dipole oasis” [144, 145] employed in real-world table-top experiments, this approximation is well justified. Since the dispersion relations of momentum to energy are fundamentally different for photons and electrons, the influence of the linear photon momentum is usually overshadowed by the momentum gain of the electron due to the imparted photon energy. However, nondipole effects become more important with increasing energy of the photoelectrons, e.g., by increasing the laser wavelength or intensity. Hence, the development of strong mid-infrared laser systems challenges the applicability of the dipole approximation. While the transfer of energy in strong-field ionization is well understood, nondipole effects were only studied in recent years.

In the dipole approximation, electron momentum distributions from strong-field ionization of atoms are symmetric under interchange of forward and backward direction. Here, “forward” denotes the light-propagation direction. However, a nonzero forward average momentum was observed in a pioneering experiment for nonscattered electrons [146]. The major part of this forward shift is caused by the momentum gain of the electron during its acceleration in the laser field [147–149] and only a small fraction is attributed to its liberation by tunneling [150, 151]. Despite years of research, there are still open questions about the underlying microscopic mechanisms, e.g., on the contributions of the magnetic part of the Lorentz force and the spatial dependence of the electric field. In linearly-polarized fields, nondipole effects are also affected by rescattering. As a result, for the low-energy electrons, the peak of the momentum distribution is shifted against the light-propagation direction. This was attributed to the exchange of momentum between electron and ion during rescattering [152–157]. In this context various questions emerge such as: How does large-angle scattering in HATI influence the momentum transfer? Are interference structures in PMDs such as in photoelectron holography also modified by nondipole effects?

This thesis has the following structure: Following this introduction, Chapter 2 describes the basic concepts and methods used to interpret and to theoretically describe strong-field phenomena. In the first part of this thesis, we use the dipole approximation to study several aspects of strong-field ionization such as the importance of focal-point phases, the phase structure of the wave packets from molecular strong-field ionization, or the control of low-energy electron wave packets. In contrast, the second part theoretically considers the influence of nondipole effects on various strong-field phenomena and provides answers to the questions asked above. The thesis closes with concluding remarks in Chapter 11. Several chapters are based on joint work with experimental groups, enabling a direct comparison between the simulated results and the measurements. The topics studied in the main chapters can be summarized as follows:

- The focusing of electron waves in strong-field ionization of atoms is studied in Chapter 3. We show that during Coulomb focusing electron waves pass through focal points and acquire a phase shift analogous to the Gouy phase in optical beams. The focal-point phases modify the observed interference structures in photoelectron momentum distributions. We unveil that such phases do not only appear in linear polarization but also in other waveforms that give rise to rescattering. The focal-point effects are encoded in a prefactor of the exponentiated action in semiclassical models that influences both the phase and the weight of each trajectory.

- The dynamics of electrons right at the boundary between bound Rydberg states and low-energy continuum states is studied for atoms in Chapter 4. To this end, an electron wave packet is created by a short femtosecond laser pulse. Its motion is controlled by a phase-stable terahertz pulse, which implies a high degree of temporal localization of the creation process. By varying the time delay, the signatures of various regimes of dynamics, ranging from recollision-free acceleration to coherent electron-ion scattering induced by the terahertz field, are observed in the photoelectron momentum distributions.
- The attoclock protocol is considered to microscopically investigate the strong-field ionization of atoms in Chapter 5. We explore the dependence of the attoclock offset on a lateral momentum component, i.e., on which slice of the momentum distribution is analyzed. We demonstrate that this observable is strongly influenced by the dependence of the tunnel exit—the position where the electron is born after tunnel ionization—on the velocity of the liberated electron. To study the effects of the time-dependent barrier during tunneling in the attoclock configuration, both close-to-circularly-polarized fields and quasilinear fields are used.
- The influence of the molecular structure on the momentum-space phase of the electron wave packet created by recollision-free strong-field ionization of molecules is explored in Chapter 6. As the derivative of this phase is related to the electron's position, we are able to investigate the dependence of the spatial offset of the electron's birth position on the electron's emission direction relative to the molecular axis. To this end, we study both results from numerical TDSE simulations of the phase of the continuum wave function and position offsets retrieved from photoelectron momentum distributions in an interferometric approach [69].
- Nondipole modifications of the ATI rings in strong-field ionization of atoms are investigated in Chapter 7. In the dipole approximation, the multiphoton generalization of Einstein's photoeffect law suggests that the kinetic energies of the photoelectrons do not depend on the electrons' emission direction. However, in TDSE simulations beyond the dipole approximation, we show that the geometric centers of ATI rings are displaced in the direction opposite to the light-propagation direction. The beyond-dipole change of the ac Stark effect for electron continuum states is invoked to explain this observation.
- The physical mechanisms of recollision-free strong-field ionization are investigated beyond the dipole approximation in Chapter 8. We resolve the transfer of linear momentum in time by following the idea of the attoclock and by analyzing the shift of the electron momentum distribution in the light-propagation direction as a function of the momentum in the polarization plane. The decomposition of momentum transfer into tunneling and continuum motion is considered and the influence of nonadiabaticity on nondipole effects is analyzed. Furthermore, we identify the contributions of the magnetic part of the Lorentz force as well as the spatial dependence of the electric field to the momentum-dependent nondipole shifts.
- The influence of large-angle scattering on the nondipole effects in the photoelectron momentum distribution is studied in Chapter 9. Since the electrons return close to the parent ion during scattering, the target structure vastly influences the beyond-dipole effects in HATI and, thus, the sharing of the imparted linear momentum between photoelectron and ion. We consider the hydrogen molecular ion H_2^+ as a prototype of diatomic molecules as well as the xenon atom. Even though both targets show a nondipole shift of the momentum distribution, we demonstrate that the results for atoms and molecules differ systematically.
- The nondipole modifications of the interference patterns from strong-field photoelectron holography are explored in Chapter 10. For both long-range and short-range potentials, the interference fringes are shifted in the light-propagation direction. A semiclassical model is developed for a quantitative trajectory-based description and it is shown that nondipole effects modify both the classical trajectories and their associated phases. Whereas high-order interference fringes can be

explained by two-path interference, Coulomb focusing leads to a breakdown of this picture. A glory-rescattering model [158] beyond the dipole approximation is used to resolve this problem.

This thesis is based on parts of the following peer-reviewed publications and, furthermore, contains additional details as well as some important generalizations of these results.

- S. Brennecke, M. Ranke, A. Dimitriou, S. Walther, M. J. Prandolini, M. Lein, and U. Fröhling, “Control of Electron Wave Packets Close to the Continuum Threshold Using Single-Cycle THz Waveforms,” *Physical Review Letters* **129**, 213202 (2022).
- K. Lin, S. Brennecke, H. Ni, X. Chen, A. Hartung, D. Trabert, K. Fehre, J. Rist, X.-M. Tong, J. Burgdörfer, L. Ph. H. Schmidt, M. S. Schöffler, T. Jahnke, M. Kunitski, F. He, M. Lein, S. Eckart, and R. Dörner, “Magnetic-Field Effect in High-Order Above-Threshold Ionization,” *Physical Review Letters* **128**, 023201 (2022).
- D. Trabert, N. Anders, S. Brennecke, M. S. Schöffler, T. Jahnke, L. Ph. H. Schmidt, M. Kunitski, M. Lein, R. Dörner, and S. Eckart, “Nonadiabatic Strong Field Ionization of Atomic Hydrogen,” *Physical Review Letters* **127**, 273001 (2021).
- S. Brennecke, and M. Lein, “Nondipole modification of the ac Stark effect in above-threshold ionization,” *Physical Review A* **104**, L021104 (2021).
- S. Brennecke, S. Eckart, and M. Lein, “Attoclock with bicircular laser fields as a probe of velocity-dependent tunnel-exit position,” *Journal of Physics B* **54**, 164001 (2021).
- D. Trabert, S. Brennecke, K. Fehre, N. Anders, A. Geyer, S. Grundmann, M. S. Schöffler, L. Ph. H. Schmidt, T. Jahnke, R. Dörner, M. Kunitski, and S. Eckart, “Angular dependence of the Wigner time delay upon tunnel ionization of H₂,” *Nature Communications* **12**, 1697 (2021).
- A. Hartung, S. Brennecke, K. Lin, D. Trabert, K. Fehre, J. Rist, M. S. Schöffler, T. Jahnke, L. Ph. H. Schmidt, M. Kunitski, M. Lein, R. Dörner, and S. Eckart, “Electric Nondipole Effect in Strong-Field Ionization,” *Physical Review Letters* **126**, 053202 (2021).
- H. Ni, S. Brennecke, X. Gao, P.-L. He, S. Donsa, I. Březinová, F. He, J. Wu, M. Lein, X.-M. Tong, and J. Burgdörfer, “Theory of Subcycle Linear Momentum Transfer in Strong-Field Tunneling Ionization,” *Physical Review Letters* **125**, 073202 (2020).
- S. Brennecke, N. Eicke, and M. Lein, “Gouy’s Phase Anomaly in Electron Waves Produced by Strong-Field Ionization,” *Physical Review Letters* **124**, 153202 (2020).
- N. Eicke, S. Brennecke, and M. Lein, “Attosecond-Scale Streaking Methods for Strong-Field Ionization by Tailored Fields,” *Physical Review Letters* **124**, 043202 (2020).
- A. Hartung, S. Eckart, S. Brennecke, J. Rist, D. Trabert, K. Fehre, M. Richter, H. Sann, S. Zeller, K. Henrichs, G. Kastirke, J. Hoehl, A. Kalinin, M. S. Schöffler, T. Jahnke, L. Ph. H. Schmidt, M. Lein, M. Kunitski, and R. Dörner, “Magnetic fields alter strong-field ionization,” *Nature Physics* **15**, 1222 (2019).
- S. Brennecke, and M. Lein, “Strong-field photoelectron holography beyond the electric dipole approximation: a semiclassical analysis,” *Physical Review A* **100**, 023413 (2019).
- S. Brennecke, and M. Lein, “High-order above-threshold ionization beyond the electric dipole approximation: Dependence on the atomic and molecular structure,” *Physical Review A* **98**, 063414 (2018).

Chapter 2

Introduction to Basic Concepts in Strong-Field Physics

What are the physical mechanisms behind ionization of atoms and small molecules with strong light fields? And how to describe these processes efficiently? To illuminate these questions, we present a short review of basic physical concepts of strong-field physics as well as an introduction to its theoretical modeling. Similar introductions to strong-field ionization can be found in the previous works [159–161].

A complete description of light-matter interaction requires quantum-field theories. However, here, we consider electromagnetic fields of low photon energies that are sufficiently strong to observe high-order multiphoton effects, but sufficiently weak to avoid radiative effects such as vacuum polarization. Hence, the electromagnetic field is treated classically. In addition, we assume that the field is not altered by the interaction with electronic system. Over the interaction region, the electromagnetic field is approximated by plane waves traveling in z -direction with speed of light c . The respective electric and magnetic fields are given by

$$\mathbf{E}(\mathbf{r}, t) = \mathbf{E}\left(t - \frac{z}{c}\right) \quad \text{and} \quad \mathbf{B}(\mathbf{r}, t) = \frac{1}{c} \mathbf{e}_z \times \mathbf{E}\left(t - \frac{z}{c}\right). \quad (2.1)$$

Here, the polarization plane is equal to the x - y -plane.

Additionally, we do not consider effects such as creation or annihilation of massive particles and, thus, treat the electronic system within ordinary quantum mechanics. One aim of this thesis is the investigation of nondipole phenomena and especially the influence of radiation pressure on photoelectron momentum distributions. Here, “nondipole” refers to effects beyond the electric dipole approximation. We only consider particles with velocities much smaller than the speed of light c and, thus, describe the interaction of an atom or a molecule with an electromagnetic field by the nonrelativistic time-dependent Schrödinger equation (TDSE). As the leading-order relativistic corrections are of the order $1/c^2$, our treatment still allows a consistent description of nondipole effects to first order of $1/c$. Despite these approximations, we still consider this description as an “exact” reference for the problems under study.

Throughout this thesis, atomic units are used unless stated otherwise. This unit system reflects the typical scales in length, time, etc. on which dynamics of valence electrons takes place and is well suited for our purpose. Atomic units are defined by setting the reduced Planck’s constant \hbar , the elementary charge e , the electron mass m_e , and the Coulomb constant $1/(4\pi\epsilon_0)$ to unity. Importantly for the work, the speed of light c is given in atomic units by the inverse of the fine structure constant: $c \approx 137.036$ a.u.

2.1 Basic ideas in strong-field ionization

The regimes of light-induced ionization of small target gases can be characterized by considering three parameters: the ionization potential I_p of the target, the frequency ω as well as the maximal field

strength E_0 of the radiation. Usually, the three characteristic quantities are combined into two dimensionless parameters (see for example Ref. [162]):

$$\gamma = \frac{\sqrt{2I_p} \omega}{E_0} \text{ (Keldysh parameter)} \quad \text{and} \quad Q = \frac{I_p}{\omega} \text{ (multiphoton parameter)}. \quad (2.2)$$

If the photon energy is larger than the ionization potential ($Q < 1$), a single photon is sufficient to ionize the system and the excess energy manifests itself as the kinetic energy of the liberated electron. However, at very high photon densities (high light intensities) it is possible to not only absorb one but multiple photons. Hence, even for multiphoton parameters $Q > 1$, i.e., multiple photons are required to overcome the ionization threshold, ionization is possible. The latter case of large Q is realized with visible or infrared laser fields and it is considered in this thesis. If more photons than necessary to overcome the ionization threshold are absorbed, a characteristic series of peaks is visible in the photoelectron energy spectra. In this process known as above-threshold ionization (ATI) [5], the peaks are separated by the photon energy ω .

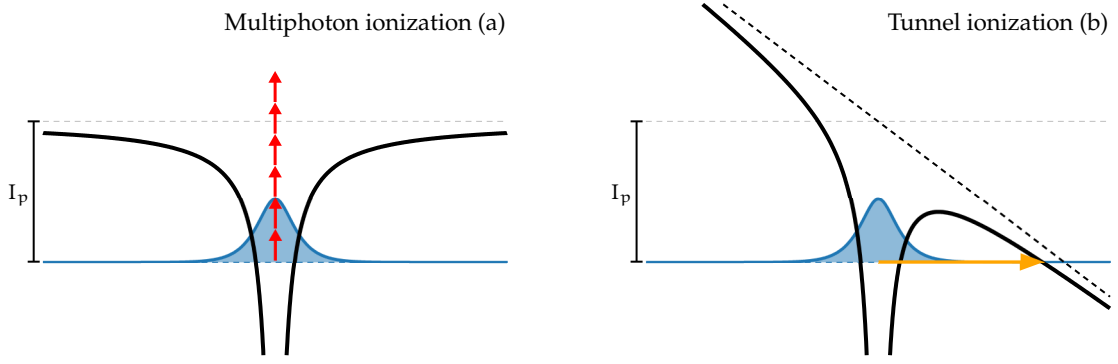


Figure 2.1: Sketch of ionization processes: (a) Multiphoton ionization. The electron of a bound-state wave function (blue area) is liberated by absorbing multiple photons (indicated as red arrows). (b) Adiabatic tunnel ionization. The potential of the light field (black dashed line) deforms the ionic potential, creating a barrier (black line) through which the previously bound electron can escape via tunneling.

In the regime $Q \gg 1$, the ionization process is usually dictated by two different time scales: the Keldysh time $\sqrt{2I_p}/E_0$ and the optical cycle $T_\omega = 2\pi/\omega$ of the external light field. The nonadiabaticity of the ionization process is characterized by their dimensionless combination, i.e., the Keldysh parameter γ [106]. The so-called multiphoton regime—the natural generalization of single-photon ionization—is indicated by large values of the Keldysh parameter $\gamma \gg 1$ (see Fig. 2.1(a)). The electron changes its energy by absorption of several photons in a first step. Hence, for this n -photon process, the ionization rate has the form $\Gamma \propto I^n$, where n is the number of absorbed photons and $I = \frac{1}{2}\epsilon_0 c E_0^2$ is the intensity (in SI units) [163, 164]. Afterwards, the created electron wave packet in the continuum travels away from the parent ion.

In the presence of a strong light field, the bound electron feels the joint electric field of the ionic core and of the external field, giving rise to a time-dependent potential barrier (see Fig. 2.1(b)). For small Keldysh parameters ($\gamma \ll 1$), the barrier changes slowly compared to the characteristic Keldysh time $\sqrt{2I_p}/E_0$ and, thus, the electron can escape through this quasistatic barrier via tunneling. In contrast to multiphoton ionization, the energy does not change, but the position changes in adiabatic tunneling. Hence, an electron that was freed at a given time t_0 , i.e., the “time of birth” or “instance of tunneling”, appears at the tunnel-exit position \mathbf{r}_0 . In this tunneling regime, the ionization probability depends exponentially on the width of the tunnel barrier and, hence, on the external field strength. The ionization rate for electrons born at time t_0 with an initial velocity \mathbf{v}_0 can be approximated by

$$w_{\text{ini}}(t_0, \mathbf{v}_0) \propto \exp\left(-\frac{2\kappa^3}{3|\mathbf{E}(t_0)|}\right) \exp\left(-\frac{\kappa v_0^2}{|\mathbf{E}(t_0)|}\right) \quad (2.3)$$

with the momentum scale $\kappa = \sqrt{2I_p}$ associated with the ionization potential I_p . Equation (2.3) is the exponential part of the Perelomov-Popov-Terent'ev (PPT) or Ammosov-Delone-Krainov (ADK) rate [165–168]. In a long-range ionic potential with an asymptotic charge Z , a third parameter $\tilde{Z} = \frac{E_0}{I_p^2} Z$ should be considered which characterizes the relative importance of Coulomb effects in the ionization process. For $\tilde{Z} > 1/4$, the external field strength is so large that the barrier is suppressed and an electron with initial energy $-I_p$ can classically escape [169].

Most of today's strong-field experiments are performed in the intermediate regime $\gamma \lesssim 1$ that can be viewed as nonadiabatic tunnel ionization. To a certain extent, the process can be treated as a first step of multiphoton absorption, promoting the initially-bound electron to a virtual intermediate state from which it is afterwards released by adiabatic tunneling [163, 164]. Hence, during nonadiabatic tunneling the energy as well as the position of the electron changes [170]. In this thesis, we will often start with the simple picture of adiabatic tunneling and afterwards include the leading-order nonadiabatic corrections.

2.1.1 The simple man's model

The physical understanding of ionization in the adiabatic or nonadiabatic tunneling regime is often greatly boosted by an interpretation in a sequence of two or three steps [7–10]. After the electron is freed in a nonclassical tunneling process (ionization step), it emerges in the continuum and it is further accelerated by the external electromagnetic field (acceleration step). If the frequency ω is sufficiently low, the electron motion can be treated classically. In this section, we restrict ourselves to the dipole approximation and discuss the most important nondipole modifications in Section 2.1.2. It is fruitful to first neglect the electron-ion interaction and study the classical dynamics induced solely by the external field, i.e., described by Newton's equation of motion

$$\ddot{\mathbf{r}}(t) = -\mathbf{E}(t). \quad (2.4)$$

We first assume that the electron is born at some time t_0 with vanishing initial velocity $\mathbf{v}_0 = \dot{\mathbf{r}}(t_0) = 0$. Hence, the time evolution of the velocity $\mathbf{v}(t)$ is given by

$$\dot{\mathbf{r}}(t) = \mathbf{v}(t) = \mathbf{A}(t) - \mathbf{A}(t_0) \quad \text{with} \quad \mathbf{A}(t) = -\int_{-\infty}^t dt' \mathbf{E}(t'). \quad (2.5)$$

Here, we introduced the quantity \mathbf{A} usually referred to as the vector potential. In a continuous wave (cw) field, the velocity can be split in a time-independent part describing the drift motion and a time-dependent part describing the electron's quivering motion. The cycle-averaged kinetic energy of the quivering motion reads

$$U_p = \frac{1}{T_\omega} \int_0^{T_\omega} dt \frac{1}{2} \mathbf{A}^2(t), \quad (2.6)$$

and it is called ponderomotive potential. In a strong field, the effective ionization potential is enhanced from I_p to $I_p + U_p$ due the required quivering energy, resulting in a shift of the positions of the ATI peaks [171–173]. This shift only appears, if the electron stays in the focus of the radiation until the end of the pulse what is typically fulfilled for the subpicosecond pulses used in today's experiments.

In reality, laser pulses have to satisfy the conditions

$$\lim_{t \rightarrow \pm\infty} \mathbf{E}(t) = 0 \quad \text{and} \quad \lim_{t \rightarrow \pm\infty} \mathbf{A}(t) = 0. \quad (2.7)$$

If the electron does not leave the focus until the end of the pulse, its asymptotic final momentum reads

$$\mathbf{p} = -\mathbf{A}(t_0). \quad (2.8)$$

This important relation between time of ionization t_0 and photoelectron momentum \mathbf{p} can be used to predict the overall shape of the photoelectron momentum distribution. For example in circularly-polarized light, one expects a distribution that is rotationally symmetric around the propagation direction of light with a maximum of the distribution in the polarization plane at $p_\perp = |\mathbf{A}(t_0)| = A_0$. In

contrast, for linearly-polarized fields with $\mathbf{E}(t) = E_0 \cos(\omega t) \mathbf{e}_x$, the vector potential is given by

$$\mathbf{A}(t) = -\frac{E_0}{\omega} \sin(\omega t) \mathbf{e}_x. \quad (2.9)$$

Thus, the distribution should be concentrated along the polarization axis with a maximal momentum $p_x^{\max} = E_0/\omega = A_0$ in polarization direction (corresponding to a maximal photoelectron energy of $(p_x^{\max})^2/2 = K_0 = 2U_p$). Here, we used the ponderomotive potential $U_p = \frac{E_0^2}{4\omega^2}$ for linearly-polarized fields. It turns out that a vanishing initial velocity \mathbf{v}_0 is a very strict assumption. Instead, a distribution of initial velocities analogous to Eq. (2.3) should be considered to describe more properly the momentum distributions in recollision-free strong-field ionization.

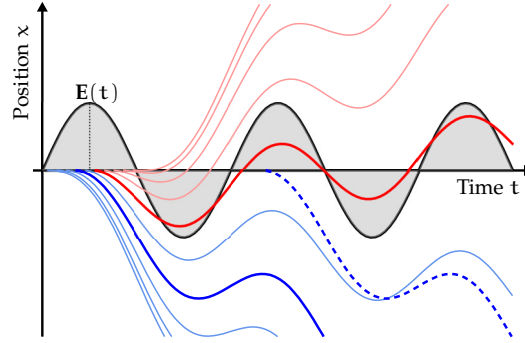


Figure 2.2: Classical simple man's trajectories (solid lines) that start in the half cycle centered around $t = 0$ of the depicted electric field (black line). The red curves indicate trajectories that are released in a descending quarter cycle of the electric-field strength and that revisit the ionic core. In contrast, the blue curves show trajectories that depart in an ascending quarter cycle and that do not revisit the ionic core. The dashed dark-blue trajectory corresponds to ionization in another cycle of the field, but is otherwise equivalent to the solid dark-blue trajectory.

By integrating the velocity (2.5), the time-dependent position of the electron is obtained

$$\mathbf{r}(t) = \mathbf{r}_0 - \mathbf{A}(t_0)(t - t_0) + \boldsymbol{\alpha}(t, t_0), \quad (2.10)$$

where we define the quiver amplitudes

$$\boldsymbol{\alpha}(t, t_0) = \int_{t_0}^t dt' \mathbf{A}(t') \quad \text{and} \quad \alpha_2(t, t_0) = \int_{t_0}^t dt' \mathbf{A}^2(t'). \quad (2.11)$$

Since the force due to the external field is independent of the position, we can simply choose the place of birth $\mathbf{r}_0 = \mathbf{r}(t_0) = 0$. In the special case of linear polarization, the dynamics is restricted to the polarization axis

$$x(t) = \frac{E_0}{\omega} \sin(\omega t_0)(t - t_0) + \frac{E_0}{\omega^2} (\cos(\omega t) - \cos(\omega t_0)). \quad (2.12)$$

Hence, the drift motion of the photoelectron is modulated by the oscillatory quiver motion with an amplitude E_0/ω^2 . Figure 2.2 shows examples of trajectories for different ionization times t_0 . Each final photoelectron momentum p_x with $|p_x| < E_0/\omega$ is reached by two trajectories starting in one optical cycle of the field. If the electrons depart in an ascending quarter cycle of the electric-field strength (see the trajectories marked in blue), they do not revisit the ionic core. However, electrons that are released in a descending quarter cycle are driven back to the parent ion, i.e., there is a return time $t_c > t_0$ with $x(t_c) = x(t_0) = 0$.

In a recollision step, the electron can undergo different processes: It can recombine with the parent ion resulting in high-harmonic generation [11, 12]. For high-harmonic generation, the return energy of the electron determines the frequency of the emitted radiation. Hence, the cutoff energy of the characteristic plateau structure in the HHG spectrum is related to the maximal return energy and is found to be $E_{\max}^{\text{HHG}} \approx 3.17 U_p + I_p$ [9, 10]. For all photon energies between I_p and E_{\max}^{HHG} , there exist two trajectories per cycle of the laser field called the short and long (HHG) trajectories. Similarly, the electron can scatter

inelastically, leading to the emission of a second electron via nonsequential double ionization [13, 15]. In the case of an elastic collision, the magnitude of the electron velocity stays constant, but its direction is changed. The target-specific field-free differential cross section (DCS) represents the probability for scattering to a certain direction [36]. After the collision a second stage of acceleration by the field takes place, resulting in high final kinetic energies such that the process is called high-order above-threshold ionization (HATI). For backscattering, the highest energy is classically found to be $E_{\max}^{\text{HATI}} \approx 10.01 U_p$ [16, 17]. Trajectories starting very close to the time of peak electric-field strength (see the trajectory drawn as dark red line in Fig. 2.2), can revisit the parent ion multiple times. However, in general, the ability of a return to the ionic core depends strongly on the shape of the external field, e.g., when increasing the ellipticity towards circular polarization recollisions are suppressed.

2.1.2 Nondipole effects

Strong-field ionization is usually described in the electric dipole approximation, i.e., the magnetic field of the laser pulse is neglected and furthermore the incident electric field is assumed to be spatially homogeneous over the field-atom interaction region. Formally, electromagnetic plane-wave fields (2.1) can be represented in Coulomb gauge with $\nabla \cdot \mathbf{A} = 0$ and $\rho = 0$, where \mathbf{A} and ρ are the vector and scalar potential, respectively. We assume that the electronic system is centered around the origin $\mathbf{r} = 0$. Mathematically, the electric dipole approximation is then realized by replacing the exact vector potential $\mathbf{A}(\mathbf{r}, t)$ by its value at the origin, i.e., by the purely time-dependent function $\mathbf{A}(t) = \mathbf{A}(\mathbf{0}, t)$. This has some important observable consequences. Here, we review for what parameters of the electromagnetic radiation the dipole approximation is expected to be accurate. To this end, following Refs. [144, 145], we consider the parameter space spanned by the frequency ω and the intensity I of the radiation (see Fig. 2.3).

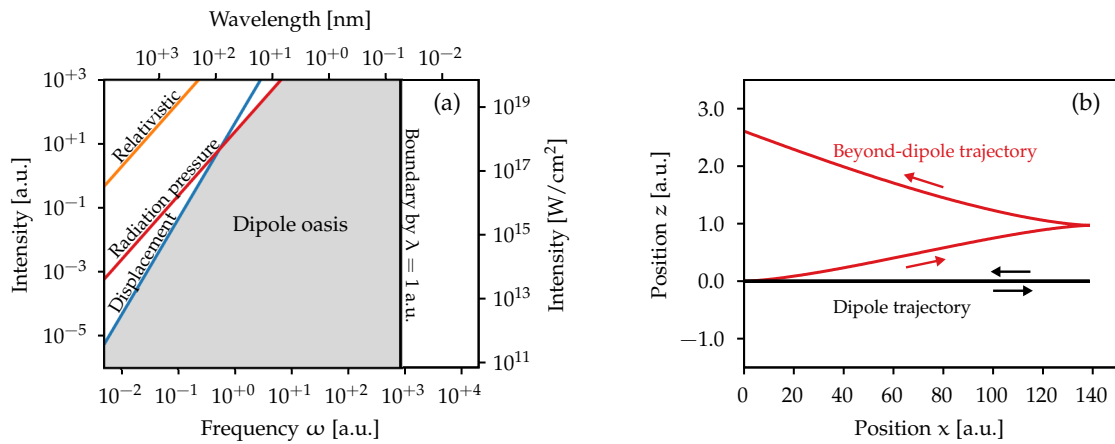


Figure 2.3: (a) Illustration of the wavelength-intensity parameter space in strong-field physics. In the various regions, different approximations of an “exact” theory are possible, e.g., in the dipole oasis the electron dynamics can be accurately described by the nonrelativistic Schrödinger equation in the dipole approximation. The indicated boundaries are explained in the main text. Adapted from Refs. [144, 145]. (b) Examples of classical trajectories in the simple man’s model starting at $t_0 = T_\omega/20$ with vanishing initial velocity for a linearly-polarized laser field with 1600 nm wavelength and a peak field strength of $E_0 = 0.1$ a.u. In contrast to the dipole approximation (black line), nondipole corrections (red line) result in a displacement of the electron and a velocity component in the light-propagation direction. Note the different scales in x -direction and z -direction.

A short-wavelength boundary of the dipole approximation is reached, if the wavelength λ of the radiation is on the order of the length scale of the target [2]. Here, the spatial variation of the electric field can palpate the electronic structure and, thus, electric quadrupole transitions become important [174]. Hence, we estimate this short-wavelength boundary by $\lambda \approx 1$ a.u. It is of importance for single-photon ionization [150, 175, 176], but does not play a practical role in the strong-field ionization with visible or infrared fields.

On the other hand, the quantum electrodynamics defines a hard relativistic boundary. Nonperturbative phenomena of (quasi)-free electrons in electromagnetic fields such as pair annihilation or Compton

scattering become important, when the parameter $z_f = 2U_p/c^2 \approx 1$ [144, 145]. Then, the characteristic kinetic energy $2U_p$ of an electron in the field is on the order of its rest energy $E = mc^2$. This boundary is usually not reached by table-top laser sources in the mid-infrared range.

In the dipole approximation, there exists no radiation pressure. Or to phrase it differently, the light field cannot transfer any momentum to the center of mass of an electron-ion system. Thus, for an atom that was initially at rest, the momentum of the residual ion is equal to the negative photoelectron momentum. As a result, one of the most fundamental concepts in physics, the conservation of momentum in the total system of photons, electrons and ion would be violated. In reality, however, every portion of energy E_γ injected by the light field during the ionization process is accompanied by a transfer of linear momentum $p_\gamma = E_\gamma/c$ to the center of mass. If we assume that after tunneling the electron is accelerated by the laser field independently of the parent ion, then we expect that the electron receives the photon momentum associated with its gain in kinetic energy $K = \mathbf{p}^2/2$. The typical drift momentum can be estimated as $p \approx A_0 \approx E_0/\omega$. Thus, linear momentum of about $K_0/c = A_0^2/(2c)$ should be transferred to the electron. The relative importance of this radiation-pressure effect can be quantified by the ratio of the transferred linear momentum to the drift momentum in the polarization plane, i.e., the ratio is given by $A_0/(2c)$.¹ In Figure 2.3(a), we use the condition $A_0/c = 0.05$ to estimate the breakdown of the dipole approximation due to importance of radiation pressure. Interestingly, nondipole effects can be observed at significantly lower intensities compared to the hard relativistic boundary. For the popular Ti:sapphire laser systems with wavelengths of 800 nm, the radiation-pressure boundary is on the order of 5×10^{15} W/cm², an intensity that is commonly accessible in modern laboratories. For the up-coming mid-infrared laser systems, this boundary will even be reached at much lower intensities.

To underpin the arguments, we study again the classical dynamics of an electron that is born with vanishing initial velocity $\mathbf{v}_0 = 0$ at the origin $\mathbf{r}_0 = 0$. Neglecting the Coulomb attraction but including the nondipole parts of the Lorentz force, Newton's equation reads

$$\ddot{\mathbf{r}}(t) = -\mathbf{E} \left(\mathbf{t} - \frac{\mathbf{z}(t)}{c} \right) - \dot{\mathbf{r}}(t) \times \mathbf{B} \left(\mathbf{t} - \frac{\mathbf{z}(t)}{c} \right). \quad (2.13)$$

Here, both the electric field inhomogeneity and the magnetic field are considered. For the laser parameters under consideration, this equation can be solved perturbatively. To first order in $1/c$, nondipole effects modify only the motion in the light-propagation direction. The time evolution of the corresponding velocity component is given by

$$\dot{z}(t) = \frac{1}{c} \left[\frac{\mathbf{A}^2(t)}{2} - \mathbf{A}(t_0) \cdot \mathbf{A}(t) + \frac{\mathbf{A}^2(t_0)}{2} \right]. \quad (2.14)$$

The first two terms represent an additional quivering motion induced by the nondipole part of the Lorentz force and vanish after the end of the laser pulse. In contrast, the last term determines the final momentum in the light-propagation direction after the end of the light pulse (see for example Ref. [177])

$$p_z = \frac{\mathbf{A}^2(t_0)}{2c}. \quad (2.15)$$

In agreement with the radiation-pressure picture, the classical description of the electron dynamics in the electromagnetic field leads to a small momentum shift in forward direction. Importantly, in Chapter 8, we will show that this simple result needs to be revised, if nonzero initial velocities of the electrons are considered.

The position of the electron in the light-propagation direction is also modified by nondipole effects. The integration of the velocity (2.14) results in

$$z(t) = \frac{1}{c} \left[\frac{1}{2} \alpha_2(t, t_0) - \mathbf{A}(t_0) \cdot \boldsymbol{\alpha}(t, t_0) + \frac{1}{2} \mathbf{A}^2(t_0)(t - t_0) \right] \quad (2.16)$$

¹The relevant parameter that characterizes the applicability of the dipole approximation is also known as the relativistic parameter $\xi = E_0/(\omega c)$.

with α and α_2 defined in Eq. (2.11). In contrast to the dipole approximation, the electron motion is not restricted to the polarization plane. A typical trajectory in a linearly-polarized field is shown in Fig. 2.3(b). The magnetic part of the Lorentz force induces a drift motion in the light-propagation direction with a position offset per optical cycle of the field given by $z_{\text{off}} = \pi E_0^2 / (2\omega^3 c)$ for $t_0 = 0$. For an electron starting with zero initial velocity, the displacement prevents an exact recollision and, thus, can influence the dynamics of recollision-based phenomena such as HHG, NSDI or HATI. The blue line in Fig. 2.3(a) shows the rough estimate of $z_{\text{off}} = 1$ a.u. similar to Ref. [178].

2.2 The time-dependent Schrödinger equation

In the nonrelativistic regime, the time evolution of atomic or molecular systems under the influence of external electromagnetic fields follows the time-dependent Schrödinger equation (TDSE)

$$i \frac{\partial}{\partial t} |\psi(t)\rangle = H(t) |\psi(t)\rangle. \quad (2.17)$$

Here, in principle, $|\psi(t)\rangle$ is the many-body state representing electronic and nuclear degrees of freedom. The Hamiltonian $H(t)$ includes effects of the time-dependent external fields as well as the interaction of the different particles with each other. For most atomic and molecular targets, this quantum-mechanical system is still too complicated to be solved numerically. Thus, we apply the following common approximations: The nuclear motion is neglected, i.e., the relative distances between the nuclei are fixed. We are interested in single-ionization processes and, hence, consider only the time evolution of one of the electrons. In this single-active-electron (SAE) approximation, the electron moves in an effective potential $V(\mathbf{r})$, representing the interaction with the nuclei as well as an averaged interaction with the other electrons. The spin degree of freedom is also not considered.²

Despite these approximations, the theoretical treatment of nondipole effects and momentum transfer in strong-field ionization is still complicated. Strictly speaking, when considering nondipole corrections, the electron-ion two-particle system does not decouple into center-of-mass and relative motion. The remaining coupling terms scale with the ratio of the electron to the ionic core masses and, thus, are nonnegligible for exotic atoms [150, 185]. However, for common atoms and molecules, it is a very good approximation to identify the electron-ion relative coordinates with the laboratory-frame coordinates of the electron. Hence, in the following, we will only consider the relative motion represented by the positions \mathbf{r} and momenta \mathbf{p} .

The central observables of this thesis are photoelectron momentum distributions (PMDs). Initially, at a time t_λ , the electronic system is prepared in a state $|\psi_0\rangle$. Afterwards, a light pulse induces ionization, i.e., the electron evolves under the influence of the electromagnetic field as well as the binding potential $V(\mathbf{r})$. After the end of the light pulse at a time t_f , the created continuum electron wave packet spreads out and its motion is only governed by the field-free Hamiltonian $H_0 = K + V(\mathbf{r})$ with $K = \frac{1}{2} \hat{\mathbf{p}}^2$. The momenta \mathbf{p} of the photoelectrons are measured experimentally at asymptotically large distances (compared to the microscopic length scales). In principle, the spreading electron waves need to be propagated till asymptotically large times $t \rightarrow \infty$. Hence, the quantum-mechanical photoelectron momentum distribution, i.e., the distribution of final asymptotic momenta \mathbf{p} , is formally given by

$$w(\mathbf{p}) = \lim_{t \rightarrow \infty} |\langle \mathbf{p} | U(t, t_\lambda) | \psi_0 \rangle|^2. \quad (2.18)$$

Here, $U(t, t_\lambda)$ is the time-evolution operator and $|\mathbf{p}\rangle$ are plane waves with momentum \mathbf{p} . In practical simulations, the limit $t \rightarrow \infty$ can never be reached. However, the field-free evolution after t_f can be

²Even though these approximations are usually assumed in strong-field physics, there are several aspirations to go beyond them. For example, effects of non-Born-Oppenheimer dynamics on the strong-field processes were studied in models in reduced dimensionality (see for example [123, 124, 179]). Furthermore, multielectron effects were considered by studying two-electron systems such as helium (see for example [180–182]) or by using models in reduced dimensionality (see for example [15, 183, 184]).

carried out efficiently by considering the spectral resolution of H_0 . The electron momentum distribution $w(\mathbf{p}) = |M(\mathbf{p})|^2$ can be expressed by means of a probability amplitude

$$M(\mathbf{p}) = \langle \mathbf{p}^{(-)} | U(t_f, t_A) | \psi_0 \rangle, \quad (2.19)$$

where we introduced the incoming stationary scattering states $|\mathbf{p}^{(-)}\rangle$ with asymptotic momentum \mathbf{p} (see Appendix A.1 for an introduction to scattering theory).

2.2.1 Minimal-coupling Hamiltonian

Based on the minimal coupling principle the dynamics of the electron in the light field is governed by the following Hamiltonian

$$H(t) = \frac{1}{2} (\hat{\mathbf{p}} + \mathbf{A}(\mathbf{r}, t))^2 - \rho(\mathbf{r}, t) + V(\mathbf{r}). \quad (2.20)$$

Although the corresponding TDSE is invariant under gauge transformations of the form

$$\mathbf{A}' = \mathbf{A} + \nabla\chi, \quad \rho' = \rho - \partial_t\chi \quad \text{and} \quad |\psi'\rangle = \exp(-i\chi)|\psi\rangle \quad (2.21)$$

with fields $\chi(\mathbf{r}, t)$, an appropriate choice of the gauge simplifies drastically the numerical solution of the TDSE and is important to construct approximate models. In this thesis, we consider effects beyond the electric dipole approximation. However, for the laser parameters under considerations, these effects are still small and can be treated as a perturbation. The vector potential of a plane-wave field (2.1) in Coulomb gauge ($\rho = 0$) can be expanded in $1/c$ (see for example [186])

$$\mathbf{A}(\mathbf{r}, t) = \mathbf{A}\left(t - \frac{z}{c}\right) = \mathbf{A}(t) + \frac{z}{c}\mathbf{E}(t) + \mathcal{O}\left(\frac{1}{c^2}\right) \quad (2.22)$$

with $\mathbf{E}(t) = -\partial_t\mathbf{A}(t)$. The corresponding physical electric and magnetic fields are

$$\mathbf{E}(\mathbf{r}, t) = -\partial_t\mathbf{A}(\mathbf{r}, t) = \mathbf{E}(t) - \frac{z}{c}\dot{\mathbf{E}}(t) + \mathcal{O}\left(\frac{1}{c^2}\right) \quad \text{and} \quad \mathbf{B}(\mathbf{r}, t) = \nabla \times \mathbf{A}(\mathbf{r}, t) = \frac{1}{c}\mathbf{e}_z \times \mathbf{E}(t) + \mathcal{O}\left(\frac{1}{c^2}\right). \quad (2.23)$$

Using the expansion of the vector potential (2.22) and neglecting terms proportional to $1/c^2$ the Hamiltonian reads

$$H(t) = \frac{1}{2} (\hat{\mathbf{p}} + \mathbf{A}(t))^2 + \frac{z}{c} (\hat{\mathbf{p}} + \mathbf{A}(t)) \cdot \mathbf{E}(t) + V(\mathbf{r}) + \mathcal{O}\left(\frac{1}{c^2}\right). \quad (2.24)$$

The theory covers the dynamics in electric quadrupole approximation, i.e., effects of the electric-field inhomogeneity are into account. However, to first order in $1/c$, only a spatially homogeneous magnetic field is considered, i.e, the magnetic dipole approximation is used. We title this choice of the Hamiltonian as generalized velocity gauge. Since relativistic corrections to Eq. (2.24) are on the order of $1/c^2$, the description is consistent with the full relativistic Dirac theory to first order in $1/c$.

The dipole approximation enables to choose a gauge with vanishing vector potential by applying a gauge transformation with [2]

$$\chi_L = -\mathbf{A}(t) \cdot \mathbf{r}. \quad (2.25)$$

When this transformation is used for the generalized velocity gauge (see Eq. (2.24)), the vector potential is still nonzero and, hence, a coupling between momenta and positions is still present

$$H_L(t) = \frac{1}{2}\hat{\mathbf{p}}^2 + \left(\mathbf{r} + \frac{z}{c}\hat{\mathbf{p}}\right) \cdot \mathbf{E}(t) + V(\mathbf{r}) + \mathcal{O}\left(\frac{1}{c^2}\right). \quad (2.26)$$

This is expected, because a nonvanishing magnetic field always requires a spatially-inhomogeneous vector potential. We refer to the Hamiltonian (2.26) as generalized length gauge.

2.2.2 Unitary transformation to “natural gauge”

In the dipole approximation, a great advantage of the velocity gauge is that the canonical momenta \mathbf{p} are classically conserved for a vanishing binding potential V . However, beyond the dipole approximation, it is impossible to find a gauge transformation (2.21) such that the resulting canonical momenta are conserved, i.e., there is always a coupling between position and momentum operators in the Hamiltonian. Luckily, we can overcome this problem by applying a more general unitary transformation $U = \exp(-i\chi_U)$ generated by a hermitian operator χ_U . The idea was first worked out in Refs. [160, 187].

Inserting the transformed state $|\tilde{\psi}\rangle = U|\psi\rangle$ into the TDSE (2.17) and ensuring its form invariance, i.e., the transformed TDSE should be given by $i\partial_t|\tilde{\psi}(t)\rangle = \tilde{H}(t)|\tilde{\psi}(t)\rangle$, we can read off the transformed Hamiltonian

$$\tilde{H}(t) = UH(t)U^\dagger + \frac{\partial}{\partial t}\chi_U. \quad (2.27)$$

We use the generating operator

$$\chi_U = \frac{z}{c} \left(\hat{\mathbf{p}} \cdot \mathbf{A}(t) + \frac{1}{2}\mathbf{A}^2(t) \right) \quad (2.28)$$

to transform the generalized velocity gauge (2.24). Importantly, the position and momentum operators do not commute. Hence, in addition to the modifications in the kinetic and the interaction terms, the transformation changes also the potential term. Using Hadamard’s lemma we find the following transformed Hamiltonian

$$\tilde{H}(t) = \frac{1}{2} \left(\hat{\mathbf{p}} + \mathbf{A}(t) + \frac{\mathbf{e}_z}{c} \left(\hat{\mathbf{p}} \cdot \mathbf{A}(t) + \frac{1}{2}\mathbf{A}^2(t) \right) \right)^2 + V \left(\mathbf{r} - \frac{z}{c}\mathbf{A}(t) \right). \quad (2.29)$$

A time-dependent shear of the potential appears due to the position-dependent shift $\mathbf{s}(t) = z\mathbf{A}(t)/c$. Because of the first term in Eq. (2.28), the transformation is not a gauge transformation (2.21) in the usual sense. Nevertheless, we refer to the transformed system as “natural gauge”. The separation of the Hamiltonian \tilde{H} in purely position- and momentum-dependent terms allows to apply the Fourier split-operator method [188] to solve numerically the TDSE (see Appendix A.2.2 for details).

2.2.3 Gordon-Volkov states

The solution of the potential-free TDSE, i.e., neglecting the potential V and considering only the dynamics induced by an external electromagnetic field, is quite helpful for the development of approximate theories in strong-field physics. Here, the time evolution is governed by the so-called Volkov Hamiltonian that reads (to first order in $1/c$)

$$H_F(t) = \frac{1}{2}\hat{\mathbf{p}}^2 + H_I(t) = \begin{cases} \frac{1}{2}\hat{\mathbf{p}}^2 + \left(\mathbf{r} + \frac{z}{c}\hat{\mathbf{p}} \right) \cdot \mathbf{E}(t) & , \text{ length gauge} \\ \frac{1}{2}(\hat{\mathbf{p}} + \mathbf{A}(t))^2 + \frac{z}{c}(\hat{\mathbf{p}} + \mathbf{A}(t)) \cdot \mathbf{E}(t) & , \text{ velocity gauge} \\ \frac{1}{2} \left(\hat{\mathbf{p}} + \mathbf{A}(t) + \frac{\mathbf{e}_z}{c} \left(\hat{\mathbf{p}} \cdot \mathbf{A}(t) + \frac{1}{2}\mathbf{A}^2(t) \right) \right)^2 & , \text{ natural gauge.} \end{cases} \quad (2.30)$$

The corresponding solutions of the TDSE consist of plane-wave states $|\mathbf{w}\rangle$ and can be labeled by a vector \mathbf{k} that is equal to the momentum before and after the end of the light pulse. We define an auxiliary vector by

$$\mathbf{v}(\mathbf{k}, t) = \mathbf{k} + \mathbf{A}(t) + \frac{\mathbf{e}_z}{c} \left(\mathbf{k} \cdot \mathbf{A}(t) + \frac{1}{2}\mathbf{A}^2(t) \right). \quad (2.31)$$

For the three considered gauges, the Gordon-Volkov states are given by (see for example [186, 189])

$$|\psi_{\mathbf{k}}^F(t)\rangle = \exp(iS_F(\mathbf{k}, t)) \times \begin{cases} |\mathbf{v}(\mathbf{k}, t)\rangle & , \text{ length gauge} \\ |\mathbf{v}(\mathbf{k}, t) - \mathbf{A}(t)\rangle & , \text{ velocity gauge} \\ |\mathbf{k}\rangle & , \text{ natural gauge.} \end{cases} \quad (2.32)$$

Here, we introduced the action

$$S_F(\mathbf{k}, t) = \frac{1}{2} \int_t d\zeta \mathbf{v}^2(\mathbf{k}, \zeta). \quad (2.33)$$

As expected, the momenta \mathbf{k} used as labels of the states are classically conserved in natural gauge. For the exact nonrelativistic Hamiltonian (2.20) with $V = 0$, a procedure was recently established to construct the Volkov states in plane-wave fields [190]. These exact states and the approximate states of Eq. (2.32) agree to first order in $1/c$.

At each time t , the Gordon-Volkov states form an orthogonal and complete basis system. Thus, the potential-free time-evolution operator U_F that propagates an arbitrary state under the influence of an electromagnetic field can be written as

$$U_F(t, t') = \int d\mathbf{k} |\psi_{\mathbf{k}}^F(t)\rangle \langle \psi_{\mathbf{k}}^F(t')|. \quad (2.34)$$

2.3 Strong-field approximation

The strong-field approximation (SFA) offers a simplified quantum-mechanical description of strong-field processes. The main idea is that the electron dynamics is governed by the electromagnetic field and is only weakly perturbed by the ionic potential. Already in 1964, Keldysh [106] developed the first approach that was later on further refined by Faisal [107] and Reiss [108]. Since then several formulations and extensions of the theory were provided that allow the description of various phenomena such as recollision-free strong-field ionization, laser-induced electron diffraction and high-harmonic generation. Here, we focus on the approximate evaluation of photoelectron momentum distributions beyond the electric dipole approximation. We assume that the electron is initially in an eigenstate with energy $-I_p$ of the field-free Hamiltonian $H_0 = \frac{\hat{p}^2}{2} + V(\mathbf{r})$. The field-free time evolution is then given by $U_0(t', t_A)|\psi_0\rangle = e^{iI_p(t'-t_A)}|\psi_0\rangle$.

To build the physical intuition of the two- and three-step models into a quantum-mechanical description, the full time-evolution operator $U(t_f, t_A)$ can be rewritten by means of a Dyson representation. Hence, the time-evolved final state is given by

$$|\psi(t_f)\rangle = U(t_f, t_A)|\psi_0\rangle = U_0(t_f, t_A)|\psi_0\rangle - i \int_{t_A}^{t_f} dt' U(t_f, t') H_I(t') U_0(t', t_A) |\psi_0\rangle. \quad (2.35)$$

In the second term, the system evolves first in its initial state. At a time t' , the application of the interaction operator $H_I(t')$ acts like a “kick” and in the spirit of the two-step model the electron is born in the continuum [191]. The integral over t' represents the summation over all possible ionization times. If the external electromagnetic fields are strong, we can hope that the continuum motion of the electron is mainly governed by these fields. Hence, we use a second Dyson representation of the time-evolution operator

$$U(t_f, t') = U_F(t_f, t') - i \int_{t'}^{t_f} dt U_F(t_f, t) V U(t, t') \quad (2.36)$$

with the Volkov propagator U_F of Eq. (2.34). Using Eqs. (2.35) and (2.36), the probability amplitude (2.19) has the following form

$$M(\mathbf{p}) = \langle \mathbf{p}^{(-)} | U(t_f, t_A) | \psi_0 \rangle = M_D(\mathbf{p}) + M_R(\mathbf{p}) \quad (2.37)$$

with an amplitude for direct electrons

$$M_D(\mathbf{p}) = -i \int_{t_A}^{t_f} dt' \langle \mathbf{p}^{(-)} | U_F(t_f, t') H_I(t') U_0(t', t_A) | \psi_0 \rangle \quad (2.38)$$

and an amplitude including rescattering

$$M_R(\mathbf{p}) = (-i)^2 \int_{t_A}^{t_f} dt' \int_{t'}^{t_f} dt \langle \mathbf{p}^{(-)} | U_F(t_f, t) V U(t, t') H_I(t') U_0(t', t_A) | \psi_0 \rangle. \quad (2.39)$$

Up to this point, the derived expressions are exact. Due to the appearance of the full time-evolution operator U in Eq. (2.39) no simplification of the numerical calculations is yet achieved. In the remaining part of this section, we discuss usual approximations for both amplitudes.

Direction ionization

In the usual strong-field approximation only the amplitude of Eq. (2.38) is considered and the exact scattering states $|\mathbf{p}^{(-)}\rangle$ are approximated by plane-wave states $|\mathbf{p}\rangle$. Inserting the Volkov propagator (2.34) into Eq. (2.38), the KFR amplitude is obtained (for a nondipole version see for example [147, 190, 192])

$$M_{\text{KFR}}(\mathbf{p}) = -i \int_{t_A}^{t_f} dt' D(\mathbf{p}, t') e^{iS_{\text{SFA}}(\mathbf{p}, t')} \quad (2.40)$$

with the generalized action of SFA

$$S_{\text{SFA}}(\mathbf{p}, t') = -\frac{1}{2} \int_{t'}^{t_f} d\zeta \mathbf{v}^2(\mathbf{p}, \zeta) + I_p(t' - t_A) \quad (2.41)$$

and the transition matrix element given by (to first order in $1/c$)

$$D(\mathbf{p}, t') = \begin{cases} \langle \mathbf{v}(\mathbf{p}, t') | (\mathbf{r} + \frac{z}{c} \hat{\mathbf{p}}) \cdot \mathbf{E}(t') | \psi_0 \rangle & , \text{ length gauge} \\ \langle \mathbf{v}(\mathbf{p}, t') - \mathbf{A}(t') | \mathbf{A}(t') \cdot \hat{\mathbf{p}} + \frac{\mathbf{A}^2(t')}{2} + \frac{z}{c} (\hat{\mathbf{p}} + \mathbf{A}(t')) \cdot \mathbf{E}(t') | \psi_0 \rangle & , \text{ velocity gauge} \\ \langle \mathbf{p} | (1 + \frac{p_z}{c}) \left(\mathbf{A}(t') \cdot \hat{\mathbf{p}} + \frac{\mathbf{A}^2(t')}{2} \right) | \psi_0 \rangle & , \text{ natural gauge.} \end{cases} \quad (2.42)$$

In a physical interpretation, the “kicked” electron experiences only the influence of the light field during its continuum propagation such that the KFR amplitude describes direct ionization without rescattering.

In general, the strong-field approximation is not gauge invariant (see for example [193]). In length gauge, unlike the velocity gauge, the field-free initial state $|\psi_0\rangle$ is usually a good approximation of the dressed ground state in the presence of the light field. Hence, the length gauge results in a more accurate description for many strong-field phenomena [194–196], e.g., it reproduces well the PMDs for short-range potentials.

Ionization including rescattering

The amplitude of Eq. (2.39) contains scattering of the electron in the potential. It can be again simplified by replacing the exact scattering states $|\mathbf{p}^{(-)}\rangle$ by plane-wave states $|\mathbf{p}\rangle$ and the full propagator U by the Volkov propagator U_F . The resulting improved SFA amplitude contains a single scattering event [18, 192, 197]

$$M_{\text{1BA}}(\mathbf{p}) = (-i)^2 \int_{t_A}^{t_f} dt' \int_{t'}^{t_f} dt \langle \mathbf{p} | U_F(t_f, t) V U_F(t, t') H_I(t') U_0(t', t_A) | \psi_0 \rangle. \quad (2.43)$$

The physical interpretation is that after a first acceleration in the continuum, the electron scatters off the parent ion at a time t . The subsequent electron motion is again governed by the electromagnetic field. Thus, two integrals over the possible ionization times t' and scattering times t appear. The laser-assisted scattering process is treated in first Born approximation (1BA) such that the distortion of an incident plane wave caused by the potential is neglected. We will redress this issue in Section 9.4.

Two major problems appear: (i) For realistic long-range potentials, the integrals in Eq. (2.43) diverge. For example, for a Yukawa potential $V(r) = -Z/r \exp(-r/\sigma)$, the integrals converge only for small cut-off parameters $\sigma \leq 1$ [190]. (ii) Formally, higher-order rescattering processes can be included in the theory by the recursive use of the Dyson Equation (2.36) in Eq. (2.39). However, in general, the resulting Born series does not converge [198].

2.3.1 Saddle-point analysis and the appearance of quantum orbits

In the KFR amplitude of Eq. (2.40), the underlying physics is still veiled by the appearing time integral. In principle, for a given momentum \mathbf{p} , the probability amplitude can be viewed as the coherent superposition of contributions from all different pathways labeled by the real-valued starting times t' . A simplified analytical treatment of the integral is provided by the saddle-point approximation (SPA). In this approach, the physical signal at each momentum \mathbf{p} is linked to a finite number of specific events.

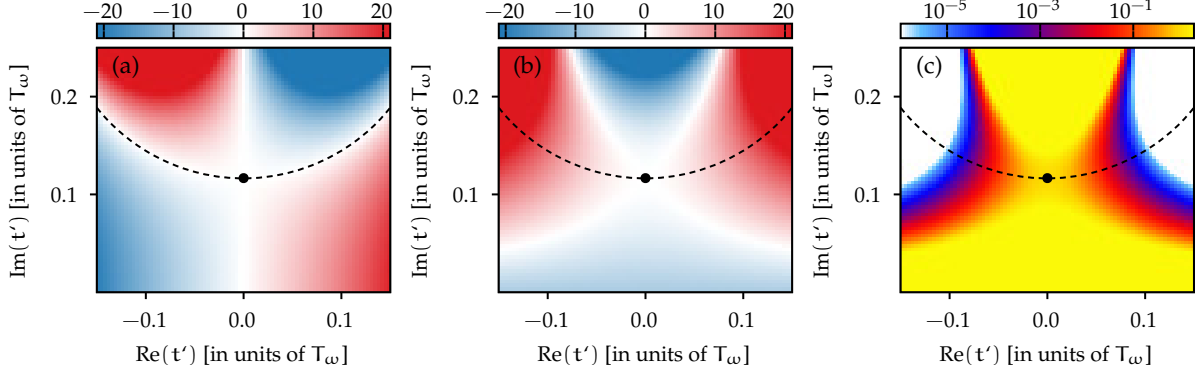


Figure 2.4: Illustration of the steepest-descent method for the KFR amplitude (2.40) in a linearly-polarized field (momentum $\mathbf{p} = 0$): (a) real part $\text{Re}(S_{\text{SFA}})$ of the action, (b) imaginary part $\text{Im}(S_{\text{SFA}})$ of the action and (c) absolute value of the integrand (in velocity gauge) shown as a function of complex time. The relevant stationary point is indicated as black dot and the dashed line marks the corresponding steepest-descent path, i.e., the path at constant phase $\text{Re}(S_{\text{SFA}})$.

The integrand in Eq. (2.40) is a product of a transition matrix element and an oscillating phase factor of the action (2.41). The time integral is well approximated in SPA, when the phase factor oscillates quickly as a function of the time t' . In the literature, there is no definite agreement what physical conditions need to be fulfilled. It sounds reasonable that the SPA works well in the low-frequency limit, i.e, when the ponderomotive energy U_p and the ionization potential I_p are large compared to the photon energy ω [122]. Importantly, stationary points $t'_s = t'_r + it'_i$ of the action (2.41) are defined by the saddle-point equation

$$\dot{S}_{\text{SFA}}(\mathbf{p}, t'_s) = \left. \frac{\partial}{\partial t'} S_{\text{SFA}}(\mathbf{p}, t') \right|_{t'=t'_s} = 0. \quad (2.44)$$

The solutions t'_s are in general complex. The probability amplitude (2.40) is then approximated as [199]

$$M_{\text{KFR}}(\mathbf{p}) \approx -i \sum_{t'_s} \sqrt{\frac{2\pi i}{\ddot{S}_{\text{SFA}}(\mathbf{p}, t'_s)}} D(\mathbf{p}, t'_s) e^{i S_{\text{SFA}}(\mathbf{p}, t'_s)}. \quad (2.45)$$

Here, the sum enables the interference of a finite number of contributions linked to the saddle points.

Mathematically, the idea behind the SPA is to deform the integration path in Eq. (2.40) into the complex time plane [200]. For a single stationary point, a steepest-descent path is chosen such that (i) it goes through the saddle point, (ii) the real part of the phase S_{SFA} is constant along the path and (iii) the imaginary part of the phase S_{SFA} increases when moving away from the saddle point.³ The integral along the deformed path is dominated by the region around the saddle point (see the schematic illustration in Fig. 2.4). Hence, the integrand can be approximated by a Gaussian function and the integral can be evaluated analytically. If multiple well-separated saddle points appear, the total integration path is split in different sections that are each chosen as steepest-descent contour and, hence, the final amplitude is given by the sum in Eq. (2.45).

The applicability of SPA is based on two critical assumptions: (i) The integrand is holomorphic in the relevant complex-time region and (ii) the saddle points are well separated. However, in the favored length gauge, the transition matrix element (2.42) has a pole at t'_s and, hence, strictly speaking a generalized approximation is needed as derived in Refs. [194, 201]. On the other hand, for a given electric field, the number of saddle points reached by the steepest-descent contour can depend on the final momenta \mathbf{p} . For example, in elliptical polarization, there are two relevant saddle points at low energies, but only a single point at high energies [202, 203]. At intermediate energies, where both points merge, the usual SPA breaks down. Here, it is not possible to consider the contributions of the two points separately and, thus, more advanced methods such as the uniform approximation are needed to obtain reliable results [204].

³Hence, the saddle points need to fulfill $\text{Im}(\ddot{S}_{\text{SFA}}(\mathbf{p}, t'_s)) > 0$.

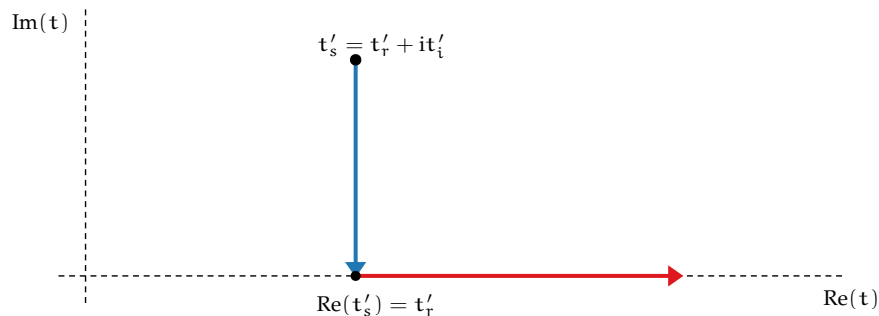


Figure 2.5: Standard integration contour in the complex-valued time plane to calculate the action of Eq. (2.41).

The overall shape of the momentum distributions and the appearance of interference are often dominated by the exponential of the action in the probability amplitude (2.45). For holomorphic functions $\mathbf{A}(t)$, the integral in the action (2.41) does not depend on the chosen integration contour. However, in the spirit of the two-step model, we can consider a standard contour consisting of two sections as depicted in Fig. 2.5. The leg from the complex-valued saddle point $t'_s = t'_r + it'_i$ down to the real axis is usually identified with the under-the-barrier motion. It determines fully the ionization probability and, thus, the shape of the electron wave packet. The second leg along the real axis from $\text{Re}(t'_s) = t'_r$ to the final time t_f can be interpreted as continuum propagating after liberation at time t'_r . Here, the electron picks up some additional phase, i.e., the real part of the action changes, which influences decisively the interference patterns.

In semiclassical theory, trajectories are introduced for a descriptive analysis of the classical action. Inspired by this concept, “quantum orbits” can be defined to evaluate the complex-valued action in SFA [110]. To this end, we solve Newton’s equation in complex time. At each time t along the integration path, the velocity is given by $\mathbf{v}(t) = \mathbf{p} + \mathbf{A}(t)$ in the dipole approximation. Formally, its integration results also in a complex-valued position

$$\mathbf{r}(t) = \int_{t'_s}^t d\tau [\mathbf{p} + \mathbf{A}(\tau)]. \quad (2.46)$$

The real parts of these orbits are frequently considered for an intuitive explanation of strong-field phenomena. In particular, the nonzero position $\text{Re}(\mathbf{r}(t'_r))$ at the liberation time t'_r is often interpreted as the SFA tunnel-exit position. However, as the SFA action does not explicitly depend on a real-valued orbit’s position, this interpretation should be viewed with caution [205–207].

2.4 Semiclassical two-step model

As motivated in Section 2.3, effects of the ionic potential can be included in the SFA by means of a Born expansion. In such a description, the electron follows potential-free paths in between two scattering events and, hence, only hard-scattering phenomena are considered properly.⁴ In contrast, even for recollision-free ionization, a long-range Coulomb potential leads to a deflection of the outgoing electrons [55]. Furthermore, in linear polarization, “soft” Coulomb effects can change the topology of the orbits and, hence, are crucial for the real physical dynamics [208]. To include such observations explicitly in the theoretical description, it is advantageous to split the ionization process into a release step and a propagation step. In the large class of “semiclassical models”, the propagation step is then described using classical trajectories that are governed by the electromagnetic field and the electron-ion

⁴In principle, under certain circumstances, the Born series describes all effects due to the ionic potential. However, effects such as Coulomb distortion and deflection are represented by higher-order terms in the series that relate to orbits undergoing multiple hard recollisions.

interaction. Here, we briefly discuss the main ideas of these models by the example of the semiclassical two-step (SCTS) model [122]. A comparison of different approaches can be found in Ref. [208].

In the first step, electrons are released by laser-induced tunnel ionization at each time t_0 . This non-classical process leads to a freed electron wave packet that is represented by a classical phase-space distribution. For adiabatic tunneling ($\gamma \rightarrow 0$), the initial velocities \mathbf{v}_0 of the electrons have to be perpendicular to the instantaneous electric field $\mathbf{E}(t_0)$ [106, 209, 210]

$$\mathbf{v}_0 \cdot \mathbf{E}(t_0) = 0. \quad (2.47)$$

The initial probability distribution $w_{\text{ini}}(t_0, v_{0,\perp}, v_{0,z})$ can be parameterized by the ionization time t_0 , a velocity component $v_{0,\perp}$ in the polarization plane and a velocity component $v_{0,z}$ in the light-propagation direction. A possible choice for w_{ini} is, for example, the ADK rate (2.3). An initial position \mathbf{r}_0 is chosen for each set of coordinates $(t_0, v_{0,\perp}, v_{0,z})$. In the original SCTS implementation, tunnel-exit positions from the tunnel ionization in parabolic coordinates with induced dipole and Stark shift (TIPIS) model were used [54, 122]. This relies on the separation of the time-independent Schrödinger equation for a Coulomb potential $V(r) = -Z/r$ under the influence of a (weak) static electric field \mathbf{E} in parabolic coordinates. The exit position is then determined by the intersection of the field-dressed potential surface with the bound-state energy [54, 122, 211]

$$\mathbf{r}_0 = -\frac{I_p + \sqrt{I_p^2 - 4\beta E}}{2E} \hat{\mathbf{E}}. \quad (2.48)$$

Here, we introduced the separation constants $\beta = Z - \sqrt{2I_p}/2$ in 3D and $\beta = Z - \sqrt{2I_p}/4$ in 2D.

In the second step, the electron is described classically. In the dipole approximation, the trajectory $\mathbf{r}_{\text{cl}}(t)$ is governed by the following Newton's equation of motion (EOM)

$$\ddot{\mathbf{r}}_{\text{cl}}(t) = -\mathbf{E}(t) - \nabla V(\mathbf{r}_{\text{cl}}(t)), \quad \mathbf{r}_{\text{cl}}(t_0) = \mathbf{r}_0, \quad \dot{\mathbf{r}}_{\text{cl}}(t_0) = \mathbf{v}_0. \quad (2.49)$$

For late final times t_f after the end of the light pulse, the velocity $\dot{\mathbf{r}}_{\text{cl}}(t_f)$ approaches some final asymptotic momentum \mathbf{p} . A key ingredient of semiclassical models is a phase associated with each trajectory. In the SCTS model, the phase is basically given by the exponential part of the semiclassical propagator

$$S_{\text{SCTS}}(t_0, \mathbf{v}_0) = -\mathbf{v}_0 \cdot \mathbf{r}_0 + I_p(t_0 - t_A) - \int_{t_0}^{t_f} dt \left[\frac{1}{2} \dot{\mathbf{r}}_{\text{cl}}^2(t) + V(\mathbf{r}_{\text{cl}}(t)) - \mathbf{r}_{\text{cl}}(t) \cdot \nabla V(\mathbf{r}_{\text{cl}}(t)) \right]. \quad (2.50)$$

To calculate electron momentum distributions, there are basically two roads. One can solve the so-called inversion problem, i.e., find all initial conditions (t_0, \mathbf{v}_0) that are mapped by the classical motion to a given final momentum \mathbf{p} . The solution of the inversion problem is in general a quite difficult task and we will study this approach further in Chapter 3. Alternatively, one uses the "shooting method" as introduced in Ref. [118]. Then, the classical ensemble is represented by a swarm of trajectories obtained by randomly sampling the initial conditions (t_0, \mathbf{v}_0) . Afterwards, the momentum distribution is then calculated by binning. For a given momentum \mathbf{p} , we consider all n_p trajectories with final momenta in the vicinity of \mathbf{p} , i.e., we determine all trajectories that end up in the bin $[p_i + \Delta p, p_i + \Delta p]$ ($i = x, y, z$). If the interference of different branches is neglected, the probability distribution of a classical-trajectory Monte Carlo (CTMC) simulation is given by

$$w(\mathbf{p}) \approx \sum_{j=1}^{n_p} w_{\text{ini}}(t_0^j, \mathbf{v}_0^j). \quad (2.51)$$

To consider interference, this formula was modified to include the phases associated with the trajectories

$$w(\mathbf{p}) \approx \left| \sum_{j=1}^{n_p} \sqrt{w_{\text{ini}}(t_0^j, \mathbf{v}_0^j)} \exp(iS_{\text{SCTS}}(t_0^j, \mathbf{v}_0^j)) \right|^2. \quad (2.52)$$

Even though this approximation works qualitatively well, we will treat in Chapter 3 the preexponential part of the semiclassical propagator more faithful and investigate the quantitative differences.

The introduced SCTS model neglects nonadiabatic effects and also to a certain extent sub-barrier Coulomb effects. To cure these deficits, different initial conditions of the classical trajectories, modified initial probability distributions as well as more advanced implementations of the semiclassical propagator can be used. This variety results in a plethora of different trajectory-based models.

2.5 Analytical R-matrix theory

Semiclassical models are usually based on many physically-motivated *ad-hoc* assumptions. In contrast, the analytical R-matrix theory is a systematic approach to include the effects of long-range Coulomb potentials and nonadiabaticity on photoelectron momentum distributions. The price, however, is that the theory includes the binding potential V only as a first-order correction to the SFA action. ARM theory was originally developed for linear polarization in Ref. [113]. Later, it was extended to close-to-circularly-polarized fields [114, 212, 213]. The main idea is to split the position space into two regions separated by a spherical boundary of radius a . For the splitting, a Bloch operator is defined as

$$L(a) = \delta(r - a) \left(\frac{\partial}{\partial r} + \frac{1 - b}{r} \right) \quad (2.53)$$

with an arbitrary constant b . The probability amplitude can be written as an integral over the matching sphere

$$M(\mathbf{p}) = -i \int_{t_\lambda}^{t_f} dt' \int d\mathbf{r} \langle \mathbf{p} | U_{\text{out}}(t_f, t') | \mathbf{r} \rangle L(a) \psi(\mathbf{r}, t'). \quad (2.54)$$

Here, the time-evolution operator U_{out} satisfies the homogeneous Schrödinger equation $i\partial_t U_{\text{out}}(t, t') = H_{\text{out}}(t) U_{\text{out}}(t, t')$ with the Hamiltonian $H_{\text{out}}(t) = H(t) - L(a)$. When the boundary radius is chosen within the tunneling barrier with $1/\kappa \ll a \ll I_p/E_0$, then different approximations for the dynamics in inner and outer space can be used. In the outer region, an eikonal-Volkov approximation of the propagator in length gauge is applied [214, 215]

$$\langle \mathbf{p} | U_{\text{out}}(t_f, t') | \mathbf{r} \rangle \approx \frac{1}{(2\pi)^{3/2}} e^{-i(\mathbf{p} + \mathbf{A}(t')) \cdot \mathbf{r}} e^{-\frac{i}{2} \int_{t'}^{t_f} d\tau (\mathbf{p} + \mathbf{A}(\tau))^2} e^{-i \int_{t'}^{t_f} d\tau V(\mathbf{r} + \mathbf{r}_L(\tau, \mathbf{p}, t'))}. \quad (2.55)$$

The potential-free trajectory of the light-driven electron reads

$$\mathbf{r}_L(\tau; \mathbf{p}, t') = \int_{t'}^{\tau} dt'' (\mathbf{p} + \mathbf{A}(t'')). \quad (2.56)$$

In the inner region, the electric field is neglected. Hence, the time-dependent wave function $\psi(\mathbf{r}, t')$ is approximated by the field-free bound-state evolution, given by $e^{i\mathbf{p} \cdot (\mathbf{r} - \mathbf{r}_\lambda)} \psi_0(\mathbf{r})$. We restrict ourselves to atoms and only consider initial states with zero angular momentum. In an asymptotically Coulomb-like potential, i.e., $V(r) \simeq -Z/r$ for large r , the bound states at large r satisfy $\psi_0(\mathbf{r}) \propto C(\kappa r)^{Z/\kappa - 1} e^{-\kappa r}$ with some constant C . These approximations lead to an expression for the probability amplitude of the following form

$$M(\mathbf{p}) \approx \frac{i\kappa}{(2\pi)^{3/2}} \int_{t_\lambda}^{t_f} dt' \int d\mathbf{r} \delta(r - a) e^{i\tilde{S}_{\text{ARM}}(\mathbf{p}, t_f; \mathbf{r}, t')} \left(C(\kappa r)^{Z/\kappa - 1} e^{-\kappa r} \right) \quad (2.57)$$

with an action phase \tilde{S}_{ARM} . Usually, the integrals are tackled by using a saddle-point approximation. For a consistent description to first order in the potential V , the corrections of the saddle-point times due to the potential can be neglected. Firstly, the saddle points t'_a are still functions of the boundary radius a . However, luckily, the dependence of the action and of the initial state on the boundary radius a approximately compensate each other. As a result, the probability amplitude is approximately independent of a .

For an explicitly a independent result, a matching procedure is considered as described in Refs. [113, 114]. The probability amplitude can be written in the following form [206, 212, 213]

$$M_{\text{ARM}}(\mathbf{p}) = R(\mathbf{p}, t'_s) e^{iS_{\text{ARM}}(\mathbf{p}, t'_s)} \quad (2.58)$$

with an atomic form factor $R(\mathbf{p}, t'_s)$ and the ARM action

$$S_{\text{ARM}}(\mathbf{p}, t'_s) = S_{\text{SFA}}(\mathbf{p}, t'_s) + S_{\text{C}}(\mathbf{p}, t'_s). \quad (2.59)$$

The shape of the momentum distribution is usually dominated by this complex-valued action, where in addition to the SFA term a Coulomb-correction appears. The correction is simply obtained by integration of the potential V along the potential-free trajectory (2.56)

$$S_{\text{C}}(\mathbf{p}, t'_s) = - \int_{t'_s - i\kappa^{-2}}^{t_f} d\tau V(\mathbf{r}_L(\tau; \mathbf{p}, t'_s)). \quad (2.60)$$

Here, the lower integration boundary $t'_\kappa = t'_s - i\kappa^{-2}$ is related to the boundary matching for a Coulomb potential. As, for example, in Ref. [212], we only consider ionization from spherically-symmetric ground states in this work and, hence, neglect the preexponential factor $R(\mathbf{p}, t'_s)$ in Eq. (2.58).

Chapter 3

Gouy's Phase Anomaly in Electron Waves Produced by Strong-Field Ionization

3.1 Introduction

When an electromagnetic wave passes through a focus, its phase is shifted by π with respect to the evolution of a plane wave. More than 100 years ago, this astonishing effect was already observed by Gouy [80]. With the advances in optical technologies, important consequences were found, e.g., for the trapping force in optical tweezers [216], in applications based on single-cycle terahertz waveforms [217] or few-cycle laser pulses [218] and for phase matching in the production of attosecond pulses [219]. Analogous phenomena were also explored in other types of waves such as acoustic waves [220], standing microwaves [221] and phonon-polariton wave packets [222]. Due to the particle-wave duality, experiments were proposed and conducted for measuring the Gouy phase anomaly in matter waves such as coherent beams of Rydberg atoms [223], Laguerre-Gaussian beams in transmission electron microscopes [224] and astigmatic electron waves [225].

In strong-field ionization of atoms or small molecules, continuum electron wave packets are formed by (nonadiabatic) tunnel ionization. Afterwards, their motion is governed by the electromagnetic field in presence of the attraction of the parent ion. In linear polarization, a part of the created wave packet is driven back to the parent ion where it scatters. In full dimensionality (3D) and for long-range potentials, the scattering electron waves pass through focal points similar to the focusing of a light wave by a lens. This so-called Coulomb focusing [77] is reflected as an enhancement of the yield in photoelectron momentum distributions [78, 79]. However, analogous to Gouy phase shift in optical waves, we will show that the scattered wave packet acquires also a $\pi/2$ phase shift while passing through focal points. Importantly, the situation need to be considered in 3D as in reduced dimensionality (2D) Coulomb focusing is absent. This phenomenon is not restricted to linear polarization, but occurs also in other waveforms that give rise to rescattering.

Even though a rigorous derivation of the focal-point phase shift is nontrivial, several illustrative explanations were given (see for example Refs. [226–228]). In an intuitive trajectory-based description, the focal-point properties are not fully determined by the selected trajectory itself, but also by the evolution of its local environment [229]. The environment can be represented as a bunch of “neighboring” trajectories or, more mathematically, as a small oriented volume element [229–231]. When the wave packet passes through a focal point, the spatial extension of the bunch of trajectories and the oriented volume go through zero. After the focus, the orientation of the volume element is inverted in the direction where the spatial extension crosses zero. In the semiclassical theory, the wave amplitudes are inversely proportional to the square root of the oriented volume. Hence, a sign change of the volume induces a

phase jump of $\pm\pi/2$. Similar to a cylindrical lens [232], Coulomb focusing in strong-field ionization acts only in one degree of freedom, it causes a bare phase shift of $\pi/2$. In contrast, in the common focusing of an optical Gaussian beam, a two-dimensional manifold of optical rays is deflected to one point, i.e., the beam is focused in two degrees of freedom. Hence, the well-known optical Gouy phase of π appears.

The absolute phase of a quantum-mechanical wave function cannot be measured in experiments. However, by considering interference structure in the photoelectron momentum distributions, relative phases of the interfering wave packets can be retrieved from the fringe positions. In this case, the emerging PMD may be viewed as a “phasometer”. For linear polarization, different parts of the released electron wave packets are always deflected to the same final momenta and, thus, rich interference patterns appear. For a cw field, wave packets are born in every cycle of the field, leading to intercycle interference that is reflected as ATI rings in the PMD. Even in recollision-free ionization, contributions that are released at different times of birth within one optical cycle are mapped to the same final momentum and, thus, create intracycle interference pattern [71–73, 76, 233]. Scattering off the parent ion induces additional “holographic patterns” with spider-like [74, 234, 235], fork-like [236], fishbone-like [28, 30] or spiral-like interference structures [79, 237].

To reveal the physical origin of the holographic patterns, the concept of conventional holography [238] was transferred to strong-field ionization. A “reference” wave is formed by a part of the released wave packet with large transverse initial velocities [28, 239]. A “signal” wave is formed by another part of the wave packet with small initial velocities that is driven back to the parent ion, where it scatters [28, 239]. The interference of the signal (scattered) and reference (nonscattered) waves creates a hologram with finger- or spider-like interference fringes. Today, a more general class of structures resulting from the interference between trajectories undergoing different types of rescattering is often referred to as holographic patterns [208]. The holograms encode spatial and temporal information about the atomic or molecular structure and dynamics on the subfemtosecond time scale. Thus, photoelectron holography was successfully used to probe the continuum electron phase in molecular ionization [29, 240], the parity of atomic and molecular orbitals [241] or momentum offsets at the tunnel exit [242]. Other achievements were the observations of nuclear motion and electronic valence-shell dynamics in molecules [30–32].

Photoelectron holography provides an ideal setting to observe Gouy’s phase anomaly in electron waves. The scattered signal wave experiences a phase shift of the fundamental value of $\pi/2$ due to Coulomb focusing and the nonscattered wave automatically acts as a Gouy-phase-free reference. In agreement with this prediction, we can already note that PMDs obtained by numerical solution of the TDSE in full dimensionality (3D) reproduce well with experimental data [74, 234]. In contrast, in reduced dimensionality (2D) where Coulomb focusing is absent, simulated PMDs show different fringe positions as well as emission strengths and do not quantitatively agree the experimental findings [29]. In this chapter, we will demonstrate that these differences are indeed related to Gouy’s phase anomaly in electron waves.

In order to decode photoelectron holograms, several attempts were undertaken to model PMDs by means of classical trajectories. In the simplest approach, an action phase is added to the simple man’s model of Section 2.1.1. The influence of the ionic potential is then only included as a hard scattering event and Coulomb-free orbits are employed during the propagation in the continuum [28, 35, 239]. This simple man’s model can be seen as a SFA-based description where the reference wave is modeled by the direct SFA (2.40) and the signal wave is represented by the improved SFA (2.43). However, such a perturbative inclusion of the ionic potential by means of a Born series results in holographic patterns that significantly differ from *ab-initio* simulations for long-range potentials and from experimental measurements. For a realistic modeling, the distortion of the electron trajectories by the long-range Coulomb attraction is essential. As a consequence, the distinction between direct and rescattered trajectories becomes blurred in long-range potentials and the topology of trajectories can be changed. To reproduce the interference pattern, several attempts based on classical Newtonian trajectories were made, e.g., trajectory-based Coulomb-corrected strong-field approximation (TCSFA) [116–119], the quantum-trajectory Monte Carlo (QTMC) model [120], the Coulomb quantum orbit strong-field approximation (CQSFA) [121], or the semiclassical two-step (SCTS) model [122]. All have in common that they assign

a certain phase to each classical trajectory and add coherently the contributions leading to a given final momentum (see also Section 2.4 for an introduction).

Qualitatively, the various types of interference structures for linear polarization are well reproduced by this zoo of semiclassical models. However, almost all models assume that a slice through the 3D dynamics is equal to the corresponding 2D dynamics. Hence, these approaches do not allow to model quantitatively the fringe position of the holographic pattern in 3D and to predict the correct relative weights of various kinds of trajectories. Putting aside the question of dimensionality, the Coulomb potential is only considered in first-order perturbation theory in the semiclassical phase in the TCSFA and QTMC models so that the number of fingers in the spider-like and the number of blades in the fan-like interference structures are not correctly reflected [122]. In contrast, the phases of the SCTS and CQSFA approaches are based on a semiclassical approximation of the time-dependent propagator formulated as Feynman's path integral. They include the Coulomb potential beyond perturbation theory. This approach is promising, because it leads to the correct number of interference fringes [72, 73, 121, 122, 243]. For photoelectrons with low transverse final momenta, the semiclassical trajectory-based description breaks down. The central maximum of the interference pattern was recently modeled by considering a glory-rescattering process [158, 244, 245]. However, since this approach does not take the interference between different types of trajectories into account, this glory model is unable to predict the full holographic pattern.

Even many years after the first measurement and first numerical calculation of interferences in strong-field photoelectron distributions, there is a puzzling discrepancy between observation and previous trajectory-based modeling. In this chapter, we resolve the existing discrepancy and explain quantitatively the interference structures in the PMDs by refining the semiclassical description. The prefactor of the exponentiated action [246, 247] is the missing piece that was not considered in detail in previous models for strong-field ionization. Its phase, known as Maslov phase, is related to Gouy's phase anomaly and influences the interference structures. Its modulus affects the relative weights of various trajectories. Here, we give a recipe how to analyze the focal-point structure of the system and determine the corresponding phase jumps. Using the rotational symmetry in linearly-polarized fields, we formulate a simple rule how to evaluate the modulus and the phase in 3D compared to 2D. In addition, we find that there exist observable Maslov phases already in the 2D situation. As a first step towards more complex systems, we show that Gouy's phase anomaly is also present in interference pattern created by bicircular fields consisting of two counter-rotating circularly-polarized fields. The analysis and classification of the semiclassical trajectories is carried out by means of a method that combines the shooting method [74, 118] with a clustering algorithm to determine all initial momenta that are classically mapped to a given final momentum (inversion problem).

Many results of this chapter are published in Ref. [248].

3.2 Anatomy of momentum distributions for linear polarization

3.2.1 Computational details

To calculate photoelectron momentum distributions in the dipole approximation, we solve numerically the TDSE in the single-active-electron approximation. The linearly-polarized laser pulse is represented by a vector potential of the form

$$\mathbf{A}(t) = -\frac{E_0}{\omega} \sin(\omega t - \phi_{\text{CEP}}) \cos^2\left(\frac{\omega t}{2n_p}\right) \mathbf{e}_x, \quad (3.1)$$

where ω is the central frequency of the field.¹ Mostly, we restrict ourselves to very short two-cycle pulses ($n_p = 2$) with a fixed carrier-envelope phase $\phi_{\text{CEP}} = 0$ and an electric-field strength $E_0 = 0.107$ a.u. corresponding to an intensity of 4×10^{14} W/cm². For 3D calculations, we use a Tong-Lin potential

¹Note the convention of the carrier-envelope phase in comparison to earlier work, e.g., in Ref. [111].

for helium (see Section A.2.3). For 2D calculations, this potential is softened by replacing the radius r by $\sqrt{r^2 + \alpha}$ and tuning α to 0.1962 such that the 1s state provides still the correct ionization potential $I_p \approx 0.904$ a.u. of helium.

In 3D, the TDSE is solved by means of the pseudospectral method in length gauge using a time step $\Delta t = 0.1$ a.u. as described in the Appendix A.2.1. To obtain PMDs, we project the wave function at the end of the laser pulse onto numerically-calculated scattering states for the ionic potential. The angular dependence of the wave function is expanded in spherical harmonics. If not stated otherwise, a maximal orbital angular momentum $l_{\max} = 512$ is used. In position representation, the wave function is represented in spherical coordinates. The radial coordinate is discretized using 2000 points on a nonuniform grid (A.44) with a core region $r_{\text{center}} = 80$ a.u. and an extension $r_{\max} = 1000$ a.u.

In 2D, the TDSE is solved using the Fourier split-operator technique on Cartesian grids as described in the Appendix A.2.2. To this end, the wave function is divided into an inner and an outer part. The inner wave function is represented on Cartesian grids of size 819.2×819.2 a.u. with spacings $\Delta x = \Delta z = 0.2$ a.u. and a time step $\Delta t = 0.01$ a.u. is used. The absorbing potential starts at a distance $r_A = 360$ a.u. from the grid center. Within the absorber, the ionic potential is set to a constant value (see Appendix A.2.2). After the end of the pulse, the simulation is usually run for a time of 800 a.u. In principle, the electron momentum distribution is obtained from the outer wave function with a resolution of $\Delta p_x = \Delta p_z = 0.0077$ a.u. However, to increase the quality at low energies, we add coherently the continuum part that is still on the inner grid and that can be extracted by projection on eikonal states (see Appendix A.2.2).

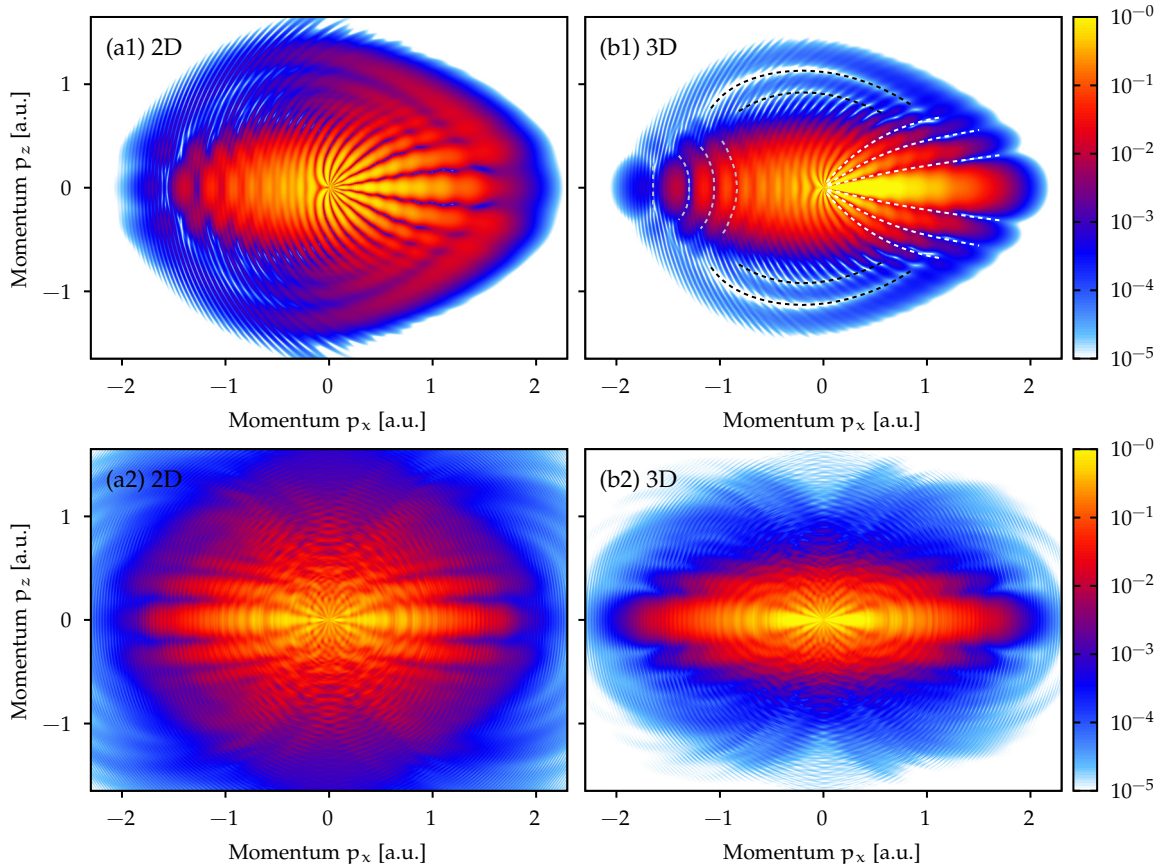


Figure 3.1: Photoelectron momentum distribution for helium ionized by linearly-polarized laser pulses with 800 nm wavelength. (a) PMDs obtained from 2D simulations and (b) slices at $p_y = 0$ through 3D distributions. Distributions for a two-cycle pulse at 4×10^{14} W/cm² intensity are presented in the upper row whereas focal-volume-averaged distributions for a ten-cycle pulse and a peak intensity of 4.5×10^{14} W/cm² are shown in the lower row. Certain structures of the PMD are highlighted in panel (b1) by dashed lines (see main text). The distributions are arbitrarily normalized. Figure is adapted from Brennecke *et al.* [248].

3.2.2 Comparison of TDSE results in 2D and 3D

The photoelectron momentum distributions for ionization of helium by short linearly-polarized laser pulses obtained by numerical solution of the TDSE are shown in Fig. 3.1(a1) for a 2D simulation and in Fig. 3.1(b1) for a 3D simulation. In 3D, it is sufficient to show a 2D slice at $p_y = 0$ through the distribution, because the system has a rotational symmetry around the polarization axis. The shortness of the laser pulses (see also Fig. 3.2) induces a strong asymmetry of the PMD along the polarization direction (p_x -direction) that depends on the chosen CEP [111, 249–251]. This offers the ability to separate different structures present in the PMDs. For momenta p_x below the classical cutoff of the simple man’s model (here at $|p_x| \approx 1.63$ a.u.), direct nonscattered and forward-scattered electrons concentrated along the polarization axis dominate for $p_x < 0$ and $p_x > 0$, respectively. According to the simple man’s model, the signal of direct electrons is dominated by trajectories starting at two different release times within the central optical cycle. Their superposition results in intracycle interference structures [71–73] that appear as signal modulations along the p_x -axis and are indicated as gray dashed lines in Fig. 3.1(b1). When ionization takes place in a quarter cycle of descending electric-field strength, the electrons are driven back to the ionic core. The interference of forward-scattered trajectories and nonscattered trajectories starting in the same quarter cycle leads to photoelectron holography [74, 234, 239]. It is observable for $p_x > 0$ as finger-like structures that are nearly parallel to the p_x -axis and that are indicated as white dashed lines in Fig. 3.1(b1). High energies can be reached by hard rescattering of electrons [16, 17]. These high-order above-threshold ionization (HATI) electrons form a weaker contribution that extends over a large range of lateral momenta p_z (mostly $|p_z| > 0.5$ a.u.). For the short pulse, only one of the “table-tennis-bat-like” structures is visible showing a cutoff energy much smaller than the $\approx 10 U_p$ expected for a cw field [252]. The high-energy plateau is overlaid by broad interference rings that are indicated as black dashed lines in Fig. 3.1(b1). In general, the same overall structures appear in the PMDs from 2D and 3D simulations. However, there are obvious differences in the positions of the interference fringes and in the relative signal strengths of the various structures.

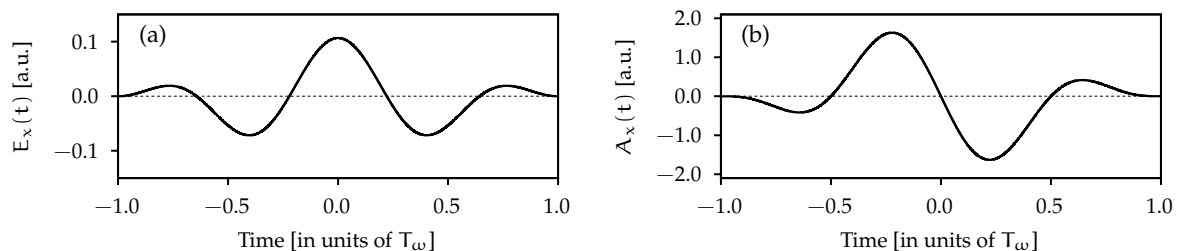


Figure 3.2: Two-cycle laser pulse with CEP $\phi_{\text{CEP}} = 0$ at an intensity of 4×10^{14} W/cm² as a function of time in units of optical cycles T_ω : (a) electric field and (b) vector potential.

In experiments, longer laser pulses are usually used. In addition, the intensity varies spatially over the laser focus and the contributions from the whole laser spot determine the experimentally-observed momentum distributions (see Section A.2.4). Hence, in order to more-realistically mimic a typical strong-field experiment, we show in Fig. 3.1(a2) and 3.1(b2) focal-volume averaged PMDs for a ten-cycle laser pulse with a peak intensity of $I_{\text{peak}} = 4.5 \times 10^{14}$ W/cm².² For the present laser conditions, the focal-volume averaging washes out some of the previously-visible patterns such as intracycle interference. However, the long laser pulse supports also plenty of additional structures that are partly caused by the interference of trajectories starting in different half cycles of the laser pulse. In addition, some familiar structures such as spider-like holographic fingers are visible. In agreement with the findings for a short pulse, the positions of the holographic fingers are shifted in 2D compared to 3D and, especially, the central fringe along the p_x -axis is much broader in 3D.

²Here, different numerical parameters are used for the 3D simulations. A maximal angular momentum of 768 is considered and the radial grid consists of 4000 points that cover an extension of $r_{\text{max}} = 2000$ a.u.

3.3 Semiclassical model

The semiclassical treatment of Feynman's path integral offers a unique opportunity to interpret quantum-mechanical dynamics on basis of classical physics. Naturally, a successful model should be able to describe quantitatively the appearing interference patterns in PMDs. Hence, both the ionic potential and the laser fields need to be included in the model beyond perturbation theory. In the spirit of the two-step picture and similar to the derivation of the SFA, it is advantageous [253, 254] to first express the probability amplitude (2.19) by means of a Dyson representation (2.35)

$$M(\mathbf{p}) = -i \int_{t_\Lambda}^{t_f} dt' \int d\tilde{\mathbf{r}} \langle \mathbf{p} | U(t_f, t') | \tilde{\mathbf{r}} \rangle \langle \tilde{\mathbf{r}} | H_I(t') | \psi_0 \rangle e^{iI_p(t' - t_\Lambda)}. \quad (3.2)$$

Here, we additionally approximated the exact scattering state by a plane wave and introduced the closure relation $\mathbf{1} = \int d\mathbf{r} |\tilde{\mathbf{r}}\rangle \langle \tilde{\mathbf{r}}|$. The expression has an intuitive physical interpretation in terms of field-free ground-state evolution up to a time t' when the electron is "kicked" to the continuum via interaction with the laser field [191]. Afterwards, in contrast to the strong-field approximation, the dynamics is governed by the laser field and the ionic potential. Similar to the models introduced in Refs. [121, 122], we apply a semiclassical approximation to the mixed position-momentum-space propagator $\langle \mathbf{p} | U(t_f, t') | \tilde{\mathbf{r}} \rangle$. However, in previous semiclassical models in strong-field physics, the attention was mostly paid to the appearing semiclassical phase S_{SC} and the remaining prefactor was not considered properly. Here, we fully include the prefactor and discuss its implications on PMDs.

3.3.1 Semiclassical approximation

In general, we study a system in D dimensions that is described by Cartesian coordinates \mathbf{r} and corresponding canonical momenta \mathbf{k} . The motion of the system is governed by the Hamiltonian $H(\mathbf{r}, \mathbf{k}, t)$ including both the laser field and the ionic potential. Formally, the mixed position-momentum-space propagator can be represented as a path integral (see Refs. [246, 255, 256])

$$\langle \mathbf{p} | U(t_f, t') | \tilde{\mathbf{r}} \rangle = \int_{\mathbf{r}(t')=\tilde{\mathbf{r}}}^{\mathbf{k}(t_f)=\mathbf{p}} D[\mathbf{r}(t), \mathbf{k}(t)] e^{i(S_{SC}[\mathbf{r}(t), \mathbf{k}(t)] - \mathbf{r}(t') \cdot \mathbf{k}(t'))} \quad (3.3)$$

with an action phase

$$S_{SC}[\mathbf{r}(t), \mathbf{k}(t)] = - \int_{t'}^{t_f} dt [H(\mathbf{r}(t), \mathbf{k}(t), t) + \mathbf{r}(t) \cdot \dot{\mathbf{k}}(t)]. \quad (3.4)$$

In this context, a path is represented by a 2D-dimensional vector function $\{\mathbf{r}(t), \mathbf{k}(t)\}$ with boundary conditions

$$\mathbf{r}(t') = \tilde{\mathbf{r}} \quad \text{and} \quad \mathbf{k}(t_f) = \mathbf{p}. \quad (3.5)$$

The "path differential" $D[\mathbf{r}(t), \mathbf{k}(t)]$ indicates the summation over all possible paths and can be defined in a manner similar to Feynman's polygon procedure used in a Lagrangian formulation [246, 247] (see Ref. [256] for a textbook treatment). The path integral over in general nonclassical paths can be approximated by means of the saddle-point method, if the classical action S_{SC} is much larger than the typical unit $\hbar = 1$ a.u. of a "quantum" action. In an \hbar^n expansion of the exact result, this semiclassical approximation considers only the leading-order term. The classical trajectories with positions $\mathbf{r}_{cl}(t)$ and momenta $\mathbf{k}_{cl}(t)$ are defined as stationary "points" of the action under the boundary conditions (3.5). It is well-known that the action is stationary, if Hamilton's equations of motion (EOM) are fulfilled

$$\dot{\mathbf{r}}_{cl}(t) = \frac{\partial H(\mathbf{r}_{cl}(t), \mathbf{k}_{cl}(t), t)}{\partial \mathbf{k}} \quad \text{and} \quad \dot{\mathbf{k}}_{cl}(t) = - \frac{\partial H(\mathbf{r}_{cl}(t), \mathbf{k}_{cl}(t), t)}{\partial \mathbf{r}}. \quad (3.6)$$

Usually, several classical trajectories defined by Eq. (3.6) satisfy the boundary conditions (3.5). For well-separated classical trajectories and nonvanishing second variations of the action [229], the main contributions to the path integral come from the regions around the classical trajectories. In this case, the path

integral of Eq. (3.3) can be approximated by using a saddle-point method. In Refs. [246, 247], a derivation of the semiclassical approximation in momentum-space representation was given. Here, these ideas are applied to the mixed position-momentum-space representation. The propagator is approximated by the coherent sum over all possible classical trajectories that fulfill the boundary conditions (3.5) (labeled by μ)

$$\langle \mathbf{p} | \mathbf{U}(t_f, t') | \tilde{\mathbf{r}} \rangle \approx \frac{1}{(2\pi)^{D/2}} \sum_{\mu} \frac{e^{-i\nu_{\mu}(t_f) \frac{\pi}{2}}}{\sqrt{|J_{\mu}(t_f)|}} e^{i(S_{SC}[\mathbf{r}_{cl,\mu}(t), \mathbf{k}_{cl,\mu}(t)] - \mathbf{k}_{cl,\mu}(t') \cdot \tilde{\mathbf{r}})}. \quad (3.7)$$

The phase of each contribution in Eq. (3.7) is mostly governed by the action S_{SC} evaluated along the classical trajectory. However, in addition, a prefactor consisting of the Jacobian J and a Maslov-phase term with the Maslov index ν appears.

To calculate the Jacobian J and the Maslov index ν for a given trajectory, it is advantageous to determine the Jacobian fields $\frac{\partial \mathbf{k}(t)}{\partial \tilde{\mathbf{p}}}$ and $\frac{\partial \mathbf{r}(t)}{\partial \tilde{\mathbf{p}}}$ along the trajectory. These time-dependent matrices represent the changes of the momentum $\mathbf{k}(t)$ or the position $\mathbf{r}(t)$ of classical trajectories at a time t with respect to infinitesimal changes of the initial momenta $\tilde{\mathbf{p}}$. The Jacobian fields can be efficiently calculated by integration of the Jacobi initial value problem [246, 257]. To this end, the second derivatives of the Hamiltonian with respect to the positions and momenta are needed. When using the velocity gauge (2.24) or length gauge (2.26) in the dipole approximation, these derivatives are given by

$$\left(\frac{\partial^2 H}{\partial \mathbf{k} \partial \mathbf{k}} \right) = \mathbf{1} \quad , \quad \left(\frac{\partial^2 H}{\partial \mathbf{r} \partial \mathbf{r}} \right) = \left(\frac{\partial^2 V}{\partial \mathbf{r} \partial \mathbf{r}} \right) \quad , \quad \left(\frac{\partial^2 H}{\partial \mathbf{k} \partial \mathbf{r}} \right) = 0. \quad (3.8)$$

The time evolution of the Jacobian fields is then determined by the equations

$$\frac{d}{dt} \left(\frac{\partial \mathbf{r}(t)}{\partial \tilde{\mathbf{p}}} \right)_{j,l} = \left(\frac{\partial \mathbf{k}(t)}{\partial \tilde{\mathbf{p}}} \right)_{j,l} \quad , \quad \frac{d}{dt} \left(\frac{\partial \mathbf{k}(t)}{\partial \tilde{\mathbf{p}}} \right)_{j,l} = - \sum_m \left(\frac{\partial^2 V}{\partial r_j \partial r_m} \right)_{cl} \left(\frac{\partial \mathbf{r}(t)}{\partial \tilde{\mathbf{p}}} \right)_{m,l} \quad (3.9)$$

with the initial conditions $\frac{\partial \mathbf{k}(t')}{\partial \tilde{\mathbf{p}}} = \mathbf{1}$ and $\frac{\partial \mathbf{r}(t')}{\partial \tilde{\mathbf{p}}} = 0$. Here, the subscript ‘‘cl’’ indicates the evaluation along the classical (unperturbed) trajectory.

The relevant Jacobian J is related to the Jacobian fields by

$$J(t) = \det \left(\frac{\partial \mathbf{k}(t)}{\partial \tilde{\mathbf{p}}} \right). \quad (3.10)$$

For classically-allowed processes, the Jacobian determines the classical evolution of the phase-space density around a given trajectory and, hence, it influences the particle density [122].

The Maslov index ν associated with each classical trajectory can be viewed as a time-dependent function that can only take integer values. At the initial time t' the Maslov index vanishes, $\nu(t') = 0$. It can only change at focal points, i.e., at times T when the Jacobian $J(T) = 0$ vanishes. If the multiplicity of the root is m , the rank of the matrix $\frac{\partial \mathbf{k}(T)}{\partial \tilde{\mathbf{p}}}$ is $D - m$. Hence, there are m linearly-independent zero modes $\mathbf{d}^{(i)}$ of $\frac{\partial \mathbf{k}(T)}{\partial \tilde{\mathbf{p}}}$ defined by

$$\sum_k \frac{\partial \mathbf{k}(T)}{\partial \tilde{p}_k} d_k^{(i)} = 0. \quad (3.11)$$

When considering the classical dynamics governed by the EOM (3.6), infinitesimal changes of the initial momenta $\tilde{\mathbf{p}} \rightarrow \tilde{\mathbf{p}} + \epsilon \mathbf{d}^{(i)}$ in these directions $\mathbf{d}^{(i)}$ do not change the momentum $\mathbf{k}(T)$ of the classical orbits at the time T in first order of ϵ . Thus, a plethora of initial momenta is deflected to approximately the same momentum $\mathbf{k}(T)$. This results in a strongly increased probability density and, hence, explains the name ‘‘focal point’’. The corresponding changes $\delta \mathbf{r}^{(i)}$ of the positions read

$$\delta \mathbf{r}^{(i)} = \epsilon \sum_k \frac{\partial \mathbf{r}(T)}{\partial \tilde{p}_k} d_k^{(i)}. \quad (3.12)$$

The jump of the Maslov index across the focal point can be calculated as

$$\Delta \nu(T) = m - 1 + \text{sgn} \det(g) \quad \text{with} \quad g_{i,j} = \delta \mathbf{r}^{(i)} \cdot \left(\frac{\partial^2 V}{\partial \mathbf{r} \partial \mathbf{r}} \right)_{cl} \delta \mathbf{r}^{(j)}. \quad (3.13)$$

In the definition of the $m \times m$ matrix g , the Hessian matrix of the potential $V(\mathbf{r})$ with respect to the positions is evaluated at the position $\mathbf{r}_{\text{cl}}(T)$ of the considered classical trajectory at the focal point. When the Hessian matrix is positive definite, then the change of the Maslov index is equal to the multiplicity m of the root [258]. However, in contrast to the position representation of the semiclassical propagator, this is not generally true for the discussed mixed representation [246, 247]. In general, Equation (3.13) needs to be evaluated at each focal point. The Maslov index at the final time t_f is simply obtained by tracking the changes of the index across all passed focal points of the trajectory.

The Jacobian fields determine the prefactor of the semiclassical propagator. Hence, the semiclassical propagator is not only influenced by the dynamics of the trajectories selected by the boundary conditions (3.5), but also by their local environment [229]. Mathematically, the local environment is represented by the Jacobian fields. These quantities can be viewed as small oriented volume elements in momentum or position space whose time evolution need to be followed.

Example: potential-free motion in a laser field

For illustration, we study the potential-free motion of an electron in the laser field. Using length gauge (2.26), Hamilton's equations of motion (3.6) are given by $\dot{\mathbf{r}}_{\text{cl}}(t) = \mathbf{k}_{\text{cl}}(t)$ and $\dot{\mathbf{k}}_{\text{cl}}(t) = -\mathbf{E}(t)$. For each pair of boundary conditions (3.5), there is one unique classical trajectory with

$$\mathbf{k}_{\text{cl}}(t) = \mathbf{p} + \mathbf{A}(t) \quad \text{and} \quad \mathbf{r}_{\text{cl}}(t) = \tilde{\mathbf{r}} + \mathbf{p}(t - t') + \int_{t'}^t d\tau \mathbf{A}(\tau). \quad (3.14)$$

According to Eq. (3.9), the relevant Jacobian fields are given by $\frac{\partial \mathbf{k}(t)}{\partial \mathbf{p}} = \mathbf{1}$. The Jacobian, $J(t) = 1$, and the Maslov index, $\nu(t) = 0$, are constant. Hence, no focal points appear. The semiclassical action (3.4) related to each trajectory is given by

$$S_{\text{SC}}[\mathbf{r}_{\text{cl}}(t), \mathbf{k}_{\text{cl}}(t)] = - \int_{t'}^{t_f} dt \frac{1}{2} \mathbf{k}_{\text{cl}}^2(t) = - \frac{1}{2} \int_{t'}^{t_f} dt (\mathbf{p} + \mathbf{A}(t))^2. \quad (3.15)$$

When inserting these quantities in the semiclassical approximation of the propagator (3.7), the exact result of the quantum-mechanical Volkov propagator (2.34) is reproduced. In this special case, the probability amplitude (3.2) reduces to the well-known KFR amplitude (2.40).

3.3.2 Approximation of the under-the-barrier dynamics

When including the ionic potential, the calculation of the probability amplitude (3.2) is much more complicated. Here, for a given final momentum \mathbf{p} , the semiclassical contributions of all possible times t' and all initial positions $\tilde{\mathbf{r}}$ have to be determined. This means, for each pair $(t', \tilde{\mathbf{r}})$, all classical paths that fulfill the boundary conditions (3.5) have to be identified. To avoid this cumbersome task, further approximations are desirable. One approach would be to evaluate the time and space integrals by using a saddle-point method. Then, analogous to the quantum-orbit model of Section 2.3.1, the time t' and the trajectories need to be continued into the complex plane. The appearing complex-valued orbits do not offer an intuitive interpretation and show problems with branch cuts of the potential [205–207].³

For a more intuitive route, we follow the idea of the two-step model 2.1.1 and split the motion into an ionization and a propagation step. In the spirit of the quantum-orbit model of Section 2.3.1, the two-pronged integration path shown in Fig. 2.5 is used for the time integral (3.2). The contour along the real axis is identified with the propagation of electron under the influence of the combined laser and Coulomb fields and, here, we restrict ourselves to real-valued trajectories. On the other hand, the contour down to the real axis is related to the under-the-barrier motion and, here, we neglect the potential V . Thus, the under-the-barrier dynamics is effectively treated like in the strong-field approximation. An auxiliary momentum $\tilde{\mathbf{p}}'$ exists that is conserved during the potential-free motion and would be equal to

³For the spider-like holographic structures, we followed this brute-force approach and used complex orbits. Compared to the model based on the approximations discussed below, we found only minor improvements.

the final momentum \mathbf{p} , if the potential would also be neglected in the propagating step. Similar, but not identical approaches were also used in TCSFA [118] and CQSFA [121].

For the chosen time-integration contour, the semiclassical action can be split into a complex-valued part that is related to the tunneling step (see also Eq. (3.15))

$$S_{\downarrow}^0 = - \int_{t'}^{\text{Re}(t')} dt \frac{(\tilde{\mathbf{p}}' + \mathbf{A}(t))^2}{2} \quad (3.16)$$

and a real-valued part corresponding to the propagation step

$$S_{\rightarrow} = - \int_{\text{Re}(t')}^{t_r} dt \left[\frac{1}{2} \dot{\mathbf{r}}_{\text{cl}}^2(t) + V(\mathbf{r}_{\text{cl}}(t)) - \mathbf{r}_{\text{cl}}(t) \cdot \nabla V(\mathbf{r}_{\text{cl}}(t)) \right]. \quad (3.17)$$

Under the made assumptions, for each auxiliary momentum $\tilde{\mathbf{p}}'$, the saddle-point times t'_s are approximately determined by the saddle-point equation of the plain SFA

$$\frac{1}{2} (\tilde{\mathbf{p}}' + \mathbf{A}(t'_s))^2 = -I_p. \quad (3.18)$$

For a given auxiliary momentum $\tilde{\mathbf{p}}'$, there are usually several solutions that are labeled by s . For a single trajectory and an initial s -like state, we approximate the probability amplitude corresponding to the release step by

$$M_{\text{ion}}(\tilde{\mathbf{p}}') \approx C_{\text{Coul}} \sqrt{\frac{2\pi}{|\mathbf{E}(t'_s) \cdot (\tilde{\mathbf{p}}' + \mathbf{A}(t'_s))|}} e^{i(S_{\downarrow}^0 + I_p(t'_s - t_A))}. \quad (3.19)$$

The last two factors are familiar from the saddle-point approximation (2.45) of the plain SFA.⁴ Here, the ionization probability is mostly determined by the imaginary $\text{Im}(S_{\downarrow}^0 + I_p t'_s)$ of the action. In addition, a Coulomb correction of the ionization rate [259, 260] is included

$$C_{\text{Coul}}^2 = (4I_p/|\mathbf{E}(t'_r)|)^{2Z/\sqrt{2I_p}}. \quad (3.20)$$

This factor can be derived by considering the first-order corrections of the potential V to the sub-barrier action in the adiabatic limit [259, 261].

For further simplification, a connection between the auxiliary momenta $\tilde{\mathbf{p}}'$ and the initial positions $\tilde{\mathbf{r}}$ of the classical trajectories is established to avoid the $\tilde{\mathbf{r}}$ integration in the probability amplitude (3.2). Even though there is no fundamental justification, most semiclassical models in strong-field physics rely on the concept of a defined tunnel exit (see for example Refs. [116–122, 210, 262]). We use the SFA tunnel-exit positions defined by Eq. (2.46), i.e., we assume that the trajectories are real valued at the release time $t'_r = \text{Re}(t'_s)$, $\text{Im}(\mathbf{r}_{\text{cl}}(t'_r)) = 0$, and start with a vanishing real part of the position at the saddle-point time t'_s , $\text{Re}(\mathbf{r}_{\text{cl}}(t'_s)) = 0$. The tunnel-exit position \mathbf{r}_0 is then given by

$$\mathbf{r}_0 = \text{Re} \left(\int_{t'_s}^{t'_r} d\tau \mathbf{A}(\tau) \right) \quad (3.21)$$

and the corresponding initial velocity reads

$$\mathbf{v}_0 = \tilde{\mathbf{p}}' + \mathbf{A}(t'_r). \quad (3.22)$$

This connection between the initial degrees of freedom was previously used in various different works, e.g., in Refs. [116–118]. Due to the made *ad-hoc* assumptions, this section should not be viewed as a derivations, but instead a motivation of the model. Naturally, there are cases where certain of the approximations fail. For example, it was shown that the proper modeling of the enhancement in probability for energies close to the classical $2U_p$ cutoff for direct ionization prevents a separation into sub-barrier motion up to a real-valued tunnel exit and subsequent classical dynamics [205].

⁴We neglect the phase in the square root. For linear polarization, we explicitly use $\sqrt{2I_p + \tilde{p}_{\perp}^2} |\mathbf{E}_x(t'_s)|$ for the denominator.

3.3.3 Inversion problem

The numerical solution of the classical equations of motion (3.6) for given initial conditions of Eqs. (3.21) and (3.22) defined by an auxiliary momentum $\tilde{\mathbf{p}}'$ is a relatively simple task. However, according to the recipe in Section (3.3.1), in the semiclassical simulations all classical trajectories leading to a given final momentum \mathbf{p} must be identified. This can be a cumbersome task.

In general, all initial conditions and, hence, the associated classical trajectories can be uniquely labeled by the constant $\tilde{\mathbf{p}}'$ and the index s . When restricting ourselves to a single saddle-point time t'_s per auxiliary momentum $\tilde{\mathbf{p}}'$, then the classical dynamics defines a mapping \mathbf{D} of an auxiliary momentum $\tilde{\mathbf{p}}'$ to a final momentum $\mathbf{p} = \mathbf{D}(\tilde{\mathbf{p}}')$. Thus, all initial conditions $\tilde{\mathbf{p}}'$ that are mapped to a given final momentum \mathbf{p} need to be found, i.e., mathematically, we have to calculate all roots

$$\tilde{\mathbf{p}}' = \mathbf{D}^{-1}(\mathbf{p}). \quad (3.23)$$

When scattering is important, the Coulomb attraction significantly alters the topology of the classical trajectories. Then, the function \mathbf{D} has a complicated form and it is in general not injective. The direct application of root-finding algorithms, such as in Refs. [121, 245], is difficult and requires the prior knowledge about the overall characteristics of the trajectories. Hence, this inversion approach cannot be easily adapted to different targets and driving-field shapes.

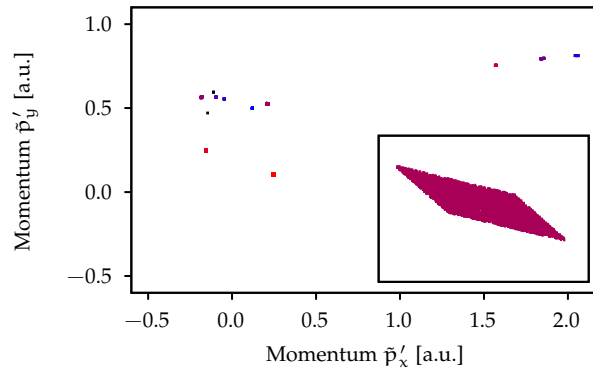


Figure 3.3: Sampled initial momenta $\tilde{\mathbf{p}}'$ that correspond to a bin centered around a momentum $\mathbf{p} = (0.3, 0.3)$ a.u. with $\Delta p = 0.01$ a.u. for the bicircular field used in Fig. 3.15. The different colors indicate the identified cluster. Each cluster consists of many points, see also the magnification of a cluster centered at $\tilde{\mathbf{p}}' = (0.21, 0.53)$ a.u. shown in the inset. 18000 points are depicted in total. The few black dots indicate points that are not assigned to any cluster.

Here, we follow an alternative approach: We use a Monte-Carlo algorithm to sample the initial momenta $\tilde{\mathbf{p}}'$ and determine the corresponding final momenta by propagating the classical EOM (3.6). Thus, we scan the function \mathbf{D} with a finite number of random points. Afterwards, for a given final momentum \mathbf{p} , we select all trajectories that have final momenta in the vicinity of \mathbf{p} , i.e., we consider all trajectories that end up in the bin $[p_i + \Delta p, p_i + \Delta p]$ ($i = x, y, z$). Up to this point, the scheme is quite similar to the shooting method introduced in Section 2.4. As an example, we show in Fig. 3.3 all initial conditions in the $\tilde{\mathbf{p}}'$ -space for a bin around a given final momentum \mathbf{p} . For a sufficiently large number of trajectories per the bin, the points in $\tilde{\mathbf{p}}'$ -space form a finite number of accumulations around the desired roots of the inversion problem. Each cluster corresponds to a different kind of trajectory. We identify the different accumulations labeled by μ and their location $\tilde{\mathbf{p}}'_\mu$ by means of clustering algorithms.⁵ It turned out that a DBSCAN (density-based spatial clustering of applications with noise) algorithm is a good choice. In this algorithm, single points can be rejected that belong to chaotic trajectories.⁶ Considering vanishing bin sizes, the area covered by the clusters goes to zero and their locations are the solutions of the inversion problem (3.23) for the given final momentum \mathbf{p} . Since this approach does not rely on any physical intuition, it is a quite versatile approach to solve the inversion problem.

⁵This idea was first formulated by Nicolas Eicke.

⁶These orbits circle around the ionic core multiple times and lead to very fuzzy structures without much weight in the PMD.

The quality of the solution is determined by the number of points per cluster. If the initial momenta $\tilde{\mathbf{p}}'$ are sampled randomly, i.e., with a uniform distribution, the number of points per cluster is proportional to the inverse of the Jacobian $|J(t_f)|$. Thus, the efficiency of the clustering approach is improved, when this effect is compensated by using a nonuniform distribution of the initial momenta in the Monte-Carlo sampling. Qualitatively, for linear polarization, this can be achieved by considering larger weights for small lateral momentum components.

3.3.4 Explicit scheme of the simulation

A recipe for a simulation, i.e., the calculation of the probability amplitude for a given momentum \mathbf{p} , is as follows:

- Solve the saddle-point equation (3.18) for each auxiliary momentum $\tilde{\mathbf{p}}'$ to obtain the corresponding saddle-point times $t'_s = t'_r + it'_i$. Establish a connection between $\tilde{\mathbf{p}}'$ and the initial conditions for the trajectories of the propagation step, i.e., determine the tunnel-exit position \mathbf{r}_0 of Eq. (3.21) and initial velocity \mathbf{v}_0 of Eq. (3.22) for each $\tilde{\mathbf{p}}'$.
- Sample the momenta $\tilde{\mathbf{p}}'$ using a Monte-Carlo algorithm. For each $\tilde{\mathbf{p}}'$, determine corresponding final momentum by solving the classical equations of motion (3.6) from time t'_r till t_f including both laser field and Coulomb attraction with the initial conditions $\mathbf{r}_{cl}(t'_r) = \mathbf{r}_0$ and $\dot{\mathbf{r}}_{cl}(t'_r) = \mathbf{v}_0$. If the electron energy at the time t_f after the end of the laser pulse is negative, the electron is trapped into Rydberg states. Hence, these trajectories are excluded from the simulation.
- Solve the inversion problem for the given final momentum \mathbf{p} by using a clustering algorithm as described in Section 3.3.3. For each branch of saddle-point times, all auxiliary momenta $\tilde{\mathbf{p}}'_\mu$ are found that lead to the given final momentum \mathbf{p} .
- For each solution $\tilde{\mathbf{p}}'_\mu$ of the inversion problem, the ingredients for the probability amplitude are calculated. To this end, determine the ionization amplitude M_{ion} of Eq. (3.19) by numerical integration of the sub-barrier action S_\downarrow^0 of Eq. (3.16). In order to calculate the phase S_{\rightarrow} of Eq. (3.17), the Jacobian J and the Maslov index ν for each trajectory, we solve once more the classical EOM, but add one equation for the phase and the set of equations (3.9) for the Jacobian fields. During the propagation of the trajectories, we monitor the time-dependent Jacobian $J(t)$ and determine the jump of the Maslov index at focal points as described in Section 3.3.1.
- Finally, the transition amplitude is approximated using these ingredients

$$M(\mathbf{p}) \approx \sum_{\mu} M_{\text{ion}}(\tilde{\mathbf{p}}'_\mu) \frac{e^{-i\nu_\mu \frac{\pi}{2}}}{\sqrt{|J_\mu(t_f)|}} e^{iS_{\rightarrow, \mu}}, \quad (3.24)$$

where μ labels all possible initial momenta $\tilde{\mathbf{p}}'_\mu$ that are classically mapped to the given final momentum \mathbf{p} , i.e., the solutions of the inversion problem. Note that in the sum all branches of saddle-point times must be included.

This model describes the quantum dynamics of the propagation step within the semiclassical approximation and, hence, considers both the laser field and the Coulomb potential in a nonperturbative manner. The solution of the inversion problem by means of a clustering algorithm enables the simulation of arbitrary targets and driving-field shapes. In contrast to previous models, the prefactor of the exponentiated action is treated properly by including both the Maslov phase and the square root of the Jacobian $1/\sqrt{|J|}$.

3.3.5 Symmetry considerations for linearly-polarized fields

In the special case of linear polarization, the dynamical system of atom and electric field has a rotational symmetry around the polarization axis (x -axis). Hence, the electron momentum distributions in 3D are

rotationally symmetric around the p_x -axis and it is sufficient to consider only a 2D slice through the PMD at $p_y = 0$. In the semiclassical model, the initial positions are on the x -axis and, thus, classical trajectories starting with initial velocities in the x - z -plane stay in this plane. To calculate a slice through the PMD at $p_y = 0$, we only need to consider initial momenta in the \tilde{p}_x - \tilde{p}_z -plane.

Importantly, the Jacobian fields depend on the dimensionality of the problem. Thus, a slice through the semiclassically-calculated PMD in 3D is not the same as a semiclassically-calculated PMD in 2D. Here, we provide the relations between Jacobians J and Maslov indices ν for 2D and 3D simulations. To this end, we follow the scheme introduced in Section 3.3.1 and restrict ourselves to potentials $V(x, r_\perp)$ with a single minimum at $r_\perp = \sqrt{y^2 + z^2} = 0$ for each x .

Under these assumptions, the rotational symmetry determines the form of the Jacobian fields in 3D

$$\left(\frac{\partial \mathbf{k}(t)}{\partial \tilde{\mathbf{p}}} \right)_{3D} \doteq \begin{pmatrix} \alpha & 0 & \beta \\ 0 & \zeta & 0 \\ \gamma & 0 & \delta \end{pmatrix} \quad \text{with} \quad \zeta = \frac{k_{cl,z}(t)}{\tilde{p}_z}, \quad (3.25)$$

where the remaining four elements belong to the Jacobian fields in 2D

$$\left(\frac{\partial \mathbf{k}(t)}{\partial \tilde{\mathbf{p}}} \right)_{2D} \doteq \begin{pmatrix} \alpha & \beta \\ \gamma & \delta \end{pmatrix}. \quad (3.26)$$

As a result, the Jacobian $J_{3D}(t)$ of the 3D system and the Jacobian $J_{2D}(t)$ of the corresponding 2D system are related by

$$J_{3D}(t) = \frac{k_{cl,z}(t)}{\tilde{p}_z} J_{2D}(t). \quad (3.27)$$

This 2D-to-3D correction factor was already used in Ref. [122]. Effects of the different Jacobians on the photoelectron momentum distributions are discussed later on.

To determine the Maslov index ν , we need to consider the jumps of the index at focal points T defined by $J(T) = 0$. According to Eq. (3.27), focal points in 3D appear, if either $k_{cl,z}(T) = 0$ or $J_{2D}(T) = 0$.

- For $k_{cl,z}(T) = 0$, but $J_{2D}(T) \neq 0$, an additional focal point appears in the 3D system compared to the 2D situation. The zero mode of the Jacobian matrix is given by $\mathbf{d} = \mathbf{e}_y$. It can be shown that the Jacobian fields $\frac{\partial \mathbf{r}(t)}{\partial \tilde{\mathbf{p}}}$ have also the form of Eq. (3.25), but with ζ replaced by $\frac{r_{cl,z}(t)}{\tilde{p}_z}$. Thus, the infinitesimal position change defined in Eq. (3.12) is

$$\delta \mathbf{r} = \epsilon \frac{r_{cl,z}(T)}{\tilde{p}_z} \mathbf{e}_y. \quad (3.28)$$

According to Eq. (3.13), the Maslov index changes across the focal point by

$$\Delta \nu(T) = \text{sgn} \left[\left(\frac{\partial^2 V}{\partial y^2} \right)_{cl} \epsilon^2 \left(\frac{r_{cl,z}(T)}{\tilde{p}_z} \right)^2 \right] = \text{sgn} \left[\left(\frac{1}{r_\perp} \frac{\partial V(x, r_\perp)}{\partial r_\perp} \right)_{cl} \epsilon^2 \left(\frac{r_{cl,z}(T)}{\tilde{p}_z} \right)^2 \right] = +1, \quad (3.29)$$

where we used that $r_{cl,y}(T) = 0$ for the trajectory and that the potential $V(x, r_\perp)$ has a single minimum at $r_\perp = 0$ for fixed x , i.e., it is monotonically-increasing function for all $r_\perp > 0$.

- For $k_{cl,z}(T) \neq 0$, but $J_{2D}(T) = 0$, the focal point is already present in the 2D situation. The form of the Jacobian matrix (3.25) implies zero modes with vanishing y -component, i.e., $\mathbf{d} = a \mathbf{e}_x + b \mathbf{e}_z$ with $a, b \in \mathbb{R}$. The infinitesimal position changes are also in the x - z -plane. Hence, the jump of the Maslov index in 3D is the same as for the corresponding 2D system and can be calculated according to Eq. (3.13).

In principle, the rare case of $k_{cl,z}(T) = 0$ and $J_{2D}(T) = 0$ could appear. Even though it does not play a role in practice, it can be treated like the two cases above. Thus, we can summarize that there are additional focal points of the electron waves in 3D compared to the corresponding 2D system. The Maslov indices of the 3D system and of the 2D system are related by

$$\nu_{3D} = \nu_{2D} + \delta \nu, \quad (3.30)$$

where $\delta \nu$ is the number of zeros of $k_{cl,z}(t)$ along the trajectory. At the additional focal points of the 3D system, the Maslov index is always increased by one.

3.4 Results and discussion

In this section, we show that the prefactor of the exponentiated action, i.e., the Maslov phase and the Jacobian, needs to be considered for a quantitative description of the interference structures in PMDs. We explore how Coulomb focusing leads to Gouy's phase anomaly in electron waves (reflected by nonzero Maslov phases) and study its influence on the various interference patterns in electron momentum distributions. Previously, this well-known phenomenon of optics and wave mechanics was simply overlooked in strong-field physics.

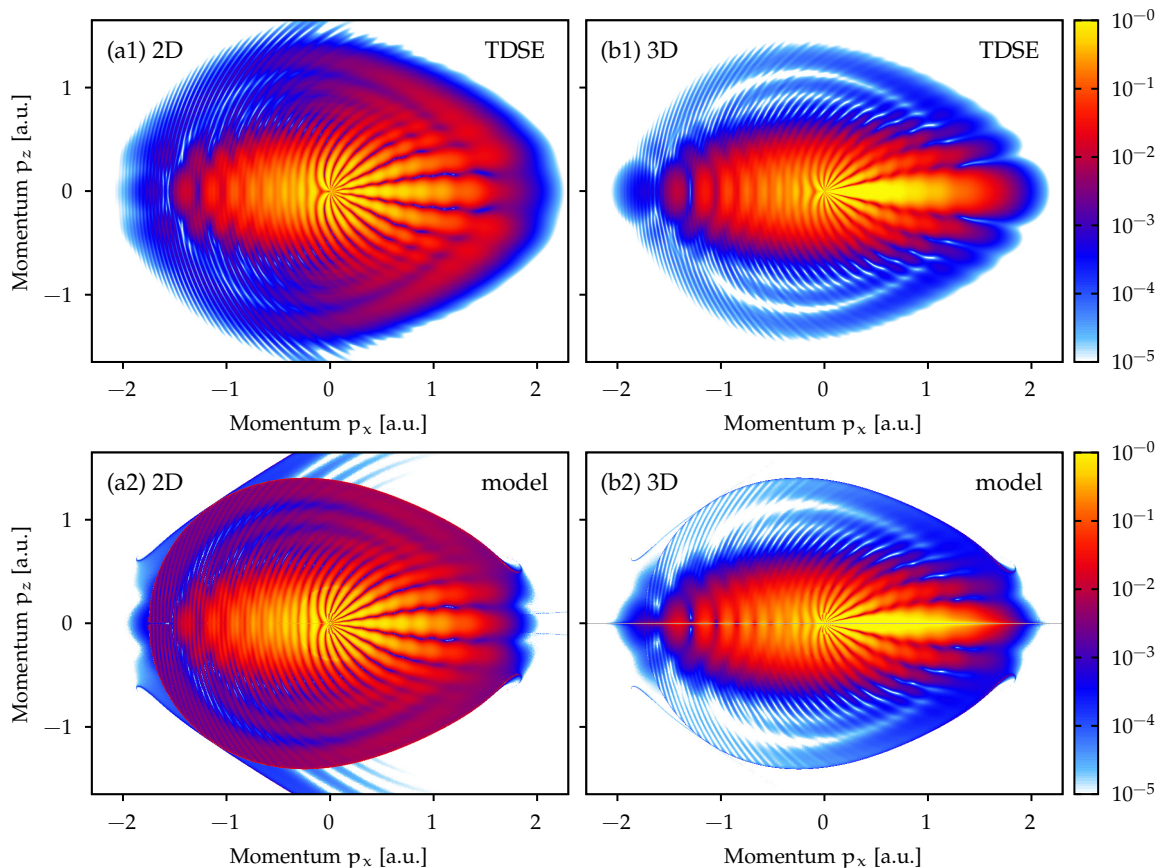


Figure 3.4: Photoelectron momentum distributions for helium ionized by two-cycle linearly-polarized laser pulses with 800 nm wavelength and 4×10^{14} W/cm² intensity as in Fig. 3.1. (a) PMDs obtained from 2D simulations and (b) slices at $p_y = 0$ through 3D distributions. The distributions are calculated by numerical solution of the TDSE in the upper row or with the semiclassical model in the lower row. Figure is adapted from Brennecke *et al.* [248].

The introduced semiclassical model is considered to simulate PMDs for helium ionized by linearly-polarized pulses with 800 nm central wavelength and an intensity of 4×10^{14} W/cm². For simplicity, we use a bare $-1/r$ potential, but insert the correct ionization potential to evaluate the amplitude (3.19) and the initial conditions for the trajectories. The resulting PMDs are shown in Fig. 3.4 for two and three dimensional calculations. Since the ionization rate depends strongly on the field strength, the contributions of the three central half cycles of the electric field are only considered (see Fig. 3.5). In addition, complicated trajectories with Maslov indices $|v_{2D}| \geq 3$ are discarded. These trajectories have very low contributions in regions, where their Jacobian $J(t_f)$ is nonzero, and lead to narrow caustic structures for momenta, where their Jacobian $J(t_f)$ vanishes. Since the appearance of caustics indicate the breakdown of the semiclassical approximation [263], the bright caustic lines would not be physical, i.e., regularization procedures would need to be applied.

The PMDs from the semiclassical model agree very well with the TDSE results (see Fig. 3.4). Especially, the differences between 2D and 3D simulations are present on both levels of theory. The considered trajectories are independent of the dimension such that the same semiclassical phase S_{\rightarrow} associated

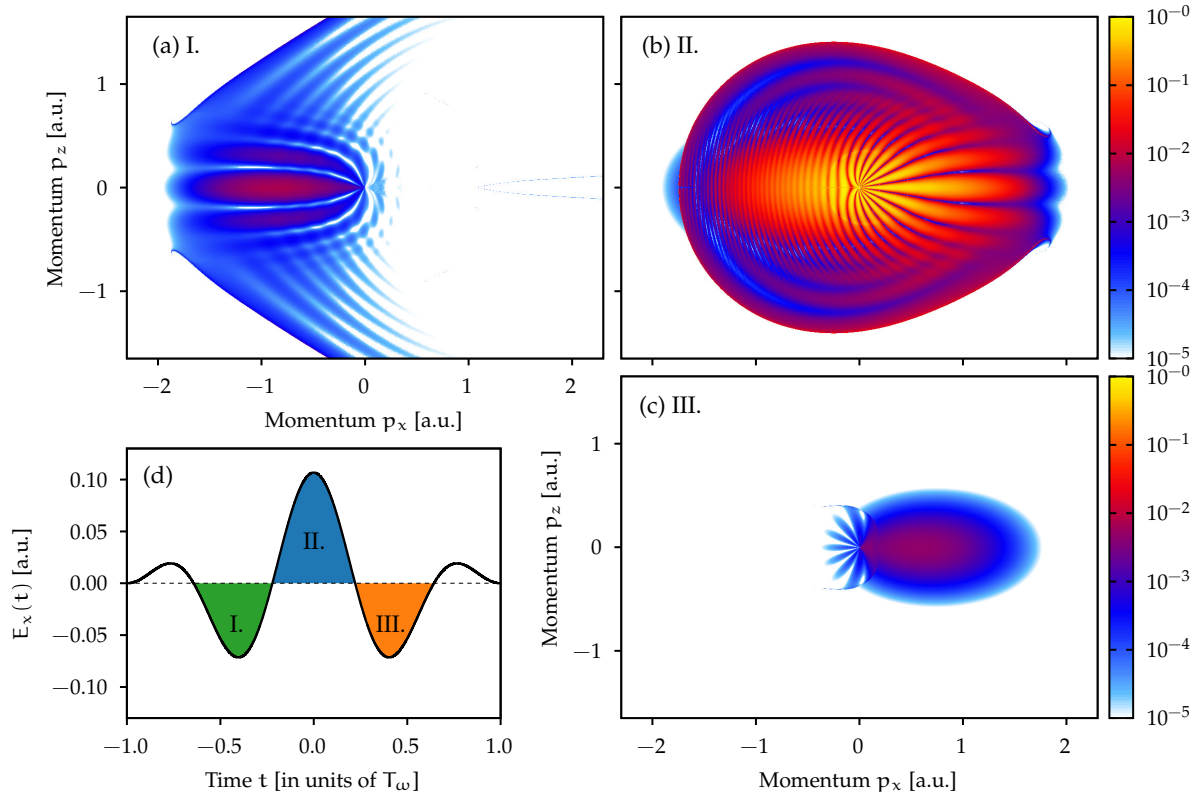


Figure 3.5: (a)-(c) PMDs from the semiclassical model in 2D for the same parameters as in Fig. 3.4, but each result only contains the contributions of trajectories starting in one of the half cycles of the electric field that are indicated in panel (d). The same normalization is used in panels (a)-(c).

with the continuum motion and same ionization amplitude M_{ion} are included in the model. The crucial ingredient to reproduce the differences between 2D and 3D simulations is the prefactor of the semiclassical propagator, i.e., the Jacobian and the Maslov index. The Jacobian reflects how a small volume in the space of initial momenta is deformed by the classical propagation into a volume in the space of final momenta. Or to phrase it otherwise, the Jacobian can be viewed as a measure of how the final momenta change under classical evolution when varying the initial momenta. As shown in Section 3.3.5 for linear polarization, the Jacobian J_{3D} of the 3D system and the Jacobian J_{2D} of the corresponding 2D system are related by

$$|J_{3D}| = \frac{p_\perp}{\tilde{p}_\perp} |J_{2D}| \quad \text{with} \quad p_\perp = \sqrt{p_y^2 + p_z^2}. \quad (3.31)$$

Here, p_\perp and \tilde{p}_\perp are the momentum components perpendicular to the polarization direction of the final and initial momenta. As an example, we may consider direct nonscattered electrons with sufficiently high energy. There, the final momenta are only weakly deflected by Coulomb attraction compared to the initial momenta. Hence, the Jacobians are typically close to one and, especially, nearly independent of the dimensionality.

When scattering plays a role, the situation is different. For large-angle scattering leading to high-energy electrons, the final momenta are very sensitive to changes of the initial momenta and, hence, the associated Jacobians are much larger than one. Classically, large scattering angles correspond to small impact parameters and to small initial perpendicular momenta \tilde{p}_\perp . At the same time, large final perpendicular momenta p_\perp can be reached. In this case, the Jacobians in 3D are even further enhanced and, thus, the weights of the trajectories in the PMDs are reduced compared to 2D. Physically, this reflects the dependence of the scattering probability on the dimension. The resulting higher emission strength in 2D compared to 3D can be clearly seen at large perpendicular momenta $|p_\perp| \gtrsim 0.8$ a.u. in Fig. 3.4.

On the other hand, for forward scattering present around the central holographic fringe, the final momenta p_{\perp} are smaller than the initial momenta \tilde{p}_{\perp} . Comparing the 3D to the 2D situation, the Jacobians of these trajectories are reduced and their weights are enhanced. This results in a concentration of the signal along the polarization axis for $p_x > 0$ in the 3D PMDs shown in Fig. 3.4. Classically, due to the cylindrical symmetry, a given final momentum \mathbf{p} on the polarization axis is reached by an infinite amount of distinct trajectories with the same magnitude \tilde{p}_{\perp} of the transverse initial velocity and with the same release time [158]. Here, the influence of the Coulomb attraction maps a circle of initial transverse velocities to a single point in final momentum space so that the effect is called Coulomb focusing [77, 78]. As a result, an axial caustic singularity emerges in the model indicating the breakdown of the semiclassical approximation. Hence, the result of the model is questionable in the vicinity of the polarization axis (for our laser parameters typically $p_{\perp} < 0.05$ a.u.). To obtain finite spectral weights, a regularization procedure that considers the quantum nature of the focusing process in terms of glory rescattering was developed [158]. We will further discuss this point in Section 10.5.3.

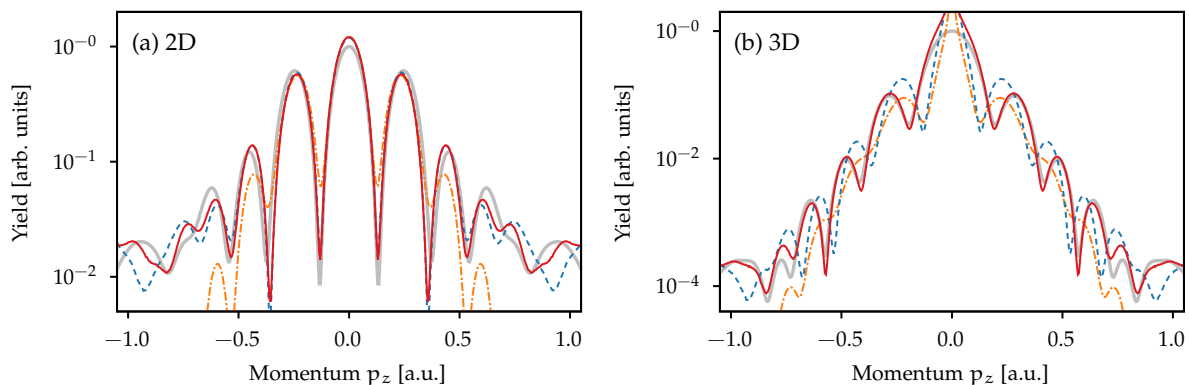


Figure 3.6: 1D slices through the momentum distributions of Fig. 3.4 at fixed $p_x = 0.81$ a.u.: TDSE results (gray thick line), semiclassical model of Eq. (3.24) (red line), neglecting Maslov's phase (blue dashed line) or neglecting Maslov's phase and using the Jacobian J_{2D} instead of its square root (orange dashed-dotted line) (see main text for further information). For better comparison, the distributions are normalized to an arbitrary value. The slices are averaged over a range of $p_x = 0.81 \pm 0.05$ a.u. Figure is adapted from Brennecke *et al.* [248].

Figure 3.6 compares slices through the momentum distributions in 2D and 3D for different modifications of our model. In many previous semiclassical models such as in Refs. [74, 118, 120, 122], the inversion problem is not solved explicitly, but instead the shooting method introduced in Section 2.4 is used. The distribution from the shooting method can be written in form of Eq. (3.24), but then a wrong power of the Jacobian must be artificially used (-1 instead of $-1/2$). In Ref. [122], the correct 2D-to-3D correction factor for the Jacobian was already used, but not derived. Then, the wrong power of the 2D Jacobian still appears (see the orange line in Fig. 3.6). This wrong weighting of the shooting method leads to a too fast decrease towards large perpendicular momenta and a too low contrast of the interference fringes. Compared to our model, the agreement with the TDSE result is worse. On the other hand, the CQSFA includes the correct power of the Jacobian [121, 264, 265], but always treats the system in 2D resulting in a diminished agreement with realistic 3D simulations.

3.4.1 Observing Gouy's phase anomaly in photoelectron holography

Coulomb focusing, i.e., the interplay between the long-range Coulomb attraction and the laser electric field, does not only result in a bunching of scattered electrons in momentum space at asymptotically large times. But in addition, similar to a lens in optics, Coulomb focusing also makes the scattered wave packets pass through focal points in momentum or position space during their propagation. Thus, it acts like a “lens” for electron waves.

For linearly-polarized fields, this can be vividly illustrated in position space (see also Fig. 3.7). Classically, the rotational symmetry dictates again that all trajectories starting at the tunnel exit with the same magnitude \tilde{p}_{\perp} , but different directions of their initial transverse velocity cross the polarization

axis $r_{\perp} = 0$ at the same position x . Hence, in a trajectory-based description, a one dimensional manifold of trajectories is deflected to a single point. As a result, whenever the wave packet crosses the polarization axis, it is focused in position space. In analogy to Gouy's phase anomaly in optics, we expect a phase shift of the electron wave packet after passing the focus. Within a semiclassical description, this phase anomaly is related to a change of Maslov's index. When describing the wave packet in position space, the associated position-space Maslov index increases indeed by one at each position-space focal point [258]. Since Coulomb focusing only appears in 3D, the position-space Maslov phases for the scattered trajectories differ by $\pi/2$ in the 3D system compared to the corresponding 2D system. The described setting in strong-field ionization is comparable to a cylindrical lens in optics that creates a line focus, i.e., the two-dimensional area of a light beam is focused in one degree of freedom and, thus, the Gouy phase only changes by $\pi/2$ [232].

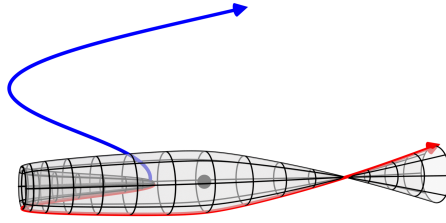


Figure 3.7: Schematic illustration of Gouy's phase anomaly in photoelectron holography. Interference between a nonscattered trajectory (blue line) and scattered trajectory (red line) that lead to the same final momentum \mathbf{p} . Due to the rotational symmetry in 3D, a one-dimensional manifold of trajectories with the same initial perpendicular momentum \tilde{p}_{\perp} (indicated as a surface) is focused on the polarization axis in position space. This results in a phase shift of $\pi/2$. Figure is adapted from Brennecke *et al.* [248]. The graphic implementation was done by Nicolas Eicke.

The absolute phases of the photoelectron wave packets are not experimentally accessible. However, when the focused signal wave packet is overlaid with a nonscattered reference wave as in photoelectron holography [74, 239], their phase difference determines the interference pattern. The resulting modulation of the signal is clearly visible in 1D slices through the distributions in 2D and 3D (see Fig. 3.6). For a quantitative modeling, we consider the semiclassical model of Section 3.3 based on a momentum-space description. Since the focal points and the Maslov phases in position space generally differ from the ones in momentum space, we first confirm the simple argumentation presented above by calculating the Maslov indices in momentum space.

For final momenta with $p_z \gg 0$, the reference trajectory is only weakly perturbed by the Coulomb attraction. It starts already with initial momentum $\tilde{p}_z > 0$ and its Jacobian J_{2D} is close to one (see Figs. 3.8(b) and (c)). Hence, its Maslov index is zero. For a given final momentum \mathbf{p} , the corresponding signal trajectory starts approximately at the same release time t_r' (see Fig. 3.8(a)), but with an initial velocity $\tilde{p}_z < 0$. It is deflected by the potential to its final momentum $p_z > 0$. The numerical calculation shows that its Maslov index is still zero in 2D. However, according to the previous sections, the Maslov indices in 2D and in 3D are related by

$$\nu_{3D} = \nu_{2D} + \delta\nu, \quad (3.32)$$

where $\delta\nu$ is the number of zeros of $p_{\perp}(t)$ along the trajectory. The signal trajectory passes one additional axial focal point in momentum space, resulting in a Maslov index in 3D of one. Thus, the Coulomb-focused trajectory in 3D indeed experiences a phase shift compared to the 2D situation. This is reflected by the different positions of the holographic fringes (see Fig. 3.6). The central fringe is broader in 3D and the higher-order maxima are systematically shifted towards larger perpendicular momenta. The predictions by the semiclassical model are in perfect agreement with the TDSE results.

In 2D, the final Maslov index of the signal trajectory in holography is still zero. The time evolution of the corresponding Jacobian $J_{2D}(t)$ is shown in Fig. 3.8(e) for selected final momenta p_z . For $p_{\perp} = p_z = 0$, the signal trajectory and the reference trajectory are indistinguishable, resulting in Jacobians close to one at all times. However, when considering larger $p_z \gg 0$, we find that the Jacobian of the signal trajectory

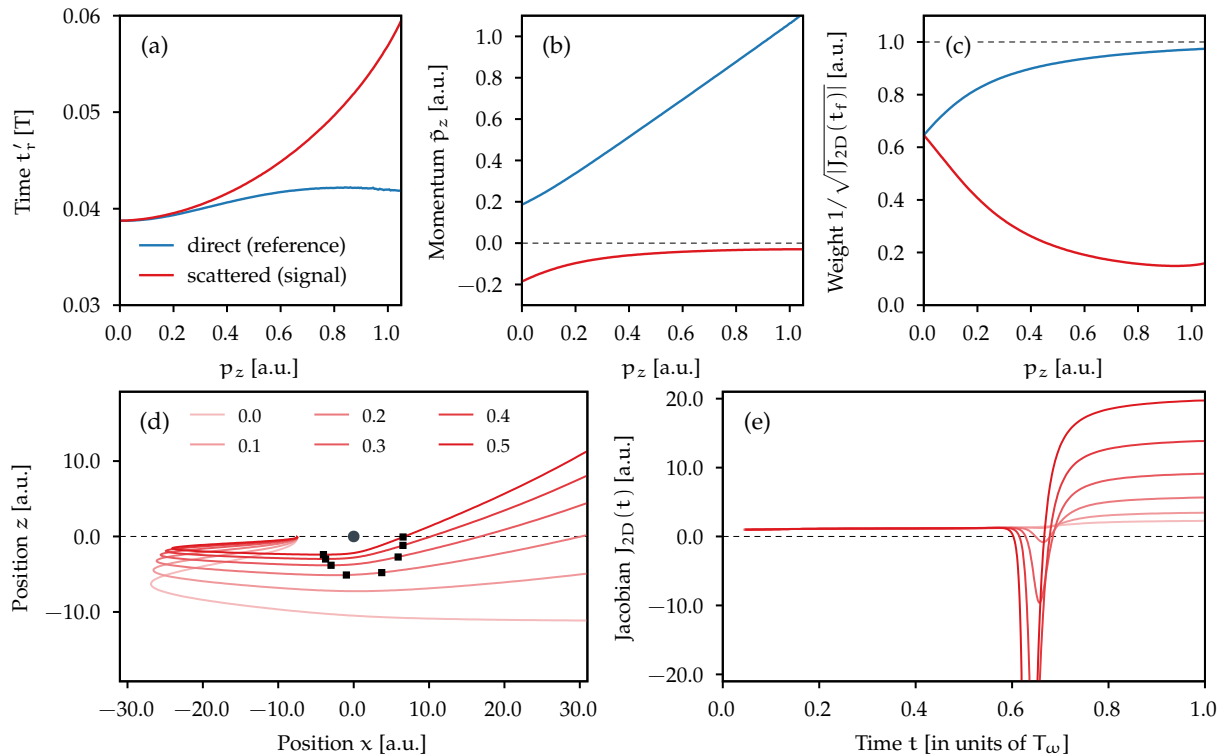


Figure 3.8: Properties of the trajectories relevant for the holographic pattern shown in Fig. 3.6 at $p_x = 0.8$ a.u.: (a) release time t_r' , (b) initial perpendicular momentum \bar{p}_z and (c) inverse of the square root of the final Jacobian in 2D. (d) Scattered (signal) trajectories shown for selected values of p_z as indicated in the legend in a.u. The black dots mark the focal points in 2D, i.e., the zeros of the time-dependent Jacobian shown in panel (e).

has two zero crossings in 2D, indicating two focal points. Compared to the previously-discussed axial caustic in Coulomb focusing, these points have another structure. Following the recipe of Section 3.3.1, the numerical calculation shows that the Maslov index is increased by $+1$ at one point, but it is decreased by -1 at the other point. This results in the final Maslov index of zero. The simple example emphasizes that it is usually not sufficient to count the number of focal points in 2D in order to determine the Maslov phases.

Scaling of the wavelength

When adding the potential-free action phase of Eq. (3.15) to the simple man's model of Section 2.1.1, the basic properties of holography can be qualitatively studied [74, 234]. The phase difference between signal and reference wave (in 2D) is mostly determined by $\Delta S \approx \frac{1}{2} p_\perp^2 (t_c - t_0)$. For adiabatic conditions, the excursion time of the signal trajectory, i.e., the time spent in the continuum between release and recollision, is nearly independent of the laser intensity. Hence, the pattern is only weakly affected by changes of the intensity and it survives focal-volume averaging. On the other hand, the excursion time is proportional to the wavelength λ and, thus, the fringe spacing is expected to scale as $\propto \lambda^{-1/2}$.

Even though this simple man's model is unable to predict the fringe positions quantitatively correct, our TDSE results show smaller fringe spacings for longer wavelengths in agreement with earlier work [234] (see Fig. 3.9).⁷ For the studied wavelengths between 400 nm and 1200 nm, the influence of Maslov's phase shift is apparent, i.e., the correct positions of the interference maxima and minima can only be reproduced, when including the Maslov phase. The agreement between our semiclassical model and the TDSE result is best for the longest wavelength, i.e., for the most adiabatic conditions. There, not only the fringe positions but also the signal strength is perfectly predicted for a broad region of perpendicular momenta p_\perp . When considering smaller wavelengths, we still find good agreement

⁷For 1000 nm and 1200 nm wavelength, a maximal angular momentum of 768 is considered in the 3D TDSE simulations.

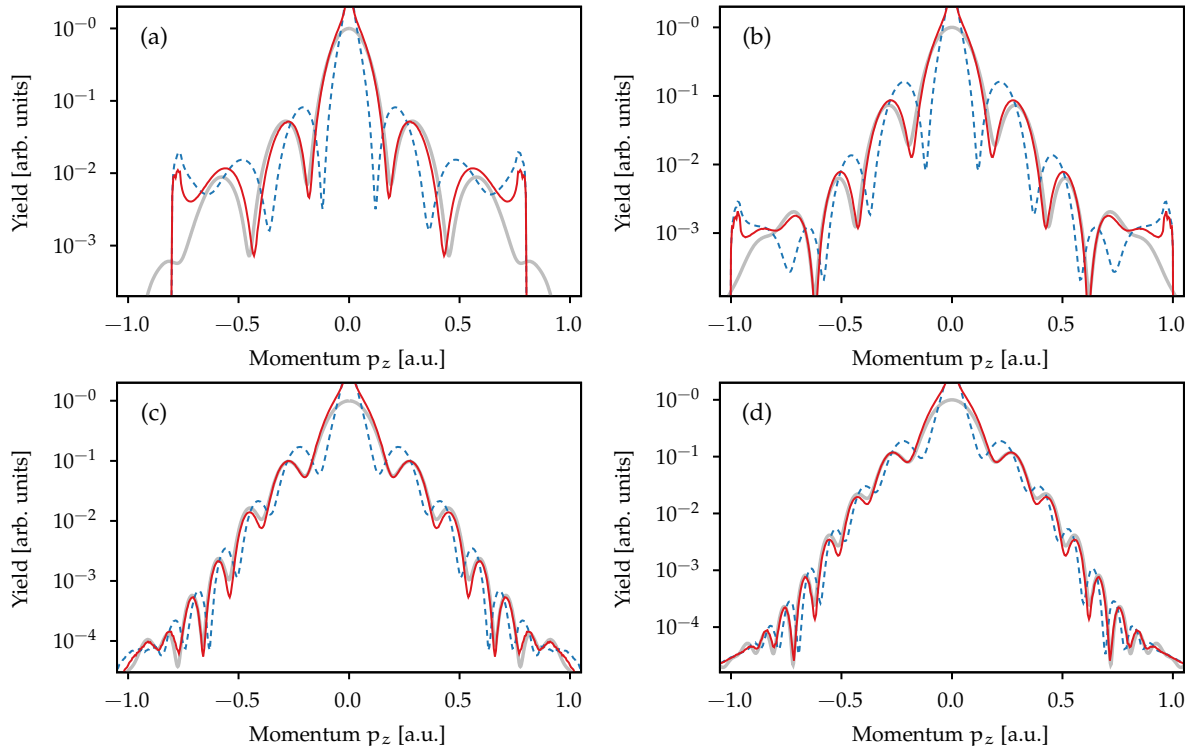


Figure 3.9: 1D slices through the momentum distributions in 3D at fixed $p_x \approx E_0/(2\omega)$ analogous to Fig. 3.6(b), but for different wavelengths: (a) $\lambda = 400$ nm, (b) $\lambda = 600$ nm, (c) $\lambda = 1000$ nm and (d) $\lambda = 1200$ nm. Again, the results are indicated as: TDSE results (gray thick line), semiclassical model including Maslov's phase (red line) and neglecting Maslov's phase (blue dashed line). For better comparison, the distributions are normalized to an arbitrary value. The slices are averaged over a range of $p_x = E_0/(2\omega) \pm 0.05$ a.u. Figure is adapted from Brennecke *et al.* [248].

for the central fringes. However, since the maximal return energy of the signal electrons scales quadratically with the wavelength, the extension of classically-reachable perpendicular momenta shrinks with decreasing wavelength. For 400 nm and 600 nm, pronounced cutoffs at $|p_z| \approx 0.8$ a.u. and $|p_z| \approx 1.0$ a.u. are visible in the semiclassical calculations. In principle, classical caustics appear at these cutoff momenta, indicating the breakdown of the semiclassical approximation. Due to the finite resolution in our simulations, the caustics are reflected by fuzzy maxima.

3.4.2 Intracycle interference

Interference appears not only between trajectories starting in the same half cycle of the pulse (see the color-marked time windows in Fig. 3.5), but also between trajectories released in different half cycles. For a cw field, the simple man's model predicts that each momentum $|p_x| < E_0/\omega$ is reached by two distinct trajectories starting at different times within an optical cycle. For the considered pulse, such intracycle interference occurs between contributions from the time windows I. and II. or from the windows II. and III. (see Fig. 3.5). It results in fringes roughly parallel to the z -axis in Fig. 3.4. Due to the shortness of the pulse and the chosen CEP $\phi_{\text{CEP}} = 0$, the contributions from windows I. and III. are much weaker than the signal from window II. Hence, the intracycle interference pattern has a low contrast.

The intracycle interference can be controlled via the CEP of short few-cycle laser pulses [71, 73]. For a CEP of $\phi_{\text{CEP}} = -\pi/2$, the pattern can be observed more clearly (see the pulse shown in Figs. 3.10(a) and (b)). This choice ensures that the signal on the positive p_x -axis is dominated by the central quarter cycles of the field. The intracycle interference leads to a series of pronounced peaks along the p_x -axis (see Fig. 3.10(c)). The positions as well as the modulation depth of the fringes are again well reproduced by the semiclassical model including Maslov's phase. In the time window marked in orange, one direct trajectory has a relevant contribution to the signal. In contrast, a direct and a scattered trajectory are

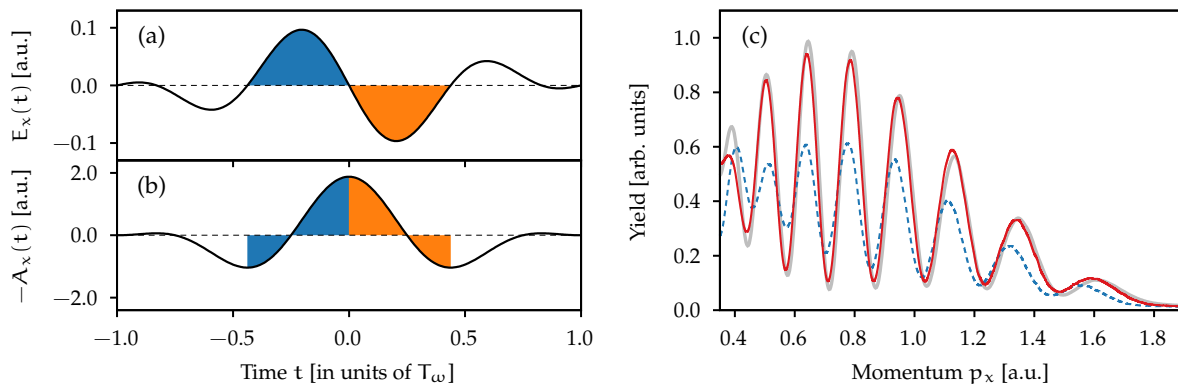


Figure 3.10: (a) Electric field of a two-cycle pulse with CEP $\phi_{\text{CEP}} = -\pi/2$ and (b) corresponding negative vector potential. The color-marked half cycles induce the dominant signal on the positive p_x -axis. (c) Signal along the p_x -axis obtained by integration over the central stripe with $p_{\perp} \leq 0.2$ a.u. of 3D distributions. Again, the results are indicated as: TDSE results (gray thick line), semiclassical model including Maslov's phase (red line) and neglecting Maslov's phase (blue dashed line).

launched in the time window marked in blue. Hence, the intracycle interference pattern is formed by scattered and direct trajectories. As a result, the nonzero Maslov phase present for the scattered trajectory also influences this type of interference. Here, however, the relative importance of the Maslov phase depends strongly on the weight of direct and scattered trajectories.

As discussed above, an axial caustic is present on the polarization axis in the semiclassical simulations. Even though the integration over a small region around the axis ensures that the calculated signal is finite, it is not guaranteed that the used Maslov phase is meaningful for momenta very close to the polarization axis. However, we obtain the same conclusions, if only the signal between $p_{\perp} = 0.05$ a.u. and $p_{\perp} = 0.2$ a.u. is considered in the integration.

For the observation of intracycle interference in more common multi-cycle pulses, the fringe spacings of the intracycle interference need to be much larger than the spacings of the ATI peaks [233]. It was shown that the visibility of the fringes can be controlled in orthogonal two-color fields by their relative phase [92, 266]. Alternatively, sculpted light pulses created by parallel two-color fields can be used as in the experiment by Xie *et al.* [76]. There, a fundamental field is superimposed with its second harmonic of equal field strength and, for a certain two-color phase, prominent intracycle interference was observed. This choice of the field leads to a pronounced asymmetry along the polarization axis already for a cw field, i.e., a preferred emission in positive p_x -direction. We use a similar field represented by a vector potential

$$\mathbf{A}(t) = - \left(\frac{E_0}{\omega} \sin(\omega t + \pi/2) + \frac{E_0}{2\omega} \sin(2\omega t + \pi/2) \right) \cos^2 \left(\frac{\omega t}{2n_p} \right) \mathbf{e}_x, \quad (3.33)$$

but choose again a two-cycle envelope ($n_p = 2$) (see the pulse shown in Figs. 3.11(a) and (b)). Compared to a single-color field with the same intensity, the sculpted field has a higher cutoff for direct ionization and the release times of the interfering wave packets are confined to a narrower time window. The latter ensures that their accumulated phase difference is smaller and, thus, the spacing of the intracycle fringes is larger. In Ref. [76], the authors interpreted their distributions using a model based on a Coulomb-corrected version of strong-field approximation and retrieved the relative phase difference between the interfering trajectories. They concluded that the valence-electron dynamics and, especially, the transient population of excited states are important to explain the interference pattern. Surprisingly, our semiclassical model including Maslov's phase can perfectly reproduce the TDSE-based interference pattern without considering valence-electron dynamics at all (see the signal along the polarization axis shown in Fig. 3.11(c)). Again, when the Maslov phase is neglected, the intracycle interference pattern cannot be quantitatively modeled. Thus, our approach offers an alternative interpretation of the experimental results [76] and suggests that the retrieval of valence-electron dynamics might actually not be possible.

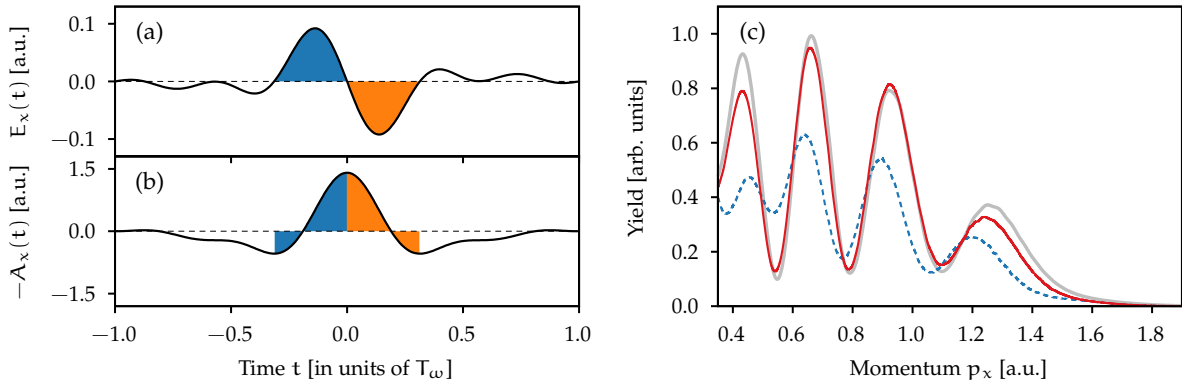


Figure 3.11: (a) Electric field, (b) corresponding negative vector potential and (c) signal along the p_x -axis as in Fig. 3.10, but for the sculpted two-color field of Eq. (3.33). A fundamental wavelength of 800 nm and a total intensity of 1×10^{14} W/cm² are used.

3.4.3 Interference of high-energy electrons

High kinetic energies can be reached by electrons which are elastically scattered by large angles and, subsequently, are further accelerated by the light field [16, 17]. Within this high-order above-threshold ionization (HATI) process, some electrons are deflected to large lateral momenta forming a plateau-like region in the PMD. Classically, two trajectories per optical cycle contribute to the same final momentum (see also the schematic illustration in Fig. 3.12). According to their excursion times, they are called “short” and “long” rescattering trajectory. A more detailed investigation of their kinematics can be found in Chapter 9. In the 2D distributions shown in Fig. 3.4, their interference pattern is visible as nearly-circular ring structures.

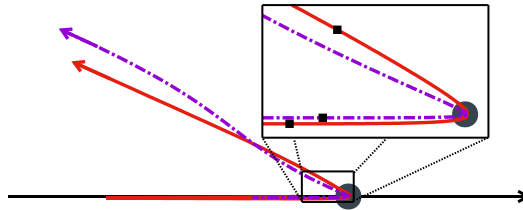


Figure 3.12: Schematic illustration of high-order above-threshold ionization. The superposition of the long rescattering trajectory (red solid line) with the short rescattering trajectory (violet dashed-dotted line) creates an interference pattern in the high-energy region. Here, the long trajectory passes two focal points in 2D (black squares) resulting in a Maslov index $\nu_{2D} = 0$. In contrast, the short trajectory only passes one focal point (black square) resulting in a Maslov index $\nu_{2D} = 1$. Figure is adapted from Brennecke *et al.* [248].

By considering this interference pattern, we will demonstrate that nonzero Maslov phases already influence the PMDs in 2D. These Maslov phases arise from passing through other types of focal points, e.g., through fold caustics, and, hence, the change of the Maslov index needs to be calculated numerically. The long trajectory is topologically equivalent to the scattered trajectory in holography (see Section 3.4.1). In 2D, it crosses through two focal points, where the Maslov index is increased at one point and it is decreased at the other. Hence, its final Maslov index is $\nu_{2D} = 0$. On the other hand, the short trajectory only passes through one focal point in 2D and has a final Maslov index of $\nu_{2D} = +1$. For a quantitative modeling of the fringe positions in the circular interference structures, the difference of these Maslov phases is crucial (see also the 1D slice through the distributions at $p_x = -0.5$ a.u. shown in Fig. 3.13). Since both trajectories become equivalent at the classical boundary (here at $|p_z| \approx 1.4$ a.u.), a caustic appears in the semiclassically-simulated PMDs.

The yield of high-energy electrons is much higher in the 2D setting compared to the 3D setting. As explained above, this overall effect is well reproduced by the semiclassical model due to the dependence of the Jacobian on the dimensionality. However, for large-angle scattering, the electron has to return very close to the parent ion such that the HATI process is very sensitive to details of the ionic potential.

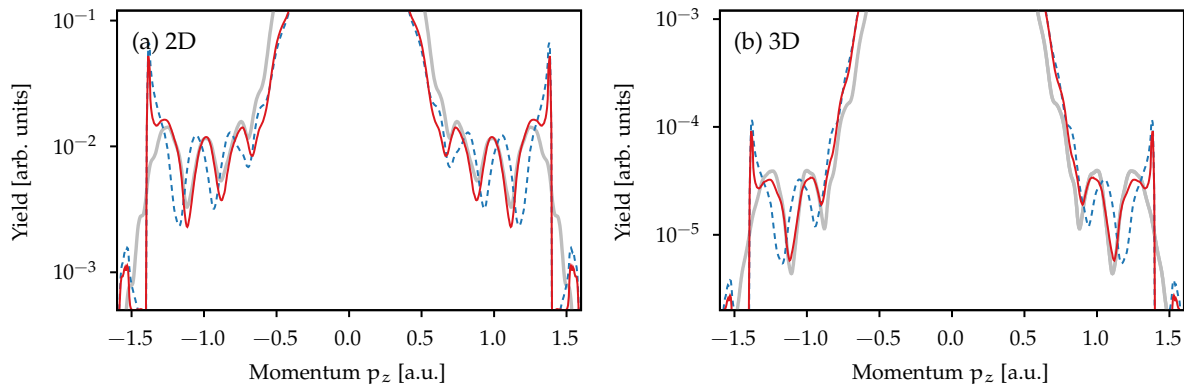


Figure 3.13: 1D slices through the momentum distributions in 2D (panel a) and in 3D (panel b) of Fig. 3.4 at fixed $p_x = -0.5$ a.u. and $p_y = 0$. Again, the results are indicated as: TDSE results (gray thick line), semiclassical model including Maslov's phase (red line) and neglecting Maslov's phase (blue dashed line). For better comparison, the distributions are normalized to an arbitrary value. Figure is adapted from Brennecke *et al.* [248].

The target-dependent elastic-scattering differential cross section (DCS) mostly determines the shape of the scattering plateau in the PMDs. Thus, it is expected that the $-1/r$ potential used in the semiclassical model cannot quantitatively reproduce all details. In principle, the problem of modeling HATI by means of classical simulations goes much deeper, because the classical DCS usually differs from the correct quantum-mechanical DCS. A prominent exception is a bare Coulomb potential in 3D.

To include the correct quantum-mechanical DCS in simplified simulations, quantum-orbit models based on the framework of the improved strong-field approximation can be used (see Section 2.3 and also Chapter 9). For sufficiently adiabatic conditions, such models are able to quantitatively predict the shape of the scattering plateau and the appearing interference pattern for short-range potentials. In these approaches, an additional phase (analogous to Maslov's phase) is also present and it is inherently included in the prefactor resulting from saddle-point approximation. For example, this prefactor was already used in Refs. [199, 204].

3.4.4 Interference in bicircular counter-rotating fields

Focusing of electron wave packets and the appearance of Gouy's phase anomaly is nothing special for cylindrically-symmetric systems under the influence of linearly-polarized pulses, but it is rather a property of light-driven rescattering in general. To demonstrate this, we consider strong-field ionization in bicircular fields consisting of two counter-rotating circularly-polarized fields with frequencies ω and 2ω . A prototype of a bicircular field can be represented by the vector potential

$$\mathbf{A}(t) = \frac{E_0}{\omega} \frac{1}{\sqrt{1+R}} \left[\begin{pmatrix} \sin(\omega t) \\ \pm \cos(\omega t) \end{pmatrix} + \frac{\sqrt{R}}{2} \begin{pmatrix} \sin(2\omega t) \\ \cos(2\omega t) \end{pmatrix} \right], \quad (3.34)$$

where a positive sign corresponds to co-rotating fields and a negative sign to counter-rotating fields. The parameter R represents the intensity ratio of the two colors. For $R \rightarrow 0$ or $R \rightarrow \infty$, circularly-polarized fields of frequency ω or 2ω are retrieved, respectively. In contrast to pure circular polarization, in counter-rotating fields at intermediate intensity ratios, more complex electron dynamics occur, allowing electrons to revisit the parent ion. Already in 1995 Eichmann *et al.* [267] demonstrated that it is possible to efficiently drive high-harmonic generation by counter-rotating bicircular fields. The HHG process was further explored to generate circularly-polarized XUV radiation [268–270]. Later on, other recollision-based phenomena such as high-order above-threshold ionization [271–277] and nonsequential double ionization [278–281] were analyzed.

Figure 3.14 shows PMDs from 2D TDSE simulations for helium ionized by four-cycle counter-rotating bicircular fields for various intensity ratios. In contrast to cw fields with their three-fold dynamical symmetry [271, 282], the finite pulse duration leads to a symmetry breaking. In the simple man's model, the main parts of the momentum distribution are expected to follow the negative vector potential $-\mathbf{A}(t)$.

Hence, for intermediate intensity ratios R , intracycle interference occurs due to the superposition of wave packets launched in different thirds of an optical cycle. In addition, high-energy electrons visible with their “scattering spheres” are again a sign of hard rescattering. The interference between direct and rescattered electrons leads to holographic interference patterns, which were theoretically predicted in Refs. [272, 273, 283]. Such interference patterns were also experimentally observed in lateral distributions [284]. A detailed analysis of various rescattering structures in bicircular fields can be found in Refs. [272, 273].

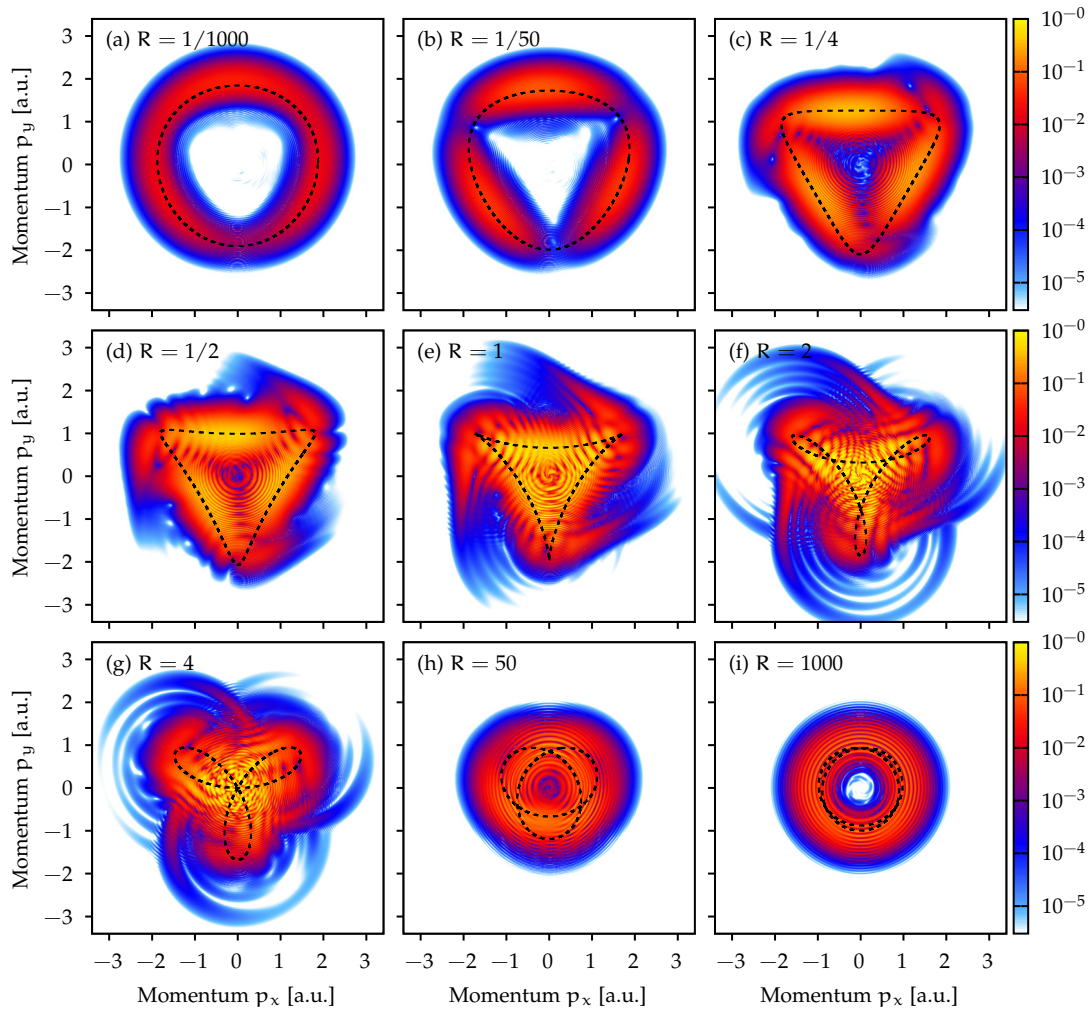


Figure 3.14: Photoelectron momentum distributions from 2D TDSE simulations for helium ionized by bicircular counter-rotating fields with 800 nm fundamental wavelength, 8×10^{14} W/cm² intensity and using a \cos^2 envelope of four cycles duration. The panels correspond to different intensity ratios R of the two colors. For each panel, the dashed black line is the negative vector potential of a cw field with the same intensity ratio.

In the following, we restrict ourselves to the intensity ratio $R = 3$, where scattering is quite pronounced. The PMDs for ionization by a short two-cycle pulse obtained by 2D and 3D simulations are shown in Fig. 3.15.⁸ Even though the same overall structures are present in both 2D and 3D PMDs, the positions of the interference fringes and the relative weight of the various regions differ. Even for these nontrivial waveforms, the semiclassical model reproduces well the various types of interference patterns and, especially, their differences of the 2D and 3D system.⁹ Due to the lack of symmetry, the Jacobian initial-value equations (3.9) have to be solved numerically to determine the Jacobians and Maslov indices in 2D and 3D. We speculate that the over-pronounced high-energy contributions of the model

⁸Here, a maximal angular momentum of 384 is used in the 3D TDSE simulations.

⁹In the semiclassical calculations of the probability amplitudes (3.24) in 2D and in 3D, we consider the same trajectories evolving in the x - y -plane.

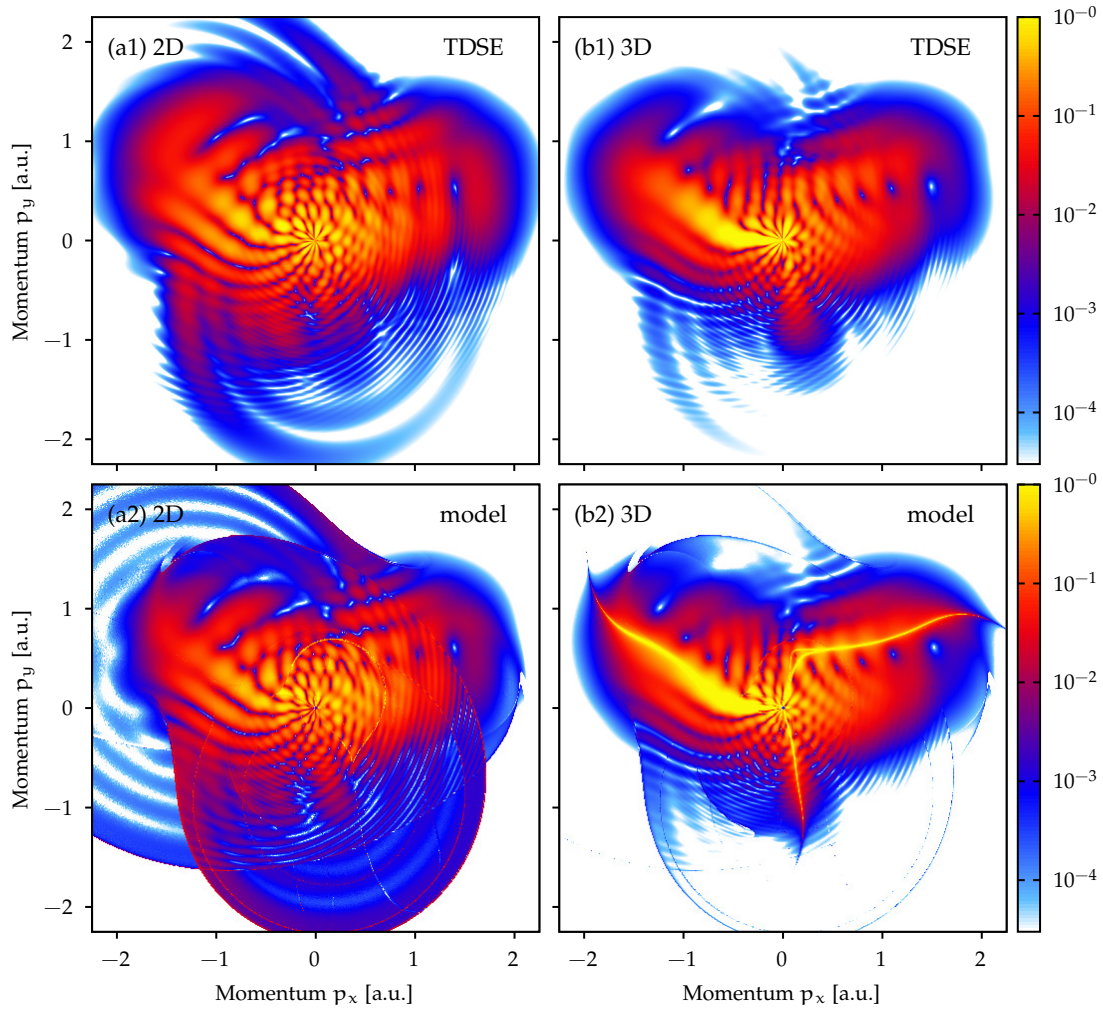


Figure 3.15: Photoelectron momentum distributions for helium ionized by two-cycle bicircular laser pulses with 800 nm fundamental wavelength, 8×10^{14} W/cm² intensity and intensity ratio $R = I_{2\omega}/I_{\omega} = 3$. (a) PMDs obtained from 2D simulations and (b) slices at $p_y = 0$ through the 3D distributions. The distributions are calculated by numerical solution of the TDSE in the upper row or with the semiclassical model in the lower row.

in 2D are caused by a too large classical cross section in 2D compared to the exact quantum-mechanical DCS (see also Section 3.4.3).

In analogy to linear polarization, the interplay between the Coulomb potential and the laser field leads in 3D to focusing of scattered electron waves into the polarization plane. Within the semiclassical model, this bunching of electrons causes three bright lines of caustics corresponding to the three thirds of an optical cycle. In the TDSE simulations, the associated enhancement of the yield in 3D compared to 2D is particularly visible for the central holographic fringe point in the upper left quadrant of Fig. 3.15(b1). A magnification of the holographic pattern is shown in Fig. 3.16(b). It is caused by the interference of a nonscattered wave packet with a scattered wave packet [283]. A schematic illustration of typical trajectories in position space is presented in Fig. 3.17. We consider the same trajectories in the 2D and 3D semiclassical simulations for the distribution in the p_x - p_y -plane. However, scattered trajectories pass additional focal points during their time evolution in 3D compared to the 2D situation. An analysis shows that the corresponding zero mode of the Jacobian field points in z -direction. Hence, trajectories starting with slightly different initial velocity in z -direction and otherwise same initial conditions are focused by Coulomb attraction to the same point in the polarization plane (see also the trajectories indicated as black lines in Fig. 3.17). In the position-space description, the focused electron wave experiences a phase shift of $\pi/2$ in 3D. In agreement with our findings for linear polarization, the numerical calculation in the momentum-space description indeed shows that those scattered trajectories experi-

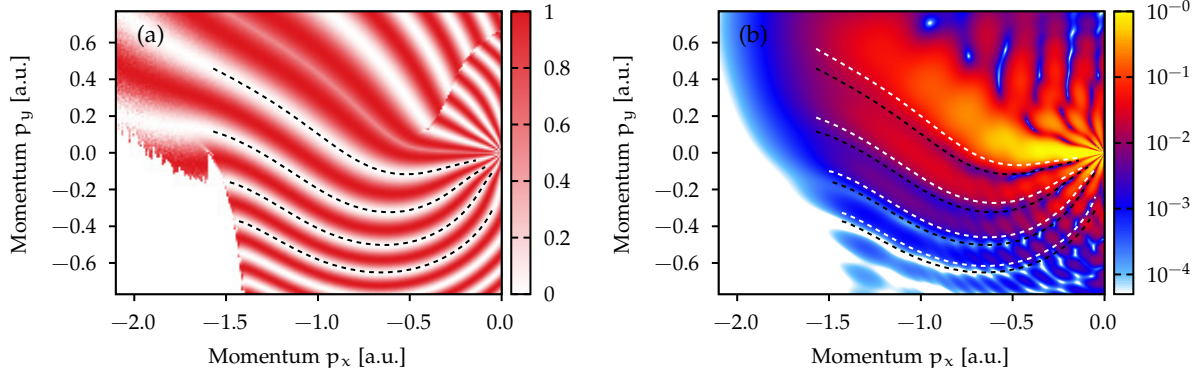


Figure 3.16: Photoelectron holography in bicircular fields. (a) Interference pattern of direct and scattered trajectories, i.e., $\cos^2(\Delta S/2)$ of their phase difference ΔS in 3D. (b) 2D slice through the 3D PMD from numerical solution of the TDSE as in Fig. 3.15(b1). The positions of the holographic interference minima of the semiclassical model are marked by black dashed lines, if Maslov's phase is included, and by white dashed lines, if Maslov's phase is neglected. Figure is adapted from Brennecke *et al.* [248].

ence an additional sign change of their Jacobian and a change of their Maslov index by $+1$ in 3D. This is an indication that the connection of Coulomb focusing and Gouy's phase anomaly is a rather general property of scattering trajectories.

The additional Maslov phases picked up in 3D become visible in the holographic interference pattern. The phase in the semiclassical model is dominated by $S \approx \text{Re}(S_{\downarrow}^0) + I_p(t_r' - t_A) + S_{\rightarrow} - v\frac{\pi}{2}$. We restrict ourselves to the two most important trajectories. Figure 3.16(a) shows the interference pattern calculated from their phase difference ΔS . The form of the fringes is reminiscent of the well-known finger-like structures in linear polarization. The positions of the predicted interference minima including Gouy's phase anomaly, i.e., Maslov's index in 3D, are depicted as black dashed lines. These positions agree well with the minima visible in the PMD from numerical solution of the 3D TDSE (see Fig. 3.16(b)).

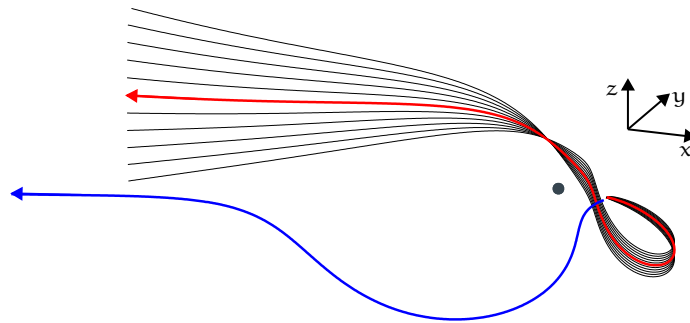


Figure 3.17: Schematic illustration of holography trajectories in a bicircular field. Both the nonscattered trajectory (blue line) and the scattered trajectory (red line) evolve in the x - y -plane. Trajectories (black lines) starting with small additional velocities in z -direction compared to the scattered trajectory are deflected by the Coulomb attraction of the ionic core (indicated as gray dot) and cross the polarization plane in the same point. Hence, this point is a focal point in position space.

3.5 Conclusion

In this chapter, the focusing of electron waves produced by strong-field ionization was analyzed. In full dimensionality (3D), the interplay of the laser electric field and the Coulomb attraction between electron and ion leads to a bunching of electron waves. As a result, similar to a lens in optics, this Coulomb focusing acts as a lens for electrons, making the waves pass through focal points. Reminiscent of Gouy's phase anomaly, the phase of the electron wave packets changes while passing through a focus. Since the bunching takes place in one degree of freedom, we found the fundamental value of $\pi/2$ for the phase shift. This can be vividly illustrated for linearly-polarized fields with their rotational symmetry around

the polarization axis. There, the scattered electron wave packets are focused in position space every time when they cross the polarization axis. However, importantly, the appearance of focal-point phases is a much more general phenomenon in strong-field ionization which is also present in other waveforms that give rise to rescattering such as in bicircular counter-rotating fields.

We demonstrated that these previously-overlooked Gouy phase shifts influence the formation of various interference structures in photoelectron momentum distributions from strong-field ionization. A simple example is the spider-like holographic pattern caused by the superposition of a nonscattered reference wave and a scattered signal wave. Since Coulomb focusing is absent in reduced dimensionality (2D), its influence on the photoelectron momentum distributions was qualitatively identified by comparing the results from TDSE simulations in 3D and in 2D. In addition to the well-known enhancement of the spectral weight, we observed a systematic shift of the interference fringes related to Gouy's phase anomaly. A similar effect is also present for the intracycle interference pattern. Aside from Coulomb focusing, we revealed that there are measurable focal-point phases already in 2D. As an example, the interference between short and long rescattering trajectories in the high-energy plateau region was considered. Hence, it turned out that strong-field ionization is an ideal setup for the natural observation of focal-point phases for electron waves.

For a quantitative, but intuitive trajectory-based modeling, we refined the semiclassical description based on an approximation of Feynman's path integral. Previous studies mostly concentrated on the action phase associated with each trajectory. However, to account for focusing effects of the electron waves, we studied an additional prefactor of the semiclassical propagator which reflects the classical evolution of the local environment around a given trajectory. The modulus of the prefactor involves the Jacobian and influences the weighting of the trajectories. In contrast, its phase, known as the Maslov phase, can be identified as a case of Gouy's phase anomaly and it affects the interference structures. We analyzed the focal-point structure of the electron trajectories and calculated the jumps of the Maslov phase. In the special case of linear polarization, the rotational symmetry enabled us to formulate a simple rule how to evaluate the Jacobian and Maslov phase in 3D compared to 2D. By considering several laser wavelengths, it was shown that the inclusion of preexponential factors is crucial for the good agreement of the model with TDSE results.

The analysis of the semiclassical trajectories relies on the solution of the inversion problem, i.e., the determination of all possible initial momenta of the electron trajectories that are classically deflected to a given final momentum. Here, we accomplished this task by means of a clustering method based on machine learning. This alternative approach is quite versatile and can be applied for different targets and electric-field configurations. Thus, the clustering scheme resolves one of the problems in the applicability of the semiclassical propagator. In principle, the idea can be transferred to other semiclassically-treated problems as long as the dynamics is not too chaotic. Compared to previously used initial-value representations, this may open the route for a clearer view on physical processes in various fields of research such as molecular spectroscopy [257, 285, 286] or interacting bosons [287].

Recently, it was shown that the inclusion of the Gouy phase anomaly results in a significant improvement in direct comparison to experimental data [288]. The quantitative interpretation of photoelectron momentum distributions for atoms by means of semiclassical models forms the foundation for the future analysis of nontrivially-polarized fields [275, 283, 284] or more complex targets such as molecules [30, 31, 240, 289]. In atoms, the properties of structured electron beams such as vortex beams generated by strong-field ionization of current-carrying orbitals [290–292] could be quite interesting, because similar effects as in the focusing of structured optical beams are expected. In molecules, the scattering off different centers may lead to new kind of electron trajectories with different focal-point properties and, thus, unexplored types of interference patterns. From a fundamental point, it would be illuminating to study the limits of the Coulomb focusing process. For example, the use of small negatively-charged molecules with permanent dipole moments results in a $1/r^2$ behavior of the ionic potential at large distances r (in contrast to the common $-1/r$ behavior), raising the question whether focusing and Gouy's phase anomaly are present in this modified situation.

Chapter 4

Control of Electron Wave Packets Close to the Continuum Threshold Using THz Waveforms

4.1 Introduction

Recollisions of high-energy electrons in strong linearly-polarized electromagnetic fields form the basis of many phenomena such as high-harmonic generation [11, 12], elastic scattering and diffraction [16–18, 33, 34, 36], or photoelectron holography [74, 239]. These processes can be qualitatively understood by means of the three-step model [7–10]: A continuum electron wave packet is created by laser-induced tunneling, afterwards it is controlled by the same light field, and it is potentially driven back to the parent ion (see also Chapter 3). However, for electron energies close to the continuum threshold, the light-driven motion of the electron wave packets is decisively influenced by the long-range Coulomb force of the parent ion. For example, low-energy structures [81–84] appear in the photoelectron spectra for atoms in strong laser field. These are caused by soft recollisions of electrons just above the continuum threshold [83–86, 118]. In addition, the long-range nature of the potential leads to a quasicontinuum of bound Rydberg states just below the continuum threshold. In strong fields, these weakly-bound states play for example an important role in the generation of coherent vacuum-ultraviolet (VUV) emission [293–296] and can be populated through multiphoton absorption [297–299] or by recapture after tunnel ionization [300–302].

For Rydberg states, the important time and length scales are hugely increased compared to the typical scales of tightly-bound atomic ground states. The dynamics of these electrons close to the continuum threshold can be modified by means of terahertz (THz) waveforms. Rydberg states can be ionized by means of half-cycle THz pulses [104] and single-cycle THz pulses [105] or their population can be redistributed [303]. Due to the different scales involved, the ionization mechanism usually works quite different compared to tunnel ionization in visible or infrared laser fields [105]. For example, the stabilization of states close to the ionization threshold were observed for single-cycle THz pulses [304, 305]. Previously, pump-probe schemes based on THz waveforms were already used to study phenomena at the continuum threshold. Examples are the control of the recombination of continuum electrons at low energies on a picosecond timescale [103, 306], the investigation of the electron dynamics in Rydberg states [101, 102] or the probing of electron interactions in double Rydberg wave packets [307].

Low-energy structures, population of Rydberg states and also other recollision-based phenomena appear quite naturally in strong visible or infrared fields. However, the control of the created electron wave packets with a single light pulse is difficult, because the same field governs both the preparation of the wave packet and its further evolution.¹ In this chapter, we investigate the natural solution and

¹One way to extend the possibilities of control is to use bichromatic fields (see for example [87–92, 308]).

decouple the creation step from the propagation step by using two very distinct light fields: a short infrared (IR) pulse with 25 fs duration and a synchronized carrier-envelope-phase-stable near-single-cycle THz pulse with a cycle length of about 1.3 ps at the central frequency. In this scheme, the IR pulse launches an electron wave packet at the continuum edge, i.e., extending across continuum and weakly-bound states. The subsequent motion of the electron wave packet is steered by the THz waveform. The creation time of the wave packet is localized on the scale of an optical cycle of the THz field such that launch process and subsequent acceleration are well separated. Compared to previous pump-probe studies using THz pulses [101–103, 306, 307], the subcycle timing enables the selection of the ongoing physical processes. Depending on the delay between the pulses, we observe effects such as Coulomb focusing of the outgoing wave packet or even more pronounced collision dynamics such as large-angle scattering and the appearance of holographic patterns. These phenomena well-known from strong-field ionization (see Chapter 3) are here observed under rather different conditions of the radiation and, hence, for quite different electron energies ($|E| < 1$ eV).

The setting is strongly reminiscent of the attosecond streak camera [63, 309, 310]. There, single-photon ionization by an XUV attosecond pulse launches a temporally-localized electron wave packet in the continuum. Afterwards, these photoelectrons are streaked in energy by means of a femtosecond infrared laser pulse. Usually, the initial kinetic energies of the freed electrons are sufficiently high such that the interaction with the parent ion can be ignored. Hence, the momenta of the photoelectrons roughly follow the negative vector potential of the streaking field [63]. However, for low electron energies (in the few-eV range), theoretical works predict that recollision-based phenomena may also be present in streaking [99, 311–315]. In a modified streak camera for strong-field ionization, based on the combination of ionization by a short visible pulse and deflection of the created wave packets by a mid-infrared pulse, scattering was already experimentally observed [100, 316]. In a RABBITT-like scheme with an attosecond pulse train phase-locked to the infrared field [65], electron wave packets at low energies were also manipulated and probed in experiment [94, 95, 97, 98]. The imprint of recollisions were observed in photoelectron distributions [96, 317] and in the emitted radiation [318, 319] by variation of the delay between the pulse train and the infrared field. However, the analysis of the momentum distributions is difficult in RABBITT-like schemes due to the series of wave packets launched by the pulse train. The main differences of our scheme to these previous works are: We consider much lower electron energies where the interplay between long-range Coulomb interaction and external electric field is even more pronounced. To control the electron dynamics, we use THz pulses. This enables us to reach a high degree of temporal localization of the initial wave packet. If this is quantified as the ratio of probe cycle length to ionizing pulse length, our THz-IR scheme reaches a ratio of about 50 whereas the previous studies only reached about 10.

The work is based on a collaboration with the group of Ulrike Fröhling in Hamburg. Martin Ranke performed an experiment using the described two-pulse scheme and measured the projection of the photoelectron momentum distributions for various delays by means of velocity-map imaging [320, 321]. We provided the theoretical simulations and developed the physical model of the ongoing processes. Most parts of this chapter are already published in Ref. [322].

4.2 Computational details

In order to calculate photoelectron momentum distributions in the presence of the THz pulse and the IR field, the TDSE is solved numerically in the electric dipole approximation for xenon modeled by a single-active-electron potential. We only consider ionization of the 5p orbital aligned along the polarization direction of the IR pulse, i.e., the orbital with magnetic quantum number $m = 0$ for the angular momentum component along x -direction. Compared to the conditions present in the other chapters of this work, the natural scales for low-energy electrons (typically with momenta $|\mathbf{p}| < 0.25$ a.u.) and for THz pulses are quite different. Hence, to obtain reliable results, several challenges have to be mastered:

- *Energy scale:* In an accurate simulation of electrons at low energies, the ionic potential V has to be considered during the whole motion of the outgoing electrons, i.e., two-grid methods as described in the Appendix A.2.2 cannot be used. Thus, we use the pseudospectral method in length gauge as described in the Appendix A.2.1 and store the position-space wave function on a single grid till the end of the THz pulse. To determine the PMDs, we project the final wave function onto numerically-calculated scattering states for the ionic potential (see Eq. (2.19)).
- *Time scale:* The THz field has an optical cycle length of about 1.3 ps and, thus, a time interval of several picoseconds must be covered in the simulations. The accuracy of the splitting scheme in the pseudospectral method is mostly determined by the error term of Eq. (A.23) which is proportional to $\sim \mathbf{E}(t) \cdot [\mathbf{E}(t) + 2\nabla V(\mathbf{r})] \Delta t^3$. Hence, the error in length gauge is strongly influenced by the electric-field strength (in contrast to velocity gauge where the error is proportional to the vector potential). Since the THz electric field is much weaker than the IR electric field with a ratio of about $E_{\text{THz}}/E_{\text{IR}} \approx 10^{-3}$, we use a time step of $\Delta t = 0.15$ a.u. when the IR is present, but we choose a large step of $\Delta t = 1.5$ a.u. when only the THz field is present.
- *Length scale:* The quiver amplitude of the electrons in the THz field is given by $E_{\text{THz}}/\omega_{\text{THz}}^2 \approx 1400$ a.u. However, even electrons with small momenta as 0.15 a.u. can travel large distances as 15500 a.u. in the time interval between their liberation and the end of the THz pulse (maximal time span of ≈ 2.5 ps). The radial part of the wave function is discretized using 6000 points on a nonuniform grid (A.44) with an extension $r_{\text{max}} = 19000$ a.u. and a core region $r_{\text{center}} = 100$ a.u. The grid spacing in the asymptotic part is approximately given by $\Delta r_{\text{max}} \approx 3.3$ a.u. such that a maximal momentum of $p_{\text{max}} \approx 1.1$ a.u. can be represented. This choice ensures that the low-energy part of the wave function remains on the grid until the end of the THz pulse. However, depending on the time delay, electrons from higher-order ATI peaks of the IR field (see Section 4.3) can reach the grid boundary and are absorbed by a mask function (A.53) of $\Delta r_{\Lambda} = 200$ a.u. width.
- *Angular-momentum scale:* For a rough classical estimate, we consider the product of a characteristic lateral momentum of 0.15 a.u. and a quiver amplitude of 1400 a.u. which results in an angular momentum of about 210 a.u.² In the expansion of the angular dependence of the wave function in spherical harmonics, we include states with maximal orbital angular momentum $l_{\text{max}} = 512$. For selected delays, the simulations were repeated with $l_{\text{max}} = 768$ and similar results were obtained for the low-energy part of the PMDs. To speed up the calculations, we monitor the populations of the angular momentum components during the propagation and only consider states with appreciable population.

4.3 THz-field-free distributions

The IR pulse prepares the electron wave packet that is afterwards steered by the THz waveform. The shape of the wave packet at the end of the IR pulse is a central ingredient that decisively influences the subsequent motion. For this reason, we first study the photoelectron momentum distributions in the absence of the THz field, i.e., the continuum part of the prepared wave packet. The experimentally-measured projection of the PMD is shown in Figs. 4.1(a) for ionization with an IR pulse of 795 nm central wavelength and a peak intensity of about 8.5×10^{12} W/cm². Here, the polarization of the light pulses (x -axis) is parallel to the detector plane. For the calibration of the momentum axis and the laser intensity, the measured distribution was compared to distributions from numerical simulations of the TDSE taking focal-volume averaging into account. The simulated distributions are further discussed below.

In a multiphoton picture for above-threshold ionization [5, 172], the positions of the ATI peaks are determined by the condition $E_n = n\omega - I_p - U_p$ with the ionization potential I_p of xenon and the

²In the used length gauge, states with even higher angular-momentum quantum numbers are populated.

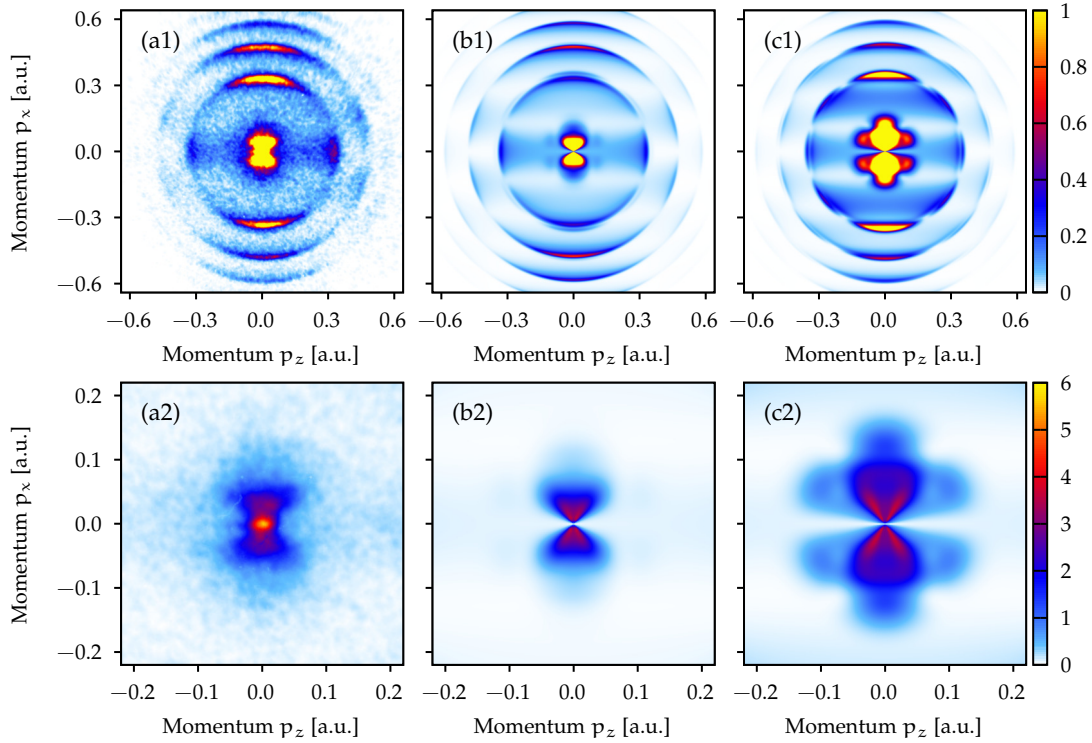


Figure 4.1: Photoelectron momentum distributions projected onto the p_x - p_z -plane for ionization of xenon by an IR pulse. The experimental results are shown in panels (a). The focal-volume-averaged distributions from numerical simulations of the TDSE for the GSZ potential and for the Tong-Lin potential are depicted in panels (b) and (c), respectively. The lower row contains a magnification of the low-energy region. Arbitrary normalization is used for panels (a), (b) and (c). The experimental data were provided by Ranke [320]. Figure is adapted from Brennecke *et al.* [322].

ponderomotive potential $U_p \propto E_0^2/\omega^2$ (see Section 2.1.1). For ionization with the xenon ion ending up in a $^2P_{3/2}$ state with an ionization potential $I_p \approx 0.4458$ a.u., a number of $n = 9$ photons is at least required to form an ATI peak in the continuum.³ We can assign the photon numbers $n = 9, \dots, 12$ to the ATI peaks centered at momenta $|\mathbf{p}| \approx 0.33, \dots, 0.64$ a.u. The chosen laser intensity is just above the closing of the eight-photon ionization channel occurring at an intensity defined by $E_8 = 8\omega - I_p - U_p = 0$. Thus, the eight-photon peak is centered slightly below the continuum edge. Due to its finite spectral width, its high-energy tail still reaches positive electron energies. In the low-energy part of the measured PMD, it is visible as an extended “butterfly-like”-shaped pattern (see also the magnification shown in Fig. 4.1(a2)).

For the TDSE simulations, we use IR pulses with a \cos^2 envelope of 26 optical cycles duration (≈ 25 fs FWHM in intensity) and perform calculations for a broad range of intensities. To consider the influence of focal-volume averaging, we assume a Gaussian beam profile and follow the scheme introduced in the Appendix A.2.4. The xenon atom is either model by a Tong-Lin potential [324] (see Section A.2.3) or by a modified Green-Sellin-Zachor (GSZ) potential [325].⁴ The projected PMDs are shown in Figs. 4.1(b) and (c), respectively. The overall structure of the PMDs is similar as the experimental one. However, in the simulated distributions, we find that each ATI peak is split in two sub peaks with a different angular structure. We identify the inner peak with the nonresonant ionization channel whereas the outer peak is related to a Freeman resonance [172] of 6d states. Due to this resonance behavior, the simulated PMDs are quite susceptible to the exact electronic structure and to the laser parameters. For example, the resonant ionization path is much more pronounced in the Tong-Lin potential compared to the GSZ potential. In the low-energy region, the resonant channel is visible as an extended structure

³In agreement with Ref. [323], the analysis of the signal along the p_z -axis and some symmetry arguments suggest that the channel ending up in a $^2P_{1/2}$ state can be neglected.

⁴In order to accurately reproduce the ionization potential of xenon, we slightly modified the parameter $H = 6.8163$ of the GSZ potential of Ref. [326].

with f character and it is too pronounced for the Tong-Lin potential compared to the experimental result. Hence, since we are mostly interested in this low-energy region, we use the GSZ potential for all further simulations. Note that for this choice the emission strength of the higher-order ATI peaks ($n > 8$) is only qualitatively reproduced (see also the 1D distributions in Fig. 4.2(a)).

In the presence of the THz pulse, we are unable to perform focal-averaged simulations for all delays. When only considering a single intensity, the low-energy part of the PMD is most accurately reproduced for an intensity of $7 \times 10^{12} \text{ W/cm}^2$. In this case, compared to the focal-averaged simulations, the yield is underestimated in the region between $p \approx 0.08 \text{ a.u.}$ and $p \approx 0.2 \text{ a.u.}$, but matches well in all other regions (see Fig. 4.2(b)).

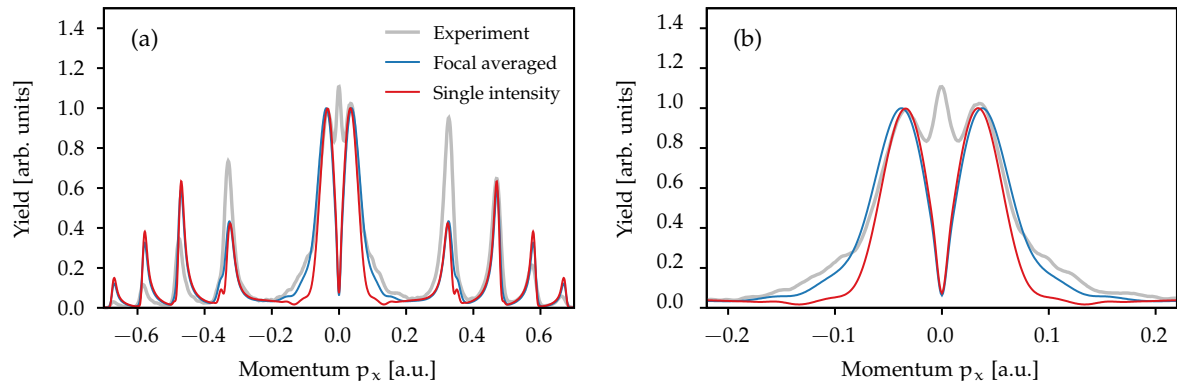


Figure 4.2: Photoelectron momentum distributions along the polarization direction (p_x -direction) for the same conditions as in Fig. 4.1. The distributions are calculated by integration of the 2D projections over $|p_z| < 0.1 \text{ a.u.}$ In addition to the focal-volume-averaged result for the GSZ potential (blue line), the distribution for a fixed intensity of $7 \times 10^{12} \text{ W/cm}^2$ is shown (red line). Panel (b) is a magnification of the low-energy region. The experimental data were provided by Ranke [320].

A characteristic difference between the TDSE simulations and the experiment is a bright spot centered at $p = 0$. These “zero-energy electrons” (ZEEs) have been neglected so far. As explained, the $n = 8$ photon peak is centered at slightly negative energies and, hence, there is a strong population in Rydberg states with very weak binding energies. After the end of the IR pulse, the ionization of these states by the static electric field of the VMI [327–329] or by blackbody radiation [330] leads to the additional zero-energy signal. We will consider this part of the PMD in more detail in Section 4.6.

In the remaining part of this chapter, we will study the influence of the THz field on the released electron wave packet. To this end, we investigate the following three regions of the PMDs separately:

- *High-energy electrons*: ATI peaks with energies $E_n = n\omega - I_p - U_p$ and $n > 8$.
- *Low-energy electrons*: the region corresponding to the “peak” at the threshold with $n = 8$ photons, but only momenta with $\sqrt{p_x^2 + p_z^2} > 0.04 \text{ a.u.}$
- *Zero-energy electrons*: identified with the region $\sqrt{p_x^2 + p_z^2} < 0.04 \text{ a.u.}$ in momentum space and mostly related to additional ionization of Rydberg states.⁵

4.4 Streaking of ATI peaks

After the preparation of the electron wave packet by the IR pulse, the interplay between the THz pulse and the electron-ion interaction controls its subsequent dynamics. Figure 4.3 shows the experimental momentum distributions along the polarization axis as a function of the time delay τ between THz waveform and IR pulse. The ATI peaks for $n \geq 9$ all behave similarly and are mostly streaked in energy

⁵The exact choice of the boundary between zero-energy and low-energy electrons has no deeper physical motivation. In spite of an experimental broadening of the zero-energy peak, the value of $p = 0.04 \text{ a.u.}$ ensures that all additional electrons released by the detector field are assigned to “zero-energy electrons”. For a value of $p = 0.03 \text{ a.u.}$, the observables discussed in this chapter show a quite similar behavior.

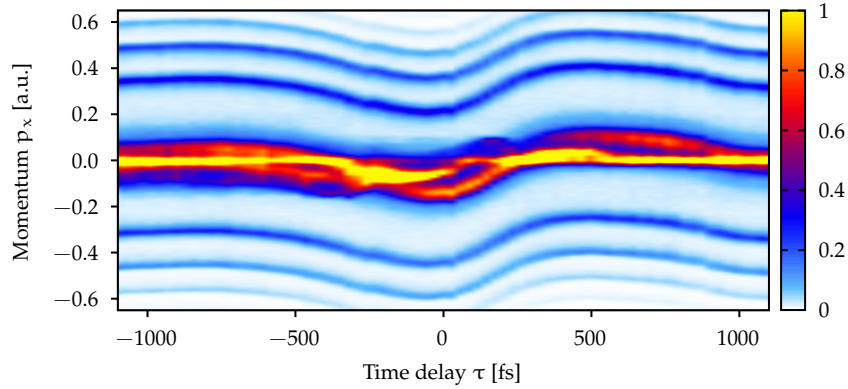


Figure 4.3: Experimental photoelectron momentum distributions along the polarization axis as a function of time delay τ between the THz waveform and the IR pulse. The distributions are calculated by integration of the 2D projections over $|p_z| < 0.1$ a.u. The experimental data were provided by Ranke [320].

by the THz field [63]. For these electrons with high initial kinetic energy, the effect of the Coulomb attraction can be neglected and their dynamics is solely determined by the THz field. Following the same idea as in attosecond streaking, the momentum change induced by the THz pulse is approximated classically as [63, 331, 332]

$$\Delta p_x = - \int_{\tau}^{\infty} dt E_{\text{THz}}(t) = -A_{\text{THz}}(\tau). \quad (4.1)$$

Here, τ is the creation time of the wave packet and it is equal to the time delay. E_{THz} and A_{THz} are the electric field and the vector potential of the THz waveform, respectively.

The relation of Eq. (4.1) is used to reconstruct the experimentally-applied THz pulse. To this end, we determine the central momenta of the ATI peaks as a function of the delay τ . To extract the relative variation due to the THz field, the THz-field-free positions are subtracted. The reconstructed vector potentials for the three ATI peaks with $n = 9 - 11$ are in very good agreement with each other (see Fig. 4.4(a)). Although the maximal THz field strength is only about $81 \text{ kV/cm} \approx 1.58 \times 10^{-5}$ a.u., the long acceleration time of the THz field leads to momentum changes on the order of 0.1 a.u. For the simulations, we apply a smoothed spline fit to the data for the ATI peak with $n = 9$. In order to reduce the computational effort and obtain a manageable pulse duration, the retrieved waveform is truncated at -1500 fs and $+1350$ fs by using a \sin^2 mask. The resulting “short” pulse is shown in Fig. 4.4 as black line.

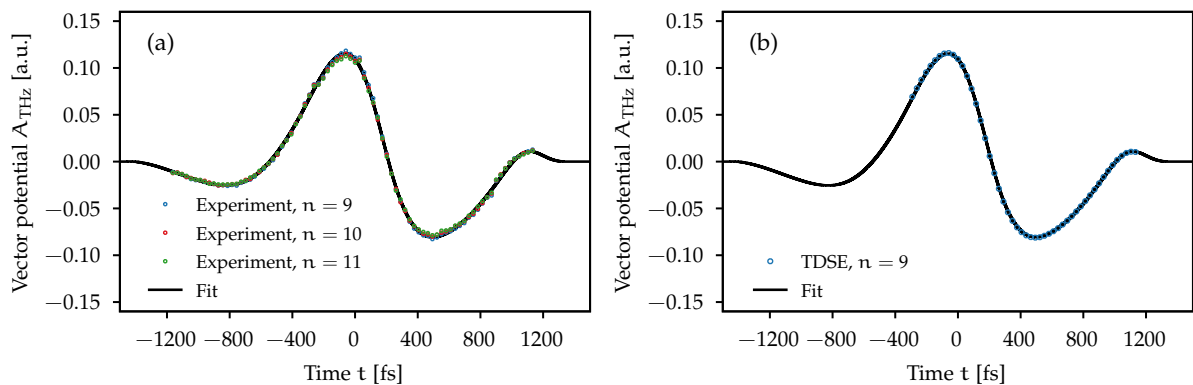


Figure 4.4: Vector potential of the THz pulse retrieved from experimental data for several ATI peaks indicated in the legend (left panel) and retrieved from TDSE simulations (right panel). The black solid line shows the vector potential for the short THz pulse used in the TDSE simulations. The experimental data were provided by Ranke [320].

In the extraction procedure of the THz pulse, the influence of the Coulomb attraction is neglected. We can test this approximation by using the PMDs from numerical TDSE simulations, including both the IR pulse and the THz pulse. The same procedure as for the experimental data is applied to reconstruct the vector potential. For the ATI peak with $n = 9$, the retrieved result is shown in Fig. 4.4(b) as blue dots.

The reconstruction is in perfect agreement with the vector potential used for the simulations (deviations lower than 0.002 a.u.). For large negative delays $\tau < -290$ fs, higher-order ATI peaks are absent in the simulations, because these electrons reach the boundary of the radial simulation grid.

4.5 Dynamics of low-energy electrons

The low- and zero-energy electrons exhibit major deviations from the simple momentum shift of the higher-order ATI peaks. Figure 4.5(a) shows a magnification of the experimental distributions along the polarization directions as a function of the time delay τ . An animated presentation of the complete 2D projections of the PMDs is available as Supplemental Material of Ref. [322]. Even though some parts of the momentum distribution at low energies still roughly follow the momentum shift of Eq. (4.1), their signal strength is modulated and their corresponding angular distribution is deformed as a function of the delay. Additionally, localized spots are visible in the PMDs, e.g., at $p_x \approx 0.09$ a.u. for the delay $\tau \approx 174$ fs or at $p_x \approx 0.14$ a.u. for the delay $\tau \approx 400$ fs. Furthermore, the creation of the wave packet before the main THz pulse arrives (large negative delays) results in noticeably broader p_x -distributions compared to its launch after the main THz pulse has already passed (large positive delays). All in all, we observe a variation of the total electron emission probability as a function of the delay.

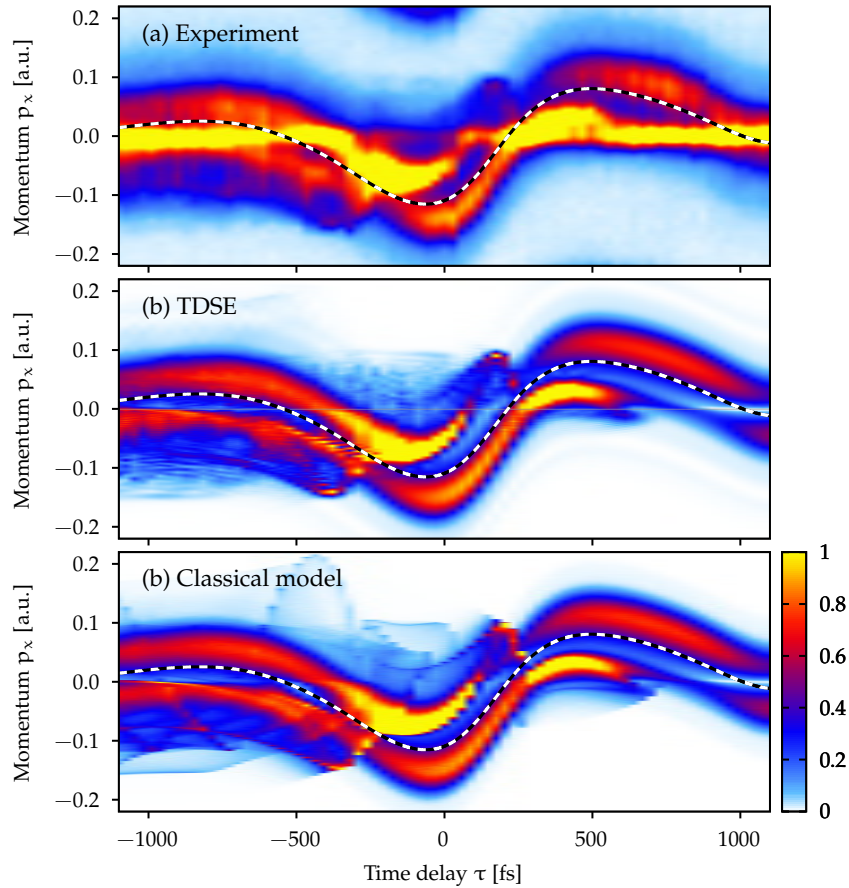


Figure 4.5: Low-energy part of the photoelectron momentum distributions along the polarization axis as a function of time delay τ analogous to Fig. 4.3. The dashed line indicates the momentum shift of Eq. (4.1) which is usually considered in streaking experiments, i.e., estimated by neglecting the electron-core interaction. The experimental data were provided by Ranke [320]. Figure is adapted from Brennecke *et al.* [322].

The PMDs from numerical solution of the TDSE well reproduce the major features of the experiment in the low-energy region (see Fig. 4.5(b)). However, as expected, the bright line centered at $p_x = 0$ of zero-energy electrons is visible in the experiment and it is not contained in the TDSE simulations. We will separately discuss zero-energy electrons in Section 4.6. To avoid a background resulting from the projection of higher-order ATI peaks ($n \geq 9$), we subtracted the corresponding signal in all simulations.

4.5.1 Classical model

The observations for low-energy electrons are already a clear indication that the interplay between the THz field and the electron-ion interaction plays a crucial role. To reveal the physics behind these observations, a classical-trajectory Monte Carlo (CTMC) model is established. Since the creation of the wave packet takes a much shorter duration than the length of an optical cycle of the THz field, the whole ionization process is split into two steps:⁶

- *Creation of the wave packet.* The IR field prepares the initial wave packet at a time τ by multiphoton ionization. To properly describe this nonclassical process, we perform a TDSE simulation without THz field. The low-energy part of the quantum-mechanical energy distribution is shown in Fig. 4.6(a). Here, we select the peak at the continuum edge, i.e., extending across weakly-bound Rydberg states ($E < 0$) and continuum states ($E > 0$).

The main idea is to use the quantum-mechanical wave function from the TDSE and to convert it into a classical phase-space distribution. To this end, we consider the quantum-mechanical velocity distribution at the end of the IR pulse and assign to every velocity \mathbf{v}_0 a unique initial position $\mathbf{r}_0(\mathbf{v}_0)$. The angular structure of the velocity distribution shown in Fig. 4.6(b) is caused by the superimposition of contributions with small orbital angular momentum (here $l = 1, 3$ and 5). For simplicity, we assume zero initial angular momentum in the classical calculation and, thus, choose a mapping of the form $\mathbf{r}_0(\mathbf{v}_0) = r_0(v_0)\hat{\mathbf{v}}_0$. The function $r_0(v_0)$ is optimized to reproduce the THz-field-free quantum-mechanical energy distribution (energy-optimization method).⁷ After the end of the IR pulse, the wave packet is still localized in the vicinity of the ionic core (see the initial positions shown in Fig. 4.6(c)). By construction, this approach assigns a unique energy value to each initial velocity. This enables the identification of regions with negative and positive energies in the wave packet (see the white dotted line in Fig. 4.6(b)).

An alternative way to define the mapping $r_0(v_0)$ is offered by the local-position method [333, 334]. To this end, for each velocity \mathbf{v}_0 , a local position is defined as $\mathbf{r}_0(\mathbf{v}_0) = -\nabla_{\mathbf{v}_0} \arg \tilde{\psi}(\mathbf{v}_0)$ with the momentum representation $\tilde{\psi}(\mathbf{v}_0)$ of the wave packet (for a more detailed discussion see the classical backpropagation method of Section 5.2.4). To avoid complications caused by interference, we only analyze the dominant contribution of the quantum-mechanical wave packet with orbital angular momentum $l = 1$. Besides some additional oscillations, the result of the local-position method is in good agreement with the energy-optimization method (see Fig. 4.6(c)). Hence, in the following, all presented results are obtained with the energy-optimized mapping.

- *Propagation in the presence of the THz pulse.* The dynamics induced by the THz pulse is treated classically by propagating the phase-space distribution forward in time. To this end, we simulate a swarm of classical trajectories following Newton's equation including the THz field and the attractive force of a $-1/r$ potential (see the EOM (2.49)). For the chosen initial conditions, the electron motion is restricted to the plane spanned by the polarization direction and the initial velocity. At large times t_f after the end of the THz pulse, we determine the final momenta \mathbf{p} of the electrons and calculate the electron momentum distributions. Similar to the discussion in Section 3.3.5, it is sufficient to only consider trajectories in a 2D plane. However, in order to account for focusing in the third dimension, we use an additional weighting factor of $|v_{0,\perp}|/|p_\perp|$ in the calculation of PMDs (see the relation of the Jacobians in 2D and 3D presented in Eq. (3.31)).

The result of the classical model shown in Fig. 4.5(c) contains all major features of the TDSE distributions. As expected, small quantitative differences are visible. For example, a slight shift (up to ≈ 50 fs) is present for some of the structures. We believe that these deviations are partially attributed to the chosen initial distribution and to the neglect of the THz pulse during the release by the IR pulse.

⁶This idea is similar to the well-known two-step model of strong-field physics [8].

⁷To this end, the coefficients of a fourth-order polynomial representing the auxiliary function $v_0(E)$ are varied to optimally reproduce the quantum-mechanical energy distribution. The numerical inversion of $v_0(E)$ and the use of $E = v_0^2/2 - 1/r_0$ results in the desired mapping $r_0(v_0)$.

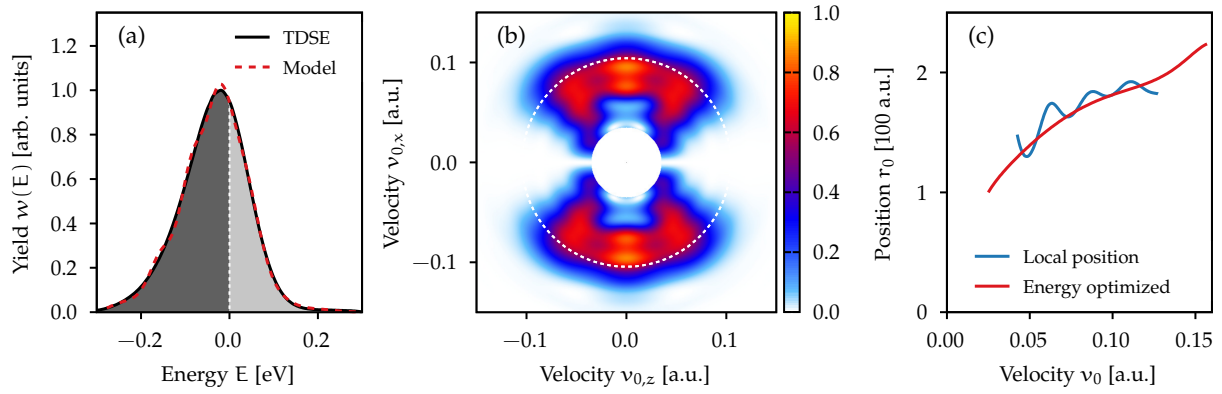


Figure 4.6: Properties of the initial wave packet used in the classical simulations: (a) energy distribution from the TDSE simulation without THz pulse (black solid line) and used in the classical model (red dashed line). (b) Representation as a slice through the electron velocity distribution. The white dotted line indicates zero energy in the classical model. (c) Mapping $r_0(v_0)$ of the initial velocity v_0 to the initial position r_0 determined by an optimization of the energy distribution (red line) or by the local-position method (blue line). Figure is adapted from Brennecke *et al.* [322].

4.5.2 Discussion

In the absence of Coulomb effects, the electron motion is only influenced in polarization direction by the THz pulse. On the other hand, if the THz pulse is absent and the created wave packet only evolves under the influence of the binding forces, it expands radially outwards. For the chosen initial conditions, the classical trajectories follow straight lines. In both special cases, the trajectories do not cross the polarization axis ($r_{\perp} = \sqrt{y^2 + z^2} = 0$). Thus, an axis crossing of trajectories is a sign of the interplay between THz pulse and Coulomb attraction. Figure 4.7 shows the classical distributions where the trajectories are selected with respect to their number δ of axis crossings. As expected, for late delays, no crossings ($\delta = 0$) occur and the main characteristics of trajectories are unchanged compared to the Coulomb-free case. However, for intermediate and very early delays, trajectories undergoing one or even multiple axis crossings play an important role. In this section, we will first discuss the limiting scenarios of wave packets created before the main THz pulse arrives (large negative delays) or after the main THz pulse has already passed (large positive delays). Afterwards, we will turn to intermediate delays.

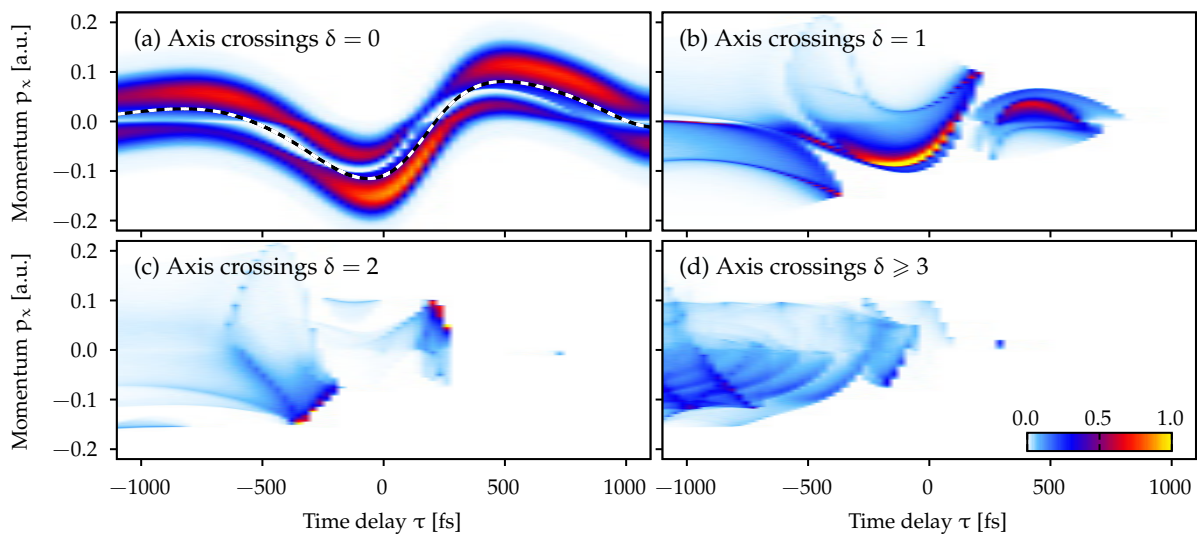


Figure 4.7: Low-energy part of the photoelectron momentum distributions along the polarization axis as a function of time delay τ from classical simulations analogous to Fig. 4.5. For the panels, only trajectories with a given number δ of crossing of the polarization axis are selected. Summing up the results of all panels leads to the total distribution of Fig. 4.5(c).

Late delays: THz-field-free dynamics

For the short THz pulse of the simulations and for late delays, i.e., at the right edge of Fig. 4.5(c), the wave packet is created after the THz pulse has already passed. In this situation, the energy of the outgoing electrons is classically conserved. The wave packet expands radially outwards and is only decelerated by the Coulomb attraction. Classically, after a certain finite time, electrons with negative energies ($E < 0$) reach their turning points and, thus, are trapped in bound orbits, i.e., correspond to the population of Rydberg states. In contrast, electrons with positive energies ($E > 0$) escape and form the THz-field-free PMD. Importantly, this division into bound and escaping orbits is an asymptotic concept in the sense that both types of electrons only show qualitatively different behavior after sufficiently long propagation times.

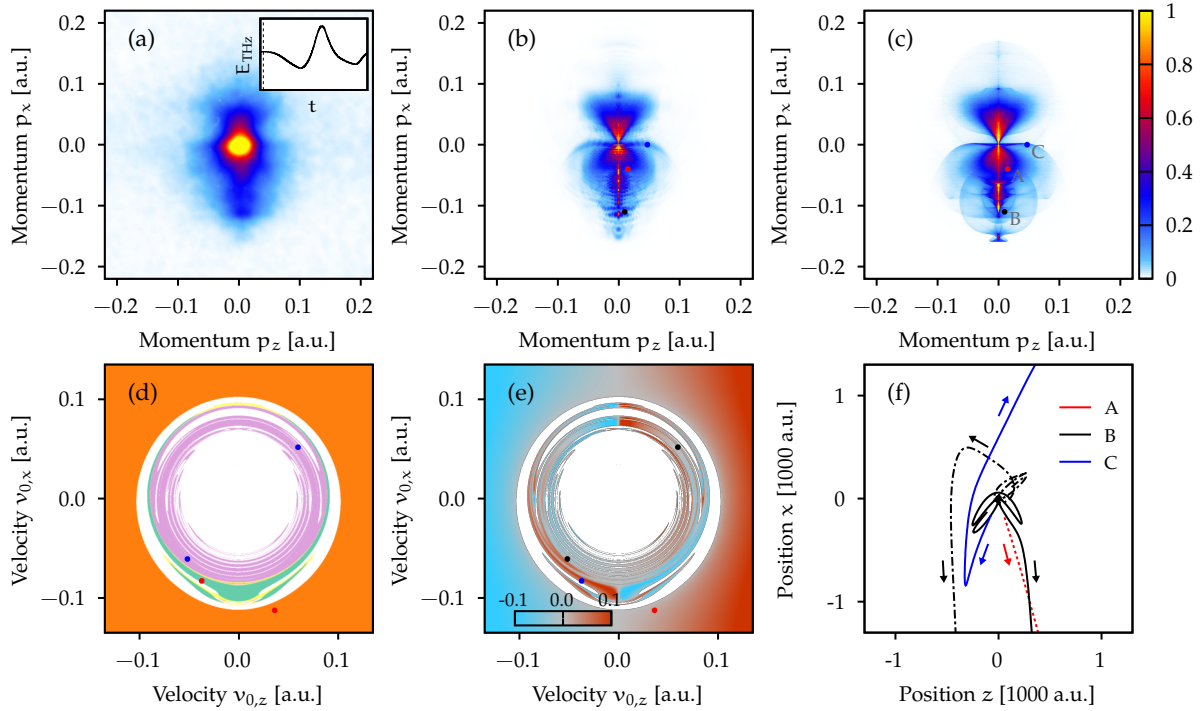


Figure 4.8: Electron dynamics for a delay of -1133 fs. (a)-(c) 2D projections of the PMDs from the experiment, the TDSE simulation and the classical model. (d) Classification of trajectories in the initial-velocity space according to their number of axis crossings: trapped trajectories (white), $\delta = 0$ (orange), $\delta = 1$ (green), $\delta = 2$ (yellow) and $\delta \geq 2$ (rose). (e) Final lateral momentum component (p_z -component) in a.u. as a function of the initial velocity. (f) Characteristic trajectories leading to a given final momentum marked by points in panels [(b),(c)]. The corresponding initial velocities are also indicated by the points in panels [(d),(e)]. The electric field E_{THz} is shown in the inset of panel (a). The experimental data were provided by Ranke [320].

Early delays: ionization of Rydberg states by a single-cycle THz pulse

For very early delays, the continuum part of the wave packet has already traveled far away from the core, when the main part of the THz pulse arrives. Hence, the coupling between the THz pulse and the Coulomb potential can be neglected such that the trajectories do not cross the polarization axis (see the red trajectory in Fig. 4.8(f)). Since these electrons experience the whole THz pulse, their final momenta deviate only slightly from the THz-field-free situation. Weakly-bound electrons with negative initial energy also experience the whole THz pulse and, hence, they can be liberated by the single-cycle THz pulses as in earlier works [105, 304, 335]. Here, the ionization mechanism is mostly determined by the relative duration of the THz pulse, i.e., for the single-cycle pulse the optical period, compared to Kepler period $\tau_K = 2\pi n^3$ of the orbit with an effective quantum number $n = 1/\sqrt{-2E}$.

For high binding energies (e.g. -0.1 eV), the Kepler periods are much smaller than the pulse duration and an adiabatic over-the-barrier ionization mechanism dominates as discussed in Ref. [105]. The

ionization probability increases with decreasing binding energy, i.e., for too small initial velocities ionization is suppressed (see Fig. 4.8(d)). In this regime, the interplay between the THz pulse and the ionic potential results in a complex motion with multiple revisits of the core (see the trajectories shown as black lines in Fig. 4.8(f)). The chaotic dynamics leads to a fragmentation of the initial-velocity space into regions of escaping trajectories and of trapped trajectories. As a result, very different initial conditions are mapped to the same final momenta. For example, about 20 different trajectories contribute to the momentum indicated as a black point in Figs. 4.8(b),(c). In the 2D PMDs, these contributions lead to a concentrated signal with very fuzzy structures along the polarization axis. This additional signal is also visible in the distributions along the polarization in the region between $p_x \approx -0.15$ a.u. and $p_x \approx 0.1$ a.u. (see Figs. 4.5 and 4.7(d)). The various structures cannot be resolved in the experiment and only appear as a blurred region.

When going towards the ionization threshold, the binding energy decreases and the associated Kepler period increases. For certain initial energies, the magnitude of Kepler period is on the same order as the duration of the THz pulse. Hence, the orbits do not circle around the ionic core multiple times. A typical trajectory is shown as blue solid line in Fig. 4.8(f). The related structures in the PMD are more extended compared to the chaotic dynamics discussed above. Very close to the ionization threshold, the Kepler times become much larger than the THz duration. In this regime, ionization can occur by displacement and a counter-intuitive stabilization was observed [304, 305]: More weakly-bound electrons are less likely to be liberated (see the white area around $v_0 \approx 0.1$ a.u. in Fig. 4.8(d) that indicates trapping of electrons). The energies in our initial wave packet span both the regime of displacement and the regime of adiabatic ionization. The combination of both mechanisms leads to an “ionization window” in the energy distribution with high ionization probability.

Intermediate delays: reminiscence of strong-field phenomena

In the intermediate time range, i.e., when the wave packet is created during the main part of the THz pulse, very interesting dynamics occurs. Here, the interplay between the electron-ion interaction and the THz pulse is still very important, but the dynamics can be interpreted by means of a few characteristic trajectories. For large regions of initial conditions, the motion is regular in the sense that small changes of external parameters such as the THz field or the initial wave packet only weakly perturb the electron dynamics and the structures in the PMD.

In conventional strong-field ionization, the release time and the transverse initial velocity of the electrons determine the characteristics of their motion (see Chapter 3 and references therein). For example, rescattering is only possible for electrons born slightly after the maximum of the electric field. Here, in contrast, we only “ionize” at a well-defined time given by the delay τ . However, we have to pay the price that the initial wave packet contains a broad range of parallel initial velocities. Hence, for a given delay, the initial velocity defines the ongoing dynamics and the structures visible in the PMD. In the following, we discuss the several physical phenomena through the example of two selected delays.

Streaking of low-energy electrons

When the wave packet is created close to a zero crossing of the THz electric field, the electrons are accelerated in the same direction for the following half cycle of the THz pulse. Hence, parts of the wave packet with initial velocity components $v_{0,x}$ antiparallel to the electric field are driven away from the parent ion. For example, the electric field points in x -direction for time larger than about -58 fs and a corresponding trajectory is indicated as red dotted line in Fig. 4.9(f). For sufficiently large initial velocities, these parts of the wave packet are only weakly decelerated by the Coulomb attraction. In the projected PMD, this results in the triangle-like region at $p_x < -0.1$ a.u. (see Figs. 4.9(b),(c)). The situation is similar to streaking of high-energy electrons or recollision-free strong-field ionization.

Classically, the triangular region is formed of trajectories with both negative and positive initial energies E . The white dotted line in Fig. 4.9(b),(c) marks $E = 0$ from the classical model. In the TDSE simulations as well as in the classical calculations, the shape of this structure in the PMD is sensitive to

the angular structure of the initial velocity distribution. Thus, the PMD contains not only information on the energy distribution of Rydberg states but also on the initial shape of their angular distribution. Unfortunately, the current classical model is not able to fully reproduce the angular dependence of the quantum-mechanical TDSE results. We think that more advanced modeling is necessary for an appropriate reconstruction of the initial wave packet from a photoelectron momentum distribution. A promising approach could be a simple quantum-mechanical model based on eikonal-Volkov states [215].

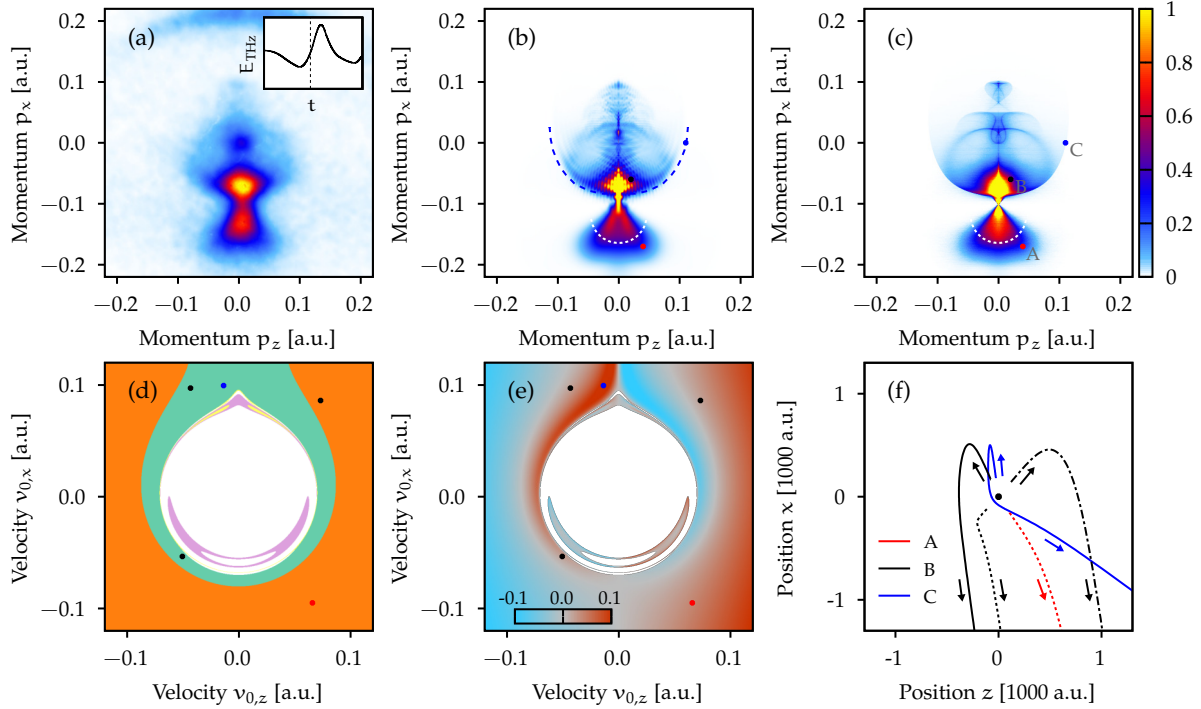


Figure 4.9: Electron dynamics analogous to Fig. 4.8, but for a delay of -58 fs. In addition, the white dotted line in panels (b) and (c) indicates zero initial energy ($E = 0$). The blue dashed line marks the classical boundary of the scattering plateau. The experimental data were provided by Ranke [320]. Figure is adapted from Brennecke *et al.* [322].

Recollision-based phenomena

When considering smaller initial velocities (but still a delay of -58 fs and $v_{0,x} < 0$), the influence of the Coulomb potential becomes more prominent. Here, we observe a strong deflection and focusing of electrons in the lateral direction. This results in an enhancement of the yield in the vicinity of the polarization axis at the upper edge of the triangle-like region. The corresponding trajectories form the boundary between zero and a single axis crossing and, hence, their initial conditions lay on the boundary between the green and orange area in Fig. 4.9(d). Even though trajectories with even smaller initial velocities can still escape in negative x -direction, they cross the polarization axis during the motion (see the trajectory indicated as the black dotted line in Fig. 4.9(f)).

On the other hand, trajectories initially launched with $v_{0,x}$ -components parallel to the THz electric field are first decelerated and may reverse their direction. For large transverse initial velocities, the electron makes a wide turn around the ion. Its trajectory is still only weakly influenced by the Coulomb field and can be attributed to recollision-free ionization. An example is shown as black dashed-dotted line in Fig. 4.9(f). For smaller transverse initial velocities, Coulomb focusing appears similar to conventional strong-field ionization [77, 78] (see Section 3.4 for further discussions). Here, the electrons are deflected to very small transverse final momenta and the signal is enhanced in the vicinity of the polarization axis (see the bright region around $p_x \approx -0.08$ a.u. in Fig. 4.9(b),(c)).

For even smaller transverse initial velocities, the electrons are driven back to the vicinity of the parent ion during their acceleration in the THz field and scatter off the potential, resulting in strong changes of

their velocities. Afterwards, they are further accelerated by the THz field. Typical trajectories are shown as the blue and black solid lines in Fig. 4.9(f). The trajectories cross the polarization axis such that their topology changes, i.e., their Maslov index changes and a Gouy phase is picked up as discussed in Chapter 3. Due to the large deflection of the scattered electrons, different parts of the initial wave packet can be mapped to the same final momentum and interfere. Similar to strong-field photoelectron holography [74, 239] introduced in Section 3.4.1, we find interference fringes roughly parallel to the polarization axis in the TDSE simulations. The pattern is caused by the superposition of a nonscattered and a scattered trajectory (see trajectories indicated as dashed-dotted and solid black lines in Fig. 4.9(f)). For small final perpendicular momenta p_{\perp} , a third type of trajectories is important (indicated as dotted black line). Their interference with the holography trajectories results in a coarse signal modulation in p_x -direction. The characteristics of interfering trajectories are similar to those leading to intracycle interference in strong-field ionization [71, 72, 233]. Here, however, the trajectories are released at the same time τ defined by the IR pulse, but have different initial velocities (in contrast to the “double-slit in time” present in strong-field ionization).

Classically, smaller transverse initial velocities and, thus, smaller impact parameters lead to larger the scattering angles of the electrons (see the trajectory indicated as blue solid line in Fig. 4.9(f)). Analogous to the high-order above-threshold ionization (HATI) process introduced in Section 3.4.3, some electrons are deflected to large lateral momenta and form a circular plateau-like region [16, 17]. Its classical boundary is indicated in Fig. 4.9(b) as blue dashed line. In our numerical simulations, “backscattered” electrons, i.e., those that are elastically scattered into large angles close to 180° , also appear in this THz-driven situation. Analogous to HATI, these particular electrons can acquire “high” kinetic energies. It is important to note that even though we observed phenomena known from conventional strong-field ionization, the time, length and momentum scale on which the electron dynamics appears are quite different in our THz-field-driven situation.

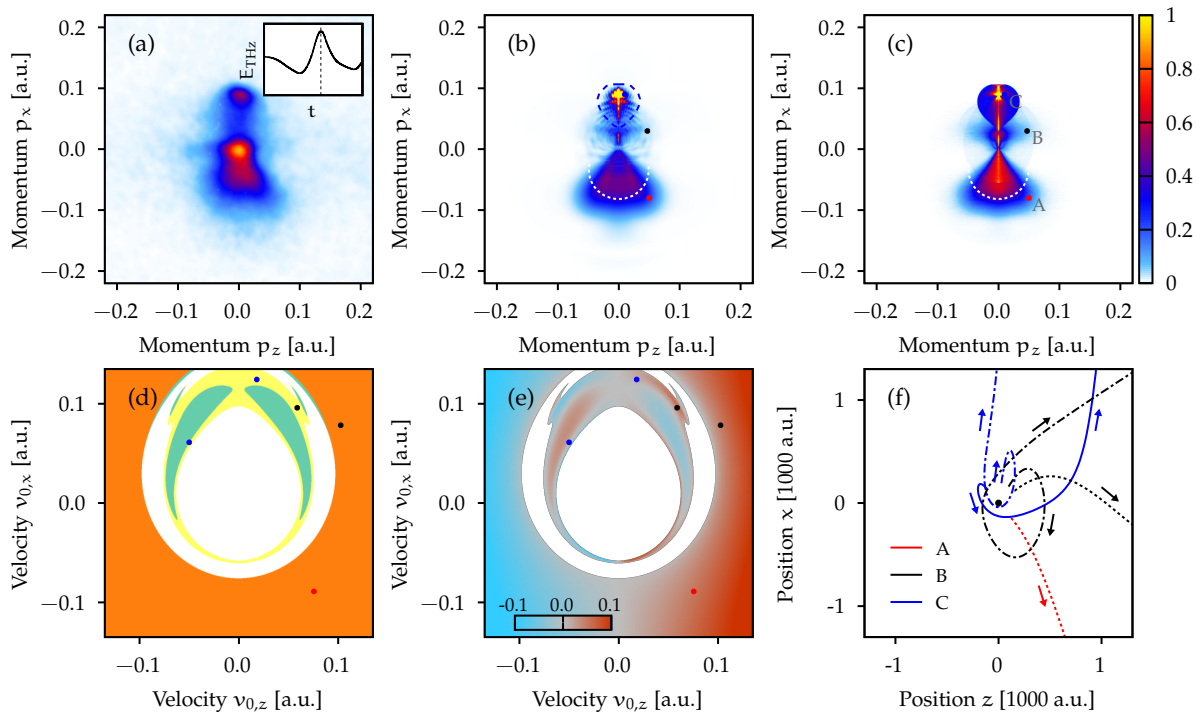


Figure 4.10: Electron dynamics analogous to Fig. 4.8, but for a delay of 174 fs. In addition, the white dotted line in panels (b) and (c) indicates zero initial energy ($E = 0$). The blue dashed line marks the classical boundary of the scattering plateau. The experimental data were provided by Ranke [320]. Figure is adapted from Brennecke *et al.* [322].

Bunching effects

For slight variations of the delay around the zero crossing of the electric field at $\tau \approx -58$ fs, the electron motion is only weakly modified and the overall shape of the PMDs remains unchanged. In this region, the different vector potentials $A_{\text{THz}}(\tau)$ at the release times τ solely alter the exact positions and sizes of the various structures (see the contributions corresponding to zero or one axis crossing in Fig. 4.7). Despite the shortness of our near-single-cycle THz pulse, similar recollision-free and recollision-based structures appear in the PMD in reversed direction for delays half an optical cycle later. In the transition region, i.e., for delays around the maximum of the THz electric field, the physical processes are drastically changed. In conventional strong-field ionization, electrons liberated directly after the peak of the electric-field strength can revisit the core multiple times (see for example Fig. 2.2). This complicated dynamics leads to the appearance of low-energy structures [86]. In the THz field similar effects occur, involving additional axis crossings of the trajectories (see for example the strong contributions of trajectories with two axis crossings for delays around $\tau = 200$ fs in Fig. 4.7).

To investigate the transition region, we start with the well understood delays around $\tau = -58$ fs and track the changes towards delays around $\tau = 200$ fs. When going to later delays, the time span in which the THz field accelerates the electrons in negative x -direction gets shorter. Thus, the electric field changes its sign when the electron is still in the close vicinity of the ionic core. In this region of delays, it is not justified to divide the electron motion in THz-driven sections and a “scattering” process. Instead, the intriguing interplay between the THz field and the ionic attraction defines the exact electron trajectories. Besides a shift of the whole distribution, we find that the extension of the rescattering plateau shrinks (see the blue dashed line in Fig. 4.10(b) for a delay of ≈ 174 fs). An analysis shows that all trajectories with a single axis crossing (see the green area in Fig. 4.10(d)) are deflected to this tiny region in final momentum space. A typical trajectory is shown as blue solid line in Fig. 4.10(f). Importantly, for slightly changed initial velocities, the electron circles once around the core and crosses the polarization axis twice (see the trajectory indicated as blue dashed-dotted line). At the boundary between these two topologically different types of trajectories bunching occurs, resulting in caustics in the classical simulations. For a delay of ≈ 174 fs, the bunching effect is also visible as bright spot at $p_x \approx 0.08$ a.u. in the experimental and TDSE results (see Figs. 4.10(a),(b)). For even later delays, after the maximum of the THz electric field, electrons with velocity components $v_{0,x} > 0$ are not efficiently driven back to the parent ion by the THz field. Thus, similar to conventional strong-field ionization, the dynamics and the resulting structures in the PMDs are substantially altered in this region of delays.

4.6 Dynamics of zero-energy electrons

The probability of low-energy electrons (expect for zero-energy electrons) is shown in Fig. 4.11(a) as a function of the delay τ . In the simulations, the normalization is chosen such that the whole wave packet at the continuum edge has a probability of one. In contrast, the experimental yield is arbitrarily normalized to best match the TDSE result. The dependence of the yield of low-energy electrons on the delay is well reproduced by the TDSE and by CTMC simulations.

In contrast, the yield of zero-energy electrons (with $\sqrt{p_x^2 + p_z^2} < 0.04$ a.u.) is systematically underestimated in the simulations (see Fig. 4.11(b)). The experimental result is majorly influenced by the contribution of the bright spot approximately centered at vanishing momentum in the electron momentum distributions. In earlier works [327–330], this additional signal was attributed to depletion of Rydberg states after end of the light pulses by the VMI detector field or by blackbody radiation. However, we find that even when the wave packet is created after the main part of the THz pulse has already passed ($\tau > 1100$ fs) the yield enhancement is much larger in the measurements with THz source compared to the THz-field-free situation of Section 4.3. Importantly, in earlier experiments with a similar THz source [332], it was shown that the applied THz pulses have a weak, but long pulse tail. So far, in the simulations, we only considered a near-single-cycle THz pulse with vanishing field strength outside the pulse length of 2.9 ps. In the following section, we investigate the influence of the THz pulse tail and the static detector field of the VMI to explain the variation of the yield of zero-energy electrons.

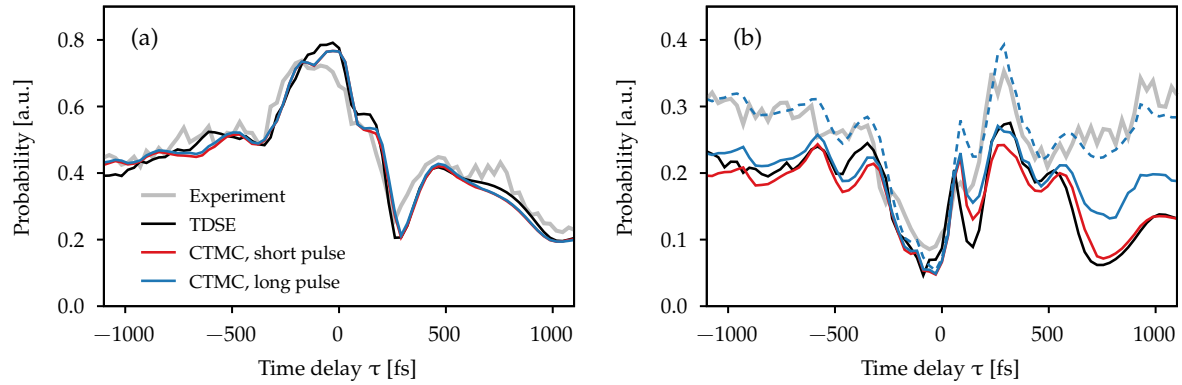


Figure 4.11: Integrated probabilities from 3D results versus time delay. (a) Probability of low-energy electrons except for zero-energy electrons, obtained by integration over all momenta satisfying $|p_x + A_x(\tau)| < 0.2$ a.u., $|p_z| < 0.1$ a.u. and $\sqrt{p_x^2 + p_z^2} > 0.04$ a.u. (b) Zero-energy electrons' probability with $\sqrt{p_x^2 + p_z^2} < 0.04$ a.u. The dashed line shows the sum of the classical model result for a long THz pulse and a selected amount of Rydberg electrons freed by the detector field (see main text at the end of Section 4.6). The theoretical results are normalized such that the probability of the initial wave packet is chosen to one. The experimental results were provided by Ranke [320] and are arbitrarily normalized. Figure is adapted from Brennecke *et al.* [322].

The classical trajectory simulations enable us to include both a tail of the THz pulse and a static electric field of the VMI. Without detector field, the system is rotationally symmetric around the polarization axis of the THz radiation. Hence, it was sufficient to only consider trajectories in a 2D plane. The inclusion of a detector field breaks this symmetry. Nevertheless, to keep the simulations computationally feasible, we restrict ourselves to the 2D dynamics in the plane spanned by the polarization axis (x -axis) and the detector field F pointing in negative y -direction. After the end of the THz pulse and at sufficiently large distances r such that $V(r) \approx -Z/r$, the situation simplifies to the well-known Stark problem (see for example Ref. [336]). The corresponding Hamilton-Jacobi equation is separable in semiparabolic coordinates ($\zeta = \sqrt{r+y}$ and $\sigma = \pm\sqrt{r-y}$). For this choice, the Stark barrier is formed in ζ -direction. The characteristic energy scale of the problem is given by

$$E_c = 2\sqrt{ZF}. \quad (4.2)$$

For a detector field strength $F = 20.5$ kV/m $\approx 4 \times 10^{-8}$ a.u. and an asymptotic charge $Z = 1$, we obtain the energy $E_c = 4 \times 10^{-4}$ a.u. Similar to the field-free situation, all electrons with $E > 0$ are asymptotically free. The detector field induces additional over-the-barrier ionization of electrons with energy $0 > E > -E_c$. However, not all trajectories which fulfill the energy condition will actually escape. In addition, a sufficiently large amount of energy needs to be in the degree of freedom ζ , resulting in the condition

$$\Gamma_\zeta - \frac{E^2}{F} > 0 \quad (4.3)$$

with the conserved quantity $\Gamma_\zeta = 4r^2\dot{\zeta}^2 - F\zeta^4 - 2E\zeta^2$. In the simulations, we propagate all trajectories till the end of the THz pulse. Afterwards, to speed up the simulations, we restrict ourselves to orbits that satisfy Eq. (4.3). These escaping trajectories are further propagated till they are sufficiently far away from the ionic core. From their final momenta \mathbf{p} , the momentum distributions are determined. Here, however, we only consider the distributions along the polarization axis obtained by integration over the p_y -direction.

For vanishing detector field strength and for the short THz pulse of Fig. 4.4, the 1D distributions are shown in Fig. 4.13(a) as a function of the delay. Even though the same overall structures as in the 3D simulations (see Fig. 4.5(c)) are present, their relative weight is slightly changed due to the reduced dimensionality (2D).⁸ In order to study the effect of a more realistic THz pulse, we perform additional simulations for a long pulse with an extended pulse tail of maximal field strength of ≈ 15 kV/cm at $t \approx 1.4$ ps. The tail reaches zero at $t = 10$ ps (see Fig. 4.12).⁹ In the low-energy region with $|p_x| > 0.04$ a.u.,

⁸Here, in contrast to the 3D simulations, the focusing in the third dimension has been ignored. The effect is similar to the dependence on the dimensionality studied in Chapter 3.

⁹In additional simulations, we confirmed that our conclusions do not depend on the precise length of the THz pulse tail.

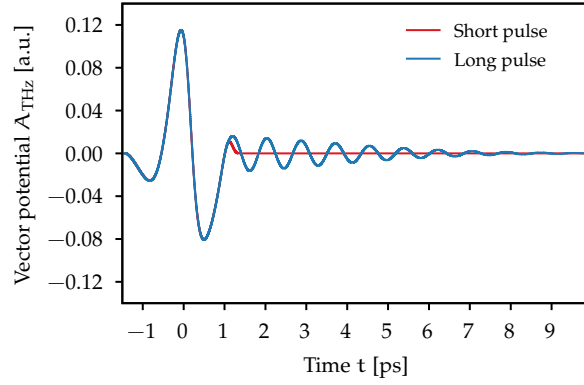


Figure 4.12: Vector potential of the THz waveforms used in the classical simulations for a short pulse or a long pulse with a pulse tail. Figure is adapted from Brennecke *et al.* [322].

all prominent structures are basically unchanged compared to the short pulse result (see Fig. 4.11(b)). As expected, slightly more electrons with very low kinetic energies ($|p_x| < 0.04$ a.u.) are liberated by the pulse tail. However, we find that even the inclusion of a pulse tail cannot fully reproduce the strong enhancement of zero-energy electrons visible in the experiment.

For zero-energy electrons, the detector field of the VMI plays a crucial role [329, 336, 337]. Even for electrons with small positive energies, the static field may induce an additional collision with the ionic core and modifies the dynamics. Thus, the influence of the detector field in the presence of the long-range electron-ion interaction results in deviations from parabolic trajectories that are usually assumed in the interpretation of VMI measurements [43]. The inclusion of the detector field in the classical simulations leads to the p_x -distributions shown in Figs. 4.13(b) and (d) for the short and long THz pulses, respectively. For low-energy electrons (discussed in the previous section), the detector field does not change the types of structures and their intensity is only very weakly altered. The corresponding electron trajectories are approximately parabolic after the end of the THz pulse so that a nontrivial influence of the detector field can be neglected in this region. In contrast, for very low energies ($|p_x| < 0.04$ a.u.), the projected momentum distributions are affected by the detector field and new bright structures appear. Our findings are in agreement with the momentum scale of $p_c = \sqrt{2E_c} \approx 0.028$ a.u. estimated by considering the energy of Eq. (4.2).

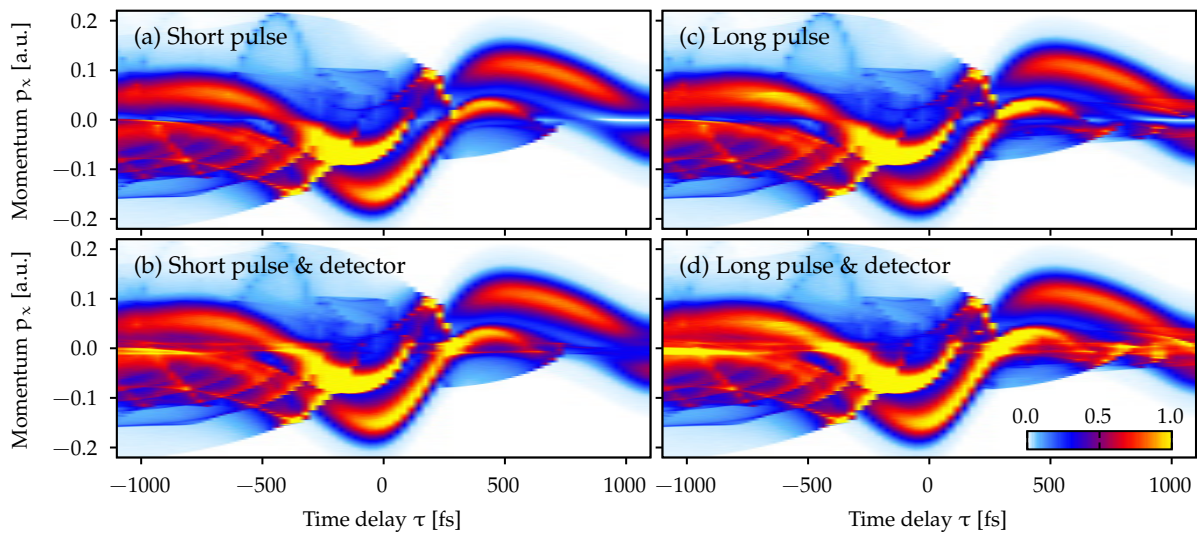


Figure 4.13: Photoelectron momentum distributions along the polarization direction from classical simulations in 2D versus time delay. The distributions are obtained by integration of the 2D momentum distributions over the p_y -component. Panels (a)-(d) show the results for the four possible settings based on a short or long THz pulse and the detector field being included or neglected. Figure is adapted from Brennecke *et al.* [322].

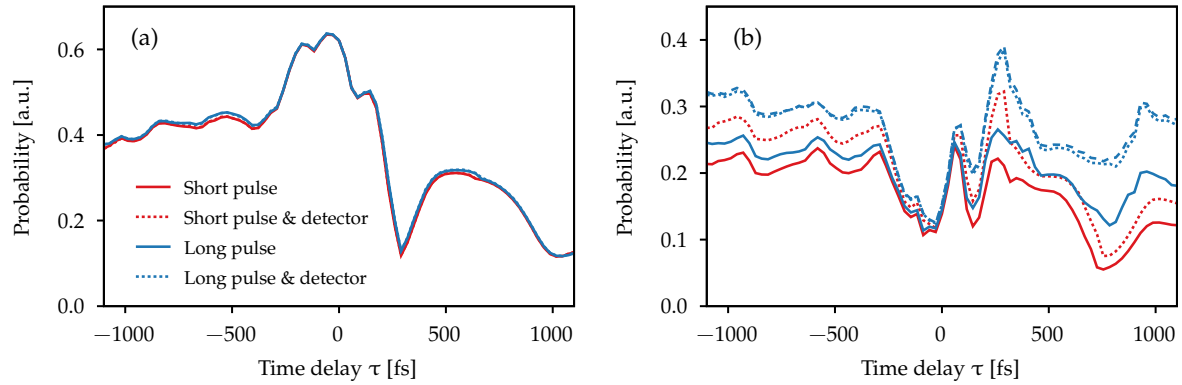


Figure 4.14: Integrated probabilities from 2D classical simulations versus time delay. (a) Probability of low-energy electrons except for zero-energy electrons, obtained by integration over all momenta satisfying $|p_x| > 0.04$ a.u. (b) Probability of zero-energy electrons with $|p_x| < 0.04$ a.u. The solid and dotted lines correspond to the four settings of Fig. 4.13 as indicated in the legend. In addition, the dashed line shows the sum of the classical model result for a long THz pulse and a selected amount of electron freed by the detector field (see main text). Figure is adapted from Brennecke *et al.* [322].

When considering both the THz pulse tail and the detector field of the VMI, the signal of zero-energy electrons is strongly enhanced in the classical simulations. We only discuss further the integrated yield of zero-energy electrons which is shown in Fig. 4.14(b) for the four settings introduced above. For delays around $\tau = 0$ fs, the main part of the THz pulse already liberates efficiently all weakly-bound electrons and, hence, neither the tail nor the detector field leads to additional ionization. Thus, all settings give approximately the same zero-energy yield. In contrast, for large positive and negative delays, both the pulse tail and the detector field give rise to additional zero-energy electrons. We find that in the presence of a long pulse tail the electrons may pick up some additional energy and, hence, a large amount of electrons appear directly at the continuum threshold. Even though only a fraction is ionized by the pulse tail itself, the additional excitation leads to more electrons that are freed by the detector field compared to the short pulse case. Thus, in principle, the enhancement of the zero-energy yield contains information on the population of Rydberg states after the main part of the THz pulse.

For a simplified treatment, we can split the process in two parts: (i) The THz pulse dominates the dynamics as long as it is present and the detector field can be neglected. (ii) After the end of the THz pulse, there is still population left in very weakly-bound states that is subsequently liberated by the detector field. In Ref. [329], it was shown the static field frees approximately *two-thirds* of the electrons with energies $-E_c < E < 0$.¹⁰ For the 2D system, we find that this simple estimate (blue dashed line) reproduces reasonably well the result of a full classical simulation including both the THz pulse tail and the static field (blue dotted line). Hence, we apply the analogous procedure to estimate the amount of zero-energy electrons freed by the detector field in 3D (see blue dashed line in Fig. 4.11(b)). Despite the simple modeling, the predicted variation of the zero-energy yield agrees with the experimental result.

4.7 Conclusion

The strong-field ionization process is often described as a sequence of two steps: (i) preparation of an electron wave packet and (ii) its subsequent light-driven dynamics. Both stages are usually governed by the same electromagnetic field. In this chapter, we provided a theoretical analysis of the natural extension based on two light fields with very distinct properties so that each field is only responsible for one of the steps. The wave packet is created by multiphoton ionization using an infrared pulse with 25 fs duration. Afterwards, wave-packet motion is steered by a carrier-envelope-phase-stable near-single-cycle THz pulse with a cycle length of about 1.3 ps at the central frequency. Hence, the preparation

¹⁰In their derivation, it was assumed that the energy and the cosine of the angle of the initial electron velocity in the x - y -plane are uniformly distributed. For a uniform distribution of the energy and the angle itself, one would instead get a fraction of $2/\pi$ of freed electrons.

time of the wave packet is well localized on the scale of an optical cycle of the THz field. We mostly concentrated on the part of the created electron wave packet at the continuum threshold with energies extending across weakly-bound and continuum states. For these low-energy electrons, the interplay between the Coulomb attraction and the external THz field is of major importance.

To image the electron dynamics, we considered the projections of the photoelectron momentum distributions for a wide range of delays between both pulses. Our TDSE simulations in 3D reproduced well the main features of the experimental results [322] in the low-energy region. The THz-field-free situation is retrieved when the wave packet is created after the main THz pulse has already passed (large positive delays). In contrast, chaotic ionization of Rydberg states is observed when the wave packet is created before the main THz pulse arrives (large negative delays). Importantly, in the intermediate delay range, the subcycle timing of the pulses allowed us to control what physical processes take place ranging from weak deceleration of the outgoing wave packet by the Coulomb attraction to pronounced electron-ion-scattering phenomena. We identified the different regions of electron dynamics by means of a simple trajectory-based model.

For certain delays, recollision-free motion was observed so that the PMDs contain information on the prepared electron wave packet for both continuum states and weakly-bound Rydberg states. Not only the energy distribution, but also the angular structure of the wave packet leaves its imprint on the PMD. In the future, this might be exploited to image the shape of Rydberg wave packets and may enable a deeper understanding of electron trapping in Rydberg states during strong-field ionization in single-color [299, 300] or two-color fields [338, 339].

In addition, we demonstrated that the electron can be driven back by the THz field to the parent ion, resulting in scattering phenomena reminiscent of well-known strong-field processes. In the PMDs, regions of Coulomb-focused electrons and holographic interference patterns were identified. For certain delays, even a high-energy plateau structure is formed by electrons that undergo large-angle scattering. Our findings show a remarkable correspondence between common strong-field dynamics in visible or infrared laser pulses and the electron motion under scaled conditions in THz fields. Therefore, it should be possible to transfer imaging techniques from conventional strong-field and attosecond physics to electron dynamics at the continuum threshold with its much longer time and larger length scales. This could pave the way for the investigation of so far unexplored dynamics of Rydberg electrons in molecules [340, 341] or of multielectron phenomena [307]. For example, in rare gas dimers, the recapture of multiple electrons was observed during dissociation [340]. Since the time scale of dissociation and the THz period are comparable, THz fields could allow for the manipulation of the number of recaptured electrons and their site of recombination.

For electrons at very-low energies, termed zero-energy electrons in this chapter, the TDSE simulations based on a short THz pulse were unable to reproduce the experimental PMDs. We found that the dynamics of these electrons is influenced by a weak, but long tail of the THz pulse that is usually present in experimentally-accessible THz waveforms. Within the trajectory-based model, we identified that the pulse tail directly creates zero-energy electrons and, furthermore, leads to additional excitation within the Rydberg states. After the end of the THz pulse, the static detector field present in experiments in combination with the long-range potential induces additional ionization of those weakly-bound Rydberg states. This two-step mechanism leads to a further enhancement of zero-energy electrons.

For a clean observation of phenomena reminiscent of strong-field processes, the energy gap between the zero-energy electrons and higher-order ATI peaks (from absorption of additional IR photons) should be as wide as possible. In the future, this could be achieved by using visible laser pulses (for example at 400 nm wavelength). Since higher photon energies increase the spacing between the ATI peaks, background effects in the low-energy region are reduced. Furthermore, the use of short circularly-polarized THz pulses and the control of the ATI peak positions via the ponderomotive shift in the IR field could enable us to time resolve the wave-packet creation by means of the attoclock technique [52–54].

Chapter 5

Momentum-Resolved Attoclock

5.1 Introduction

Simple man's picture

The attoclock technique, also known as “attosecond angular streaking”, was introduced by Eckle *et al.* to measure ionization times in strong-field physics [52, 53]. The scheme is based on the idea that the light field deflects the photoelectrons according to their ionization time t_0 to a final momentum \mathbf{p} , i.e., a time stamp is put on the ionization process [52, 213]. In the simple man's model, i.e., when the electron-ion interaction is neglected, an electron starting with vanishing initial velocity \mathbf{v}_0 is mapped by the external field to the final momentum $\mathbf{p} = -\mathbf{A}(t_0)$ [7, 8]. For circularly-polarized cw fields with a vector potential

$$\mathbf{A}(t) = -A_0 \begin{pmatrix} \cos(\omega t) \\ \sin(\omega t) \end{pmatrix}, \quad (5.1)$$

this time-to-momentum mapping is particularly simple. Here, the release times t_0 are uniquely related to the electron's emission direction $\phi_{\mathbf{p}} = \angle(p_x, p_y)$ in the polarization plane by $\phi_{\mathbf{p}} = \omega t_0$. The situation is schematically illustrated in Fig. 5.1(a).

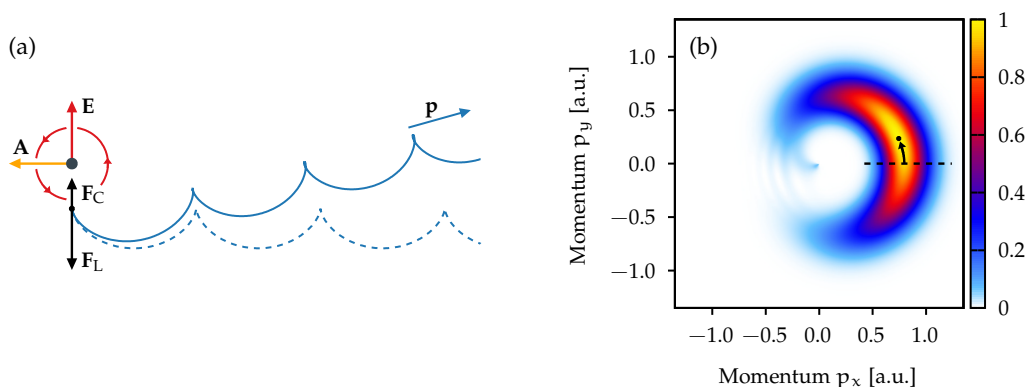


Figure 5.1: (a) Schematic illustration of the attoclock principle in circularly-polarized cw fields. Electrons released at time $t_0 = 0$ appear at a tunnel exit \mathbf{r}_0 (here in $-y$ -direction). If the electrons are afterwards only accelerated by the external electric field (with force \mathbf{F}_L), they follow the dashed trajectory and are finally detected with a momentum $\mathbf{p} = A_0 \mathbf{e}_x$, i.e., at an angle $\phi_{\mathbf{p}} = 0$. However, the force \mathbf{F}_C due to the electron-core interaction perturbs their motion such that the electrons are deflected to an offset angle ϕ_{off} compared to the potential-free case (see the trajectory shown as the solid line). Adapted from Refs. [161, 213]. (b) Observable of the attoclock: slice at $p_z = 0$ through the electron momentum distribution for strong-field ionization of hydrogen in a short circularly-polarized laser pulse. The maximum of the distribution is rotated towards positive angles. The PMD is calculated by numerical solution of the TDSE in 3D for a two-cycle pulse at 800 nm wavelength and $1 \times 10^{14} \text{ W/cm}^2$ intensity.

For atoms ionized by a cw field with circular polarization, there is no preferred emission direction of the electrons due to the cylindrical symmetry of the system. To break the symmetry and induce a clear

maximum in the photoelectron momentum distribution, many implementations use close-to-circularly-polarized laser fields [52–54, 342–345], e.g., slightly elliptically-polarized fields or a short pulse envelope. Here, we choose the laser fields such that the field strength reaches a maximum at time $t = 0$ and the corresponding electric field points in y -direction. In the simple man’s model, electrons liberated at time zero ($t_0 = 0$) are first accelerated in $-y$ -direction and, afterwards, are deflected by the laser field to the positive x -direction. Hence, the electron momentum distribution is expected to maximize at a momentum $\mathbf{p} = -\mathbf{A}(0)$, i.e., along the direction with $\phi_p = 0$.

The influence of Coulomb effects

In the experiment (see for example Refs. [52–54]) or when solving the TDSE (see for example Refs. [346–348]) for close-to-circularly-polarized fields, however, the presence of the ionic potential leads to a distortion of the distribution and an angular offset between the actual maximum of the momentum distribution in the polarization plane and the simple man’s estimate. This measurable offset in the orientation of the distribution is usually the main observable in attoclock experiments and it is termed *global attoclock offset* in the following. As an example, the momentum distribution for ionization of hydrogen with a short two-cycle laser pulse is shown in Fig. 5.1(b). The distribution is clearly “rotated” forward with respect to the handedness of the electric field [161, 346] and a global attoclock offset of $\phi_{\text{off}} \approx 18^\circ$ can be read off.

To interpret the photoelectron momentum distributions and to reveal the underlying physical mechanisms, intuitive theoretical models are required which are based on additional assumptions. Usually, for strong-field ionization, the interpretation heavily relies on trajectory-based approaches (see for example Refs. [52–54, 342]). In a classical two-step picture [7, 8, 210], the ionization step creates an electron wave packet that is represented by an initial probability distribution and characterized by initial conditions (release time, velocity and position). The subsequent acceleration by the laser electric field in the presence of the electron-ion interaction deflects the wave packet to a final momentum distribution. Qualitatively, the Coulomb-induced changes of the electron’s motion and the resulting offset angle relative to the Coulomb-free case are already evident by considering only a single trajectory launched at $t_0 = 0$ (see the blue solid line in Fig. 5.1(a)). More generally, the present Coulomb force of the residual ion leads to a more complicated classical mapping of the release time t_0 to the final momenta \mathbf{p} compared to the simple man’s model. This mapping depends on the tunnel-exit position \mathbf{r}_0 and the initial velocity \mathbf{v}_0 of the electrons. For example, under adiabatic conditions, the Coulomb-induced momentum change of an electron with vanishing initial velocity can be approximated as [210, 347]

$$\Delta\mathbf{p} = \frac{\pi Z}{2\sqrt{2r_0^3 E(t_0)}} \hat{\mathbf{E}}(t_0) = \frac{\pi Z}{(2I_p)^{3/2}} \mathbf{E}(t_0), \quad (5.2)$$

where we used an approximation of the tunneling barrier width as $r_0 = I_p/E(t_0)$. For circularly-polarized fields, the classically-expected radial momentum is given by $p_\perp = A_0 = E_0/\omega$ such that the momentum shift results in a global offset angle

$$\phi_{\text{off}} = \frac{\pi\omega Z}{(2I_p)^{3/2}}. \quad (5.3)$$

Many theoretical studies based on various techniques indeed confirmed that the global attoclock offset is mostly attributed to the influence of the Coulomb attraction on the outgoing electron. Examples of recently used approaches are the analytical R-matrix theory [213], classical-trajectory Monte Carlo simulations [349], the classical backpropagation method [211, 350, 351], a classical Rutherford scattering model [352] and trajectory-free ionization times from Dyson integrals [353]. Hence, the attoclock scheme can be viewed as a concept to probe the interplay between laser field and Coulomb interaction on microscopic scale in a setting where intracycle interference and recollisions are negligible. The comparison of experimentally-accessible photoelectron momentum distributions to theoretical simulations allows us to study strong-field ionization on a very fundamental level and to benchmark its theoretical

modeling.¹ The detailed understanding is a key challenge, because the ionization step is the starting point for more complex processes such as high-harmonic generation, laser-induced electron diffraction or nonsequential double ionization. A summary of several developments in attoclock-like setups and their interpretation can be found in Refs. [55, 56].

Modern developments and the goals of this chapter

Most previous attoclock experiments were performed on noble gases, where multielectron effects [54, 182, 213] and initial states carrying angular momentum [354, 355] may influence the ionization process. For a long time, the simplest target, atomic hydrogen, with its well-known electronic structure defined by the electrostatic potential of the proton was only studied theoretically. Recently, Sainadh *et al.* performed the first attoclock experiment with atomic hydrogen to study tunnel ionization [342, 356], verifying the theoretically-predicted global attoclock offsets quantitatively. Trabert *et al.* conducted a similar experiment, but considered more nonadiabatic ionization conditions by using an elliptically-polarized femtosecond laser pulse with a central wavelength of 390 nm [357]. The experiment shows four above-threshold ionization peaks in the photoelectron energy spectrum. By determining the attoclock offset for each peak separately, an increasing offset as a function of energy was observed. In Section 5.2.3, we use the unique opportunity and provide numerical results from *ab-initio* simulations of the TDSE to benchmark theoretical predictions against experimental findings.

More generally, the attoclock offset depends on the lateral momentum in the polarization plane and on the momentum in the light-propagation direction. Residuals of this momentum dependence were already noted in the theoretical works [358, 359] and also observed in different experimental studies [343–345, 357, 360]. Even though close-to-circularly-polarized fields were used in all mentioned settings, some experiments found increasing attoclock offsets and others decreasing attoclock offsets as a function of energy. In this chapter, we systematically study the *momentum-dependent attoclock offsets*. For close-to-circularly-polarized laser fields, we show that the opposite trends are related to the geometry of the liberated electron wave packets, i.e., to the way how the rotational symmetry of circular polarization is broken. As motivated above, the global attoclock shift is strongly influenced by the tunnel-exit position of the electron such that the attoclock can act as a fine “nano-ruler” [55] that measures the tunnel-barrier width (see Eq. (5.2) and for example Ref. [54]). By analyzing higher-dimensional observables such as the momentum-dependent attoclock offsets, we can investigate the influence of an initial electron velocity on the ionization process. We demonstrate that momentum-dependent attoclock offset is affected by the velocity dependence of the tunnel-exit position.

To study the momentum-dependent offsets, the attoclock setting should first be as simple as possible such that liberation of electrons by an adiabatic tunnel-ionization process is highly desirable. In the adiabatic limit, ionization becomes a quasistatic process and, thus, it is independent of the concrete electric-field shape. However, it is the question how to approach this limit in a simple way. In general, the nonadiabatic corrections depend on the change of the tunneling barrier with time and, thus, on the particular waveform. For circular polarization, the tunnel’s direction rotates, resulting in an offset of the initial perpendicular velocities of the electrons and, thus, in an increased mean of the photoelectron energy compared to the simple man’s model [170]. The additional nonadiabatic velocity can be explained by considering energy transfer to the electron during its under-the-barrier motion [163, 164]. In contrast, for linear polarization, the rotational symmetry around the polarization axis enforces a symmetric distribution of the perpendicular initial velocities. Importantly, the quantum-orbit model results in a nonzero velocity component along the direction of the electric field [162] which vanishes in the vicinity of the peak electric-field strength. In the usually studied elliptically-polarized attoclock configuration, there is a debate on the the transverse [361] and the parallel [362–366] momentum distributions in nonadiabatic ionization.

¹Importantly, this does not mean that the attoclock method is able to select a single correct model. For example, even in a trajectory-based picture, the origin of the offset could be explained by different features such as the effect of Coulomb attraction on the outgoing electron, a time delay relative to the time of peak field strength or an initial velocity of the electron in instantaneous field direction. The interpretation depends always on the concrete assumptions made in a model.

In principle, complications due to nonadiabatic velocity offsets of the transverse distribution could be avoided in the attoclock analysis by studying the dynamics in linearly-polarized fields. However, pure linear polarization is not well suited. As discussed in Chapter 3, for ionization at peak electric-field strength, recollisions in the Coulomb field strongly affect the electron dynamics [78, 79, 81, 82]. Additionally, intracycle interference distracts the signal [71, 72] and prevents an interpretation of the distribution by means of a single ionization time. To avoid these problems, the strong-field dynamics can be studied in an alternative waveform introduced by Eicke *et al.* [359]. They used a specific bicircular ω - 2ω field composed of two counter-rotating fields (as introduced in Section 3.4.4) such that the electric field resembles linear polarization three times per optical cycle of the fundamental field. At the same time, the field shape provides a time-to-momentum mapping similar to the conventional attoclock [359, 367]. For this particular “bicircular” or “quasilinear” attoclock, the Coulomb attraction on the outgoing electron induces a shift of the electron momentum distribution along the instantaneous field direction [359]. Similar to pure linear polarization, the setting is nearly isotropic in the directions perpendicular to the instantaneous field in the vicinity of the peak electric-field strength. Thus, the bicircular field provides a clean setup to investigate the dependence of the attoclock shift on the electron’s initial velocity. The momentum-dependent attoclock offsets for the quasilinear field are studied in Section 5.3.

In the regime of adiabatic ionization, the picture of tunneling through a potential barrier is most useful. In a stationary one-dimensional scenario, the zero-kinetic-energy principle naturally dictates the tunnel-exit position [368]. In higher spatial dimensions, the choice of the tunneling coordinate is not unique and ambiguities already arise. For a Coulomb potential, the separation of Schrödinger’s equation in parabolic coordinates is possible and leads to the TIPIS tunnel-exit position [54, 260, 347] (see Eq. (2.48)). The TIPIS result differs from the tunnel exit of the field-direction model based on Cartesian coordinates [77, 347]. For a time-dependent barrier in a nonadiabatic ionization scenario, the situation is even more complex, because the energy is not conserved anymore during tunneling [163]. The classical backpropagation method [211, 350, 351] offers an approach to extract characteristic features of the ionization process from *ab-initio* simulations. Within this framework, the ionization step is first treated quantum mechanically. The ejected electron wave packet is then used to define a swarm of classical trajectories that are propagated backwards in time until a tunneling criterion is met. At that time, the observables at the tunnel exit are extracted. In contrast to the original work [211, 350, 351], we propose a momentum-space-based implementation to study the relation between initial velocity and initial position of the electrons. This (independent) approach on the tunneling characteristics is used to support our understanding of the momentum-dependent attoclock shifts.

A major goal of this chapter is to provide a more complete picture of existing attoclock implementations and, especially, to address their limitations and problems in their interpretation. The first part of this chapter considers results for the attoclock with close-to-circularly-polarized fields and is based on joint work with the group of Reinhard Dörner in Frankfurt, especially Daniel Trabert and Sebastian Eckart. Trabert *et al.* performed the attoclock experiment on atomic hydrogen using the COLTRIMS technique whereas we provided results from TDSE simulations for the publication [357]. Inspired by discussions with Sebastian Eckart, the momentum-resolved bicircular attoclock was studied. Parts of this work are published in Ref. [369].

5.2 Attoclock using close-to-circularly-polarized fields

We begin to study the momentum-dependent attoclock offsets by considering the commonly-used close-to-circularly-polarized attoclock settings. Here, we focus on three important cases:

- *Circularly-polarized pulses with very short envelope* represented by a vector potential

$$\mathbf{A}(t) = -A_0 \begin{pmatrix} \cos(\omega t) \\ \sin(\omega t) \end{pmatrix} \cos^4 \left(\frac{\omega t}{4} \right). \quad (5.4)$$

These pulses were used in various theoretical studies, e.g., in Refs. [213, 350, 353].

- *Two-color co-rotating bicircular fields* represented by a vector potential

$$\mathbf{A}(t) = -A_0 \frac{2}{2 + \sqrt{R}} \left[\begin{pmatrix} \cos(\omega t) \\ \sin(\omega t) \end{pmatrix} + \frac{\sqrt{R}}{2} \begin{pmatrix} \cos(2\omega t) \\ \sin(2\omega t) \end{pmatrix} \right]. \quad (5.5)$$

For small intensity ratios R of the two colors, the perturbation by the second-harmonic field induces a single maximum of the electric field and also of the vector potential. This field shape was recently used in Ref. [344].

- *Elliptically-polarized fields* with ellipticity ζ represented by a vector potential

$$\mathbf{A}(t) = -A_0 \begin{pmatrix} \cos(\omega t) \\ \sin(\omega t)/\zeta \end{pmatrix}. \quad (5.6)$$

For $|\zeta| \rightarrow 1$, a circularly-polarized field is retrieved. For $|\zeta| \neq 1$, the semi-major axis is aligned along the y -axis. Elliptically-polarized fields were used in the original attoclock implementation [52, 53] and also in the recent experiments on atomic hydrogen [342, 357].

For these choices, the Lissajous figures of the negative vector potentials at 800 nm fundamental wavelength are shown as black dashed lines in Figs. 5.2(a). The definitions ensure that the vector potentials at $t = 0$ are the same, i.e., $\mathbf{A}(0) = -A_0 \mathbf{e}_x$. A gray circle with radius $A_0 \approx 0.66$ a.u. indicates the negative vector potential of pure circular polarization with 800 nm wavelength and 1×10^{14} W/cm² intensity.

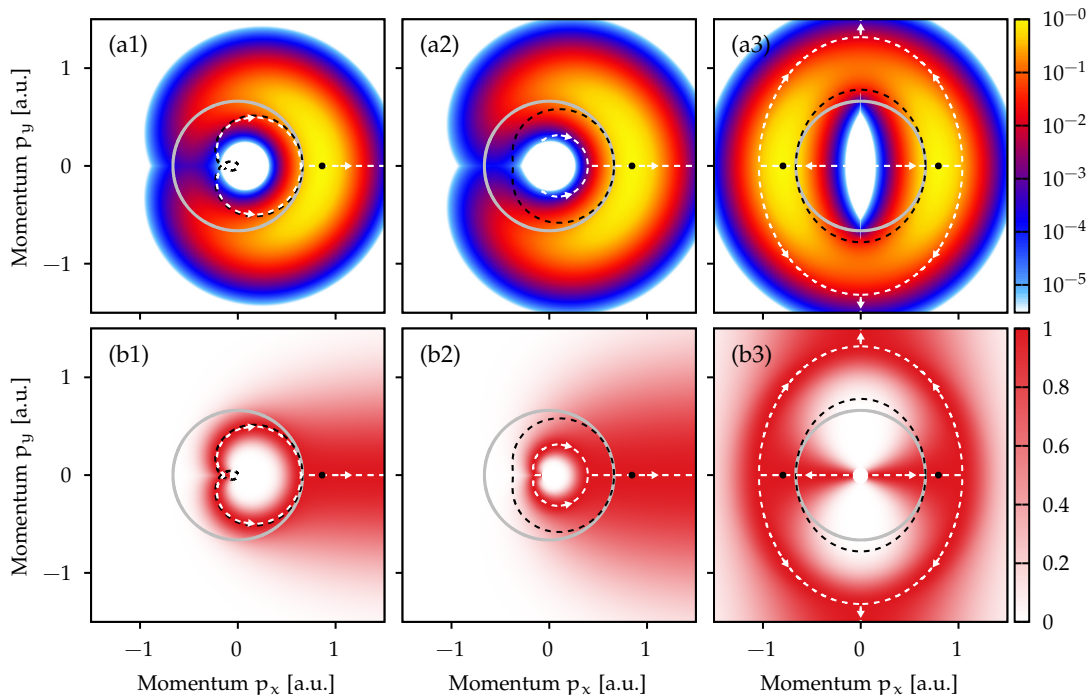


Figure 5.2: (a) Photoelectron momentum distributions for strong-field ionization of atomic hydrogen at 800 nm fundamental wavelength modeled by strong-field approximation using a saddle-point method. (b) Corresponding distributions individually normalized for each radial momentum p_{\perp} . Results for a short circularly-polarized pulse (5.4) are shown in panels [(a1),(b1)], for a co-rotating bicircular field (5.5) with $R = 0.1$ in panels [(a2),(b2)], and for an elliptically-polarized field (5.6) with $\zeta = 0.85$ in panels [(a3),(b3)]. The negative vector potentials are depicted as black dashed lines. The gray thick line marks a circle of radius $A_0 \approx 0.66$ a.u. The white dashed lines indicate the positions of angular offsets $\phi_{\text{off}}(p_{\perp})$ for each radial momentum p_{\perp} (see main text).

5.2.1 Geometry of the electron wave packets

Before including the effects of Coulomb attraction on the momentum distributions, we first explore the geometry of the liberated electron wave packets in the strong-field approximation.² Slices at $p_z = 0$ through the PMDs for ionization of atomic hydrogen are shown in Figs. 5.2(a). For short circularly-polarized pulses and the bicircular waveform, the single maximum of the electric-field strength is reflected as a unique global maximum in the PMD marked with a black dot. In contrast, the elliptically-polarized field is invariant under a time shift by $T_\omega/2$ and a simultaneous rotation by 180° . This dynamical two-fold symmetry is carried over to the PMD. Two equivalent maxima appear that are attributed to the two instants of maximal field strength within an optical cycle (at $t = 0$ and $t = T_\omega/2$). Hence, for elliptical polarization, we restrict ourselves to the half plane with $p_x \geq 0$ linked to one half cycle of ionization times. As expected, for all three field shapes, the global maxima of the PMDs are on the p_x -axis and are attributed to ionization at the time of peak electric-field strength.

For further characterization of the PMD's geometry, in addition to the global attoclock maximum, we analyze the maximum's position $\phi_{\text{off}}(p_\perp)$ for each fixed radial momentum p_\perp separately. To improve the visibility of the angular distributions for less probable p_\perp , panels (b) of Fig. 5.2 show the distributions normalized to maximum value one at each radial momentum p_\perp individually. For elliptical polarization, Figure 5.3(a) shows 1D slices through the PMD as a function of the angle ϕ_p at various fixed radial momenta p_\perp . In agreement with Ref. [210], there is only a single maximum at $\phi_{\text{off}} = 0^\circ$ for small momenta p_\perp . However, when going towards larger p_\perp , the maximum gets broader and it splits in two maxima at $p_\perp \approx 1.05$ a.u. (here a bifurcation occurs). The maximum's angle changes continuously from 0° to $\pm 90^\circ$. For the branch with increasing angle, the maximum's angle $\phi_{\text{off}}(p_\perp)$ is shown in Fig. 5.3(b) as a function of p_\perp . Translated back into Cartesian coordinates, positions of the maxima at fixed momenta p_\perp are reprinted in Fig. 5.2 as white dashed lines.³

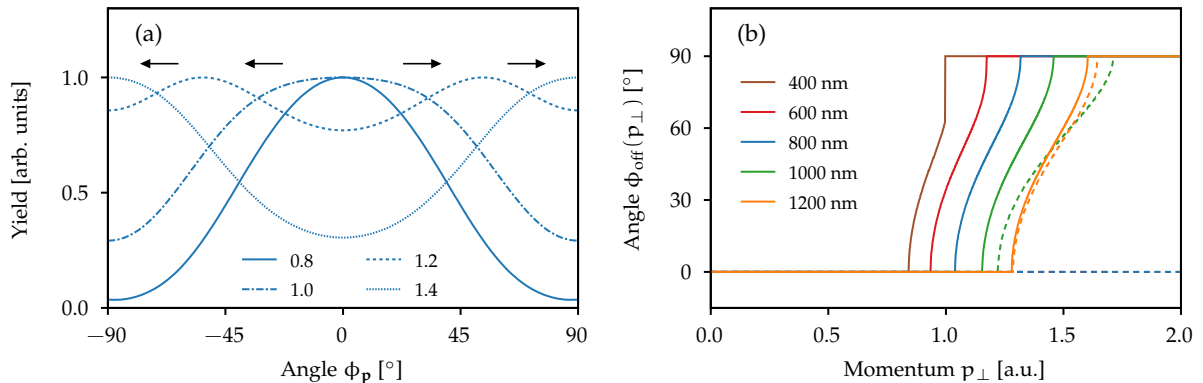


Figure 5.3: Maximum splitting of the angular distribution for elliptical polarization: (a) 1D slices through the PMD of Fig. 5.2(a3) for fixed radial momenta p_\perp given in the legend in a.u. Each distribution is individually normalized. When going from small p_\perp towards larger p_\perp , the maximum of the distribution is split in two maxima. (b) Offset angle $\phi_{\text{off}}(p_\perp)$ as a function of p_\perp : SFA results (solid lines) and results from an ADK-based model (dashed lines). Shown are the results for five different wavelengths indicated in the legend and for the same intensity as in Fig. 5.2. The results of the ADK-based model for 400 nm to 800 nm wavelength are on top of each other.

In the vicinity of the global maximum, the angles $\phi_{\text{off}}(p_\perp)$ vanish for the three field shapes. However, when going to small p_\perp and large p_\perp , the three waveforms show different trends. As discussed above, the maximum is split into two at large p_\perp for elliptical polarization whereas this branching occurs at small p_\perp for short circularly-polarized pulses and for the bicircular waveform. Even though the SFA distributions are mirror symmetric in p_y , it is not guaranteed that there is a maximum on the p_x -axis for every momentum p_\perp . For angles $\phi_{\text{off}}(p_\perp) \neq 0$, the associated real parts of the saddle-point times are not equal to zero anymore. Since these nonzero offset angles already exist in SFA, it is questionable whether they should be called ‘‘attoclock’’ or ‘‘deflection’’ angles.

²We apply the saddle-point approximation to the KFR amplitude and include only the contribution (2.45) of a single saddle-point time t'_s for each final momentum \mathbf{p} . Therefore, Fig. 5.2 does not exhibit any ATI rings.

³For a given p_\perp , several equivalent maxima may appear due to the symmetry of the PMDs.

The use of polar coordinates in the attoclock analysis is inspired by the rotational symmetry in pure circular polarization and the resulting time-to-angle mapping. However, to observe attoclock offsets, the introduced waveforms break this symmetry and, thus, the time-to-momentum mapping as well as the geometry of the PMDs changes. In general, the PMDs roughly follow the negative vector potential $-\mathbf{A}(t)$. For elliptical polarization, the vector potential bends (in the vicinity of $t = 0$) outwards compared to a circle of constant radius A_0 . Hence, already in a simple man's model, radial momenta with $p_\perp > A_0$ are preferred for angles $|\phi_p| \gg 0$. As a result, when using polar coordinates for the final momentum distribution, it is plausible that the offset angles are nonzero at large p_\perp . In contrast, for the short circularly-polarized pulses and the bicircular waveform, the vector potential bends inwards compared to a circle and, hence, the opposite behavior is observed (here the splitting occurs at small p_\perp). In elliptical polarization, the problem of nonvanishing angles $\phi_{\text{off}}(p_\perp)$ could be partially cured by analyzing the PMD in symmetry-adapted coordinates and determining the maximum's positions along lines of constant generalized radii [362]. For our analysis, however, we keep polar coordinates and view the angle dependence $\phi_{\text{off}}(p_\perp)$ as one possible way to characterize the geometry of the wave packet.⁴

In the remaining part of this section, we quantify the branching of the offset angle, i.e., a transition of the angles from $\phi_p = 0^\circ$ to $\phi_p = 90^\circ$, for elliptical polarization and consider the influence of nonadiabaticity. The splitting of the maximum can be studied by comparing the signal along the p_y -axis (at $\phi_p = 90^\circ$ corresponding to $t_0 = T_\omega/4$) to the p_x -axis (at $\phi_p = 0^\circ$ corresponding to $t_0 = 0$).⁵ Using a two-step model as in Section 2.4 based on the adiabatic ADK rate (2.3), the ratio at fixed p_\perp is given by

$$\frac{w(p_\perp, \phi_p = 90^\circ)}{w(p_\perp, \phi_p = 0^\circ)} = \exp\left(-\frac{\kappa}{E_0} \left(\frac{2}{3} k^2 \left(\frac{1}{\zeta} - 1\right) + \left[\frac{(p_\perp - A_0/\zeta)^2}{\zeta} - (p_\perp - A_0)^2\right]\right)\right). \quad (5.7)$$

Splitting of the maxima occurs when the ratio crosses one, i.e., when the exponent has a zero crossing. This is the case, if the following condition is fulfilled

$$A_0 \geq \sqrt{\frac{2}{3}} \zeta \kappa. \quad (5.8)$$

For hydrogen with $\kappa = 1$ a.u. and an ellipticity of $\zeta = 0.85$, a splitting of the maxima should only appear for $A_0 \gtrsim 0.75$ a.u. For sufficiently adiabatic conditions, the angles $\phi_{\text{off}}(p_\perp)$ of the ADK-based model reproduce the SFA result well (see Fig. 5.3(b)). However, the SFA predicts a maximum splitting for all considered wavelengths. The difference compared to the ADK-based result is mostly caused by nonadiabatic corrections of the initial lateral velocity distribution [170, 354, 370–372]. To first order in the Keldysh parameter, the most probable initial velocity (at fixed release time t_0) is shifted by [161]

$$\Delta \mathbf{v}_0 = -\frac{I_p}{3E^2(t_0)} (\dot{\mathbf{E}}(t_0) - (\dot{\mathbf{E}}(t_0) \cdot \hat{\mathbf{E}}(t_0)) \hat{\mathbf{E}}(t_0)). \quad (5.9)$$

As a result, for elliptical polarization, the radial distribution at $\phi_p = 90^\circ$ is further shifted outwards by nonadiabatic effects compared to the radial distribution at $\phi_p = 0^\circ$. This explains qualitatively that there is also a transition of $\phi_{\text{off}}(p_\perp)$ towards 90° for large p_\perp in the SFA for small wavelength.⁶

5.2.2 The influence of the Coulomb potential

To go beyond the SFA and include the influence of the ionic potential, we perform numerical simulations of the TDSE for a bare Coulomb potential. To this end, we use the pseudospectral method and include

⁴This choice works well when ATI rings are present and it is the same as in the previous experimental studies [343–345, 357].

⁵The radial distribution along the p_y -axis is located at larger p_\perp compared to the distribution along the p_x -axis due to a larger magnitude of the associated vector potential $|\mathbf{A}(T_\omega/4)| > |\mathbf{A}(0)|$. On the other hand, the ionization rate is higher at the maximum of the electric-field strength at $t = 0$ compared to $t = T_\omega/4$. This interplay determines whether branching occurs.

⁶In the Supplemental Material of Ref. [357], we present a systematic study of the wavelength dependence and compare results from TDSE simulations to semiclassical models. In agreement with the results of this section, the inclusion of nonadiabatic effects in the initial distribution is important to reproduce the offset angles ϕ_{off} of about 90° for large perpendicular momenta p_\perp (that are visible in the TDSE simulations for all studied wavelengths).

spherical harmonics up to $l_{\max} = 384$. More computational details are presented in the next section. For the simulations, the elliptically-polarized field and the bicircular field are augmented by a \cos^2 envelope of ten cycles total duration. The resulting distributions are averaged over eight CEPs between 0 and 2π . Figure 5.4 shows the PMDs for the three field shapes. In order to avoid the influence of ATI rings on the renormalized distributions of panels (b2) and (b3), these distributions were first averaged over an energy interval ω .

Even though the overall structure of the PMDs from TDSE is quite similar compared to the SFA results, the reflection symmetry in y -direction is broken [210, 373]. Importantly, the Coulomb-induced deflection of the electrons is not a uniform rotation of the momentum distribution. For example, in an adiabatic classical picture, the final momentum is shifted in the direction of the instantaneous electric field (see Eq. (5.2)). Moreover, in a trajectory-based description, the deflection in momentum space depends on the ionization time and the initial velocity. For radial momenta p_{\perp} with a single maximum of their angular distribution in the SFA, the maximum's angle is displaced forward with respect to the handedness of the electric field, in analogy to the global attoclock offset. However, when the angular distribution in the SFA has two maxima in the interval $[-90^{\circ}, 90^{\circ}]$, the Coulomb effects lead to a selection of one dominant maximum [210, 373].

The comparison of the PMDs from SFA (see Fig. 5.2) and from TDSE (see Fig. 5.4) shows that the overall dependence of the maximum's angle $\phi_{\text{off}}(p_{\perp})$ on the radial momentum p_{\perp} has a similar trend (see white dashed lines). Depending on the field shape, large angles are observed either at small p_{\perp} (panels (a1),(a2)) or at large p_{\perp} (panel (a3)). This explains the discrepancy of decreasing angles $\phi_{\text{off}}(p_{\perp})$ as a function of p_{\perp} for short circularly-polarized fields [353] as well as for co-rotating bicircular fields [344] and the increasing angles $\phi_{\text{off}}(p_{\perp})$ as a function of p_{\perp} for elliptical polarization [343, 345, 357]. We find that, for either small or large p_{\perp} , the angles are fixed by the geometric constraints and relatively insensitive to the ionic potential. In the intermediate region, especially close to maximum splitting in the SFA, the PMD is extremely flat and, thus, small perturbations can induce large angular offsets. As a result, the maximum's angle $\phi_{\text{off}}(p_{\perp})$ is very sensitive to the ionic potential.

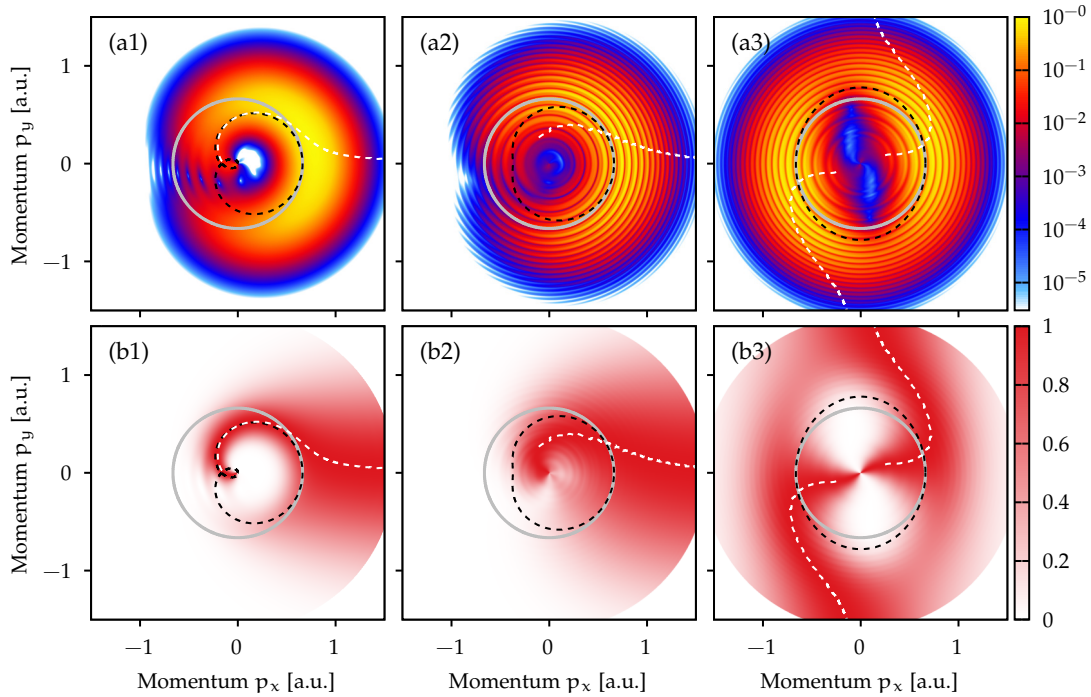


Figure 5.4: Comparison of slices at $p_z = 0$ through the photoelectron momentum distributions of hydrogen for three different waveforms analogous to Fig. 5.2, but calculated by numerical solution of the TDSE in 3D. For the co-rotating bicircular field and the elliptically-polarized field, ten-cycle pulses with \cos^2 envelope are used and the results are averaged over eight CEP values.

5.2.3 Nonadiabatic ionization of atomic hydrogen

Atomic hydrogen with its single electron is the simplest system to study light-matter interaction. Since multielectron effects are absent, the electron only experiences the laser field and the well-defined electrostatic potential $V(r) = -1/r$ of a proton. As a result, the hydrogen atom is *the* most-frequently discussed benchmark system in theoretical studies and textbooks. However, experiments on the strong-field ionization of atomic hydrogen are rare, because the preparation of hydrogen atoms out of molecular H_2 and the separation of atomic events from those resulting from nondissociated H_2 is quite challenging. Sainadh *et al.* [342, 356] conducted the first attoclock experiments to study adiabatic ionization of atomic hydrogen. More recently, Trabert *et al.* [357] used an attoclock geometry based on elliptically-polarized pulses to investigate nonadiabatic ionization. To this end, atomic hydrogen was irradiated using femtosecond laser pulses at a central wavelength of 390 nm and a peak intensity of 1.4×10^{14} W/cm². The conditions correspond to a Keldysh parameter of about 3. The aim of this section is to benchmark these experimental results against numerical simulations of the TDSE and to further explore the geometry of the electron momentum distributions. All shown experimental data are kindly provided by Daniel Trabert *et al.* [357].

Computational details

To calculate photoelectron momentum distributions in the dipole approximation, we solve numerically the TDSE in the single-active-electron approximation by means of the pseudospectral method in length gauge as described in the Appendix A.2.1. For the nonadiabatic conditions, the main part of the PMD is located at small energies and, hence, a major challenge is to determine accurately the signal in this region. To this end, we numerically propagate the wave function till the end of the laser pulse and calculate the photoelectron momentum distribution (2.19) by projection on the exact scattering states of the Coulomb potential.⁷ Elliptically-polarized laser pulses centered at a wavelength of 390 nm with an ellipticity $\zeta = 0.85$ and a \cos^2 envelope of the vector potential are used. Most of the results are calculated for a total duration of 20 optical cycles. The PMDs are averaged over four CEPs between 0 to 2π . In an experiment, the intensity spatially varies over the laser focus. The measured electron momentum distributions contain the contributions of the whole laser focus. To include this focal-volume-averaging effect, we follow the scheme introduced in the Appendix A.2.4 and assume a Gaussian beam profile. If not stated otherwise, we use a peak intensity in the focus of $I_{\text{peak}} = 1.4 \times 10^{14}$ W/cm² and perform calculations for 27 intensities ranging from 0.1×10^{14} W/cm² to 1.4×10^{14} W/cm².

During the time propagation with a time step of $\Delta t = 0.08$ a.u., the wave function is represented in spherical coordinates and its angular dependence is expanded in spherical harmonics. For most calculations, a maximal orbital angular momentum $l_{\text{max}} = 192$ is used. The radial coordinate is discretized using $N_r = 1000$ points on a nonuniform grid (A.43) with an extension $r_{\text{max}} = 900$ a.u. and parameters $L = 300$ a.u., $\beta = 0.25$.

Results

Four ATI rings are clearly visible in the projection of the electron momentum distribution onto the polarization plane shown in Fig. 5.5(a). These are reflected as peaks that are approximately spaced by the photon energy of 3.18 eV in the electron energy spectrum (see Fig. 5.5(b)). In order to calibrate the laser intensity, the experimental energy distribution was compared to the theoretical simulations. The best agreement was found for the used peak intensity of $I_{\text{peak}} = 1.4 \times 10^{14}$ W/cm². In general, the experimental distributions and in particular the relative signal strength of the different peaks are well reproduced by the TDSE results. The largest deviation of about 15% of the emission strength is visible for the peak centered at ≈ 4 eV. To explore the origin of this deviation, we performed additional simulations for a

⁷A comparison of the global attoclock offsets from our implementation to previous works [213, 352] is shown for short circularly-polarized laser pulses in Fig. A.8 of the appendix.

changed beam profile of the laser focuses, i.e., a modified weighting of the PMDs for the different intensities, and also for different pulse envelopes. Both properties can change the energy distributions on the order of 10%, but are typically not precisely known in experiments. The pulse duration in the simulations differs from the experiment: 50 fs (FWHM in intensity) pulse are used in the measurements whereas pulses of 20 cycles total duration (corresponding to about 9.5 fs FWHM) are used for most simulations. However, for total pulse lengths in the range between 10 and 30 optical cycles, we confirmed that all presented quantities do not significantly change.

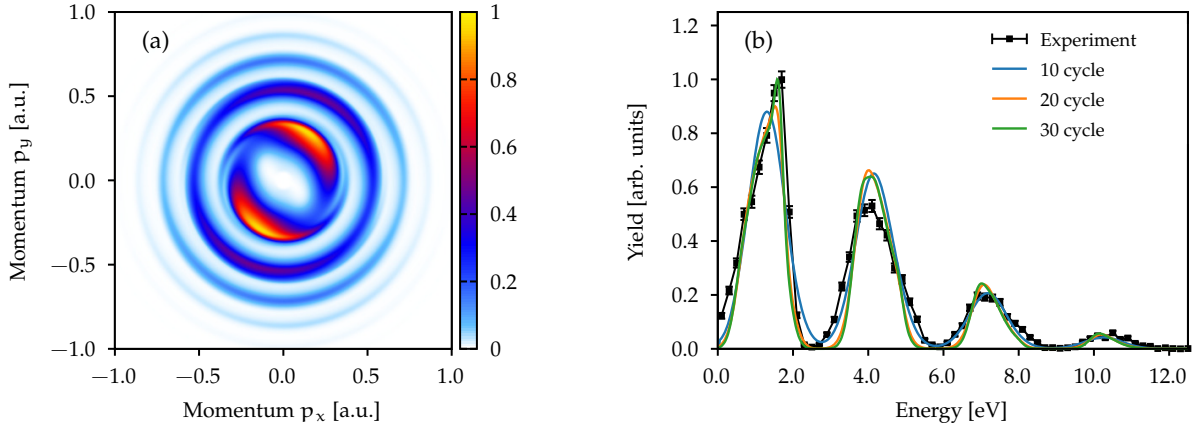


Figure 5.5: (a) Photoelectron momentum distribution projected onto the polarization plane for ionization of atomic hydrogen by elliptically-polarized pulses ($\zeta = 0.85$) at 390 nm central wavelength calculated by numerical solution of the TDSE in 3D for a total pulse duration of 20 cycles. A peak intensity of $I_{\text{peak}} = 1.4 \times 10^{14} \text{ W/cm}^2$ is used for the focal-volume averaging. (b) Simulated energy spectra for three different pulse durations are compared to the experimental result of Trabert *et al.* [357]. Figure is adapted from Trabert *et al.* [357].

An angular modulation of the signal on the ATI rings due to the finite ellipticity is clearly visible in the projected PMD (see Fig. 5.5(a)). For a quantitative comparison, we calculate the angular distributions $w(\phi)$ by integration of the projected PMD over a ring around each ATI peak. For the different ATI peaks, the theoretically-simulated angular distributions are in quantitative agreement with the experimentally-measured ones (see Fig. 5.6). The experimental uncertainty is the largest for the highest energy, where 153 events were only detected. The major axis of the polarization ellipse is again aligned along the y-axis. The four angular distributions show two distinct minima and maxima, but their modulation depth depends on the energy. The most probable emission angles increase with energy. To avoid complications due to experimental noise, the offset angles are not directly determined by maximum's search. Instead, the angular distribution for each peak is approximated using a Fourier series

$$w(\phi) = \frac{B_0}{2} + \sum_{k=1}^N B_k \cos(k(\phi - \phi_k)). \quad (5.10)$$

The coefficients B_k and ϕ_k can be easily calculated by using the sine-cosine-form of the Fourier series. The coefficients B_k vanish for odd k due to the two-fold symmetry of the signal after CEP averaging. Typically, the second-order coefficients dominate the angular dependence such that the offset angles can be approximated as $\phi_{\text{off}} \approx \phi_2$. For the different ATI peaks, the angles ϕ_{off} are shown in Fig. 5.7 as a function of their radial momentum p_{\perp} . The quantitative comparison of the focal-volume-averaged results presented in panel (b) again underlines the excellent agreement between TDSE simulation and experimental measurement. The largest deviation of about 6° between TDSE and experiments appears for the ATI at $p_{\perp} \approx 0.53 \text{ a.u.}$ However, as discussed in the previous section, the angular distribution has the weakest modulation depth in this intermediate energy region such that the angular distribution is most susceptible to perturbations (see Figs. 5.3(a) and 5.4(b3)). Thus, in the simulations, the offset angle for the ATI peak at $p_{\perp} \approx 0.53 \text{ a.u.}$ can be changed by a few degrees by the ellipticity, the considered envelope of the laser pulses or the beam profile in the laser focus.

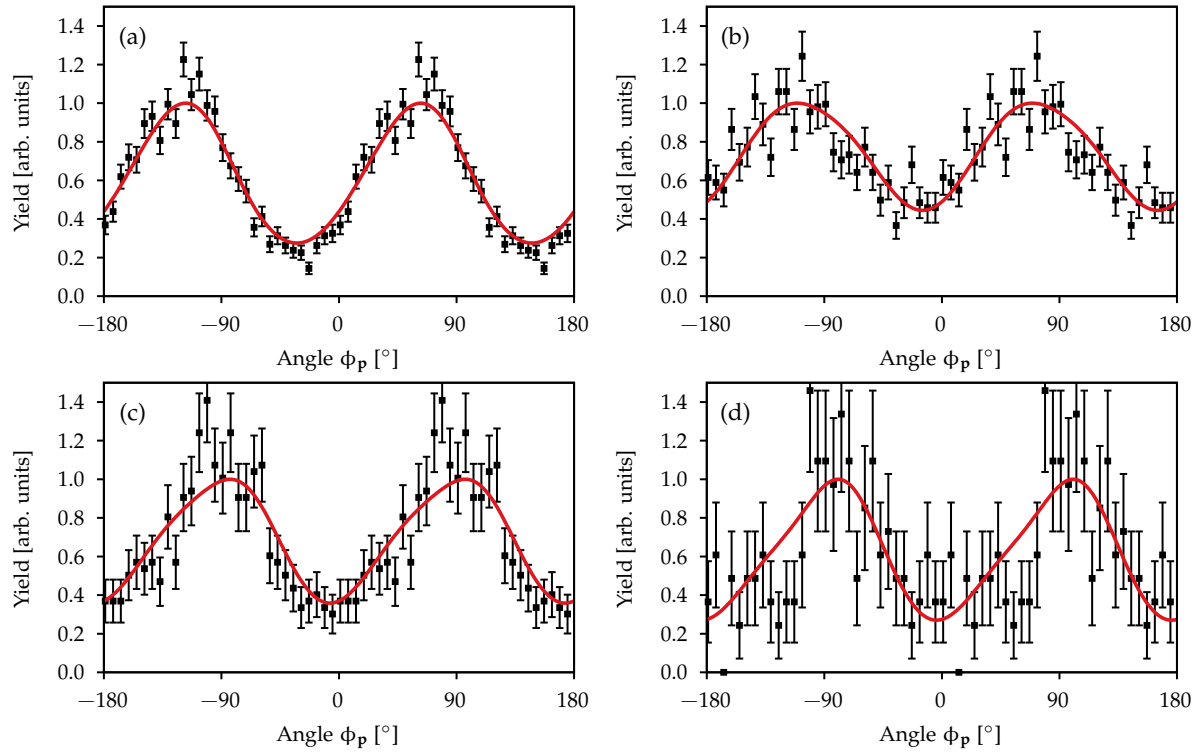


Figure 5.6: Angular distributions for various ATI peaks obtained by integration of the projected PMD of Fig. 5.5(a): TDSE results (red lines) and experimental results provided by Trabert *et al.* [357] (black dots). Panels (a)-(d) show the results for the peaks centered at $p_{\perp} \approx 0.30$ a.u., $p_{\perp} \approx 0.53$ a.u., $p_{\perp} \approx 0.71$ a.u. and $p_{\perp} \approx 0.86$ a.u., respectively. The TDSE distributions are normalized to maximum signal of one. The experimental data are normalized to the same integral as the theory results.

Repeating the steps above for simulations at fixed intensity, i.e., without focal-volume averaging, we find the offset angles ϕ_{off} shown in Fig. 5.7(a). For large radial momenta, the maximum's positions are again mostly determined by the geometrical constraints of the electron wave packet in elliptical polarization, i.e., the angles are close to 90° independently of the intensity. However, the offset angles decrease monotonically as a function of intensity for the lowest-order peaks. Qualitatively, the same intensity dependence was observed for short circularly-polarized pulses in Ref. [352]. In a Rutherford (half) scattering scenario [352], the trend is explained by a decreasing final radial momentum E_0/ω of the electron. In our case, however, the radial momentum p_{\perp} is nearly constant for a given ATI peak.

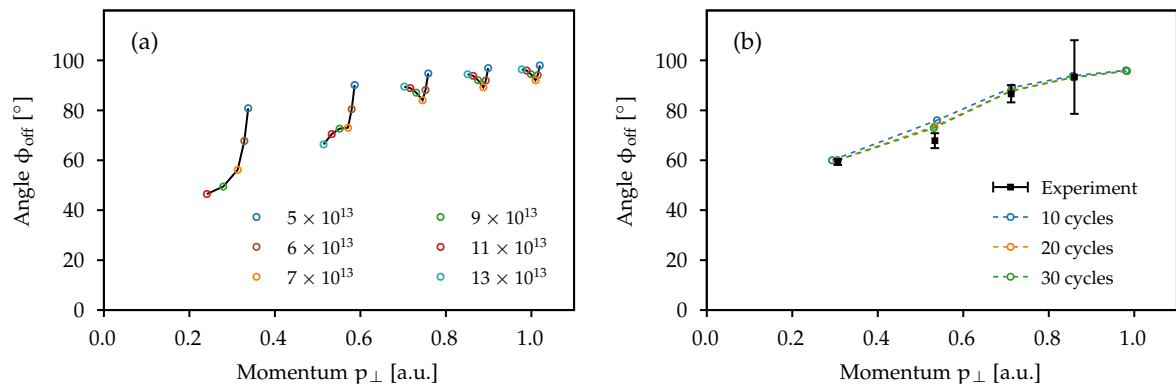


Figure 5.7: Offset angles ϕ_{off} extracted from angular distributions for different ATI peaks shown as a function of their radial momenta p_{\perp} . (a) TDSE results for fixed intensity of the laser pulses indicated in the legend in W/cm^2 . (b) Comparison of focal-averaged TDSE results for three pulse durations and the experimental result provided by Trabert *et al.* [357]. Figure is adapted from Trabert *et al.* [357].

In an experiment, contributions from the whole laser focus are collected. Since the effective intensity changes over the focus, we include this effect in the simulations by adding up incoherently the weighted distributions for fixed intensities I (see Appendix A.2.4). Here, we explore the influence of this focal-volume averaging on the final PMD. The relative weight is determined by the spatial volume occupied by a given intensity I in the laser focus, i.e., more precisely by the derivative $-\frac{\partial V(I_{\text{peak}}, I)}{\partial I}$ of the cumulated volume function $V(I_{\text{peak}}, I)$. For each given intensity I , the weighted radial momentum distributions in the polarization plane from TDSE simulations are shown in Fig. 5.8(a), i.e., the product of the bare TDSE result times the volume weighting factor. The integration over the intensity I would result in the focal-volume-averaged radial distribution. Due to the ponderomotive shift of the effective ionization potential [172, 374], the ATI peaks move towards smaller p_{\perp} with the increasing intensity. The lowest-order peak corresponding to five absorbed photons experiences a channel closing around the peak intensity of $1.4 \times 10^{14} \text{ W/cm}^2$, i.e., five photons are not sufficient to overcome the field-dressed ionization threshold. The contributions of the different intensities to the several ATI peaks (the integrated signal over the peaks) are shown in Fig. 5.8(b). The higher-order peaks ($n \geq 6$) are dominated by intensities around $\approx 1.2 \times 10^{14} \text{ W/cm}^2$. However, the channel closing of the five-photon peak leads to strong contributions of lower intensities, i.e., this peak is influenced by a broad range of intensities.

Even for the laser pulses of the simulations at fixed intensity, the energy bandwidth of the ATI peaks is much smaller than the ponderomotive energy shifts when going from the smallest intensities with finite contribution to the peak intensity. As a result, for the focal-volume-averaged data, the different radial momenta p_{\perp} of an ATI peak can be attributed to different intensities within the laser focus [374]. However, as shown above, the angular distributions and their offset angles strongly depend on the intensity. To improve the visibility, the angular distribution for each radial momentum p_{\perp} in the polarization plane is separately normalized to one (see Fig. 5.8(c)). For the two lowest ATI peaks, the offset angles $\phi_{\text{off}}(p_{\perp})$ increase indeed as a function of p_{\perp} when going from the center towards higher energies within a peak. The same trend was also observed in the experiment [357]. The momentum-dependent maximum's position can be explained by considering the offset angles of Fig. 5.7(a) for calculations at fixed intensities between $3 \times 10^{13} \text{ W/cm}^2$ and $13 \times 10^{13} \text{ W/cm}^2$ (see black dots). When going to higher order peaks, the observation is less clear for two reasons: (i) The dependence of $\phi_{\text{off}}(p_{\perp})$ on the intensity is weaker and (ii) a smaller range of intensities contributes.

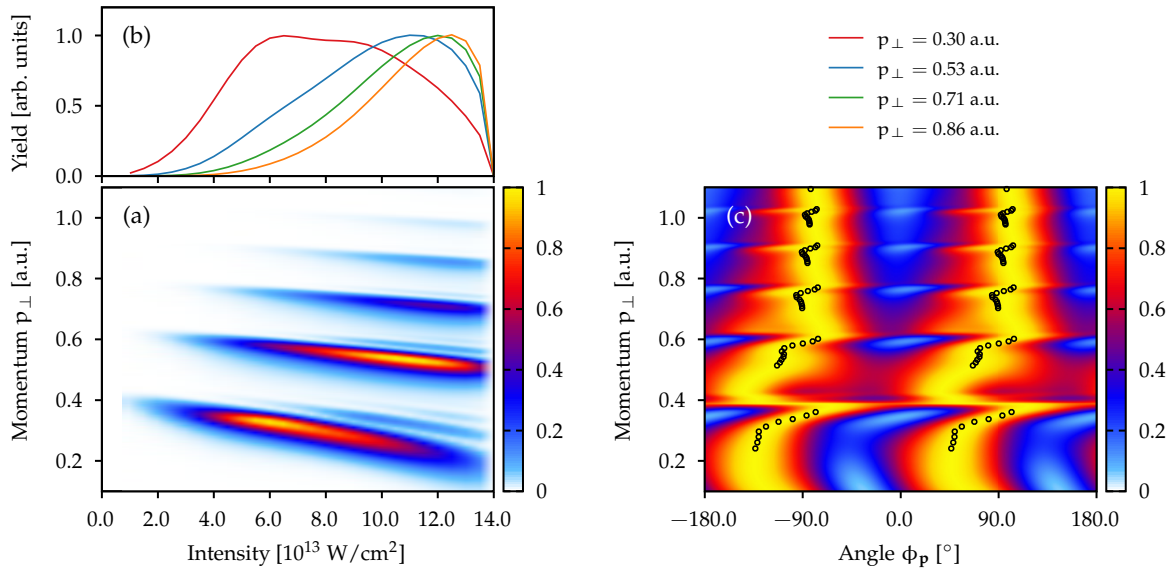


Figure 5.8: Investigation of the substructure for the ATI peaks. (a) Radial momentum distribution from TDSE simulations weighted as in a Gaussian focus in 3D versus laser intensity (see main text). The other parameters are the same as in Fig. 5.5. (b) Relative contribution for the intensities to the yield of the different ATI peaks. All four distributions are normalized to maximum signal of one. (c) Focal-volume-averaged distribution in cylindrical coordinates after rowwise normalization. The black dots indicate the offset angles ϕ_{off} from TDSE simulations at fixed intensities between $3 \times 10^{13} \text{ W/cm}^2$ and $13 \times 10^{13} \text{ W/cm}^2$ analogous to Fig. 5.7(a). Figure is adapted from Trabert *et al.* [357].

Classical trajectory-based model

Trajectory-based two-step models are a common approach to interpret the strong-field dynamics in the presence of Coulomb interaction and were successfully used to model the global attoclock shifts (see for example Refs. [54, 371]). In these classical-trajectory Monte Carlo (CTMC) simulations, an entire distribution of release times and initial velocities is sampled to calculate a final momentum distribution. As introduced in Section 2.4, the basic idea is to split the dynamics into the release of an electron wave packet and its subsequent acceleration. Here, we roughly follow the model for strong-field ionization of Section 3.3 that can be summarized as follows: The ionization step is modeled by the strong-field approximation using a saddle-point method. For each auxiliary momentum $\tilde{\mathbf{p}}'$, the corresponding real part t_r' of the saddle-point time t_s' is identified as release time. In order to represent the geometry of the liberated wave packet well, the ionization probability is approximated by the KFR amplitude (2.45), i.e., it includes nonadiabatic corrections. The electron is born at the tunnel-exit position \mathbf{r}_0 with an initial velocity $\mathbf{v}_0 = \tilde{\mathbf{p}}' + \mathbf{A}(t_r')$. During its acceleration in the continuum, the electron follows a real-valued trajectory governed by Newton's equation of motion (2.49) including the laser field and the Coulomb attraction. Hence, the initial momentum $\tilde{\mathbf{p}}'$ is deflected to a final momentum $\mathbf{p} = \mathbf{D}(\tilde{\mathbf{p}}')$. To solve the inversion problem, i.e., to determine the relevant initial momenta $\tilde{\mathbf{p}}'$ for a given final momentum \mathbf{p} , a clustering algorithm is used (compare Section 3.3.3 for details). We restrict ourselves to the dynamics in the polarization plane and only include release times within one optical cycle of the field. The final probability distribution is then given by

$$w(\mathbf{p}) = \frac{|M_{\text{KFR}}(\tilde{\mathbf{p}}')|^2}{|J|}. \quad (5.11)$$

The Jacobian J of Eq. (3.10) is calculated numerically by considering the variation of the final momentum \mathbf{p} with the auxiliary momentum $\tilde{\mathbf{p}}'$ for a fixed tunnel-exit point and for a release time t_r'

$$J = \det \mathbf{D}'(\tilde{\mathbf{p}}'). \quad (5.12)$$

For the classical simulations, we use top-flat pulses with a falling edge of 12 optical cycles and only consider a fixed intensity of $9 \times 10^{13} \text{ W/cm}^2$. In previous works on the global attoclock offsets [54, 211, 260], tunnel-exit positions from the TIPIS model were used successfully. Here, the Stark shift of the ionization potential can be neglected due to the small polarizability of hydrogen. The initial positions of Eq. (2.48) include a Coulomb correction, but follow adiabatically the instantaneous electric field $\mathbf{E}(t_r')$. Hence, the tunnel exit depends solely on the release time t_r' and it explicitly is independent of the initial velocity \mathbf{v}_0 (see Fig. 5.9(a)). The resulting PMD is used to extract the offset angle $\phi_{\text{off}}(p_{\perp})$ for each radial momentum p_{\perp} (see Fig. 5.9(b)). The offset angle of the classical simulation decreases for small radial

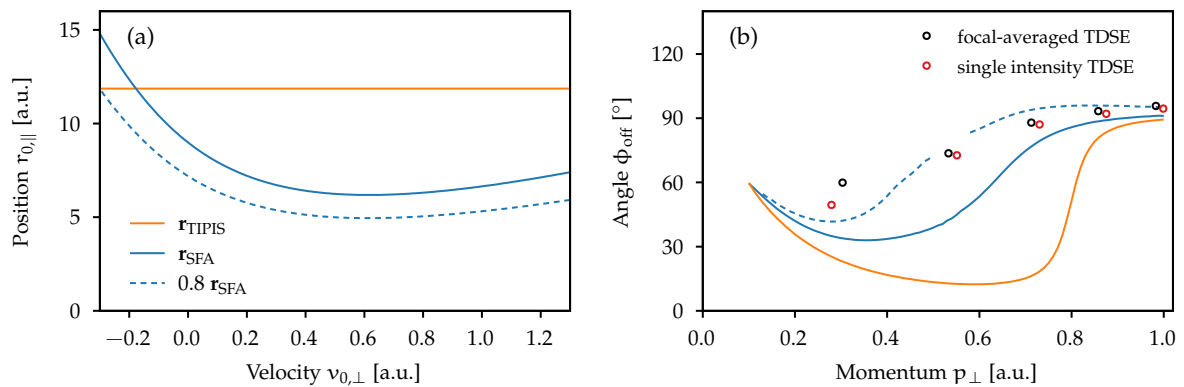


Figure 5.9: (a) Illustration of the tunnel-exit positions as a function of the initial velocity component $v_{0,\perp}$ perpendicular to the instantaneous field $\hat{\mathbf{E}}(t_r')$ for ionization at $t_r' = 0$ and an intensity of $9 \times 10^{13} \text{ W/cm}^2$. The corresponding initial velocity distribution in SFA is approximately centered at $v_{0,\perp} \approx 0.25$ a.u. (b) Comparison of the offset angles ϕ_{off} from TDSE to the classical trajectory-based model for three different choices of the tunnel exit (see panel a). In addition to the focal-volume averaged TDSE result, the offset angles for a fixed intensity of $9 \times 10^{13} \text{ W/cm}^2$ are shown. Figure is adapted from Trabert *et al.* [357].

momenta p_{\perp} . However, the geometrical constraints of the released electron wave packet lead again to a strong increase of the angle around $p_{\perp} \approx 0.8$ a.u. and a convergence towards 90° for even larger p_{\perp} . In the intermediate p_{\perp} -range, the TDSE results are not well reproduced by the classical model.

In contrast to the adiabatic exit position of the TIPIS model, the tunnel-exit position \mathbf{r}_{SFA} from the strong-field approximation of Eq. (3.21) contains nonadiabatic corrections, but it neglects Coulomb corrections. The SFA exit position depends strongly on the velocity \mathbf{v}_0 at the release time t'_r . Thus, for the laser conditions at hand, much shorter tunnel-barrier widths compared to the TIPIS exit point occur around the maximum of the initial velocity distribution. These modified initial conditions give rise to a significant increase of the offset angles and result in an improved agreement with TDSE simulations. For an *ad-hoc* correction of SFA exit point due to Coulomb effects during the under-the-barrier motion, we simply use $0.8\mathbf{r}_{\text{SFA}}$. This artificial exit point leads to an even better agreement with TDSE simulations. Our results suggest that the offset angles and, hence, the shape of the photoelectron momentum distributions are strongly influenced by the choice of the tunnel-exit position and the shape of the initial electron wave packet.

5.2.4 Classical backpropagation

The fundamental question arises whether it is a good choice to consider tunnel-exit positions that depend on the electron's initial velocity and are sensitive to nonadiabatic effects. The classical backpropagation method [211, 350, 351] offers the opportunity to extract characteristic features of the liberated electron wave packet from *ab-initio* simulations. In the attoclock discussion so far, we only considered the experimentally-accessible momentum distributions, i.e., the modulus squared of the probability amplitudes of the electron wave packet. The idea of the classical backpropagation method is to use the phase information of the asymptotic electron wave function and to define a relation between the asymptotic momentum and the final position of the electron. These final conditions are used to propagate classical trajectories back in time till a tunneling criterion is reached so that release times, tunnel-exit positions and initial velocities of the electrons can be extracted.

The classical backpropagation was already used to show that nonadiabatic effects for circular polarization result in reduced tunnel-barrier widths compared to the estimates for adiabatic tunneling [211, 350, 351]. However, to the best of our knowledge, the dependence of the exit positions \mathbf{r}_0 on the initial velocity \mathbf{v}_0 was not studied so far. Here, we close this gap to support our model of Section 5.2.3.

Introducing a momentum-space backpropagation method

The starting point is an *ab-initio* simulation of the TDSE till a final time t_f after the end of the laser pulse, i.e, the initial state is first propagated quantum-mechanically forward in time by solving the TDSE. The asymptotic continuum wave packet is then transcribed to a classical phase-space distribution. In previous implementations (for example in Refs. [211, 350, 351, 359]), the position representation $\psi(\mathbf{r}, t_f)$ of the wave packet was used to define the phase-space distribution. Inspired by the semiclassical physics with its relation between action phase and canonical momenta, a local momentum is assigned to each position by using the phase gradient of the wave function [333, 334]

$$\mathbf{p}_{\psi}(\mathbf{r}, t_f) = \nabla_{\mathbf{r}} \arg \psi(\mathbf{r}, t_f). \quad (5.13)$$

Below we will show that, even for short-range potentials, the position-space representation changes its form due to dispersion and, hence, the defined correlation (5.13) also depends on the time t_f . In contrast, the momentum representation $\tilde{\psi}(\mathbf{p}, t_f)$ of the wave packet only picks up a phase in such a scenario. This motivates us to use the momentum representation to initiate the classical backpropagation. For each final momentum \mathbf{p} , we propose to define a local position by⁸

$$\mathbf{r}_{\tilde{\psi}}(\mathbf{p}, t_f) = -\nabla_{\mathbf{p}} \arg \tilde{\psi}(\mathbf{p}, t_f). \quad (5.14)$$

⁸A similar idea was already used to study Wigner time delays in single-photon ionization [375]. In order to flatten the phase in the numerical implementation, a phase of $-\mathbf{p}^2 t_f / 2$ is subtracted at each momentum \mathbf{p} before calculating the derivative in Eq. (5.14). Afterwards, this is compensated by adding a position offset of $\mathbf{p} t_f$.

The defined relation between momenta and local positions is only meaningful in the absence of interference in the final electron momentum distribution.

The pairs of momenta and positions are used to start classical trajectories that propagate backward in time. Their dynamics follows Newton's equation including both the electron-ion interaction and the driving light field. For each trajectory, the backpropagation is terminated at a time t_0 , when a tunneling criterion is met. Here, the velocity criterion is applied, i.e., the trajectory is stopped when the velocity of the electron is perpendicular to the instantaneous electric field $\mathbf{E}(t_0)$.⁹ Then, the time t_0 , the remaining velocity component in the polarization plane $v_{0,\perp}$ and the velocity component in the light-propagation direction $v_{0,z}$ can be used to parameterize other quantities such as the tunnel-exit position. Both, the momentum-space and the position-space versions define mappings of the final momenta \mathbf{p} or final positions \mathbf{r} to the initial coordinates

$$(t_0, v_{0,\perp}, v_{0,z}) = \mathbf{D}_M(\mathbf{p}) \quad \text{and} \quad (t_0, v_{0,\perp}, v_{0,z}) = \mathbf{D}_P(\mathbf{r}). \quad (5.15)$$

The position of the electron at the ionization time t_0 can be interpreted as the tunnel-exit position. Note that the mappings \mathbf{D}_M , \mathbf{D}_P and the defined tunnel-exit positions are solely retrieved from the phase information of the asymptotic electron wave packet (either in momentum or position representation).

The modulus squared of the amplitudes of the electron wave packets in combination with the relations of Eqs. (5.13) and (5.14) define a classical phase-space distribution at time t_f that can also be propagated backwards in time. The extracted initial probability distributions read

$$w_{\text{ini}}(t_0, v_{0,\perp}, v_{0,z}) = \frac{|\tilde{\Psi}(\mathbf{p})|^2}{|\det \mathbf{D}'_M(\mathbf{p})|} \quad \text{and} \quad w_{\text{ini}}(t_0, v_{0,\perp}, v_{0,z}) = \frac{|\Psi(\mathbf{r})|^2}{|\det \mathbf{D}'_P(\mathbf{r})|}. \quad (5.16)$$

The first equation is for the momentum-space approach, whereas the second equation is for the position-space approach. In general, both results may differ from each other. By construction, the momentum-space approach ensures that the quantum-mechanical PMD is exactly reproduced by classical trajectories that are launched according to the distribution $w_{\text{ini}}(t_0, v_{0,\perp}, v_{0,z})$ at the velocity- and time-dependent tunnel-exit positions. One remaining question is always whether the extracted initial distributions have an intuitive and simple interpretation.

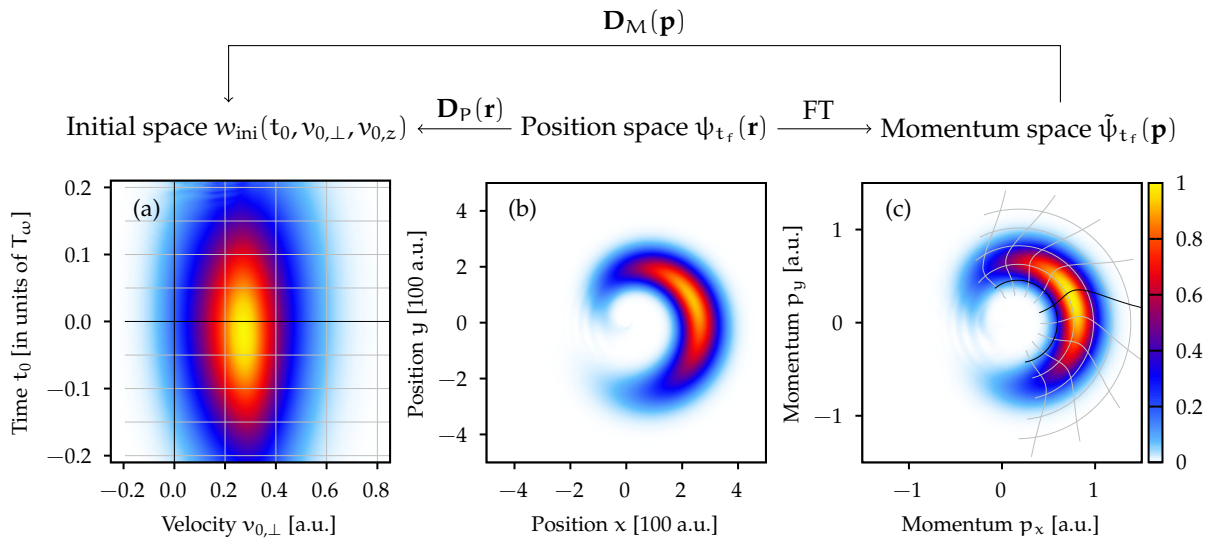


Figure 5.10: Classical backpropagation of an electron wave packet released in a circular attoclock configuration with 800 nm wavelength and 1×10^{14} W/cm² intensity. (a) Initial probability distribution w_{ini} of the backpropagated trajectories. (b) Position-space probability distribution at final time $t_f = 3 T_\omega$. (c) Photoelectron momentum distribution, i.e., momentum-space probability distribution at final time $t_f = 3 T_\omega$. The radial contour lines mark constant initial velocity with a spacing of 0.2 a.u.. The black line shows $v_{0,\perp} = 0$. The angular contour lines mark constant time of ionization with a spacing of 0.05 T_ω . The black line shows $t_0 = 0$. All distributions are independently normalized to maximum signal of one. Inspired by Ref. [161].

⁹Several other criteria were studied in Refs. [211, 350, 351].

As a first example, we consider strong-field ionization of hydrogen in 2D modeled by a potential

$$V(\mathbf{r}) = -\frac{Z + (Z_{\text{core}} - Z)e^{-r^2/r_{\text{core}}^2}}{\sqrt{r^2 + \epsilon}} \quad (5.17)$$

with $Z = Z_{\text{core}} = 1$ and $\epsilon = 0.64$ in order to reproduce the ionization potential $I_p = 0.5$ a.u. To avoid interference, a short two-cycle circularly-polarized laser pulse of Eq. (5.4) with 1×10^{14} W/cm² intensity is chosen. For the momentum-space approach, we solve the TDSE numerically using the split-operator method on two grids of size 819.2×819.2 a.u. with spacings of $\Delta x = 0.2$ a.u. as described in the Appendix A.2.2. For radial distances $r > 350$ a.u., the potential is set flat. For the position-space approach, only one large grid of size 1638×1638 a.u. with spacings of $\Delta x = 0.2$ a.u. is used and the wave function is propagated up to a given time t_f . Figure 5.10 shows the position-space as well as momentum-space representation of the final wave packet in panels (b) and (c).¹⁰ The initial distribution obtained by classical backpropagation based on the momentum-space approach is presented in panel (a). In order to visualize the mapping \mathbf{D}_M^{-1} of the initial conditions $(t_0, v_{0,\perp})$ to the final momenta \mathbf{p} , contour lines show fixed ionization times and initial velocities. Due to the Coulomb interaction, the lines of constant time strongly deviate from straight lines in the space of final momenta.

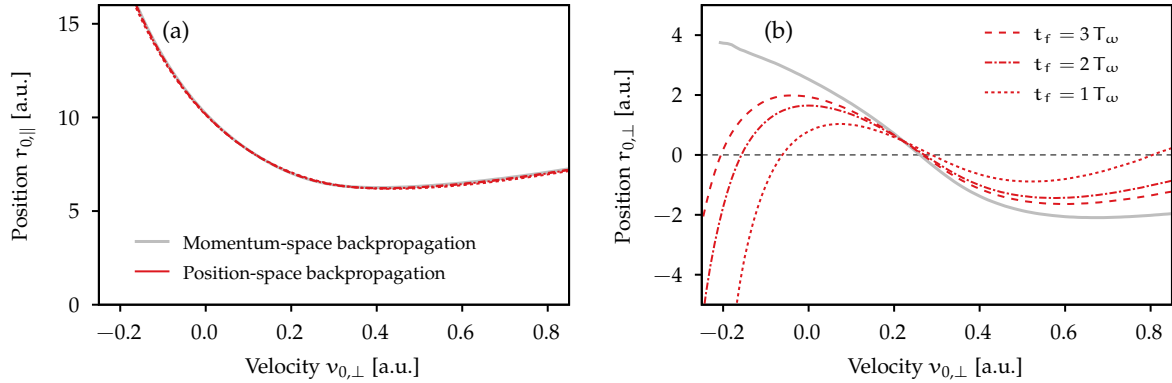


Figure 5.11: Tunnel exits for a release time $t_0 = 0$ as a function of the initial velocity $v_{0,\perp}$ from momentum-space and position-space backpropagation approaches using the setting of Fig. 5.10. (a) Component antiparallel to and (b) component perpendicular to the instantaneous electric field $\mathbf{E}(0)$. For the position-space approach, different final times t_f are used as indicated in the legend in units of optical cycles.

Comparison of the momentum-space approach and the position-space approach

For the newly-proposed momentum-space version, two important properties need to be investigated: (i) Are results of the classical backpropagation independent of the final time t_f ? (ii) What is the relation of the proposed momentum-space version to the earlier-used position-space approach?

To address these questions, we first consider the results shown in Fig. 5.10. Here, we restrict ourselves to ionization at time of peak electric-field strength, i.e., we only analyze those trajectories for which the backpropagation stops at $t_0 = 0$. The tunnel-exit positions calculated by the momentum-space approach are shown in Fig. 5.11 as a function of the initial velocity $v_{0,\perp}$. In additional simulations, we find that the tunnel-exit positions are in good approximation independent of the time t_f when the forward quantum propagation is stopped. The stability of the momentum-space version can be seen as follows. At a time t_f , the momentum-space wave packet can be written as $\tilde{\psi}(\mathbf{p}, t_f) = \tilde{A}(\mathbf{p}) \exp(i\tilde{B}(\mathbf{p}))$ with a real-valued amplitude \tilde{A} and a phase \tilde{B} . If t_f is sufficiently large, the detached wave packet is located at large distances r where a vanishing ionic potential can be assumed. Hence, the time evolution over an additional interval Δt is quantum-mechanically given by

$$\tilde{\psi}(\mathbf{p}, t_f + \Delta t) = \tilde{A}(\mathbf{p}) e^{i\tilde{B}(\mathbf{p})} e^{-i\frac{\mathbf{p}^2}{2}\Delta t}. \quad (5.18)$$

¹⁰In contrast to the Monte Carlo simulations used in Refs. [211, 350, 351], we determine for each tuple of initial conditions $(t_0, v_{0,\perp})$ the corresponding final momentum $\mathbf{p} = \mathbf{D}_M^{-1}(t_0, v_{0,\perp})$ by using the multidimensional Newton method. Afterwards, the Jacobian in Eq. (5.16) is approximated by a finite-difference formula.

According to Eq. (5.14), the associated position for the wave packet at a time $t_f + \Delta t$ reads

$$\mathbf{r}_{\tilde{\psi}}(\mathbf{p}, t_f + \Delta t) = -\nabla_{\mathbf{p}} \arg \tilde{\psi}(\mathbf{p}, t_f + \Delta t) = \mathbf{r}_{\tilde{\psi}}(\mathbf{p}, t_f) + \mathbf{p}\Delta t. \quad (5.19)$$

The relation between the positions for transcription at time t_f and $t_f + \Delta t$ is equal to a classical motion with a momentum \mathbf{p} . Thus, in the momentum-space version, the defined trajectories are independent of the final time t_f .

In contrast, if the position-space approach of previous implementations [211, 351] is used, the retrieved initial positions depend on the final time t_f (see Fig. 5.11). For the special choice of $t_0 = 0$, the position component parallel to the instantaneous field $\mathbf{E}(t_0)$ is nearly stable. However, in general for $t_0 \neq 0$, we find that both components change with t_f . The numerical results suggest of the position-space approach gets closer to the momentum-space version for large $t_f \rightarrow \infty$. To understand the relation of both approaches, we need to consider the transformation between the position and momentum representations of an electron wave packet

$$\psi(\mathbf{r}, t_f) = \frac{1}{(2\pi)^{D/2}} \int d\mathbf{p} \tilde{\psi}(\mathbf{p}, t_f) e^{i\mathbf{p}\cdot\mathbf{r}} = \frac{1}{(2\pi)^{D/2}} \int d\mathbf{p} \tilde{\Lambda}(\mathbf{p}) e^{i\tilde{\mathbf{B}}(\mathbf{p})} e^{i\mathbf{p}\cdot\mathbf{r}}. \quad (5.20)$$

For large times t_f , the phase factor $\exp(i\tilde{\mathbf{B}}(\mathbf{p}))$ is a quickly oscillating function of the momentum \mathbf{p} (see Eq. (5.18)). Hence, the integral can be evaluated by means of the saddle-point approximation. The saddle-point equation reads

$$0 = \nabla_{\mathbf{p}} (\tilde{\mathbf{B}}(\mathbf{p}) + \mathbf{p} \cdot \mathbf{r}) = -\mathbf{r}_{\tilde{\psi}}(\mathbf{p}, t_f) + \mathbf{r}. \quad (5.21)$$

For a given position \mathbf{r} , the equation selects the corresponding saddle-point momentum, i.e., it establishes a mapping $\mathbf{p}(\mathbf{r})$. The mapping can be explicitly calculated by inverting the positions $\mathbf{r}_{\tilde{\psi}}(\mathbf{p}, t_f)$ of the local-position method (5.14). If the backpropagation is started using the position-space wave function from the saddle-point approximation of Eq. (5.20), the associated local momentum of Eq. (5.13) is given by

$$\begin{aligned} \mathbf{p}_{\psi}(\mathbf{r}, t_f) &= \nabla_{\mathbf{r}} \arg \psi(\mathbf{r}, t_f) = \nabla_{\mathbf{r}} (\mathbf{r} \cdot \mathbf{p}(\mathbf{r}) + \tilde{\mathbf{B}}(\mathbf{p}(\mathbf{r}))) \\ &= \mathbf{p}(\mathbf{r}) + \nabla_{\mathbf{r}} \mathbf{p}(\mathbf{r}) \cdot (\nabla_{\mathbf{p}} \tilde{\mathbf{B}}(\mathbf{p}(\mathbf{r})) + \mathbf{r}) = \mathbf{p}(\mathbf{r}). \end{aligned} \quad (5.22)$$

In the last step, we used the saddle-point equation (5.21). The position-to-momentum mapping from the position-space approach is the inverse of the momentum-to-position mapping from the momentum-space approach, if the saddle-point approximation is applied to their connection via Fourier transformation. For binding potentials with finite support, the phase factor $\exp(i\tilde{\mathbf{B}}(\mathbf{p}))$ oscillates more quickly as a function of \mathbf{p} for larger times t_f . Hence, in the limit of large times t_f , the saddle-point approximation becomes exact so that position-space and momentum-space approaches become indeed equivalent.

As a result, we consider the outcome of momentum-space approach to be the correct result for the backpropagation scheme. Importantly, the slow convergence of the position-space approach is also present when considering short-range potentials or even in wave packets from strong-field approximation. It is mostly caused by the dispersion of the outgoing wave packet in position space. Thus, to obtain converged results, a huge spread of the position-space wave packet needs to be covered in the theoretical simulations. In contrast, for the momentum-space implementation, only a relatively small region of the position space needs to be represented explicitly. This is, in particular, beneficial for long-wavelength driving fields and in 3D simulations. In the following, we will only present backpropagation results based on the momentum approach.

Nonadiabatic corrections to the tunnel-exit positions

The tunnel-exit positions from classical backpropagation shown in Fig. 5.11 lead to following conclusions: (i) The exit positions depend strongly on the initial velocity $v_{0,\perp}$, which is in agreement with the previously-considered SFA exit points of Eq. (3.21). (ii) The results are not symmetric with respect to $v_{0,\perp} \rightarrow -v_{0,\perp}$, which is a hint for nonadiabatic effects. (iii) A nonzero component of the initial position perpendicular (here along x -direction) to the direction of the instantaneous field $\mathbf{E}(t_0)$ appears.

In order to further explore the tunnel-exit positions, we consider ionization for a long-range potential as well as a short-range potential in an attoclock setting with identical laser conditions of 1200 nm wavelength and 1×10^{14} W/cm² intensity. We again use the potential (5.17) with $Z = Z_{\text{core}} = 1$ and $\epsilon = 0.64$ for a 2D long-range model of hydrogen and with $Z = 0$, $Z_{\text{core}} = 1$, $\epsilon = 0.344$ and $r_{\text{core}} = 3$ a.u. for a 2D short-range model with approximately the same ionization potential. For fixed release time $t_0 = 0$, the observables extracted from classical backpropagation simulations are shown in Fig. 5.12 as a function of initial velocity $v_{0,\perp}$. In agreement with Ref. [351], the initial velocity distributions are quite similar for long- and short-range potentials (see panels 2 of Fig. 5.12). However, the retrieved initial positions exhibit some qualitative differences.

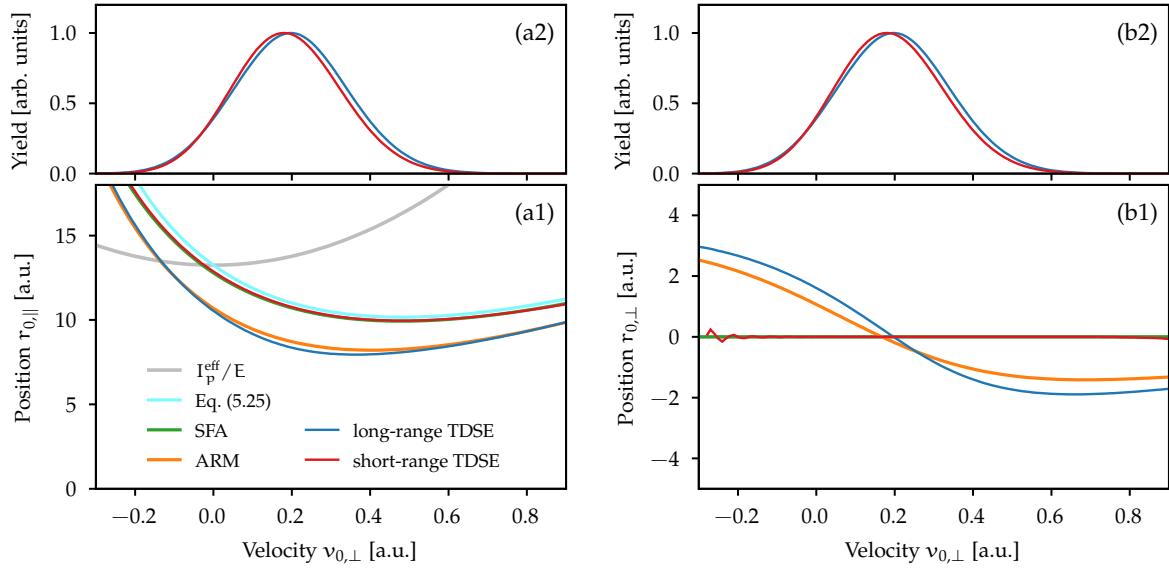


Figure 5.12: Comparison of tunnel-exit positions for a release time $t_0 = 0$ as a function of the initial velocity $v_{0,\perp}$ from different levels of theory for two-cycle circularly-polarized pulses at 1200 nm wavelength and 1×10^{14} W/cm² intensity. (a1) Component antiparallel to and (b1) component perpendicular to the instantaneous electric field $E(0)$. [(a2),(b2)] Initial velocity distributions from backpropagation.

For short-range potentials, the strong-field approximation evaluated by means of a saddle-point method usually describes the recollision-free ionization dynamics very well. Within this simplified treatment, the classical backpropagation method can be carried out analytically. For an initial $1s$ state, the phase of the asymptotic wave function in momentum representation is dominated by the SFA action of Eq. (2.41) (see the KFR amplitude (2.45)). Thus, in our momentum-space version of Eq. (5.14), we find a final local position at time t_f

$$\begin{aligned} \mathbf{r}_{\tilde{\Psi}}(\mathbf{p}, t_f) &= -\nabla_{\mathbf{p}} \text{Re}(S_{\text{SFA}}(\mathbf{p}, t'_s)) = \text{Re} \left(\int_{t'_s}^{t_f} d\tau (\mathbf{p} + \mathbf{A}(\tau)) - \nabla_{\mathbf{p}}(t'_s(\mathbf{p})) \dot{S}_{\text{SFA}}(\mathbf{p}, t'_s) \right) \\ &= \text{Re} \left(\int_{t'_s}^{t_f} d\tau (\mathbf{p} + \mathbf{A}(\tau)) \right), \end{aligned} \quad (5.23)$$

where the saddle-point equation (2.44) is used in the last step. Considering classical potential-free motion to propagate backwards until a time t_0 , the following tunnel-exit position appears

$$\mathbf{r}_{\text{SFA}} = \mathbf{r}_{\tilde{\Psi}}(\mathbf{p}, t_f) + \int_{t_f}^{t_0} d\tau (\mathbf{p} + \mathbf{A}(\tau)) = \text{Re} \left(\int_{t'_s}^{t_0} d\tau (\mathbf{p} + \mathbf{A}(\tau)) \right). \quad (5.24)$$

For a given trajectory, the corresponding time t_0 is determined by the tunneling criterion. For the chosen velocity criterion and in the vicinity of the peak electric-field strength, the time t_0 is approximately equal to the real part t'_r of the SFA saddle-point time. Hence, we find that the backpropagation result \mathbf{r}_{SFA} from SFA input is equal to the well-known SFA tunnel-exit point of Eq. (3.21).

For short-range potentials, the SFA exit points perfectly agree with the full numerical result from TDSE simulations for a broad range of laser wavelengths (see Fig. 5.13 for results between 800 nm and 2000 nm corresponding to Keldysh parameters between 1.5 and 0.6). For a release time $t'_r = t_0 = 0$, the component of the exit position perpendicular to the instantaneous electric field vanishes. The component antiparallel to the field depends strongly on the initial velocity $v_{0,\perp}$. This velocity dependence considerably changes with the degree of nonadiabaticity. For a simplified analytical analysis, Equation (3.21) can be expanded to first order in the Keldysh parameter¹¹

$$\mathbf{r}_{\text{SFA}} \approx -\frac{I_p^{\text{eff}}}{E(t'_r)} \hat{\mathbf{E}}(t'_r) - \frac{I_p^{\text{eff}}}{E(t'_r)} \frac{\mathbf{v}_0 \cdot \dot{\mathbf{E}}(t'_r)}{E^2(t'_r)} \hat{\mathbf{E}}(t'_r), \quad (5.25)$$

where the possible ionization times t'_r and initial velocities \mathbf{v}_0 are selected by the saddle-point equation (see Appendix A.4.1). The first term is also present in the adiabatic limit and it is dominated by the increased effective ionization potential $I_p^{\text{eff}} = I_p + \mathbf{v}_0^2/2$ due to the initial velocity \mathbf{v}_0 . It is called the I_p^{eff}/E exit position in the following. For circular polarization, the first-order nonadiabatic correction is quite crucial as it induces the asymmetry of the tunnel exits as a function of $v_{0,\perp}$ (see Fig. 5.12). In the vicinity of the maximum of the velocity distribution (for small positive $v_{0,\perp}$), the nonadiabatic correction leads to reduced tunnel-barrier widths compared to the adiabatic I_p^{eff}/E estimate. Our analysis is in agreement with the qualitative finding of Refs. [211, 350, 351] that the tunnel-exit positions (averaged over the initial distribution) decrease due to nonadiabatic effects.

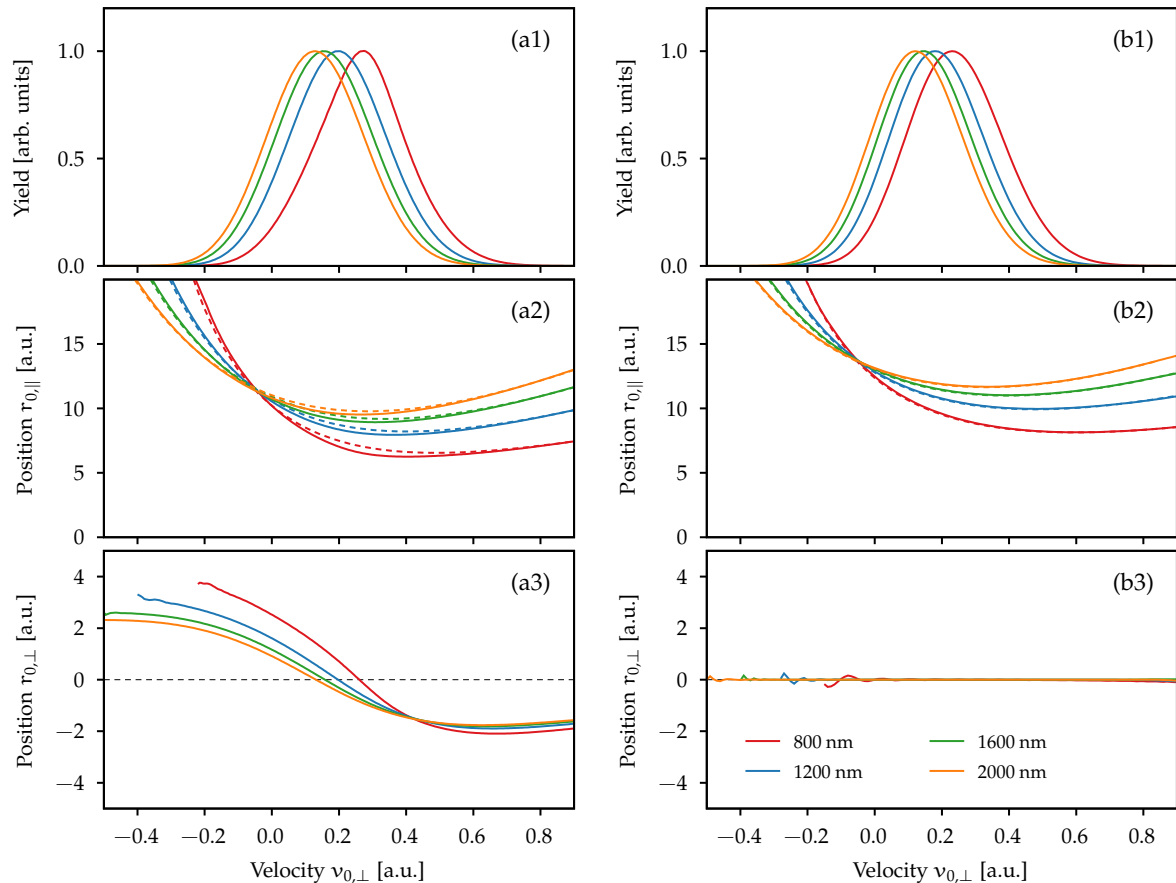


Figure 5.13: Classical backpropagation results for different wavelengths as indicated in the legend either obtained for a long-range potential (panels a) and a short-range potential (panels b). Slices through the initial distributions as well as antiparallel and perpendicular components of tunnel-exit position are shown in the different rows. For comparison, the backpropagation results for ARM theory are shown as dashed lines in panel (a2) and the backpropagation results for SFA are shown in panel (b2).

¹¹A similar expression was also found in Ref. [211].

Eckart [357] suggested to interpret the velocity-dependent exit positions as follows: Ionization under nonadiabatic conditions allows a change of energy during the under-the-barrier motion [191]. This ionization process can be modeled as nonresonant multiphoton interaction promoting the initially-bound electron to a virtual intermediate state and as the subsequent release by adiabatic tunneling [163, 164, 376]. For pure circular polarization, change of energy is accompanied by a defined change of the angular momentum L_z of the electron, i.e., its effective energy at the release can be expressed as $-I_p^{\text{eff}} + \omega L_z$. The classical angular momentum $L_z = r_{0,\parallel} v_{0,\perp}$ at the release position $\mathbf{r}_0 = -r_{0,\parallel} \mathbf{e}_y$ should be equal to the quantum-mechanical angular momentum after multiphoton interaction. Then, the tunnel-barrier width can be defined by the intersection of a triangular tunneling barrier with the effective electron energy

$$r_{0,\parallel} \approx \frac{I_p^{\text{eff}}}{E_0} - \frac{I_p^{\text{eff}} \omega}{E_0^2} v_{0,\perp}. \quad (5.26)$$

We find that the result of this model is equal to the expansion (5.25) of the SFA exit. For $v_{0,\perp} > 0$, multiphoton absorption during tunneling increases the field-dressed energy of the electron and, hence, results in an inward shift of the tunnel-exit position.

For long-range potentials, the components of the exit positions antiparallel to the instantaneous electric field (here negative y -direction) extracted by classical backpropagation are systematically shifted towards smaller distances compared to the short-range results (see Fig. 5.12(a1)). The simplest adiabatic approach assumes that the electron tunnels in a 1D slice along the direction of the instantaneous electric field [77]. This is called field-direction model (FDM). The introduction of Cartesian coordinates results in a one-dimensional potential barrier formed by the ionic potential $-Z/r$ and the potential of the light field (in length gauge). The remaining directions lead again to an increased effective ionization potential I_p^{eff} and the tunnel-exit position reads [347]

$$\mathbf{r}_0 = -\frac{I_p^{\text{eff}} + \sqrt{(I_p^{\text{eff}})^2 - 4ZE}}{2E} \hat{\mathbf{E}}. \quad (5.27)$$

If the binding potential is neglected ($Z = 0$), the exit position reduces to the simpler I_p^{eff}/E estimate. The first-order Coulomb correction reads $\Delta r = -Z/I_p^{\text{eff}}$. In agreement with the backpropagation result, the tunnel-exit positions from FDM are shifted towards smaller distances and depend of the initial velocity.

However, when considering close-to-circularly-polarized fields, the interplay between nonadiabatic corrections and the long-range potential must be included for a quantitative description. The analytical R-matrix (ARM) theory introduced in Section 2.5 enables a simplified modeling of electron momentum distributions, including the binding potential V to first order correctly in the exponent. We use the analytical form (2.58) of the asymptotic electron wave packet in ARM as input for a classical backpropagation calculation. It allows us to derive an analytical estimate for the Coulomb correction with respect to the potential-free SFA exits (see Appendix A.4.2 for details). This ARM result agrees very well with the full numerical result from TDSE (see Fig. 5.12(a1)).

When tunneling at the time of peak field strength, both the field-direction model and the strong-field approximation predict that the electron appears exactly in the direction antiparallel the instantaneous field $\mathbf{E}(0)$. Surprisingly, for both TDSE and ARM input, the backpropagation results for long-range potentials show nonzero components $r_{0,\perp}$ of the initial position perpendicular to the instantaneous field. In additional 3D simulations, we find that such additional components are not limited to the dynamics in the polarization plane, but are present in any direction that is perpendicular to the direction of the electric field at the instant of tunneling. The exact perpendicular components $r_{0,\perp}$ depend on the used wavelengths, e.g., for 800 nm values as large as 3 a.u. are reached. Even though the components $r_{0,\perp}$ decrease for more adiabatic conditions, they do not entirely vanish (not shown). Furthermore, in additional simulations, we observe that the perpendicular component changes only weakly with the laser intensity. Importantly, we want to note that the exact outcome of a classical backpropagation simulation depends on the used tunneling criterion [211]. In this sense, the perpendicular component can be seen as a consequence of the chosen velocity criterion. In the future, it would be interesting to study whether generalized tunneling criteria also show such an effect (see also Section 6.2.3).

5.3 Bicircular attoclock

The dependence of the Coulomb-induced deflection of the photoelectrons on their initial position (see also Eq. (5.2)) offers the opportunity to study the tunneling geometry by means of the momentum-dependent attoclock offsets. For elliptically-polarized fields, we already found that the variation of tunnel-exit positions as a function of the electron's initial velocity leaves an imprint on the offset angles (see Section 5.2.3). Unfortunately, in close-to-circularly-polarized fields, the geometry of the wave packet as well as nonadiabatic effects complicate the analysis of the momentum-dependent attoclock offsets.

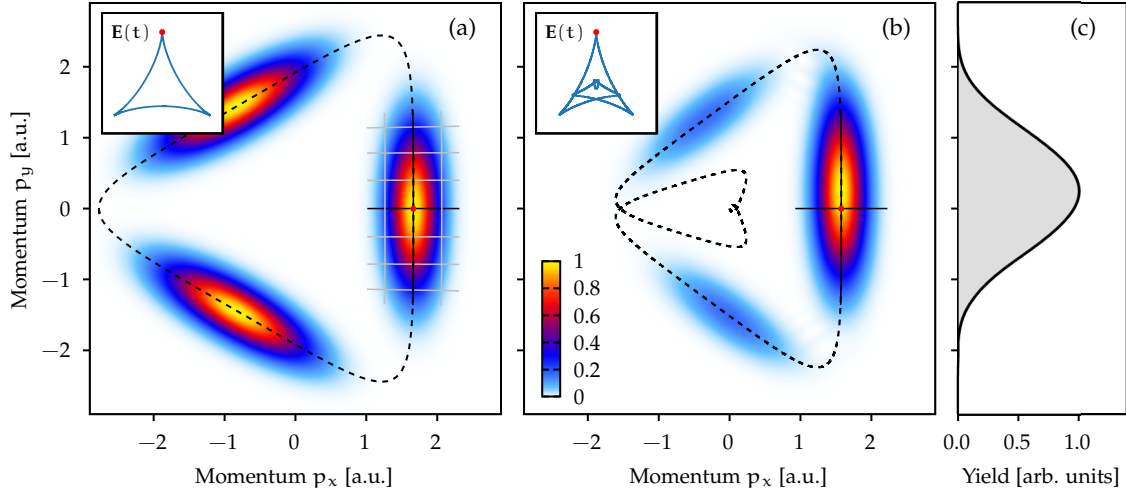


Figure 5.14: Setup of the bicircular attoclock. 2D slices at $p_z = 0$ through the photoelectron momentum distribution for ionization of helium by a bicircular field with 800 nm effective wavelength and 7×10^{14} W/cm² intensity: (a) strong-field approximation for a cw field ($R = 1/4$) and (b) numerical simulation of the TDSE for a three-cycle pulse with an optimized intensity ratio of $R \approx 0.292$ (see Eq. (5.31)). The dashed lines show the negative vector potentials and the insets indicate the electric fields. In panel (a), the nearly-horizontal solid contour lines mark constant time of ionization with a spacing of $0.4/E_p$. The black line shows $t_0 = 0$. The nearly-vertical lines mark constant initial velocity with a spacing of 0.4 a.u. The black line shows $v_{0,\perp} = 0$. (c) 1D Slice through the maximum of the PMD from TDSE as a function of p_y , i.e., at constant $p_x = -A_x(0) \approx 1.58$ a.u. Figure is adapted from Ref. [359] and from Brennecke *et al.* [369].

To avoid these problems, a quasilinear field can be used. In the vicinity of the maximal electric-field strength, the direction of the field is approximately constant, and simultaneously it provides a simple time-to-momentum mapping. This waveform was introduced to study the global attoclock shift by Eicke *et al.* [161, 359]. To this end, a bicircular field similar to Eq. (3.34) consisting of two counter-rotating circularly-polarized fields with the following vector potential

$$\mathbf{A}(t) = -\frac{1}{1+\sqrt{R}} \frac{E_p}{\omega} \left[\begin{pmatrix} \cos(\omega t) \\ \sin(\omega t) \end{pmatrix} + \frac{\sqrt{R}}{2} \begin{pmatrix} -\cos(2\omega t) \\ \sin(2\omega t) \end{pmatrix} \right] \quad (5.28)$$

is optimized. For a particular intensity ratio $R = 1/4$ of the fundamental to the second harmonic, the light field resembles linear polarization three times per optical cycle of the fundamental field. The negative vector potential and electric field are presented in Fig. 5.14(a). Due to the three-fold symmetry, we can restrict ourselves to ionization in one third cycle of the electric field centered around a peak of the electric-field strength. In the vicinity of $t = 0$, we find

$$\begin{aligned} \mathbf{A}(t) &= A_x(0) \mathbf{e}_x - \frac{E_p}{\omega_{\text{eff}}} \sin(\omega_{\text{eff}} t) \mathbf{e}_y + \mathcal{O}(t^4), \\ \mathbf{E}(t) &= E_p \cos(\omega_{\text{eff}} t) \mathbf{e}_y + \mathcal{O}(t^3). \end{aligned} \quad (5.29)$$

Hence, the field is indeed approximately linearly polarized along the y -axis with an effective frequency $\omega_{\text{eff}} = \sqrt{2} \omega$ and a peak field strength E_p . The time-averaged intensity is given by $I = \frac{5}{9} c \epsilon_0 E_p^2$ and the nonadiabaticity of the ionization process is characterized by the Keldysh parameter $\gamma_{\text{eff}} = \sqrt{2I_p} \omega_{\text{eff}}/E_p$.

Figure 5.14(a) shows a typical momentum distribution for strong-field ionization by a quasilinear cw field. The PMD is calculated for helium in the strong-field approximation.¹² It consists of three separated cigar-like regions of high probability that belong to the three maxima of the electric-field strength per optical cycle. Within this potential-free setting, a electron liberated at a time t_0 with an initial velocity \mathbf{v}_0 is deflected by the light field to a final momentum $\mathbf{p} = -\mathbf{A}(t_0) + \mathbf{v}_0$. Ionization at maximal field strength (here at $t_0 = 0$), with vanishing initial velocity leads to the maximum of the cigar centered at a final momentum $\mathbf{p} = -\mathbf{A}(0) = A_0 \mathbf{e}_x$ (see the red dot in Fig. 5.14(a)). For adiabatic conditions, the initial velocity \mathbf{v}_0 must be perpendicular to the electric field $\mathbf{E}(t_0)$ at the instant of tunneling (see Eq. (2.47)). Thus, in the vicinity of $t = 0$ where the direction of the electric field is nearly constant, the $v_{0,y}$ -component vanishes and the setting is nearly isotropic in the $v_{0,\perp}$ - $v_{0,z}$ -plane perpendicular to the field $\mathbf{E}(t_0)$. Using the form of the initial velocity $\mathbf{v}_0 \approx v_{0,\perp} \mathbf{e}_x + v_{0,z} \mathbf{e}_z$, the final momenta are approximately given by

$$\mathbf{p}_\perp = -\mathbf{A}(t_0) + \mathbf{v}_0 \approx (v_{0,\perp} - A_x(0)) \mathbf{e}_x + v_{0,z} \mathbf{e}_z + E_y(0) t_0 \mathbf{e}_y. \quad (5.30)$$

Hence, the release time t_0 is mapped to the p_y -component of the final electron momentum and the initial velocity $\mathbf{v}_0 \approx v_{0,\perp} \mathbf{e}_x + v_{0,z} \mathbf{e}_z$ to the p_x - and p_z -components [359]. To visualize the mapping, contour lines at fixed ionization times and initial velocities are shown in Fig. 5.14(a). A change of the release time t_0 leaves the p_x - and p_z -components of the momentum almost unchanged. On the other hand, a variation of the initial velocity does nearly not alter the p_y -component. Hence, the quasilinear field provides a clean setting to investigate the momentum dependence of attoclock offsets.

For a numerical solution of the TDSE in 3D, we use the Fourier split-operator method on two grids as described in the Appendix A.2.2. An effective potential V for helium is chosen as by Tong *et al.* [324], but with the singularity removed using a pseudopotential for the 1s state with a cutoff radius $r_{c1}=1.5$ a.u. (see Appendix A.2.3). The binding potential is fully included on the inner grid that spans 409.6 a.u. in each dimension with a spacing of $\Delta x = 0.4$ a.u. At the edge of the inner grid, we set the potential to a constant and use an absorbing potential (A.53) with $\Delta r_A = 40$ a.u. A 2D slice at $p_z = 0$ through the PMD is shown in Fig. 5.14(b). In order to avoid ATI rings, we used again a short three-cycle pulse such that a single global maximum of the electric field is selected. The corresponding cigar is still approximately centered in p_x -direction at $p_x = -A_x(0)$. However, in p_y -direction, it is clearly displaced towards positive momenta. This global attoclock shift of $\Delta p_{\max} \approx 0.24$ a.u. is determined by the maximum of the total distribution. It can be more clearly seen in a 1D slice through the PMD presented in Fig. 5.14(c) and was investigated in Refs. [161, 359].

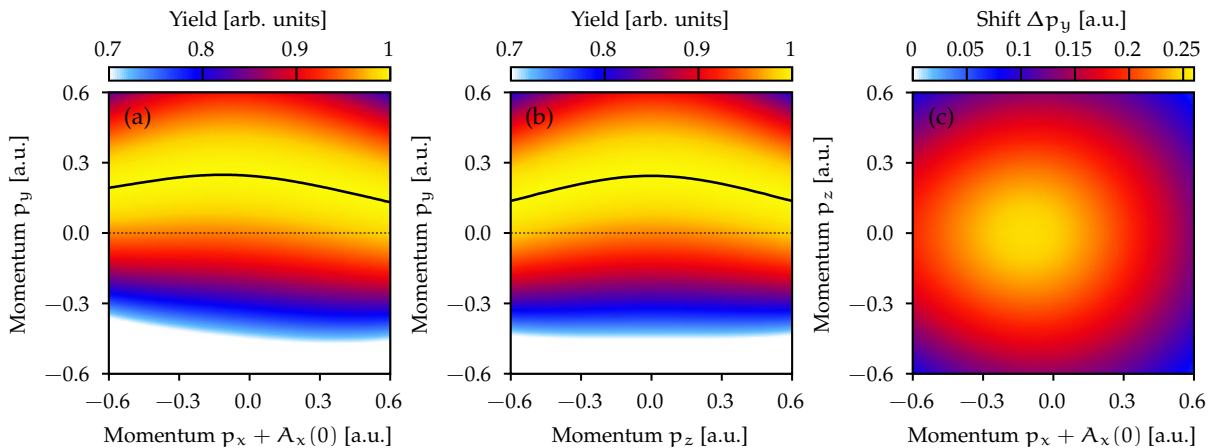


Figure 5.15: Momentum-dependent attoclock shift for a bicircular field. (a) Signal in the p_x - p_y -plane at $p_z = 0$ and (b) signal in the p_z - p_y -plane at $p_x = -A_x(0) \approx 1.58$ a.u. In both panels, each column is individually normalized and the resulting momentum-dependent attoclock shift Δp_y is indicated as black solid line. The dotted black line at $p_y = 0$ guides the eye. (c) Momentum-dependent attoclock shift Δp_y as a function of $p_x + A_x(0)$ and p_z . Figure is adapted from Brennecke *et al.* [369].

¹²We apply the saddle-point approximation to the KFR amplitude and include only the contribution (2.45) of a single saddle-point time t'_s for each final momentum \mathbf{p} . Therefore, Fig. 5.14(a) does not exhibit any ATI rings.

Momentum-dependent attoclock shifts

The attoclock offset can be individually analyzed for each momentum in the p_x - p_z -plane, i.e., we again determine the momentum dependence of the attoclock shift. For an illustration, the signal in the p_x - p_y -plane at constant $p_z = 0$ is depicted in Fig. 5.15(a). Here, each column is normalized individually. We determine the most probable momentum Δp_y at each momentum p_x by means of a Gaussian fit.¹³ The result is shown as black line. At the maximum of the lateral distribution at $p_x \approx -A_x(0)$, the momentum-dependent shift is equal to the global attoclock shift Δp_{\max} . The procedure can be repeated for all lateral momenta in the vicinity of the global maximum. Figure 5.15(c) shows the momentum-dependent attoclock shift as a function of p_x and p_z . For the used laser conditions, the maximal attoclock shift of $\Delta p_y \approx 0.249$ a.u. is not found exactly at $p_x + A_x(0) = 0$, but instead at $p_x + A_x(0) = -0.11$ a.u. When going away from this point, the magnitude of the attoclock shift decreased as a function of p_x and p_z . It reaches values as small as ≈ 0.155 a.u. at $p_z = 0$ and $p_x + A_x(0) = 0.5$ a.u. corresponding to only $\approx 65\%$ of the global attoclock shift. In order to check the numerical convergence, we additionally solved the TDSE by means of the pseudospectral method introduced in the Appendix A.2.1. In these additional simulations, we scaled the extension and the spacing of the radial grid as well as the maximal-included orbital angular momentum. The momentum-dependent attoclock shifts from both numerical methods are in very good agreement. From their comparison, the numerical error is estimated to be smaller than 5% for the attoclock shift in the shown region of p_x and p_z .

The slight asymmetry of the momentum-dependent attoclock shift as a function of $p_x + A_x(0)$ can be attributed to the deviations of the quasilinear field from pure linear polarization and to the finite nonadiabaticity of the ionization process. To minimize the former point, we did not exactly use the intensity ratio $R = 1/4$ of the two colors in the TDSE simulations for the short pulse. Note that an envelope of the vector potential of n_p cycles duration influences the expansion (5.29) of the electric field around $t = 0$. Hence, for $R = 1/4$, the envelope would induce additional deviations from a pure linearly-polarized field. To compensate for this effect, Paul Winter suggested an optimized intensity ratio which is given by (for the \cos^4 envelope)

$$R_{n_p} = \left(\frac{2n_p^2 + 2}{4n_p^2 + 1} \right)^2. \quad (5.31)$$

In the limit of long pulses, the ratio converges to $1/4$. However, for short pulses, corrections are present, e.g., for three-cycle pulses $R_3 = (20/37)^2 \approx 0.292$ and for seven-cycle pulses $R_7 = (100/197)^2 \approx 0.258$.

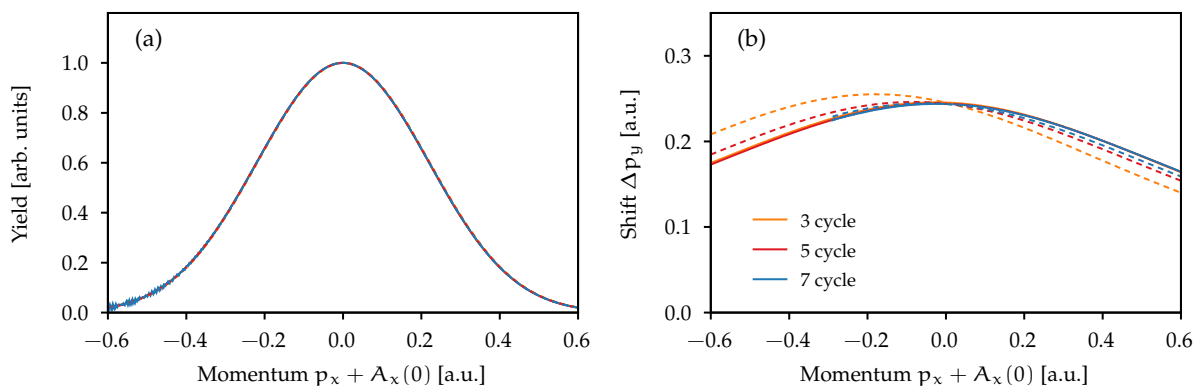


Figure 5.16: Scaling of the pulse length. (a) Slice through the momentum distributions (at $p_y = 0$) and (b) momentum-dependent attoclock shift as a function of $p_x + A_x(0)$. The results are extracted from 2D TDSE simulations for 1500 nm effective wavelength, an intensity of 7×10^{14} W/cm² and different pulse durations indicated in the legend. The dashed lines correspond to a fixed intensity ratio $R = 1/4$ whereas the solid lines use the optimized ratio of Eq. (5.31). The probability distributions in panel (a) are on top of each other and cannot be distinguished in the graph. Figure is adapted from Brennecke *et al.* [369].

¹³An iterative procedure is used where the fit range is centered around the previous maximum's position with a width of one quarter of the previous standard deviation σ . Other methods such as the "power method" [161] give virtual identical results.

To further study the asymmetry in the momentum-dependent attoclock shifts, additional 2D TDSE simulations are performed for a longer effective wavelength of 1500 nm (see Fig. 5.16). For the more adiabatic ionization conditions and for pulses with the optimized ratio (5.31), the momentum-dependent attoclock shifts are approximately independent of the pulse duration and the asymmetry nearly disappears. In contrast, for three-cycle pulses with an intensity ratio $R = 1/4$, we find that the deviations from linear polarization lead to a tiny rotation of the probability distribution (by only a few degrees in the polarization plane). Hence, even for the considered adiabatic conditions, a slight asymmetry appears. As expected, for longer pulses with an intensity ratio $R = 1/4$, the results approaches the shifts for the optimized ratio (5.31). In the following, we only apply three-cycles pulses with the optimized intensity ratio.

5.3.1 Classical adiabatic model

We further investigate the momentum-dependent attoclock shifts by using a trajectory-based two-step model [210, 301, 347]. To this end, the classical connection between the initial electron velocity \mathbf{v}_0 at its time of release t_0 to the final momentum \mathbf{p} must be established. Compared to the potential-free simple man's model, the momentum change $\Delta\mathbf{p}_C$ due to Coulomb attraction modifies this mapping of the initial conditions to the final momenta

$$\mathbf{p}(t_0, \mathbf{v}_0) = -\mathbf{A}(t_0) + \mathbf{v}_0 + \Delta\mathbf{p}_C(t_0, \mathbf{v}_0). \quad (5.32)$$

In the following, we restrict ourselves to ionization in the vicinity of peak field strength at $t = 0$ and we are only interested in the adiabatic limit reached by scaling the wavelength of the radiation.

For the calculation, it is advantageous to measure the different quantities in the natural scales of strong-field ionization (see Section 2.1). Time is measured in units of $\sqrt{I_p}/E_p$ (which is a multiple of the Keldysh time $\sqrt{2I_p}/E_p$), i.e., $\tilde{t} = E_p/\sqrt{I_p}(t - t_0)$. Positions are measured in units of I_p/E_p with $\tilde{\mathbf{r}} = E_p/I_p \mathbf{r}$. Hence, the tunnel-exit position reads $\mathbf{r}_0 = I_p/E_p \tilde{\mathbf{r}}_0$ and the initial velocity is given by $\mathbf{v}_0 = \sqrt{I_p} \tilde{\mathbf{v}}_0$. The electric field and its derivatives are written as $\mathbf{E}^{(n)}(t) = E_p \omega_{\text{eff}}^n \tilde{\mathbf{E}}^{(n)}(\tilde{t})$. Since the magnitude of the static electric field of the ion is given by Z/r^2 with the asymptotic charge Z , we find that the effective interaction strength between electron and ion is represented by

$$\tilde{Z} = \frac{E_p}{I_p^2} Z. \quad (5.33)$$

We can write the electron trajectory as the potential-free laser-driven part plus a correction $\Delta\tilde{\mathbf{r}}(\tilde{t})$:

$$\begin{aligned} \tilde{\mathbf{r}}(\tilde{t}) &= \Delta\tilde{\mathbf{r}}(\tilde{t}) + \tilde{\mathbf{r}}_0 + \tilde{\mathbf{v}}_0 \tilde{t} - \int_0^{\tilde{t}} d\tau' \int_0^{\tau'} d\tau \tilde{\mathbf{E}}\left(t_0 + \sqrt{I_p}/E_p \tau\right) \\ &= \Delta\tilde{\mathbf{r}}(\tilde{t}) + \tilde{\mathbf{r}}_0 + \tilde{\mathbf{v}}_0 \tilde{t} - \frac{1}{2} \tilde{\mathbf{E}}(t_0) \tilde{t}^2 - \sum_{n=1}^{\infty} \frac{\tilde{\mathbf{E}}^{(n)}(t_0)}{\sqrt{2^n} (n+2)!} \gamma_{\text{eff}}^n \tilde{t}^{n+2}. \end{aligned} \quad (5.34)$$

In the second line, the electric field is expanded around the time t_0 and the appearing integrals are performed analytically. The zeroth-order term in the effective Keldysh parameter γ_{eff} is simply the trajectory in a constant electric field. Inserting this form (5.34) in Newton's equation (2.49) for a bare $-Z/r$ potential, the time evolution of the Coulomb correction $\Delta\tilde{\mathbf{r}}(\tilde{t})$ is governed by

$$\frac{d^2}{d\tilde{t}^2} \Delta\tilde{\mathbf{r}}(\tilde{t}) = -\tilde{Z} \frac{\tilde{\mathbf{r}}(\tilde{t})}{\tilde{r}^3(\tilde{t})}. \quad (5.35)$$

Note that so far no approximation was made to the classical motion. In contrast to pure linear polarization, the electron is driven by the quasilinear field away and does not come back close to the parent ion. Importantly, the Coulomb attraction rapidly decreases as a function of the distance from the ion. Thus, in the adiabatic limit of vanishing Keldysh parameter ($\gamma_{\text{eff}} \rightarrow 0$), the Coulomb-induced momentum change is mainly gained in a time interval much shorter than an optical cycle of the light field [210].

In the quasilinear field, the derivative of the electric field $\dot{\mathbf{E}}(0)$ vanishes at the time of peak electric-field strength. Hence, the first-order correction in γ_{eff} of the trajectory (5.34) disappears. Therefore, it is a good approximation to only consider the trajectory in a constant electric field given by¹⁴

$$\tilde{\mathbf{r}}(\tilde{t}) = \Delta\tilde{\mathbf{r}}(\tilde{t}) + \tilde{\mathbf{r}}_L(\tilde{t}) \approx \Delta\tilde{\mathbf{r}}(\tilde{t}) + \tilde{\mathbf{r}}_0 + \tilde{\mathbf{v}}_0\tilde{t} - \frac{1}{2}\tilde{\mathbf{E}}(t_0)\tilde{t}^2. \quad (5.36)$$

Interestingly, in scaled coordinates, the equation of motion and the tunnel exit from the field-direction model (5.27) only depend on $|\tilde{\mathbf{E}}(t_0)|$, \tilde{Z} and $\tilde{\mathbf{v}}_0$. Around $t \approx 0$, the field strength is approximately constant ($|\tilde{\mathbf{E}}(t)| \approx 1$) and we find for the FDM tunnel exit

$$\tilde{\mathbf{r}}_0 = -\frac{(1 + \tilde{\mathbf{v}}_0^2/2) + \sqrt{(1 + \tilde{\mathbf{v}}_0^2/2)^2 - 4\tilde{Z}}}{2}\hat{\mathbf{E}}(0). \quad (5.37)$$

As a result, under the made assumptions, the Coulomb-induced momentum changes $\Delta\mathbf{p}_C$ in reduced units ($\Delta\tilde{\mathbf{p}}_C = \Delta\mathbf{p}_C/\sqrt{I_p}$) are also only functions of the velocity $\tilde{\mathbf{v}}_0$ and the combination $\tilde{Z} = \frac{E_p}{I_p^2}Z$ of the peak field strength E_p , the ionization potential I_p and the asymptotic charge Z . However, it is worth to note that for other choices of tunnel-exit positions such as the TIPIS model such a universal scaling is not present.

To obtain a simplified analytical result, we consider the Coulomb field a weak perturbation. The first-order correction of the final momentum in the interaction strength \tilde{Z} is calculated by integration of the Coulomb force along the light-driven trajectory $\tilde{\mathbf{r}}_L(\tilde{t})$ [210]

$$\Delta\tilde{\mathbf{p}}_C = -\tilde{Z} \int_0^\infty d\tau \frac{\tilde{\mathbf{r}}_L(\tau)}{\tilde{r}_L^3(\tau)}. \quad (5.38)$$

Inserting the trajectory of Eq. (5.36) in Eq. (5.38) leads to a momentum change $\Delta\mathbf{p}_C = \sqrt{I_p}\Delta\tilde{\mathbf{p}}_C$ with¹⁵

$$\Delta\tilde{\mathbf{p}}_C = \left[\frac{\pi}{2} \frac{\tilde{Z}}{\sqrt{2\tilde{r}_0^3\tilde{\mathbf{E}}(t_0)}} - \frac{3\pi}{16} \frac{\tilde{Z}\tilde{\mathbf{v}}_0^2}{\sqrt{2\tilde{r}_0^5\tilde{\mathbf{E}}^3(t_0)}} \right] \hat{\mathbf{E}}(t_0) - \frac{1}{2} \frac{\tilde{Z}}{\tilde{r}_0^2\tilde{\mathbf{E}}(t_0)} \tilde{\mathbf{v}}_0. \quad (5.39)$$

Equation (5.39) is only correct to second order in the initial velocity \mathbf{v}_0 . The Coulomb attraction focuses the wave packet in the directions perpendicular to the instantaneous electric field, resulting in a narrower final transverse momentum distribution compared to the initial velocity distribution (see the last term in Eq. (5.39)). Additionally, the wave packet is decelerated in the direction of the instantaneous field $\mathbf{E}(t_0)$ (see the first term in Eq. (5.39)). Thus, for the quasilinear field, the p_y -component of the electron momentum is shifted.

A common assumption is that the attoclock shifts in the final momentum distribution, which are obtained by peak search, correspond to ionization at the time of peak field strength. Then, within the presented simple model, the momentum-dependent attoclock shifts are given by $\Delta p_{C,y}$ of Eq. (5.39). In the following, we will explore their dependence on the tunnel-barrier width r_0 and the ability to utilize the attoclock as a ‘‘nano-ruler’’.

Before proceeding the analysis of the attoclock shift, we consider the properties of the main ingredient of the classical model: the tunnel-exit positions. For close-to-circularly-polarized fields, we found in Section 5.2.4 that a decisive dependence of the tunnel-exit positions on the initial electron velocity \mathbf{v}_0 is present in the classical backpropagation approach. Here, we apply this method to the quasilinear setting and restrict ourselves again to ionization at $t_0 = 0$, i.e., at the peak of the electric-field strength. Since the setting is nearly isotropic in the directions perpendicular to the instantaneous field, it is sufficient to analyze the tunnel-exit positions along one coordinate axis of the initial velocity. The $r_{0,\parallel}$ -component of the initial position antiparallel to the field $\mathbf{E}(t_0)$ shows a quadratic dependence on the initial velocity $v_{0,z}$ (see Fig. 5.17(a)). For nonzero initial velocities \mathbf{v}_0 , the increased effective ionization potential $I_p^{\text{eff}} = I_p + \mathbf{v}_0^2/2$

¹⁴For vanishing initial velocity, this idea was already used in Refs. [210, 301, 347].

¹⁵We assume a tunnel exit of the form $\tilde{\mathbf{r}}_0 = -\tilde{r}_0\hat{\mathbf{E}}(t_0)$ such as in the field-direction model and assume $\tilde{\mathbf{v}}_0 \cdot \hat{\mathbf{E}}(t_0) = 0$.

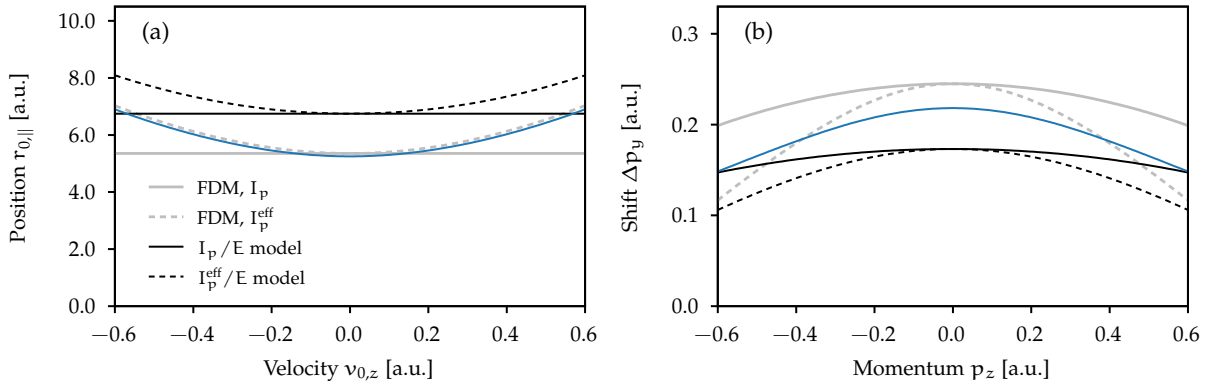


Figure 5.17: (a) Component of tunnel-exit position antiparallel to the instantaneous electric field $E(0)$ as a function of the initial velocity $v_{0,z}$ for ionization at $t_0 = 0$. The result from classical backpropagation (blue line) is compared to the I_p^{eff}/E model (black dashed line) and the field-direction model of Eq. (5.27) with velocity dependence (gray dashed line). (b) Momentum-dependent attoclock shift as a function of p_z at fixed $p_x = -A_x(0) \approx 2.96$ a.u. extracted from the solution of TDSE in 3D (blue line). In addition, the momentum shift $\Delta p_{C,y}$ of the model in Eq. (5.39) is shown for the different choices of the tunnel exit from panel (a). The intensity is 7×10^{14} W/cm 2 ($E_p = 0.134$ a.u.) and an effective wavelength of 1500 nm is used in the TDSE simulation. The other parameters are the same as in Fig. 5.14. Figure is adapted from Brennecke *et al.* [369].

leads to an outward shift of the exit position. In contrast to circular polarization, the first-order non-adiabatic corrections vanish for the quasilinear field in the vicinity of its maximum. As a result, the backpropagation result for a long-range potential agrees very well with the adiabatic FDM of Eq. (5.27). When repeating the backpropagation calculation for a short-range potential (not shown), we find perfect agreement with the simple I_p^{eff}/E estimate.

In the classical model, the influence of the Coulomb force on the outgoing electron is smaller for a larger tunnel-exit position (see also Eq. (5.39)). Thus, the increasing tunnel-barrier width as a function of v_0^2 results in a decreasing attoclock shift in the classical model. This explains already qualitatively the observed momentum dependence of the attoclock shift in Fig. 5.15. It is instructive to first consider a further simplification of the model by using the I_p^{eff}/E tunnel-exit position. To second order in v_0 , the momentum change of Eq. (5.39) is then given by

$$\Delta \bar{p}_{C,y} = \frac{\pi}{2\sqrt{2}} \tilde{Z} - \frac{9\pi}{16\sqrt{2}} \tilde{Z} \tilde{v}_0^2. \quad (5.40)$$

The first term describes the global attoclock shift at $\mathbf{v}_0 = 0$ or equivalently at the final momentum $p_x + A_x(0) = 0$ and $p_z = 0$ which was already found in Refs. [210, 347]. When using the approximate relation $\mathbf{v}_0 \approx (p_x + A_x(0))\mathbf{e}_x + p_z\mathbf{e}_z$, the second velocity-dependent term in Eq. (5.40) leads to a reduction of the attoclock shift for nonzero $p_x + A_x(0)$ and p_z . We find that within the model two thirds of the velocity-dependent term are attributed to the velocity dependence of the tunnel-exit position \mathbf{r}_0 and one third is related to the linear velocity dependence of the electron trajectory (see Eq. (5.36)).

The estimate $\Delta p_{C,y}$ of the classical model (5.39) is depicted in Fig. 5.17(b) for different choices of the tunnel-exit position. In all cases, a clear variation of the attoclock shift as a function of the momentum p_z is visible. If the dependence of the tunnel-barrier width on the velocity is artificially neglected by setting $I_p^{\text{eff}} = I_p$, the dependence of the attoclock shift on p_z is drastically reduced. For a comparison to results from the numerical solution of the TDSE in 3D, we choose adiabatic ionization conditions by considering an effective wavelength of 1500 nm (Keldysh parameter $\gamma_{\text{eff}} \approx 0.3$). The model leads to a slightly too large global attoclock shift compared to the TDSE result. Even though the momentum dependence of the attoclock shift is qualitatively correctly reproduced, the simplified model is unable to precisely predict the curvature. To investigate these deviations, we will study the influence of additional effects such as higher-order Coulomb corrections, the initial probability distribution or the interplay between nonadiabatic and Coulomb effects in the following Sections 5.3.2 and 5.3.3.

5.3.2 Scaling towards the adiabatic limit

Motivated by the classical adiabatic model with its universal dependence of the attoclock shift on the interaction strength \tilde{Z} , we further explore the attoclock shift in the adiabatic limit. Again, the TDSE is solved numerically by means of the split-operator method on two Cartesian grids as described in Section A.2.2, but the dynamics is only considered in a reduced 2D setting. The potential of Eq. (5.17) is used with the parameters $Z_{\text{core}} = 3$ and $\epsilon = 0.64$. One goal of this section is to study the influence of the ionization potential I_p and the asymptotic charge Z on the attoclock shift. To this end, for a given charge Z , the desired ionization potential is fixed by adjusting the screening distance r_{core} .

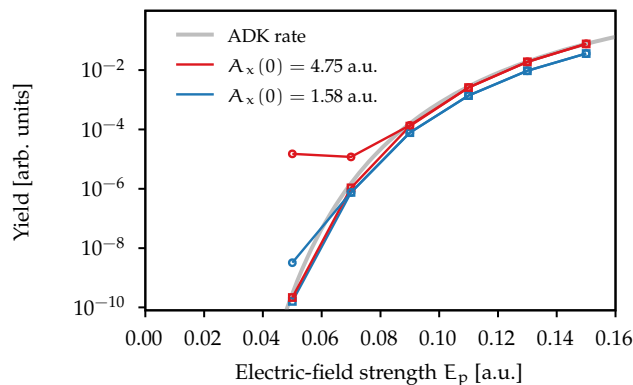


Figure 5.18: Ionization probability as a function of the peak field strength for ionization with three-cycle bicircular pulses. Results from velocity gauge (circles) are compared to results from length gauge (squares) for the same numerical parameters. For each field strength, the vector potential $A_x(0)$ and, hence, the Keldysh parameter are fixed (see the legend) by scaling the wavelength. The results are calculated by numerical solution of the 2D TDSE for an initial $1s$ state with $I_p \approx 0.904$ a.u. For comparison, the ADK rate (2.3) is scaled by an arbitrary factor.

To determine results in the adiabatic limit, we extrapolate results for finite nonadiabaticity by scanning the wavelength of the radiation. A problem is that, for a fixed ionization potential, small Keldysh parameters are related to huge vector potentials, $\gamma_{\text{eff}} = \sqrt{2I_p} \omega_{\text{eff}}/E_p = 5/3 \sqrt{I_p}/|A_x(0)|$. When solving the TDSE for helium in velocity gauge on Cartesian grids spanning 409.6 a.u. in each direction with spacings of $\Delta x = 0.2$ a.u. (as used in the previous chapters), we observe nonphysical behavior for those large vector potentials. To illustrate this, Figure 5.18 shows that ionization yield as a function of the field strength, but for fixed values of the vector potential. The comparison of the velocity-gauge TDSE results with the ADK rate (2.3) multiplied by the pulse length reveals a large amount of artificial ionization for low field strength. In order to avoid this numerical problem, the length gauge is chosen in this section.¹⁶ For sufficiently high field strengths related to large ionization probabilities, both gauges give virtually identical results for the same grid sizes. In addition, for adiabatic conditions, the length-gauge result also perfectly follows the ADK rate for smaller field strengths.

For a systematic study, we perform a series of TDSE calculations for a target (modeled by the potential (5.17)) with ionization potential $I_p = 1$ a.u. and an asymptotic charge $Z = 1$ by varying the peak field strength E_p while keeping the effective Keldysh parameter fixed. Hence, for given E_p and I_p , we adjust the frequency ω of the radiation. As suggested by the classical model (5.40) the global attoclock shift varies approximately linearly with the field strength as long as the fields are sufficiently weak (see Fig. 5.19(a)). For strong fields, we observe a turn to smaller offsets. Here, as discussed in Refs. [213, 350, 351], depletion shifts the peak of the ionization rate to earlier times such that the attoclock offsets from TDSE decrease. In a model introduced in Ref. [161], it can be shown that, for fixed field strength, the distributions for long laser wavelengths are most influenced by depletion.

¹⁶In length gauge, the field-free initial state is usually a good approximation to the state in the presence of the laser field. Since both gauges are connected by $|\psi_V\rangle = \exp(-i\mathbf{r} \cdot \mathbf{A}(t))|\psi_L\rangle$, the state in the presence of the field is shifted in momentum space by the vector potential $\mathbf{A}(t)$ in velocity gauge. When working on Cartesian grids, the maximal momentum in one direction $p_{\text{max}} = \pi/\Delta x$ is defined by the spacing Δx , e.g., $p_{\text{max}} \approx 15.7$ a.u. for a spacing of $\Delta x = 0.2$ a.u. However, the momentum-space representation of bound s states can be approximated as $\tilde{\Psi}_0(\mathbf{k}) \propto 1/(\mathbf{k}^2 + \kappa^2)^{1+Z/\kappa}$ and it decreases very slowly as a function of \mathbf{k} on a scale given by $\kappa = \sqrt{2I_p}$. Hence, in velocity gauge, large shifts $\mathbf{A}(t)$ by several atomic units of the state in momentum

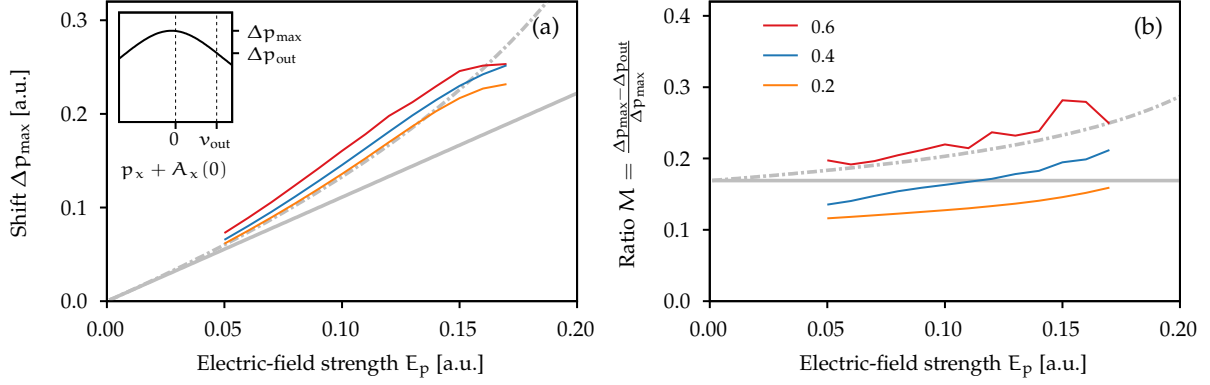


Figure 5.19: (a) Global attoclock shift Δp_{\max} as a function of the field strength. (b) Relative variation of the attoclock shift represented by the ratio $M = \frac{\Delta p_{\max} - \Delta p_{\text{out}}}{\Delta p_{\max}}$ with Δp_{out} being the attoclock shift at $v_{\text{out}} = 0.4$ a.u. A sketch of the situation is shown in the inset of panel (a). The colored lines show the TDSE results for fixed values of the Keldysh parameter γ_{eff} as indicated in the legend. The gray lines show the adiabatic estimate (5.39) for the I_p^{eff}/E tunnel exit (gray solid lines) or the field-direction model (gray dashed-dotted lines). Figure is adapted from Brennecke *et al.* [369].

In general, the observed attoclock shifts slightly increase for more nonadiabatic conditions. This can be more clearly seen when studying the global attoclock shifts as a function of the Keldysh parameter (see Fig. 5.20(a) for a fixed field strength $E_p = 0.1$ a.u.). As expected, in the vicinity of peak electric-field strength, the first-order nonadiabatic corrections are small such that the shift scales approximately quadratically with the Keldysh parameter. To extract the value Δp_{\max}^0 in the adiabatic tunneling limit ($\gamma_{\text{eff}} \rightarrow 0$), we use a quadratic fit $\Delta p_{\max}(\gamma_{\text{eff}}) = \Delta p_{\max}^0 + b\gamma_{\text{eff}}^2$ to the range of Keldysh parameters between 0.2 and 0.5. The extrapolated results are shown in Fig. 5.22(a). To check the extraction procedure, we performed fits including an additional linear in γ_{eff} . However, if depletion can be neglected, i.e., for not to high intensities, both fitting functions give virtually-identical results.

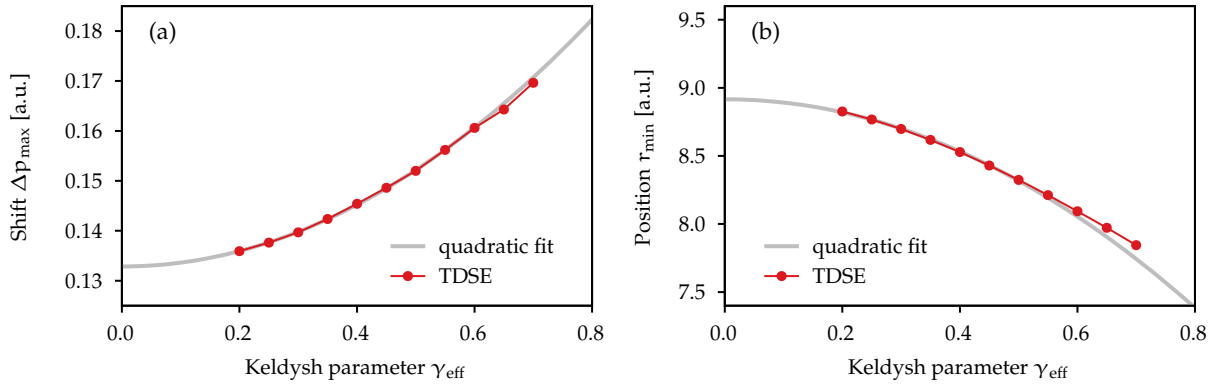


Figure 5.20: Extrapolation of the global attoclock shift (panel a) and the tunnel-barrier width (panel b) towards the adiabatic limit. Shown are the TDSE results versus Keldysh parameter γ_{eff} for fixed field strength $E_p = 0.1$ a.u. and corresponding quadratic fits.

To investigate the momentum dependence of the attoclock offsets, we quantify the relative variation of the attoclock shifts by a single figure of merit. To this end, a relative difference M between the global attoclock shift Δp_{\max} and an outer attoclock shift Δp_{out} is defined

$$M = \frac{\Delta p_{\max} - \Delta p_{\text{out}}}{\Delta p_{\max}} \quad (5.41)$$

with Δp_{out} being the attoclock shift at a given value of $v_{\text{out}} = p_x + A_x(0)$. The ratio M increases when using larger values of v_{out} . However, for values between 0.3 a.u. and 0.5 a.u., we observed the same qualitative behavior in the TDSE calculations. Thus, in the following, we only discuss results for $v_{\text{out}} = 0.4$ a.u. (see Fig. 5.19(b)). In the simple formula (5.40) where the I_p/E exit position is used, the relative difference M is independent of the field strength. For fixed Keldysh parameter, the relative difference M

space induce errors, if common grid parameters are used.

from TDSE indeed increases weakly as a function of the electric-field strength.¹⁷ The trend is qualitatively reproduced by classical adiabatic model of Section 5.3.1 when considering the FDM tunnel exit. Furthermore, for the TDSE results, we observe an increase of the relative variation M as a function of the Keldysh parameter γ_{eff} . For the most adiabatic conditions with $\gamma_{\text{eff}} = 0.2$, the ratios M from TDSE are smaller than the prediction of the classical adiabatic model of Eq. (5.39). It is evident that there is a systematic difference between the TDSE and the model which will be further studied in Section 5.3.3.

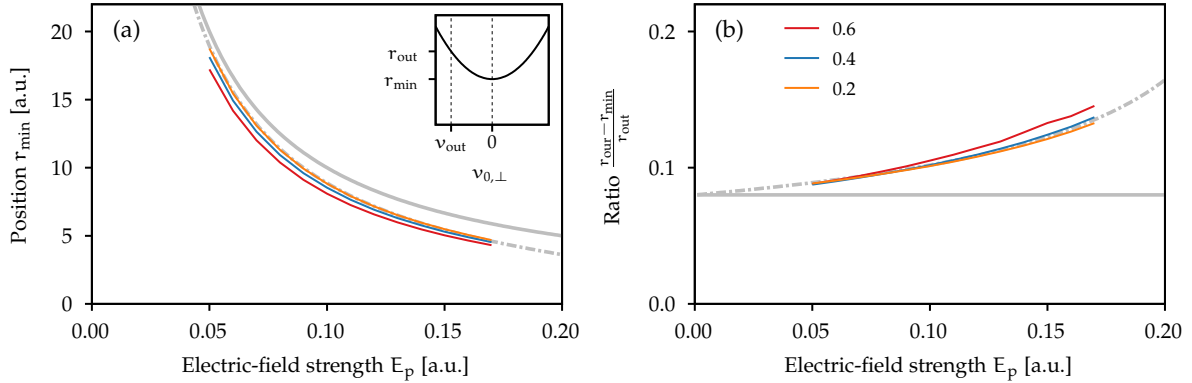


Figure 5.21: (a) Tunnel-barrier width r_{min} for vanishing initial velocity. (b) Velocity-dependent variation of the tunnel-barrier width represented by the ratio $\frac{r_{\text{out}} - r_{\text{min}}}{r_{\text{out}}}$ with r_{out} being the tunnel-barrier width at $v_{\text{out}} = 0.4$ a.u. The colored lines show the backpropagation results based on TDSE input for fixed values of the Keldysh parameter γ_{eff} as indicated in the legend. The gray lines show the I_p^{eff}/E tunnel exit (gray solid lines) or the field-direction model (gray dashed-dotted lines). Figure is adapted from Brennecke *et al.* [369].

In the microscopic analysis of the momentum-dependent attoclock shifts, the tunnel-exit positions play a crucial role. The results of the tunnel-barrier width at vanishing initial velocity from the classical backpropagation method are presented in Fig. 5.21(a) for the various laser conditions. In addition, we also quantify the variation of the tunnel-barrier width as a function of the initial velocity in a single figure of merit (see Fig. 5.21(b)). For the considered conditions, the exit positions roughly follow the estimate of the field-direction model. To investigate nonadiabatic effects, the tunnel-barrier width is analyzed as a function of the Keldysh parameter for fixed field strength (see Fig. 5.20(b)). Again, the first-order nonadiabatic correction vanishes in the vicinity of peak field strength. In agreement with the prediction in Ref. [163], we find a nonadiabatic reduction of the barrier width that scales quadratically with the Keldysh parameter. To determine the adiabatic limit, we again use a quadratic fit $r_{\text{min}}(\gamma_{\text{eff}}) = r_{\text{min}}^0 + b\gamma_{\text{eff}}^2$ to the range of Keldysh parameters between 0.2 and 0.5. The agreement of the extrapolated results from classical backpropagation with the field-direction model is quite remarkable (see Fig. 5.22(b)).

Repeating the steps above, we find the global attoclock shifts and the tunnel-barrier width in the adiabatic limit for various combinations of the asymptotic charge Z and the ionization potential I_p . As long as over-the-barrier ionization is unimportant, the tunnel-barrier width measured in units of I_p/E_p is a universal function of the interaction strength \tilde{Z} (see Fig. 5.22(b)). Similarly, a nearly universal behavior of the global attoclock shift measured in units of $\sqrt{I_p}$ on the interaction strength \tilde{Z} is observed, if depletion can be neglected. For small values of \tilde{Z} , the prediction of the adiabatic model (5.40) agrees reasonably well with the TDSE result, i.e., the attoclock offset is approximately a linear function of \tilde{Z} . Here, the TDSE solution is consistent with the assumption of vanishing ionization times. Going to larger interaction strength, higher-order corrections in \tilde{Z} become relevant. To consistently include these corrections in the classical modeling, the Coulomb effects on the trajectories are determined by numerical solution of Eq. (5.35) for the adiabatic trajectories (5.36) with vanishing initial velocities. The resulting Coulomb-induced momentum changes $\Delta p_{C,y}$ are shown in Fig. 5.22(a) as gray lines. The initial positions from FDM (dashed-dotted line) leads to a better agreement with the TDSE results compared to the I_p/E exit points (solid line).

¹⁷The oscillations for large Keldysh parameters are mostly caused by weak intracycle interference of the three different cigars in the PMD.

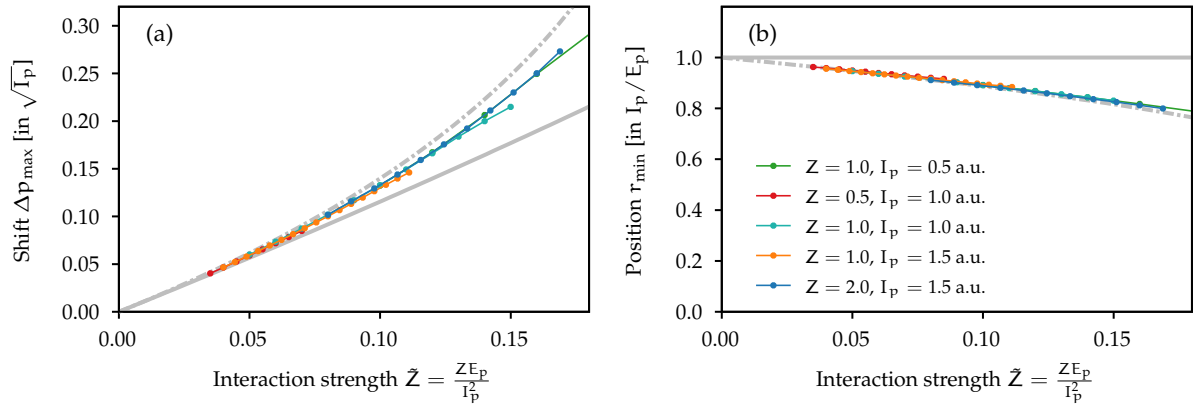


Figure 5.22: Adiabatic limit of the global attoclock shift (panel a) and the tunnel-barrier width (panel b) as a function of the interaction strength \tilde{Z} . The colored lines indicate data sets for various combinations of the asymptotic charge Z and the ionization potential I_p as indicated in the legend. For comparison, the classical attoclock shifts for the I_p/E tunnel exit (gray solid line) and for the field-direction model (gray dashed-dotted line) are calculated by the numerical solution of Eq. (5.35) with the adiabatic trajectory (5.36).

Even though the exit positions from the FDM are in perfect agreement with the positions from backpropagation, the attoclock shifts from TDSE are slightly smaller than classical FDM-based estimate.¹⁸ It is important to note that both considered quantities are in one respect fundamentally different: The backpropagation result for the tunnel exit is solely based on the phase information of the outgoing wave packet in momentum-space representation [350, 377]. In contrast, the attoclock shift represents the corresponding modulus squared of the probability amplitude. The discrepancy can be interpreted in the sense that, for large interaction parameters (typically related to large field strength) and even under adiabatic conditions, in a trajectory-based description (with the initial conditions from backpropagation) the most probable ionization time needs to be slightly negative in order to reproduce the TDSE distributions. Importantly, compared to more nonadiabatic conditions [161, 359], these time delays are quite small (only a few attoseconds).

5.3.3 Advanced models based on probability distributions

For adiabatic conditions and small interaction strength \tilde{Z} , the variation of the attoclock shift as a function of the momentum is overestimated by the classical adiabatic model of Section 5.3.1 (see Fig. 5.19(b)). For an easier comparison, we also consider a quadratic fit to determine the adiabatic limit of the relative variation M from the TDSE results. The extrapolated ratios are nearly independent of the electric-field strength (see Fig. 5.23(b)). However, in contrast to the global attoclock shift, the extrapolation including a linear term in the Keldysh parameter leads to slightly larger ratios M .¹⁹

The classical adiabatic model is based on two main assumptions: (i) The process is treated adiabatically, e.g., the initial velocity has no component along the ionizing field and the Coulomb-induced momentum change is calculated for a trajectory in a constant electric field. (ii) The attoclock shift is modeled by following the classical trajectories starting at the peak of the electric-field strength, i.e., in contrast to the TDSE simulations no distribution of final momenta is considered. To “refine” the model, a CTMC simulation based on sampling an entire initial probability distribution can be used to extract the attoclock shifts from final momentum distributions (as done in Section 5.2.3 for elliptical polarization). If \mathbf{p}' was the final momentum in the absence of the Coulomb interaction, the final momentum in the presence of the Coulomb interaction can be written as $\mathbf{p} = \mathbf{p}' + \Delta\mathbf{p}_C$. For small \tilde{Z} , the momentum

¹⁸For initial positions from the TIPIS model, the results are not universal functions of \tilde{Z} . However, in general, we find that the attoclock offsets predicted for the TIPIS exits agree slightly better with the offsets from TDSE compared to the FMD model.

¹⁹For the highest-considered field strength, the results of both fits agree very well. However, when going to the weakest fields, the ratios M of extrapolation including a linear term systematically increase and reach values as high as 0.15 for $E_p = 0.05$ a.u. We cannot rule out that this is a numerical issue.

change $\Delta\mathbf{p}_C$ of the CTMC method can be treated by perturbation theory

$$\Delta\mathbf{p}_C = - \int_{t_0}^{t_f} dt \nabla V \left(\mathbf{r}_0 + \int_{t_0}^t d\tau (\mathbf{p} + \mathbf{A}(\tau)) \right). \quad (5.42)$$

Usually, the change $\Delta\mathbf{p}_C$ depends on the given final momentum \mathbf{p} . If the initial distribution is chosen from SFA²⁰, the distribution of final momenta \mathbf{p} from a CTMC simulation can be approximated as

$$w_{\text{CTMC}}(\mathbf{p}) \approx e^{-2\text{Im}S_{\text{SFA}}(\mathbf{p}')} \approx e^{-2\text{Im}S_{\text{SFA}}(\mathbf{p}-\Delta\mathbf{p}_C)}. \quad (5.43)$$

Using the PMD of Eq. (5.43) to extract the momentum offsets analogous to the TDSE, the global attoclock shift is in perfect agreement with the adiabatic estimate of Eq. (5.40) (see Fig. 5.23(a)). In contrast, the variation M is even further overestimated in a CTMC simulation compared to the classical adiabatic model of Eq. (5.40) and the TDSE results (see panel (b) in Fig. 5.23). This systematic deviation is related to the form of Coulomb-free momentum distribution. Its width in longitudinal direction (p_y -direction) is proportional to the laser wavelength whereas the width in lateral direction is nearly wavelength independent. In combination with nonadiabatic modifications of the classical trajectories²¹, a wavelength-independent correction of the momentum-dependent attoclock offsets appears that persists in the adiabatic limit. Hence, the *ad-hoc* combination of initial distributions from quantum-mechanical theories with the classical Newtonian trajectories leads to slight inconsistencies in the CTMC simulations.

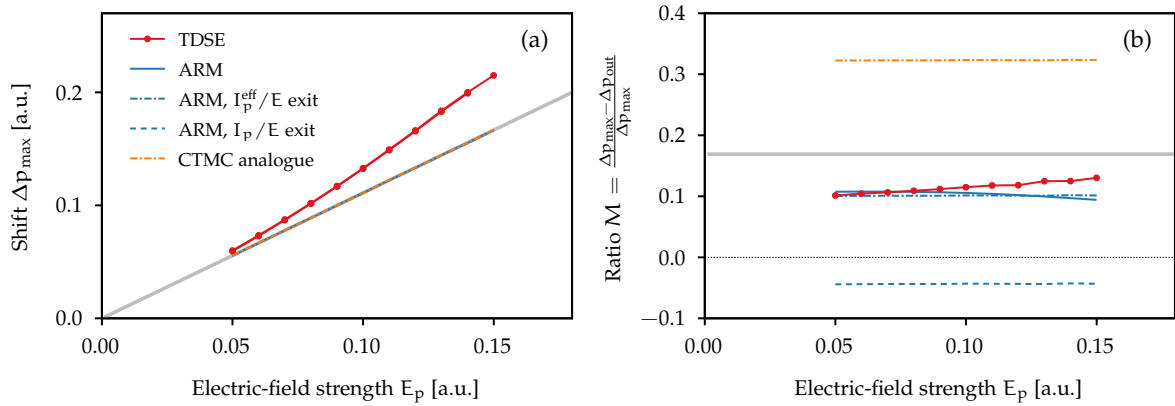


Figure 5.23: Comparison of different levels of approximation for the adiabatic limit of the global attoclock shifts (panel a) and of the relative variations M of the attoclock shifts (panel b). In addition to the results from TDSE, various approximations of ARM theory, the CTMC model of Eq. (5.43) and the simple estimate of Eq. (5.40) (gray lines) are shown. In panel (a), the global attoclock shifts for all versions of ARM theory and for the CTMC analogue are on top of the gray lines and cannot be distinguished. The other parameters are the same as in Fig. 5.19.

For a simplified modeling of PMDs which includes nonadiabatic effects and Coulomb effects in a systematic manner, we use the ARM theory introduced in Section 2.5. The ARM theory only takes the potential V to first order in the action into account. Thus, for consistency, we perform the simulations for $Z = 0.01$ and use a linear extrapolation to estimate the observables for the desired value of $Z = 1$. In addition, the same extraction procedure of the attoclock shifts in the adiabatic limit as for the TDSE is used. By construction the global attoclock shifts from ARM theory scale linearly with the parameter \tilde{Z} and exactly follow the classical estimate (5.40). The ARM results for the variation M agree very well with the full numerical TDSE results and are superior compared to the classical adiabatic model of Section 5.3.1 and the CTMC simulations.

In the following, we study the difference between the CTMC simulations and the ARM theory. For the global attoclock shift, a similar procedure was already applied in Ref. [161]. In ARM theory, the Coulomb correction of the action is calculated along a complex-valued quantum orbit (2.56) evolving in complex time from the saddle point t_s' to the final time t_f . When using the standard two-pronged

²⁰Here, preexponential factors and the Jacobian are neglected.

²¹Both an initial velocity component along the instantaneous field and nonadiabatic corrections during the continuum motion contribute.

integration path from t'_s down to the real axis $t'_r = \text{Re}(t'_s)$ and then to the final time t_f , the Coulomb correction of Eq. (2.60) can be split into two parts:

$$\text{Im } S_C^\downarrow(\mathbf{p}, t'_s) = -\text{Im} \int_{t'_s - i\kappa^{-2}}^{t'_r} d\tau V(\mathbf{r}_L(\tau; \mathbf{p}, t'_s)), \quad \text{Im } S_C^\rightarrow(\mathbf{p}, t'_s) = -\int_{t'_r}^{t_f} d\tau \text{Im } V(\mathbf{r}_L(\tau; \mathbf{p}, t'_s)). \quad (5.44)$$

In the adiabatic limit, virtually-identical results are obtained, if the first part (corresponding to under-the-barrier motion) is neglected. For the part $\text{Im } S_C^\rightarrow$ corresponding to the subsequent beyond-the-barrier motion, we only need to study the quantum orbit \mathbf{r}_L for real-valued times in the interval $\tau \in [t'_r, t_f]$

$$\begin{aligned} \mathbf{r}_L(\tau; \mathbf{p}, t'_s) &= \int_{t'_s}^{\tau} dt'' (\mathbf{p} + \mathbf{A}(t'')) = \int_{t'_s}^{t'_r} dt'' (\mathbf{p} + \mathbf{A}(t'')) + \int_{t'_r}^{\tau} dt'' (\mathbf{p} + \mathbf{A}(t'')) \\ &= i \text{Im } \mathbf{r}_L(t'_r; \mathbf{p}, t'_s) + \mathbf{r}_0 + \int_{t'_r}^{\tau} dt'' (\mathbf{p} + \mathbf{A}(t'')). \end{aligned} \quad (5.45)$$

The last two terms represent a classical real-valued potential-free trajectory starting at the time t'_r at the SFA tunnel exit \mathbf{r}_0 of Eq. (3.21). However, the first purely imaginary-term does not have a classical counterpart and can be written as [161]

$$\text{Im } \mathbf{r}_L(t'_r; \mathbf{p}, t'_s) = -\nabla_{\mathbf{p}} \text{Im } S_{\text{SFA}}(\mathbf{p}). \quad (5.46)$$

In the adiabatic limit, the SFA exit position can be approximated by the I_p^{eff}/E tunnel-exit position (see Eq. (5.25)). Using the trajectory of Eq. (5.45) in combination with the I_p^{eff}/E tunnel-exit position, we find nearly perfect agreement with the full ARM simulations (see Fig. 5.23(b)). However, if the velocity dependence of the tunnel exit is artificially neglected, the attoclock shift as a function of $p_x + A_x(0)$ increases. Hence, negative values of the relative variation M appear which are in contradiction with the TDSE results. Hence, even in ARM theory, we observe a decisive influence of the velocity-dependent tunnel-exit positions on the momentum-resolved attoclock shifts.

Naturally, the question about the difference between the ARM theory and the CTMC model appears. Around the global maximum of PMD, the gradient of the imaginary part of the SFA action is small. Thus, it was suggested in Ref. [161] that the Coulomb correction $\text{Im } S_C^\rightarrow$ of Eq. (5.44) can be expanded in terms of $\text{Im } \mathbf{r}_L(t'_r; \mathbf{p}, t'_s)$ by using Eq. (5.46). To first order in $\text{Im } \mathbf{r}_L(t'_r; \mathbf{p}, t'_s)$, the relevant imaginary part of the ARM action reads

$$\begin{aligned} \text{Im } S_{\text{ARM}}(\mathbf{p}, t'_s) &= \text{Im } S_{\text{SFA}}(\mathbf{p}) + \text{Im } S_C(\mathbf{p}, t'_s) \approx \text{Im } S_{\text{SFA}}(\mathbf{p}) + \text{Im } S_C^\rightarrow(\mathbf{p}, t'_s) \\ &\approx \text{Im } S_{\text{SFA}}(\mathbf{p}) - \Delta \mathbf{p}_C \cdot \nabla_{\mathbf{p}} \text{Im } S_{\text{SFA}}(\mathbf{p}) \approx \text{Im } S_{\text{SFA}}(\mathbf{p} - \Delta \mathbf{p}_C). \end{aligned} \quad (5.47)$$

Here, we used the classical momentum change of Eq. (5.42). If this first-order expansion in $\text{Im } \mathbf{r}_L$ is sufficient, the ARM theory gives the same results as the CTMC model of Eq. (5.43). For the global maximum

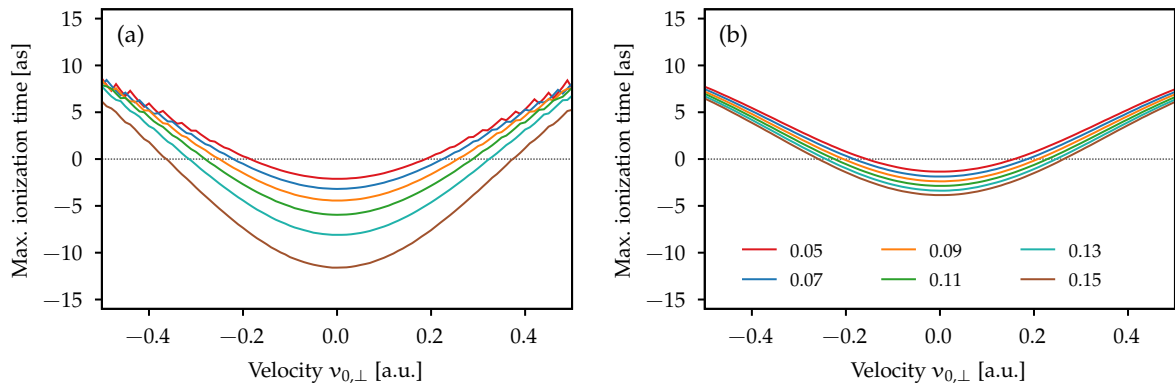


Figure 5.24: Most probable ionization time as a function of the lateral velocity $v_{0,\perp}$ extracted from classical backpropagation simulations based on TDSE input (panel a) or on input from ARM theory (panel b). The different curves show the results for various peak field strength as indicated in the legend in a.u. but fixed Keldysh parameter $\gamma_{\text{eff}} = 0.3$. The other parameters are the same as in Fig. 5.19.

of the distribution, the expansion indeed works well. Hence, for sufficiently adiabatic conditions, the ARM theory results in the same global attoclock shift as the CTMC model [161]. However, when going towards nonzero lateral momenta $p_x + A_x(0)$, we find that $\text{Im } r_L$ is nonzero and higher-order contributions become important such that a truncation of the expansion is not even appropriate in the adiabatic limit.

As pointed out above, CTMC simulations based on initial coordinate distributions from the SFA do not consider these additional terms in ARM theory due to the nonzero imaginary part of the quantum orbits. However, in principle, we can choose an initial phase-space distribution in a way that a CTMC simulation would exactly reproduce the PMD from TDSE. One approach to determine the required initial distribution is the backpropagation method (see Eq. (5.16)). For various field strengths and a fixed Keldysh parameter of $\gamma_{\text{eff}} = 0.3$, we apply the classical backpropagation to the electron wave packets from either TDSE simulations in 2D or ARM calculations. To characterize the required initial distributions, the most probable ionization time is separately determined for each lateral velocity $v_{0,\perp}$. We find that the most probable ionization time increases as a function of $|v_{0,\perp}|$ (see Fig. 5.24).²² In a (possible) CTMC simulation, this property of the initial distribution would be important to reproduce the ratio M of the momentum-dependent attoclock shift observed in TDSE and ARM theory.

5.4 Conclusion

In this chapter, photoelectron momentum distributions from recollision-free strong-field ionization of atoms were studied using the attoclock protocol. Two implementations were considered based either on close-to-circularly-polarized laser fields or quasilinear fields, i.e., bicircular counter-rotating laser fields with an intensity ratio 4 : 1 of fundamental to second harmonic field. We concentrated on the attoclock offsets related to the influence of the Coulomb attraction on the outgoing electrons. Previous theoretical works mostly investigated the global attoclock offset, i.e., the global maximum of the electron momentum distribution. However, in general, the attoclock offset depends on the lateral momentum component of the electron (orthogonal to the direction of the attoclock shift), i.e., it depends on which slice through the momentum distribution is analyzed. Within a trajectory-based modeling, these momentum-dependent attoclock offsets are sensitive to the tunnel-exit positions. Throughout the whole chapter, we explored this concept of a “nano-ruler” [54, 55] to probe the tunnel-exit positions with subangstrom precision. However, our study also revealed that there are several complications in the actual implementation of this idea.

In close-to-circularly-polarized fields, we considered the angular offset in polar coordinates as a function of the electron momentum in the plane of polarization. Even in a Coulomb-free situation, we found that the shape of the electron wave packet already leads to nonzero offset angles for radial momenta away from the global maximum. For example in elliptically-polarized fields, the angular maxima are aligned along the semi-minor axis of the polarization ellipse for small radial momenta whereas they are aligned along the semi-major axis at large radial momenta. Even though the Coulomb attraction induces finite offset angles for all radial momenta, the general trend of the angular offsets is already defined by the shape of the released wave packet. For nonadiabatic strong-field ionization of atomic hydrogen by elliptically-polarized laser pulses, the comparison of photoelectron momentum distributions from TDSE simulations to a recent experimental data showed quantitative agreement [357]. There, the simple electronic structure of atomic hydrogen and, especially, the absence of multi-electron effects provided a clean setting to benchmark the theoretical description and the experimental capabilities against each other. The observed attoclock offsets were also modeled in a trajectory-based simulation. We found that the agreement with the TDSE results was greatly improved by using nonadiabatic initial conditions

²²For the backpropagation of ARM results, the small negative ionization times at $v_{0,\perp} = 0$ are solely attributed to a not-consistently-treated Jacobian in Eq. (5.16). The quadratic dependence of the most probable ionization time on the initial velocity is nearly unchanged for a “nonadiabatic velocity criterion” (as introduced in Ref. [211]) which takes a parallel component of the initial velocity into account.

from the strong-field approximation and, especially, by considering tunnel-exit positions that depend on the initial velocity of the electron.

The geometry of the liberated electron wave packet as well as nonadiabatic effects complicate the interpretation of the momentum-dependent attoclock offsets in close-to-circularly-polarized fields. To a certain extent, these problems can be avoided in the bicircular attoclock. In this setting, the electric field mimics linear polarization for times close to the peak field strength while the overall shape of the vector potential still provides a meaningful time-to-momentum mapping [359]. The special geometry simplifies the analysis of the attoclock offset as a function of the lateral momentum. The Coulomb attraction on the outgoing electrons basically leads to a shift of the most probable electron momentum along the direction of the instantaneous electric field. Based on numerical simulations of the TDSE we determined the momentum-dependent attoclock offsets for a large range of laser parameters and extracted their adiabatic limit. Within a classical adiabatic model, we confirmed that the dependence of the tunnel-exit position on the initial electron velocity strongly influences the momentum dependence of the attoclock offset. However, while the classical model reproduces the global attoclock shift well, the momentum dependence of the attoclock shift is only qualitatively described. Within the analytical R-matrix (ARM) theory, we showed that nonclassical terms of the underlying quantum orbits play a crucial role. However, also in ARM theory, a velocity-dependent tunnel-exit position is needed to correctly model the momentum-dependent attoclock shifts.

To support the assumption of a velocity-dependent tunnel-exit position (as it is suggested by the strong-field approximation), we considered the classical backpropagation method for both shapes of the laser field. In our momentum-space backpropagation approach, the momentum-space phase of the outgoing electron packet is used to derive initial conditions for classical electron trajectories propagating backwards in time. For short-range potentials, we found that the exit positions based on the velocity criterion in backpropagation are in excellent agreement with the exit positions from the strong-field approximation. For long-range Coulomb potentials, the tunnel-barrier width is systematically reduced. By extrapolating the tunnel-exit positions from backpropagation for a quasilinear field towards the adiabatic limit, we found that these positions perfectly agree with the field-direction model.

In the future, it could be interesting to derive an analytical estimate for the electron wave packet from ARM theory in the adiabatic limit and to further investigate the observed discrepancies in momentum-dependence of the attoclock shift. In addition, the application of classical backpropagation to ARM input might enable the derivation of an analytical tunnel-exit position including leading-order Coulomb corrections. Both considerations could serve as a starting point to investigate the small negative ionization times observed in the classical backpropagation simulations with TDSE input.

By analyzing the momentum-resolved attoclock offsets more information on the released electron wave packet are accessible compared to the bare observation of the global attoclock offset. Thus, in the future, this new class of experiments may enable a deeper and more sensitive study not only of the strong-field ionization process but also of properties of the ionized target. The quasilinear attoclock with its approximately constant direction of the electric field during the electron's release provides an excellent setting to investigate the orientation-dependent ionization dynamics in molecules [367]. Based on the idea of a "nano-ruler" this offers the potential to retrieve tunnel-exit positions for molecules. Furthermore, a deeper theoretical study of chiral molecules in close-to-circularly-polarized attoclock configurations with their chiral-active properties could be interesting (as in Refs. [344, 360]). However, as pointed out above, a meaningful interpretation of such a setting is difficult and requires further investigation.

Chapter 6

Position Offsets in Strong-field Ionization of Small Molecules

6.1 Introduction

The desire to image atomic or molecular structures by means of photoelectron momentum distributions from strong-field ionization has already a long history. The first simulations and experiments studied the orientation dependence of the total yield for small molecules such as N_2 , O_2 or CO_2 by variation of the alignment of the molecular axis relative to the polarization direction of linearly-polarized lasers [57, 58, 378, 379]. A cleaner imaging configuration—avoiding recollisions and intracycle interference—is offered by considering the 3D momentum distributions from ionization in attoclock-like field configurations such as circularly-polarized fields [59–61]. If the molecular axis is fixed, then in the simple man’s model each electron emission direction is linked to a specific relative orientation of the molecule with respect to the instantaneous ionizing field. Hence, the ionization process in circular polarization contains a 360° scan of the molecular response. Using the COLTRIMS technique, Staudte *et al.* [59] and Odenweller *et al.* [380] measured the first molecular-frame-resolved PMDs in the polarization plane for H_2 and H_2^+ . The structural information encoded in PMDs was used, for example, to study asymmetric molecules [381], to probe the nodal structure of molecular orbitals for various species [382–386], to imagine valence-orbital motion [387] or to investigate the two-path inference in dimers [388]. Furthermore, the subcycle timing of molecular ionization was explored in Refs. [389, 390] and later on refined by using an attoclock technique with elliptical polarization [391–394].

Strong-field ionization prepares an electron wave packet in the continuum which can be represented by a complex-valued wave function, e.g., $\tilde{\psi}(\mathbf{p})$ in momentum space. However, experiments can only measure the electron momentum distribution, i.e., the modulus square of the final momentum-space wave function $|\tilde{\psi}(\mathbf{p})|^2$ (see the definition in Section 2.2). Hence, the previously-mentioned works with their intracycle-interference-free settings do not characterize the phase of the momentum-space wave function. In quantum mechanics, the position and momentum representation are related to each other by a Fourier transformation. Therefore, substantial information on the position distribution of the wave packet is encoded in the phase of the momentum-space wave function. Inspired by the semiclassical physics [255, 256, 375], we define the negative derivative of the spectral phase with respect to the momentum as the *local position*. A deeper motivation of this relation is given in Section 6.2.1.

The position distribution of an electron wave packet is determined by the release process as well as by the subsequent continuum motion under the influence of the external field. For molecules, the release process is especially sensitive to the orbital structure. The orbital dependence of the wave packet can for example influence recollision-based phenomena such as laser-induced electron diffraction [70]. In general, not only the emission probability depends on the direction of the ionizing field relative to the molecular orientation, but also the release position of the wave packet, i.e., its phase in momentum

space [240, 408]. This important piece of knowledge is lost when only considering interference-free PMDs. In theoretical simulations, on the other hand, the momentum-space phase of the outgoing wave packet and, thus, the position information are directly accessible. Thus, in the first part of this section, we perform numerical simulations based on the TDSE to investigate the spatial displacement of the electron wave packets in molecular strong-field ionization. The influence of nonadiabaticity on the position offsets is explored by considering both circularly-polarized fields and quasilinear fields (see Section 5.3). The long-range molecular potential also modifies the dynamics of the outgoing electron wave packet. To investigate its effect on the displacement of the asymptotic wave packet, we apply the classical backpropagation method (see Refs. [211, 350, 351] and Section 5.2.4).

While the absolute phase of wave function is not experimentally accessible, relative phases can be measured by analyzing the interference of different pathways. For single-photon ionization, the RABBITT scheme [65, 66, 395] enables studying phases of electron wave packets. There, the absorption of an infrared photon by a wave packet created via single-photon ionization in an XUV attosecond pulse train results in two independent interfering pathways. In atoms, RABBITT is sensitive to the energy derivative of the scattering phase which is known as the Wigner time delay [62]. In its original meaning, a Wigner delay is caused by modulation of the electron's wavelength upon passage over a potential during a scattering process. As a result, the scattered wave packet is shifted in space compared to a freely-traveling wave packet, i.e., retardation occurs. Single-photon ionization can be viewed as a "half-scattering" process where the electron is initially located in the vicinity of its parent ion and finally escapes from it. Thus, for atoms, RABBITT has a well-defined interpretation using the "original" Wigner time delay. For more complex targets as molecules [67, 396], the RABBITT scheme is sensitive to the derivative of the phase of the complex-valued photoionization amplitude [396]. However, in general, this quantity is not simply given by the derivative of a scattering phase and can be influenced by further parameters such as characteristics of the interaction process that creates the electron wave packet [397] or the initial location of the electron wave packet in a molecule [68].

In contrast to RABBITT, a huge number of photons is absorbed in strong-field ionization and, thus, a plethora of interference pathways emerge in the energy domain. Here, a trajectory-based description of interference in the time domain is beneficial. In principle, for linear polarization, various types of interference pattern were already introduced in Chapter 3 and could be used to explore the phase structure of the electron wave packets. Indeed, an influence of the continuum phase in molecular strong-field ionization was observed in photoelectron holography [29]. There, the orientation-dependent shift of the interference fringes is related to a variation of the initial phase of the tunneled wave packets [240]. Based on this idea, photoelectron holography was also theoretically studied to resolve birth positions of electron wave packets in molecular ionization [398, 399]. However, the main drawback of holography is that it inherently relies on scattering of electrons such that information on the initial electron wave packet is mixed up by orientation-dependent scattering properties (see for example Ref. [208]).

To avoid this drawback, a strong-field ionization process can be probed by a second weak field of a different color such that—similar to the RABBITT scheme—interference is artificially created. The perturbation of a strong field with frequency ω by a weak field of frequency $\omega/2$ induces an interference pattern of electron waves liberated in two consecutive optical cycles of the ω field. The modulation of the electron yield as a function of the relative phase between both colors was already observed for linearly-polarized fields in 1994 [400]. By considering the variation of the interference pattern as a function of this tunable parameter, information on the ionization process in the strong fundamental field can be extracted. Using linear polarization, the idea was first applied for the characterization of the relative spectral phases of different ATI peaks in atomic ionization [401]. This linearly-polarized setting was further theoretically studied by means of various methods such as the numerical solution of the TDSE or a simplified SFA-based model [402, 403]. To avoid complications due to recollisions, it is advantageous to use co-rotating circularly-polarized fields instead of linear polarization. This enables to retrieve of both phases and modulus squared of the emitted electron wave packets for atoms [404] or to study the time structure of strong-field ionization [405].

Recently, Eckart [69] proposed a scheme called holographic angular streaking of electrons (HASE) based on such co-rotating circularly-polarized fields in order to extract spatial displacements of the liberated electron wave packets from molecular strong-field ionization. In this method, the interfering wave packets involve slightly different initial velocities, so that the pattern contains information on the derivative of the phase in momentum space, i.e., on the local positions. For a theoretical description of the interference pattern, a semiclassical trajectory-based model assuming adiabatic tunneling was applied in Ref. [69]. The modeling allowed to reconstruct the derivative of the momentum-space phase of the liberated wave packet. In the second part of this section, we will theoretically evaluate the capabilities of the HASE interferometer. To this end, we first introduce the interference scheme in co-rotating fields. Afterwards, we use a potential-free description in the strong-field approximation to derive analytically a relation between the signal modulation in the two-color field and the position offsets in molecular strong-field ionization. Compared to the original modeling in Ref. [69] our description includes important nonadiabatic effects. Finally, we perform numerical experiments, i.e., we simulate the interference pattern in HASE based on TDSE, and retrieve from the two-color momentum distributions the position offsets in molecular hydrogen H_2 . The results from the interferometric approach are compared to the direct calculation of the position offsets based on the phase of the outgoing wave packet.

This chapter is based on joint work with the Dörner group in Frankfurt, especially with Daniel Trabert and Sebastian Eckart. In an experiment by Trabert *et al.* the HASE interferometer was first used to reconstruct orientation-dependent position offsets upon strong-field ionization of H_2 . Afterwards, we provided theoretical reference data for the position offsets for the joint publication [377]. These were directly extracted based on the phase of the outgoing wave packets from the numerical solution of the TDSE or the strong-field approximation.

6.2 Ab-initio calculation of position offsets

6.2.1 Motivation based on the PFT model

In the simple man's model, strong-field ionization is treated as a two-step process [7, 8]. Under adiabatic conditions, the electron is released via tunneling through a quasistatic barrier formed by bending of the ionic potential due to the laser field. For atoms, the liberated wave packet is centered at the tunnel-exit position $\mathbf{r}_0 = -r_{0,\parallel} \hat{\mathbf{E}}(t_0)$, i.e., in the direction opposite to the instantaneous field $\mathbf{E}(t_0)$ (see for example the discussion in Chapter 5). When molecules are ionized, we expect that their structure influences the momentum distribution as well as the position distribution of the freed electronic wave packet. In this chapter, we will mostly consider hydrogen molecules H_2 . For parallel or perpendicular alignment of the molecular axis with respect to an applied electric field, the freed wave packet is expected to be still centered along the direction $-\hat{\mathbf{E}}(t_0)$ due to the system's symmetry. However, if the molecular axis is tilted with respect to the electric field, the situation is less obvious (see Fig. 6.1 for a schematic illustration).

For a simplified modeling of the detached electron wave packet, the partial Fourier-transform (PFT) approach is used first. PFT was introduced for atoms [406] and later on generalized to describe the ionization of small molecules [407–409]. Analogous to the ARM theory, the main idea is to treat the wave function close to the ionic core like in the field-free situation and approximate the outer dynamics by means of the WKB method. We define the unit vectors \mathbf{e}_\perp and \mathbf{e}_\parallel that are perpendicular and antiparallel to the instantaneous field $\hat{\mathbf{E}}(t_0)$.¹ Then, the matching is performed along a line $\mathbf{r}_0 + r_\perp \mathbf{e}_\perp$ perpendicular to the atomic tunneling direction $\mathbf{r}_0 = r_{0,\parallel} \mathbf{e}_\parallel$ (see the dashed line in Figs. 6.1(a1)-(c1)).² As a result, the shape of the liberated wave packet is influenced by the slice of the initial wave function $\psi_M(\mathbf{r}_0 + r_\perp \mathbf{e}_\perp)$

¹For the cases of circularly-polarized fields and quasilinear fields discussed below, the unit vector \mathbf{e}_\perp is chosen parallel to the negative vector potential $-\mathbf{A}(t_0)$.

²In the PFT theory, as described in Ref. [406], the matching should be performed along a line with parallel distance $r_{M,\parallel}$ such that $\kappa < r_{M,\parallel} < I_p/E(t_0)$. However, we found that the later discussed results for the orientation-dependent position offsets only weakly change with the exact matching point and, hence, choose $r_{M,\parallel} = r_{0,\parallel}$ for simplicity.

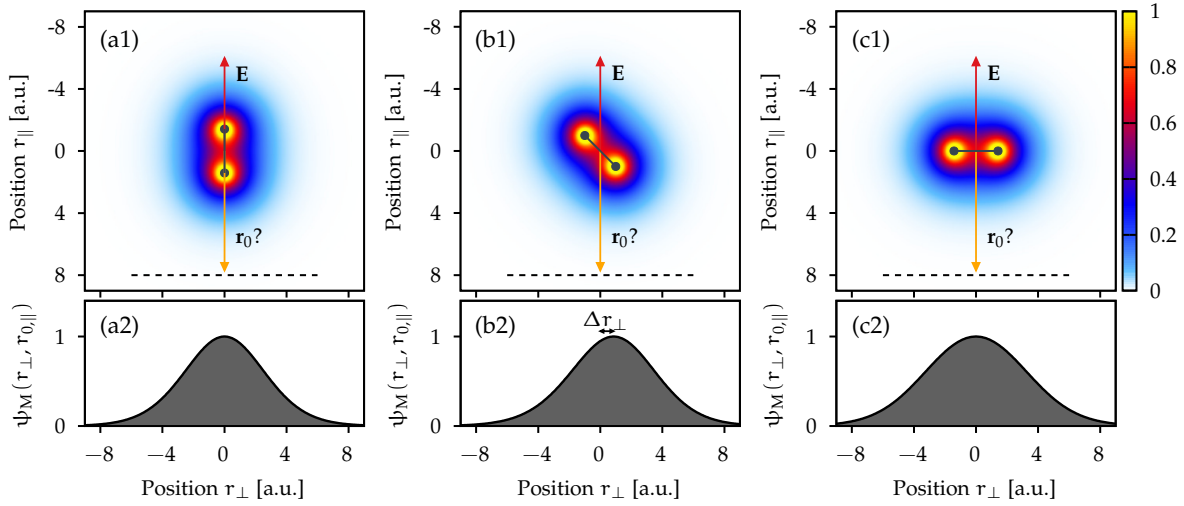


Figure 6.1: Position offsets in strong-field ionization of small molecules. (a1)-(c1) Position-space wave function $\psi_M(\mathbf{r})$ of the molecular orbital of H_2 for three orientations (with an exaggerated bond length $R_{\text{eff}} = 2.8$ a.u.). In PFT theory, the shape of the liberated electron wave packet from tunnel ionization in an electric field (red arrow) is influenced by the slice through the bound wave function along the dashed line (see main text). These slices are shown in panels (a2)-(c2). Due to the symmetric configuration, the wave functions are centered at $r_{\perp} = 0$ for parallel and perpendicular alignment ($\beta = 0^\circ$ and $\beta = 90^\circ$). However, in all other cases, the freed wave packet is not symmetric about the $\hat{\mathbf{E}}$ -axis and a position offset Δr_{\perp} is visible.

along the perpendicular line (see panels (a2)-(c2)). Due to the structured molecular orbitals (MOs), the central positions Δr_{\perp} of the wave packets depend on the relative angle β between the molecular axis $\hat{\mathbf{R}}$ and the electron's tunneling direction \mathbf{r}_0 . As expected, for parallel and perpendicular alignment ($\beta = 0^\circ$ and $\beta = 90^\circ$), the system consisting of field and molecule is mirror symmetric and the position offsets vanish, i.e., $\Delta r_{\perp} = 0$. In all other cases, this symmetry is broken and the peak position of the wave packet is shifted to $|\Delta r_{\perp}| > 0$. The simple picture suggests positive offsets $\Delta r_{\perp} > 0$ for angles β between 0° and 90° (see panel (b2) for $\beta = 45^\circ$).

After tunnel ionization, the motion of the wave packet can be described by means of classical trajectories. If the ionic potential is neglected, the classical dynamics is solely determined by the external electric field such that an initial velocity \mathbf{v}_0 at the birth time t_0 is mapped to a final momentum $\mathbf{p} = \mathbf{v}_0 - \mathbf{A}(t_0)$. When starting at the exit point \mathbf{r}_0 , the final position at a time t_f reads

$$\mathbf{r}_f = \mathbf{r}_0 + \int_{t_0}^{t_f} d\tau (\mathbf{p} + \mathbf{A}(\tau)). \quad (6.1)$$

In this potential-free setting, a shift of the liberated wave packet (at time t_0) translates directly to an offset of the wave packet at a later time t_f . Hence, the offsets could be observed by a detector placed far away from the parent ion. For circular polarization, the scenario is sketched in Fig. 6.2(a). Here, the final momentum \mathbf{p} is known to be perpendicular to the ionizing field $\mathbf{E}(t_0)$, i.e., $\mathbf{p} = (A_0 + v_{0,\perp})\mathbf{e}_{\perp}$. Thus, the introduced position offsets are parallel (antiparallel) for $\Delta r_{\perp} > 0$ ($\Delta r_{\perp} < 0$) to the final emission direction of the electron given by \mathbf{p} . Hypothetically, the arrival time of an electron can be measured at a fixed position far away from the parent ion [69]. Then, a position offset Δr_{\perp} of the liberated wave packet results in a change of the arrival time by $\Delta\tau = -\Delta r_{\perp}/p_{\perp}$. A wave packet that is shifted in the direction parallel (antiparallel) to the final momentum arrives earlier (later) on the detector [69]. For ionization of molecules, the delay depends on the relative molecular orientation and it is some tens of attoseconds. For example, an offset $\Delta r_{\perp} = 1$ a.u. and a final momentum $p_{\perp} = 1$ a.u. leads to an additional time delay of $\Delta\tau \approx 24.18$ as.

In strong-field ionization, the momentum-space representation of the outgoing electron wave packets is usually characterized in experiments. However, a basic property of quantum mechanics is that a translation by $\Delta\mathbf{r}$ in position space, $\psi(\mathbf{r}) \rightarrow \psi(\mathbf{r} - \Delta\mathbf{r})$, manifests itself as a phase gradient in momentum space, $\tilde{\psi}(\mathbf{p}) \rightarrow \exp(-i\Delta\mathbf{r} \cdot \mathbf{p})\tilde{\psi}(\mathbf{p})$. Thus, the position offsets in molecular ionization leaves an imprint

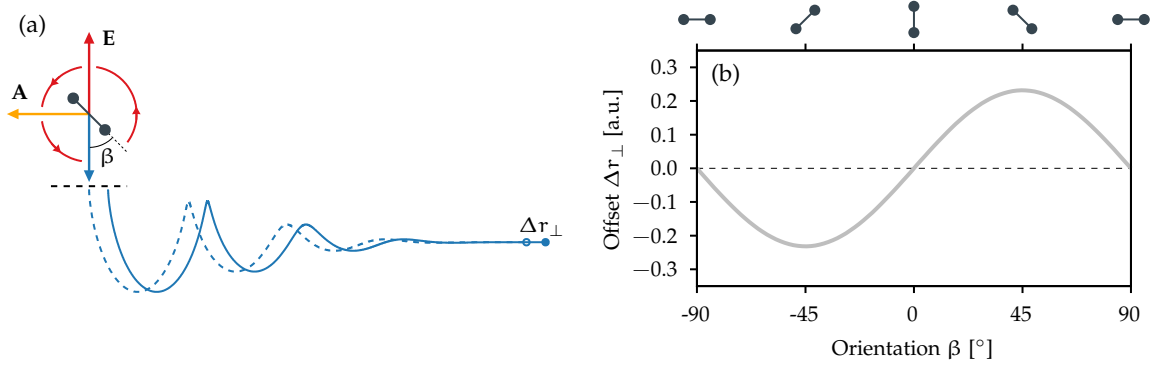


Figure 6.2: (a) Illustration of the continuum motion for ionization of molecule by circularly-polarized laser pulses. At the time of ionization $t_0 = 0$, the electron wave packet appears approximately in $-\mathbf{E}(t_0)$ -direction. However, due to the molecular structure, its center may be shifted by an offset Δr_{\perp} . In the absence of an ionic potential, the electron follows a laser-driven trajectory. Thus, a position offset of the released wave packet is translated into an offset of the wave packet at a final time t_f after the end of the pulse (see the trajectories shown as blue solid and dashed lines). (b) Perpendicular component Δr_{\perp} of the position offsets based on the PFT theory of Eq. (6.9) as a function of the relative angle β between the molecular axis $\hat{\mathbf{R}}$ and the negative direction $\mathbf{e}_{\parallel} = -\hat{\mathbf{E}}(t_0)$ of the electric field. Figure is adapted from Trabert *et al.* [377].

on the phase structure of the momentum representation. In general, for example for nonadiabatic ionization, the liberated wave packets are not Fourier-transform limited. Hence, even in a potential-free setting, they undergo a nontrivial time evolution in position space. In this situation, the local position introduced in the momentum-space version of the classical backpropagation of Section 5.2.4 still contains valuable information on the position distribution of the wave packet. At a time t_f , the local position is defined for each momentum \mathbf{p} by means of the phase gradient of the momentum-space wave function

$$\mathbf{r}(\mathbf{p}, t_f) = -\nabla_{\mathbf{p}} \arg \tilde{\psi}(\mathbf{p}, t_f). \quad (6.2)$$

As shown in Eq. (5.19), during potential-free time evolution the local position defined in Eq. (6.2) simply follows the classical trajectory. We can decompose the local position in a component antiparallel and a component perpendicular to the instantaneous electric field:

$$r_{\parallel} = -\mathbf{e}_{\parallel} \cdot \nabla_{\mathbf{p}} \arg \tilde{\psi}(\mathbf{p}) \quad \text{and} \quad r_{\perp} = -\mathbf{e}_{\perp} \cdot \nabla_{\mathbf{p}} \arg \tilde{\psi}(\mathbf{p}). \quad (6.3)$$

In the following, we will consider Eqs. (6.2) and (6.3) to determine molecular position offsets.

The time delay introduced above can be generalized by means of the local position. For the special case of circularly-polarized fields and when only considering the polarization plane, a time τ can be defined as [69, 375]

$$\tau := -\frac{r_{\perp}}{p_{\perp}} = \frac{1}{p_{\perp}} \mathbf{e}_{\perp} \cdot \nabla_{\mathbf{p}} \arg \tilde{\psi}(\mathbf{p}, t_f) = \frac{1}{p_{\perp}} \frac{\partial}{\partial p_{\perp}} \arg \tilde{\psi}(\mathbf{p}, t_f) = \frac{\partial}{\partial E} \arg \tilde{\psi}(\mathbf{p}, t_f), \quad (6.4)$$

where $\tilde{\psi}$ is viewed as a function of energy E and an additional angle. The last expression is usually referred to as Wigner time delay τ_{Wigner} (see for example Refs. [68, 375, 410]), because it has the same functional form as the expression introduced by Wigner in the context of electron scattering [62]. From a fundamental point of view, both the position offset of Eq. (6.3) and the delay of Eq. (6.4) can be viewed as a characterization of the phase change of the wave packet in momentum representation [377, 411].

The position offsets for H_2 can be estimated by means of PFT theory. For ionization at time t_0 , the structural dependence of the electron wave packet as a function of the initial velocity $\mathbf{v}_0 = v_{0,\perp} \mathbf{e}_{\perp}$ is given by the Fourier transformation of the slice through the initial wave function ψ_M along the line $\mathbf{r}_0 + r_{\perp} \mathbf{e}_{\perp}$ (see discussion above). The resulting complex-valued amplitude reads in $2D^3$

$$\tilde{\mathcal{A}}(v_{0,\perp}) = \frac{1}{\sqrt{2\pi}} \int d\mathbf{r}_{\perp} \psi_M(\mathbf{r}_0 + r_{\perp} \mathbf{e}_{\perp}) e^{-iv_{0,\perp} r_{\perp}}. \quad (6.5)$$

³Note that for a full representation of the liberated wave packet, the structure factor $\tilde{\mathcal{A}}(v_{0,\perp})$ must be multiplied by a Gaussian function of the lateral velocity $v_{0,\perp}$ (similar to the ADK rate of Eq. (2.3)) [406]. This can be interpreted as a filtering effect during tunnel ionization.

This is not the bare Fourier transformation of the bound wave function, but instead a mixed position-momentum-space representation. In order to derive an analytical estimate, we employ a linear combination of atomic orbitals (LCAO) to approximate the molecular orbital

$$\psi_M(\mathbf{r}) \propto \psi_A\left(\mathbf{r} - \frac{\mathbf{R}}{2}\right) + \psi_A\left(\mathbf{r} + \frac{\mathbf{R}}{2}\right) \quad (6.6)$$

with an internuclear distance $R = 1.3983$ a.u. and a molecular orientation given by $\hat{\mathbf{R}}$. The ground state of atomic hydrogen is chosen as the orbital $\psi_A \propto \exp(-\kappa r)$. In the PFT theory, the matching position can be approximated by the I_p/E tunnel exit, i.e., $\mathbf{r}_0 = I_p/E(t_0)\mathbf{e}_{\parallel}$. Under these assumptions and using $|R| \ll r_{0,\parallel}$ and $|r_{\perp}| \ll r_{0,\parallel}$, the amplitude of Eq. (6.5) can be written as

$$\tilde{A}(v_{0,\perp}) \approx 2\tilde{A}_A(v_{0,\perp}) \cos\left(\frac{(v_{0,\perp}\mathbf{e}_{\perp} + i\kappa\mathbf{e}_{\parallel}) \cdot \mathbf{R}}{2}\right). \quad (6.7)$$

Here, the first term is the amplitude for atomic orbitals whereas the second term represents the dependence on the molecular structure. Note that both vectors \mathbf{e}_{\parallel} and \mathbf{e}_{\perp} depend on the direction of the instantaneous electric field and, thus, in general on the time of ionization t_0 . Following the classical potential-free dynamics, in pure circularly-polarized fields with a magnitude A_0 of the vector potential, the release time t_0 and the initial velocity component $v_{0,\perp}$ are mapped to the final momenta by $p_{\perp} = v_{0,\perp} + A_0$ and $\phi_p = \omega t_0$. Thus, for a fixed molecular orientation, a given final direction ϕ_p in momentum space is linked to a relative angle β between molecular axis and instantaneous electric field.

The electron yield shows a well-known orientation-dependent modulation that can be approximated by the factor $\cosh^2(\kappa\mathbf{e}_{\parallel} \cdot \mathbf{R}/2) = \cosh^2(\cos(\beta)\kappa R/2)$ (see for example Refs. [240, 409]). However, the phase of the wave packet is also influenced by the molecular structure [240, 408]. For small initial velocities and small internuclear distances, the orientation-dependent part of the phase reads

$$\arg \tilde{A}(v_{0,\perp}) = -\frac{\sqrt{2I_p}}{8} R^2 v_{0,\perp} \sin(2\beta) \quad \text{with} \quad v_{0,\perp} = p_{\perp} - A_0. \quad (6.8)$$

According to Eq. (6.2), the variation of the local position in \mathbf{e}_{\perp} -direction is given by

$$\Delta r_{\perp} = \frac{\sqrt{2I_p}}{8} R^2 \sin(2\beta). \quad (6.9)$$

Within this model, the position offset is independent of the initial velocity $v_{0,\perp}$, i.e., the whole initial wave packet is shifted by Δr_{\perp} in position space. The predicted dependence of the position offset on the orientation β , shown in Fig. 6.2(b), is in qualitative agreement with the simple position-space-based argumentation presented above. For example, the offsets are positive for orientations $\beta \in (0^\circ, 90^\circ)$ and vanish for parallel or perpendicular alignment.

6.2.2 Computational details

The spatial information about the wave packets from strong-field ionization of small molecules can also be extract from *ab-initio* calculations. To this end, we perform numerical simulations of the TDSE in 2D and analyze the phase structure of the outgoing electron wave packets. The TDSE in the dipole approximation is solved on Cartesian grids using the Fourier split-operator method (see Section A.2.2 for details). The grids span 409.6×409.6 a.u. with spacings $\Delta x = \Delta y = 0.2$ a.u. and a time step of $\Delta t = 0.01$ a.u. is used. The momentum distributions are calculated with a resolution of $\Delta p_x = \Delta p_y = 0.0077$ a.u. In two dimensions, we consider a model H_2 molecule defined by the potential

$$V(\mathbf{r}) = -\sum_{j=1,2} \frac{Z_{\text{core}}}{\sqrt{r_j^2 + \epsilon}} \quad \text{with} \quad \mathbf{r}_j = \mathbf{r} - \mathbf{R}_j. \quad (6.10)$$

Here, $\mathbf{R}_1 = \mathbf{R}/2$ and $\mathbf{R}_2 = -\mathbf{R}/2$ are the fixed positions of the nuclei at equilibrium distance $R = 1.3983$ a.u. The effective charges $Z_{\text{core}} = 0.5$ are used such that an asymptotic charge of $Z = 1$ appears.

To reproduce the ionization potential $I_p \approx 0.56$ a.u. of real H_2 , the parameter $\epsilon = 0.265$ is chosen. Furthermore, effects of the Coulomb attraction on the outgoing electrons are switched off in the simulations for a short-range potential defined by

$$V(\mathbf{r}) = - \sum_{j=1,2} \frac{Z_{\text{core}}}{\sqrt{r_j^2 + \epsilon}} \exp\left(-\left(\frac{r_j}{r_{\text{core}}}\right)^4\right) \quad \text{with} \quad \mathbf{r}_j = \mathbf{r} - \mathbf{R}_j. \quad (6.11)$$

The parameters are tuned to $Z_{\text{core}} = 0.5$, $\epsilon = 0.1975$, a cutoff parameter $r_{\text{core}} = 3$ a.u. and an effective core distance $R = 1.2724$ a.u. This choice ensures that: (i) The correct ionization potential of real H_2 is reproduced. (ii) The ground states of the long- and short-range potentials result in similar perpendicular position offsets when calculated by numerical evaluation of the PFT theory based on Eqs. (6.3) and (6.5). Mostly, we consider recollision-free ionization in circularly-polarized laser pulses of n_p cycles duration defined by the vector potential

$$\mathbf{A}(t) = -A_0 \begin{pmatrix} \cos(\omega t) \\ \sin(\omega t) \end{pmatrix} \cos^4\left(\frac{\omega t}{2n_p}\right). \quad (6.12)$$

If not stated otherwise, we choose a three-cycle envelope ($n_p = 3$) in order to suppress the influence of ATI peaks. The effects due to the shortness of the pulse are minimized by only analyzing the part of electron wave packet that is liberated in the vicinity of maximal electric-field strength. Then, to study the orientation dependence, we use the field of Eq. (6.12) and vary the orientation of the molecular axis.

6.2.3 Results and discussion

Before proceeding with the study of the full dynamics in long-range potentials, we explore the structure of the wave packets from ionization in a short-range potential. Within this setting, an electron detached at the time of peak electric-field strength (here at $t_0 = 0$) is classically deflected by the light field to a final momentum $\mathbf{p} = -\mathbf{A}(0) + \mathbf{v}_0 = (A_0 + v_{0,\perp})\mathbf{e}_\perp = (A_0 + v_{0,\perp})\mathbf{e}_x$ (see the illustration in Fig. 6.2(a)). Thus, we only analyze the observables along the p_x -direction.

The initial-velocity distribution as a function of $v_{0,\perp} = p_\perp - A_0$ is shown in Fig. 6.3(a1) for each relative molecular orientation.⁴ In agreement with earlier works (see for example Refs. [59, 378, 379]) the ionization yield maximizes when the instantaneous electric field is aligned with the molecular axis ($\beta = 0^\circ$) (see Fig. 6.3(a2)). In contrast to the adiabatic prediction of the PFT model, the distributions are centered at positive initial velocities $p_\perp - A_0 = v_{0,\perp} > 0$ due to finite nonadiabaticity in the ionization process [170, 354, 370–372]. A precise investigation shows that this nonadiabatic effect also depends on the molecular orientation: For orthogonal alignment ($\beta = 90^\circ$), the distribution is centered at slightly larger $v_{0,\perp} = p_\perp - A_0$ compared to parallel alignment.

In order to study the spatial structure of the wave packet, the local positions of Eq. (6.2) are calculated from the momentum-space representation at the final time t_f . Classically, the positions at time t_f are linked to the initial positions at the release time t_0 (see the classical backpropagation method of Section 5.2.4). In short-range potentials, their relation is simply given by Eq. (6.1), i.e., a shift of the positions at time t_f is equivalent to a shift of the initial positions at release time t_0 . For ionization at time of peak field strength $t_0 = 0$ or equivalently momenta along the p_x -direction, the initial positions $\mathbf{r}(v_{0,\perp}, \beta)$ can be seen as functions of the relative orientation β and the initial velocity $v_{0,\perp}$. To extract the orientation dependence of these positions, i.e., relative position offsets, we define

$$\Delta\mathbf{r}(v_{0,\perp}, \beta) = \mathbf{r}(v_{0,\perp}, \beta) - \langle \mathbf{r}(v_{0,\perp}, \beta) \rangle_\beta \quad (6.13)$$

by subtracting the average value $\langle \mathbf{r}(v_{0,\perp}, \beta) \rangle_\beta$ over all possible orientations β for fixed $v_{0,\perp}$. We find that the average value $\langle \mathbf{r}(v_{0,\perp}, \beta) \rangle_\beta$ resembles very well the velocity-dependent initial positions for atoms

⁴Formally, we use the classical backpropagation method of Section 5.2.4 to determine the velocity-dependent quantities. The distribution of initial velocities is defined by evaluating the initial distribution $w_{\text{ini}}(t_0, v_{0,\perp})$ of Eq. (5.16) at $t_0 = 0$. However, in this potential-free situation, the final momenta are linear functions of the initial velocities at the tunnel exit such that their distributions are the same up to a Jacobian factor which is independent of the molecular geometry.

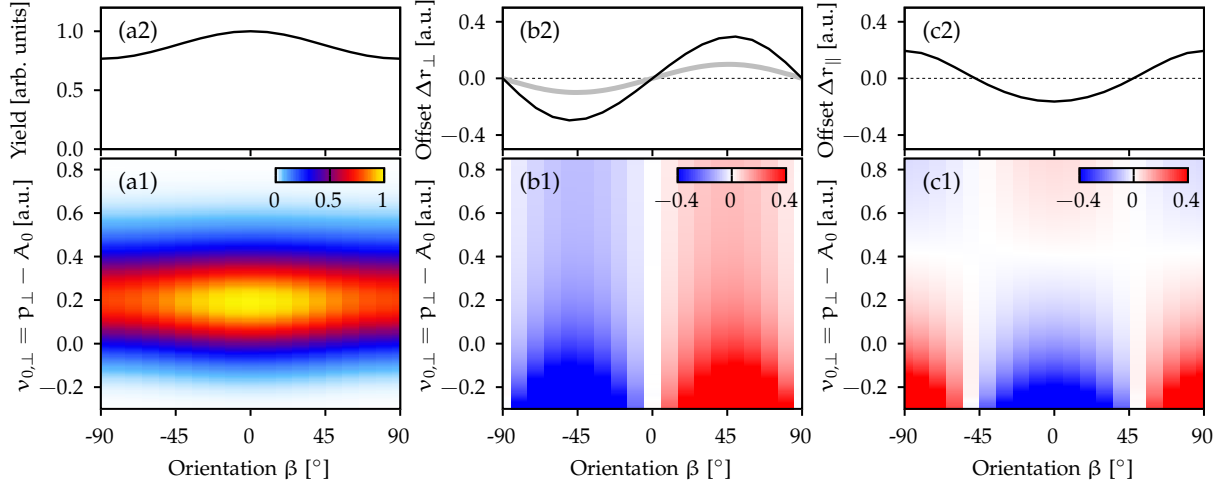


Figure 6.3: Properties of the electron wave packet for strong-field ionization of H_2 modeled by a short-range potential with three-cycle circularly-polarized laser pulses at 800 nm wavelength and $2 \times 10^{14} \text{ W/cm}^2$ intensity. (a1) Initial-velocity distribution as a function of $v_{0,\perp} = p_{\perp} - A_0$ (defined in Eq. (5.16)) and (a2) integrated yield for various molecular orientations β . (b1) Perpendicular component Δr_{\perp} and (c1) antiparallel component Δr_{\parallel} of the position offsets. (b2) and (c2) Corresponding slices at a velocity $v_{0,\perp} = 0$. The quantities are extracted from TDSE simulations (see main text). For comparison, the result from the numerical evaluation of the PFT model (see Eqs. (6.3) and (6.5)) is shown as a gray thick line in panel (b2).

with the same ionization potential which are discussed in Section 5.2.4. For each orientation β , the relative offsets defined in Eq. (6.13) are shown in Figs. 6.3(b1) and (c1) for the perpendicular and antiparallel components defined in Eq. (6.3).⁵ In agreement with the prediction by the PFT model of Eq. (6.9), the perpendicular component Δr_{\perp} extracted from TDSE simulations shows a nearly sinusoidal modulation as a function of the orientation β . However, in contradiction with the PFT theory, the modulation depth depends strongly on the initial velocity $v_{0,\perp}$. In addition, we observe a strong variation of the antiparallel component Δr_{\parallel} that is on the same order of magnitude as the perpendicular component Δr_{\perp} .

The variation of the antiparallel component can also be modeled by the PFT approach. For circular polarization, the derivative in \mathbf{e}_{\parallel} -direction (see Eqs. (6.2) and (6.3)) can be written as the derivative with respect to the angle $\phi_{\mathbf{p}}$ in the polarization plane. Importantly, slightly different angles $\phi_{\mathbf{p}}$ correspond to slightly different ionization times t_0 and, thus, to different relative orientations β of the direction \mathbf{r}_0 and the molecular axis \mathbf{R} . For the phase of Eq. (6.8) based on PFT theory, we find a position offset in the antiparallel component given by

$$\Delta r_{\parallel} = \frac{\sqrt{2I_{\text{p}}}}{4} R^2 \frac{v_{0,\perp}}{A_0 + v_{0,\perp}} \cos(2\beta). \quad (6.14)$$

In qualitative agreement with this estimate, the position offsets from TDSE indeed show a nearly sinusoidal modulation as a function of β . The PFT estimate (6.14) vanishes at $v_{0,\perp} = 0$, whereas the TDSE result vanishes at nonzero $v_{0,\perp} = p_{\perp} - A_0 \approx 0.4 \text{ a.u.}$ due to the influence of nonadiabatic effects. In contrast to the perpendicular offsets, the estimate of Eq. (6.14) suggests that the antiparallel offsets depend on the laser parameters and vanish in the adiabatic limit ($\gamma = \sqrt{2I_{\text{p}}}/A_0 \rightarrow 0$). The antiparallel components are related to the variation of the tunneling direction relative to the fixed molecular axis \mathbf{R} induced by a variation of the momentum \mathbf{p} . Thus, they depend on the time-to-momentum mapping and on the shape of the laser field. For example, in a quasilinear field (see Section 5.3), the relative orientation of the molecular axis and the instantaneous electric field does not change in the vicinity of peak field strength. Hence, we expect that the orientation dependence of the antiparallel component vanishes.

⁵In this special situation, the perpendicular component is proportional to the derivative in p_x -direction and the antiparallel component is proportional to the derivative in p_y -direction.

The influence of nonadiabaticity

To explore the dependence of the position offsets on the initial velocity $v_{0,\perp}$ and to discuss the influence of the laser conditions, we want to quantify the orientation dependence of the offsets. Inspired by the PFT theory of Eqs. (6.9) and (6.14), we use a Fourier expansion to represent the dependence on the angle β for each fixed $v_{0,\perp}$. For the TDSE results, we indeed find that the second-order Fourier coefficients dominate the angular dependence. Hence, the perpendicular components of the offsets can be approximately written as

$$\Delta r_{\perp} = \Delta r_{\perp}^{\max} \sin(2(\beta - \beta_{\perp}^{\text{def}})), \quad (6.15)$$

whereas the antiparallel components can be written as $\Delta r_{\parallel} = \Delta r_{\parallel}^{\max} \cos(2(\beta - \beta_{\parallel}^{\text{def}}))$. For short-range potentials, the deflection angles are given by $\beta_{\perp}^{\text{def}} \approx 0$ and $\beta_{\parallel}^{\text{def}} \approx 0$ or $\approx \pm\pi/2$ (due to the sign change of this component). The retrieved modulation amplitudes Δr_{\perp}^{\max} and $\Delta r_{\parallel}^{\max}$ are shown as a function of $v_{0,\perp}$ in Figs. 6.4(b2) and (c2) for various wavelengths. In all cases, the perpendicular and antiparallel components are on the same order of magnitude and depend strongly on the initial velocity $v_{0,\perp}$. The deviations of the TDSE results relative to the PFT model decrease for increasing wavelength, i.e., for more adiabatic ionization conditions. Hence, for a wavelength of 2000 nm corresponding to a Keldysh parameter $\gamma \approx 0.45$, the perpendicular offsets Δr_{\perp}^{\max} well resemble the adiabatic PFT estimate at large velocities $v_{0,\perp}$. However, even under these conditions, the perpendicular offsets from TDSE strongly increase when going from the high-energy to the low-energy edge of the wave packet.

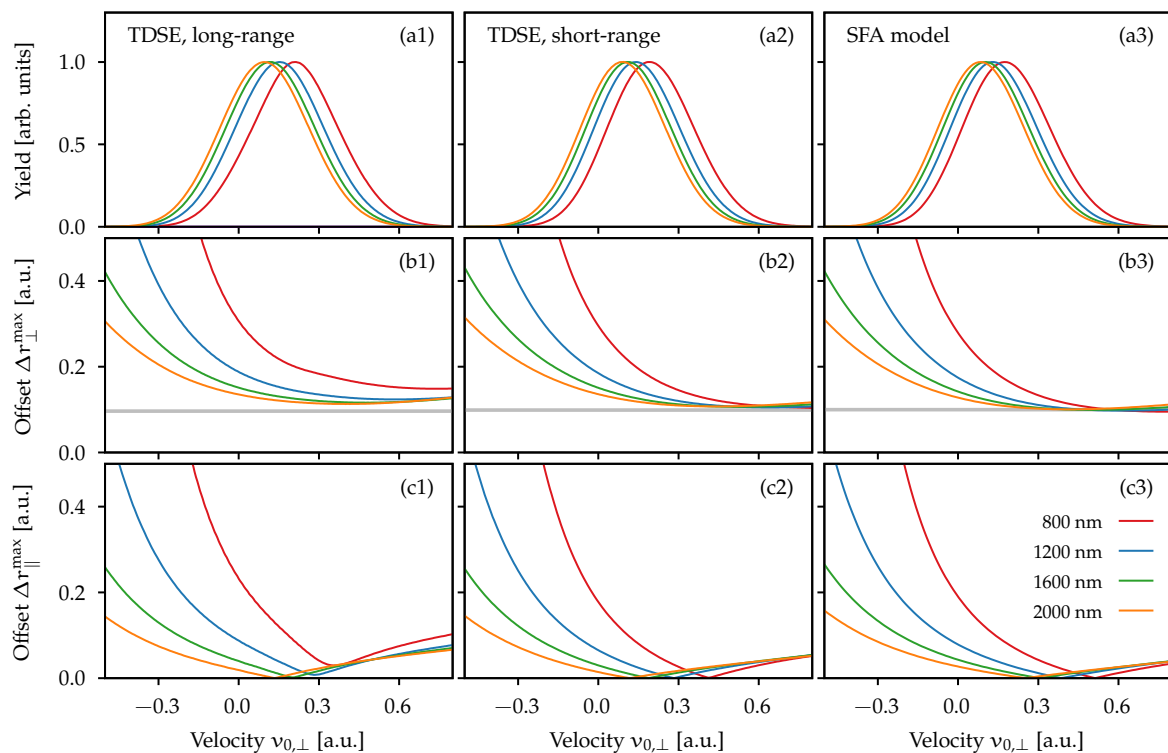


Figure 6.4: Position offsets and initial-velocity distributions corresponding to a release time $t_0 = 0$ for strong-field ionization of H_2 at various wavelengths given in the legend. The results are extracted from Fig. 6.6 for a long-range potential (panels (a1)-(c1)), from Fig. 6.3 for a short-range potential (panels (a2)-(c2)) or based on the SFA model of Eq. (6.20) (panels (a3)-(c3)). (a) Slices through the initial-velocity distribution for $\beta = 0^\circ$. (b) Modulation amplitude Δr_{\perp}^{\max} of the perpendicular component of the position offsets (see Eq. (6.15)). The gray thick line shows the numerical evaluation of the PFT theory. (c) Modulation amplitude $\Delta r_{\parallel}^{\max}$ of the antiparallel component of the position offsets. The other parameters are the same as in Fig. 6.3.

In order to investigate the huge influence of nonadiabatic effects on the phase structure in momentum space, i.e., on the position offsets, the molecular strong-field approximation (MO-SFA) [196, 412–414] can be used. In this approach, ionization is described as a transition from a field-free initial state to a Volkov state and, hence, the influence of intermediate bound states, the other electrons and the

Coulomb interaction are neglected. For molecules, its forecasting power strongly depends on the studied systems.⁶ Here, we use the favored length gauge and follow Refs. [111, 194] to rewrite the probability amplitude. Based on a saddle-point approximation, the dominant part of the probability amplitude of Eq. (2.40) takes the form⁷

$$\tilde{\Psi}(\mathbf{p}, t_f) \propto \tilde{\Psi}_M(\mathbf{p} + \mathbf{A}(t'_s)) e^{i S_{\text{SFA}}(\mathbf{p}, t'_s)}. \quad (6.16)$$

Here, we include a single saddle-point time t'_s and neglect orientation-independent prefactors, e.g., the second-order derivatives of the action in Eq. (2.45). The momentum representation $\tilde{\Psi}_M$ of the initial state is evaluated at the complex-valued quantity $\mathbf{v}(\mathbf{p}, t'_s) = \mathbf{p} + \mathbf{A}(t'_s)$. For the local position (6.2), the exponential of the SFA action results in an orientation-independent part (see Section 5.2.4). Information on the molecular structure is contained in the first factor $\tilde{\Psi}_M$. For the further analysis, we rewrite this prefactor as an exponential $\tilde{\Psi}_M = \exp(i\Phi)$ of a complex-valued phase

$$\Phi(\mathbf{v}(\mathbf{p}, t'_s)) = -i \ln \tilde{\Psi}_M(\mathbf{v}(\mathbf{p}, t'_s)). \quad (6.17)$$

According to Eqs. (6.2) and (6.16), the orientation dependence of the local position is contained in

$$\begin{aligned} \mathbf{r}(\mathbf{p}) &= -\nabla_{\mathbf{p}} \arg \tilde{\Psi}_M(\mathbf{v}(\mathbf{p}, t'_s)) = -\nabla_{\mathbf{p}} \text{Re}(\Phi(\mathbf{v}(\mathbf{p}, t'_s))) = -\text{Re} \left(\frac{\partial \mathbf{v}(\mathbf{p}, t'_s)}{\partial \mathbf{p}} \nabla_{\mathbf{v}} \Phi(\mathbf{v}(\mathbf{p}, t'_s)) \right) \\ &= -\text{Re}(\nabla_{\mathbf{v}} \Phi(\mathbf{v}(\mathbf{p}, t'_s))) + \text{Re}([\mathbf{E}(t'_s) \cdot \nabla_{\mathbf{v}} \Phi(\mathbf{v}(\mathbf{p}, t'_s))] \nabla_{\mathbf{p}}(t'_s(\mathbf{p}))). \end{aligned} \quad (6.18)$$

Importantly, the position offsets are given by a derivative with respect to the momentum \mathbf{p} . Thus, in the first row, we use the chain rule express the \mathbf{p} -derivative by the derivative with respect to the argument of Φ . Then, the first term in the second line is related to the explicit \mathbf{p} -dependence of the complex-valued velocity $\mathbf{v}(\mathbf{p}, t'_s)$. It is closely related to the adiabatic PFT result. In contrast, the second term is a result of the implicit dependence via the saddle-point time $t'_s(\mathbf{p})$. Note that in general both terms have nonadiabatic corrections.

To get an analytical estimate for the phase structure of the wave packet of an H_2 molecule in a circularly-polarized field, we again approximate the molecular orbital by the LCAO wave function of Eq. (6.6). Its Fourier transform results in

$$\tilde{\Psi}_M(\mathbf{k}) \propto \tilde{\Psi}_A(\mathbf{k}) \cos \left(\frac{\mathbf{k} \cdot \mathbf{R}}{2} \right), \quad (6.19)$$

where $\tilde{\Psi}_A$ is the Fourier transform of an atomic hydrogen orbital. The orientation-dependent position offsets are caused by the phase variation of the cosine term, i.e, the relevant phase reads

$$\text{Re}(\Phi(\mathbf{v}(\mathbf{p}, t'_s))) = \text{Im} \ln \cos \left(\frac{\mathbf{v} \cdot \mathbf{R}}{2} \right) \approx -\frac{1}{8} \text{Im}(\mathbf{v} \cdot \mathbf{R})^2 = -\frac{1}{8} R^2 v_{\parallel} v_{\perp} \sin(2\beta). \quad (6.20)$$

In the second step, an expansion is performed based on a small extension $|\mathbf{R}|$ of the molecule. In the last step, the explicit form of $\mathbf{v} = v_{\perp} \mathbf{e}_{\perp} + iv_{\parallel} \mathbf{e}_{\parallel}$ for circularly-polarized cw fields is used. The real-valued quantities $v_{\perp}, v_{\parallel} \in \mathbb{R}$ depend nonlinearly on the initial velocity $v_{0,\perp} = p_{\perp} - A_0$ and, hence, they influence the modulation of the position offsets.

Despite the inclusion of nonadiabaticity in the SFA framework, the dependence of the phase and, thus, the perpendicular position offset on the orientation β is still approximately given by a sinus function. The modulation amplitudes $\Delta r_{\perp}^{\text{max}}$ and $\Delta r_{\parallel}^{\text{max}}$ based on the phase $\text{Im} \ln \cos \left(\frac{\mathbf{v} \cdot \mathbf{R}}{2} \right)$ in Eq. (6.20) are depicted in Figs. 6.4(b3) and (c3). To account for deviations of the LCAO state from the initial state of the TDSE calculations, we use an effective distance $R_{\text{eff}} \approx 0.9$ a.u.⁸ The saddle-point version of the MO-SFA very well reproduces the features of the position offsets from TDSE simulations for a short-range

⁶For example, even for a simple molecule such as CO_2 , significant disagreement of the angular distribution between the experiment and MO-ADK theory as well as MO-SFA theory was noted. This was later resolved by considering the influence of multiple ionizing orbitals [415], multielectron effects [416], exchange interactions [126], the interplay of coordinate- and momentum-space properties of the ionizing orbital [407] and the laser-induced orbital deformation [417].

⁷Usually, the transition matrix element has a pole at t'_s which will be ignored (for an improved treatment see Ref. [194]).

⁸This choice ensures that the position offsets of Eq. (6.9) for the LCAO state and from the numerical calculation based on the PFT theory, Eqs. (6.3) and (6.5), for the initial TDSE state are nearly the same.

potential. We find that the discussed deviations from the PFT theory are indeed mainly caused by non-adiabatic corrections. Using an expansion of the vector potential as introduced in the Appendix A.3.1, we find up to first order in the Keldysh parameter γ

$$\text{Re}(\Phi(\mathbf{v}(\mathbf{p}, t'_s))) \approx -\frac{1}{8}R^2 \sqrt{2I_p + v_{0,\perp}^2} \left[v_{0,\perp} - \frac{\omega}{E_0} (I_p + v_{0,\perp}^2) \right] \sin(2\beta) + \mathcal{O}(\gamma^2). \quad (6.21)$$

The first term in the square brackets can be considered as the adiabatic limit. It is similar to the PFT result (6.8), except that the ionization potential I_p in the prefactor is replaced by an effective term $I_p^{\text{eff}} = I_p + v_{0,\perp}^2/2$. However, for the laser conditions used above, the nonadiabatic corrections in the second term in the square brackets are equally important and modify the modulation depth of the position offsets.

The influence of a long-range potential

In a realistic neutral molecule, the ionic potential behaves like a Coulomb potential $V(r) \simeq -1/r$ at large distances r . To study its influence on the ionization process, we repeat the TDSE simulations for the long-range potential of Eq. (6.10) under the same laser conditions as for the short-range potential. Figure 6.5 shows some characteristic observables of the asymptotic electron wave packet at time $t_f = 1050$ a.u. that could be measured by a detector placed far away from the ion. In Fig. 6.5, we analyze the quantities along the p_x -axis, i.e., the direction of final momenta that would correspond to ionization at $t_0 = 0$ in a Coulomb-free setting.

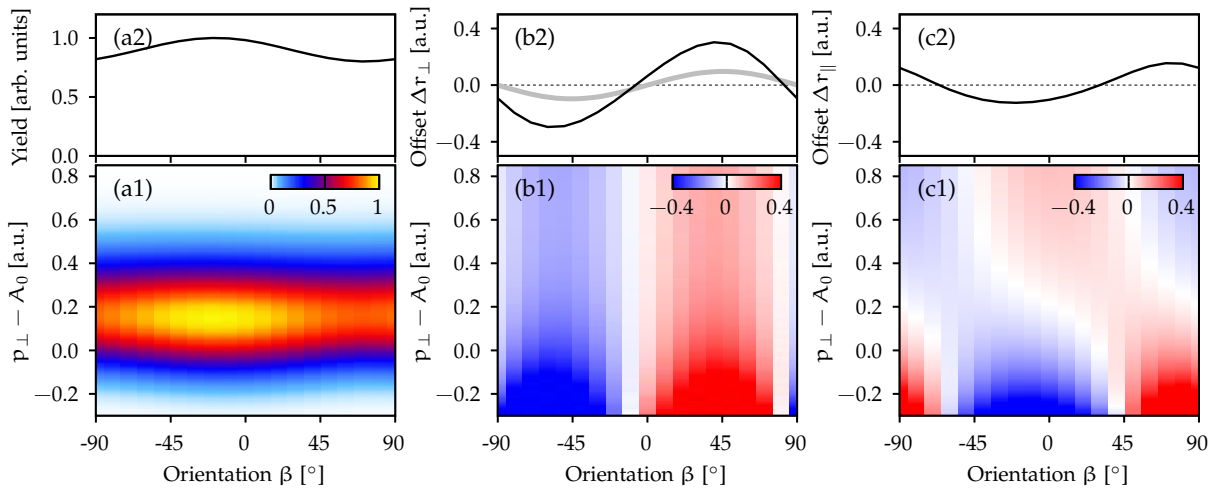


Figure 6.5: Properties of the asymptotic electron wave packet at time $t_f = 1050$ a.u. for strong-field ionization of H_2 modeled by a long-range potential with three-cycle circularly-polarized laser pulses at 800 nm wavelength and 2×10^{14} W/cm² intensity. (a1) Lateral momentum distribution as a function of $p_{\perp} - A_0$ and (a2) integrated yield for various molecular orientations β (measured against the negative y -direction). (b1) Perpendicular component Δr_{\perp} and (c1) antiparallel component Δr_{\parallel} of the position offsets. (b2) and (c2) Corresponding slices at a momentum $p_{\perp} = A_0$. The quantities are extracted from TDSE simulations (see main text). For comparison, the result from the numerical evaluation of the PFT model (see Eqs. (6.3) and (6.5)) is shown as a gray thick line in (b2).

In reality, the electron-ion interaction influences the continuum motion of the liberated electron wave packet (analogous to the attoclock discussed in Chapter 5). For example, the angular deflection of the outgoing electrons by the ionic potential induces a “rotation” of the probability distribution. Hence, in agreement with earlier work [61, 380], the orientations for minimal and maximal probabilities in Fig. 6.5(a) does not correspond to $\beta = 0^\circ$ or $\beta = 90^\circ$ anymore. Qualitatively, the position offsets for the long-range potential are similar to the short-range ones (see Figs. 6.5(b) and (c)). However, similar to the orientation dependence of the yield, the position offsets are also slightly “rotated” in the angle β . For example, the zero crossings of Δr_{\perp} are not at $\beta = 0^\circ$ and $\beta = 90^\circ$ anymore.

In order to disentangle the modification by the Coulomb attraction of the continuum motion and of the under-the-barrier motion, we again consider the classical backpropagation method (introduced in Section 5.2.4). There, classical trajectories starting with momentum \mathbf{p} at the local position $\mathbf{r}(\mathbf{p})$ of

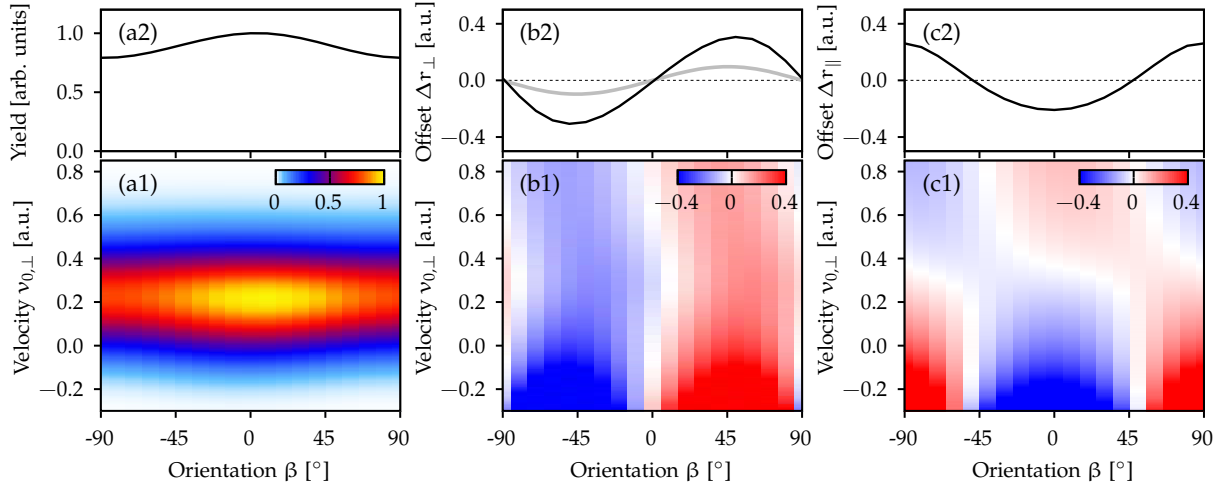


Figure 6.6: Properties of the initial electron wave packet corresponding to a release time $t_0 = 0$ obtained by classical backpropagation simulations based on input from TDSE simulations for a long-range H_2 model (see Fig. 6.5). (a1) Initial-velocity distribution as a function of $v_{0,\perp}$ and (a2) integrated yield for various molecular orientations β . (b1) Perpendicular component Δr_{\perp} and (c1) antiparallel component Δr_{\parallel} of the position offsets. (b2) and (c2) Corresponding slices at a velocity $v_{0,\perp} = 0$. For comparison, the result from the numerical evaluation of the PFT model (see Eqs. (6.3) and (6.5)) is shown as a gray thick line in (b2).

Eq. (6.2) are propagated backwards in time under the influence of the laser field and of the Coulomb interaction with the molecular ion. Here, the velocity criterion is chosen to stop the backpropagation. For each orientation of the molecule, we use the input from a TDSE simulation and perform such a backpropagation simulation. We again restrict ourselves to the quantities corresponding to electron release at $t_0 = 0$, i.e., at the time of peak field strength.

The initial-velocity distribution is shown in Fig. 6.6(a) for each relative molecular orientation. In agreement with an adiabatic tunneling picture of the PFT theory and with the results for a short-range potential presented above, the ionization yield at the tunnel exit maximizes for parallel alignment of the instantaneous electric field and the molecular axis at $\beta = 0^\circ$ (see the integrated yield in panel (a2) of Fig. 6.6). Similarly, the perpendicular components Δr_{\perp} of the position offsets at the tunnel exit approximately vanish for parallel or perpendicular alignment of the ionizing field to the molecular axis. Within this backpropagation approach, the attoclock-like rotation visible in the quantities for the asymptotic wave packet (see Fig. 6.5) are indeed mostly attributed to the influence of the ionic potential on the outgoing electrons. However, the Coulomb-correction in the backpropagation leads to an overrotation for certain initial velocities $v_{0,\perp}$. For example, at intermediate initial velocities around $v_{0,\perp} = 0.3$ a.u. the zero crossing of Δr_{\perp} is located at slight positive $\beta > 0$ (compared to its location at negative $\beta < 0$ in the asymptotic wave packet). We believe that this observation is closely related to the slight deviations of the most probable ionization times from time zero visible in the attoclock (see Sections 5.3.2 and 5.3.3 as well as Refs. [350, 359]).

For a quantitative comparison, we again determine the modulation amplitudes Δr_{\perp}^{\max} and $\Delta r_{\parallel}^{\max}$ by considering the second-order Fourier coefficients (see Eq. (6.15)) for the backpropagation results in Fig. 6.6. The amplitudes Δr_{\perp}^{\max} and $\Delta r_{\parallel}^{\max}$ for long-range and short-range potentials are overall in very good agreement (see Fig. 6.4). For the longest wavelength of 2000 nm, the deviations of the position offsets are less than 10%. However, for the shorter wavelengths such as 800 nm, the interplay between nonadiabatic effects and the long-range potentials leads to quantitative deviations compared to the short-range case. Two reasons for this are plausible: A physical deviation caused by Coulomb corrections during the under-the-barrier motion or an inconsistency of the classical backpropagation method due to the classical (i.e. incorrect) treatment of the continuum dynamics.

For atoms in circularly-polarized fields, the velocity criterion (used to stop the backpropagating trajectories) results in initial probability distributions and initial positions that are in good agreement with approximate theories such as SFA (see Section 5.2.4 and Refs. [211, 351]). In the adiabatic limit, this criterion can be derived from the saddle-point equation in SFA for atoms (see Appendix A.3.1).

For molecules, we also studied certain modified tunneling criteria (not shown). In particular, we considered the following two additional conditions: $\mathbf{r}(t_0) \cdot \mathbf{v}(t_0) = 0$ (“modified position criterion”) and $(-\mathbf{E}(t_0) - \nabla V(\mathbf{r}(t_0))) \cdot \mathbf{v}(t_0) = 0$ (“force criterion”). Qualitatively, we found similar results compared to the velocity criterion. Quantitatively, however, the modified position criterion leads to a diminished agreement compared to the results for short-range potentials. On the other hand, the force criterion slightly improves the agreement as it results in less overrotation (not shown).

Possible extensions

In circularly-polarized fields, the relative orientation of the laser electric field and the molecular axis changes with time. Hence, nonadiabatic effects during the tunnel ionization and during the continuum propagation decisively influence the position offsets in molecular strong-field ionization. In contrast, a big advantage of the quasilinear field configuration setting introduced in Section 5.3 is that its electric field has an approximately constant direction in the vicinity of the field-strength maximum. Hence, the electric field has a well-defined orientation relative to the molecule over the whole release step. For the asymmetric helium hydride molecular ion HeH^+ , the quasilinear configuration was already used to probe the orientation-dependent yield as well as the subcycle timing of ionization [367].

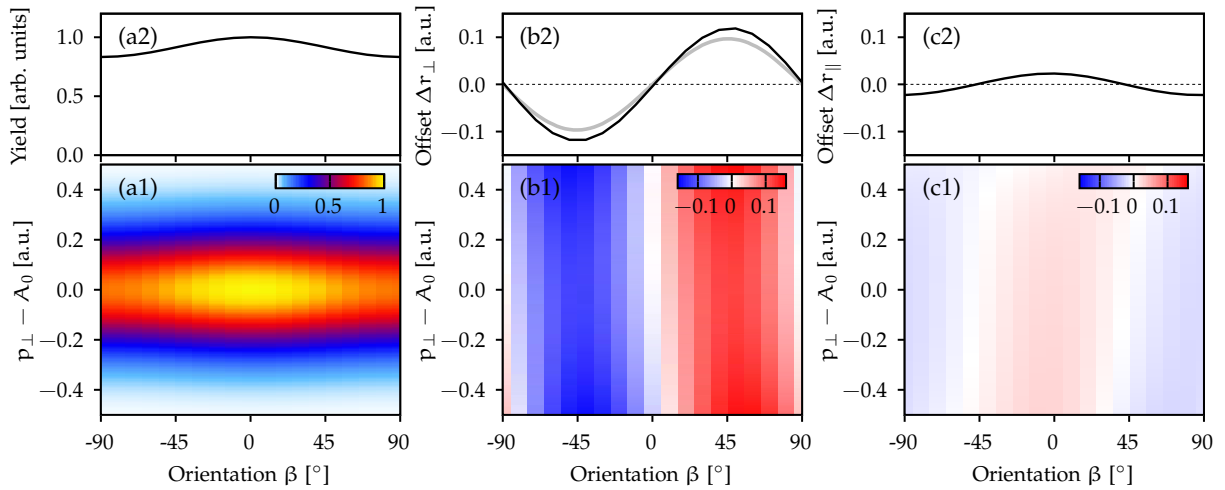


Figure 6.7: Properties of the asymptotic electron wave packet for strong-field ionization of H_2 modeled by a long-range potential as in Fig. 6.5, but in a quasilinear field with 2000 nm effective wavelength and 0.053 a.u. peak field strength (see main text).

To study the position offsets of the outgoing electron wave packets for ionization by a quasilinear field, we solve the TDSE for the long-range model of H_2 in the presence of a three-cycle pulse. An effective wavelength of 2000 nm is chosen and a peak electric-field strength of $E_p \approx 0.053$ a.u. is used (which is similar to the previously-considered circularly-polarized fields). The observables are only analyzed along the p_x -direction, i.e., the direction of final momenta that would correspond to ionization at $t_0 = 0$ in a Coulomb-free setting. The nearly constant direction of the electric field has several important consequences: Despite the presence of the long-range potential, the ionization yield maximizes for parallel alignment between the molecular axis and the instantaneous field (see Figs. 6.7(a)). Similarly, the perpendicular components Δr_\perp of the position offsets are perfectly symmetric functions of β , i.e., the deflection angles are $\beta_\perp^{\text{def}} \approx 0^\circ$ (see Figs. 6.7(b)). Furthermore, the antiparallel components Δr_\parallel approximately vanish (see Figs. 6.7(c)).

In the quasilinear configuration, the first-order nonadiabatic corrections vanish in the vicinity of peak electric-field strength. Hence, the lateral momentum distributions are centered around $p_\perp - A_0 = 0$ (with $A_0 = -A_x(0)$) for each orientation (see Figs. 6.7(a)). Additionally, the extracted perpendicular offsets are very well reproduced by the adiabatic PFT model (see Figs. 6.7(b)).⁹ Compared to circular polarization, a much weaker modulation of the perpendicular offsets Δr_\perp as a function of the “velocity” $p_\perp - A_0$

⁹Note also the different scale for the position offsets compared to the previous figures for circular polarization.

is present. For fixed β , we find that the position offsets Δr_{\perp} are approximately quadratic functions of $p_{\perp} - A_0$ what can be explained by an increased effective ionization potential, i.e., $I_p^{\text{eff}} = I_p + v_{0,\perp}^2/2$ with $v_{0,\perp} \approx p_{\perp} - A_0$ (see also Eq. (6.21)). The small deviations of the TDSE results compared to the PFT model are partially caused by Coulomb effects on the continuum motion. Using the classical backpropagation method, we confirmed that the agreement with PFT theory even improves for the initial electron wave packet (not shown). We ensured that these statements are also true for more nonadiabatic ionization conditions such as a quasilinear field with only 800 nm effective wavelength.

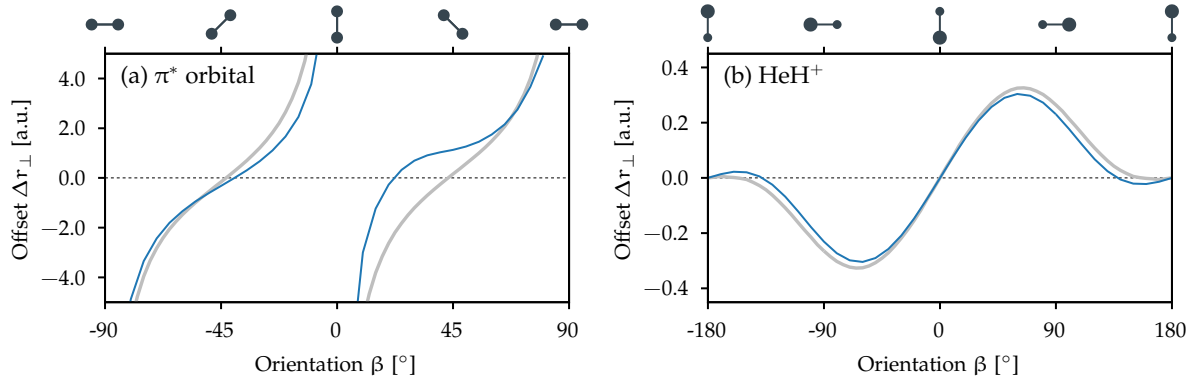


Figure 6.8: Position offsets for strong-field ionization of an oxygen model with its π^* -antibonding orbital (panel a) and of a helium hydride model (panel b). The offsets are extracted at a momentum $\mathbf{p} = A_0 \mathbf{e}_x$ from the asymptotic electron wave packets created by ionization in quasilinear fields with 2000 nm effective wavelength (analogous to Fig. 6.7). A peak field strength of 0.03 a.u. is used for the oxygen model with an ionization potential of ≈ 0.45 a.u. and a peak field strength of 0.12 a.u. is used for the helium hydride model with an ionization potential of ≈ 1.66 a.u. For comparison, the results from the numerical evaluation of the PFT model (see Eqs. (6.3) and (6.5)) are shown as gray thick lines.

To underline the sensitivity of the position offsets to the molecular structure, we present results for two additional molecules. As a simple example of polar molecules, the helium hydride molecular ion HeH^+ is considered by using a 2D model introduced in Ref. [418]. In addition, as an example with nodal planes in the molecular orbital, we choose a 2D toy model for an oxygen molecule O_2 with its π^* -antibonding orbital. The used 2D potential reads

$$V(\mathbf{r}) = - \sum_{j=1,2} \frac{Z + (Z_{\text{core}} - Z) \exp(-\eta \mathbf{r}_j^2)}{\sqrt{\mathbf{r}_j^2 + \epsilon}}. \quad (6.22)$$

Here, the parameters are $R = 2.2827$ a.u., $Z = 0.5$, $Z_{\text{core}} = 2$, $\epsilon = 0.15$ and $\eta = 0.24$. We again consider ionization by a quasilinear field of 2000 nm effective wavelength. The perpendicular components of the position offsets at $p_{\perp} = A_0$ extracted from the asymptotic electron wave packet are shown in Fig. 6.8. Compared to the hydrogen molecule, we observe a vastly different orientation dependence which is already a clear sign of the sensitivity to the orbital structure. For example, a nodal plane in the π^* -orbital translates to a minimum in the photoelectron momentum distribution [382–385]. However, simultaneously, the sign of the initial wave function changes at a nodal plane which is imprinted on the phase of the outgoing electron wave packet. The phase jump results in a discontinuity of the derivative of the phase when the position offset is calculated. The results from TDSE are well reproduced by numerical evaluation of the PFT theory using the same states as in the TDSE.

6.3 Holographic angular streaking of electrons

In our theoretical simulations, the phase of the outgoing electron wave packet is directly accessible. In contrast, in experiments, the electron momentum distributions can only be measured, i.e., the modulus squared of the probability amplitudes in momentum space can be studied. However, the relative phases of two wave packets can be characterized by interferometric approaches. Recently, Eckart suggested a scheme to measure variations of the phase gradients in momentum space [69], i.e., to study variations of the local positions (6.2). In the so-called “holographic angular streaking of electron” (HASE) scheme, the perturbation of the ionization process by a probe field with half of the fundamental frequency induces an interference pattern. The pattern can be analyzed to retrieve information on the derivative of phase in momentum space.

The original work [69] is based on an *ad-hoc* combination of a semiclassical description of the adiabatic ionization process (similar to the SCTS model of Section 2.4) and an added initial phase term with a gradient in perpendicular direction. There, a one-to-one mapping between the variation of the interference pattern and the inserted initial derivative of the phase naturally exists. However, in reality, molecules also modify other quantities of the electron wave packets. For example, the yield depends on the orientation and we found for circular polarization an orientation-dependent component of the local position in the direction of the instantaneous electric field (see Section 6.2.3). It is a priori unclear how such effects influence the HASE interferometer. In order to confirm the retrieval mechanism of Ref. [69], we derive an analytical description of the HASE approach based on the molecular strong-field approximation. This allows us to refine the mapping between the variation of the interference pattern and perpendicular components of the position offsets (phase gradients). Afterwards, we perform numerical experiments based on the solution of the TDSE and simulate the HASE interference pattern in photoelectron momentum distributions for a hydrogen molecule. For an *ab-initio* verification of the HASE approach, the retrieved position offsets from the interference patterns are compared to the theoretically-accessible position offsets from the phase gradients of the outgoing wave packet (see the discussion in the previous section).

6.3.1 Co-rotating two-color fields

The HASE approach probes phase gradients or local positions of the detached electron wave packets in circular polarization. To this end, a strong circularly-polarized field $\mathbf{E}_\omega(t)$ of frequency ω is perturbed by weak circularly-polarized probe field $\mathbf{E}_P(t)$ of frequency $\omega/2$ with the same helicity. These co-rotating two-color fields can be represented by the vector potential

$$\mathbf{A}(t) = \mathbf{A}_\omega(t) + \mathbf{A}_P(t) = -A_0 \left[\begin{pmatrix} \cos(\omega t - \phi_{\text{CEP}}) \\ \sin(\omega t - \phi_{\text{CEP}}) \end{pmatrix} + 2\epsilon \begin{pmatrix} \cos(\omega/2t + \alpha/2 - \phi_{\text{CEP}}/2) \\ \sin(\omega/2t + \alpha/2 - \phi_{\text{CEP}}/2) \end{pmatrix} \right] f(t). \quad (6.23)$$

An example of the negative vector potential $-\mathbf{A}(t)$ is shown in Fig. 6.9(a). The relative phase α between the fields determines the orientation of the Lissajous figure in space (2π periodic). The deviations from pure circular polarization are controlled by the relative field strength ϵ of the probe field compared to the fundamental field. For a nontrivial envelope $f(t) \neq 1$, the carrier-envelope phase ϕ_{CEP} can vary between $-\pi$ and π . If not stated otherwise, we use a trapezoidal envelope $f(t)$ with ramps of $1.5 T_\omega$ duration.

A typical photoelectron momentum distribution for ionization of a model atom by a co-rotating two-color field with 400 nm central frequency and 2×10^{14} W/cm² intensity is shown in Fig. 6.9(b1).¹⁰ To first investigate the Coulomb-free case, the PMD is calculated by numerical integration of the KFR amplitude (2.40). In a pure ω -field, ATI rings with a spacing in energy of ω would only be present (see the blue-marked peaks in Fig. 6.9(b2)). However, even a weak probe field (here $\epsilon = 0.02$) leads to the appearance of sidebands between the ATI peaks [401] (see the red-marked peaks in Fig. 6.9(b2)). When viewing the combined co-rotating field with a total optical cycle of $T_{\omega/2} = 2T_\omega$, both peaks would

¹⁰The ionization potential is chosen to the same value as for real H₂.

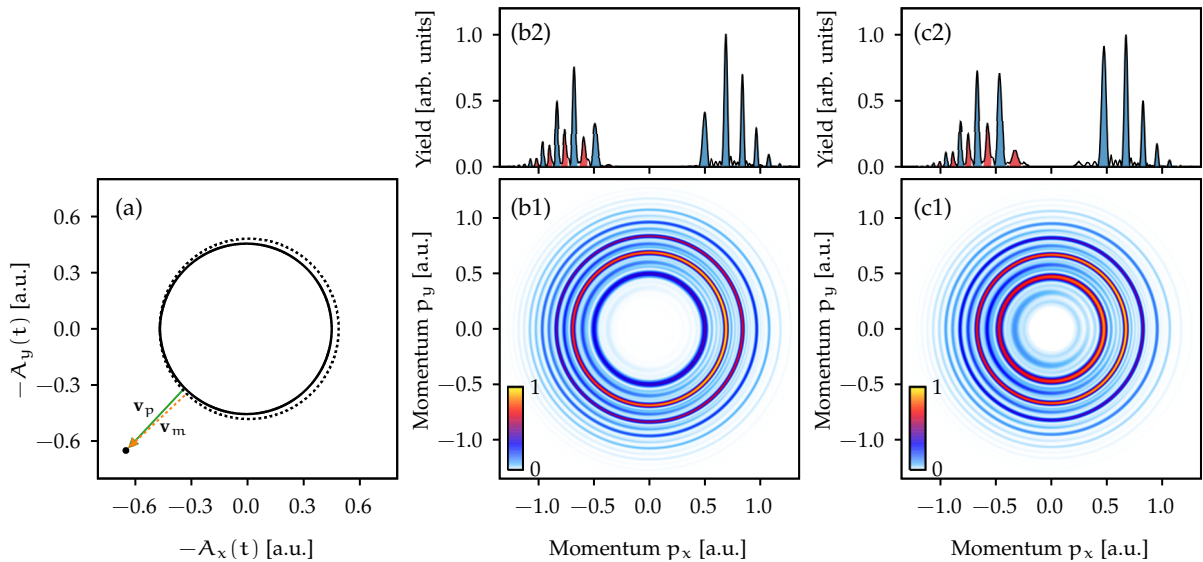


Figure 6.9: Strong-field ionization in co-rotating two-color fields. (a) Negative vector potential $-\mathbf{A}(t)$ for a waveform consisting of a strong fundamental field at 400 nm wavelength and 2×10^{14} W/cm² intensity as well as of a weak probe field at 800 nm wavelength with a relative field strength $\epsilon = 0.02$ and a relative phase $\alpha = 0$. The solid and dotted lines mark the two distinct T_ω cycles. The black dot indicates a selected final momentum \mathbf{p} that is classically reached by two different combinations of release times t_p, t_m and of initial velocities $\mathbf{v}_p, \mathbf{v}_m$, i.e., $\mathbf{p} = -\mathbf{A}(t_p) + \mathbf{v}_p = -\mathbf{A}(t_m) + \mathbf{v}_m$. Adapted from Ref. [69]. (b1) and (c1) photoelectron momentum distributions for ionization of a model atom obtained by numerical evaluation of the SFA and by the numerical solution of the TDSE. (b2) and (c2) Corresponding 1D slices through the PMD at $p_y = 0$. Here, the ATI peaks and sidebands are marked in blue and red. For the numerical SFA and TDSE simulations, the field is augmented with a trapezoidal envelope with 4 T_ω cycles of constant intensity and the results are averaged over 16 values of the CEP.

usually be denoted as ATI peaks. Here, we use a slightly different terminology and only denote the peaks present in a pure ω -field as ATI peaks. For the co-rotating field, the electron emission strength on the rings depends on the direction of the final momentum [404]. For one ATI peak and one sideband, the modulation of the yield as a function of the angle ϕ_p in the polarization plane is shown in Fig. 6.10(a). Neglecting the influence of the Coulomb potential and considering an atom, the yield for ATI rings maximizes at $\phi_p = \alpha$ (here at $\phi_p = 0^\circ$). In contrast, the modulation of the sidebands is shifted by 180° ; in fact the yield approximately vanishes at $\phi_p = \alpha$. The present structure in momentum space is sometimes called alternating half-ring (AHR) pattern [69, 419].

The yield modulation on the rings is caused by the interference of electron waves detached in two consecutive optical cycles of the ω -field. Or, to phrase it differently, it is an intracycle interference between wave packets released in two half cycles of the probe field [404, 420]. The simple man's model predicts the possible final momenta $\mathbf{p} = -\mathbf{A}(t_0) + \mathbf{v}_0$ for given release times t_0 , where the initial velocities \mathbf{v}_0 should be perpendicular to the instantaneous electric field $\mathbf{E}(t_0)$ (see Eq. (2.47)). Due to the presence of the probe field, the vector potential and the electric field in the two consecutive cycles of the ω -field slightly differ (see the solid and dotted lines in Fig. 6.9(a)). Hence, per optical cycle of the probe field, two trajectories with release times t_p, t_m and slightly different initial velocities $\mathbf{v}_p, \mathbf{v}_m$ are classically deflected to the same final momentum $\mathbf{p} = -\mathbf{A}(t_p) + \mathbf{v}_p = -\mathbf{A}(t_m) + \mathbf{v}_m$ [69, 419]. The situation is schematically illustrated in Fig. 6.9(a) for one selected final momentum. These two contributions interfere and result in the observed pattern. Importantly, the phase of the interfering wave packets is probed at different initial velocities. Therefore, the pattern contains information on the derivatives of the initial phase in momentum space [69, 419], i.e., on the local positions.

The long-range Coulomb interaction slightly alters the results. For illustration, we solve numerically the TDSE in 2D for a model potential $V(\mathbf{r}) = -1/\sqrt{\mathbf{r}^2 + 0.415}$ reproducing the ionization potential of H₂. Compared to the SFA result, the whole electron wave packet is decelerated and, thus, centered at smaller kinetic energies (see the envelopes of the distributions in Figs. 6.9(b2) and (c2)). The modulation depth of the half-ring pattern is slightly modified, but more importantly the pattern is rotated by a nonzero offset

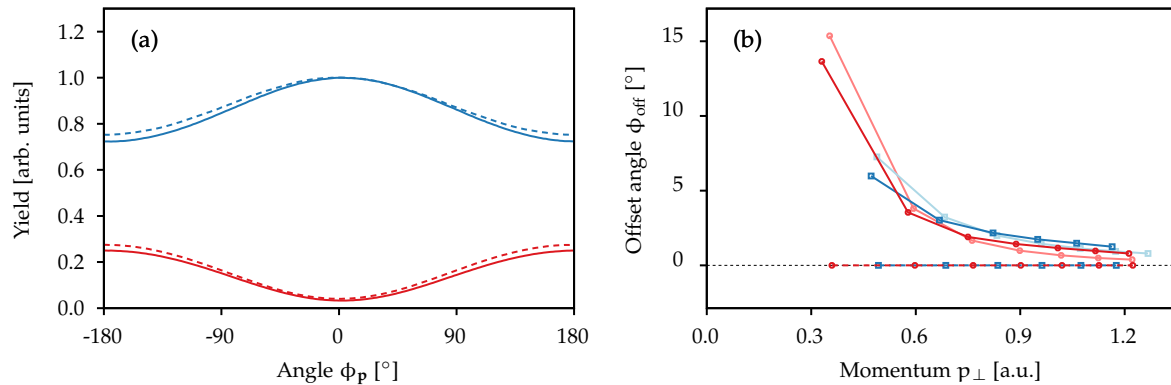


Figure 6.10: (a) Angular distribution for an ATI peak centered at $p_{\perp} \approx 0.67$ a.u. (blue lines) and a sideband centered at $p_{\perp} \approx 0.76$ a.u. (red lines) extracted from the PMDs of Fig. 6.9: SFA results (dashed lines) and TDSE results (solid lines). The distributions for the ATI peaks are normalized to one. In the TDSE results, the Coulomb potential leads to a slight rotation compared to the potential-free SFA results. (b) Offset angle ϕ_{off} extracted for each ATI peak (blue lines) and for each sideband peak (red lines). For comparison, the results from ARM theory are shown as pale blue and pale red lines.

angle [404]. The angular structure can be represented by a Fourier series (5.10) that is dominated by the fundamental components ($k = 1$). Analogous to the attoclock offsets in Section 5.2.3, we approximate the offset angle compared to the Coulomb-free case by $\phi_{\text{off}} = \phi_1$ (see Fig. 6.10(b)). Interestingly, the rotation of the AHR pattern is much smaller than the attoclock angles observed for similar laser parameters.¹¹ Here, in contrast to the attoclock of Chapter 5, the rotation of the pattern is mainly caused by a Coulomb-induced phase difference of the paths. Hence, the analysis of the AHR pattern and the attoclock protocol are fundamentally different. Since we are mostly interested in a modification of the interference pattern by the structure of small molecules, the interpretation of the Coulomb-induced rotation is left for the future.

6.3.2 Quantum-orbit model

In the HASE scheme [69], variations of the phase gradient of the initial electron wave packet or equivalently changes of the local positions influence the interference pattern in the photoelectron momentum distribution. To measure position offsets based on the HASE scheme, the modification of the pattern must be uniquely mapped to these offsets. Here, a few questions arise: What quantity does the HASE scheme measure exactly, e.g., the total position offset or only a selected component? How to make sure that the orientation-dependent ionization probability of molecules does not spoil or even dominate the measurements? What about the influence of nonadiabatic effects on the interferometer? Before proceeding with the full numerical study based on the TDSE simulations, we explore these questions in a Coulomb-free quantum-orbit model based on the strong-field approximation. This allows us to analytically describe the interference pattern of the HASE interferometer and investigate the influence of the molecular structure.

Modeling of the interference pattern

The SFA framework was introduced in Section 2.3 and already used for molecules in Section 6.2.3. Here, we again use a length-gauge version and apply a saddle-point approximation. Hence, for a single saddle-point time, the complex-valued probability amplitude is given by Eq. (6.16). Analogous to the discussion above, the amplitude can be written as $M = \exp(i(\Phi + S_{\text{SFA}}))$ with a complex-valued “phase” Φ that contains information on the electronic structure of the initial bound state ψ_M (see Eq. (6.17)). For a cw field of the form (6.23) with $\phi_{\text{CEP}} = 0$, we indeed find two relevant saddle-point times (t'_m and t'_p) with real parts within one optical cycle of the $\omega/2$ -field. The interference of both

¹¹The offset angles from TDSE are well reproduced by a simulation based on ARM theory of Section 2.5.

contributions leads to the angular modulation of the signal on the ATI peaks and sidebands

$$w(\mathbf{p}) = \left| e^{i(\Phi(\mathbf{v}(\mathbf{p}, t'_m)) + S_{\text{SFA}}(\mathbf{p}, t'_m))} + e^{i(\Phi(\mathbf{v}(\mathbf{p}, t'_p)) + S_{\text{SFA}}(\mathbf{p}, t'_p))} \right|^2. \quad (6.24)$$

Here, the probe field should only slightly perturb the dominant dynamics induced by the fundamental field. Hence, we expand the structure-dependent “phase” Φ and the SFA action of Eq. (2.41) to first order in the relative field strength ϵ .

We first determine the modification of the saddle points in the co-rotating field (defined by Eq. (2.44)) compared to the saddle-point times $t_s^{(0)}$ of pure circular polarization. For momenta $\mathbf{p} = p_\perp \mathbf{e}_\perp$ in the polarization plane, the unperturbed times can be explicitly written as [354] (in a single T_ω cycle)

$$\omega t_s^{(0)} = \phi_p + i\omega\tau_i \quad \text{with} \quad \omega\tau_i = \text{acosh}(\chi) \quad \text{and} \quad \chi = \frac{1}{2A_0 p_\perp} [p_\perp^2 + A_0^2 + 2I_p] \in \mathbb{R}. \quad (6.25)$$

Additionally, we define the unperturbed action for circular polarization

$$S_{\text{SFA}}^{(0)}(\mathbf{p}, t') = -\frac{1}{2} \int_{t'}^{t_f} dt (\mathbf{p} + \mathbf{A}_\omega(t))^2 + I_p(t' - t_A) \quad (6.26)$$

and the perturbation

$$\Delta S(\mathbf{p}, t') = - \int_{t'}^{t_f} dt \mathbf{A}_P(t) \cdot (\mathbf{p} + \mathbf{A}_\omega(t)). \quad (6.27)$$

Including only first-order corrections, the perturbed saddle-point times can be written as $t_s' = t_s^{(0)} + t_s^{(1)}$ with the correction due to the probe field

$$t_s^{(1)} = - \frac{\partial_{t'} \Delta S(\mathbf{p}, t_s^{(0)})}{\partial_{t'}^2 S_{\text{SFA}}^{(0)}(\mathbf{p}, t_s^{(0)})} = \frac{\mathbf{A}_P(t_s^{(0)}) \cdot (\mathbf{p} + \mathbf{A}_\omega(t_s^{(0)}))}{\mathbf{E}_\omega(t_s^{(0)}) \cdot (\mathbf{p} + \mathbf{A}_\omega(t_s^{(0)}))}. \quad (6.28)$$

Thus, the corresponding perturbed complex-valued velocity reads (to first order in ϵ)

$$\mathbf{v}(\mathbf{p}, t_s') = \mathbf{v}^{(0)}(\mathbf{p}, t_s^{(0)}) + \Delta \mathbf{v}(\mathbf{p}, t_s^{(0)}) = \mathbf{p} + \mathbf{A}_\omega(t_s^{(0)}) + \mathbf{A}_P(t_s^{(0)}) - \mathbf{E}_\omega(t_s^{(0)}) t_s^{(1)}. \quad (6.29)$$

The expansion of the structure-dependent “phase” leads to

$$\Phi(\mathbf{v}(\mathbf{p}, t_s')) = \Phi(\mathbf{v}(\mathbf{p}, t_s^{(0)})) + \Delta \Phi(\mathbf{p}, t_s^{(0)}) = \Phi(\mathbf{v}^{(0)}(\mathbf{p}, t_s^{(0)})) + \nabla \Phi(\mathbf{v}^{(0)}(\mathbf{p}, t_s^{(0)})) \cdot \Delta \mathbf{v}(\mathbf{p}, t_s^{(0)}). \quad (6.30)$$

Since a first-order correction of the saddle-point time changes the SFA action only to second order, we can evaluate the action at the unperturbed saddle-point times $t_s^{(0)}$. The expansion of the action to first order in ϵ is given by

$$S_{\text{SFA}}(\mathbf{p}, t_s') = S_{\text{SFA}}^{(0)}(\mathbf{p}, t_s^{(0)}) + \Delta S(\mathbf{p}, t_s^{(0)}). \quad (6.31)$$

We only need to take ionization from two consecutive cycles of the circularly-polarized ω -field into account. Due to its periodicity, the unperturbed quantities evaluated at the two distinct saddle points have simple relations:

$$t_p^{(0)} = t_m^{(0)} + T_\omega, \quad \mathbf{v}^{(0)}(\mathbf{p}, t_p^{(0)}) = \mathbf{v}^{(0)}(\mathbf{p}, t_m^{(0)}), \quad \text{and} \quad \Phi(\mathbf{v}^{(0)}(\mathbf{p}, t_p^{(0)})) = \Phi(\mathbf{v}^{(0)}(\mathbf{p}, t_m^{(0)})). \quad (6.32)$$

The difference of the unperturbed action phase between the two orbits is given by (with $n \in \mathbb{Z}$)

$$S_{\text{SFA}}^{(0)}(\mathbf{p}, t_p^{(0)}) - S_{\text{SFA}}^{(0)}(\mathbf{p}, t_m^{(0)}) = \left(I_p + U_p + \frac{p^2}{2} \right) T_\omega = \begin{cases} 2\pi n & , \text{ at ATI peaks} \\ \pi(2n + 1) & , \text{ at sidebands.} \end{cases} \quad (6.33)$$

In the following, we will only consider the signal on the ATI peaks and sidebands defined by the fundamental field. For case distinction, an upper index will always denote the ATI peak result whereas a lower index marks the sideband result.

We investigate the relations of the corrections of the action and “phase” for the two saddle-points t'_p and t'_m . For the perturbation of the vector potential, we have $\mathbf{A}_P(t_p^{(0)}) = -\mathbf{A}_P(t_m^{(0)})$. Thus, we find

$$\Delta\mathbf{v}(\mathbf{p}, t_p^{(0)}) = -\Delta\mathbf{v}(\mathbf{p}, t_m^{(0)}) \quad \Rightarrow \quad -\Delta\Phi(\mathbf{p}, t_p^{(0)}) = \Delta\Phi(\mathbf{p}, t_m^{(0)}) =: \Delta\Phi \quad (6.34)$$

and similarly

$$-\text{Im} \left[\Delta S(\mathbf{p}, t_p^{(0)}) \right] = \text{Im} \left[\Delta S(\mathbf{p}, t_m^{(0)}) \right] := \text{Im} \Delta S_m. \quad (6.35)$$

We define the difference in the action $\Delta S = \Delta S(\mathbf{p}, t_m^{(0)}) - \Delta S(\mathbf{p}, t_p^{(0)})$, which satisfies $\text{Im} \Delta S = 2\text{Im} \Delta S_m$.

Using the expansion of the action and of the “phase” to first order in ϵ , the signal of Eq. (6.24) can be approximated as

$$\begin{aligned} w(\mathbf{p}) &\approx w^{(0)}(\mathbf{p}) \left| e^{i(\Delta\Phi(\mathbf{p}, t_m^{(0)}) + \Delta S(\mathbf{p}, t_m^{(0)}))} \pm e^{i(\Delta\Phi(\mathbf{p}, t_p^{(0)}) + \Delta S(\mathbf{p}, t_p^{(0)}))} \right|^2 \\ &= w^{(0)}(\mathbf{p}) \left| e^{i(\Delta\Phi + i\text{Im} \Delta S_m)} \pm e^{i(-\Delta\Phi - i\text{Im} \Delta S_m - \text{Re} \Delta S)} \right|^2. \end{aligned} \quad (6.36)$$

Here, $w^{(0)}(\mathbf{p})$ is the unperturbed signal for pure circular polarization. As expected, if the probe pulse is switched off, the sideband signal vanishes due to destructive interference, whereas constructive interference occurs on the ATI peaks. For weak perturbations, the arguments of the exponential function are small so that we can use a Taylor expansion. In addition, we assume that the change of the structure-dependent “phase” $\Delta\Phi$ is small compared to the difference in the action ΔS . When neglecting second-order terms in $\Delta\Phi$ and terms higher than ϵ^2 , Equation (6.36) can be rewritten as

$$w(\mathbf{p}) = w^{(0)}(\mathbf{p}) \begin{cases} 4 - \text{Re}(\Delta S^2) - 4 \text{Re}(\Delta S \Delta\Phi) + \dots & , \text{ at ATI peaks} \\ |\Delta S|^2 + 4 \text{Re}(\Delta S^* \Delta\Phi) + \dots & , \text{ at sidebands.} \end{cases} \quad (6.37)$$

For the further analysis, we have to explicitly evaluate the quantities ΔS and $\Delta\Phi$. To this end, we define the real-valued coefficient functions

$$\begin{aligned} A_1 &= \frac{1}{\omega} (p_\perp + A_0) \cosh\left(\frac{\omega\tau_i}{2}\right), & A_2 &= \frac{1}{\omega} (p_\perp - A_0) \sinh\left(\frac{\omega\tau_i}{2}\right), \\ B_1 &= -\frac{A_0}{p_\perp} \cosh\left(\frac{\omega\tau_i}{2}\right), & B_2 &= -\frac{p_\perp - A_0\chi}{p_\perp \sqrt{\chi^2 - 1}} \sinh\left(\frac{\omega\tau_i}{2}\right), \\ C_1 &= +\frac{A_0}{p_\perp} \sinh\left(\frac{\omega\tau_i}{2}\right), & C_2 &= -\frac{p_\perp - A_0\chi}{p_\perp \sqrt{\chi^2 - 1}} \cosh\left(\frac{\omega\tau_i}{2}\right), \end{aligned} \quad (6.38)$$

with τ_i and χ defined in Eq. (6.25). Using Eq. (6.27), the action correction ΔS reads

$$\Delta S = \int_{t_p^{(0)}}^{t_m^{(0)}} dt \mathbf{A}_P(t) \cdot (\mathbf{p} + \mathbf{A}_\omega(t)) = 8\epsilon A_0 \left[A_1 \sin\left(\frac{\Phi_p - \alpha}{2}\right) - iA_2 \cos\left(\frac{\Phi_p - \alpha}{2}\right) \right]. \quad (6.39)$$

Importantly, according to Eq. (6.30), the correction of the “phase” $\Delta\Phi$ is a linear function of the gradient of the quantity Φ . We can write this correction as

$$\begin{aligned} \Delta\Phi &= 2\epsilon A_0 \left[\left(B_1 \cos\left(\frac{\Phi_p - \alpha}{2}\right) + iC_1 \sin\left(\frac{\Phi_p - \alpha}{2}\right) \right) (\mathbf{e}_\perp \cdot \nabla\Phi) \right. \\ &\quad \left. + \left(B_2 \sin\left(\frac{\Phi_p - \alpha}{2}\right) + iC_2 \cos\left(\frac{\Phi_p - \alpha}{2}\right) \right) (\mathbf{e}_\parallel \cdot \nabla\Phi) \right], \end{aligned} \quad (6.40)$$

where we use the unit vectors \mathbf{e}_\perp and \mathbf{e}_\parallel that are perpendicular and antiparallel to $\mathbf{E}_\omega(\text{Re } t_s^{(0)})$. We omit the argument $\mathbf{v}^{(0)}(\mathbf{p}, t_s^{(0)})$ of the gradient $\nabla\Phi$.

Using Eqs. (6.39) and (6.40), the electron signal of Eq. (6.37) for ATI rings and sidebands can be expressed as

$$w(\mathbf{p}) = w^{(0)}(\mathbf{p}) \left[(2 \pm 2) \mp 32\epsilon^2 A_0^2 (\eta_\pm - \kappa_\pm \cos(\Phi_p - \alpha) - \delta_\pm \sin(\Phi_p - \alpha)) \right]. \quad (6.41)$$

The introduced quantities η_{\pm} , κ_{\pm} and δ_{\pm} depend on the laser parameters, on the final momentum \mathbf{p} and on the gradient $\nabla\Phi$, but not on the relative phase α . An explicit calculation results in

$$\begin{aligned}\delta_{\pm} &= -(A_1B_1 \pm A_2C_1) \operatorname{Re}(\mathbf{e}_{\perp} \cdot \nabla\Phi) + (A_1C_2 \mp A_2B_2) \operatorname{Im}(\mathbf{e}_{\parallel} \cdot \nabla\Phi) \\ &= -\frac{A_0}{p_{\perp}\omega} \left(-\operatorname{Re}(\mathbf{e}_{\perp} \cdot \nabla\Phi) + \frac{p_{\perp} - A_0\chi}{A_0\sqrt{\chi^2 - 1}} \operatorname{Im}(\mathbf{e}_{\parallel} \cdot \nabla\Phi) \right) \tilde{\delta}_{\pm}\end{aligned}\quad (6.42)$$

with the definitions $\tilde{\delta}_{+} = A_0\chi + p_{\perp}$ and $\tilde{\delta}_{-} = p_{\perp}\chi + A_0$. We want to compare this expression to the position offsets of the unperturbed electron wave packet, i.e., to the derivatives of the real-valued momentum-space phase. In the MO-SFA framework, the perpendicular component of the position offsets is given by Eq. (6.18). The evaluation for a circularly-polarized ω -field leads to the expression

$$\begin{aligned}\Delta r_{\perp} &= -\mathbf{e}_{\perp} \cdot \nabla_{\mathbf{p}} \operatorname{Re} \left(\Phi(\mathbf{v}^{(0)}(\mathbf{p}, t_s^{(0)})) \right) = -\mathbf{e}_{\perp} \cdot \operatorname{Re} \left(\frac{\partial \mathbf{v}^{(0)}(\mathbf{p}, t_s^{(0)})}{\partial \mathbf{p}} \nabla\Phi \right) \\ &= \frac{\chi A_0}{p_{\perp}} \left(-\operatorname{Re}(\mathbf{e}_{\perp} \cdot \nabla\Phi) + \frac{p_{\perp} - A_0\chi}{A_0\sqrt{\chi^2 - 1}} \operatorname{Im}(\mathbf{e}_{\parallel} \cdot \nabla\Phi) \right).\end{aligned}\quad (6.43)$$

Here, the “ Δ ” indicates that we are only considering the orientation-dependent part of the local position that is induced by the prefactor in the strong-field approximation. In general for asymmetric molecules, the quantity in Eq. (6.43) can differ from the relative position offsets defined in Eq. (6.13) by an orientation-independent shift. However, for the special case of H_2 , the symmetry enforces that the quantities of Eqs. (6.13) and (6.43) are equal.

Importantly, we find that the quantity δ_{\pm} in the signal of Eq. (6.41) is proportional to the structure-dependent position offset Δr_{\perp} of Eq. (6.43):

$$\delta_{\pm} = -\frac{\tilde{\delta}_{\pm}}{\omega\chi} \Delta r_{\perp}.\quad (6.44)$$

Hence, we showed within the MO-SFA framework that the experimentally-accessible electron signal in the two-color field contains information on the perpendicular component Δr_{\perp} of position offsets from molecular strong-field ionization in the ω -field (the parallel component does not influence the signal). This assumption was already made in Refs. [69, 377], but not formally derived.

How to extract the position offsets?

To this end, we study the electron distribution in the two-color field approximated by Eq. (6.41). In the special case of an initial s state for an atom, the first factor $w^{(0)}$ for pure circular polarization is independent of the angle $\phi_{\mathbf{p}}$, the coefficients η_{\pm} , κ_{\pm} are also isotropic and the position offsets Δr_{\perp} vanish. In agreement with the numerical results in Fig. 6.10(b), the angular modulation of the signal is determined by the $\cos(\phi_{\mathbf{p}} - \alpha)$ term in Eq. (6.41). Thus, a change of the relative phase α is equivalent to a change in the orientation of the interference pattern. On the other hand, for molecules, the first factor $w^{(0)}$, the coefficients η_{\pm} , κ_{\pm} and also the position offsets Δr_{\perp} generally depend on the direction of the final momentum \mathbf{p} . As a result, for a fixed relative phase α and a fixed molecular axis \mathbf{R} , the dependence of the yield on the angle $\phi_{\mathbf{p}}$ is strongly influenced by the angle-dependent ionization probability $w^{(0)}$ for pure circular polarization. This makes it more difficult to access the position offsets Δr_{\perp} . We believe that the recent experiment on CO with a scheme similar to HASE suffers from this problem [421].

Instead of studying the yield as a function of the angle $\phi_{\mathbf{p}}$, the signal can also be investigated as a function of the relative phase α between the two colors at a fixed final momentum \mathbf{p} and for a fixed molecular orientation. Then, the variation of the yield as a function of α is solely determined by the $\cos(\phi_{\mathbf{p}} - \alpha)$ term and the $\sin(\phi_{\mathbf{p}} - \alpha)$ term in Eq. (6.41). Here, the first factor $w^{(0)}$ and the quantities η_{\pm} , κ_{\pm} , δ_{\pm} are kept fixed. Thus, for a given momentum \mathbf{p} on an ATI peak (sideband), the optimal relative phase α_{opt} that maximizes (minimizes) the signal is given by the simple relation

$$\tan(\phi_{\mathbf{p}} - \alpha_{\text{opt}}) = \frac{\delta_{\pm}}{\kappa_{\pm}} = -\frac{\tilde{\delta}_{\pm}}{\omega\chi\kappa_{\pm}} \Delta r_{\perp}.\quad (6.45)$$

In Eq. (6.45), the quantities κ_{\pm} have the form

$$\kappa_{\pm} = A_1^2 \pm A_2^2 + \mathbf{b} \cdot \nabla \Phi, \quad (6.46)$$

with coefficients A_1, A_2 defined in Eq. (6.38) and a function \mathbf{b} of the final momentum \mathbf{p} , I_p and A_0 . Even though, in principle, κ_{\pm} also depends on the target structure because of the gradient $\nabla \Phi$, we find that, in practice, the first structure-independent terms dominate for small molecules. Hence, we neglect the last term proportional to $\nabla \Phi$ in κ_{\pm} .

For vanishing position offsets, the yield as a function of α is maximized (minimized) at $\alpha_{\text{opt}} = \phi_p$ for ATI peaks (sidebands). Usually, for small molecules, the offset $\Delta\alpha_{\text{opt}} = \alpha_{\text{opt}} - \phi_p$ of the optimal phase compared to the angle ϕ_p is sufficiently small so that Eq. (6.45) can be linearized. Hence, we get an analytical mapping of the experimentally-accessible offset $\Delta\alpha_{\text{opt}}$ of the optimal phase to the position offset Δr_{\perp}

$$\Delta\alpha_{\text{opt}} \approx \frac{\tilde{\delta}_{\pm}}{\omega\chi\kappa_{\pm}} \Delta r_{\perp}, \quad (6.47)$$

where the coefficients are given by $\kappa_{+} = ((A_0^2 + p_{\perp}^2)\chi + 2A_0p_{\perp})/\omega^2$ and $\kappa_{-} = ((A_0^2 + p_{\perp}^2) - 2A_0p_{\perp}\chi)/\omega^2$ as well as $\tilde{\delta}_{+} = A_0\chi + p_{\perp}$ and $\tilde{\delta}_{-} = p_{\perp}\chi + A_0$ with $\chi = \frac{1}{2A_0p_{\perp}} [p_{\perp}^2 + A_0^2 + 2I_p] \in \mathbb{R}$. As a result, we find that, for a fixed momentum \mathbf{p} and a fixed molecular axis \mathbf{R} , the variation of the yield as the function of the relative phase α can be considered to measure position offsets Δr_{\perp} . We confirm the assumption of Refs. [377, 419] that the offset $\Delta\alpha_{\text{opt}}$ of the optimal phase is uniquely linked to the position offset Δr_{\perp} and that this mapping is not influenced by other molecule-specific quantities (such as the orientation dependence of the yield).

The presented scheme is similar to the phase-of-the-phase (PoP) spectroscopy [422–425]. In PoP spectroscopy, parallel two-color fields are used and the yield is studied as a function of the relative phase between a strong fundamental field and a weak second-harmonic probe field. Then, the phase-of-the-phase which maximizes the ionization yield at a given momentum can be used to investigate the ionization process. The important difference is that the HASE scheme considers changes of an interference pattern caused by a probing field with half of the fundamental frequency.

On the first glance, the problem with an orientation-dependent yield was avoided in a slightly different way in the recent work [377]. In the experiment by Trabert *et al.* using the COLTRIMS technique, the orientation of the two-color field in space was fixed, but the measurement contained the distributions for all possible orientations of the molecular axis. In their analysis, all configurations with a given relative orientation β were selected. Hence, a momentum distribution for a given β (see for example Fig. 2(b) of Ref. [377]) contains events corresponding to different absolute orientations of the molecule in laboratory frame. On the other hand, the orientation of the Lissajous figure of the vector potential in the laboratory frame can be varied by the relative phase α (see the schematic sketch of Fig. 6.11(a)). Hence, the special selection of events and the analysis of the signal as a function of ϕ_p in Ref. [377] is equivalent to the approach described above, i.e., using a fixed final momentum and molecular orientation (in the laboratory frame) and analyzing the yield as a function of the relative phase α . From a theoretical perspective, however, it is more intuitive to work with a molecule fixed in the laboratory frame.

Dependence on the laser parameters

The sensitivity of the HASE interferometer is mainly determined by modulation depth of the signal as a function of α and by the conversion of a position offset Δr_{\perp} to a phase offset $\Delta\alpha_{\text{opt}}$. According to Eq. (6.41), the signal modulation of the ATI peaks is approximately given by $8\epsilon^2 A_0^2 \kappa_{+}$. For adiabatic conditions, the modulation depth is proportional to $\epsilon^2 E_0^4/\omega^6$ (at $p_{\perp} = A_0$) and can be controlled by the relative field strength ϵ . On the other hand, the conversion factor of Eq. (6.47) only depends on the properties of the fundamental laser field, the ionization potential and the magnitude of the momentum p_{\perp} . Hence, as long as the probe field is sufficiently weak, the mapping is independent of the probe-field strength. For adiabatic ionization conditions, the conversion factor scales with $\Delta\alpha_{\text{opt}}/\Delta r_{\perp} \propto \omega^2/E_0$, i.e., with the inverse of the position-space quiver amplitude of the electron in the fundamental field. Thus, the HASE interferometer is less sensitive to position offsets for longer wavelengths.

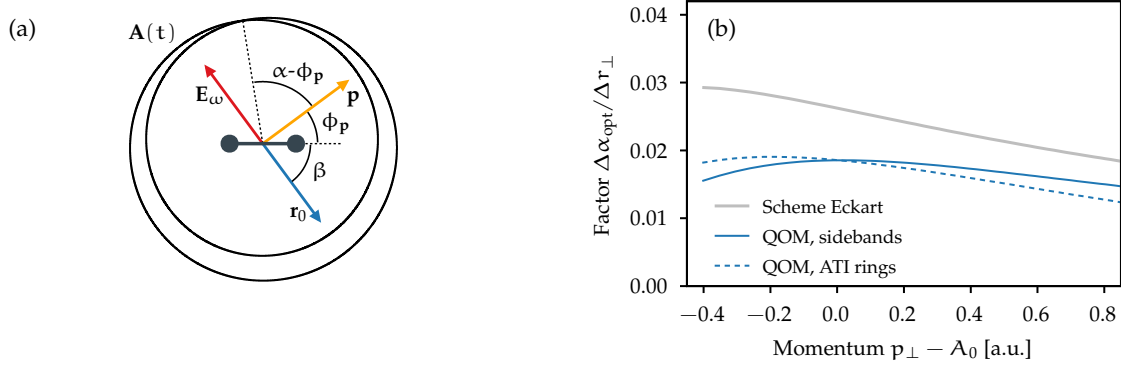


Figure 6.11: Geometry of the HASE interferometer. (a) The orientation of the vector potential (black line) of the co-rotating two-color laser field can be varied by the relative phase α . For a given final momentum \mathbf{p} and a fixed molecular orientation β , the relative phase of the probe field α is scanned and the yield is recorded. From the offset $\Delta\alpha_{\text{opt}} = \alpha_{\text{opt}} - \phi_{\mathbf{p}}$ of the optimal phase, the position offsets Δr_{\perp} can be reconstructed. (b) Conversion factor of position offsets Δr_{\perp} to offsets $\Delta\alpha_{\text{opt}}$ of the optimal phase as a function of the momentum p_{\perp} for 800 nm fundamental wavelength and 2×10^{14} W/cm² intensity. In addition to the factor (6.47) from the quantum-orbit model (blue lines), the conversion factor used by Eckart in Ref. [69] is shown as gray line.

Figure 6.11(b) shows the conversion factor of Eq. (6.47) as a function of the momentum component p_{\perp} for 800 nm fundamental wavelength and 2×10^{14} W/cm² intensity. Compared to the previously-used retrieval algorithm by Eckart [69] based on an adiabatic semiclassical model, we find significantly smaller conversion factors for both ATI peaks and sidebands. Hence, once again, we observe a decisive influence of nonadiabatic effects in circularly-polarized fields. Interestingly, for $p_{\perp} \neq A_0$, Equation (6.47) predicts systematically different offsets $\Delta\alpha_{\text{opt}}$ for the sidebands and for the ATI rings (due to the different conversion factors).

In the recent experimental work [377], the conversion factor by Eckart based on a semiclassical model was used which does not discriminate between ATI peaks and sidebands. There, in order to avoid the systematic difference between both kinds of peaks, the authors first determined the envelope of the momentum distribution as a function of p_{\perp} for fixed α and fixed $\phi_{\mathbf{p}}$, e.g., by Fourier filtering. Afterwards a “normalized” distribution, i.e., the division of the full distribution by the envelope, was considered in the analysis. When applying this normalization approach to the distribution of Eq. (6.41) obtained in the quantum-orbit model, we can approximate the envelope at each p_{\perp} by the sum of the expressions for ATI peaks and for sidebands. For the corresponding normalized distribution, we find that the systematic difference of the phase offset $\Delta\alpha_{\text{opt}}$ between ATI peaks and sidebands indeed vanishes. The effective conversion factor is then given by the factor for the sidebands in Eq. (6.47). However, for numerical reasons, we do not use this normalization approach in the following and instead we stick to the theory of Eq. (6.47) with different conversion factors for ATI peaks and for sidebands.

6.3.3 Results for a short-range potential

In this section, we conduct numerical experiments to simulate the HASE interferometer by means of TDSE calculations. We extract the orientation-dependent position offsets in molecular ionization by analyzing experimentally-accessible interference structures in the photoelectron momentum distributions for the two-color field. In addition, we independently determine the offsets from the momentum-space phase of the liberated electron wave packet created by strong-field ionization in a circularly-polarized field with fundamental frequency ω (see Eq. (6.2)). To verify the HASE scheme, both results are compared to each other.

We first avoid the complications by a Coulombic tail of the potential by studying the HASE interferometer for a short-range model of H₂ with the potential (6.11). To calculate the photoelectron momentum distributions for ionization by the co-rotating two-color field (6.23), we solve the TDSE numerically on Cartesian grids as described in Section 6.2.2. Here, the molecular axis is fixed along the x -direction, i.e., the molecular frame is equal to the laboratory frame. The laser pulse has a trapezoidal envelope with

8 T_ω -cycles of constant intensity. To minimize envelope effects, the electron momentum distributions are averaged over 16 values of the CEP between -2π and 2π .¹² The fundamental field has a wavelength of 800 nm wavelength and an intensity of 2×10^{14} W/cm², i.e., a vector potential of $A_0 = 0.932$ a.u. The applied probe field has a relative field strength $\epsilon = 0.003$. For these parameters, the modulation of the yield on the ATI rings is on the order of 20%. The simulations are repeated for 180 values of the relative phase α between the fundamental and the probe field, using the range from $-\pi$ to π . The setting is sketched in Fig. 6.11(a).

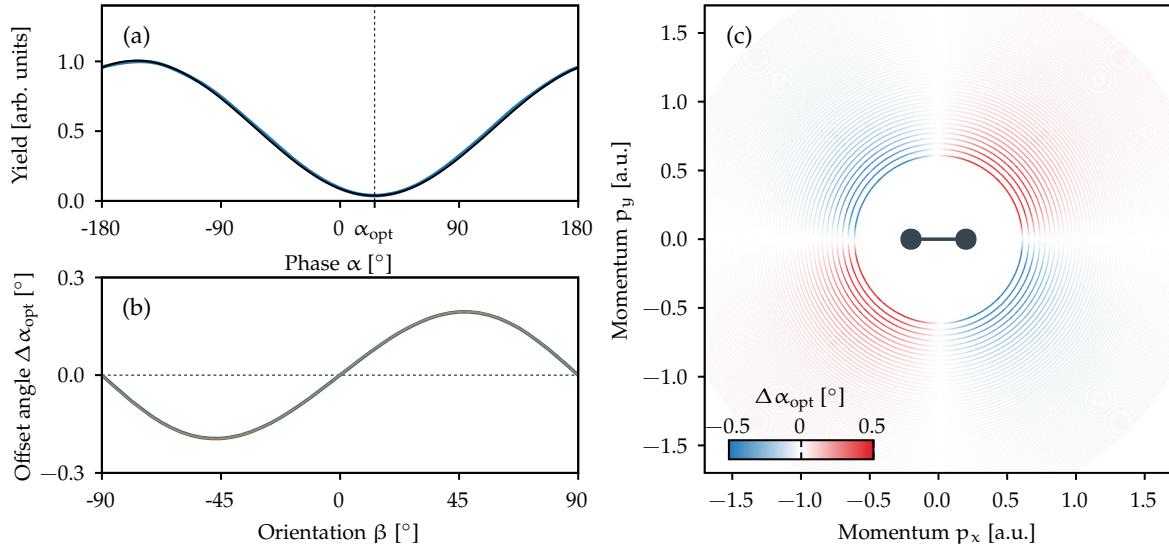


Figure 6.12: Experimentally-accessible observables to retrieve the orientation-dependent position offsets. (a) Signal modulation as a function of the relative phase α for a given final momentum $\mathbf{p} = (0.948, 0.460)$ a.u. ($\phi_{\mathbf{p}} = 25.9^\circ$) on a sideband extracted from TDSE simulations (blue line). The truncated Fourier series is shown as black line and the retrieved optimal phase α_{opt} is indicated as dashed vertical line. (c) Phase offset $\Delta\alpha_{\text{opt}} = \alpha_{\text{opt}} - \phi_{\mathbf{p}}$ in degrees as a function of the momenta \mathbf{p} . (b) Lineout of the phase offset as a function of the relative orientation β for a sideband centered at $p_{\perp} \approx 1.05$ a.u. The (small) orange points indicate the results for all neighboring momenta on the Cartesian grid. The blue curve shows the extracted dependence on an equally-spaced grid in β .

The TDSE simulations provide a sequence of 2D electron momentum distributions parameterized by the relative phase α . Each distribution corresponds to another orientation of the vector potential of the two color field in the laboratory frame. For a given final electron momentum \mathbf{p} , we consider the variation of the signal as a function of the relative phase α . An example for a momentum on a sideband is shown in Fig. 6.12(a). As explained above, the variation of the yield is caused by the interference between two wave packets detached in two consecutive cycles of the fundamental field. Since the signal versus α is 2π -periodic, for each final momentum \mathbf{p} , the change of the yield can be represented by a Fourier series

$$w(\mathbf{p}, \alpha) = \frac{B_0(\mathbf{p})}{2} + \sum_{k=1}^N B_k(\mathbf{p}) \cos(k(\alpha - \alpha_k(\mathbf{p}))). \quad (6.48)$$

In agreement with the predicted α -dependence of the quantum-orbit model (6.41), the fundamental component with $k = 1$ is found to dominate over higher-harmonic contributions for sufficiently small relative field strength ϵ . An example for the truncation of the series at $N = 1$ is shown as black line in Fig. 6.12(a). For each final momentum \mathbf{p} , the optimal phase α_{opt} is approximated by the value $\alpha_1(\mathbf{p})$. As expected from the quantum-orbit model (6.45), for a short-range potential, the optimal phase α_{opt} roughly follows the angle $\phi_{\mathbf{p}}$ in the polarization plane.

The subtraction of the structure-independent angle $\phi_{\mathbf{p}}$ from the optimal phase α_{opt} results in the offset $\Delta\alpha_{\text{opt}} = \alpha_{\text{opt}} - \phi_{\mathbf{p}}$ of the optimal phase. This offset $\Delta\alpha_{\text{opt}}$ clearly shows an orientation-dependent modulation with sign changes for the different quadrants (see Fig. 6.12(c)). Here, we selected regions

¹²We sample the CEPs on a equally-spaced grid with an offset of α . This offset ensures that, for each relative phase α , the same (rotated) Lissajous figures of the field are included in the simulations.

around the ATI rings and sidebands to avoid problems for low signal in between the peaks. The phase offsets vary on the order of one degree as a function of both the angle ϕ_p as well as the magnitude p_\perp . Due to the fixed molecular axis (along the x -axis), a variation of the optimal phase as a function of ϕ_p is directly related to a modulation with respect to the relative orientation between the final momentum and the molecular axis. The mapping of the angle ϕ_p of the momentum in the polarization plane and the relative angle β is given by $\beta = 90^\circ - \phi_p$. To extract the offset $\Delta\alpha_{\text{opt}}$ as a function of the relative angle β for a given peak, we consider the offsets for all momenta on the Cartesian grid in the vicinity of the peak and apply a moving average to define a single value on an equally-spaced grid for β . For a sideband at $p_\perp \approx 1.05$ a.u., Figure 6.12(b) shows the phase offsets $\Delta\alpha_{\text{opt}}$ at the selected momenta on the Cartesian grid as orange points and the extracted smooth function as blue line.

The offsets $\Delta\alpha_{\text{opt}}$ of the phase as a function of the lateral momenta p_\perp and the relative orientation β contain all information that is needed to reconstruct the perpendicular component Δr_\perp of the position offsets or, to phrase it otherwise, of the phase gradients of the wave packet. To this end, we use the mapping (6.47) derived in the quantum-orbit model and convert the phase offsets $\Delta\alpha_{\text{opt}}$ to the position offset Δr_\perp . For selected ATI rings and sidebands, the results Δr_\perp are shown as a function of the orientation β in Fig. 6.13. Importantly, we only used the experimentally-accessible information on the variation of the yield as a function of the relative phase α in this numerical experiment.

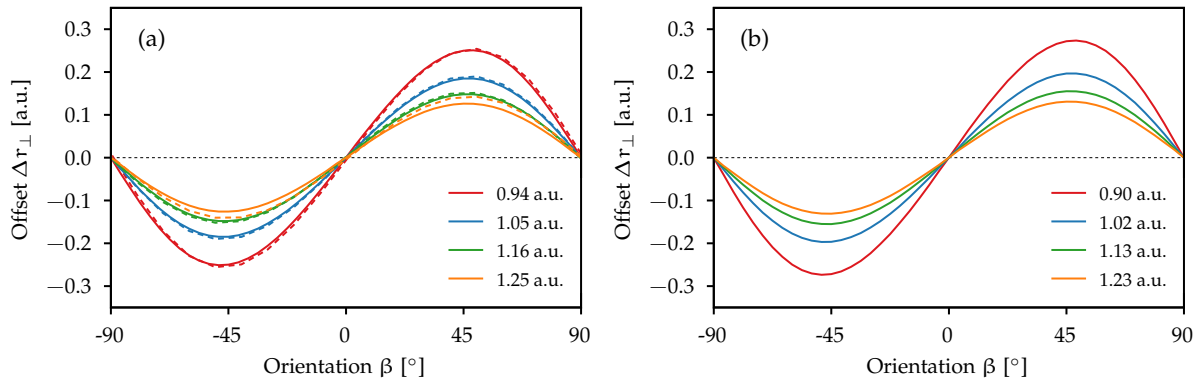


Figure 6.13: Reconstructed orientation-dependent position offsets for a short-range potential. The results based on the HASE scheme are shown for selected sidebands and ATI peaks in panels (a) and (b), respectively. The corresponding momenta p_\perp are indicated in the legends. For comparison, the results based on the phase gradient of the continuum wave packet from ionization in the fundamental field are shown as dashed lines in panel (a).

To benchmark the results from HASE, we consider ionization of H_2 by the fundamental field and determine the position offsets from the phase of the continuum wave packet (similar to Section 6.2.3). This purely theoretical approach is independent of the numerical HASE experiment performed above. Since the position offsets are influenced by nonadiabatic effects (see Section 6.2.3), we use the same envelope of the laser pulse as in the HASE simulations. Due to intercycle interference, we can only extract the phase of the wave packet in momentum space at the positions of the ATI peaks. At the sidebands of HASE scheme, the derivative of the phase in Eq. (6.2) can be approximated by using the neighboring ATI peaks. For each sideband, we extract the orientation-dependent variation of the position offsets by subtraction of the average value over all possible orientations β (analogous to the procedure in Eq. (6.13)). The theoretical results from the derivative of the phase are shown in Fig. 6.13(a) as dashed lines. For the shown peaks, the phase gradient results from TDSE are in remarkable agreement with the position offsets extracted using the HASE scheme. In agreement with Section 6.2, the orientation dependence of the position offsets approximately follows a $\sin(2\beta)$ function.

To quantitatively compare the position offsets, we use again the ansatz $\Delta r_\perp = \Delta r_\perp^{\text{max}} \sin(2(\beta - \beta_\perp^{\text{def}}))$ of Eq. (6.15).¹³ Here, $\Delta r_\perp^{\text{max}}$ represents the modulation depth of the position offset and the deflection angle β_\perp^{def} determines for which orientations β the offsets vanish. The results are presented in Fig. 6.14(a) and (b). The deflection angles β_\perp^{def} are very small over the main part of the lateral distribution indicating

¹³We use a fit to determine the parameters (in contrast to Section 6.2.3).

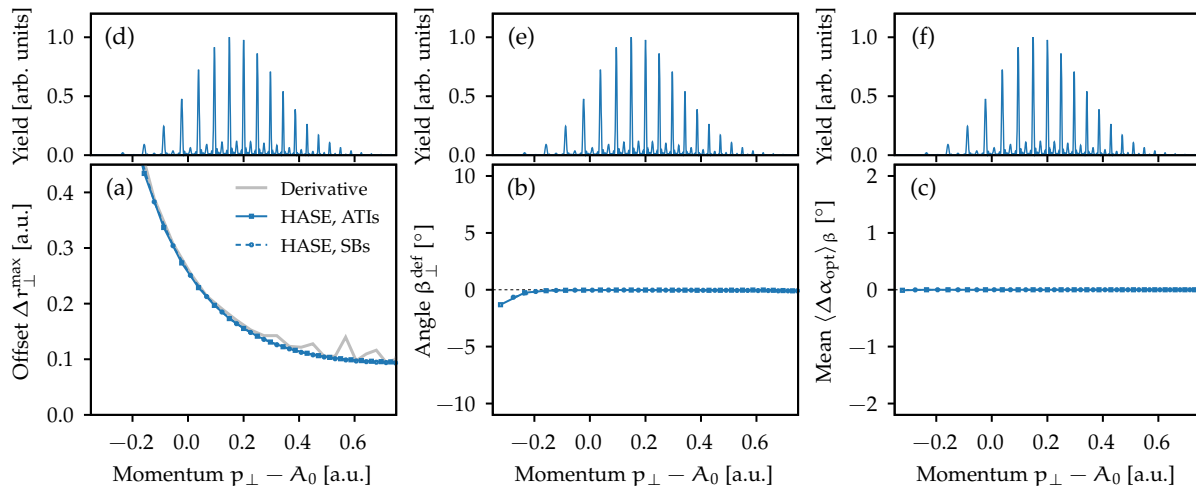


Figure 6.14: Reconstructed quantities of the HASE interferometer for a short-range potential. (a) Amplitude Δr_{\perp}^{\max} of the orientation-dependent position offsets and (b) deflection angle $\beta_{\perp}^{\text{def}}$ calculated by a Fourier expansion (see Eq. (6.15)). (c) Expectation value of the phase offset $\Delta\alpha_{\text{opt}}$. In addition to the results from the interferometric approach for ATI peaks (solid blue lines) and sidebands (dashed blue lines), the results based on the phase gradient of the continuum wave packet from ionization in the fundamental field are depicted as gray thick line in panel (a). (d)-(f) Lateral momentum distribution for the two-color field.

that the perpendicular position offsets maximize (minimize) at 45° (-45°) and vanish for parallel or perpendicular alignment. The modulation amplitudes Δr_{\perp}^{\max} extracted from the ATI peaks and from the sidebands are in perfect agreement. This shows that the separate conversion factors of Eq. (6.47) for both types of peaks work well. The results from the HASE interferometer are in excellent agreement with the directly-calculated phase derivatives (see Fig. 6.14(a)). Especially, the decisive momentum dependence related to nonadiabatic effects is well reproduced by the interferometric approach. The small, but visible deviations in Fig. 6.14(a) at large perpendicular momenta are likely to be caused by an insufficient resolution of the ATI rings in the simulations on Cartesian grids.

6.3.4 Results for a long-range potential

For a more realistic investigation, we apply the HASE interferometer to molecular hydrogen modeled by a potential V that behaves at large distances r like a Coulomb potential $-1/r$. To this end, we repeat the TDSE simulations for the long-range potential of Eq. (6.10).¹⁴ Due to Coulomb interaction, even for atoms, the optimal phase α_{opt} differs from the angle ϕ_{p} in the polarization plane (see also Fig. 6.10). This effect is also present in the simulations for molecules. For the short-range potential used in Section 6.3.3, the expectation value $\langle\Delta\alpha_{\text{opt}}\rangle_{\beta}$ obtained by averaging $\Delta\alpha_{\text{opt}} = \alpha_{\text{opt}} - \phi_{\text{p}}$ over all molecular orientation at fixed perpendicular momentum p_{\perp} vanishes in agreement with the potential-free quantum-orbit model (see Fig. 6.14(c)). However, for long-range potentials, the expectation value $\langle\Delta\alpha_{\text{opt}}\rangle_{\beta}$ is nonzero (see Fig. 6.16(c)). Since this offset is mostly induced by the long-range tail of the potential, we expect that it depends only weakly on the molecular orientation.

To convert the offsets $\Delta\alpha_{\text{opt}}$ of the optimal phase to the position offset Δr_{\perp} , we still want to use the conversion factor (6.47) that was derived in the Coulomb-free quantum-orbit model. Furthermore, we are only interested in the relative change of the position offsets as a function of the emission direction relative to the molecular axis. Hence, similar to Ref. [377], we first subtract the reference values $\langle\Delta\alpha_{\text{opt}}\rangle_{\beta}$ from the phase offsets $\Delta\alpha_{\text{opt}}$ and, afterwards, we apply the conversion factor to extract the position offsets.¹⁵ Figure 6.15 shows the reconstructed results as a function of the relative orientation $\beta = 90^{\circ} - \phi_{\text{p}}$ for selected sidebands and ATI peaks. Despite the presence of the long-range potential, the reconstructed position offsets are similar to the short-range simulation. For comparison,

¹⁴At the edges of the inner grid used in the simulations, the ionic potential is truncated over a distance of 40 a.u. using a \sin^2 function (see also Appendix A.2.2). This ensures that, even for finite box sizes, the correct ionization potential is obtained.

¹⁵This is similar to the procedure used in Eq. (6.13).

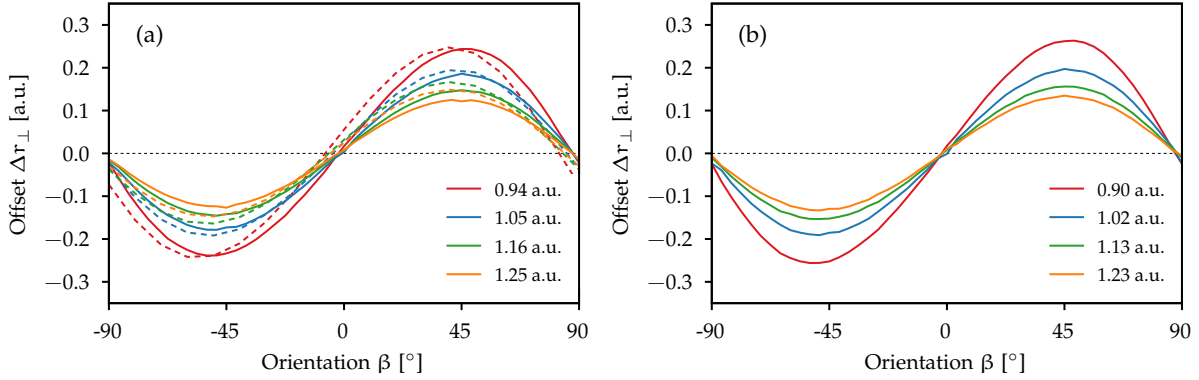


Figure 6.15: Reconstructed orientation-dependent position offsets as in Fig. 6.13, but for a long-range potential. The results based on the HASE scheme are shown for selected sidebands and ATI peaks in panels (a) and (b), respectively. For comparison, the results based on the phase gradient of the continuum wave packet from ionization in the fundamental field are shown as dashed lines in panel (a).

we again consider ionization of the long-range model by the fundamental field and determined the position offsets from the phase of the continuum wave packet. The position offsets from the derivative of the continuum phase are shown in Fig. 6.15(a) as dashed lines. Generally, the results from the HASE scheme and from the phase derivative also match well for the used long-range potential.

In agreement with the findings in Section 6.2.3, the derivative of the (asymptotic) phase shows an attoclock-like rotation with deflection angles $\beta_{\perp}^{\text{def}}$ between six and eight degrees in the relevant p_{\perp} -range. However, the orientation dependence of the position offset from HASE is nearly uninfluenced by the Coulomb potential. The deflection angles $\beta_{\perp}^{\text{def}}$ are about two degrees for momenta close to the maximum of the lateral distribution (see Fig. 6.16(b)). The approximate invisibility of Coulomb effects was also observed in other approaches with two-color fields. An example is the streaking of electron with a weak external electric field that is polarized perpendicular to a strong linear driving field [367, 426]. Similar to these situations, we believe that the absence of an attoclock rotation is at least partially related to the use of a Coulomb-free phase-offset-to-position-offset mapping.

The amplitudes $\Delta r_{\perp}^{\text{max}}$ of the position offsets depend strongly on the momentum p_{\perp} (see Fig. 6.16(a)). For the laser parameters at hand, the comparison with the short-range potential shows that this is again mostly caused by the influence of nonadiabaticity. For momenta p_{\perp} slightly smaller than the maximum of the lateral distribution, the amplitudes $\Delta r_{\perp}^{\text{max}}$ from the HASE scheme and from the derivative of the

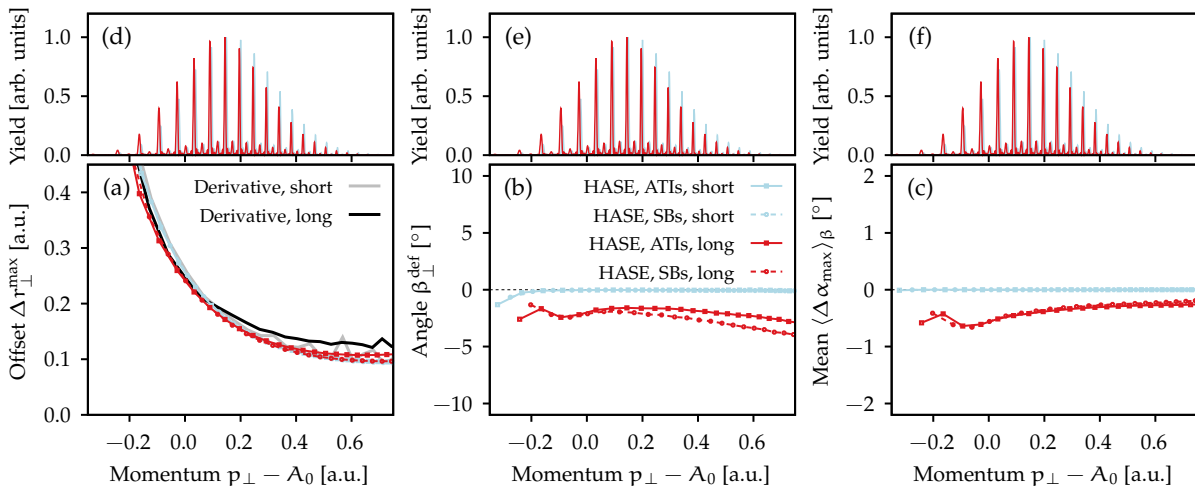


Figure 6.16: Reconstructed quantities of the HASE interferometer as in Fig. 6.16, but for a long-range potential (red lines). For comparison, the results for a short-range potential are shown as pale blue lines. In addition, the results based on the phase gradient of the continuum wave packet from ionization in the fundamental field are shown in panel (a) for the long-range potential (black thick line) and for the short-range potential (gray thick line).

phase are in very good agreement. However, at large p_{\perp} , the HASE interferometer leads to systematically smaller values compared to the derivative of the phase. Interestingly, the results from HASE for a long-range and a short-range potential are also in very good agreement for large p_{\perp} .

Our theoretical study based on TDSE simulations shows that, for a fundamental field with 800 nm wavelength, Coulomb effects modify only weakly the operating principle of the HASE interferometer. Using the Coulomb-free retrieval procedure based on a quantum-orbital model, the reconstructed position offsets are in satisfying agreement with the results from the derivative of the phase in a single-color simulation. Thus, the presented results confirm many predictions that were made in Ref. [69] based on a semiclassical model. However, the weak influence of the long-range potential on the HASE interferometer leaves some room for speculations. For example, whether the HASE scheme measures (in the presence of a long-range potential) the asymptotic position offsets at the detector or the position offsets at the tunnel exit, i.e., at the time of ionization.

In the recent pioneering experiment [377] that implemented the HASE scheme to study electron wave packets from strong-field ionization of molecular hydrogen, a fundamental wavelength of 390 nm was used. There, the situation is more delicate, because both nonadiabatic and Coulomb effects are very prominent. Thus, a Coulomb-free modeling of the HASE interferometer as used in our simulations is questionable. Therefore, the experimental data were interpreted based on a semiclassical model with adiabatic initial conditions that includes the Coulomb potential during the continuum motion [69]. However, unfortunately, we found in Section 6.3.2 that this semiclassical model does not give quantitatively correct results in a potential-free setting due to the improper treatment of nonadiabaticity (see also in Fig. 6.11(b)). To resolve this problem in the interpretation of the HASE scheme for long-range potentials, more sophisticated modeling is needed which should properly include nonadiabatic as well as Coulomb effects. We expect that a good starting point for future work would be the ARM theory introduced in Section 2.5.

6.4 Conclusion

In this chapter, we studied electron wave packets produced by recollision-free strong-field ionization of small (aligned) molecules. The properties of the released wave packet depend on the relative orientation of the molecular axis with respect to the tunneling direction. Usually, only the modulus squared of the probability amplitudes in momentum space of the outgoing wave packets is characterized by considering interference-free photoelectron momentum distributions. However, the phase of the momentum-space wave functions carries important spatial information on the ionized molecular orbital and the ionization process itself. For the hydrogen molecule H_2 , a prototypical dimer, we examined the orientation dependence of the local positions—defined as the negative derivative of the spectral phase with respect to the momentum. The simple prolate shape of the molecular orbital allows for an intuitive analytical interpretation of the observed changes in the local positions. These spatial offsets are related to the variations of the wave-packet's release position after tunnel ionization, leading to elongated/shortened travel paths of the wave packets. We followed two independent approaches to extract the local positions from TDSE simulations: (i) We directly analyzed the theoretically-accessible phase of the continuum wave function after the end of the laser pulse. (ii) We performed numerical experiments based on an interferometric scheme [69] to reconstruct the variation of the local positions from experimentally-accessible photoelectron momentum distributions.

Based on the phase of the continuum wave function, the local positions were determined for fields with circular polarization. We found that both the component perpendicular and the component antiparallel to the instantaneous electric field depend on the relative alignment of the molecular axis. For H_2 , the perpendicular position offsets basically show a sinusoidal modulation as a function of the molecular orientation. However, we found that the modulation depth strongly varies with the lateral momentum of the electrons in the polarization plane. As shown in a simple model based on the strong-field approximation, the enhancement of the modulation depth is related to nonadiabatic effects during the

release of the electron wave packets. We demonstrated that this complication due to nonadiabaticity can be avoided by considering ionization in a quasilinear field geometry with a nearly constant direction of the electric field around the time of peak field strength. The long-range Coulomb potential also influences the position offsets of the asymptotic wave packets. To disentangle the effect of the potential during tunnel ionization and during subsequent continuum motion, we performed classical backpropagation simulations.

Experimentally, the phase of the electron wave packets is not directly accessible. In the HASE scheme, a weak probe field with twice the wavelength of the fundamental circularly-polarized field is applied and the resulting interference pattern is considered to reconstruct position offsets [69]. A major goal of this chapter was to evaluate and to refine this interferometric scheme. Based on the strong-field approximation, we proved that there is a one-to-one correspondence between the optimal phase of the measurable interference pattern and the perpendicular component of the position offsets in molecular strong-field ionization. It turned out that this mapping based on the SFA contains important nonadiabatic corrections which were not included in the previous adiabatic modeling [69]. For the special case of a fundamental field with 800 nm wavelength, we performed TDSE simulations and directly compared the position offsets from the continuum wave packet to the position offsets retrieved from the HASE scheme. For a short-range model of H_2 , both results are in perfect agreement. For the considered laser parameters, we found that the long-range tail of a more realistic potential for H_2 only weakly influences the position offsets from the HASE scheme. This theoretical *ab-initio* study of the HASE interferometer in combination with the recent pioneering experimental implementation [377] demonstrated that the orbital imprint on the spatial information of the emitted electron wave packets is indeed experimentally accessible in strong-field ionization.

To improve the HASE scheme in the future, it would be advantageous to minimize the influence of nonadiabaticity on the measurement. To this end, the quasilinear field could be considered and the appearing position offsets could be probed by means of a linearly-polarized orthogonal streaking field of twice the effective wavelength. Similar to the co-rotating circularly-polarized fields, we expect that a scan of the yield as a function of the relative phase should encode the position information for small molecules. Furthermore, an obvious extension is the study of molecules with additional molecular orbitals as in nitrogen N_2 or with nodal planes as in oxygen O_2 . Furthermore, the influence of Stark effects in polar molecules such as helium hydride molecular ion HeH^+ or carbon monoxide CO (as recently used in Ref. [421]) on the position offsets would be worth studying. In principle, it should also be possible to perform pump-probe schemes and characterize the time-dependent change of the bound wave functions in position space. The simple analysis of the HASE scheme provided in this chapter was mainly based on the assumption that the molecular orbital can be interpreted as a single ionizing center, i.e., that its shape only weakly differs from typical atomic orbitals. However, when stretching the bond length, the double-slit interference of the two electron wave packets released at the two centers [388] becomes important. Recently, a HASE experiment on argon dimers was already performed in the group of Reinhard Dörner. It would be interesting to theoretically study the evolution of the position offsets when varying the internuclear distance from small molecules such as H_2 or N_2 to large molecules such as noble gas dimers. In TDSE simulations, this should be (artificially) possible by simply stretching the bond length.

Chapter 7

Nondipole Modification of the AC Stark Effect in Above-Threshold Ionization

7.1 Introduction

Placing an electronic system in a static external electric field leads to a shift of its energy levels compared to the field-free situation. This dc Stark effect is *the* textbook example for perturbation theory in quantum mechanics. Similarly, the electronic structure of matter is modified by an oscillating electromagnetic field, known as dynamical or ac Stark effect. In contrast to the dc Stark effect, the available intense laser pulses can strongly disturb the electronic systems. Resonant dipole transitions between bound electronic states are affected by the ac Stark effect, leading to a plethora of observations such as the Autler-Townes effect [427] and the Mollow triplet in resonance fluorescence [428, 429]. Here, we only focus on the nonresonant ac Stark effect in intense laser pulses which have important implications for the shaping of potential energy surfaces [430], the time-dependent modification of propagating laser pulses [431, 432] or the alignment of molecules [433].

The absorption of more photons than necessary to overcome the ionization threshold results in above-threshold ionization [5]. The electron energy spectra consist of peaks that are separated by the photon energy ω and correspond to the various numbers of absorbed photons. In the photoelectron momentum distributions, this is reflected as rings. As explained in Section 2.1.1, both continuum states and weakly-bound states are approximately shifted by the ponderomotive potential U_p . In strong laser pulses, the ponderomotive potential can reach several tens of electron volts. In contrast, the nonresonant ac Stark effect only weakly affects the tightly-bound states. For multi-cycle subpicosecond laser pulses, the electrons stay in the laser focus till the end of the pulse. Hence, the positions of the ATI rings are modified by the continuum ac Stark effect [171–173]. For nonresonant ionization (as for example in circularly-polarized fields), the positions of the ATI rings are usually estimated as

$$n\omega = I_p + \frac{\mathbf{p}^2}{2} + U_p \quad (7.1)$$

with $n \in \mathbb{N}$ being interpreted as the number of absorbed photons [171, 374]. The situation is more complex, when Rydberg states are shifted by the ac Stark effect into resonance with the ground state and are populated during the laser pulse [172, 434]. These Freeman resonances result in a rich additional substructure of the ATI peaks. Here, we restrict ourselves to circularly-polarized fields to avoid Freeman resonances [374].

Above-threshold ionization is usually discussed in the electric dipole approximation. In this case, the photoelectron momentum distributions from ionization of atoms are symmetric under reflection

about the laser polarization plane, i.e., under the transformation $p_z \rightarrow -p_z$. The ATI rings are centered at momentum $\mathbf{p} = 0$ (see Eq. (7.1)). However, nondipole effects cause the breaking of the forward-backward symmetry (see also Section 2.1.2 for an introduction). In recent experiments, the transfer of photon momentum to the photoelectrons and, hence, nondipole-induced shifts of the photoelectron momentum distributions were observed [51, 146, 152, 157, 435, 436]. The investigations of nondipole effects in strong-field ionization mostly considered the shift of the envelope of the probability distribution (usually represented by the average momentum in the light-propagation direction) or rescattering phenomena. These aspects will be discussed in detail in Chapters 8, 9 and 10. However, even though ATI peaks were one of the earliest manifestations of multiphoton effects in light-matter interaction, so far the influence of nondipole effects on the ATI peak geometry received little attention. The question arises whether the positions of the ATI rings in momentum space and, thus, the corresponding photoelectron energy depends on the electron's emission direction. This question was only addressed in various implementations of the strong-field approximation [147, 437, 438]. Here, we present the first *ab-initio* TDSE simulations for circularly-polarized laser pulses that resolve the nondipole effects on individual ATI rings. We find that the ATI rings are not lines of constant kinetic energy anymore. Interestingly, the centers of the ATI rings are displaced into the direction that is opposite to the on-average transferred photon momentum. We attribute the shift of the ATI rings to the influence of nondipole effects on the ac Stark effect for continuum electrons.

Most of the results discussed in this chapter are published in Ref. [439]. Simultaneously, a theoretical work based on the strong-field approximation discussed the positions of the ATI rings [440] and a measurement on molecular hydrogen ionized by linearly-polarized laser pulses experimentally confirmed the shift of the rings [441].

7.2 Ponderomotive shift of ATI rings

The nondipole modification of the ac Stark effect can be classically motivated by considering the ponderomotive energy of an electron in an electromagnetic field (see Section 7.2.1). Its influence on the photoelectron momentum distributions is afterwards studied. The appearance of ATI rings can be explained by means of two complementary pictures. In Section 7.2.2, we introduce a nondipole version of the *multiphoton picture*. Here, ATI rings appear due to the absorption of multiple photons with quantized energy ω and the energy conservation dictates the possible final kinetic energies of the liberated electrons. Alternatively, ATI rings can be explained in a *time-domain picture* as interference between electron bursts liberated in the various cycles of a sufficiently-long laser pulse. The latter picture is closely related to the nondipole SFA-based calculations in Refs. [147, 437, 438] and will be shortly discussed in Section 7.2.3.

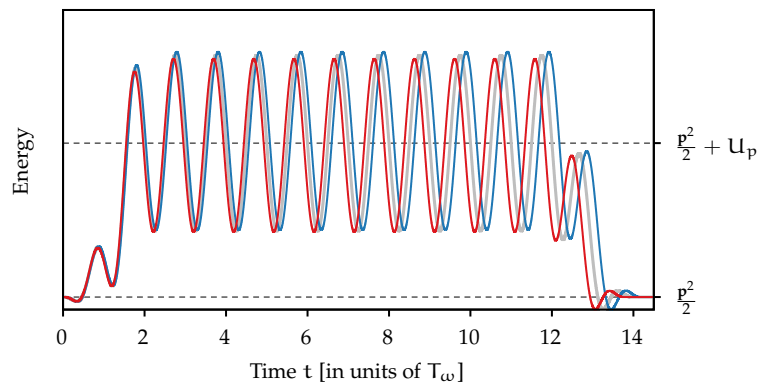


Figure 7.1: Classical kinetic energy of an electron in a circularly-polarized trapezoidal laser pulse ($E_0 = 0.1$ a.u., $\omega = 0.05695$ a.u.). The gray line shows the result from the electric dipole approximation for an initial momentum $\mathbf{p} = (0.5, 0.0, \pm 2.0)$ a.u. For both momenta, the full nondipole dynamics under the influence of the Lorentz force (magnetic field and spatially-inhomogeneous electric field) is also considered: $p_z = 2$ a.u. (blue line) and $p_z = -2$ a.u. (red line).

7.2.1 The (classical) ponderomotive energy

When a (potential-free) electron with an initial momentum \mathbf{p} is accelerated by an electromagnetic field, its classical kinetic energy is modified (see Fig. 7.1). In general, the average kinetic energy $\langle K \rangle$ of the quivering electron is increased compared to the field-free case, i.e., the electron experiences a ponderomotive shift of its energy. The electron loses this additional energy, when the laser pulse is switched off. Afterwards, the electron's momentum is again equal to \mathbf{p} , i.e., a potential-free electron is not accelerated by a laser pulse. When considering a T_ω -periodic field, i.e., $\mathbf{A}(t) = \mathbf{A}(t + T_\omega)$, the kinetic energy $K(t)$ is also a T_ω -periodic function in the dipole approximation. Hence, the ponderomotive energy is obtained by averaging over a single optical cycle T_ω (see also Eq. (2.6)):

$$U_p = \langle K \rangle - \frac{\mathbf{p}^2}{2} = \frac{1}{T_\omega} \int_0^{T_\omega} dt \frac{1}{2} \mathbf{A}^2(t). \quad (7.2)$$

The inclusion of nondipole corrections in the Lorentz force leads to a modified oscillatory behavior of the kinetic energy (see Fig. 7.1). Both the period and the magnitude of the oscillation depend on the initial momentum component p_z of the electron in the light-propagation direction. The changed periodicity can be explained in analogy to the Doppler effect.¹ In the laboratory frame, the Lorentz force depends on the argument $\omega\eta = \omega(t - z/c)$ (see Eq. (2.13)). Therefore, electrons that move with a velocity $p_z \neq 0$ effectively feel an oscillating force with a slightly-changed frequency $\omega_{\text{eff}}(p_z) = \omega(1 - p_z/c)$. Electrons propagating parallel (antiparallel) to the light-propagation direction experience a slightly lower (higher) frequency compared to the frequency ω of the incident laser field. As a result, even for a T_ω -periodic laser field, the kinetic energy of the electrons is not T_ω -periodic, but instead we expect (to first order in $1/c$) a period of $T_{\text{eff}}(p_z) = T_\omega(1 + p_z/c)$.

The changed magnitude of the field-dressed energy results in a nondipole modification of the ponderomotive shift. This nondipole modification of the ponderomotive potential was already noted in several works based on the strong-field approximation [147, 437, 438]. To classically determine the leading-order correction, we treat the terms beyond the dipole approximation as a perturbation and evaluate their contribution to the electron's velocity by integration of the nondipole part of the Lorentz force along a trajectory in the dipole approximation (for a detailed calculation with slightly different initial conditions see also Section 8.3.1). For an electron starting at a position \mathbf{r}_0 with an initial momentum \mathbf{p} (at time t_0 before the laser pulse arrives), the time-dependent velocity is given by (to first order in $1/c$)

$$\dot{\mathbf{r}}_\perp(t) = \mathbf{p}_\perp + \mathbf{A}(t) + \frac{z_0 + p_z(t - t_0)}{c} \mathbf{E}(t) + \mathcal{O}\left(\frac{1}{c^2}\right) \quad (7.3)$$

for the components in the polarization plane and

$$\dot{z}(t) = p_z + \frac{1}{c} \left[\mathbf{p} \cdot \mathbf{A}(t) + \frac{1}{2} \mathbf{A}^2(t) \right] + \mathcal{O}\left(\frac{1}{c^2}\right) \quad (7.4)$$

for the component in the propagation direction of light. Hence, the kinetic energy reads

$$K(t) = \frac{1}{2} \mathbf{p}^2 + \left(1 + \frac{p_z}{c}\right) \left[\mathbf{p} \cdot \mathbf{A}(t) + \frac{1}{2} \mathbf{A}^2(t) \right] + \frac{z_0 + p_z(t - t_0)}{c} (\mathbf{p} + \mathbf{A}(t)) \cdot \mathbf{E}(t) + \mathcal{O}\left(\frac{1}{c^2}\right). \quad (7.5)$$

For a T_ω -periodic laser field, we find that $K(t + T_{\text{eff}}(p_z)) = K(t) + \mathcal{O}\left(\frac{1}{c^2}\right)$, i.e., the kinetic energy has indeed a period of T_{eff} (to first order in $1/c$). Hence, it is only meaningful to calculate the average kinetic energy in the presence of the field by taking the mean value over an interval T_{eff} instead of T_ω . To first order in $1/c$, this results in

$$\langle K \rangle = \frac{1}{T_{\text{eff}}(p_z)} \int_{t_b}^{t_b + T_{\text{eff}}(p_z)} dt K(t) = \frac{\mathbf{p}^2}{2} + \left(1 + \frac{p_z}{c}\right) U_p + \mathcal{O}\left(\frac{1}{c^2}\right), \quad (7.6)$$

for arbitrary times t_b in the cw part of the pulse. Thus, we find an effective ponderomotive energy $(1 + \frac{p_z}{c}) U_p$.² As in the dipole approximation, the electrons are shifted up in energy due to the presence

¹A further discussion of Doppler-like effects in strong-field physics is presented in our work [436] and in Chapter 8.

²In SFA-based descriptions, the same expression was already found in Refs. [147, 437, 438].

of an electromagnetic field. However, the nondipole correction depends on the momentum component p_z in the light-propagation direction. Hence, electrons traveling in the light-propagation direction ($p_z > 0$) experience a larger ponderomotive shift compared to those electrons that travel against the light-propagation direction ($p_z < 0$).

7.2.2 Multiphoton picture using the ac Stark effect

If an atom is placed in an intense low-frequency radiation field, its electronic structure is modified. In this situation, it is advantageous to consider the “dressed” quasienergy states of an atom in a periodic electromagnetic field instead of the eigenstate of the field-free Hamiltonian [442, 443]. Here, we treat the electromagnetic fields classically and use Floquet theory to describe the dressed electron. For a time-periodic Hamiltonian $H(t) = H(t + T_\omega)$, the Floquet theorem guarantees that the TDSE has solutions of the form $|\gamma_F(t)\rangle = e^{-iE_F t}|\theta(t)\rangle$ with quasienergies E_F and time-periodic states $|\theta(t)\rangle = |\theta(t + T_\omega)\rangle$. We assume that it is possible to associate a unique field-free state to a time-periodic Floquet state (see for example the review [444] for a discussion). Then, the ac Stark shift of the state is given by the difference between its quasienergy and its field-free energy eigenvalue.

For infrared or visible radiation, the photon energies are much smaller than the transition energies from the tightly-bound ground state of an atom (such as helium) to its excited states. Hence, the ac Stark shift of the ground state is given by a quasistatic Stark shift and can at first be neglected, i.e., $E_{F,g} \approx -I_p$. We will discuss the influence of the ac Stark shift of the initial state in Section 7.3.3. On the other hand, the ac Stark shifts of the continuum states are much larger in strong fields. To estimate their nondipole corrections, we consider the potential-free TDSE. Here, we treat the system in the natural gauge of Section 2.2.2, but the argumentation can be adapted to the generalized length or velocity gauge. To first order in $1/c$, the solutions of the potential-free TDSE are given by (see Section 2.2.3)

$$|\psi_p^F(t)\rangle = e^{iS_F(\mathbf{p},t)}|\mathbf{p}\rangle \quad (7.7)$$

with plane-wave states $|\mathbf{p}\rangle$ and the generalized action S_F of Eq. (2.33). For T_ω -periodic fields, the time-periodic Floquet states can be expressed using the Volkov states by $|\theta_p(t)\rangle = |\psi_p^F(t)\rangle e^{iE_{F,c}(\mathbf{p})t}$. Hence, the quasienergy of a continuum state with label \mathbf{p} reads

$$E_{F,c}(\mathbf{p}) = \frac{\mathbf{p}^2}{2} + \left(1 + \frac{p_z}{c}\right) U_p. \quad (7.8)$$

For sufficiently short pulses, the electrons stay in the laser focus throughout the whole pulse.³ Thus, electrons in a Floquet state with label \mathbf{p} will be detected with a final momentum \mathbf{p} , when the laser field is switched off adiabatically. Hence, the quasienergy of Eq. (7.8) can be interpreted as the ac-Stark-shifted energy of a continuum state with momentum \mathbf{p} . As in the dipole approximation, the ac Stark shift $(1 + \frac{p_z}{c})U_p$ of the continuum states agrees with the classical ponderomotive energy of a potential-free electron in the presence of an electromagnetic field (see Section 7.2.1).

In the argumentation above, the bound states and the potential-free continuum were treated separately. In reality, however, the light field induces transitions between the bound and the continuum states.⁴ The energy conservation dictates: An electron that starts in a field-dressed state with quasienergy $E_{F,g}$ and that absorbs n photons can only reach continuum states with quasienergies $E_{F,c} = E_{F,g} + n\omega$. Inserting the approximations for the quasienergies, we find the condition

$$\frac{\mathbf{p}^2}{2} + \left(1 + \frac{p_z}{c}\right) U_p = n\omega - I_p. \quad (7.9)$$

Here, the energy conservation (7.9) selects all final electron momenta \mathbf{p} that may be reached by absorbing n photons. These momenta still form spheres (analogous to the dipole limit). However, the centers of

³On the other hand, the pulses must be sufficiently long such that they resemble a periodic field in the vicinity of the pulse maximum. Both requirements can be fulfilled by visible or infrared pulses in the subpicosecond range.

⁴In a Floquet calculation including bound as well as continuum states, this leads to complex quasienergies and decaying states.

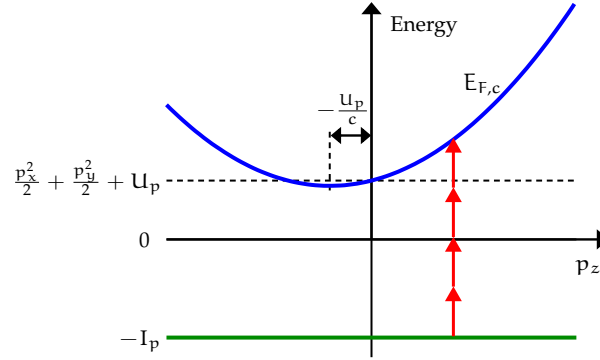


Figure 7.2: Schematic illustration of the ac-Stark-shifted quasienergies (with exaggerated value of $1/c$). The blue line shows the quasienergies (7.8) of the potential-free continuum states as the function of the p_z -momentum component in the light-propagation direction (for fixed $p_x^2 + p_y^2$). If a continuum state with a given momentum $p_z > 0$ can be reached by the absorption of n photons, then the continuum state with $-p_z$ cannot be reached by the absorption of the same number of photons. Figure is adapted from Brennecke *et al.* [439].

the spheres are uniformly shifted towards negative p_z

$$p_z^{\text{ATI}} = -\frac{U_p}{c} < 0. \quad (7.10)$$

Interestingly, the possible momenta for a given number n do not correspond to the same final kinetic energy $\mathbf{p}^2/2$. As an example, consider the situation that a continuum state with momentum component p_z can be populated by the absorption of n photons (see Eq. (7.9)). Then, the continuum state with momentum component $-p_z$ (but the same $p_x^2 + p_y^2$) is not accessible by the absorption of the same number of photons due to their different ac Stark shifts. Figure 7.2(a) schematically illustrates the situation.

7.2.3 Time-domain picture

Alternatively, the appearance of ATI rings can be modeled by considering the interference of electron wave packets liberated in each optical cycle of the laser field. In the strong-field approximation beyond the dipole approximation (introduced in Section 2.3), this was done in Refs. [147, 437, 438]. There, the probability density is given by

$$w(\mathbf{p}) = |M_{\text{KFR}}(\mathbf{p})|^2 = \left| \int_{t_A}^{t_f} dt' D(\mathbf{p}, t') e^{iS_{\text{SFA}}(\mathbf{p}, t')} \right|^2 \quad (7.11)$$

with the action (2.41) and the matrix elements (2.42). For laser pulses of n_p cycles duration, the integral can be split into

$$w(\mathbf{p}) = \left| \sum_{n=0}^{n_p-1} \int_{t_A + T_\omega n}^{t_A + T_\omega (n+1)} dt' D(\mathbf{p}, t') e^{iS_{\text{SFA}}(\mathbf{p}, t')} \right|^2. \quad (7.12)$$

This sum can be interpreted as the superposition of emitted electron bursts that are freed in each cycle of the field. When the intensity of the pulse is constant, the transition matrix element is T_ω periodic and the action fulfills (to first order in $1/c$)

$$S_{\text{SFA}}(\mathbf{p}, t' + T_\omega) = S_{\text{SFA}}(\mathbf{p}, t') + \left[\frac{\mathbf{p}^2}{2} + I_p + \left(1 + \frac{p_z}{c}\right) U_p \right] T_\omega := S_{\text{SFA}}(\mathbf{p}, t') + \Delta S. \quad (7.13)$$

Thus, the phase difference ΔS between the emission in consecutive laser cycles determines the interference pattern in the PMD. The positions of the maxima are defined by the condition for constructive interference, $\Delta S = 2\pi j$ with $j \in \mathbb{Z}$. This condition was already found in Refs. [147, 437, 438] and it is equivalent to the energy conservation of Eq. (7.9). However, its implications on the photoelectron momentum distribution was neither discussed in detail nor was it verified by numerical *ab-initio* simulations.

7.3 TDSE results

7.3.1 Computational details

To simulate the quantum dynamics of the light-driven system, we numerically solve the 3D TDSE in the single-active-electron approximation for a plane-wave light pulse. To mimic a helium atom, we choose the ionic binding potential proposed by Tong and Lin [324], but remove the singularity by using a pseudopotential for the 1s state with a cutoff radius $r_{cl} = 1.5$ a.u. The procedure is described in Appendix A.2.3 and the used parameters of the potential are given in Table A.2. The circularly-polarized light pulse is defined by

$$\mathbf{A}(\eta) = \frac{E_0}{\omega} f(\eta) \begin{pmatrix} \cos(\omega\eta) \\ -\sin(\omega\eta) \end{pmatrix} \quad (7.14)$$

with the light-cone coordinate $\eta = t - z/c$ and the frequency ω . The parameter E_0 characterizes the peak electric-field strength and is chosen to reproduce a presumed intensity. In order to minimize effects of a changing pulse envelope $f(\eta)$, we either use (i) trapezoidal pulses of two ascending cycles, then 5.5 cycles of constant intensity and afterwards two descending cycles; or (ii) pulses with a \cos^2 envelope of 14 cycles total duration.

The natural gauge introduced in Section 2.2 is applied such that the theory covers the dynamics within the magnetic dipole and the electric quadrupole approximation. For the numerical solution, the Fourier split-operator technique on two Cartesian grids is used (see Appendix A.2.2). Here, the full electronic state is divided into an inner and an outer part. The inner wave function is represented on Cartesian grids of size $409.6 \times 409.6 \times 409.6$ a.u. with spacings $\Delta x = \Delta y = \Delta z = 0.4$ a.u. and a time step of 0.03 a.u. is used. The complex absorbing potential starts at a distance $r_A = 160$ a.u. from the grid center. Before the absorber starts, the ionic potential is truncated over a distance of 25 a.u. using a \sin^2 function. This ensures that, even for finite box sizes, the correct field-free ionization potential is obtained. The electron momentum distribution is calculated from the outer wave function. We use slices through the full 3D momentum distributions in the p_x - p_y -, p_x - p_z - and p_y - p_z -planes with a resolution of $\Delta p_x = \Delta p_y = \Delta p_z = 0.0019$ a.u.

7.3.2 Nondipole shift of the ATI rings

Figure 7.3(a) shows a slice in the polarization plane through the photoelectron momentum distribution from ionization of helium by a trapezoidal laser pulse with 800 nm wavelength and an intensity of 4×10^{14} W/cm². As expected for circularly-polarized multi-cycle laser pulses, the PMD has a donut-like

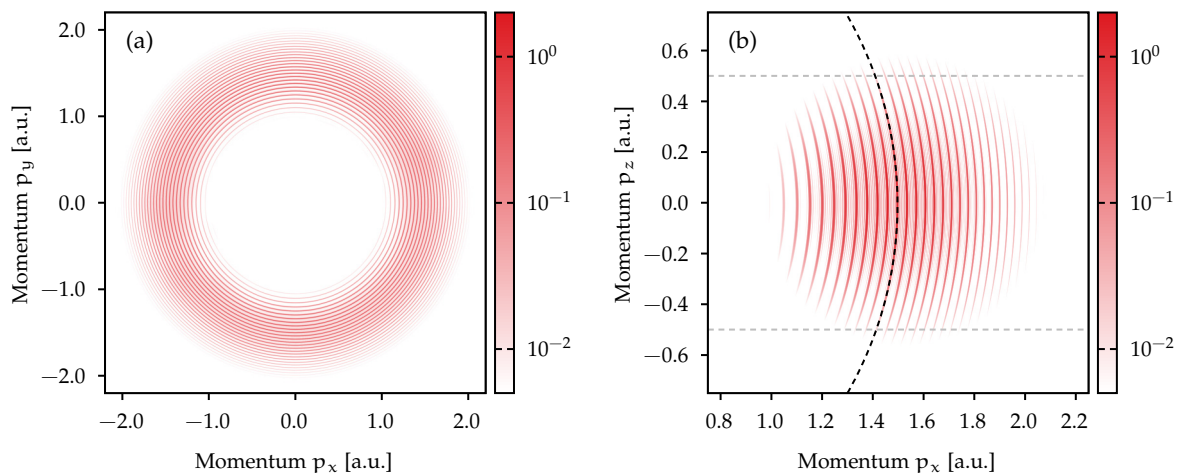


Figure 7.3: 2D slices through the photoelectron momentum distributions at $p_z = 0$ (panel a) and at $p_y = 0$ (panel b) for ionization of helium by a trapezoidal laser pulse with 4×10^{14} W/cm² intensity and 800 nm wavelength. The black dashed line in panel (b) indicates the position $p_x^n(p_z)$ of one selected ATI ring. Figure is adapted from Brennecke *et al.* [439].

shape, i.e., it is approximately rotationally symmetric in the polarization plane. Formally, the whole distribution can be separated in an envelope of the distribution and an underlying ATI-peak pattern. In order to study the nondipole modification of the ATI ring structure, we restrict ourselves to a 2D slice in the p_x - p_z -plane (see Fig. 7.3(b)). In the dipole approximation, the PMDs would be symmetric under interchange of the forward and backward directions. However, the comparison of 1D slices through the distribution at $p_z = \pm 0.5$ a.u. (see gray dashed lines in Fig. 7.3(b)) clearly reveals the symmetry breaking in propagation direction due to nondipole effects (see Fig. 7.4(a)). In agreement with earlier works (see for example Ref. [146]), the envelope of the momentum distribution is shifted in forward direction, i.e., the probability in forward direction is higher than in backward direction. This radiation pressure effect will be further discussed in Chapter 8. However, in addition, we find a difference in the positions of the ATI peaks in forward and backward direction. The observation is already a sign of a nondipole modification of the ac Stark effect (see the prediction of Section 7.2.2). The TDSE simulations confirm that the ATI peaks are still approximately given by spheres in momentum space that are shifted in the direction opposite to the propagation direction of the radiation. Hence, the envelope of the momentum distribution and the ATI-peak structure are displaced in opposite directions.

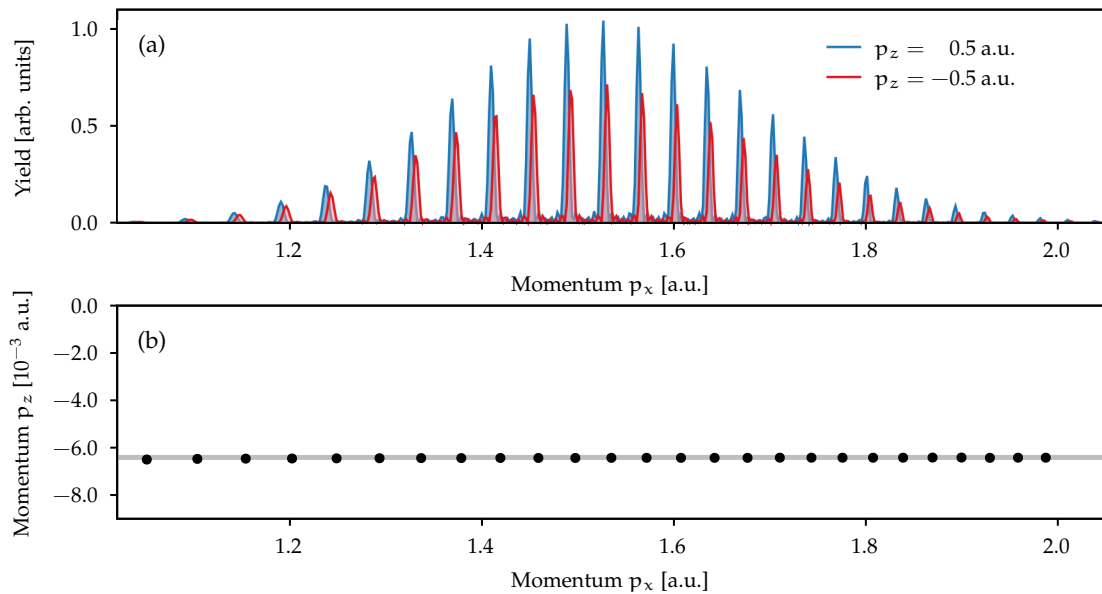


Figure 7.4: (a) 1D slices at $p_z = \pm 0.5$ a.u. ($p_y = 0$) through the distribution of Fig. 7.3. (b) Shift p_z^{ATI} of the ATI rings against the propagation direction of the light shown as a function of p_x^n (p_z^{ATI}) for various ATI rings. For comparison, the simple estimate of Eq. (7.10) is depicted as gray thick line. Figure is adapted from Brennecke *et al.* [439].

To quantify the offsets of the ATI rings, we numerically determine their positions. For every ATI ring labeled with n , the position of the peak maximum in p_x -direction is calculated at each fixed p_z .⁵ The resulting function $p_x^n(p_z)$ represents the geometry of the ATI ring in p_x - p_z -plane (see for example the ATI ring indicated as black dashed line in Fig. 7.3(b)). The center of the ATI ring is identified with position p_z^{ATI} of the maximum of $p_x^n(p_z)$.⁶ The selected ring is shifted slightly backwards by nondipole effects and is centered at $p_z^{\text{ATI}} \approx -0.0064$ a.u. The analysis is repeated for a large range of ATI rings and the corresponding results are shown in Fig. 7.4(b). For all analyzed rings, the numerically-determined positions perfectly agree with the simple model of Eq. (7.10): the rings are centered at $p_z^{\text{ATI}} = -U_p/c$ (independently of the number of absorbed photons).

⁵For each ATI peak, a small region around the maximum's position on the numerical momentum grid is selected and the "power method" [161] is applied to determine the peak position.

⁶This position is numerically determined by means of a quadratic fit to the p_z -range between -0.3 and 0.3 a.u.

Intensity and wavelength scaling

In the dipole domain, the ponderomotive shifts of the ATI peaks were first identified by scaling the intensity of the radiation [172, 374, 434]. The ponderomotive potential U_p depends linearly on the laser intensity and quadratically on its wavelength. Hence, Equation (7.10) predicts that both the radius of the ATI rings and the positions of their centers depend on these laser parameters. The nondipole shift of the center along the p_z -direction is shown in Fig. 7.5 for various intensities ranging from 3×10^{14} to 8×10^{14} W/cm². Both for 800 nm and 400 nm wavelength (shown in panel (a) and panel (b)), the results from TDSE simulations are in perfect agreement with the simple estimate of Eq. (7.10), i.e., we indeed observe a linear scaling of the center's position with the ponderomotive potential U_p .

In a real experiment, focal-volume averaging complicates the observation of well-separated ATI rings in circularly-polarized laser pulses with 800 nm wavelength. In addition, a trapezoidal pulse envelope used so far for the TDSE simulations is quite unrealistic. To study the influence of stronger contributions from the leading and falling edges of the pulse with smaller instantaneous intensities, we repeat the calculations for a more-realistic \cos^2 pulse of 14 optical cycles duration with 400 nm central wavelength. The extracted positions of the ATI peaks are also in perfect agreement with the $-U_p/c$ estimate, indicating that the detailed form of the laser pulse is only of minor importance (see the crosses in Fig. 7.5(b)).

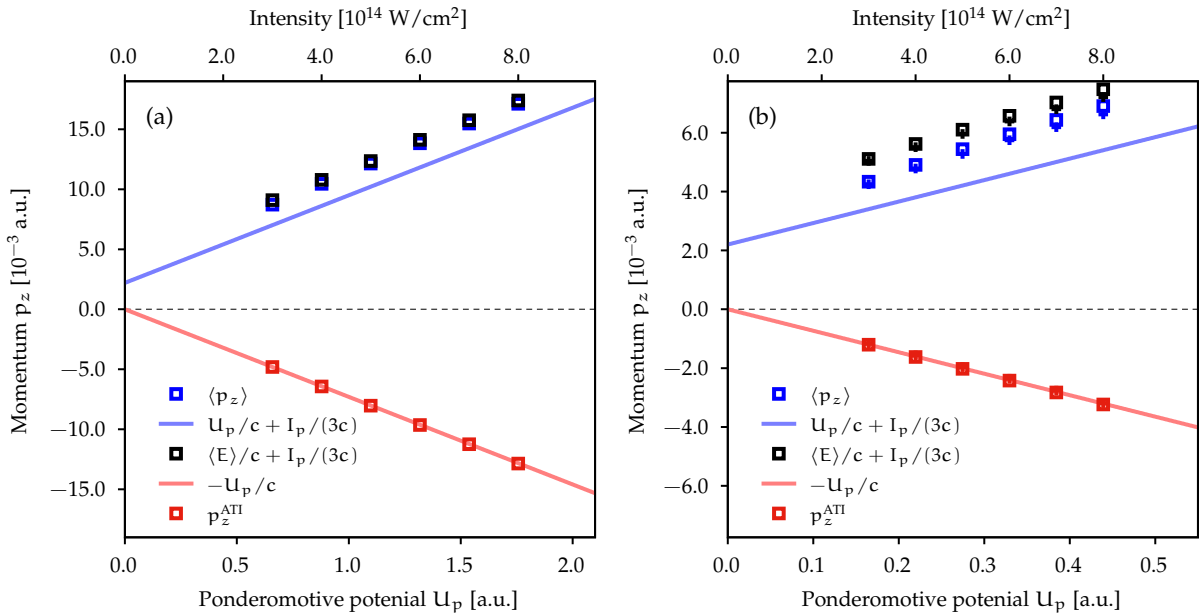


Figure 7.5: Shift of the ATI ring positions p_z^{ATI} and expectation value $\langle p_z \rangle$ of the momentum in the light-propagation direction as a function of the ponderomotive potential. The results are extracted from PMDs obtained by numerical solution of the TDSE for various laser parameters: (a) 800 nm wavelength and (b) 400 nm wavelength. The results for trapezoidal pulses (squares) or for pulses with a \cos^2 envelope (crosses) at 400 nm wavelength are very close to each other. For comparison, the red line indicates the simple estimate for the ATI peak position of Eq. (7.10) and the blue line shows a simple estimate for the average momentum $\langle p_z \rangle = \frac{U_p}{c} + \frac{I_p}{3c}$ in circularly-polarized fields. For the black dots, the expectation value of the energy is numerically calculated from the TDSE distributions. Figure is adapted from Brennecke *et al.* [439].

For comparison, Figure 7.5 also shows the average values $\langle p_z \rangle$ of the momentum component in the light-propagation direction for all studied laser parameters. The positive expectation value $\langle p_z \rangle$ indicates that the envelope of the momentum distribution is slightly displaced in the propagation direction of light. This is expected for recollision-free strong-field ionization [51, 150, 151, 190]. We find that the shifts of the ATI ring positions p_z^{ATI} are in the same order of magnitude as the expectation values $\langle p_z \rangle$ but point in the opposite direction. Previously, an estimate for the average momentum transfer in circularly-polarized light was given by $\langle p_z \rangle \approx \langle E \rangle/c + I_p/(3c)$ (see for example Refs. [150, 190]). For 800 nm wavelength, the TDSE results indeed follow this simple scaling (in agreement with the earlier work in Ref. [445]). However, a systematic deviation between TDSE result and estimate for $\langle p_z \rangle$ is present for the more nonadiabatic ionization conditions at 400 nm wavelength. The momentum transfer will be further discussed in Chapter 8.

7.3.3 AC Stark shift of the ground state

The tightly-bound ground state of helium also experiences an ac Stark shift [434]. Even though the shift is quite small, it influences the final energies of the photoelectrons. To test the accuracy of the simulations, we retrieve the ac-Stark-shifted ground-state energy $E_{F,g}$ from the absolute positions of the ATI peaks. These results are compared to numerical calculations of the quasi-energies using Floquet theory.

To calculate the ac Stark shift in Floquet theory, we again solve numerically the TDSE for a nearly monochromatic laser field [446].⁷ The modulus of the Fourier transform of the autocorrelation function $\langle \psi_0 | \psi(t) \rangle$ of the time-evolved state $|\psi(t)\rangle$ with the ground state $|\psi_0\rangle$ has peaks at the quasienergies of the field-dressed system [447]. The extracted ac-Stark-shifted energy $E_{F,g}$ of the ground state is shown in Fig. 7.6(b) as a function of the intensity for a wavelength of 800 nm. Since the dipole moment of the ground state vanishes, the ac Stark shift scales linearly with the intensity in the considered parameter range. In the limit of vanishing electric-field strength, the quasienergy $E_{F,g}$ converges to the field-free energy of the ground state represented on the numerical grid ($E_g \approx -0.9025$ a.u.). The small discrepancy to the exact ground-state energy of the Tong-Lin potential of about -0.9038 a.u. is caused by our finite resolution of the used Cartesian grids.

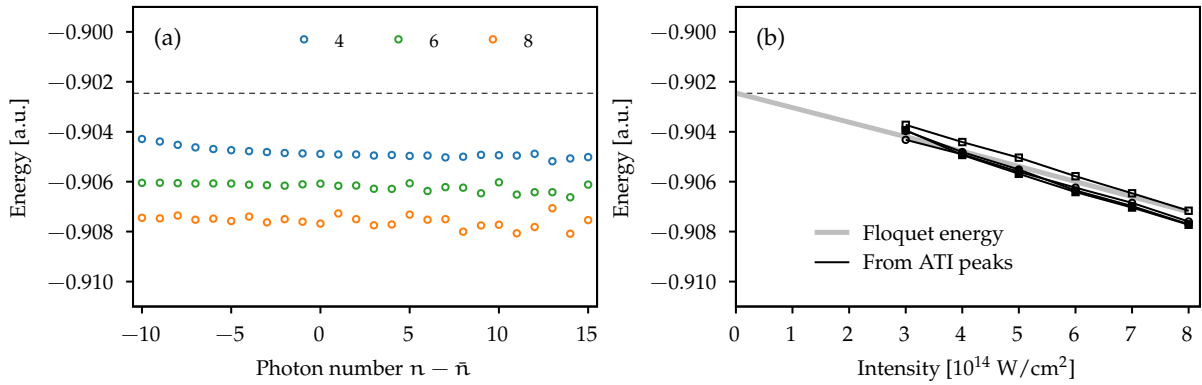


Figure 7.6: AC-Stark-shifted energy of the ground state at 800 nm wavelength. (a) Energies retrieved from the ATI peaks along p_x -direction for different photon numbers n . The colors indicate the results for three intensities given in the legend in units of 10^{14} W/cm². (b) Comparison of the quasienergies calculated using Floquet theory and the energies retrieved from the ATI peaks. The black curves show the results obtained from peaks along $\pm p_x$ -directions and $\pm p_y$ -directions, respectively.

On the other hand, the ac-Stark-shifted energy of the ground state also influences the exact locations of the ATI rings or more precisely their radii (see also the argumentation of Section 7.2.2). Here, we restrict ourselves to the polarization plane (p_x - p_y -plane) and determine the positions \mathbf{p}_n of the ATI peaks (associated to the absorption of n photons). The field-dressed energy is then approximated as

$$E_{F,g} = \frac{\mathbf{p}_n^2}{2} + U_p - n\omega. \quad (7.15)$$

The retrieved ac-Stark-shifted energy is shown separately for each ATI ring in Fig. 7.6(a). For the selected intensities, we find that the variation of the reconstructed energy with respect to n is much smaller than the ac Stark shift. Note that the spacing of the ATI rings in momentum space of the ATI rings decreases with increasing energy. Since the momentum distribution for the highest-considered intensity of 8×10^{14} W/cm² is located at the largest momenta, this case involves the largest uncertainty in the reconstructed field-dressed energy.

For each intensity, the retrieved energies are averaged over several ATI rings around the maximum of the lateral distribution. These averaged energies $E_{F,g}$ are shown in Fig. 7.6(b). To check for effects of the carrier-envelope phase, the procedure is applied along all four directions of the coordinate axes. We believe that the small deviations of the results from the p_y -direction (compared to the other directions) are caused by larger contributions from the leading and falling edge of the laser pulse. Nevertheless, the results retrieved from the PMDs are generally in good agreement with the results from Floquet calculations. The difference between both approaches is much smaller than the ac Stark shift itself.

⁷We use a trapezoidal pulse with two ascending cycles and 20 cycles of constant intensity.

7.4 Conclusion

In the dipole approximation, the multiphoton generalization of Einstein's photoeffect law predicts above-threshold ionization rings that are centered at zero momentum, i.e., the photoelectrons on a ring all have the same final kinetic energy. In this chapter, we theoretically analyzed the beyond-dipole modifications of the structure of the ATI rings based on the numerical solution of the TDSE for helium. For nonresonant ionization in circularly-polarized fields, we observed that the centers of the ATI rings are uniformly shifted against the light-propagation direction, in agreement with the prediction of the strong-field approximation [147, 437, 438]. Therefore, the ring centers are displaced to the opposite direction of the radiation pressure.

We explained the shift of the ATI peaks by a nondipole modification of the ac Stark effect for continuum states. Motivated by the classical ponderomotive energy, we showed that the upward shift in energy of the continuum states depends on the electron momentum in the light-propagation direction. Electrons that travel with the light wave experience larger ponderomotive shifts compared to those electrons that travel against the light-propagation direction. Assuming energy conservation for transitions from the initial bound state to the field-dressed continuum states, the shift of the ATI ring position is simply given by $p_z^{\text{ATI}} = -U_p/c$ with the common ponderomotive potential U_p . This estimate is in perfect agreement with the results from the numerical TDSE solutions for a broad range of laser parameters.

We expect that similar nondipole shifts of the ATI rings are also present for other waveforms as long as nonresonant ionization dominates. However, the appearance of Stark-shifted bound-state resonances (Freeman resonances) [172] may alter the ATI peak structure. This might be a reason why in the recent measurement on molecular hydrogen ionized by linearly-polarized laser pulses, deviations from the theoretically-predicted peak positions were observed [441].

Chapter 8

Microscopic Study of Nondipole Effects in Recollision-Free Ionization

8.1 Introduction

Motivation: Linear-momentum transfer in strong-field ionization

In strong light fields, atoms or molecules may absorb multiple photons (typically tens or hundreds). The well-known conservation laws imply that energy, angular momentum and linear momentum of the photons are transferred to the total system consisting of electron and ion. Even though in strong-field physics the external electromagnetic field is usually treated as a classical plane-wave field (see also Chapter 2), these classical fields also carry energy and linear momentum.¹ The associated linear momentum is related to the cycle-averaged Poynting vector $\mathbf{S} \propto \mathbf{E} \times \mathbf{B}$ of the field and manifests itself for example as radiation pressure on matter. For both classical light fields and photons, every portion of energy E_γ traveling with speed of light c is accompanied by a linear momentum of $p_\gamma = E_\gamma/c$ in the light-propagation direction. However, an amount of energy E transferred from the photons to the electrons leads to photoelectron momenta on the scale $p_{el} \sim \sqrt{2E}$. As a result, the imparted energy usually dominates the observations in the photoelectron momentum distribution compared to the “small” linear momentum.² Thus, the transfer of energy to the system is very well understood, but there are many open questions regarding linear-momentum transfer. As in the electric dipole approximation the magnetic field is neglected and furthermore the incident electric field is assumed to be spatially homogeneous over the field-atom interaction region, the transfer of linear momentum is not covered by this approximation (see also Section 2.1.2). In this chapter, we include leading-order nondipole corrections to describe various effects in recollision-free strong-field ionization. Especially, the amount of linear momentum delivered to the photoelectrons, resulting in a forward shift of the photoelectron momentum distribution, is considered. Recollision-based phenomena will be discussed in Chapters 9 and 10.

Important previous investigations

In a pioneering work on strong-field ionization at very high intensities on the order to 10^{18} W/cm², Moore *et al.* [450, 451] demonstrated that the angle between the electron momentum and the propagation direction of the light is on average smaller than 90° . There, an average of 90° would be expected within the dipole approximation. This observation of nondipole effects was in agreement with the earlier classical predictions (see for example Ref. [177]) and the pioneering calculations of photoelectron momentum distributions beyond the dipole approximation using SFA-based approaches [147, 452–454]. After-

¹Hence, strictly speaking, quantization effects of the radiation field and “photons” (interpreted as elementary excitations of normal modes of the field) are not considered.

²Other properties of light-matter interaction such as angular momentum or helicity were also investigated in strong-field ionization (see for example Refs. [354, 355, 448, 449]).

wards, the total transition rate as well as photoelectron energy and angular distributions were calculated for circularly-polarized as well as linearly-polarized strong fields based on SFA-like treatments of the Dirac equation [147, 455, 456], of the Klein-Gordon equation [453, 456, 457] or of the TDSE [192, 458]. Interestingly, even under relativistic ionization conditions, the Klein-Gordon equation can be exactly solved for an electron in a short-range separable potential interacting with a circularly-polarized laser field [459]. The asymptotics of the SFA theory and simple expressions for the direct ionization rates were developed based on WKB theory [460–462]. Quasi-classical approaches (more precisely an adiabatic Landau-Dykhne approximation) lead to simple analytical expressions for the angular and energy distributions of photoelectrons beyond the electric dipole approximation [463–469].

For moderate intensities in the region of 10^{14} W/cm², the influence of the radiation pressure on single ionization in circularly-polarized fields was first experimentally studied by Smeenck *et al.* in 2011 [146]. At 800 nm and 1400 nm wavelength, they observed an overall shift of the photoelectron momentum distributions in the propagation direction of the laser beam such that the average momentum component in the light-propagation direction is positive. Within the error bars, the shift is consistent with the forward momentum of $\langle p_z \rangle = A_0^2/(2c)$ as classically predicted for the acceleration of an electron with zero initial velocity by the electromagnetic field (see also Section 2.1.2). This important result was already earlier derived in Refs. [147, 149] and later on is was theoretically supported by SFA-based calculations [148] and by classical simulations [470].

Importantly, refined theoretical simulations showed that a part of the linear momentum transferred during the laser-induced tunnel ionization is also given to the photoelectron [150, 151, 471]. In a WKB approximation, the additional momentum shift can be modeled as the action of the laser's magnetic field on the electron during the under-the-barrier motion [151, 471].³ Based on numerical SFA simulations, it was suggested to parameterize the on-average transferred momentum as [150, 190]

$$\langle p_z \rangle = \frac{\langle K \rangle}{c} + \beta \frac{I_p}{c}, \quad (8.1)$$

where $K = \mathbf{p}^2/2$ is the final kinetic energy of the electron. In a sense, the fraction of the momentum transferred to the electron during tunnel ionization is represented by β . For the ground state of a hydrogen atom, values between 0.3 and 1/3 were found [150, 151, 190, 471]. Deviations from $\beta \approx 1/3$ are expected for other initial states [190] and for exotic atoms [185]. The first TDSE simulations beyond the electric dipole approximation for hydrogen ionized by circularly-polarized pulses at 800 nm wavelength lead to values $\beta \approx 0.1$ for $I = 0.5 \times 10^{14}$ W/cm² and $\beta \approx 0.26$ for $I = 3.0 \times 10^{14}$ W/cm² [445].⁴

The goals of this chapter

To reveal the physical origin of the forward shift of the momentum distribution, the ionization process can be interpreted as a sequence of (i) laser-induced ionization and (ii) potential-free acceleration of the electron as a classical particle by the electromagnetic field (similar to Section 2.1.1). Classically, the deflection of the electron in the light-propagation direction is caused by the effects of the temporospatial-dependent electric field and magnetic field. For an electron that is released at time t_0 with an initial velocity \mathbf{v}_0 , the final momentum \mathbf{p} after the end of the light pulse is given by (to first order in $1/c$)

$$\mathbf{p}_\perp = \mathbf{v}_{0,\perp} - \mathbf{A}_\perp(t_0) \quad (8.2)$$

for the components in the polarization plane and

$$p_z = v_{0,z} - \frac{1}{c} \left(\mathbf{p} \cdot \mathbf{A}(t_0) + \frac{1}{2} \mathbf{A}^2(t_0) \right) \approx v_{0,z} + \frac{1}{c} \left(\frac{\mathbf{p}^2}{2} - \frac{\mathbf{v}_0^2}{2} \right) \quad (8.3)$$

³Interestingly, the result was already found but not discussed in Refs. [466, 467].

⁴For linearly-polarized fields, two-dimensional simulations of the TDSE [153] and the Dirac equation [151, 471] already existed. However, targets with ionization potential $I_p \approx 9000$ a.u. are considered in Refs. [151, 471] and scattering phenomena dominate the dynamics in Ref. [153].

for the component in the propagation direction of the light.⁵ The last terms of Eq. (8.3) are quite intuitive as the classical momentum gain in the field is equal to the energy gain during the continuum motion divided by c . For vanishing initial velocity $\mathbf{v}_0 = 0$, the well-known heuristic estimate of $p_z = A_0^2/(2c)$ is retrieved. However, for nonzero initial velocity $\mathbf{v}_0 \neq 0$, classical mechanics suggests that only the energy gain rather than the total kinetic energy determines the final momentum component p_z of the electron in the light-propagation direction.

Within in the simple man's model, Equation (8.2) defines the possible release time t_0 and the required initial velocity $\mathbf{v}_{0,\perp}$ for a given momentum component \mathbf{p}_\perp in the polarization plane.⁶ Hence, according to Eq. (8.3), we expect that the momentum gain during the continuum motion depends on both the release time t_0 and the initial velocity $\mathbf{v}_{0,\perp}$. However, most of the previous works only discussed the entire momentum transfer induced by the laser pulse, i.e., the main observable is the total average $\langle p_z \rangle$ of the momentum component in the light-propagation direction.⁷ It is difficult to observe effects of the initial velocity $\mathbf{v}_{0,\perp}$ and of the release time t_0 on the momentum transfer in the total expectation value $\langle p_z \rangle$. In order to extract additional information on the nondipole effects, the average value of the momentum component in the light-propagation direction can be separately studied for each momentum \mathbf{p}_\perp in the polarization plane⁸

$$\langle p_z \rangle(\mathbf{p}_\perp) = \frac{\int dp_z p_z w(\mathbf{p}_\perp, p_z)}{\int dp_z w(\mathbf{p}_\perp, p_z)}. \quad (8.4)$$

Here, w is the photoelectron momentum distribution. The differential quantity (8.4) is referred to as partial average and it is the central observable of this chapter. The main goal of our studies is to develop a more complete picture of the physical mechanisms underlying the nondipole effects in recollision-free strong-field ionization. To this end, we discuss the following aspects.

For circular polarization, the initial velocity in the polarization plane is simply linked to the radial momentum p_\perp in the polarization plane (see Chapter 5). Hence, using numerical simulations of the TDSE and a simplified theoretical description based on the strong-field approximation, we study the most probable momentum $p_z^{\max}(p_\perp)$ in the light-propagation direction or equivalently $\langle p_z \rangle(p_\perp)$ as a function of the radial momentum. This allows us to investigate the dependence of the nondipole shift on the initial electron's velocity. Especially, we evaluate whether the total kinetic electron energy or only its energy gain during the continuum acceleration determines the nondipole shift. In a pioneering experiment based on the COLTRIMS technique, Hartung *et al.* were able to measure the deflection of the momentum distribution as a function of the radial momentum with high accuracy [473]. A part of this chapter is based on our joint work where we directly compared the nondipole shift from theoretical simulations to experimental measurements [51].

Usually, in previous studies, nondipole effects were included to a given order in $1/c$, i.e., both effects of the magnetic field and of the electric-field inhomogeneity were simultaneously considered. Recently, it was suggested in Alexander Hartung's thesis to separately study both influences on the photoelectron momentum distributions [473]. To this end, the most probable radial momentum $p_\perp^{\max}(p_z)$ was analyzed as a function of the momentum p_z in the light-propagation direction (analogous to the previous work [170]). The observed forward-backward asymmetry of this observable is mainly related to the temporospatial dependence of the electric field. My main contribution to the joint publication [436] was to provide an *ab-initio* verification based on TDSE simulations and to work out a simplified theoretical description of the observed phenomenon. To this end, we introduce a simple classical adiabatic model which allows the separate investigation of magnetic and electric nondipole effects. This enables us to show that the observations on the momentum dependence of the non dipole shift $p_z^{\max}(p_\perp)$ and the

⁵Note that this classical solution is known (see for example Ref. [177]).

⁶In principle, one additional condition is need (see for example Eq. (2.47) for adiabatic ionization conditions).

⁷Exceptions are Refs. [151, 471, 472] that study recollision-free ionization in linearly-polarized fields and consider the dependence of the nondipole shift on the momentum along the polarization direction.

⁸This observable was already introduced in my master thesis [160] and calculated for circular as well as bicircular fields. However, in Ref. [160], the physical interpretation was only barely considered. Here, we close this gap by presenting many additional numerical results and by exploring the underlying physics.

nondipole modifications of $p_{\perp}^{\max}(p_z)$ are two sides of the same coin, i.e., both have the same physical origin.

In close-to-circularly-polarized fields, the release time t_0 of the electron is approximately mapped to the angle ϕ_p of the electron in the polarization plane (see Chapter 5). Based on this attoclock concept, Willenberg *et al.* experimentally studied the angular dependence of the nondipole shift for strong-field ionization with elliptical polarization [435] and, hence, “time-resolved” the momentum transfer within an optical cycle of the field. In general, attoclock-like settings provide an excellent ground for studying the interplay between nondipole and Coulomb effects acting on the outgoing electrons. This stimulates us to theoretically analyze and model nondipole effects in the elliptical attoclock as well as in the quasilinear attoclock setting introduced in Section 5.3. Some of these results are published in Ref. [367].

From a theoretical perspective, it is interesting to disentangle the momentum transfer during the tunnel ionization and during the subsequent continuum motion of the electrons. Hongcheng Ni suggested to apply the classical backpropagation method [211, 350, 351] for this purpose (see also Section 5.2.4 for an introduction). This allows us to consider the previously-unexplored interplay between nonadiabatic and nondipole effects. In the joint work, my main contribution was to perform SFA-based simulations and to derive a simplified model that includes leading-order nonadiabatic corrections [474]. Here, this work is further extended with a particular focus on the influence of the long-range electron-ion interaction.

To study recollision-free ionization, we mainly use three laser geometries: circular polarization, elliptical polarization and a quasilinear field. For didactic reasons, the work is not presented in chronological order. Instead, we will first study the effect of the Coulomb attraction on the outgoing electrons in attoclock settings. Afterwards, the electron wave packet is analyzed by means of the classical backpropagation method and the influence of nonadiabaticity is considered. With this important knowledge on the released electron wave packet, we investigate the interplay of magnetic and electric nondipole effects and reveal their imprint on photoelectron momentum distributions.

8.2 The influence of Coulomb and nonadiabatic effects

8.2.1 Computational details

To describe the dynamics of the electron in the light field beyond the electric dipole approximation, we numerically solve the 3D TDSE for a plane-wave laser pulse. Analogous to Chapter 7, we use the Fourier split-operator technique (see Appendix A.2.2) and employ the natural gauge introduced in Section 2.2. If not stated otherwise, a helium atom is considered and described by a pseudopotential for the 1s state.

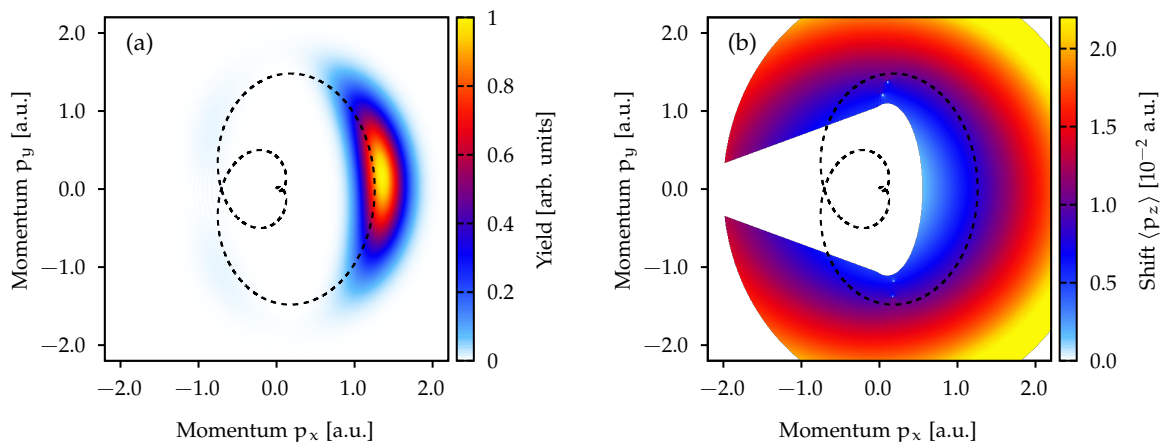


Figure 8.1: Nondipole effects in recollision-free strong-field ionization by elliptically-polarized fields: (a) 2D slice at $p_z = 0$ through the photoelectron momentum distribution obtained by numerical solution of the TDSE for helium ionized by a three-cycle laser pulse ($\zeta = 0.75$) with 800 nm wavelength and 5×10^{14} W/cm² intensity. The black dashed line shows the negative vector potential. The distribution is normalized to maximum signal of one. (b) Nondipole shift of the momentum distribution represented by the momentum-resolved partial average $\langle p_z \rangle(\mathbf{p}_{\perp})$ of Eq. (8.4).

The numerical propagation scheme based on two grids is explained in the Appendix A.2.2. The inner wave function is represented on a Cartesian grid of size $409.6 \times 409.6 \times 409.6$ a.u. with spacings $\Delta x = \Delta y = \Delta z = 0.4$ a.u. and a time step of 0.03 a.u. is used. The absorbing boundary starts at a distance of $r_A = 160$ a.u. from the grid center. The ionic potential is set to a constant value in the absorption region. The photoelectron momentum distribution in 3D is calculated using the outer wave function with a resolution of $\Delta p_x = \Delta p_y = \Delta p_z = 0.0077$ a.u.

8.2.2 Angle-resolved nondipole shifts for elliptical polarization

To time-resolve the momentum transfer in the light-propagation direction, Willenberg *et al.* [435] performed an experiment using an attoclock protocol based on elliptically-polarized laser fields. Within this attoclock setting (see Chapter 5), the angle detection angle ϕ_p of the photoelectron in the polarization plane is related to the release time t_0 of the electron. Hence, the measurement of the nondipole shift in the light-propagation direction as a function of the angle ϕ_p allows us to study the momentum transfer on a sub-optical-cycle time scale. This so far unexplored aspect of the momentum sharing between ejected electron and its parent ion is studied in the following theoretically.

We consider ionization of helium by an elliptically-polarized laser pulse of the form

$$\mathbf{A}(\eta) = -\frac{E_0}{\omega\sqrt{1+\zeta^2}} \begin{pmatrix} \zeta \cos(\omega\eta) \\ \sin(\omega\eta) \end{pmatrix} f(\eta) \quad (8.5)$$

with the light-cone coordinate $\eta = t - z/c$ and the frequency ω . The parameter E_0 is determined by the chosen intensity of the field and the parameter ζ represents the ellipticity (circularly-polarized light is retrieved for $|\zeta| = 1$). Here, we use an ellipticity $\zeta = 0.75$, a central wavelength of 800 nm and an intensity of 5×10^{14} W/cm². In order to avoid ATI rings, short three-cycle pulses with a \cos^4 envelope are applied. The electric field is chosen such that the maximum of the electric-field strength corresponds to $t = 0$. In

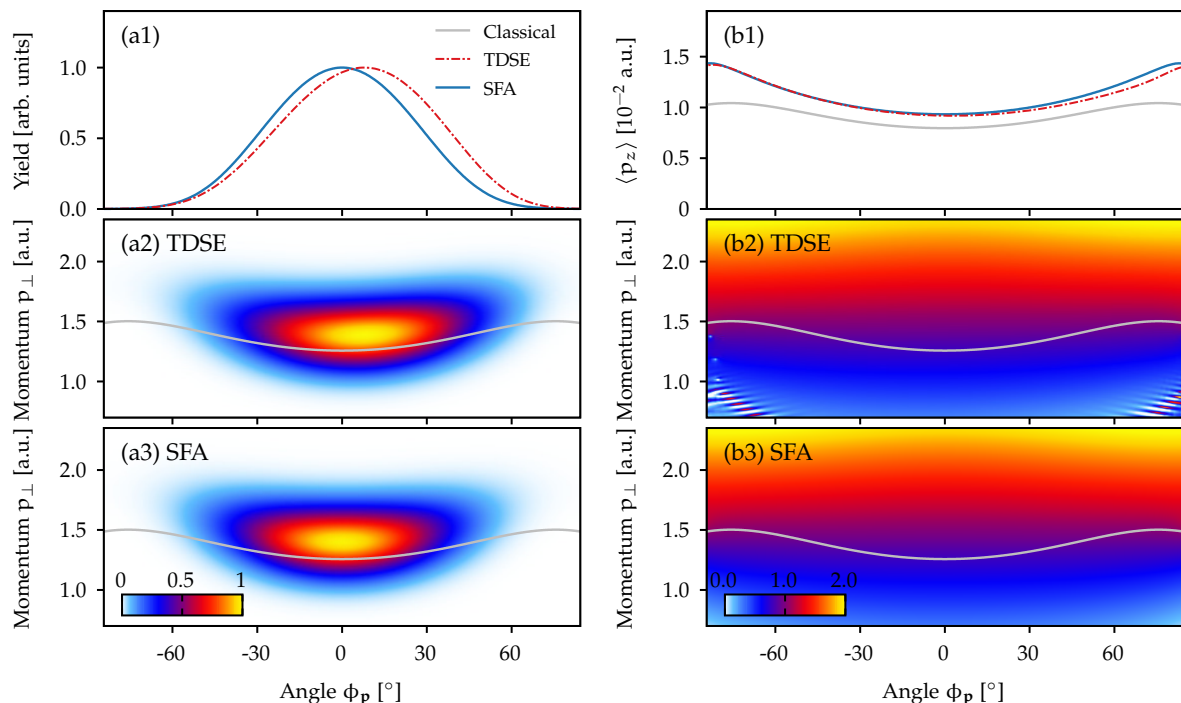


Figure 8.2: Analysis of the PMD for elliptical polarization as in Fig. 8.1 in cylindrical coordinates: (a1) angular distribution (normalized to maximum signal of one). [(a2),(a3)] Projection of the PMD onto the p_\perp - ϕ_p -plane from TDSE simulation and from SFA in saddle-point approximation. Both distributions are normalized to maximum signal of one. [(b2,b3)] Partial average $\langle p_z \rangle(p_\perp, \phi_p)$ in the polarization plane in units of 10^{-2} a.u. The gray lines show the classical estimate of Eqs. (8.2) and (8.3) with $\mathbf{v}_0 = I_p/(3c)\mathbf{e}_z$. Figure is adapted from Ni *et al.* [474].

the simple man's model, ionization at time $t_0 = 0$ corresponds to final momenta \mathbf{p} with angle $\phi_p = 0$. A slice ($p_z = 0$) through the photoelectron momentum distribution calculated by numerical solution of the TDSE in 3D is shown in Fig. 8.1(a). Due to the shortness of the pulse, only one clear maximum of the momentum distribution in the vicinity of the positive p_x -axis is present that roughly follows the negative vector potential (see black dashed line). For each momentum \mathbf{p}_\perp in the polarization plane, we separately determine the average momentum $\langle p_z \rangle(\mathbf{p}_\perp)$ in the light-propagation direction (see Eq. (8.4)). In the vicinity of the probability maximum, the result is a smooth function (see Fig. 8.1(b)), depending on both the radial momentum p_\perp and the angle ϕ_p in the polarization plane.⁹

To study the angular dependence of the nondipole shift, we convert the momentum distribution to cylindrical coordinates. The projection of the 3D distribution from TDSE on the polarization plane is shown in Fig. 8.2(a2) and the partial average in Fig. 8.2(b2). By integration of the projected distribution along the p_\perp -momentum component in the polarization plane, the angular distribution $w(\phi_p)$ is obtained (see Fig. 8.2(a1)). In an analogous way, by averaging the partial average (8.4) over p_\perp , the angle-resolved nondipole shift is calculated

$$\langle p_z \rangle(\phi_p) = \frac{\int dp_\perp \int dp_z p_z p_\perp w(p_\perp, \phi_p, p_z)}{\int dp_\perp \int dp_z p_\perp w(p_\perp, \phi_p, p_z)}. \quad (8.6)$$

The result from TDSE is shown in Fig. 8.2(b1). As discussed in Chapter 5, the peak position of the angular distribution is shifted towards nonzero angles $\phi_{\text{off}} \approx 7.8^\circ$ due the influence of the Coulomb attraction on the outgoing electron. The angle-resolved nondipole shift $\langle p_z \rangle(\phi_p)$ shows also a clear modulation with a pronounced minimum at $\phi_{\text{min}} \approx 2^\circ$. In agreement with the experimental results [435], the angle ϕ_{min} corresponding to minimal momentum transfer is much smaller compared to the attoclock offset ϕ_{off} . In the next sections, we explore this variation of the nondipole shift and study the influence of Coulomb effects during the continuum motion.

8.2.3 Coulomb effects during the continuum motion

As discussed in Chapter 5, for close-to-circularly-polarized attoclock settings, some difficulties arise in the interpretation of the observables (e.g. due to nonadiabatic effects). To avoid these complications, we first use the quasilinear field configuration created by a bicircular ω - 2ω -field (see Section 5.3 for an introduction) and study the interplay between Coulomb effects on the outgoing electrons and nondipole effects.

A slice at $p_z = 0$ through the momentum distribution for ionization of helium in the quasilinear setting is shown in Fig. 8.3(a). We again use a three-cycle laser pulse with an effective wavelength of 800 nm. The global maximum corresponds to the region of almost linear polarization in the vicinity of the peak of the pulse at $t = 0$. In the dipole approximation, the flow of time t_0 through the PMD follows the p_y -momentum component and initial velocities $\mathbf{v}_0 \approx v_{0,x}\mathbf{e}_x + v_{0,z}\mathbf{e}_z$ are mapped to the p_x - and p_z -momentum components (see Section 5.3 for details). We only analyze a slice through the maximum of the PMD that corresponds approximately to vanishing initial velocities $v_{0,\perp} \approx v_{0,x} = 0$ and, thus, the final momentum components in the polarization plane are given by $\mathbf{p}_\perp = -\mathbf{A}(t_0) \approx -A_x(0)\mathbf{e}_x + E_y(0)t_0\mathbf{e}_y$ (see the black vertical line in Fig. 8.3(a)). The maximum's position of the probability distribution is located at positive momenta p_y . As discussed in Section 5.3, this attoclock shift is a well-known signature of Coulomb effects (see also Fig. 8.3(b)). The nondipole shifts $\langle p_z \rangle(-A_x(0), p_y)$ of Eq. (8.4) from TDSE simulations are perfectly quadratic functions of p_y with a pronounced minimum centered very close to $p_y \approx 0$ (see the dashed-dotted lines in Fig. 8.3(c)). In agreement with the observation for elliptical polarization, the point of minimum momentum transfer is also unaffected by Coulomb effects compared to the attoclock shift of the probability distribution.¹⁰

When first neglecting Coulomb effects and treating the continuum motion classically, the nondipole part of the Lorentz force leads to a deflection of the electrons in the light-propagation direction (see

⁹We only analyze $\langle p_z \rangle(\mathbf{p}_\perp)$ in regions with sufficiently high probability. In the remaining part, $\langle p_z \rangle(\mathbf{p}_\perp)$ is set to zero.

¹⁰For example at an intensity of 10^{15} W/cm², the point of minimal nondipole shift is at $p_y \approx 0.015$ a.u. and the probability maximizes at $p_y \approx 0.276$ a.u.

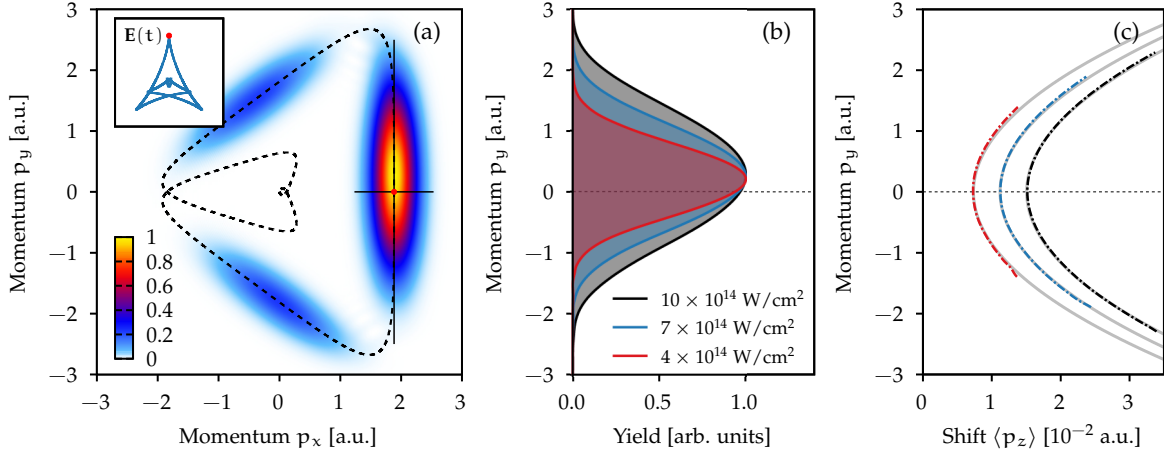


Figure 8.3: Nondipole effects in recollision-free strong-field ionization by quasilinear fields: 2D slice at $p_z = 0$ through the photoelectron momentum distribution obtained by numerical solution of the TDSE for helium ionized by a three-cycle laser pulse with 800 nm effective wavelength and $10 \times 10^{14} \text{ W/cm}^2$ intensity. The distribution is normalized to maximum signal of one. The black dashed line shows the negative vector potential and the inset shows the electric field. (b) 1D slices through the maximum of the PMD calculated along a line at fixed $p_x = -A_x(0)$ as a function of p_y (see black vertical line in panel (a)) for three different intensities (independently normalized to maximum signal of one). (c) Corresponding nondipole shift $\langle p_z \rangle(p_y)$ of Eq. (8.4). The gray lines show the classical estimate of Eqs. (8.2) and (8.3) with $\mathbf{v}_0 = I_p/(3c)\mathbf{e}_z$. Figure is adapted from Eicke *et al.* [367].

Eq. (8.3) and, hence, we expect an average transferred momentum

$$\langle p_z \rangle(p_x, p_y) \approx \langle v_{0,z} \rangle + \frac{1}{c} \left(\frac{\mathbf{p}^2}{2} - \frac{\mathbf{v}_0^2}{2} \right). \quad (8.7)$$

The slice (considered in Fig. 8.3(c)) corresponds to vanishing initial velocity in the polarization plane. Thus, this potential-free simple man's model predicts a quadratic dependence of the nondipole shift on the p_y -momentum component. This classical result for the quasilinear field is similar to the recollision-free result in pure linearly-polarized light except for a constant offset by $\approx p_x^2/(2c) = A_x^2(0)/(2c)$ caused by the displacement of the momentum distribution in p_x -direction.¹¹ The model is in almost perfect agreement with the TDSE result. In particular, the point of minimal momentum transfer corresponds to $p_y = 0$. In the remaining part of this section, we further explore the influence of Coulomb effects on the classical motion of the electron.

To this end, we consider the classical motion of the released electron, but include the electron-ion interaction as well as the nondipole effects perturbatively (similar to the model introduced in Section 5.3.1). For simplicity, we still restrict ourselves to the slice with $v_{0,x} \approx 0$ and, thus, assume an initial velocity $\mathbf{v}_0 = v_{0,z}\mathbf{e}_z$. We calculate the deflection of the electron by the Coulomb attraction by evaluating the Coulomb force (see Eq. (5.38)) along the adiabatic light-driven trajectory of Eq. (5.36). If the electron starts at the I_p/E tunnel-exit position of Eq. (5.25), its velocity as a function of time t in the dipole approximation is approximately given by

$$\mathbf{r}_D(t) = \mathbf{A}(t) - \mathbf{A}(t_0) + \mathbf{v}_0 + \Delta\mathbf{r}_C(t, t_0) \quad (8.8)$$

with the Coulomb correction (to first order in Z and in \mathbf{v}_0)

$$\Delta\mathbf{r}_C(t, t_0) \approx \frac{Z}{\sqrt{2}} \frac{E(t_0)}{I_p^{3/2}} \hat{\mathbf{E}}(t_0) \left[\frac{\tau(t, t_0)}{\tau^2(t, t_0) + 1} + \arctan(\tau(t, t_0)) \right] - \frac{Z}{2} \frac{E(t_0)}{I_p^2} \mathbf{v}_0 \left[1 - \frac{1}{(\tau^2(t, t_0) + 1)^2} \right] \quad (8.9)$$

and the dimensionless time $\tau(t, t_0) = E(t_0)/\sqrt{2I_p}(t - t_0)$. To include leading-order nondipole effects for the motion in the light-propagation direction, we again use perturbation theory. For plane waves (2.1) with $\mathbf{B} = \mathbf{e}_z \times \mathbf{E}/c$ and, thus, $|\mathbf{B}| = |\mathbf{E}|/c$, the shift $z(t)/c$ in the argument of the magnetic part of the

¹¹The result for pure linear polarization was already given in Refs. [151, 471, 472]. However, in reality, the recollisions taking place in linearly-polarized fields prevent an observation of the recollision-free scenario (see Chapter 10).

Lorentz force can be neglected, if we are only interested in the corrections to first order in $1/c$. The integration of the Lorentz force along the dipole trajectory $\mathbf{r}_D(t)$ results in¹²

$$\begin{aligned} \Delta p_{ND,z} &= - \int_{t_0}^{\infty} dt (\dot{\mathbf{r}}_D(t) \times \mathbf{B}(t))_z = \frac{\mathbf{A}^2(t_0)}{2c} - \frac{1}{c} \int_{t_0}^{\infty} dt \Delta \dot{\mathbf{r}}_C(t, t_0) \cdot \mathbf{E}(t) \\ &\approx \frac{\mathbf{A}^2(t_0)}{2c} - \frac{1}{c} \Delta \mathbf{p}_C \cdot \mathbf{A}(t_0) + \frac{Z}{c} \frac{E(t_0)}{I_p}. \end{aligned} \quad (8.10)$$

Here, we used the momentum change in the dipole approximation due to the Coulomb force given by $\Delta \mathbf{p}_C = \pi Z \mathbf{E}(t_0) / (2I_p)^{3/2}$ (see Eqs. (5.40) and (8.9)). The first two terms were already used in Ref. [435]. There it was argued that the attoclock shift is gained in a time interval much shorter than an optical cycle of the light field and, hence, the influence of the Coulomb potential can be viewed as an initial velocity offset in the potential-free mapping of Eq. (8.3). We find that the nonzero time of deceleration compared to a short-kick picture, however, leads to the last term in Eq. (8.10). In conclusion, for given release time t_0 , the Coulomb-induced change of the velocity in the polarization plane affects the final momentum in the light-propagation direction through the magnetic part of the Lorentz force (see the last two terms in Eq. (8.10)).

However, importantly, the Coulomb effects also change the time-to-momentum mapping for components in the polarization plane: $\mathbf{p}_\perp \approx -\mathbf{A}(t_0) + \Delta \mathbf{p}_C$. As a result, for example, the final momentum $\mathbf{p} = -A_x(0)\mathbf{e}_x$ on the p_y -axis does not correspond to ionization at $t_0 = 0$ anymore, but instead it corresponds to ionization at a slightly negative time $t_0 < 0$. To analyze the nondipole shift as a function of the final momentum, we have to account for this Coulomb-corrected mapping. The final momentum in the light-propagation direction can be expressed as

$$p_z = \left(1 - \frac{Z}{2} \frac{E(t_0)}{I_p^2} \right) v_{0,z} + \frac{\mathbf{p}^2}{2c} - \frac{(\Delta \mathbf{p}_C)^2}{2c} + \frac{Z}{c} \frac{E(t_0)}{I_p}. \quad (8.11)$$

The first term represents the focusing of the initial velocity distribution in z -direction due to the Coulomb attraction (see also Eq. (5.39)). The second term represents the nondipole shift in the absence of the potential whereas the last terms are the Coulomb-induced corrections. Here, in a short-kick picture, the Coulomb corrections of the time-to-momentum mapping and of the nondipole shift in Eq. (8.10) compensate each other to first order in the charge Z . Thus, the third term in Eq. (8.11) remains which is of second order in Z . Only the nonzero time of deceleration leads to a term proportional to Z (see the fourth term in Eq. (8.11)). For usual system parameters like $I_p = 0.9$ a.u., $E_0 = 0.15$ a.u., we find $\frac{(\Delta \mathbf{p}_C)^2}{2c} \approx 1.4 \times 10^{-4}$ a.u. as well as $\frac{Z}{c} \frac{E(t_0)}{I_p} \approx 1.2 \times 10^{-3}$ a.u. indicating that the last term in Eq. (8.11) is usually the dominant Coulomb correction.

In the vicinity of the attoclock maximum, the electric-field strength is approximately constant and the corrections of the nondipole shift of Eq. (8.11) only depend very weakly on the momentum component p_y . Hence, the Coulomb corrections lead to an overall increase of the nondipole shift, but they do not affect the momentum p_y at which the minimal nondipole shift occurs. Qualitatively, the same arguments can also be applied for elliptically-polarized fields (see also Ref. [435]), explaining the much smaller angle ϕ_{\min} corresponding to minimal momentum transfer compared to the attoclock offset ϕ_{off} .¹³ Within the classical model (including the Coulomb effects), the maximum of the probability distribution corresponds to the time $t_0 = 0$ of peak field strength. In contrast, the point of minimal momentum transfer corresponds to ionization at a slightly negative release time $t_0 < 0$. A similar effect was observed in the streaking of electrons with a weak external electric field that is polarized perpendicular to a strong driving field [367, 426]. Both for HHG [426] as well as photoelectrons [367], the reconstructed ionization times are in agreement with the ionization times of the strong-field approximation, i.e., these methods

¹²To arrive at the second line, we wrote $\Delta \dot{\mathbf{r}}_C(t, t_0) = \Delta \mathbf{p}_C + (\Delta \dot{\mathbf{r}}_C(t, t_0) - \Delta \mathbf{p}_C)$ in the integral. Afterwards, the integral over the first term proportional to $\Delta \mathbf{p}_C$ can be directly evaluated. For the second term, we applied an adiabatic approximation of the electric field $\mathbf{E}(t) \approx \mathbf{E}(t_0)$.

¹³The approximately two degrees offset from the potential-free estimate is likely to be caused by geometric effects as well as nonadiabatic effects. We expect that for larger field strength its relative importance decreases compared to the attoclock offset.

measure ionization times as if the outgoing electron did not experience the Coulomb attraction [161]. All these observations have in common that the perturbing forces act in the direction perpendicular to the ionizing electric field.

8.2.4 The influence of nonadiabaticity on the momentum transfer

Now, we turn back to the slightly more complicated situation in elliptically-polarized fields. Similar to the quasilinear field, the angular dependence of the nondipole shift $\langle p_z \rangle$ can be qualitatively explained by the classical motion of a potential-free electron in the laser field [435]. When neglecting nonadiabatic corrections, the distribution of initial velocities in the polarization plane is centered around $v_{0,\perp} = 0$. Hence, for each angle ϕ_p in the polarization plane, the final momentum distribution is approximately centered at $-\mathbf{A}(t_0(\phi_p))$, where $t_0(\phi_p)$ is the classical time-to-momentum mapping defined by Eq. (8.2). The deflection due to the full Lorentz force again leads to a momentum component in forward direction $p_z \approx v_{0,z} + A^2(t_0(\phi_p))/(2c)$ (see the gray line in Fig. 8.2(b2)). Here, the variation of the average final electron energy as a function of the angle ϕ_p mostly determines the angular dependence of the average momentum $\langle p_z \rangle$. For example, the local minimum of the vector potential $|\mathbf{A}(t)|$ at $t = 0$ is mapped to an angle $\phi_p = 0^\circ$ and, hence, results in a local minimum of the nondipole shift $\langle p_z \rangle$. However, in contrast to the perfect agreement of the classical model with the TDSE result for the quasilinear setting (see Fig. 8.3(c)), there are two obvious differences visible for elliptical polarization: (i) In this classical adiabatic model, the nondipole shift is systematically underestimated and (ii) the difference between TDSE and classical adiabatic model increase as a function of $|\phi_p|$. These observations are also present in the experimental results in Ref. [435] and raise questions about their physical origins.

For further investigation, we consider a simplified description in the strong-field approximation beyond the electric dipole approximation of Section 2.3. The application of a saddle-point approximation offers a useful analytical treatment in a quantum-orbit model (see Section 2.3 for an introduction). This approach covers nonadiabatic effects, but neglects the Coulomb potential after interaction with the field. We only include the signal for a single saddle-point time $t'_s = t'_r + it'_i$ defined by the following equation

$$\dot{S}_{\text{SFA}}(\mathbf{p}, t'_s) = \frac{1}{2} \left[\mathbf{p} + \mathbf{A}(t'_s) + \frac{\mathbf{e}_z}{c} \left(\mathbf{p} \cdot \mathbf{A}(t'_s) + \frac{1}{2} \mathbf{A}^2(t'_s) \right) \right]^2 + I_p = 0 \quad (8.12)$$

with the generalized action

$$S_{\text{SFA}}(\mathbf{p}, t') = -\frac{1}{2} \int_{t'}^{t_f} dt \left[\mathbf{p} + \mathbf{A}(t) + \frac{\mathbf{e}_z}{c} \left(\mathbf{p} \cdot \mathbf{A}(t) + \frac{1}{2} \mathbf{A}^2(t) \right) \right]^2 + I_p(t' - t_A). \quad (8.13)$$

For an 1s initial state, the electron momentum distribution is given by (to first order in $1/c$ and up to a normalization factor)

$$w(\mathbf{p}) \approx \frac{1}{|\dot{S}_{\text{SFA}}(\mathbf{p}, t'_s)|^\alpha} e^{-2\text{Im}S_{\text{SFA}}(\mathbf{p}, t'_s)}. \quad (8.14)$$

In length gauge, the parameter α in the preexponential factor is given by $\alpha = 1 + Z/\sqrt{2I_p}$, where Z is the asymptotic charge of the ion.¹⁴ Even though the SFA neglects Coulomb effects, the SFA result agrees well with the nondipole shift from the TDSE for elliptically-polarized fields (see Figs. 8.2(b2) and 8.2(b3)). Especially, the angular dependence of $\langle p_z \rangle(\phi_p)$ is quantitatively reproduced by the SFA result.

To explain the difference between the classical adiabatic model and the more advanced theories, it is important to note that we average $\langle p_z \rangle(\mathbf{p}_\perp)$ over the \mathbf{p}_\perp -distribution to calculate the angle-resolved quantity $\langle p_z \rangle(\phi_p)$ of Fig. 8.2(b1). The momentum transfer during the continuum motion (see the terms $1/c (\mathbf{p}^2/2 - \mathbf{v}_0^2/2)$ in Eq. (8.7)) leads to a strong increase of the average $\langle p_z \rangle(\mathbf{p}_\perp)$ as a function of the momentum component p_\perp (see Figs. 8.2(b2) and 8.2(b3)). However, for close-to-circularly-polarized fields,

¹⁴The parameter α can be derived by considering a generalized saddle-point approximation which takes the pole in the transition matrix element into account [194].

the most probable momenta p_{\perp} are increased due to the well-known nonadiabatic offset of the initial velocity distribution as discussed in Refs. [170, 354, 370–372] (see also Figs. 8.2(a2) and 8.2(a3)). As a result, the averaged nondipole shift $\langle p_z \rangle(\phi_p)$ is enhanced compared to the simple adiabatic model. The more nonadiabatic ionization conditions at the minima of the electric-field strength lead to a further increase of $\langle p_{\perp} \rangle$ and thus of $\langle p_z \rangle(\phi_p)$ around $\phi_p \approx \pm 90^\circ$ compared to ionization at the time of peak electric-field strength corresponding to $\phi_p \approx 0^\circ$. This explains the enhanced angular modulation of $\langle p_z \rangle(\phi_p)$ visible in the TDSE and SFA compared to the classical adiabatic model.

The asymptotic nondipole shift $\langle p_z \rangle$ is also influenced by the initial velocity $\langle v_{0,z} \rangle$ in the light-propagation direction, i.e., by possible momentum transfer during the tunneling process. Hence, a nontrivial dependence of $\langle v_{0,z} \rangle$ on the liberation time t_0 would modify the angle-resolved nondipole shift $\langle p_z \rangle(\phi_p)$. To study the initial velocity $\langle v_{0,z} \rangle$ and, thus, to disentangle the nondipole effects during the tunnel ionization and during the subsequent acceleration of the electron on a subcycle time scale, Hongcheng Ni suggested to employ the classical backpropagation method introduced in Section 5.2.4.

The basic idea is to classically propagate the asymptotic electron wave packet back in time until a defined tunneling criterion is reached. This enables the calculation of various observables of the liberated electron wave packet at the tunnel exit. Here, we define an initial distribution $w_{\text{ini}}(t_0, v_{0,\perp}, v_{0,z})$ as a function of the release time t_0 , of the initial velocity component $v_{0,\perp}$, which is in the polarization plane and perpendicular to the instantaneous electric field $\mathbf{E}(t_0)$, and of the initial velocity component $v_{0,z}$ in the light-propagation direction. Before proceeding with the full numerical calculation using TDSE input, we explore the potential-free case by using the SFA input (see also Appendix A.3). In this special case, the mapping of the initial coordinates $(t_0, v_{0,\perp}, v_{0,z})$ to the final momenta \mathbf{p} is given by Eqs. (8.2) and (8.3). For ionization by an elliptically-polarized pulse, the initial probability distribution of Eq. (5.16) is calculated based on the wave packet of Eq. (8.14). The projection of the initial distribution on the t_0 - $v_{0,\perp}$ -plane is shown in Fig. 8.4(a2). To quantify the momentum transfer during the tunneling process, we define the expectation value of the initial velocity in the light-propagation direction for each t_0 and $v_{0,\perp}$

$$\langle v_{0,z} \rangle(t_0, v_{0,\perp}) = \frac{\int dv_{0,z} v_{0,z} w_{\text{ini}}(t_0, v_{0,\perp}, v_{0,z})}{\int dv_{0,z} w_{\text{ini}}(t_0, v_{0,\perp}, v_{0,z})}. \quad (8.15)$$

To further quantify the temporal evolution of the sub-barrier momentum transfer, $\langle v_{0,z} \rangle(t_0)$ is calculated by additional averaging over the perpendicular velocity $v_{0,\perp}$. The results for $\langle v_{0,z} \rangle(t_0, v_{0,\perp})$ and $\langle v_{0,z} \rangle(t_0)$

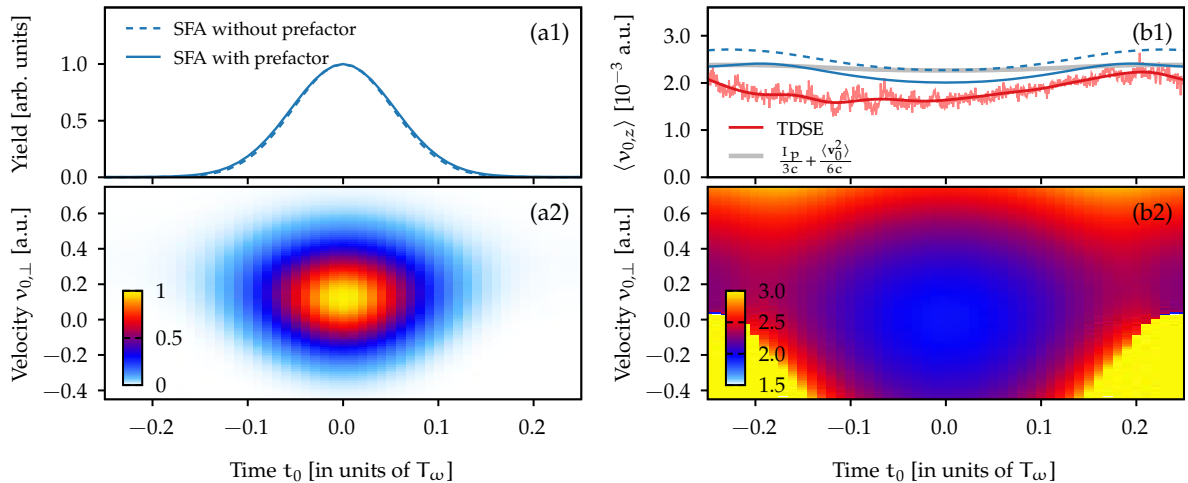


Figure 8.4: Electron wave packet at the tunnel exit for ionization by an elliptically-polarized field calculated by classical backpropagation for input from the SFA. (a1) Time-dependent ionization rate. (a2) Initial probability distribution projected onto the t_0 - $v_{0,\perp}$ -plane. (b1) Subcycle-resolved average initial velocity $\langle v_{0,z} \rangle$ as a function of the release time t_0 . (b2) Average initial velocity $\langle v_{0,z} \rangle(t_0, v_{0,\perp})$ of Eq. (8.15) in units of 10^{-3} a.u. For comparison, the simple estimate of Eq. (8.17) is shown in panel (b1) as gray line and the classical backpropagation result from TDSE (provided by Hongcheng Ni [474]) is shown as red line. For the results in panels (a2) and (b2) and the blue solid lines in panels (a1) and (b1), the distribution of Eq. (8.14) with $\alpha = 1 + Z/\sqrt{2}I_p$ is considered. In addition, the blue dashed lines show the results for input with $\alpha = 0$, i.e., neglecting the prefactor in Eq. (8.14). Figure is adapted from Ni *et al.* [474].

are presented in Figs. 8.4(b2) and (b1), respectively. In agreement with earlier works [150, 151], the average initial velocity is on the order of $I_p/(3c) \approx 2.2 \times 10^{-3}$ a.u. for helium. However, the average initial velocity $\langle v_{0,z} \rangle$ shows a small variation with the initial velocity $v_{0,\perp}$ and the ionization time t_0 within an optical cycle. Note that for times around $t_0 \pm 0.25 T$, the two saddle points in time corresponding to different half cycles of the electric field approach each other in the region with $v_{0,\perp} < 0$. Hence, the saddle-point approximation breaks down [202, 203]. This prevents a meaningful time-resolved study within the backpropagation method, i.e., the observed large values of $\langle v_{0,z} \rangle$ in Fig. 8.4(b2) have no physical significance.

For the laser parameters at hand (Keldysh parameter ≈ 0.8), nonadiabatic effects during tunnel ionization must be considered. To study further the properties of the ionized wave packet, we derived an analytical expression based on SFA in saddle-point approximation which takes leading-order nonadiabatic corrections into account. When neglecting the preexponential factor in Eq. (8.14) ($\alpha = 0$), the initial wave packet is given to first order in the Keldysh parameter γ by (see Appendix A.3.2)

$$w_{\text{SFA}}(t_0, v_{0,\perp}, v_{0,z}) \approx \exp \left(-\frac{2}{3E(t_0)} \left[2I_p + v_{0,\perp}^2 + (v_{0,z} - \langle v_{0,z} \rangle)^2 \right]^{3/2} \left[1 + \frac{1}{2} \frac{\mathbf{v}_0 \cdot \dot{\mathbf{E}}(t_0)}{E^2(t_0)} \right] \right). \quad (8.16)$$

The expectation value of the initial velocity can be approximated as (to first order in $1/c$)

$$\langle v_{0,z} \rangle(t_0, v_{0,\perp}) \approx \frac{I_p + v_{0,\perp}^2/2}{3c}. \quad (8.17)$$

Importantly, for fixed $v_{0,\perp}$ and t_0 , we find that the first-order nonadiabatic corrections to the under-the-barrier momentum transfer vanishes. Thus, the first term of Eq. (8.17) is in agreement with earlier works [150, 151, 471]. Here, however, a nonzero initial velocity $v_{0,\perp}$ increases the effective ionization potential $I_p + v_{0,\perp}^2/2$. This explains qualitatively the quadratic dependence of the nondipole shift $\langle v_{0,z} \rangle$ on $v_{0,\perp}$ visible in Fig. 8.4(b2) in the vicinity of $t_0 = 0$. The observed variation of $\langle v_{0,z} \rangle(t_0)$ as a function of release time t_0 is caused by the interplay between nonadiabatic and nondipole effects (see Fig. 8.4(b1)). Even though the $v_{0,\perp}^2$ term in Eq. (8.17) induces a weak subcycle modulation of $\langle v_{0,z} \rangle(t_0)$ (see gray line in Fig. 8.4(b1)), we find that the time dependence of $\langle v_{0,z} \rangle(t_0)$ is mostly caused by nonadiabatic corrections in second order of the Keldysh parameter.

Our results show that the subcycle variation of the initial velocity $\langle v_{0,z} \rangle(t_0)$ is approximately one order of magnitude smaller than the angular modulation of the nondipole shift $\langle p_z \rangle(\phi_p)$ in the final momentum distribution. Hence, for the considered elliptical attoclock, the time dependence of the initial velocity $\langle v_{0,z} \rangle(t_0)$ influences the measurable quantity $\langle p_z \rangle(\phi_p)$ only weakly.¹⁵

8.2.5 Momentum transfer during the under-the-barrier motion

The classical backpropagation simulations can also be performed with input from TDSE for a long-range potential. For elliptical polarization, the initial velocity $\langle v_{0,z} \rangle(t_0)$ at the tunnel exit shows a weak subcycle modulation (see Fig. 8.4(b1)).¹⁶ However, the average value $\langle v_{0,z} \rangle(t_0)$ is significantly smaller than the value $I_p/(3c)$ expected for a short-range potential (the minimal nondipole shift is about 1.6×10^{-3} a.u. $\approx 0.24 I_p/c$). To investigate this reduced sub-barrier momentum transfer and avoid complications due to nonadiabaticity, we again consider the quasilinear attoclock configuration. For the quasilinear setting and a long-range potential, the average initial velocity $\langle v_{0,z} \rangle$ for ionization at $t_0 = 0$ from backpropagation with input from TDSE is shown in Fig. 8.5(a) as a function of the velocity $v_{0,\perp}$ in the polarization plane. In agreement with the potential-free estimate of Eq. (8.17), $\langle v_{0,z} \rangle$ is a quadratic function of $v_{0,\perp}$. However, similar to the simulations for elliptical polarization, we find that the nondipole shifts are significantly reduced compared to $I_p/(3c)$. For a further study, we repeat the

¹⁵This observation is in contrast to the speculations in Ref. [435] about an additional ellipticity-dependent initial velocity in the light-propagation direction.

¹⁶This backpropagation result for elliptical polarization was kindly provided by Hongcheng Ni [474].

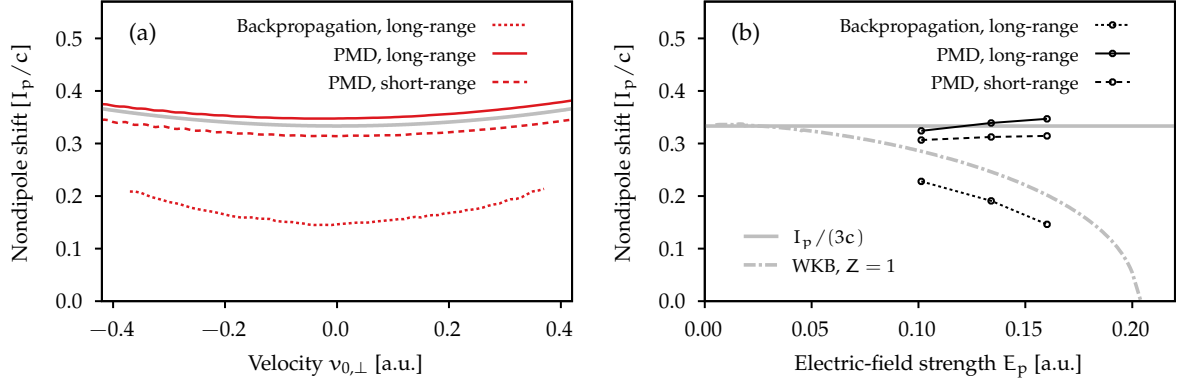


Figure 8.5: Under-the-barrier momentum transfer in strong-field ionization by a quasilinear field of Fig. 8.3 from TDSE simulations: (a) Average velocity $\langle v_{0,z} \rangle$ in the light-propagation direction as a function of the initial velocity $v_{0,\perp} = v_{0,x}$ at fixed release time $t_0 = 0$ for an intensity of 10×10^{14} W/cm². The solid and dashed lines are calculated by subtracting the classical potential-free nondipole shift during the continuum motion (see Eq. (8.3)) from the asymptotic average momentum $\langle p_z \rangle$. In addition, for the long-range potential, results from full classical backpropagation calculations including the electron-ion interaction during the continuum motion are shown as the dotted lines. (b) Average velocity $\langle v_{0,z} \rangle$ at $v_{0,\perp} = 0$ as a function of the peak electric-field strength. The gray thick line is the simple estimate of Eq. (8.17) and the gray dashed-dotted line is numerically calculated by WKB approximation (see Eq. (8.19)).

simulations for the short-range potential

$$V(r) = -\frac{6.15 \exp(-1.26 \sqrt{r^2 + 0.2})}{\sqrt{r^2 + 0.35}} \quad (8.18)$$

with the same ionization potential as helium. The corresponding initial velocity $\langle v_{0,z} \rangle$ is in much better agreement with the simple estimate of Eq. (8.17). Their small difference can be attributed to corrections from the preexponential factor in SFA that depend on the initial state of the electron [474]. This indicates the reduction of the under-the-barrier nondipole shift for long-range potentials is indeed caused by the presence of the Coulomb interaction.

In the adiabatic limit, the tunneling process can be quasi-classically described by means of a Wentzel-Kramers-Brillouin (WKB) approximation. Within this framework, Klaiber and Yakaboylu *et al.* [151, 471] included magnetic nondipole effects on the under-the-barrier motion. We follow their approach and consider the static situation of an electric field of strength E_p pointing in positive y -direction and a magnetic field pointing in negative x -direction. During its quasi one-dimensional motion the electron tunnels through the barrier $V_{\text{eff}}(y) = V(y) + yE_p$ formed by the binding potential V and the electric field. Here, the magnetic field can be included by means of a nonvanishing vector potential $A_z = -yE_p/c$ such that the velocity in propagation direction of the light reads $v_z = p_z - yE_p/c$. Assuming $p_x = 0$, the total energy of the electron $\epsilon(y) = -I_p - (p_z - yE_p/c)^2/2$ is position dependent and the WKB tunneling probability

$$w_{\text{tunnel}} \propto \exp\left(-2 \int_{y_i}^{y_0} dy \sqrt{2(V_{\text{eff}}(y) - \epsilon(y))}\right) \quad (8.19)$$

through the classically-forbidden region $y_0 < y < y_i$ is changed compared to the dipole approximation.¹⁷ For a short-range potential, the integral can be evaluated analytically. In agreement with the adiabatic limit of the SFA (8.17), the velocity distribution in $v_{0,z}$ -direction at the tunnel exit maximizes at $v_{0,z}^{\text{max}} = I_p/(3c)$ [151]. A long-range Coulomb potential $V(r) = -Z/r$ leads to a reduced tunnel-barrier width reflected by a reduced amount of transferred momentum [471] (see gray dashed-dotted line in Fig. 8.5(b)). Qualitatively, this simple model reproduces the observed reduction of the under-the-barrier momentum transfer present in the backpropagation calculations.

Experiments can only access the nondipole shifts in the asymptotic momentum distributions and do not measure the electron wave packets at the tunnel exit. However, we found that during the continuum

¹⁷Note that this approximation does not properly consider the dynamics very close to the center of the potential. For an improved treatment, the WKB solution should be matched to the initial state (analogous to ARM theory [113]).

motion of the electron, a long-range Coulomb potential enhances the nondipole shift by approximately $ZE_p/(cI_p)$ (see the last term in Eq. (8.11)). Thus, the Coulomb effects on the nondipole shift in the tunneling step and in the subsequent continuum motion nearly compensate each other. In all studied cases, we find that the nondipole shift in the final momentum distribution agrees well with the potential-free estimate of Eq. (8.7) in combination with the initial velocity of Eq. (8.17). To underline this, we subtract the nondipole contribution of the potential-free continuum motion from the asymptotic average momentum transfer $\langle p_z \rangle$ for a long-range potential. The results are shown as solid lines in Fig. 8.5 and match very well the $I_p/(3c)$ estimate of Eq. (8.17). Hence, for us, it seems that the separation of the momentum transfer into under-the-barrier and continuum motion in the backpropagation is to a certain extent artificial.

8.3 Disentanglement of magnetic and electric nondipole effects

In previous studies, nondipole effects were included to a given order in $1/c$, i.e., both the effect of the magnetic field and the electric-field inhomogeneity were simultaneously incorporated. Commonly, in strong-field ionization, the magnetic component of the light field was considered as the dominating source of nondipole effects (see for example the review [475]). Alexander Hartung [473] proposed to study the effects of the magnetic field and the temporospatial dependence of the electric field separately.¹⁸ In Ref. [473], (numerical) simulations based on single trajectories and an ensemble of trajectories were used to study the nondipole asymmetry of the maximum's position of the radial momenta p_\perp as a function of the momentum p_z . In Section 8.3.1, we follow this idea, but derive an analytical description. In a quantum-mechanical calculation based on a Hamiltonian of the form (2.20) it is not possible to include only one of the two nondipole contributions. Thus, we use a two-step model where the influence of the laser magnetic field and electric-field inhomogeneity on the classical motion of the electron can be studied separately. In Sections 8.3.2 and 8.3.3, the model used to interpret photoelectron momentum distributions from numerical TDSE simulations and especially the influence of nonadiabatic effects is considered.

8.3.1 Simple man's model

The release of the electron is a nonclassical process. In this section, we use an adiabatic approximation for the distribution of the initial coordinates. According to Eq. (8.16), the released wave packet is then given by

$$w_{\text{adia}}(t_0, v_{0,\perp}, v_{0,z}) \approx \exp \left(-\frac{2}{3E(t_0)} \left[2I_p + v_{0,\perp}^2 + \left(v_{0,z} - \frac{I_p + v_{0,\perp}^2/2}{3c} \right)^2 \right]^{3/2} \right). \quad (8.20)$$

A schematic sketch of a slice in the $v_{0,\perp}$ - $v_{0,z}$ -plane at fixed t_0 through the initial distribution is shown in Fig. 8.6(a). To characterize the geometry of the wave packet, we determine the most probable electron velocity $v_{0,z}^{\text{max}}$ for each fixed $v_{0,\perp}$. Similarly, we can also consider the most probable velocity $v_{0,\perp}^{\text{max}}$ in the polarization plane for each fixed $v_{0,z}$. For the adiabatic distribution, these lines of maxima are given by

$$v_{0,z}^{\text{max}}(v_{0,\perp}) = \frac{1}{3c} \left(I_p + \frac{v_{0,\perp}^2}{2} \right) \quad \text{and} \quad v_{0,\perp}^{\text{max}}(v_{0,z}) = 0. \quad (8.21)$$

Thus, the global maximum of the distribution is approximately located at

$$v_{0,z}^{\text{max}} = \frac{I_p}{3c} \quad \text{and} \quad v_{0,\perp}^{\text{max}} = 0. \quad (8.22)$$

In the vicinity of the global maximum, the initial distribution of Eq. (8.20) is approximately rotationally symmetric, i.e., its Hessian matrix evaluated at the maximum is invariant under rotations.

¹⁸A similar approach was also earlier used in my master thesis [160] to disentangle electric and magnetic nondipole effects in the high-energy rescattering region.

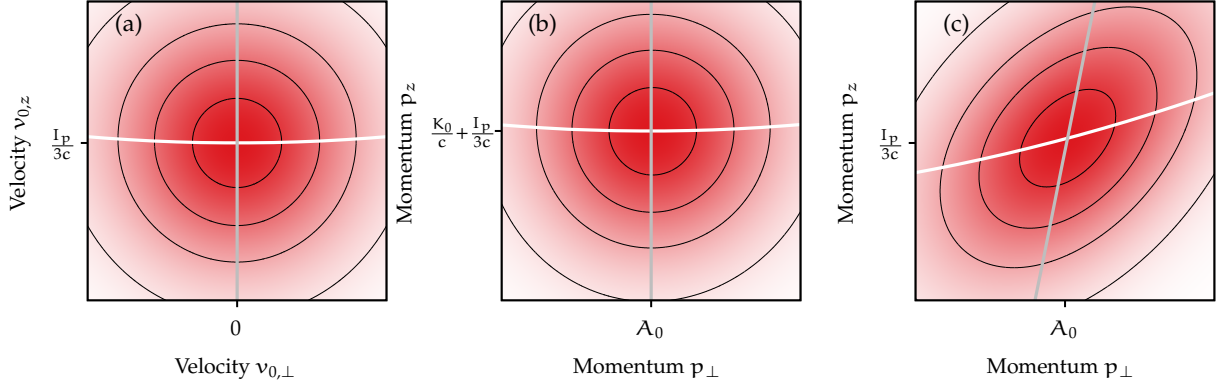


Figure 8.6: Schematic visualization of the effects of the magnetic field and the electric-field inhomogeneity on the photoelectron momentum distributions for an exaggerated value of $1/c$. (a) Initial-velocity distribution of Eq. (8.20) for fixed t_0 . The gray and white lines indicate the position of the maxima for fixed $v_{0,z}$ or for fixed $v_{0,\perp}$ (see Eq. (8.21)), respectively. (b) Slice through the final momentum distribution when only taking spatially-homogeneous electric and magnetic fields into account. The gray and white lines again indicate the position of the maxima for fixed p_z or for fixed p_{\perp} (see Eq. (8.29)), respectively. (c) Slice through the final momentum distribution when only taking the spatially-inhomogeneous electric field into account (and neglecting the magnetic field). The gray and white lines again indicate the maximum's position (see Eq. (8.32)). Figure is adapted from Hartung *et al.* [436].

Classical dynamics

The light-induced dynamics during the continuum motion deflects the initial wave packet to its final asymptotic shape. The continuum motion is approximated by means of classical mechanics. When the electron-ion interaction is neglected, the classical dynamics is governed by the Newton equation

$$\ddot{\mathbf{r}}(t) = -\mathbf{E}\left(t - \frac{z(t)}{c}\right) - \dot{\mathbf{r}}(t) \times \mathbf{B}\left(t - \frac{z(t)}{c}\right). \quad (8.23)$$

The term due to the magnetic field is printed in red and the term due to the electric-field inhomogeneity is printed in blue, respectively. In the dipole approximation, only a spatially-homogeneous electric field is present and the mapping of the initial velocity \mathbf{v}_0 to the final momentum \mathbf{p} is given by $\mathbf{p} = \mathbf{v}_0 - \mathbf{A}(t_0)$. For plane waves (2.1) with $\mathbf{B} = \mathbf{e}_z \times \mathbf{E}/c$ and, thus, $|\mathbf{B}| = |\mathbf{E}|/c$, the shift $z(t)/c$ in the argument of the magnetic part of the Lorentz force can be neglected, if we are only interested in the corrections to first order in $1/c$. To include leading-order nondipole corrections for the components in the polarization plane, the force of Eq. (8.23) is integrated along the dipole trajectory in the light-propagation p_D direction (here along $z_D(t) = v_{0,z}(t - t_0)$):

$$\begin{aligned} \mathbf{p}_{\perp} &= \mathbf{v}_{0,\perp} - \int_{t_0}^{\infty} dt \left[\mathbf{E}\left(\left(1 - \frac{v_{0,z}}{c}\right)t + \frac{v_{0,z}t_0}{c}\right) + v_{0,z}\mathbf{e}_z \times \mathbf{B}(t) \right] + \mathcal{O}\left(\frac{1}{c^2}\right) \\ &= \mathbf{v}_{0,\perp} - \frac{1}{1 - \frac{v_{0,z}}{c}}\mathbf{A}(t_0) + \frac{v_{0,z}}{c}\mathbf{A}(t_0) + \mathcal{O}\left(\frac{1}{c^2}\right) = \mathbf{v}_{0,\perp} - \mathbf{A}(t_0) + \mathcal{O}\left(\frac{1}{c^2}\right). \end{aligned} \quad (8.24)$$

Here, we use the definition of $\mathbf{A}(t)$ in Eq. (2.5).

The effect of the temporospatial dependence of the electric field can be interpreted in analogy to the Doppler effect. In the laboratory frame, electrons traveling in (against) the light-propagation direction feel an oscillating force due to the electric field with an effective frequency which is lower (higher) than the frequency of the external light field. The effective frequency $\omega_{\text{eff}}(v_{0,z}) = \omega(1 - v_{0,z}/c)$ can be read off the upper line in Eq. (8.24). As discussed in Section 7.2.1, the effective frequency changes the ponderomotive energy of the electron. In addition, its drift momentum (in the dipole approximation given by $\mathbf{v}_0 - \mathbf{A}(t_0)$) is also modified, because the quantity \mathbf{A} scales with the inverse of the frequency (see the blue-marked correction in the lower line of Eq. (8.24)). To confirm that the electron “feels” an electric field with frequency ω_{eff} , we can analyze the motion in an inertial frame Σ' that moves with velocity $\mathbf{v} = v_{0,z}\mathbf{e}_z$ relative to the rest frame of the ionic core. In Σ' , because $t = t' + \mathcal{O}(1/c^2)$ and $z = z' + v_{0,z}t' + \mathcal{O}(1/c^2)$, the electric and magnetic fields read according to the Lorentz transformation

(to first order in $1/c$)

$$\begin{aligned}\mathbf{E}'(\mathbf{r}', t') &= \mathbf{E}(\mathbf{r}, t) + v_{0,z} \mathbf{e}_z \times \mathbf{B}(\mathbf{r}, t) \\ &= \left(1 - \frac{v_{0,z}}{c}\right) \mathbf{E}\left(t - \frac{z}{c}\right) = \left(1 - \frac{v_{0,z}}{c}\right) \mathbf{E}\left(\left(1 - \frac{v_{0,z}}{c}\right) t' - \frac{z'}{c}\right), \\ \mathbf{B}'(\mathbf{r}', t') &= \mathbf{B}(\mathbf{r}, t).\end{aligned}\quad (8.25)$$

The electric-field inhomogeneity results indeed in a modified effective frequency in the moving frame Σ' . However, for a correct description of the dynamics in the moving frame Σ' , a modification of the magnitude of the electric field appears that is related to the magnetic field in the rest frame. This is a well-known ambiguity in the separation of the total electromagnetic field into electric and magnetic field components. In an ionization process, the fixed position of the nucleus defines a natural rest frame, to which we will restrict ourselves in the following.

The motion in the light-propagation direction is solely influenced by the magnetic part of the field. Analogous to Eq. (8.24), the nondipole correction is determined perturbatively along the dipole trajectory. The final momentum in the light-propagation direction is given by (to first order in $1/c$)

$$p_z = v_{0,z} + \frac{1}{c} \left(\frac{1}{2} \mathbf{A}^2(t_0) - \mathbf{v}_{0,\perp} \cdot \mathbf{A}(t_0) \right) + \mathcal{O}\left(\frac{1}{c^2}\right) = v_{0,z} + \frac{1}{c} \left(\frac{\mathbf{p}^2}{2} - \frac{\mathbf{v}_0^2}{2} \right) + \mathcal{O}\left(\frac{1}{c^2}\right). \quad (8.26)$$

The relations between the initial conditions and the final momenta (see Eqs. (8.24) and (8.26)) are the well-known results of Eqs. (8.2) and (8.3). In the final result, nondipole corrections are solely given by magnetic-field-induced terms in the light-propagation direction. However, it is important that the nondipole corrections in the \mathbf{p}_\perp -momentum component due to the magnetic field and due to the temporospatial dependence of the electric field cancel each other (to first order in $1/c$).

The initial distribution of Eq. (8.20) is transformed into the final electron momentum distribution by the light-induced dynamics in the continuum. Hence, these distributions are classically related by the mappings of Eqs. (8.24) and (8.26). In the following, we will separately consider the effects of both nondipole contributions (electric and magnetic) on the experimentally-measurable momentum distributions. To simplify the discussion, we restrict ourselves to times t_0 with $\mathbf{A}(t_0) \cdot \mathbf{E}(t_0) = 0$ such that under adiabatic conditions the initial velocity \mathbf{v}_0 is parallel or antiparallel to the vector potential $\mathbf{A}(t_0)$ (see Eq. (2.47)). Thus, for fixed t_0 , the plane of final momenta spanned by $-\mathbf{A}(t_0)$ and \mathbf{e}_z must only be considered. This simplification is possible for the usual attoclock settings close to their maxima of the electric-field strength (see Section 5.2.1).

Spatially-homogeneous fields

Taking only a homogeneous electric field and the magnetic field into account (and neglecting the spatial dependence of the electric field) gives the mapping¹⁹

$$\begin{pmatrix} p_\perp \\ p_z \end{pmatrix} = \begin{pmatrix} A_0 \\ K_0/c \end{pmatrix} + \begin{pmatrix} 1 & -A_0/c \\ A_0/c & 1 \end{pmatrix} \begin{pmatrix} v_{0,\perp} \\ v_{0,z} \end{pmatrix}. \quad (8.27)$$

Here, $\mathbf{A}(t_0) = A_0 \hat{\mathbf{A}}(t_0)$ and $K_0 = A_0^2/2$ is the kinetic drift energy. The first term describes the effect of an homogeneous electric field (i.e. a shift by A_0 in the polarization plane) and the well-known nondipole shift of the electron momentum distribution by K_0/c in the light-propagation direction. In addition, the second term represents a small rotation of the distribution by an angle of about A_0/c around the origin. To first order in $1/c$, the initial distribution of Eq. (8.20) is invariant under small rotations. To exponential accuracy, the resulting final momentum distribution is still approximately rotationally symmetric around the global maximum of the distribution at

$$p_z^{\max} \approx \frac{K_0}{c} + \frac{I_p}{3c} \quad \text{and} \quad p_\perp^{\max} \approx A_0. \quad (8.28)$$

¹⁹For the discussion, the upper components of the vectors correspond to a basis vector $-\hat{\mathbf{A}}(t_0)$, e.g., $v_{0,\perp} = -\mathbf{v}_0 \cdot \hat{\mathbf{A}}(t_0)$.

Hence, it is effectively only displaced in the p_{\perp} - p_z -momentum plane compared to the initial-velocity distribution (see Fig. 8.6(b)). For each fixed p_{\perp} , we represent the forward shift of the distribution in the light-propagation direction by the most probable momentum p_z^{\max} . Similarly, the most probable momentum p_{\perp}^{\max} in the polarization plane can be determined for each fixed value of p_z . We find

$$p_z^{\max}(p_{\perp}) \approx \frac{K_0}{c} + \frac{1}{3c} \left(I_p + \frac{(p_{\perp} - A_0)^2}{2} \right) \quad \text{and} \quad p_{\perp}^{\max}(p_z) \approx A_0. \quad (8.29)$$

p_{\perp}^{\max} is constant in this case. The nondipole shift p_z^{\max} is nearly constant, i.e., its slope vanishes at the global maximum at $p_{\perp} = A_0$.

Spatially-inhomogeneous electric field

Taking only the temporospatial dependence of the electric field into account (and neglecting the magnetic field) gives the simplified mapping

$$\begin{pmatrix} p_{\perp} \\ p_z \end{pmatrix} = \begin{pmatrix} A_0 \\ 0 \end{pmatrix} + \begin{pmatrix} 1 & A_0/c \\ 0 & 1 \end{pmatrix} \begin{pmatrix} v_{0,\perp} \\ v_{0,z} \end{pmatrix}. \quad (8.30)$$

The electric-field inhomogeneity results in a shearing of the electron momentum distribution that is schematically shown in Fig. 8.6(c). The global maximum of the distribution is approximately located at

$$p_z^{\max} \approx \frac{I_p}{3c} \quad \text{and} \quad p_{\perp}^{\max} \approx A_0. \quad (8.31)$$

Importantly, the electric-field inhomogeneity induces the breaking of the rotational symmetry. Close to the global maximum, the electron momentum distribution has an elliptic shape with semi-minor axis $1 - \frac{A_0}{c}$ and semi-major axis $1 + \frac{A_0}{c}$ both tilted by 45° compared to the p_{\perp} - p_z -axis. Hence, the lines of maxima at fixed p_{\perp} and at fixed p_z are given by

$$p_z^{\max}(p_{\perp}) \approx \frac{1}{3c} \left(I_p + \frac{(p_{\perp} - A_0)^2}{2} \right) + \frac{A_0}{c} (p_{\perp} - A_0) \quad \text{and} \quad p_{\perp}^{\max}(p_z) \approx A_0 + \frac{A_0}{c} p_z. \quad (8.32)$$

Both the momentum dependencies of $p_{\perp}^{\max}(p_z)$ and of $p_z^{\max}(p_{\perp})$ have a nonzero slope of A_0/c in the vicinity of the maximum. The comparison with the homogeneous-field setting shows that this nonzero slope is a characteristic property of the temporospatial dependence of the electric field. For the dependence of $p_{\perp}^{\max}(p_z)$ on p_z , this was already noted in Ref. [473]. Here, we have additionally shown that the electric-field inhomogeneity also influences the nondipole shift of the momentum distribution in the light-propagation direction.

Spatially-inhomogeneous electric field and magnetic field

Taking the spatially-inhomogeneous electric field and the magnetic field into account results in the mapping of Eqs. (8.24) and (8.26). The global maximum of the final electron momentum distribution is then approximately located at

$$p_z^{\max} \approx \frac{K_0}{c} + \frac{I_p}{3c} \quad \text{and} \quad p_{\perp}^{\max} \approx A_0. \quad (8.33)$$

The magnetic-field effect during the continuum motion causes a forward shift of $\frac{K_0}{c}$. However, the influence of the electric-field inhomogeneity again leads to a shearing of the electron momentum distribution. The lines of maxima at fixed p_{\perp} and at fixed p_z are given by

$$p_z^{\max}(p_{\perp}) \approx \frac{K_0}{c} + \frac{1}{3c} \left(I_p + \frac{(p_{\perp} - A_0)^2}{2} \right) + \frac{A_0}{c} (p_{\perp} - A_0) \quad \text{and} \quad p_{\perp}^{\max}(p_z) \approx A_0 + \frac{A_0}{c} p_z. \quad (8.34)$$

Similar to the electric-field-only case, we find a nonzero slope of these lines of maxima in the vicinity of the global maximum.

8.3.2 Results for quasilinear fields

In the simple man's model of the previous section, an adiabatic ionization process was considered. In a quasilinear attoclock configuration, the first-order nonadiabatic corrections vanish in the vicinity of the field-strength maximum. Thus, the setting is well-suited to begin the study of nondipole effects. Afterwards, we discuss the ionization process in circularly-polarized fields which are easier to implement in experiments. However, for circular polarization, the distribution of initial velocities perpendicular to the instantaneous field is modified by nonadiabatic effects [170, 354, 370–372].

The cigar-like photoelectron momentum distribution from ionization of helium by a quasilinear field is shown in Fig. 8.3(a). To analyze the effects of the spatial dependence of the electric field, we restrict ourselves to a slice through the PMD at $p_y = 0$ (see black horizontal line in Fig. 8.3(a)). This slice would correspond to ionization at the time of peak field strength ($t_0 = 0$) in the absence of Coulomb effects. For fixed momenta $p_\perp = p_x$, the forward shift $p_z^{\max}(p_x)$ of the distribution in the light-propagation direction can be approximated by the partial average $\langle p_z \rangle(p_x, p_y = 0)$ of Eq. (8.4). For the recollision-free and interference-free ionization, we find that the partial average $\langle p_z \rangle(p_x, p_y)$ perfectly agrees with the maximum's position extracted by a quadratic fit. The result $p_z^{\max}(p_x)$ from TDSE is in perfect agreement with the simple man's model including both the magnetic field and the electric field inhomogeneity (see Fig. 8.7(a1)). At the global maximum located at $p_x + A_x(0) \approx 0$, the nondipole shift is indeed given by $\mathbf{p}^2/(2c) + I_p/(3c) = K_0/c + I_p/(3c)$. In the vicinity of the maximum, the nondipole shift p_z^{\max} varies linearly as a function of $p_x + A_x(0)$. For the studied intensity range between 5×10^{14} W/cm² and 10×10^{14} W/cm², we find that the slope is in perfect agreement with the estimate A_0/c . If the temporospatial dependence of the electric field is neglected, the momentum dependence is not correctly reproduced (see gray dashes line).

Importantly, for nonzero initial velocities (here given by $v_{0,\perp} \approx p_x + A_x(0)$), the TDSE results systematically deviate from the often-used (parabolic) estimate $K/c + I_p/(3c) = \mathbf{p}^2/(2c) + I_p/(3c)$. It shows that the final kinetic energy does not determine the nondipole shift or to phrase it differently the momentum transfer. Instead, according to Eq. (8.34), the electron picks up a momentum of $(I_p + v_{0,\perp}^2/2)/(3c)$ in forward direction during the tunnel ionization process (see also Eq. (8.17)). In the subsequent continuum motion, the kinetic energy of the electron changes by $\Delta E = \mathbf{p}^2/2 - \mathbf{v}_0^2/2$. In this step, only the light-field momentum associated with the gain in energy is transferred to the electron (see also Eq. (8.26)).

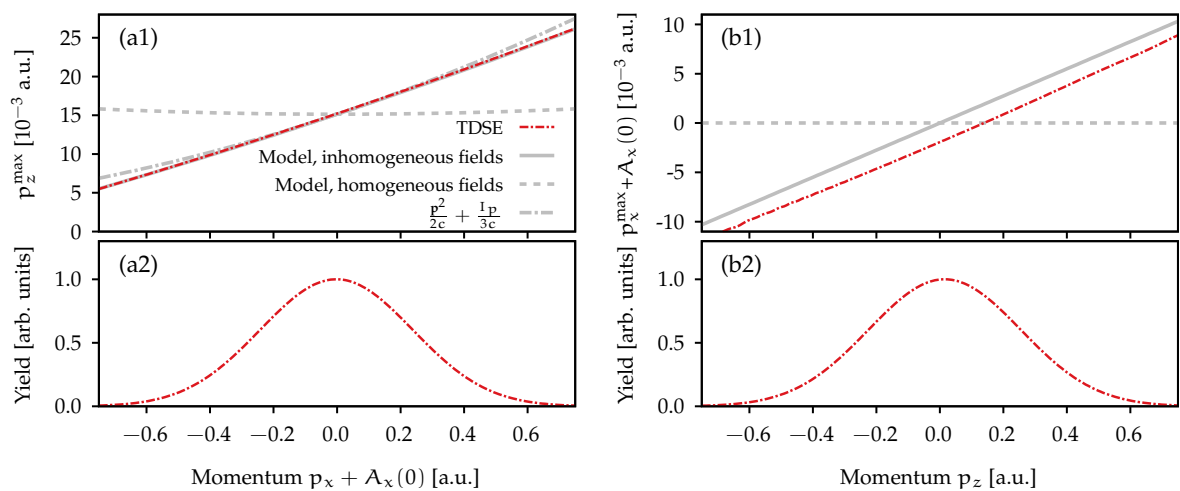


Figure 8.7: Momentum-resolved nondipole observables for a quasilinear field of Fig. 8.3(a): (a1) most probable momentum p_z^{\max} for fixed p_x and (b1) most probable momentum p_x^{\max} for each fixed p_z extracted from a slice at $p_y = 0$ through the PMD from TDSE. The gray dashed lines show the estimate (8.29) neglecting the temporospatial dependence of the fields whereas the gray solid lines include both the effect of the magnetic field and the temporospatial dependence of the electric field (see Eq. (8.34)). In addition, the dashed-dotted gray line in panel (a1) depicts the often-used parabolic estimate. (a2) and (b2) Slices through the PMD at fixed $p_z = 0$ or at fixed $p_x + A_x(0) = 0$ (individually normalized to maximal value of one), respectively.

For a deeper study, we also determine the most probable momentum p_x^{\max} in the polarization plane for each fixed momentum p_z .²⁰ The TDSE result is shown in Fig. 8.7(b1). As suggested by the simple man's model including the temporospatial dependence of the electric field, we find that $p_x^{\max}(p_z)$ is approximately a linear function of p_z . Thus, electrons flying in forward direction ($p_z > 0$) have on average larger momenta in the polarization plane (here in p_x -direction) than those emitted into backward direction ($p_z < 0$). The slope of $p_x^{\max}(p_z)$ at $p_z = 0$ is again in good agreement with the simple estimate given by A_0/c . However, compared to the simple man's model, the lateral distribution in TDSE is systematically shifted to smaller p_x -momenta. This is caused by the deceleration of the outgoing electrons by the long-range Coulomb attraction. An additional calculation showed that this difference is already present in the dipole approximation.

8.3.3 Results for circularly-polarized fields

Circular polarization provides the simplest experimentally-accessible setting for recollision-free ionization. For multi-cycle femtosecond laser pulses, the resulting photoelectron momentum distributions have a donut-like shape, i.e., they are approximately rotationally symmetric around the light-propagation direction (see also Fig. 7.3). Hence, it is sufficient to study a slice in the p_\perp - p_z -plane with $p_\perp > 0$ through the PMD. For the field defined in Eq. (8.5), the actual electric-field strength is $|\mathbf{E}| = E_p = E_0/\sqrt{2}$ and the magnitude of the vector potential is given by $|\mathbf{A}| = A_0 = E_0/(\sqrt{2}\omega)$.

Before proceeding with the full numerical solution of the TDSE, we study the PMD by means of the strong-field approximation, i.e., neglecting the long-range potential after interaction with the laser field. The following equations for a circularly-polarized cw field were already derived in my master thesis [160]. To obtain an analytical expression, we apply the saddle-point approximation. The resulting saddle-point equation (2.44) can be analytically solved (to first order in $1/c$)

$$\omega t'_s = \phi_p + 2\pi n + i \operatorname{acosh}(\chi) \quad \text{with} \quad n \in \mathbb{Z}. \quad (8.35)$$

Here, we defined the auxiliary quantity

$$\chi = \frac{1}{A_0 p_\perp} \frac{\frac{1}{2} p^2 + I_p + \left(1 + \frac{p_z}{c}\right) K_0}{1 + \frac{p_z}{c}} \quad \text{with} \quad K_0 = A_0^2/2. \quad (8.36)$$

Neglecting preexponential factors, the momentum distribution can be approximated as

$$w(\mathbf{p}) \approx e^{-2 \operatorname{Im} S_{\text{SFA}}(\mathbf{p}, t'_s)} \quad (8.37)$$

with the imaginary part of the SFA action given by

$$\operatorname{Im} S_{\text{SFA}}(\mathbf{p}, t'_s) = \left(1 + \frac{p_z}{c}\right) \frac{p_\perp A_0}{\omega} \left(\chi \operatorname{acosh}(\chi) - \sqrt{\chi^2 - 1}\right). \quad (8.38)$$

This is the nondipole generalization of the result in Ref. [354]. As expected, the PMD is independent of the angle ϕ_p in the polarization plane and of the rotation sense of the field.

Nondipole forward shift

Based the SFA distribution of Eqs. (8.37) and (8.38) for circular polarization, the forward shift p_z^{\max} of the distribution is determined for each lateral momentum p_\perp , we find to first order in $1/c$ [160]

$$p_z^{\max}(p_\perp) = \frac{1}{c} \left(p_\perp A_0 \frac{\sqrt{\chi_\perp^2 - 1}}{\operatorname{acosh}(\chi_\perp)} - K_0 \right) \quad \text{with} \quad \chi_\perp = \frac{1}{A_0 p_\perp} \left(\frac{1}{2} p_\perp^2 + I_p + K_0 \right). \quad (8.39)$$

This expression includes all orders of nonadiabatic corrections. In agreement with the approximation in Section 8.2.4, we find that the first-order nonadiabatic corrections (that are proportional to the Keldysh parameter) vanish. When only considering small initial velocities $v_{0,\perp} = p_\perp - A_0$, the shift of Eq. (8.39)

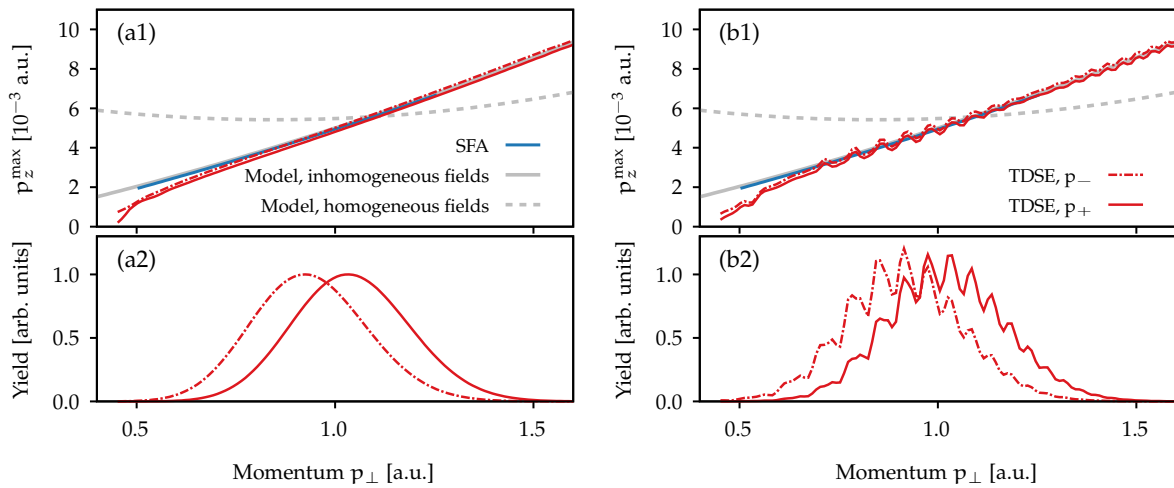


Figure 8.8: Nondipole shift $p_z^{\max}(p_{\perp})$ of the PMD from ionization of argon by circularly-polarized laser pulses with 800 nm central wavelength and 1.6×10^{14} W/cm² intensity. (a1) and (b1) Results for three-cycle and for ten-cycle laser pulses with \cos^2 envelope (see main text). (a2) and (b2) Corresponding momentum distributions obtained by integration over p_z (arbitrarily normalized). For the TDSE simulations, the initial state is chosen as p_{+} or p_{-} orbital (red solid or dashed-dotted lines). For comparison, the blue line shows the SFA result (8.39). The gray dashed lines show the estimate (8.29) of the simple man’s model neglecting the electric-field inhomogeneity whereas the gray solid lines include both the effects of the magnetic field and of the temporospatial dependence of the electric field (see Eq. (8.34)).

can be expanded. This leads to the same result for $p_z^{\max}(p_{\perp})$ as in the simple man’s model of Eq. (8.34) when taking both magnetic corrections and the electric-field inhomogeneity into account.

In an experiment by Hartung *et al.* [51], the momentum transfer in recollision-free strong-field ionization was studied for argon atoms. To model this system, we choose a Tong-Lin potential with singularity removed by using a pseudopotential for the 3p states (see Appendix A.2.3). The valance shell of the ground state with an ionization potential $I_p \approx 0.58$ a.u. consists of three degenerate p orbitals (p_{+} , p_{-} and p_0), where the index indicates the magnetic quantum number m of the orbital angular momentum in the light-propagation direction. We first consider short circularly-polarized pulses with a three-cycle \cos^2 envelope, 800 nm central wavelength and 1.6×10^{14} W/cm² intensity. From the photoelectron momentum distributions from the numerical solution of the TDSE (as described in Section 8.2.1), we again approximate the nondipole shift p_z^{\max} as a function of p_{\perp} by means of the partial average $\langle p_z \rangle(p_{\perp})$ of Eq. (8.4) calculated for electrons in the vicinity of the p_x -axis.

For electrons in initial p_{\pm} states, the momentum-dependent nondipole shifts $p_z^{\max}(p_{\perp}) \approx \langle p_z \rangle(p_{\perp})$ are separately shown in Fig. 8.8(a1).²¹ The momentum-dependent nondipole shifts are only weakly affected by the angular momentum of the initial state.²² In the central region of the distributions, the TDSE results are well reproduced by the saddle-point SFA of Eq. (8.39) and the simple man’s model of Eq. (8.34). For small lateral momenta p_{\perp} , the SFA result slightly overestimates the nondipole shifts compared to the TDSE solution. In additional simulations for a short-range argon model, we confirmed that this deviation is mainly caused by the long-range tail of the potential [160]. In agreement with Refs. [170, 354], the lateral distributions for the p_{\pm} orbitals are centered at different momenta (see Fig. 8.8(a2)). Thus, the total average $\langle p_z \rangle$ over the whole distribution is different for the p_{\pm} orbitals [190].

In the experiment [51], laser pulses of 25 fs duration were used. To study the dependence of the nondipole shift on the pulse length, we repeat the simulations for ten-cycle laser pulses. The resulting PMDs are converted to cylindrical coordinates. Afterwards, 2D projections are calculated by integration of the signal along the angle ϕ_p in the polarization plane. To reduce the influence of ATI rings, the 2D distributions $w(p_{\perp}, p_z)$ are averaged in p_{\perp} -direction over slices of $\Delta p_{\perp} = 0.1$ a.u. width. The nondipole shift is again represented by the partial average $\langle p_z \rangle(p_{\perp})$ (see Fig. 8.8(b1)). Except for small oscillations

²⁰The “power method” [161] is applied to determine the peak position for each fixed momentum p_z .

²¹This observable was already considered for helium in my master thesis [160].

²²The difference between the p_{+} and p_{-} states is on the order of 10^{-4} a.u.

caused by the ATI rings, the TDSE results for the short and long laser pulses agree reasonably well. Hence, in the present situation, the pulse length is only of minor importance for the momentum transfer.

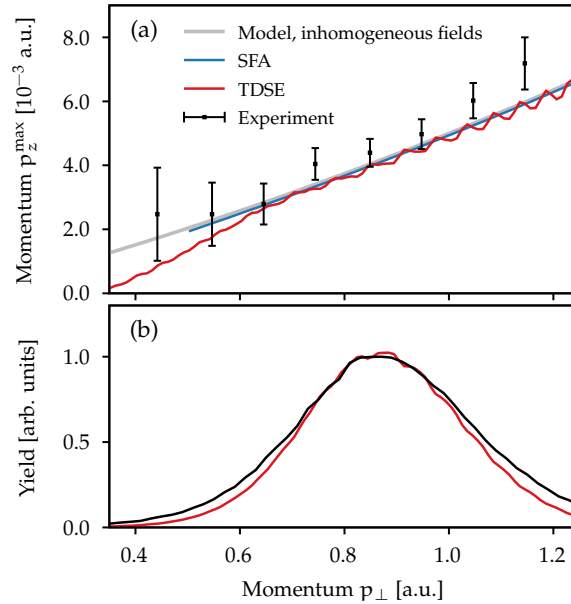


Figure 8.9: (a) Nondipole shift $p_z^{\max}(p_{\perp})$ of the PMD from ionization of argon by circularly-polarized laser pulses with 800 nm central wavelength and a peak intensity of 1.6×10^{14} W/cm²: experimental result provided by Hartung *et al.* [51] (black symbols) and focal-volume-averaged result obtained from the numerical solution of the TDSE (red line). For comparison, the blue line and the gray line show the SFA result (8.39) and the simple man's estimate (8.34) for a fixed intensity of 1.6×10^{14} W/cm². The arbitrarily-normalized momentum distributions are depicted in panel (b) for visual orientation. Figure is adapted from Hartung *et al.* [51].

For a more realistic comparison, the electron momentum distributions are also averaged over the focal-volume distribution for a peak intensity of $I_{\text{peak}} = 1.6 \times 10^{14}$ W/cm² (see the scheme introduced in Appendix A.2.4). To this end, 13 TDSE simulations are performed for ten-cycle laser pulses with a central wavelength of 800 nm and intensities ranging from 0.4×10^{14} W/cm² to 1.6×10^{14} W/cm². Since ionization in circularly-polarized fields preferentially depletes the states co- and counter rotating with respect to the field compared to the p_0 states, we only consider the incoherent sum of the momentum distributions for the p_{\pm} states. The good agreement between the lateral distribution of the experiment and the focal-averaged TDSE result confirms the intensity calibration (see Fig. 8.9(b)). We find that intensity averaging changes the nondipole shift only slightly compared to the simulations for a single fixed intensity (see Figs. 8.8(b1) and 8.9(a)). Both the TDSE simulations and the simplified model well reproduce the experimental dependence of the nondipole shift on the momentum p_{\perp} . The approximately linear increase of the nondipole shift as a function of p_{\perp} can be seen as the first experimental observation of an electric nondipole effect (see the discussion in Section 8.3.1).

The forward shift of $I_p/(3c)$ caused by the influence of the magnetic field on the electron during its laser-induced tunnel ionization [151] is given by $\approx 1.4 \times 10^{-3}$ a.u. Thus, for the present laser conditions, $I_p/(3c)$ is on the same order of magnitude as the transferred momentum during the continuum motion of the electron ($K_0/c \approx 2.7 \times 10^{-3}$ a.u.). Since the experimental result [51] is closely described by our simulations, the data show the first experimental evidence of magnetic-field effects acting during the tunnel-ionization step.

Nondipole modification of the most probable radial momentum

The dependence of the most probable radial momentum p_{\perp}^{\max} on the momentum p_z is an alternative observable to study the effect of the electric-field inhomogeneity. This idea was first used in Ref. [473]. Here, we follow the scheme introduced therein for the analysis of our simulation data. In order to first

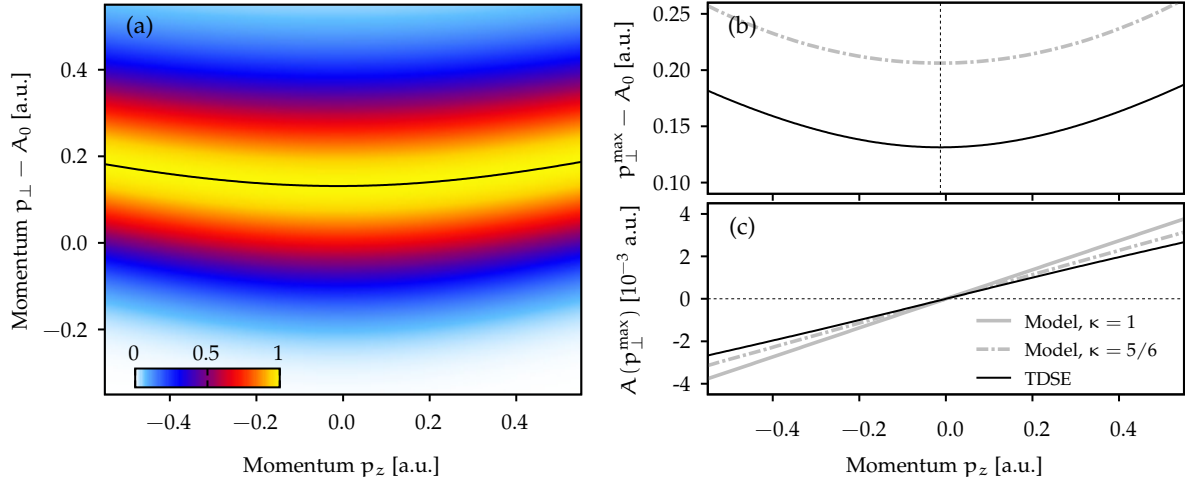


Figure 8.10: Analysis of the photoelectron momentum distributions from ionization of argon by circularly-polarized three-cycle laser pulses of 800 nm wavelength and 2×10^{14} W/cm² intensity calculated by numerical solution of the TDSE. (a) Distribution in the p_z - p_\perp -plane at $p_y = 0$. To study the most probable radial momentum for each p_z , every column is normalized individually. The resulting momentum-dependent maximum's position $p_\perp^{\max}(p_z)$ is shown as black line. A magnification of the line of maxima $p_\perp^{\max}(p_z)$ is shown in panel (b). There, the simplified result (8.45) for a nonadiabatic initial-velocity distribution is also depicted as gray dashed-dotted line. The thin dotted vertical line indicates the position of the minimal value of $p_\perp^{\max}(p_z)$ from TDSE. (c) Antisymmetrization $A(p_\perp^{\max}(p_z))$ as defined in Eq. (8.41) for the TDSE result as well as the simple man's estimates for an adiabatic ($\kappa = 1$) and a nonadiabatic initial distribution ($\kappa = 5/6$).

avoid the further complications of initial states carrying angular momentum, we use the potential

$$V(r) = -\frac{1 + \exp(-0.66r)}{\sqrt{r^2 + 0.5}}. \quad (8.40)$$

The resulting 1s state reproduces the ionization potential of argon and is considered as initial state in the TDSE simulations. We numerically calculate the photoelectron momentum distribution for ionization by circularly-polarized three-cycle pulses. Analogous to the approach in Ref. [170], we analyze a slice at $p_y = 0$ through the momentum distribution and normalize the radial distribution for fixed p_z individually (see Fig. 8.10(a)). For each p_z , the most probable momentum p_\perp^{\max} is determined by means of a Gaussian fit.²³ The maxima are located at larger radial momenta compared to the simple man's estimate of $p_\perp = A_0$ and have a close to parabolic shape as a function of p_z (see black line in Fig. 8.10(a)). In the dipole approximation, the function $p_\perp^{\max}(p_z)$ is forward-backward symmetric and the deviation compared to $p_\perp = A_0$ is mostly caused by nonadiabatic effects as described in Refs. [170, 354, 370–372]. In reality, as first experimentally observed in Ref. [473], the forward-backward symmetry is broken, i.e., the minimum of $p_\perp^{\max}(p_z)$ is not located at $p_z = 0$. The TDSE simulations confirm that the minimum is shifted to slightly negative p_z (see dotted vertical line in Fig. 8.10 (b)).

The parabolic shape of $p_\perp^{\max}(p_z)$ (already present in the dipole approximation) complicates the analysis of nondipole effects for circular polarization. To disentangle the (leading-order) nondipole effects from the symmetric contributions, the antisymmetrization of $p_\perp^{\max}(p_z)$ is considered

$$A(p_\perp^{\max}(p_z)) = \frac{p_\perp^{\max}(p_z) - p_\perp^{\max}(-p_z)}{2}. \quad (8.41)$$

In the dipole approximation, $A(p_\perp^{\max}(p_z))$ vanishes. However, the results from TDSE beyond the dipole approximation show an approximately linear dependence of $A(p_\perp^{\max}(p_z))$ on p_z (see Fig. 8.10(c)). The slope of $A(p_\perp^{\max}(p_z))$ around $p_z = 0$ can be determined by means of a fit

$$A(p_\perp^{\max}(p_z)) = \kappa \frac{A_0}{c} p_z + \dots \quad (8.42)$$

²³An iterative procedure is used where the fit range is centered around the previous maximum's position with a width of one quarter of the previous standard deviation σ .

Here, we introduced a dimensionless parameter κ . In the simple man's model of Section 8.3.1 based on an adiabatic initial-velocity distribution, we find $\kappa = 1$. However, the TDSE simulation for circular polarization of Fig. 8.10 only results in $\kappa \approx 0.75$.²⁴

The interplay between nonadiabatic initial-velocity offsets and nondipole effects can be studied by considering the momentum distributions of Eq. (8.38) from the SFA. We are only interested in leading-order nonadiabatic corrections and, hence, expand the SFA expression to first order in the Keldysh parameter γ . Alternatively, the same results can also be obtained by using the initial distribution of Eq. (8.16) and the mappings of initial velocities to final moment of Eqs. (8.24) and (8.26) (similar to the analysis in simple man's model of Section 8.3.1). We find that the global maximum of the distribution is located at (to first order in $1/c$)

$$p_z^{\max} \approx \frac{K_0}{c} + \frac{2I_p}{3c} \quad \text{and} \quad p_{\perp}^{\max} \approx A_0 + \frac{I_p}{3A_0}. \quad (8.43)$$

Already in the dipole approximation, the nonadiabatic effects displace the radial distribution by $\frac{I_p}{3A_0}$ (see also Eq. (5.9) and Ref. [354]). When inserting p_{\perp}^{\max} into Eq. (8.34), the nondipole shift p_z^{\max} of the global maximum is obtained in Eq. (8.43). Within this SFA treatment, we find that the most probable radial momentum as a function of p_z is given by

$$p_{\perp}^{\max, \text{SFA}}(p_z) \approx A_0 + \frac{1}{3A_0} \left(I_p + \frac{p_z^2}{2} \right) + \frac{A_0}{c} p_z, \quad (8.44)$$

where $p'_z = p_z - (K_0 + 2I_p/3)/c$ is the momentum relative to the global maximum. In the second term, an increased effective ionization potential results in a quadratic dependence of the nonadiabatic offset on the momentum p'_z in the light-propagation direction [170]. The gray dashed-dotted line in Fig. 8.10(b) shows the analytical result of Eq. (8.44). The too large nonadiabatic offset and the slightly different curvature compared to the TDSE result can be partially attributed to higher-order nonadiabatic corrections as well as to the influence of the electron-ion interaction [170].

At the global maximum (see Eq. (8.43)), the slope of $p_{\perp}^{\max, \text{SFA}}(p_z)$ in Eq. (8.44) is to first order in $1/c$ given by A_0/c . Importantly, the quadratic term in Eq. (8.44) is centered at the global maximum of the distribution and not at $p_z = 0$. Hence, when using the SFA result of Eq. (8.44) for the antisymmetrization in Eq. (8.41), we find²⁵

$$A(p_{\perp}^{\max, \text{SFA}}(p_z)) \approx \frac{5}{6} \frac{A_0}{c} p_z. \quad (8.45)$$

Even in the adiabatic limit ($\gamma \rightarrow 0$), the slope $\kappa = 5/6 \approx 0.83$ is changed compared to the simple man's model based on the adiabatic initial distribution. The difference is caused by the forward shift $\sim K_0/c$ of the distribution induced by the magnetic field. When only taking spatially-homogeneous fields during the continuum propagation into account, the SFA-based model already predicts a nonvanishing slope for the antisymmetrization that is given by $\kappa = -1/6$. We can conclude that the deviation between the slope from TDSE and the simple man's model ($\kappa = 1$) can be mainly attributed to the interplay between nonadiabatic initial-velocity offsets and nondipole effects.

Wavelength and intensity scaling

In the simple man's model, the slope of the nondipole shift $p_z^{\max}(p_{\perp})$ as a function of p_{\perp} and the slope of the antisymmetrization $A(p_{\perp}^{\max}(p_z))$ as a function of p_z scale linearly with the parameter A_0/c . Thus, we expect both slopes to increase with the intensity and wavelength of the radiation. For the argon model of Eq. (8.40) with an 1s initial state and short three-cycle laser pulses, we perform two parameter scans: The wavelength is scaled between 454 nm and 2400 nm for a fixed intensity of 2.5×10^{14} W/cm² or the intensity is scaled between 1.0×10^{14} W/cm² and 5.0×10^{14} W/cm² for a fixed central wavelength of 800 nm. The results cover a range of Keldysh parameters between 0.34 and 1.8. The slopes of $p_z^{\max}(p_{\perp})$

²⁴The slope is determined by means of a cubic fit to the p_z -range between -0.1 and 0.1 a.u.

²⁵In principle, a second term of the form $(I_p p_z)/(A_0 c)$ appears. However, compared to A_0/c , this term is on the order of γ^2 , but our derivation is only consistent to first order in γ .

at $p_{\perp} = A_0$ and of $A(p_{\perp}^{\max}(p_z))$ at $p_z = 0$ are determined as explained above. The results are shown in units of A_0/c in Figs. 8.11 and 8.12. In addition, TDSE results for a short-range potential given by

$$V(\mathbf{r}) = -\frac{3.36 \exp(-0.7\sqrt{r^2 + 0.2})}{\sqrt{r^2 + 0.5}} \quad (8.46)$$

with an 1s initial state and the same ionization potential as argon are presented.

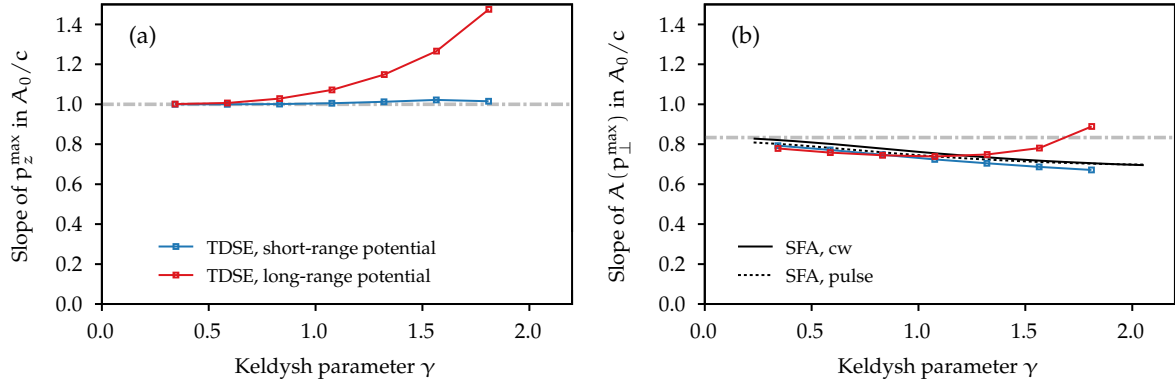


Figure 8.11: Dependence of the electric nondipole effect on the laser wavelength at a constant intensity of $2.5 \times 10^{14} \text{ W/cm}^2$. (a) Slope of the function $p_z^{\max}(p_{\perp})$ evaluated at $p_{\perp} = A_0$ and (b) slope of the function $A(p_{\perp}^{\max}(p_z))$ evaluated at $p_z = 0$ in units of A_0/c . The blue and red lines are the TDSE results for an argon atom modeled by a short-range potential (8.46) and a long-range potential (8.40), respectively. The gray lines show the adiabatic estimates of one for panel (a) and of $5/6$ for panel (b). In addition, the black lines in panel (b) indicate the results from the saddle-point SFA for a cw field (solid line) and for a three-cycle pulse (dotted line) as used in the TDSE simulations.

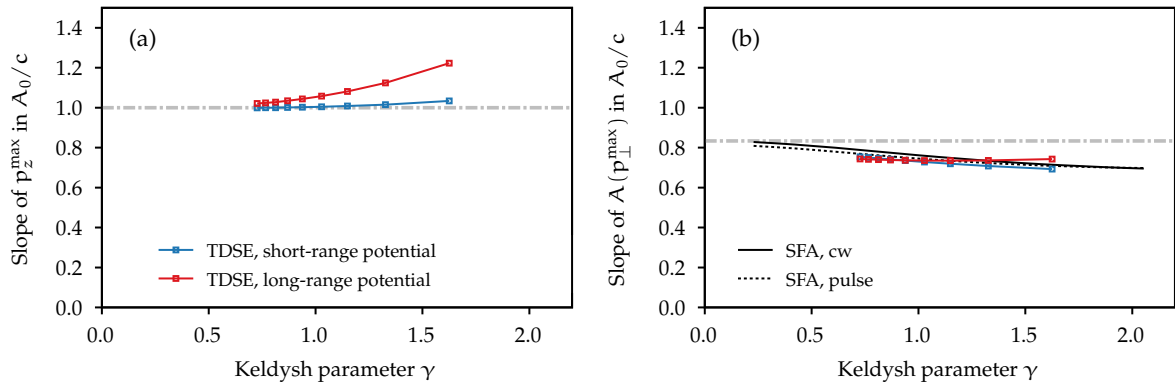


Figure 8.12: Dependence of the electric nondipole effect analogous to Fig. 8.11, but for various intensities at a fixed central wavelength of 800 nm. The SFA results are the same as in Fig. 8.11.

For the short-range potential, the slope of $p_z^{\max}(p_{\perp})$ perfectly follows the adiabatic result A_0/c of Eq. (8.34) for all studied laser parameters. Here, nonadiabatic corrections to the slope of $A(p_{\perp}^{\max}(p_z))$ are also visible for the short-range potential. For a circularly-polarized cw field, it can be shown in the SFA framework that both slopes expressed in units of A_0/c only depend on the Keldysh parameter γ . Already in the strong-field approximation, we find that higher-order nonadiabatic corrections appear for the slope of $A(p_{\perp}^{\max}(p_z))$ (compared to the first-order nonadiabatic estimate of Eq. (8.45)). The numerically-determined slope for the PMD in SFA (see Eq. (8.37)) is shown as black solid lines in panels (b) of Figs. 8.11 and 8.12 and very well reproduces the TDSE results for the short-range potential.

For sufficiently adiabatic ionization conditions, the slopes for short-range and long-range potentials are in very good agreement. However, deviations arise when the Keldysh parameter increases, i.e., when the ionization process becomes more nonadiabatic.²⁶ To include the influence of the ionic potential in the SFA framework, we extended the analytical R-matrix (ARM) method introduced in Section 2.5

²⁶Note that even for a Keldysh parameter of one the deviations are smaller than 10%.

beyond the electric dipole approximation. The resulting theory systematically includes nondipole effects, nonadiabaticity and the ionic potential. Additional simulation showed that the nondipole ARM method is capable of reproducing the differences between long-range and short-range simulations.

Finally, we compare the theoretical simulations to experimental results. The slope of $p_z^{\max}(p_{\perp})$ observed in the experiment [51] for argon is in very good agreement with the theoretical prediction (see Fig. 8.9). However, for the same data set, Hartung *et al.* also determined slope of $A(p_{\perp}^{\max}(p_z))$ and found a value of $(1.69 \pm 0.62) A_0/c$ [436, 473] which is larger than the theoretical prediction. Surprisingly, for xenon ionized by laser pulses with 800 nm wavelength, slopes of $(1.51 \pm 0.31) A_0/c$ at $6.8 \times 10^{13} \text{ W/cm}^2$ intensity and of $(3.1 \pm 0.1) A_0/c$ at $1.2 \times 10^{14} \text{ W/cm}^2$ were measured by Hartung and Lin *et al.* [436].²⁷

To model the measurements for xenon atoms, we repeat the TDSE simulations and use a pseudopotential based on the Tong-Lin potential for the 5p states (see Appendix A.2.3). Again, three-cycle laser pulses with 800 nm central wavelength are considered. If the spin-orbit splitting is neglected, the outermost sub-shell of the ground state of xenon is formed by three degenerate p orbitals (p_+ , p_- and p_0). Figure 8.13 separately shows the dependence of the slope of $A(p_{\perp}^{\max}(p_z))$ on the intensity for the p_{\pm} initial states. Even though the slopes for both states differ slightly, the difference compared to the SFA result (for an 1s state) is smaller than 15% for all studied intensities. As expected, using the incoherent sum of the distributions for p_{\pm} states, the result for the slope is in between the results for the individual p states. We also confirmed that the inclusion of the remaining p_0 orbital leads only to insignificantly smaller values of the slope.²⁸ Therefore, for a broad range of laser intensities and wavelength, our simulations predict significantly smaller slopes compared to the experimental measurements.

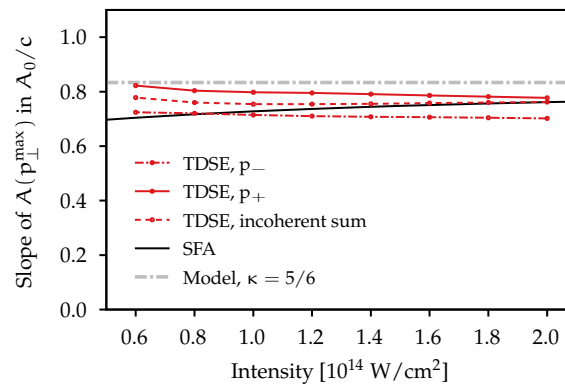


Figure 8.13: Dependence of the slope of $A(p_{\perp}^{\max}(p_z))$ evaluated at $p_z = 0$ on the light intensity for xenon ionized by three-cycle laser pulses with 800 nm central wavelength: results for initial p_+ and p_- orbitals from TDSE (red solid and dashed-dotted lines), the result for the incoherent sum of their distributions (red dashed line), and the SFA result (black line). The gray dashed-dotted line indicates the adiabatic limit of $5/6$. Figure is adapted from Hartung *et al.* [436].

We performed several additional calculations to explore the quantitative difference between the slopes in experiment and theory. Using the SFA as well as the nondipole version of ARM theory, we found that, for reduced ellipticity of the radiation, the slope of $A(p_{\perp}^{\max}(p_z))$ depends on the angle ϕ_p in the polarization plane. For an ellipticity of 0.75, the slope is increased by about 60% along the directions of the major axis of the polarization ellipse compared to the directions along the minor axis. However, when averaging the distribution over the angle ϕ_p , the resulting slope is only increased by about 25% compared to circular polarization. Furthermore, focal-volume averaging causes insignificant changes of the slopes. In principle, the spin-orbit splitting of the valence states in the xenon ion is quite significant. We investigated this effect in the SFA framework following the ideas in Ref. [476] which is able to predict the spin polarization in strong-field ionization of heavy noble gas atoms [477]. However, for the nondipole effects, we found that spin-orbit splitting changes the extracted slopes by less than 5%.

All these uncertainties in the experiment and in the theoretical modeling can potentially explain the moderate deviations of the slopes observed for argon and xenon at the lower laser intensities. However,

²⁷The stated errors are statistical errors.

²⁸For the experimentally-relevant intensities, the slope changes by less than 10%.

the significantly-increased slope observed in the xenon experiment at higher intensity warrants further research. Possibly, some of the applied theoretical approximations need to be reconsidered. For example, the ionic potential was approximated by means of a pseudopotential and, thus, the initial state is effectively treated as a 2p state in contrast to the physical 5p state. In addition, this possibly leads to a nonphysical structure of the excited states and, hence, could influence the field dressing of the initial state present at high intensities [478]. Multielectron effects were also not considered in the simulations either.

8.4 Conclusion

In this chapter, an in-depth analysis of photoelectron momentum distributions from strong-field ionization beyond the electric dipole approximation was presented. The total linear momentum of the photons absorbed during ionization is transferred to the photoelectron and the residual ion. For recollision-free ionization, we investigated the amount of momentum delivered to the photoelectron which results in an overall shift of the photoelectron momentum distribution in the light-propagation direction, i.e., a nonzero average forward momentum. Most previous studies observed the total average momentum in the light-propagation direction. However, in order to extract additional information, we considered the partial average and showed that the momentum transfer depends on the final momentum of the electron in the polarization plane. Studying this differential observable allowed us to deepen the picture of the underlying physical mechanisms. Previously, the forward momentum was divided into a contribution from the tunnel ionization [150, 151] and a contribution from the continuum motion [147, 149]. An important message of this chapter is that the continuum contribution is proportional to the kinetic energy ΔE gained due to the acceleration in the laser field and *not* to the final kinetic energy of the electrons.

In order to time resolve the momentum transfer on a subcycle time scale, attoclock settings can be used [435]. We theoretically studied this protocol for both an elliptical and a quasilinear attoclock configuration. In agreement with the experimental observation in Ref. [435], we found that the point of minimal momentum transfer corresponds rather to the point where the maximum yield in a Coulomb-free situation is expected than to the actual Coulomb-shifted attoclock maximum of the yield. Considering a classical model, we showed that, to leading order, the Coulomb interaction does indeed not shift the point of minimal momentum transfer. In contrast to the quasilinear setting, nonadiabatic tunneling modifies the angle-resolved momentum transfer in elliptically-polarized fields. To explore the influence of nonadiabaticity on the liberated electron wave packet at the tunnel exit, we applied the classical backpropagation approach. For elliptical polarization, nonadiabatic effects cause a slight subcycle modulation of the average forward velocity at the tunnel exit. However, since this modulation is much smaller than the angular dependence of momentum transfer in the final electron wave packet, it is hard to observe the subcycle variation experimentally. The Coulomb interaction does not only influence the continuum motion, but also the tunneling step. Surprisingly, we found that the Coulomb effects on the momentum transfer during both steps nearly cancel each other. Hence, the nondipole forward shifts of the experimentally-accessible final electron momentum distributions are usually well approximated by the potential-free estimate.

When considering both the laser magnetic field and the spatial inhomogeneity of the electric field during the continuum propagation, their effects compensate each other for the motion along the polarization plane and, effectively, only the final momentum along the light-propagation direction is influenced by nondipole effects. However, within a classical description, we can separately study magnetic and electric nondipole effects on the photoelectron momentum distributions. To characterize their imprint, we analyzed two observables: (i) the most probable momentum $p_z^{\max}(p_{\perp})$ in the light-propagation direction as a function of the radial momentum in the polarization plane and (ii) the most probable radial momentum $p_{\perp}^{\max}(p_z)$ as a function of the momentum in the light-propagation direction. Under adiabatic conditions, the magnetic field effectively leads to a uniform forward shift of the electron mo-

mentum distribution, i.e., the slopes of $p_z^{\max}(p_{\perp})$ and $p_{\perp}^{\max}(p_z)$ vanish. However, for different initial electron velocities in the light-propagation direction, the spatial dependence of the electric field induces slightly different effective frequencies of the force due to the laser field experienced by electrons. This leads to a shearing of the momentum distribution and is reflected by finite slopes of both $p_z^{\max}(p_{\perp})$ and $p_{\perp}^{\max}(p_z)$. Analyzing the momentum distributions from the numerical solution of the TDSE for a quasi-linear field, we indeed found nonvanishing slopes for both observables and a perfect agreement with the simple man's prediction. For circularly-polarized fields, the momentum dependence of the forward shift $p_z^{\max}(p_{\perp})$ from TDSE also follows the simple man's model and agrees very well with experimental data [51]. However, in circular polarization, we discovered that the momentum dependence of the most probable radial momentum $p_{\perp}^{\max}(p_z)$ is influenced by nonadiabatic effects.

In the future, the application of tailored laser fields could improve the visibility and allow for a separation of the different nondipole contributions in photoelectron momentum distributions. For example, the comparison of the momentum transfer between co- and counter-rotating bicircular fields [170] could enable a cleaner experimental observation of the interplay between nonadiabatic and nondipole effects. To this end, the combination of an elliptically-polarized field with its circularly-polarized third harmonic could also be advantageous, because this field configuration may provide a constant magnitude of the vector potential combined with a time-dependent magnitude of the electric field. In addition, the interplay between nondipole and Coulomb effects is only barely investigated for recollision-free ionization (see for example Refs. [479–481]). In the first preliminary simulations, we found that the nondipole effects also influence the momentum-dependent attoclock offsets discussed in Chapter 5. This might allow the investigation of nondipole corrections of the tunnel-exit positions. Such a study would also be particularly important to rule out nondipole contributions in the attoclock studies of chiral molecules as in Refs. [344, 360].

Usually, the nondipole effects in recollision-free strong-field ionization are dominated by the influence of the electromagnetic field far away from the parent ion. Hence, the nondipole modifications of photoelectron momentum distributions are only weakly susceptible to the electronic structure of the target. However, the disagreement between the experimental measurement for xenon [436] and our theoretical prediction for the momentum dependence of the most probable radial momentum $p_{\perp}^{\max}(p_z)$ could suggest that the nondipole effects are influenced by the complex electronic structure. To resolve the differences, the development of theoretical methods including both multielectron and nondipole effects could be crucial. Furthermore, in order to study the target dependence of nondipole effects in recollision-free scenarios, it could be interesting to scale the internuclear distance of diatomic molecules [482] and observe the transition from an "atomic-like" behavior for small distances to a molecular-interference-dominated regime for large distances.

Chapter 9

High-Order Above-Threshold Ionization Beyond the Electric Dipole Approximation

9.1 Introduction

During the ionization process in linearly-polarized fields liberated electrons may be driven back to the parent ion and may elastically scatter off the ionic potential (see Chapter 3). Electrons that are scattered into large angles and that are subsequently further accelerated by the laser field can reach high kinetic energies. Thus, this process is known as high-order above threshold ionization (HATI). The high-energy contributions form a plateau in the photoelectron energy spectra reaching up to the famous $\approx 10 U_p$ cutoff [16, 17]. Classically, for large angle scattering, the electrons need to come close to the parent ion during recollision. Hence, the HATI process is very sensitive to the details of the ionic potential and can be used for atomic and molecular imaging (as suggested in Refs. [33, 34]). In the laser-induced electron diffraction (LIED) technique, structural information of the ionic species is encoded in the diffraction pattern visible in the photoelectron momentum distributions. LIED was used to retrieve differential cross sections (DCS) of atoms [36–38] and to measure static bond lengths in molecules [41]. Since the rescattering process occurs within an optical cycle after the liberation of the electrons, the nuclear dynamics in molecules [40, 42] as well as the electronic valence-shell dynamics [31] can be monitored. In almost all works on HATI, the dipole approximation is employed to interpret the electron momentum distributions. However, recently mid-infrared few-cycle laser sources were used in LIED to achieve high scattering energies and to drive recollisions in the quasistatic regime (see for example Ref. [42]). As motivated in Section 2.1.2, for these long wavelengths, the dipole approximation is questionable.

In general, the theory of recollision-based phenomena in strong fields beyond the electric dipole approximation has already a considerable history. However, most works on high-energy recollisions focus on high-harmonic generation [186, 189, 483–486] or nonsequential double ionization [487–491]. For single ionization, recollision-based processes were either studied at low kinetic energies (see Chapter 10) or in extremely intense fields [192, 457, 492, 493]. In our previous work [187] that was related to my master thesis [160], we discussed the high-energy region of the photoelectron momentum distributions for ionization of helium in the regime of moderate laser intensities. The distributions were calculated by numerical solution of the TDSE in 2D beyond the electric dipole approximation. Compared to recollision-free ionization (see Chapter 8), the nondipole effects and, especially, the momentum transfer to the photoelectrons are vastly different in HATI. The central finding in Ref. [187] was a modification of the shape of the plateau region, which can be explained in terms of a nondipole extension of the three-step model. In addition, the emission probability differs in forward and backward directions, which is outside the scope of a purely kinematic model. During the recollision of the electron with the

much heavier ion an arbitrary amount of momentum can be exchanged and, thus, no universal scaling of the transferred momentum with respect to the light parameters exists. Instead, the asymmetry and, hence, the transferred momentum strongly depend on the target gas [160].

To properly model the emission strength of the photoelectron momentum distributions, quantum-mechanical theories need to be considered. As introduced in Section 2.3, scattering can be included in the context of the strong-field approximation by means of Born series what was introduced in Refs. [197, 494] and later on extended beyond the dipole approximation in Ref. [457]. The application of a saddle-point approximation leads to a simplified analytical treatment and provides an intuitive interpretation of the physical processes [110, 111]. In the improved SFA, the scattering process is treated in the first Born approximation (1BA). Hence, the quality of the results strongly depends on the energy of the scattering electrons, on the dimensionality of the problem and on the shape of the potential. To describe laser-assisted scattering beyond the 1BA, Kroll and Watson derived a low-frequency approximation (LFA) in the context of laser-assisted electron-atom scattering [495]. The LFA was later introduced to the context of HATI (in the dipole approximation) by Milošević *et al.* [496, 497]. This approach enables a derivation of the factorization of probability amplitudes in HATI into one factor describing the field-free elastic scattering and another factor representing the returning electron wave packet. Under additional assumptions, this results in the quantitative rescattering theory (QRS) [36, 498].

In this chapter, the nondipole effects in the HATI process are further investigated and, especially, their sensitivity to the atomic and molecular structure is explored. The various nondipole modifications of the photoelectron momentum distributions are first introduced by considering distributions for ionization of small molecules from the numerical solution of the TDSE. As a prototypical of diatomic molecules, the hydrogen molecular ion H_2^+ is considered for the special cases of parallel and perpendicular alignment of the molecular axis relative to the ionizing field.¹ We show that the nondipole modifications of the molecular-interference pattern are orientation dependent. To shed light on the ongoing processes, we consider a nondipole three-step model as introduced in my master thesis [160] and Ref. [187]. Later, in the first experiment on nondipole effects in HATI by Lin *et al.* [500], xenon was ionized by strong laser pulses and the nondipole shift of the central maximum in the momentum distribution was analyzed. We consider a quantum-orbit model based on a nondipole generalization of the low-frequency approximation to quantitatively interpret the photoelectron momentum distributions for xenon. The appearing nondipole shift can also be intuitively explained based on the classical three-step model. Interestingly, we find that the nondipole shifts of the central maximum are different for atoms such as xenon and molecules such as H_2^+ .

The first part of this chapter considers strong-field ionization of the hydrogen molecular ion H_2^+ beyond the electric dipole approximation. Some of these results are published in Ref. [501]. The second part of this chapter on the HATI process for xenon is based on joint work with the group of Reinhard Dörner in Frankfurt, especially Kang Lin. For the publication [500], Lin *et al.* performed the experiment based on the COLTRIMS technique, Ni *et al.* provided data from TDSE simulations and we developed a simplified interpretation based on the three-step model as well as a more advance description based on the LFA.

9.2 Anatomy of nondipole effects in HATI

9.2.1 Computational details

We focus on the dynamics in linearly-polarized fields. To this end, n_p -cycle laser pulses described by the following vector potential are used

$$\mathbf{A}(\eta) = -\frac{E_0}{\omega} \sin(\omega\eta - \phi_{\text{CEP}}) \cos^4\left(\frac{\omega\eta}{2n_p}\right) \mathbf{e}_x. \quad (9.1)$$

¹At about the same time, the photon-momentum transfer in strong-field ionization of H_2^+ was also considered in Ref. [499]. There, however, the main focus was on the total momentum transfer in recollision-free ionization.

Here, $\eta = t - z/c$ is the light-cone coordinate. The chosen frequency of $\omega = 0.05695$ a.u. corresponds to 800 nm wavelength and E_0 is the electric-field strength. If not stated otherwise, the carrier-envelope phase is $\phi_{\text{CEP}} = 0$. The electric field points along the x -axis of the coordinate system and the corresponding magnetic field points along the y -axis (see also Eq. (2.1)).

To illustrate the dependence of the nondipole effects on the structure of the target, we first study the hydrogen molecular ion modeled in 2D as described in Ref. [502] with the potential

$$V(\mathbf{r}) = \frac{-1}{\sqrt{(\mathbf{r} - \mathbf{R}/2)^2 + \epsilon}} + \frac{-1}{\sqrt{(\mathbf{r} + \mathbf{R}/2)^2 + \epsilon}}. \quad (9.2)$$

The soft-core parameter is chosen as $\epsilon = 0.5$ such that the ground-state energy of ≈ -1.11 a.u. is reproduced. The nuclei are kept fixed during the time evolution at the equilibrium internuclear distance of $R = 2$ a.u. The molecular axis \mathbf{R} is either aligned parallel or perpendicular to the electric field. This choice ensures that in the dipole approximation the system is symmetric under the interchange of the forward and backward directions (invariant under reflections at the x -axis).

For the introduced plane-wave laser pulse, the electron dynamics is modeled by numerical simulations of the TDSE in 2D. Analogous to Chapter 7, we use Fourier split-operator technique on Cartesian grids (see Appendix A.2.2) and employ the natural gauge introduced in Section 2.2. A numerical grid of size 409.6×409.6 a.u. with spacings of $\Delta x = \Delta z = 0.1$ a.u. and a time step of $\Delta t = 0.003$ a.u. is used. After the end of the laser pulse, the electron momentum distributions are calculated with a resolution of $\Delta p_x = 0.0077$ a.u. and $\Delta p_z = 0.0038$ a.u.

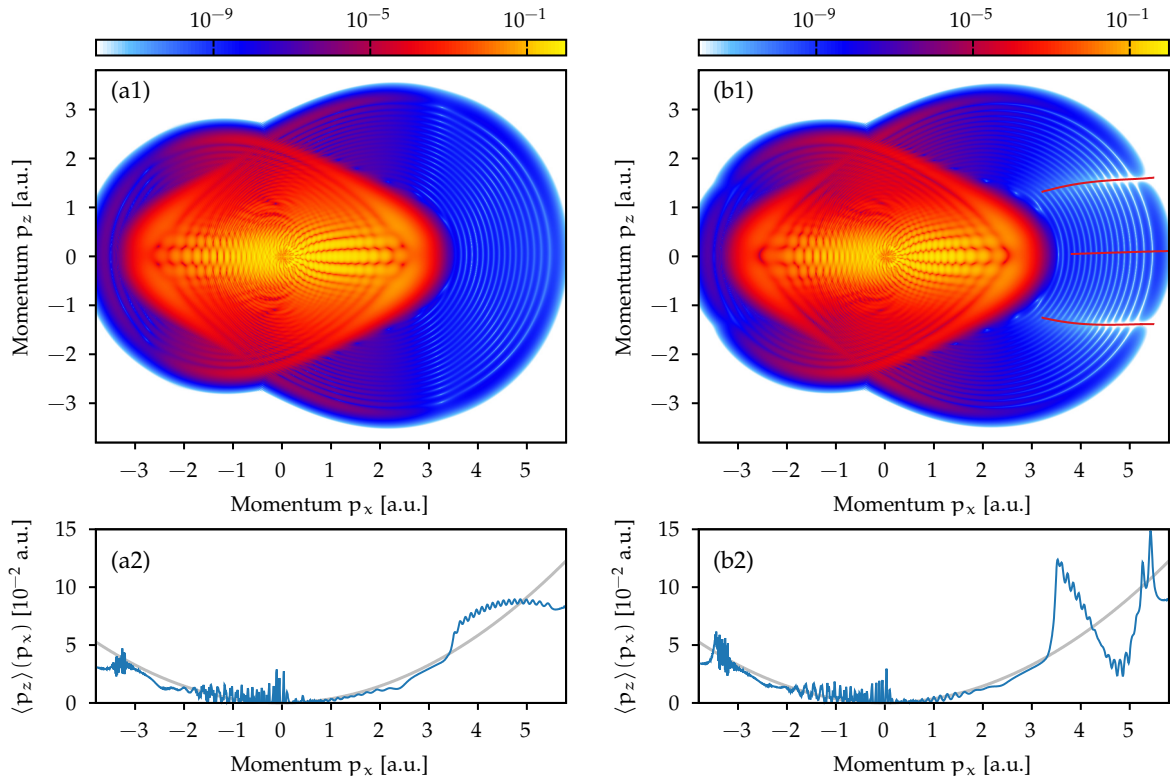


Figure 9.1: Photoelectron momentum distributions for ionization of H_2^+ with parallel (panel a1) and perpendicular (panel b1) alignment of the molecular axis with respect to the electric field by four-cycle pulses with 8×10^{14} W/cm² intensity from TDSE simulations. The red lines in panel b1 indicate the numerically-determined positions of the molecular-interference maximum and minima. [(a2),(b2)] Corresponding partial averages $\langle p_z \rangle(p_x)$ and the heuristic estimate $p_x^2/(2c)$ (gray lines). Figure is adapted from Brennecke *et al.* [501].

9.2.2 TDSE results for the hydrogen molecular ion

The photoelectron momentum distributions for ionization of the hydrogen molecular ion H_2^+ by four-cycle laser pulses obtained by the numerical solution of the TDSE are shown in Fig. 9.1. Panel (a1) and panel (b1) contain the results for parallel and perpendicular alignment of the molecular axis with respect to the electric field. Both PMDs exhibit the same overall structures that are familiar for linearly-polarized pulses (see Chapter 3 for an introduction). The strong contributions of direct and forward-scattered electrons are concentrated along the p_x -axis and approximately reach up to the classical cutoff for nonscattered electrons (here at $|p_x| \approx 2.8$ a.u.). This region of the PMD will be further discussed in Chapter 10.

HATI leads to the weaker contribution of high-energy electrons, covering a large range of lateral momenta p_z [16, 17]. The asymmetry of the PMD along the polarization axis (between the positive and the negative p_x -direction) is caused by the shortness of the laser pulse [111, 249–251]. For the chosen CEP ($\phi_{\text{CEP}} = 0$), the rescattering electrons with the highest energies are emitted in positive p_x -direction. However, the observations in this chapter can also be transferred to multi-cycle femtosecond laser pulses usually used in strong-field experiments. The plateau-like structure for $p_x > 0$ is overlaid by nearly-circular interference rings caused by the interference of long and short rescattering trajectories [18, 202, 503]. The outermost ring, i.e., the boundary of this plateau-like structure, is significantly broader than the other interference fringes and is called backward rescattering ridge (BRR) [36].

The shape of the electron momentum distribution in the HATI region is influenced strongly by the differential cross section that depends on the target structure [36, 498]. For the H_2^+ , the returning electron wave packets scatter off the two centers of the diatomic molecular ion. The interference of these two possible pathways creates a double-slit interference pattern in the DCS and, hence, results in a nontrivial structure-dependent variation of the yield [39, 504]. For perpendicular alignment, pronounced minima appear parallel to the p_x -axis (see the red lines in Fig. 9.1(b1)). For parallel alignment, a reduced emission strength is also visible along a line nearly parallel to the p_z -axis at $p_x \approx 3.3$ a.u.

Due to the inclusion of nondipole effects, the PMDs are not forward-backward symmetric along the light-propagation direction (z -direction). For each momentum p_x in polarization direction, the nondipole effects can be quantified by means of the partial average $\langle p_z \rangle(p_x)$ of Eq. (8.4) (see Figs. 9.1(a2) and (b2)). For momenta smaller than the classical cutoff, the average $\langle p_z \rangle$ roughly follows the simplest

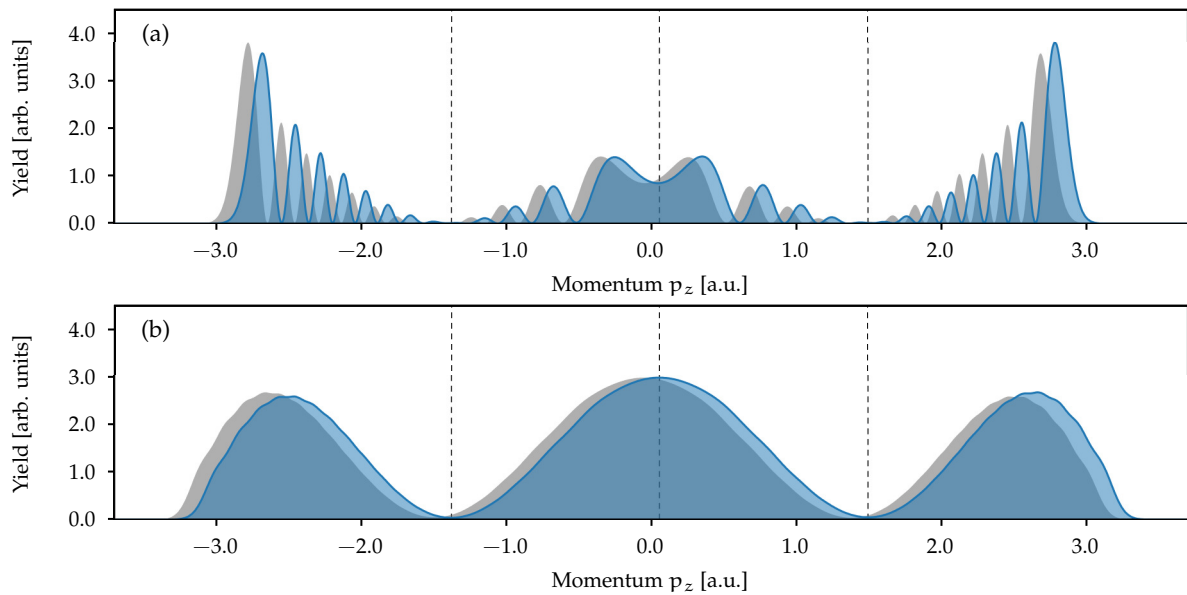


Figure 9.2: 1D slices at $p_x = 4$ a.u. through the photoelectron momentum distributions for perpendicular alignment (blue lines): result for a single intensity of 8×10^{14} W/cm² as in Fig. 9.1 (panel a) and focal-volume-averaged result for a peak intensity of 9.5×10^{14} W/cm² (panel b). To highlight the nondipole effects, the mirror images, i.e., 1D slices through $w(p_x, -p_z)$, are shown additionally (gray lines).

classical estimate $p_x^2/(2c)$ for recollision-free ionization (see Chapter 8). In contrast, the average $\langle p_z \rangle$ deviates strongly from the parabolic estimate at high electron energies [187]. For parallel alignment, the partial average is approximately independent on p_x between $p_x \approx 3.5$ a.u. and $p_x \approx 6$ a.u. and, thus, it is quite similar to our findings for helium [187]. However, for perpendicular alignment, a pronounced local minimum appears in the partial average. This shows already that the nondipole effects in the HATI region are highly sensitive to the molecular orientation and more generally to the target structure.

The nondipole modifications are only barely visible in the full 2D distributions. Therefore, a slice through the PMD for perpendicular alignment at $p_x = 4$ a.u. is shown in Fig. 9.2(a). The following three major deviations compared to the dipole approximation are visible:

- (i) The boundary of the rescattering plateau represented by the location of the BRR structure is shifted along the light-propagation direction [187]. In addition, the interference extrema caused by the superposition of the short and long rescattering trajectories are displaced [187]. We find that these shifts are nearly independent of the molecular alignment and they agree with the result for helium within the numerical accuracy [187].
- (ii) When considering one interference maximum in forward direction and one in backward direction, their probabilities are in general different [187]. For example, the signal on the BRR in forward direction is up to 17% higher than in backward direction for perpendicular alignment. We find that this effect depends strongly on the used targets and, for molecules, also on their orientation.
- (iii) The molecular-interference pattern is modified. The positions of the corresponding broad minima and maxima are shifted in the light-propagation direction (see the red solid lines in Fig. 9.1(b) and the dashed vertical lines in Fig. 9.2(a)). We find that the shifts depend on the momentum component along the polarization direction and increases from ≈ 0.05 a.u. at $p_x \approx 4$ a.u. to ≈ 0.12 a.u. at $p_x \approx 6$ a.u.

In a real experiment, the contributions of the whole laser focus influence the the measured signal. We mimic this effect by averaging several TDSE distributions for different intensities (see Section A.2.4). For a peak intensity of $I_{\text{peak}} = 9.5 \times 10^{14}$ W/cm², a slice at $p_x = 4$ a.u. through the focal-volume-averaged distribution is shown in Fig. 9.2(b). Since the interference pattern of long and short trajectories is very susceptible to changes of the light intensity [18], these fringes are not visible in the averaged distribution. Even though the boundary of the scattering plateau is smeared out, the shift of the BRR and the asymmetry of the yield can in principle be observed. Importantly, the molecular-interference pattern are very prominent in the averaged distribution and, especially, their nondipole shift is preserved. Hence, the nondipole modifications of these structure-dependent features in the PMD are very promising for experimental observation of nondipole effects in HATI.

9.3 Simple man's model beyond the dipole approximation

To reveal the physics beyond high-order above-threshold ionization, we use a nondipole extension of the three-step model [10, 16] (see Section 2.1.1). The model was first introduced in Ref. [187] and in my master thesis [160] such that the following section is based on these previous works. Here, the dynamics is divided into a sequence of four well-separated steps: (i) laser-induced ionization, (ii) acceleration of the released electron away and back to the parent ion by the light field, (iii) scattering off the ionic potential, and (iv) further acceleration by the electromagnetic field.

Tunneling ionization launches electrons at each release time t_0 with initial velocities $\mathbf{v}_0 \perp \mathbf{E}(t_0)$. The subsequent motion of the electron in the presence of the electromagnetic field is described classically by Newton's equation. For certain ionization times, a part of the electron wave packet is driven back to the vicinity of the ionic core at $\mathbf{r} = 0$. If we neglect the influence of the ionic potential, the time-dependent velocity of an electron starting at $\mathbf{r} = 0$ can be determined similar to Section 2.1.2 and it is to first order

in $1/c$ given by

$$\dot{\mathbf{r}}(t) = \mathbf{v}_0 - \mathbf{A}(t_0) + \mathbf{A}(t) + \frac{\mathbf{e}_z}{c} \left(\frac{1}{2} \mathbf{A}^2(t_0) - \mathbf{v}_0 \cdot \mathbf{A}(t_0) \right) + \frac{\mathbf{e}_z}{c} \left((\mathbf{v}_0 - \mathbf{A}(t_0)) \cdot \mathbf{A}(t) + \frac{1}{2} \mathbf{A}^2(t) \right). \quad (9.3)$$

Integrating (9.3) again, the electron's position reads

$$\begin{aligned} \mathbf{r}(t) = & (\mathbf{v}_0 - \mathbf{A}(t_0)) (t - t_0) + \boldsymbol{\alpha}(t, t_0) \\ & + \frac{\mathbf{e}_z}{c} \left(\frac{1}{2} \mathbf{A}^2(t_0) - \mathbf{v}_0 \cdot \mathbf{A}(t_0) \right) (t - t_0) + \frac{\mathbf{e}_z}{c} \left((\mathbf{v}_0 - \mathbf{A}(t_0)) \cdot \boldsymbol{\alpha}(t, t_0) + \frac{1}{2} \alpha_2(t, t_0) \right) \end{aligned} \quad (9.4)$$

with $\boldsymbol{\alpha}$ and α_2 defined in Eq. (2.11). To first order in $1/c$, the nondipole part of the Lorentz force only modifies the trajectory (9.4) along the light-propagation direction. Hence, for an exact return to the ionic core at $\mathbf{r} = 0$, the motion in polarization direction leads to the condition

$$0 = x(t_0) = x(t_c) = -A_x(t_0)(t_c - t_0) + \alpha_x(t_c, t_0). \quad (9.5)$$

The condition defines the relation between the release time t_0 and the return (or collision) time t_c . For the four-cycle laser pulses used in Fig. 9.1, only one half cycle of ionization times is relevant for the high-energy region with $p_x > 0$. Figure 9.3(a) shows the corresponding mapping of excursion time $t_c - t_0$ as a function of the energy at time of return t_c . Due to the shortness of the pulse, the maximal return energy of about $2.79 \frac{E_0^2}{4\omega^2}$ is slightly reduced compared to the maximal energy of about $3.17 \frac{E_0^2}{4\omega^2}$ in a cw field [10]. Below this classical cutoff, there are two distinct times of ionization with the same return energy. For each energy, the trajectory with larger excursion time is referred to as long trajectory whereas the other is denoted as short trajectory.

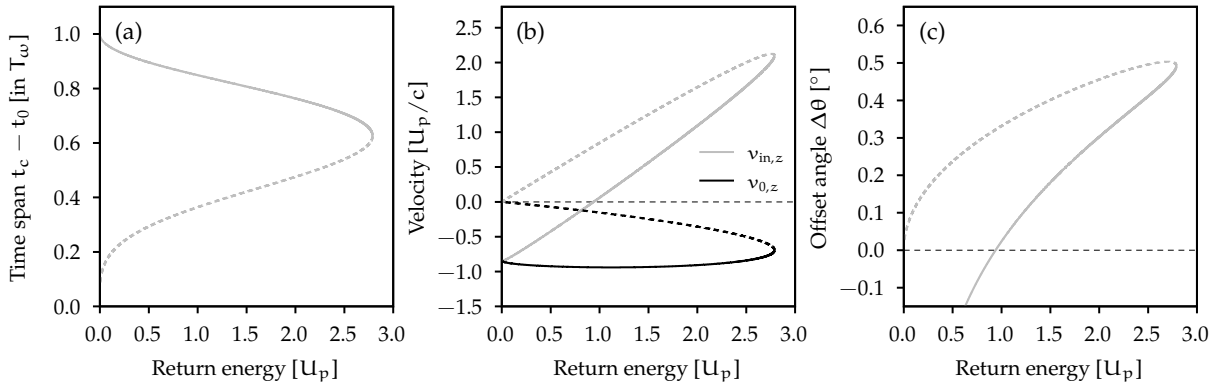


Figure 9.3: Properties of the simple man's trajectories as a function of the recollision energy in units of $U_p = \frac{E_0^2}{4\omega^2}$ for the laser parameters of Fig. 9.1. (a) Time difference between ionization and recollision in units of optical cycles T_ω . (b) Components in the light-propagation direction of the initial velocity $v_{0,z}$ and of the incoming velocity $v_{in,z}$. (c) Offset angle $\Delta\theta$ of the incoming electron with respect to the polarization axis. The observables for short (long) trajectories are shown as dashed (solid) lines. Figure is adapted from Brennecke *et al.* [501].

As illustrated in Fig. 2.3(b), the magnetic part of the Lorentz force causes a drift motion of the electron in the light-propagation direction such that the center of the electron wave packet does not exactly return to its initial position [189]. Classically, small impact parameters only lead to large scattering angles. For an exact return to the initial position $\mathbf{r} = 0$ at the collision time t_c , a small initial velocity $\mathbf{v}_0 = -|v_0|\mathbf{e}_z$ of the electron pointing against the propagation direction of the light is necessary. The required initial velocity is given by

$$v_{0,z} = -\frac{1}{2c(t_c - t_0)} \int_{t_0}^{t_c} d\tau (\mathbf{A}(\tau) - \mathbf{A}(t_0))^2 \quad (9.6)$$

and is shown in Figure 9.3(b) as a function of the return energy. The absolute values of the initial velocity are larger for long trajectories, because these are more strongly displaced by the Lorentz force than short trajectories.

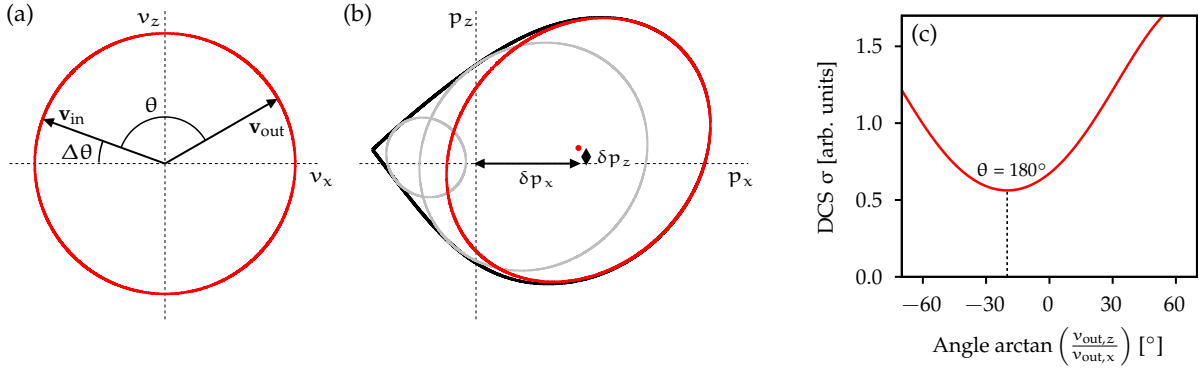


Figure 9.4: Schematic illustrations with exaggerated value of $1/c$: (a) scattering circle in the v_x - v_z -plane on which the possible outgoing velocities \mathbf{v}_{out} (shortly after scattering) lie for a given incoming velocity \mathbf{v}_{in} (shortly before scattering). Due to the nondipole part of the Lorentz force, the incoming velocity is at an angle $\Delta\theta$ relative to the v_x -axis. (b) The acceleration by the laser field after scattering maps a circle of outgoing velocities to an ellipse in the final momentum space. Its center is located at $\delta p_x = -A_x(t_c)$ and $\delta p_z = A_x^2(t_c)/(2c)$. The black line shows the classical boundary, i.e., the envelope of all possible ellipses. Figure is adapted from Brennecke *et al.* [187]. (c) Hypothetical scattering probability on the scattering circle of panel (a) for a given incoming velocity \mathbf{v}_{in} . Due to the offset $\Delta\theta$ (here 20°) the scattering probability is not invariant under the transformation given by $v_{\text{out},z} \rightarrow -v_{\text{out},z}$.

Neglecting the ionic potential, the returning electron (at $\mathbf{r} = 0$) has an incoming velocity

$$\mathbf{v}_{\text{in}} = \mathbf{A}(t_c) - \mathbf{A}(t_0) + \frac{1}{2c}(\mathbf{A}(t_c) - \mathbf{A}(t_0))^2 \mathbf{e}_z + \mathbf{v}_0. \quad (9.7)$$

During the scattering the electron motion is strongly influenced by the ionic potential. We assume that the light-induced change of the electron velocity is small while the electron passes over the nonzero part of the potential. For short-range potentials, the assumption is appropriate, if the kinetic energy of the incident electrons is high and the optical cycle of the laser field is sufficiently long. Naturally, the assumption is questionable for long-range potentials. The energy conservation during rescattering then reads

$$\frac{1}{2}\mathbf{v}_{\text{out}}^2 = \frac{1}{2}\mathbf{v}_{\text{in}}^2. \quad (9.8)$$

Hence, for a given return time t_c , the possible outgoing velocities \mathbf{v}_{out} of the electron (directly after the scattering event) form a sphere of radius $v_{\text{scat}}(t_c, t_0) = |\mathbf{A}(t_c) - \mathbf{A}(t_0)| + \mathcal{O}(\frac{1}{c^2})$.

The scattering process is usually not isotropic, i.e., the probability of the outgoing velocities on the scattering sphere depend on their relative orientation with respect to the incoming velocity and, for molecules, also on the molecular structure. Assuming a field-free elastic scattering process, the scattering probability can be approximated by means of the elastic scattering differential cross section

$$\sigma(\mathbf{v}_{\text{out}} \leftarrow \mathbf{v}_{\text{in}}) = |f(\mathbf{v}_{\text{out}} \leftarrow \mathbf{v}_{\text{in}})|^2 \quad (9.9)$$

with the scattering amplitude f . An introduction to scattering theory is given in Section A.1. First, we restrict ourselves to atoms, where the DCS only depends on the relative scattering angle $\theta = \angle(\mathbf{v}_{\text{out}}, \mathbf{v}_{\text{in}})$ and on the magnitude of the velocity v_{scat} . In the dipole approximation, the electron moves along the polarization axis during its first stage of acceleration. Hence, the scattering probabilities for opposite outgoing velocities $v_{\text{out},z}$ and $-v_{\text{out},z}$ but the same $v_{\text{out},x}$ are equal. However, when taking nondipole effects into account, the z -component of the incoming velocity is nonzero. Thus, the scattering probability is rotated by an angle $\Delta\theta = |\arctan(v_{\text{in},z}/v_{\text{in},x})| \approx |v_{\text{in},z}/v_{\text{in},x}|$ with respect to the polarization axis compared to the dipole approximation. As a result, the symmetry of the scattering probability for outgoing velocities \mathbf{v}_{out} with respect to the polarization axis is broken (see the schematic illustration in Figs. 9.4(a) and (c)).

The z -component of the incoming velocity is shown in Fig. 9.3(b). For high return energies $v_{\text{scat}}^2/2$ close to the cutoff, the momentum gain $v_{\text{scat}}^2/(2c)$ of the electron associated with the first stage of acceleration dominates $v_{\text{in},z}$. In this region, the initial velocity $v_{0,z}$ is approximately smaller by a factor of ≈ 4 .

For the laser parameters of Fig. 9.1, the offset angles $\Delta\theta$ are mostly positive and reach a maximum of about 0.5° close to the cutoff energy (see Fig. 9.3(c)). In general, the x -component of the incoming velocity scale linearly with the electric-field strength E_0 and the wavelength λ . In contrast, the z -component varies quadratically in both parameters. As a result, the offset angle increases linearly with the field strength and the wavelength.

The motion of the electron after scattering is again solely determined by the light field. This step is similar to the classical motion in the recollision-free ionization discussed in Section 8.3.1. Here, the second stage of acceleration maps the outgoing velocities \mathbf{v}_{out} to the final measurable momenta \mathbf{p} . From Eq. (9.3) applied to the motion starting at t_c , the mapping is given by (to first order in $1/c$)

$$\mathbf{v}_{\text{out}} = \mathbf{p} + \mathbf{A}(t_c) + \frac{\mathbf{e}_z}{c} \left(\mathbf{p} \cdot \mathbf{A}(t_c) + \frac{1}{2} \mathbf{A}^2(t_c) \right) \quad \text{or} \quad \mathbf{p} = \mathbf{v}_{\text{out}} - \mathbf{A}(t_c) + \frac{\mathbf{e}_z}{c} \left(\frac{\mathbf{p}^2}{2} - \frac{\mathbf{v}_{\text{out}}^2}{2} \right). \quad (9.10)$$

In Eq. (9.10), $\mathbf{p}^2/2$ is the final kinetic energy of the electron and $\mathbf{v}_{\text{out}}^2/2$ the kinetic energy immediately after the scattering event. Thus, as intuitively expected, the linear momentum gain associated with the second acceleration stage is given by the energy gain over the speed of light c . Again, the temporospatial dependence of the electric field leads to a deformation of the scattering spheres of outgoing velocities (defined by the energy conservation (9.8)) to ellipsoids in the final momentum space. The magnetic field shifts the centers of the ellipsoids in the light-propagation direction, i.e., they are located at a momentum $\delta\mathbf{p} = -\mathbf{A}(t_c) + \mathbf{A}^2(t_c)/(2c)\mathbf{e}_z$. For return times t_c with $A_x(t_c) < 0$, the centers are displaced to positive $p_x > 0$ and $p_z > 0$. Classically, the total momentum distribution is formed by adding up the ellipsoids corresponding to all possible times of return. A schematic illustration of a few ellipses in 2D is shown in Fig. 9.4(b).

For comparison of the simple man's model to TDSE results in 2D, we consider the dynamics in a short-range soft-core potential

$$V_Y(r) = -\frac{2.0}{\sqrt{r^2 + 0.5}} e^{-0.41r}. \quad (9.11)$$

Its ground state reproduces the ionization potential $I_p \approx 0.905$ a.u. of helium. For the used laser parameters, the excursion amplitude of the electron can be estimated as $E_0/\omega^2 \approx 47$ a.u. Thus, the region of nonnegligible ionic potential (represented by the cutoff radius ≈ 2.4 a.u.) is much smaller than the distance of excursion in the light field. In PMDs from the numerical solution of the TDSE, we again find a shift of the rescattering plateau and a forward-backward asymmetry in the emission strength.

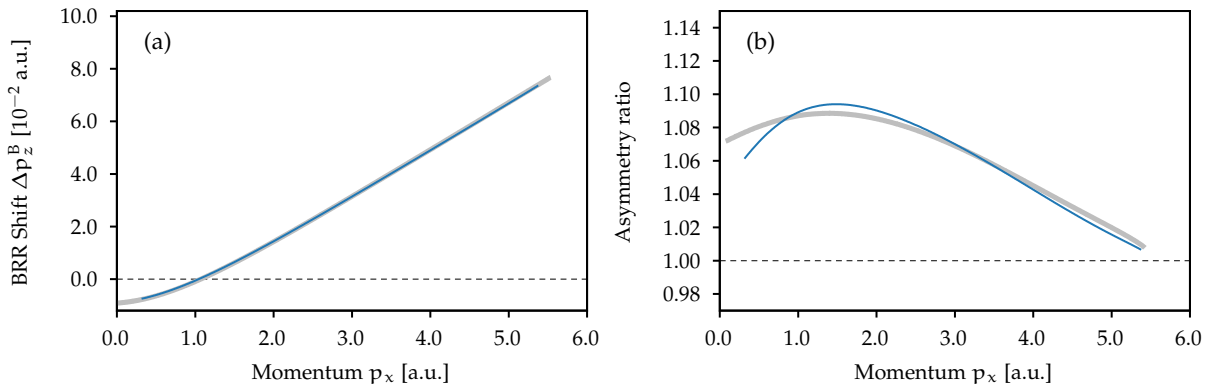


Figure 9.5: (a) Shift of the BRR structure and (b) forward-backward asymmetry of the emission strength on the BRR structure quantified as the ratio of the signal strength at fixed p_x for the short-range potential (9.11). Shown are numerical TDSE results (blue lines) and results of the simple man's model (gray lines) for ionization by four-cycle laser pulses with 800 nm wavelength and 8×10^{14} W/cm² intensity. Figure is adapted from Brennecke *et al.* [187, 501].

Shift of the rescattering plateau

In the PMDs from TDSE, we identify the boundary of the rescattering plateau with the position of the BRR structure. The shift of this boundary in the light-propagation direction is then quantified by

$$\Delta p_z^B(p_x) = \frac{p_z^+ + p_z^-}{2}, \quad (9.12)$$

where p_z^+ and p_z^- are the maxima's position of the BBR structure at fixed p_x in forward direction and backward direction, respectively. The classical boundary of all ellipses in the simple man's model is in perfect agreement with the TDSE result (see Fig. 9.5(a)). The shift can be approximated by using the two opposite points on a single ellipse with the same p_x . According to Eq. (9.10), this results in [160, 187]

$$\Delta p_z^B(p_x) \approx \frac{1}{c} \left(\frac{\mathbf{p}^2}{2} - \frac{v_{\text{scat}}^2(t_c, t_0)}{2} \right). \quad (9.13)$$

Within the simple man's model, the shift of the BRR structure is caused by the electron's deflection in the electromagnetic field after the scattering event. Here, the gained momentum in the light-propagation direction is equal to the light-field momentum associated with the energy gain of the electrons after rescattering.

Forward-backward asymmetry of the emission strength

To quantify the forward-backward asymmetry of the emission strength (see Section 9.2), we determine the signals on the BBR structure in forward and in backward directions at each p_x . For each p_x , the asymmetry is then quantified by the ratio of these signal strengths. For the short-range potential, the TDSE result is shown in Fig. 9.5(b). The asymmetry is mostly attributed to a different scattering probability and effects such as the ionization probability and the spreading of the electron wave packet during the first acceleration stage are neglected.² In the simple man's model, the asymmetry is approximated by taking the ratio of the DCSs calculated on the classical boundary in forward direction and in backward direction. Despite the simplicity, the model reproduces well the asymmetry from TDSE [160].

For the considered short-range potential, the DCS is basically a monotonic falling function of the return energy and of the scattering angle θ (between 0° and 180°) in the relevant energy range. Hence, for each return energy, it has a minimum at $\theta = 180^\circ$ corresponding to a backreflection of electron direction during scattering. For high return energies, the electrons have a positive $v_{\text{in},z}$ -component of their incoming velocity (see Fig. 9.3(b)). Hence, the scattering angle for an electron with positive component $v_{\text{out},z} > 0$ is smaller than the scattering angle for an electron with velocity component $-v_{\text{out},z} < 0$ (but the same $v_{\text{out},x}$). As a result, directly after the scattering event, electrons with positive component $v_{\text{out},z} > 0$ are more probable than electrons with velocity component $-v_{\text{out},z} < 0$. Qualitatively, this explains the asymmetry ratios larger than one for the studied potential (see also my master thesis [160]).

The asymmetry effect is mostly related to the scattering process, i.e., to the relative angle of the incoming velocity with respect to the polarization axis and to the exact shape of the field-free DCS. Thus, the asymmetry is very susceptible to the structure of the target. For example, in the limiting case of a zero-range potential [457] with a flat DCS, the signals in forward and backward directions are nearly equal. In this case, the information on the incoming velocity and, thus, the momentum transfer before the recollision is removed in the scattering process [160].

9.4 Low-frequency approximation model

For simplified quantum-mechanical simulations of the HATI process, we introduce a nondipole version of the low-frequency approximation and consider a quantum-orbit description. In my master thesis [160], the correct formulation of LFA was already guessed by means of the similarity to the description in the dipole approximation. Thus, the following section is in parts similar to my previous work.

²This is possible, because opposite points on the classical boundary with the same p_x nearly belong to the same ellipse in the simple man's model and, hence, their corresponding ionization and return times hardly differ.

For short-range potentials, the model is able to quantitatively interpret the high-energy part of the PMDs. The starting point is the rescattering amplitude derived in Eq. (2.39) in generalized length gauge. Approximating the exact final scattering state by a plane-wave state $|\mathbf{p}\rangle$, the amplitude reads³

$$M_R(\mathbf{p}) = (-i)^2 \int_{t_A}^{t_f} dt' \int_{t'}^{t_f} dt \langle \mathbf{p} | U_F(t_f, t) V U(t, t') H_I(t') U_0(t', t_A) | \psi_0 \rangle. \quad (9.14)$$

If the time-evolution operator U was replaced by the Volkov propagator of Eq. (2.34), the nondipole version of the improved SFA would arise (see Section 2.3). Then, the laser-assisted scattering would be treated in first Born approximation (1BA). For field-free scattering in 3D, the 1BA gives the correct DCS for a bare Coulomb potential. However, in general, effective single-active-electron potentials contain additional short-range contributions so that the DCS within 1BA and the exact quantum-mechanical DCS agree only asymptotically at large energies. Usually, for typical energies involved in HATI, the 1BA is not reliable.

Low-frequency approximation

To model the scattering process beyond the 1BA, we use the low-frequency approximation introduced to the context of HATI in the dipole approximation by Milošević *et al.* [496, 497]. Following the three-step model and the improved SFA, the electron dynamics is divided into stages of potential-free acceleration of the electron wave packet by the electromagnetic field and a field-free scattering event. If the light-induced change of the electron's velocity is small during the scattering process, i.e., while the electron passes over the nonzero part of the potential, it is expected that the separation works well [497]. As a prerequisite, the light-driven dynamics should take place on a much longer time scale than the scattering process. Hence, ideally, the region in space with nonzero ionic potential should be much smaller than the excursion amplitude of the electron in the light field.

In order to derive the LFA, we rewrite Eq. (9.14) by inserting the Volkov propagator of Eq. (2.34)

$$M_R(\mathbf{p}) = (-i)^2 \int_{t_A}^{t_f} dt' \int_{t'}^{t_f} dt \int d\mathbf{k} e^{iS_F(\mathbf{p}, t_f)} R_{\mathbf{p}, \mathbf{k}}(t, t') \langle \psi_{\mathbf{k}}^F(t') | H_I(t') U_0(t', t_A) | \psi_0 \rangle \quad (9.15)$$

and introduce the laser-assisted scattering amplitude

$$R_{\mathbf{p}, \mathbf{k}}(t, t') = \langle \psi_{\mathbf{p}}^F(t) | V U(t, t') | \psi_{\mathbf{k}}^F(t') \rangle. \quad (9.16)$$

Here, the action S_F of Eq. (2.33) and the Volkov states $|\psi_{\mathbf{m}}^F(\tau)\rangle$ of Eq. (2.32) are used. In order to incorporate the idea of different timescales in the theoretical description, the laser-assisted scattering amplitude is expanded in powers of the laser frequency ω . Following the derivation in Ref. [497], the LFA only considers the zeroth-order term of this expansion. When including leading-order nondipole corrections, the amplitude can be rewritten as (for a derivation see Appendix A.5)

$$R_{\mathbf{p}, \mathbf{k}}^{\text{LFA}}(t, t') = \langle \psi_{\mathbf{p}}^F(t) | V + V G_0(\tilde{E}(\mathbf{k}, t) + i0) V | \psi_{\mathbf{k}}^F(t') \rangle \quad (9.17)$$

with the "kinetic energy" of the light-driven electron

$$\tilde{E}(\mathbf{k}, t) = \frac{\mathbf{v}^2(\mathbf{k}, t)}{2}. \quad (9.18)$$

The field-free Green's operator is defined as (see also Appendix A.1)

$$G_0(z) = (z - H_0)^{-1}. \quad (9.19)$$

Using the Volkov states of Eq. (2.32) and the Lippmann-Schwinger equation (A.7) for the scattering states $|\mathbf{m}^{(+)}\rangle$, the amplitude reads

$$R_{\mathbf{p}, \mathbf{k}}^{\text{LFA}}(t, t') = \langle \mathbf{v}(\mathbf{p}, t) | V | \mathbf{v}(\mathbf{k}, t)^{(+)} \rangle e^{i(S_F(\mathbf{k}, t) - S_F(\mathbf{p}, t))} = \frac{-1}{(2\pi)^2} f(\mathbf{v}(\mathbf{p}, t) \leftarrow \mathbf{v}(\mathbf{k}, t)) e^{i(S_F(\mathbf{k}, t) - S_F(\mathbf{p}, t))}. \quad (9.20)$$

³For short-range potentials, this expression is still exact for large times t_f [497].

The modulus squared of the field-free scattering amplitude f is the DCS σ for scattering of an electron with incoming velocity \mathbf{v}_{in} to an outgoing velocity \mathbf{v}_{out} , where f is given by

$$f(\mathbf{v}_{\text{out}} \leftarrow \mathbf{v}_{\text{in}}) = -(2\pi)^2 \langle \mathbf{v}_{\text{out}} | V | \mathbf{v}_{\text{in}}^{(+)} \rangle. \quad (9.21)$$

Finally, the amplitude (9.15) for rescattered electrons in the low-frequency approximation can be expressed as

$$M_{\text{LFA}}(\mathbf{p}) = \frac{1}{(2\pi)^2} \int_{t_\lambda}^{t_f} dt' \int_{t'}^{t_f} dt \int d\mathbf{k} f(\mathbf{v}(\mathbf{p}, t) \leftarrow \mathbf{v}(\mathbf{k}, t)) D(\mathbf{k}, t') e^{iS_{\mathbf{p},\mathbf{k}}(t, t')} \quad (9.22)$$

with a transition matrix element associated with the ionization step (see also Eq. (2.42))

$$D(\mathbf{k}, t') = \langle \mathbf{v}(\mathbf{k}, t') | H_I(t') | \psi_0 \rangle \quad (9.23)$$

and an effective combination of the actions

$$S_{\mathbf{p},\mathbf{k}}(t, t') = \frac{1}{2} \int_{t_f}^t d\zeta \mathbf{v}^2(\mathbf{p}, \zeta) + \frac{1}{2} \int_t^{t'} d\zeta \mathbf{v}^2(\mathbf{k}, \zeta) + I_p(t' - t_\lambda). \quad (9.24)$$

In Eq. (9.22), the calculation of the off-shell scattering amplitude is quite demanding.⁴ In addition, the five integrations prevent a simple physical interpretation of the HATI process. Thus, for further simplification, we approximate the integrals by means of the saddle-point method introduced in Section 2.3.1 (similar to Refs. [18, 192, 199, 202]).

Saddle-point analysis

The stationary points of the action $S_{\mathbf{p},\mathbf{k}}$ with respect to the different integration variables are defined by $\partial_x S_{\mathbf{p},\mathbf{k}}(t, t') = 0$ with $x \in \{t', t, \mathbf{k}\}$. For the three kinds of integrals over the ionization time t' , the return time t and the intermediate momentum \mathbf{k} , we give a short physical interpretation that is closely related to the one in the dipole approximation [199, 202].

The saddle-point equation for the intermediate momentum \mathbf{k}_s can be solved analytically

$$\mathbf{k}_s = -\frac{\boldsymbol{\alpha}(t_s, t'_s)}{t_s - t'_s} + \frac{1}{c} \left(\frac{\boldsymbol{\alpha}^2(t_s, t'_s)}{(t_s - t'_s)^2} - \frac{\alpha_2(t_s, t'_s)}{2(t_s - t'_s)} \right) \mathbf{e}_z + \mathcal{O}\left(\frac{1}{c^2}\right). \quad (9.25)$$

The first term of Eq. (9.25) represents the constraint that the electron needs to return at time t_s to the initial position at time t'_s in the polarization plane (see also Eq. (9.5) in the classical model). To compensate for the electron's drift motion along the light-propagation direction, an initial velocity is required (see also Eq. (9.6) in the classical model), leading to the nondipole corrections in Eq. (9.25).

The saddle-point equation for the ionization time t'_s is familiar from direct ionization (see Eq. (8.12))

$$\frac{1}{2} \mathbf{v}^2(\mathbf{k}_s, t'_s) = \frac{1}{2} \left(\mathbf{k}_s + \mathbf{A}(t'_s) + \frac{\mathbf{e}_z}{c} \left(\mathbf{k}_s \cdot \mathbf{A}(t'_s) + \frac{1}{2} \mathbf{A}^2(t'_s) \right) \right)^2 = -I_p. \quad (9.26)$$

The initial velocity required for exact return leads to an increased effective ionization potential. Hence, in contrast to the dipole approximation, the solutions t'_s are not even real when $I_p = 0$ and the ionization rate is slightly reduced [189, 192].

The saddle-point equation for the recollision time t_s is given by

$$\frac{1}{2} \left(\mathbf{k}_s + \mathbf{A}(t_s) + \frac{\mathbf{e}_z}{c} \left(\mathbf{k}_s \cdot \mathbf{A}(t_s) + \frac{1}{2} \mathbf{A}^2(t_s) \right) \right)^2 = \frac{1}{2} \left(\mathbf{p} + \mathbf{A}(t_s) + \frac{\mathbf{e}_z}{c} \left(\mathbf{p} \cdot \mathbf{A}(t_s) + \frac{1}{2} \mathbf{A}^2(t_s) \right) \right)^2. \quad (9.27)$$

It can be interpreted as the energy conservation in the scattering process (see also Eq. (9.8) in the classical model). This ensures that the scattering amplitude f in Eq. (9.22) is restricted to the ‘‘scattering sphere’’ in velocity space defined by the value of the incoming velocity.

⁴In general, the incoming and outgoing velocities have different magnitudes and the energy is not conserved during scattering.

Since the intermediate momentum $\mathbf{k}_s(t_s, t'_s)$ of Eq. (9.25) depends on both ionization time and return time, the saddle-point equations (9.26) and (9.27) are coupled. To determine the complex-valued ionization time t'_s and return time t_s , we numerically solve the system of equations using Newton's method. Trajectories with travel times $\text{Re}(t_s - t'_s)$ exceeding one optical cycle are discarded. Hence, two main branches of trajectories are only considered: the "short" and "long" trajectories [202].

Within the approximations, the probability amplitude of a single quantum orbit can be written as

$$M_{\text{LFA},s}(\mathbf{p}) = \frac{1}{(2\pi)^2} C_p C_{i,r} \tilde{D} f(\mathbf{v}(\mathbf{p}, t_s) \leftarrow \mathbf{v}(\mathbf{k}_s, t_s)) e^{iS_{\mathbf{p},\mathbf{k}_s}(t_s, t'_s)}. \quad (9.28)$$

Here, the ionization matrix element D (which has a pole at the saddle points [194]) is replaced by a reduced factor \tilde{D} . \tilde{D} is chosen as one for initial s states and as $v_x(\mathbf{k}_s, t'_s)$ for initial p_x states.⁵ Since the considered orbits are launched in a small time range close to the point of maximal electric-field strength, this prefactor only has little influence on the PMD in HATI. The prefactors from the Hessian matrix elements in the integrals are given by

$$C_p = \sqrt{\frac{(2\pi i)^D}{(t'_s - t_s)^D}} + \mathcal{O}\left(\frac{1}{c^2}\right) \quad \text{and} \quad C_{i,r} = \sqrt{\frac{(2\pi i)^2}{\det(H_{t,t'}[S_{\mathbf{p},\mathbf{k}_s}(t_s, t'_s)])}}. \quad (9.29)$$

Here, the factor C_p is related to the spreading of the wave packet between ionization and recollision.

In the high-energy region, the interference structures are mostly determined by the action $S_{\mathbf{p},\mathbf{k}}$. The dependence on the target structure is caused by the scattering amplitude f which is calculated as described in Appendix A.1. However, in Eq. (9.28) the arguments of f , i.e., $\mathbf{v}(\mathbf{p}, t_s)$ and $\mathbf{v}(\mathbf{k}_s, t_s)$, have nonzero imaginary parts which are neglected for simplicity.⁶ In the usual saddle-point approximation, the total probability amplitude is given by the coherent superposition of the contributions (9.28) of all relevant solutions. In the center of the scattering plateau in the PMD, the two branches are well separated and the saddle-point approximation works well. However, in the vicinity of the BRR structure, both solutions merge. For large energies, only the long trajectory has to be considered [202]. For an adequate treatment of this situation, we use the uniform approximation [204] to obtain a description of the whole rescattering region. We refer to the resulting model as LFA model or quantum-orbit model.

9.5 Hydrogen molecular ion

The double-slit experiment with electrons [505] is a prime example of the interference of matter waves in quantum mechanics. In HATI, the liberated electron wave packet is driven back to its parent ion and scatters off the potential. Thus, for diatomic molecules, the returning wave is diffracted at both centers of the ion [41]. The situation resembles a double-slit scenario such that two-source interference effects appear (see Fig. 9.6(a) for a schematic illustration). In this section, we will explore the nondipole modifications of the molecular-interference pattern visible in the HATI region for ionization of H_2^+ .

In general, the HATI process for diatomic molecules can be described by considering four geometrical paths of the recolliding electron depending on its initial position at one or the other center of the dimer as well as the center where it scatters off [39, 504]. However, for small molecules with a σ_s bond (such as H_2^+ with its equilibrium internuclear distance of $R = 2$ a.u.), the initial molecular orbital is highly localized and does not have nodal planes. Hence, we can neglect the influence of the molecular structure on the recolliding part of the liberated electron wave packet.⁷ Hence, in the simple man's model and also in LFA, the structure dependence is solely determined by the two-center interference in the scattering amplitude.

⁵To approximate the matrix element, we imitate the direct SFA of Eq. (6.16) and we use that the p_x state can be written in the form $\tilde{\Psi}(\mathbf{p}) = p_x \mathbf{b}(\mathbf{p}^2)$. We neglect the function \mathbf{b} , because it is constant according to Eq. (9.26).

⁶For a Yukawa potential in 1BA, we found that the nondipole observables are only weakly influenced by these imaginary parts.

⁷For more complex orbitals such as in Ref. [70], this is not possible.

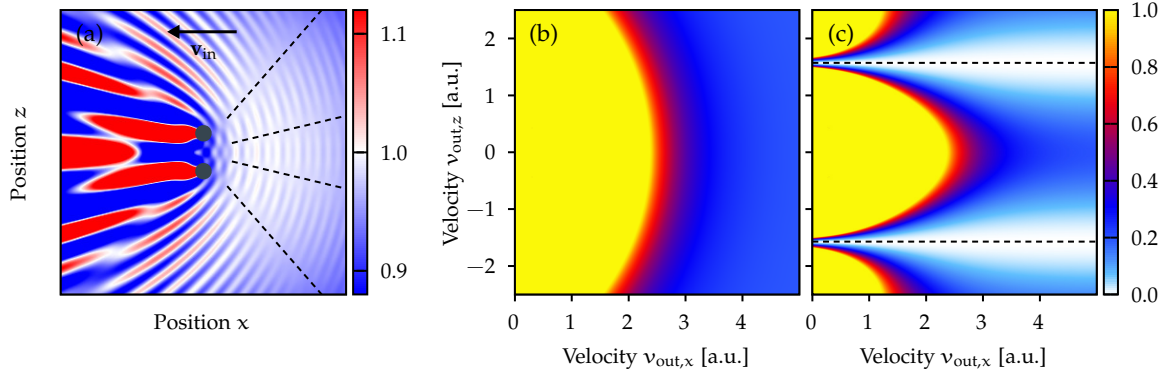


Figure 9.6: (a) Schematic illustration of electron diffraction at the two centers of a homonuclear diatomic molecule. Shown is the probability density in position space for an electron wave packet with initial velocity $\mathbf{v}_{in} = -3 \mathbf{e}_x$. The dashed lines indicate the nodal lines of the molecular-interference pattern for large-angle-scattered electrons. Inspired by Ref. [41]. (b) Differential cross section (arbitrarily normalized) for scattering of electrons with incoming velocities $\mathbf{v}_{in} = -|\mathbf{v}_{in}| \mathbf{e}_x$ off a single ionic center and (c) off the two centers of the H_2^+ molecular ion aligned along the z -axis (see Eq. (9.30)). The positions of the molecular-interference minima are indicated as dashed lines (see Eq. (9.31)).

For dimers, the molecular potential can be written as sum of potentials of the individual centers: $V(\mathbf{r}) = V_A(\mathbf{r} + \mathbf{R}/2) + V_A(\mathbf{r} - \mathbf{R}/2)$. The scattering amplitude within 1BA can be approximated as [506]

$$\begin{aligned}
 -\frac{1}{(2\pi)^2} f(\mathbf{v}_{out} \leftarrow \mathbf{v}_{in}) &\approx \langle \mathbf{v}_{out} | V | \mathbf{v}_{in} \rangle = \langle \mathbf{v}_{out} | V_A(\mathbf{r} + \mathbf{R}/2) + V_A(\mathbf{r} - \mathbf{R}/2) | \mathbf{v}_{in} \rangle \\
 &= \langle \mathbf{v}_{out} | V_A(\mathbf{r}) | \mathbf{v}_{in} \rangle \left(e^{+i(\mathbf{v}_{out} - \mathbf{v}_{in}) \cdot \mathbf{R}/2} + e^{-i(\mathbf{v}_{out} - \mathbf{v}_{in}) \cdot \mathbf{R}/2} \right) \\
 &\approx -\frac{1}{(2\pi)^2} f_A(\mathbf{v}_{out} \leftarrow \mathbf{v}_{in}) 2 \cos \left(\frac{\mathbf{R} \cdot (\mathbf{v}_{out} - \mathbf{v}_{in})}{2} \right)
 \end{aligned} \tag{9.30}$$

with the amplitude f_A representing elastic electron scattering off an atomic ion. The differential cross section $\sigma_A = |f_A|^2$ for an atomic ion is simply a monotonic function of the energy (in the relevant region) and is free of any essential structure (see Fig. 9.6(b) for the potential of Eq. (9.2)). In the second line of Eq. (9.30), the scattering amplitudes of the two centers are a product of the atomic amplitude f_A with a position-dependent phase factor. Hence, the DCS of the H_2^+ ion shows an interference pattern on top of the atomic DCS (see Fig. 9.6(c) for an incoming velocity $\mathbf{v}_{in} \perp \mathbf{R}$). According to the cosine term in Eq. (9.30), lines of constructive or destructive interference are given by [33, 39]

$$\mathbf{R} \cdot (\mathbf{v}_{out} - \mathbf{v}_{in}) = n\pi \tag{9.31}$$

with n being even for maxima and odd for minima. To observe the molecular-interference pattern in photoelectron momentum distributions, the de-Broglie wavelength of the electrons $\lambda_{dB} = 2\pi/v_{scat}$ needs to be on the same order of magnitude as the spatial extension of the molecule [41].

After scattering, the electrons are accelerated by the light field for a second time (see the simple man's model of Section 9.3). Electrons with given outgoing velocities \mathbf{v}_{out} are deflected by the electromagnetic field to their final momenta \mathbf{p} and, thus, the structure of the DCS is imprinted on the photoelectron momentum distribution. The condition of Eq. (9.31) and the mapping of the incoming and outgoing velocities to final momenta based on the simple man's model (see Eqs. (9.7) and (9.10)) predict the positions of interference extrema in final momentum space. For perpendicular alignment, these positions are defined by $v_{out,z} - v_{in,z} = \frac{n\pi}{R}$. Hence, for a given scattering event specified by an ionization time t_0 and a collision time t_c , the corresponding velocity $v_{in,z}$ fixes the outgoing velocity

$$v_{out,z} = v_{in,z} + \frac{n\pi}{R} \tag{9.32}$$

for each extremum labeled by n . In the dipole approximation, we have $v_{in,z} = 0$ and the mapping of the outgoing velocity $v_{out,z}$ to p_z is trivial: $v_{out,z} = p_z$. Thus, in the dipole approximation, the positions of the extrema in the PMD are simply given by [33]

$$p_z^{dip} = \frac{n\pi}{R} \quad \text{with } n \in \mathbb{Z}. \tag{9.33}$$

Hence, for each classically-reachable momentum p_x in the scattering plateau, the same positions of interference extrema in p_z -direction are expected.

Figure 9.7(a) shows a magnification of the scattering plateau from ionization of H_2^+ by an electric field perpendicular to the molecular axis (see Fig. 9.1(b1)). The zeroth-order maximum as well as the first-order minima are indicated as black lines. Even though the positions $p_z^{\text{dip}} = \pm\pi/2 \approx \pm 1.57$ a.u. predicted by the double-slit model for the first-order minima are slightly too large, the positions from TDSE are indeed nearly independent of p_x for large p_x . For lower momenta p_x , the lines are bend inwards towards smaller $|p_z|$ what can be explained by using an eikonal model [507]. According to Eq. (9.33), the positions of the extrema are independent of the laser parameters and are the same for the long and short trajectories. Hence, the molecular-interference structure is nearly unaffected by focal-volume averaging (see Fig. 9.7(b)).

In contrast, for parallel alignment of the field and the molecular axis, the positions of the minima are determined by the x -component of the incoming and outgoing velocities. In agreement with the TDSE result of Fig. 9.1(a1), the nodal lines are nearly parallel to the p_z -axis. However, the condition (9.31) suggest that the exact positions depend on the vector potential at the ionization and return times [39, 504]. Hence, already in PMDs for a single laser intensity, the molecular-interference structures are less pronounced. Focal averaging reduces the contrast of the interference pattern even further.

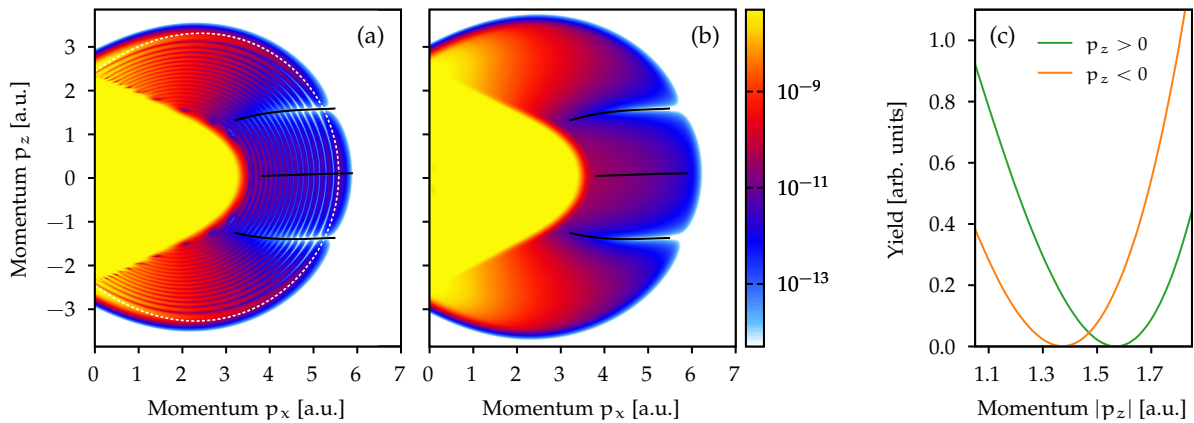


Figure 9.7: Photoelectron momentum distribution for ionization of H_2^+ with perpendicular alignment of the molecular axis relative to the electric field from TDSE simulations: (a) result for a single intensity of 8×10^{14} W/cm 2 and (b) focal-volume-averaged result assuming a peak intensity of 9.5×10^{14} W/cm 2 . The black lines indicate the numerically-determined positions of the molecular-interference maximum and minima. The white dashed line marks the boundary of the rescattering plateau. (c) Signal on this boundary in the region of the two-center interference minima for positive p_z (green line) and negative p_z (orange line) extracted from panel (a). Figure is adapted from Brennecke *et al.* [501].

Nondipole shift of the molecular-interference pattern

For perpendicular alignment, the signal of the PMD from TDSE along the classical boundary of the simple man's model is depicted in Fig. 9.7(c) as a function of p_z in the vicinity of the molecular-interference minima. Here, the nondipole effects modify the positions of these minima, i.e., they are not symmetric in forward and backward directions with respect to the polarization axis. Using a quadratic fit, we find that the minima are located $p_z \approx 1.569$ a.u. and $p_z \approx -1.372$ a.u. Thus, compared to the dipole limit, their positions are approximately shifted by $\Delta p_z^M \approx 0.099$ a.u. Interestingly, the shift of the molecular-interference pattern is larger than the classical deflection of the electron after scattering (see Eq. (9.10)). For comparison, the shift of the classical boundary of the plateau region has a maximal value of $\Delta p_z^B \approx 0.077$ a.u. (see Eq. (9.13)).

To derive a simple estimate for the nondipole shift of the molecular-interference structures, we follow the ideas of the double-slit model described above but consider the nondipole corrections for the classical electron motion before and after recollision. We are only interested in the first-order nondipole corrections, i.e., the positions of the extrema are written as $p_z = p_z^{\text{dip}} + \Delta p_z$ with p_z^{dip} of Eq. (9.33). Using

the nondipole mapping of the outgoing velocities to the final momenta (see Eq. (9.10)), the condition of Eq. (9.32) implies (to first order in $1/c$)

$$\Delta p_z = v_{in,z} + \frac{1}{c} \left(\frac{\mathbf{p}^2}{2} - \frac{\mathbf{v}_{out}^2}{2} \right) = v_{0,z} + \frac{v_{in}^2}{2c} + \frac{1}{c} \left(\frac{\mathbf{p}^2}{2} - \frac{\mathbf{v}_{in}^2}{2} \right) = \frac{\mathbf{p}^2}{2c} + v_{0,z}. \quad (9.34)$$

Here, the energy conservation of Eq. (9.8) and the incoming velocity of Eq. (9.7) were used. For a given final momentum p_x and a given interference order n , Eq. (9.34) estimates the nondipole shift in p_z -direction. In Eq. (9.34), the (positive) velocity $v_{in,z}$ of the incoming electron and the momentum gain after scattering $\Delta p_z^B = \frac{1}{c} \left(\frac{\mathbf{p}^2}{2} - \frac{\mathbf{v}_{out}^2}{2} \right)$ are added up. Hence, the total momentum gain before and after collision determines the shift of the molecular-interference pattern, i.e., it is basically given by the final kinetic energy $\mathbf{p}^2/2$ over the speed of light c . For the considered laser conditions, the required initial velocity $v_{0,z}$ of Eq. (9.6) is only a small correction. The model of Eq. (9.34) predicts a shift of ≈ 0.095 a.u. for the parameters used in Fig. 9.7(a) and, thus, reproduces the TDSE result well.⁸

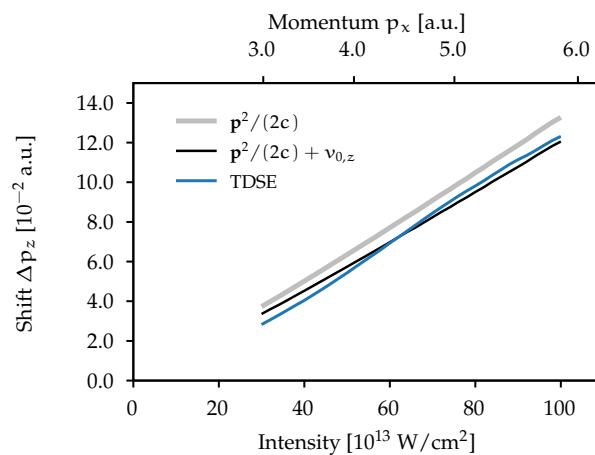


Figure 9.8: Nondipole shift of the molecular-interference minima for H_2^+ on the classical boundary as a function of the laser intensity. The TDSE result is calculated as described in the main text. The black and gray lines show the estimate of Eq. (9.34) with and without initial velocity $v_{0,z}$. The second axis illustrates the position p_x of the interference minimum extracted from TDSE.

The nondipole shift of the interference pattern depends on the energy of the outgoing electrons (see Eq. (9.34)). The cutoff energy increases with the laser intensity and wavelength. Hence, when considering the pattern shift always along the BRR structure, we expect the shift to vary with the laser parameters. The dependence on the intensity for a constant wavelength of 800 nm is investigated in Fig. 9.8. Here, for each intensity, the signal from a TDSE simulation is considered along the (intensity-dependent) classical boundary (analogous to Fig. 9.7) and the positions of the minima are determined (with momentum components p_z^+ and p_z^- in the light-propagation direction). The shift is then calculated as $\Delta p_z = (p_z^+ + p_z^-)/2$. The TDSE result is well reproduced by the estimate of Eq. (9.34) and, thus, it basically follows the total momentum transfer $\mathbf{p}^2/(2c)$ (see the gray line). However, even though the effect of the initial velocity $v_{0,z}$ in the model (9.34) is small, its inclusion slightly improves the overall agreement with the TDSE data. Note that the extension of the scattering plateau in p_z -direction shrinks for smaller intensities. For the lowest-considered intensities, the interference maxima are located close to the highest classically-possible momenta in p_z -direction such that the minima of the signal along the classical boundary are quite flat. This complication could be a reason for the slightly too small shifts observed in the TDSE.

Alternatively, the shift of the pattern can be individually determined at each momentum p_x across the scattering plateau. We consider the focal-averaged distribution of Fig. 9.7(b) and use quadratic fits of the distribution along the p_z -direction to determine the positions of the extrema for each p_x . The shift of the interference minima is shown as a function of p_x in Fig. 9.9(b). For comparison, the simple

⁸In the model, we use $v_{0,z}$ of Eq. (9.6) and insert the positions of the minima in the dipole approximation as momentum \mathbf{p} .

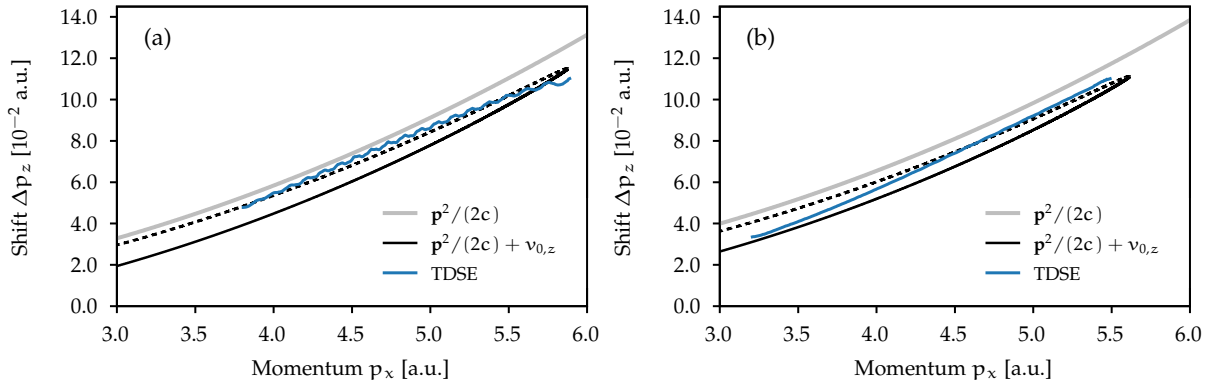


Figure 9.9: (a) Position of the central molecular-interference maximum and (b) shift of the positions of the minima as a function of p_x for H_2^+ . The TDSE results are extracted from the focal-averaged PMD of Fig. 9.7. The black and gray lines show the estimate of Eq. (9.34) with and without initial velocity $v_{0,z}$. For the model, we use $p_z \approx \pi/2.25$ a.u. and evaluate $v_{0,z}$ for a single intensity of 9×10^{14} W/cm². The dashed lines correspond to short trajectories, whereas the solid lines correspond to long trajectories.

estimate of Eq. (9.34) including $v_{0,z}$ is presented for a single fixed intensity of 9×10^{14} W/cm² and a fixed $p_z \approx \pi/2.25$ a.u. Here, an effective internuclear distance of $R_{\text{eff}} = 2.25$ a.u. is used to better match the positions of the interference minima of the TDSE simulations.⁹ In the model, the shift of the minima at fixed p_x solely depends on the laser intensity through the initial velocity $v_{0,z}$. Thus, this nondipole effect is quite stable under focal averaging and, for the whole range of momenta p_x , the TDSE results are in fair agreement with the results of the simple model. Close to the classical cutoff, where only the highest intensities dominate and the short and long trajectories merge, the model predicts a unique value. However, for smaller p_x , the initial velocities $v_{0,z}$ for both trajectories differ (and depend on the laser intensity).

The position of the central molecular-interference maximum is also influenced by nondipole effects (see Fig. 9.9(a)). According to the double-slit model, the central position has the same functional form as the shift of the interference minima and it is given by Eq. (9.34). The maximum's positions from TDSE approximately follow the estimate of the double-slit model for the short trajectories. According to Eq. (9.34), the shift is mostly determined by the final kinetic energy of the electrons. Hence, at fixed p_x , the nondipole shift of the central maximum is slightly smaller than the shift of the first-order minima, because the minima are located at larger values of $|p_z|$. This interesting non-uniformity of the nondipole shift is also qualitatively visible for the TDSE results.

For large p_x close to the high-energy cutoff, the maximum's position turns to smaller p_z compared to the model results. However, the model is only reliable, if the shape of the PMD is determined by the molecular interference. For the inner part of the rescattering plateau and for adiabatic ionization conditions, other influences such as the atomic DCS or the complex-valued action in the LFA model (see for example Eq. (9.28)) only cause minor changes of the shape of the momentum distribution. However, within the LFA model (not shown), close to and especially beyond the classical cutoff, the imaginary part of the action changes strongly such that it significantly affects the shape of the PMD and influences the maximum's position.

Forward-backward asymmetry

The molecular structure also influences the forward-backward asymmetry of the yield (quantified analogous to Section 9.3). The asymmetries on the BRR structure extracted from TDSE simulations are shown in Fig. 9.10(a) for parallel and perpendicular alignment of the H_2^+ molecular ion. For both configurations, the overall dependence of the asymmetry on p_x is well reproduced by the simple man's model with the DCS of Eq. (9.30) (see Fig. 9.10(b)).

For parallel alignment, the ratio from TDSE is above one for all p_x indicating a stronger emission in forward than in backward direction. In the vicinity of the molecular-interference minima at $p_x \approx 3.5$ a.u.

⁹The use of the numerically-determined positions p_z from the TDSE leads to similar results.

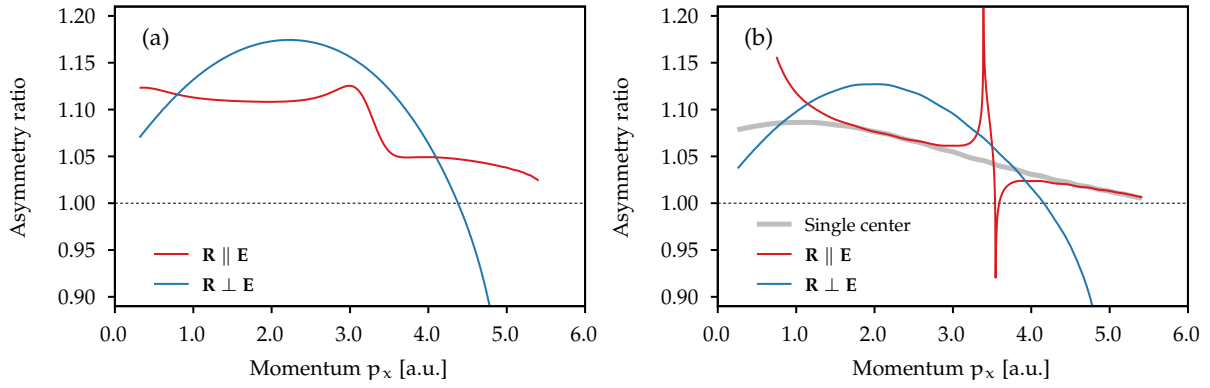


Figure 9.10: Forward-backward asymmetry of the emission strength on the BRR structure quantified as the ratio of the signal strengths at fixed p_x for H_2^+ at parallel or perpendicular alignment. (a) TDSE results and (b) results of the simple man's model using the DCS of Eq. (9.30) with an effective internuclear distance $R_{\text{eff}} = 2.25$ a.u. Additionally, the result for a single ionic center is shown as gray line. Figure is adapted from Brennecke *et al.* [501].

a modulation feature is visible. The yield of the model exactly vanishes at the molecular interference minima, resulting in a much sharper modulation structure compared to TDSE. In the simple man's model, the \cos^2 molecular-interference term of the DCS only depends on the velocity along the polarization direction. Hence, the molecular interference would not influence the asymmetry, if the two opposite points on the BRR structure at fixed p_x would belong exactly to the same scattering event, i.e., would have the same ionization and return times. However, in reality, these points belong to slightly different scattering events, i.e., they do not belong to the same ellipse in final momentum space shown in Fig. 9.4(b). Thus, the molecular-interference factor in the DCS has slightly different values in forward direction and in backward direction, inducing the sharp structure. Besides the modulation, the asymmetry follows roughly the shape of the atomic DCS shown as gray line in Fig. 9.10(b).

For the perpendicular alignment, the ratio has a single broad maximum with values as high as ≈ 1.17 . When going towards larger p_x , the emission asymmetry decreases and becomes inverted for p_x larger than ≈ 4.5 a.u., i.e., the emission in backward direction is stronger than in forward direction. In contrast to parallel alignment, the \cos^2 molecular-interference term of the DCS is influenced by the nondipole correction of the incoming velocity \mathbf{v}_{in} along the light-propagation direction, inducing strong deviations compared to a single atomic ion. In agreement with the mechanism for atomic targets, we find that the asymmetry of the yield for H_2^+ can be mostly attributed to the electron dynamics before scattering and the scattering process itself.

9.6 Xenon

Scattering of electrons off atomic ions can be interpreted as diffraction at a single slit, i.e., the incoming electron wave packet is diffracted by the ionic potential. Depending on the target, this may lead to an interference structure in the DCS.¹⁰ Classically, for large-angle scattering, the electron needs to return close to the ion such that the scattering process and the corresponding DCS are quite susceptible to the short-range part of the electron-ion interaction. Hence, even for atoms, the high-energy region of the PMD [36–38] and also its nondipole modification are very sensitive to the target. As an example, Figure 9.11(b) shows that the partial average $\langle p_z \rangle(p_x)$ in the HATI region depends indeed strongly on the used DCS. These results are calculated by means of LFA simulations (see Section 9.4) with the scattering amplitudes for various noble gases modeled by Tong-Lin potentials (see Section A.2.3).¹¹

¹⁰More precisely, the interference between the Coulomb scattering amplitude and the additional scattering amplitude due to the short-range potential may result in a nontrivial diffraction pattern (see also Eq. (A.15)).

¹¹For simple comparability, we artificially use the same ionization potential $I_p = 0.905$ a.u. for all simulations, i.e., only the scattering amplitudes are different.

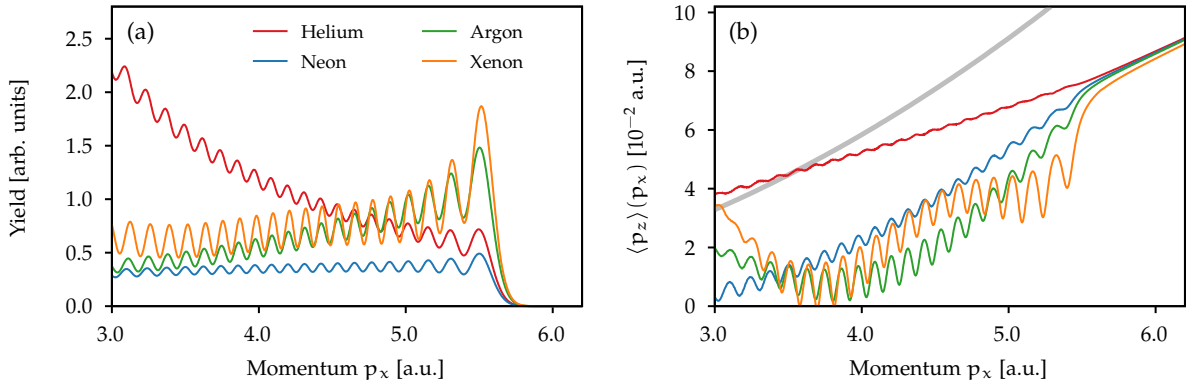


Figure 9.11: Dependence of the nondipole effects in HATI on the differential cross section. (a) Projection of the PMD on the p_x -axis and (b) corresponding partial average $\langle p_z \rangle(p_x)$ of Eq. (8.4). The gray thick line shows the heuristic estimate $p_x^2/(2c)$ and guides the eye. The PMDs are calculated in the p_x - p_z -plane by means of the LFA model of Section 9.4 using the scattering amplitudes f for various rare gases based on the Tong-Lin potential. For all simulations, the same laser parameters as in Fig. 9.1 and the same ionization potential $I_p = 0.905$ a.u. are used. In panel (a), the result for helium is magnified by a factor 100.

Recently, Lin *et al.* [500] performed the first experimental study of nondipole effects in HATI. To this end, xenon atoms were ionized by femtosecond laser pulses at a central wavelength of 800 nm and a peak intensity of 7×10^{13} W/cm². The resulting electron momentum distributions were measured by means of the COLTRIMS technique. In the remaining part of this chapter, we theoretically investigate the nondipole modifications of the momentum distributions for this special case of xenon atoms. First, we consider the overall structure of the PMD in the HATI region. To this end, we perform LFA simulations with the scattering amplitudes for xenon modeled by the Tong-Lin potential (see Section A.2.3). A laser pulse of Eq. (9.1) with ten cycles total duration and an intensity of 6×10^{13} W/cm² is chosen. In the LFA simulations, we consider three branches of long and short trajectories around the peak of the pulse. To avoid the influence of ATI rings, the contributions of the three branches are added incoherently. The results are averaged over eight values of the CEP. The projection of the 3D PMD on the p_x - p_z -plane is shown in Fig. 9.12(c). For comparison, the result from TDSE simulations (kindly provided by Hongcheng Ni [500]) is presented in Fig. 9.12(b). Here, the classical cutoff for direct ionization is around $p_x \approx 0.8$ a.u. For both levels of theory, a nontrivial angular and energy dependence of the PMD is visible in the high-energy region. As discussed above, the additional structure on the scattering plateau is mostly induced by the differential cross section [36, 37].

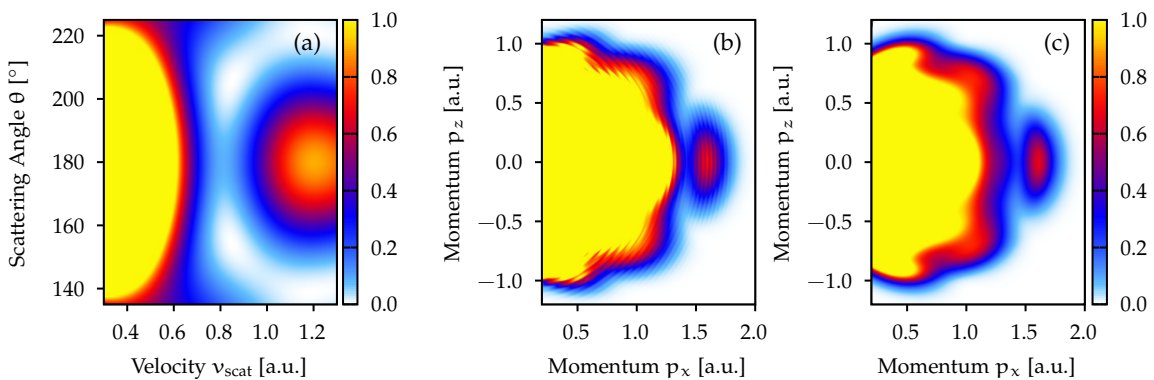


Figure 9.12: (a) Differential cross section of the Xe⁺ ion for a Tong-Lin potential (arbitrarily normalized). (b) CEP-averaged projections of the 3D PMDs on the p_x - p_z -plane from TDSE simulations (provided by Hongcheng Ni [500]) and (c) from LFA simulations. Here, xenon is ionized by ten-cycle laser pulses with 800 nm central wavelength and an intensity of 6×10^{13} W/cm² (see main text).

In the experiment, the p_z -component of the momentum is restricted to a range of about $[-0.3, 0.3]$ a.u. Hence, it is not possible to analyze the partial average $\langle p_z \rangle(p_x)$. Instead, we concentrate ourselves on the PMD in the vicinity of the polarization axis. The DCS of the Xe⁺ ion is shown in Fig. 9.12(a) in the relevant angular and velocity range. For each velocity v_{scat} , the DCS has a local maximum at a

scattering angle of $\theta = 180^\circ$ corresponding to a backreflection of electron direction during scattering. After scattering, the acceleration by the laser field maps electron's with outgoing velocities \mathbf{v}_{out} to final momenta \mathbf{p} (see Eq. (9.10)). Hence, for each p_x in the HATI region, the maximum of the DCS induces a maximum in p_z -direction in the PMD near the polarization axis (see Figs. 9.12(b) and (c)). Compared to the dipole approximation, the position of this maximum is shifted in the light-propagation direction. This is on the first glance similar to the maximum's shift for molecular H_2^+ (see Section 9.5).

Simple backreflection model

Since the maximum in the vicinity of the polarization axis is caused by the maximum of the DCS at 180° , we can estimate its nondipole shift by only considering electrons that are exactly backward scattered.¹² Hence, when modeling the electron dynamics in the simple man's approach of Section 9.3, the velocity of the electron is reversed during scattering at time t_c : $\mathbf{v}_{\text{out}} = -\mathbf{v}_{\text{in}}$. During its acceleration in the light field after scattering, the electron is deflected to its final momentum \mathbf{p} . According to Eqs. (9.7) and (9.10), the final momenta of backscattered electrons are given by (to first order in $1/c$)

$$\begin{aligned} \mathbf{p} &= -\mathbf{v}_{\text{in}} - \mathbf{A}(t_c) + \frac{1}{c} \left(\frac{\mathbf{p}^2}{2} - \frac{\mathbf{v}_{\text{in}}^2}{2} \right) \mathbf{e}_z = \mathbf{A}(t_0) - 2\mathbf{A}(t_c) - \mathbf{v}_0 - \frac{\mathbf{v}_{\text{in}}^2}{2c} \mathbf{e}_z + \frac{1}{c} \left(\frac{\mathbf{p}^2}{2} - \frac{\mathbf{v}_{\text{in}}^2}{2} \right) \mathbf{e}_z \\ &= \mathbf{A}(t_0) - 2\mathbf{A}(t_c) - v_{0,z} \mathbf{e}_z + \frac{1}{c} \left(\frac{\mathbf{p}^2}{2} - 2\frac{\mathbf{v}_{\text{in}}^2}{2} \right) \mathbf{e}_z \end{aligned} \quad (9.35)$$

with $|\mathbf{v}_{\text{out}}| = |\mathbf{v}_{\text{in}}| = v_{\text{scat}}$. For the classically-reachable momenta $p_x = A_x(t_0) - 2A_x(t_c)$ along the polarization axis, Eq. (9.35) predicts the nondipole shift of the maximum's position in p_z -direction.

The initial velocity $v_{0,z}$ and the momentum gain $\frac{v_{\text{in}}^2}{2c}$ associated with the first stage of acceleration by the electromagnetic field result in a component of incoming electron velocity \mathbf{v}_{in} along light-propagation direction (see Eq. (9.7)). During backward scattering twice the electron momentum is transferred to the parent ion and, hence, the forward momentum $v_{\text{in},z}$ before rescattering is inverted to the backward direction (see the terms with $-\mathbf{v}_0$ and $-\frac{v_{\text{in}}^2}{2c} \mathbf{e}_z$ in the first line of Eq. (9.35)). After recollision the electron picks up some additional forward momentum due to the second stage of acceleration by the electromagnetic (see the last term in the first line Eq. (9.35)).

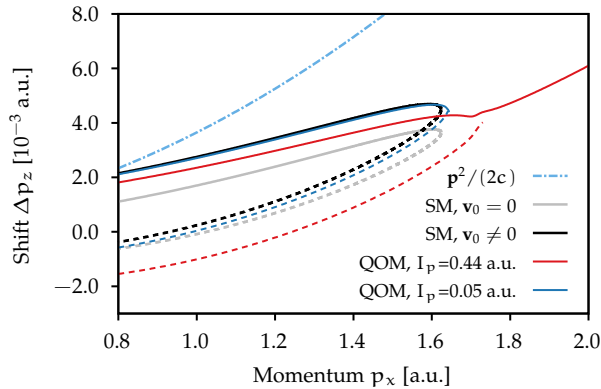


Figure 9.13: Nondipole shift of the central maximum for atomic targets as a function of p_x : simple backreflection model of Eq. (9.35) including (black lines) or neglecting (gray lines) the initial velocity \mathbf{v}_0 ; results from the quantum-orbit analysis for two different values of the ionization potential (red and blue lines). The dashed lines correspond to short trajectories, whereas the solid lines correspond to long trajectories. In all cases, a cw laser field with $6 \times 10^{13} \text{ W/cm}^2$ intensity is used. The quantum-orbit analysis is based on an artificial DCS with a pronounced maximum at $\theta = 180^\circ$. Figure is adapted from Lin *et al.* [500].

Interestingly, the predicted nondipole shifts by the backreflection model (9.35) for atoms and by the molecular-interference condition (9.34) for molecules are different. Even though the PMDs show a maximum in the vicinity of the polarization axis for both xenon atoms and H_2^+ molecules, these targets have an important difference. In H_2^+ , the molecular axis defines a preferred direction that determines

¹²To the best of my knowledge, the idea was first proposed by Reinhard Dörner. Here, it is worked out and discussed.

the DCS and, thus, the exact shape of the molecular-interference pattern in the PMD, i.e., it fixes the positions of the extrema (see also Eq. (9.31)). In contrast, for spherically-symmetric targets like xenon, the scattering probability solely depends on the energy of the electron and the angle between incoming and outgoing electron velocity. Hence, only the relative direction of the outgoing electron with respect to its incoming direction determines the structure of the probability distribution.

The result for the nondipole shift of the backreflection model is shown in Fig. 9.13 with an initial velocity $v_{0,z}$ of Eq. (9.6) being included (black lines) or neglected (gray lines). Due to the momentum transfer from the electron to the ion during scattering, the predicted shifts are significantly smaller than $p^2/(2c)$ for both long and short rescattering trajectories. To also consider the backreflection situation in the quantum-orbit model of Section 9.4, we calculate the PMDs based on an artificial DCS that is constant as a function of energy, but its angular distribution has a sharp maximum at $\theta = 180^\circ$.¹³ In this special situation, it is possible to separately analyze the PMDs for long and short trajectories and determine the corresponding positions of the central maximum at each p_x by a Gaussian fit. For small ionization potentials as $I_p = 0.05$ a.u., the QOM results reproduce well the backreflection model including an initial velocity $v_{0,z} \neq 0$ (see Fig. 9.13). However, nonadiabatic effects modify the dynamics, when considering the laser conditions in the experiment [500] and the real ionization potential $I_p \approx 0.44$ a.u. of xenon. We find that the nondipole shifts in the QOM for $I_p \approx 0.44$ a.u. are systematically smaller than for $I_p = 0.05$ a.u. and roughly follow the trend of the backreflection model with $v_{0,z} = 0$. However, the difference between the shifts for short and long rescattering trajectories is larger in the QOM compared to the classical backreflection model.

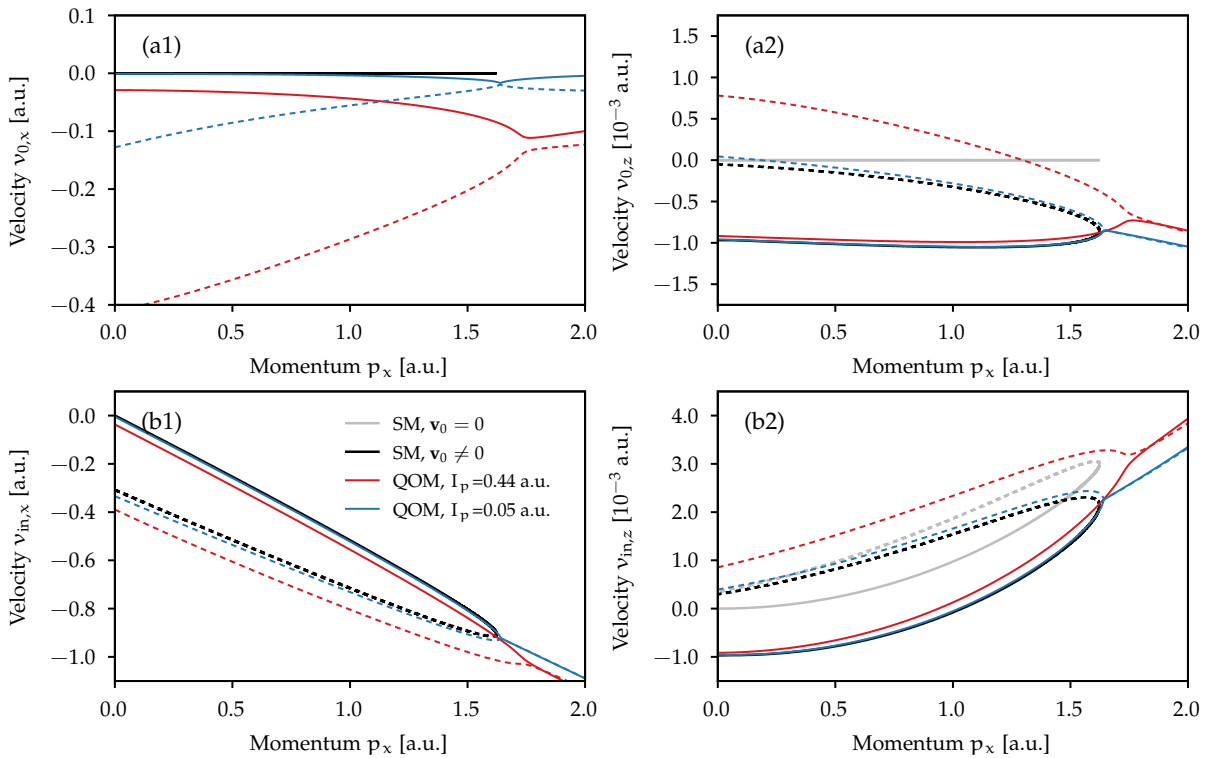


Figure 9.14: Properties of the rescattering trajectories for conditions analogous to Fig. 9.13. (a) Components of the initial velocity \mathbf{v}_0 and (b) components of the incoming velocity \mathbf{v}_{in} shortly before scattering. We interpret the following expression for the quantum-orbit model as “velocities”: $\mathbf{v}_0 = \text{Re } \mathbf{v}(\mathbf{k}_s, \text{Re}(t'_s))$ and $\mathbf{v}_{in} = \text{Re } \mathbf{v}(\mathbf{k}_s, \text{Re}(t_s))$. The dashed lines correspond to short trajectories, whereas the solid lines correspond to long trajectories.

In the quantum-orbit model, the position of the backscattering maximum is defined by the scattering amplitude $f(\mathbf{v}(\mathbf{p}, t_s) \leftarrow \mathbf{v}(\mathbf{k}_s, t_s))$ and, hence, it is influenced by the “velocities” $\mathbf{v}(\mathbf{k}_s, t_s)$ and $\mathbf{v}(\mathbf{p}, t_s)$ (see Eq. (9.28)). The imaginary part of the recollision time t_s can be neglected on the scattering plateau.

¹³For the artificial scattering amplitude f , we use $f = \exp(-(\cos \theta + 1)/\theta_w)$ with a width $\theta_w = 0.005$ corresponding to a FWHM in the angle θ of about 10° .

Thus, $\mathbf{v}(\mathbf{p}, t_s)$ provides basically the same mapping of the outgoing velocities to the final momenta as in the simple man's model. The deviations of the QOM from the simple man's model are mostly caused by the "velocity" $\mathbf{v}(\mathbf{k}_s, t_s)$, i.e., by nonadiabatic modifications of the tunnel ionization and of the propagation in the continuum before rescattering. The velocity \mathbf{v}_{in} of the electron shortly before the recollision and the velocity \mathbf{v}_0 of the electron at the tunnel exit are shown in Fig. 9.14 as a function of the final momentum p_x for the simple man's model and the quantum-orbit model. For the QOM, the real part of the complex-valued velocity $\mathbf{v}(\mathbf{k}_s, t)$ of Eq. (2.31) is used ($\mathbf{v}_0 = \text{Re } \mathbf{v}(\mathbf{k}_s, \text{Re}(t'_s))$ and $\mathbf{v}_{\text{in}} = \text{Re } \mathbf{v}(\mathbf{k}_s, \text{Re}(t_s))$). As expected, the QOM results for $I_p = 0.05$ a.u. agree very well with the simple man's model including an initial velocity $v_{0,z} \neq 0$. Additional nonadiabatic corrections are visible for the ionization potential $I_p = 0.44$ a.u. Since long trajectories are released closer to the peak of the electric-field strength, their nonadiabatic corrections are smaller compared to the short trajectories. In agreement with the strong-field approximation for direct ionization, we find that nonadiabaticity leads to a nonzero initial velocity $v_{0,x}$ along the polarization axis [116–118, 191]. Here, in addition, the $v_{0,z}$ - and $v_{\text{in},z}$ -components are increased by nonadiabatic effects. Hence, the inversion of the velocity vectors during backscattering results in smaller final momenta p_z compared to adiabatic conditions (see also Fig. 9.13).

Comparison to experimental results

In the experiment [500], the photoelectron momentum distribution has also a maximum in the vicinity of the polarization axis. For each momentum p_x , its position in p_z -direction is determined by a Gaussian fit to the central region with $|p_z| < 0.2$ a.u. The experimental nondipole shifts are depicted in Fig. 9.15(a) for momenta p_x in the HATI region. In agreement with the simple backreflection model, the experimental nondipole shifts are much smaller than $p_x^2/(2c)$. Interestingly, a pronounced local minimum of the nondipole shift is present in the high-energy region that cannot be explained by the purely kinematic backreflection model.

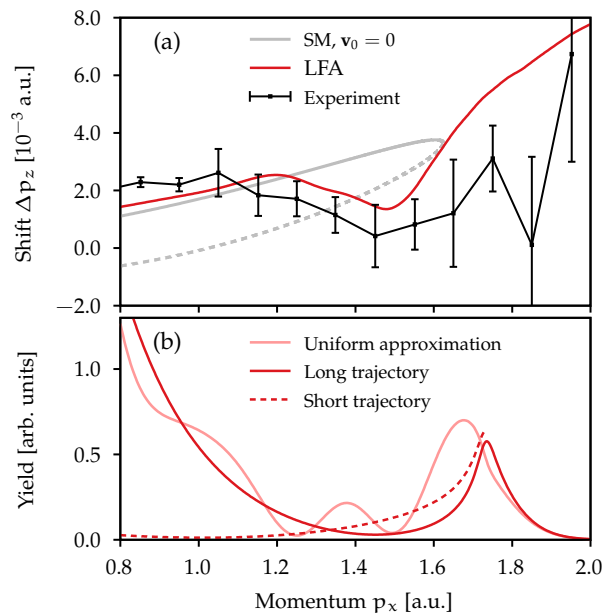


Figure 9.15: (a) Nondipole shift Δp_z of the central maximum of the PMD for ionization of xenon by linearly-polarized laser pulses with 800 nm central wavelength and a peak intensity of 7×10^{13} W/cm²: experimental result provided by Lin *et al.* [500] (black dots), focal-volume-averaged result obtained from LFA simulations with the DCS for the Tong-Lin potential including both long and short trajectories (red line) and simple backreflection model of Eq. (9.35) with $\mathbf{v}_0 = 0$ (gray line). (b) Probabilities of the individual long and short quantum orbits at $p_z = 0$ (dark red solid and dashed lines) as well as the resulting uniform approximation result (pale red line). For panel (b), a cw field with an intensity of 6×10^{13} W/cm² is used. Figure is adapted from Lin *et al.* [500].

For a more realistic theoretical description, LFA simulations are performed with the scattering amplitudes for a Tong-Lin potential (analogous to those in Fig. 9.12). Here, however, the PMDs are also averaged over the focal-volume distribution for a peak intensity of $I_{\text{peak}} = 7 \times 10^{13} \text{ W/cm}^2$. To this end, we follow the scheme introduced in Appendix A.2.4 and perform calculations for nine intensities between $3 \times 10^{13} \text{ W/cm}^2$ and $7 \times 10^{13} \text{ W/cm}^2$. Based on the LFA distributions, the nondipole shifts of the maximum are extracted analogous to the experiment (see Fig. 9.15(a)). The focal-averaged LFA results well reproduce the experimentally-observed local minimum of the nondipole shift around $p_x = 1.5 \text{ a.u.}$

In LFA, both long and short quantum orbits contribute to the measurable PMD. When only considering a single branch of long and short trajectories for fixed CEP and intensity, the superposition of both contributions creates the well-known interference pattern in the plateau region (see Fig. 9.15(b)). However, the pattern is largely washed out when averaging over the CEP and over the focal-volume distribution. In the simplified backreflection calculations shown in Fig. 9.13, the nondipole shifts for the short trajectories are significantly smaller than the shifts for long trajectories.¹⁴ Thus, in the simplest picture, the nondipole shift of the central maximum is mostly related to the shift of the individual orbits and their relative weight (see Fig. 9.15(b)). The probability of the orbits is influenced by the ionization rate and the energy dependence of the DCS. We find that in the inner part of the plateau region with $p_x \lesssim 1.3 \text{ a.u.}$ the long trajectory dominates for the Tong-Lin potential. The short trajectory becomes more important in the intermediate region between $p_x \gtrsim 1.3 \text{ a.u.}$ and the cutoff at about 1.75 a.u. In the vicinity of the cutoff, both solutions merge, a separation in long and short orbits is meaningless [18, 202] and the commonly-used saddle-point approximation breaks down [204]. For even higher p_x , only the long orbit should be included in the calculation. These constraints are automatically properly treated in the uniform approximation [204]. To summarize, the distributions are dominated by the long orbits for small p_x followed by the short orbits at intermediate p_x and again determined by the long orbits for large p_x . When considering the different nondipole shifts for both orbits, this simple picture already predicts a minimum of the nondipole shift as a function of p_x in the region where the short trajectories dominate.

Target dependence

The differential cross section depends on the exact shape of the single-active-electron potential that is used to model xenon. Following the simple argumentation above, we expect a different weighting of the trajectories and, hence, modifications of the nondipole shifts for other potentials. We perform LFA simulations for a GSZ potential (as in Section 4.3) and for the following model potential

$$V(r) = -\frac{1 + 1.985e^{-0.5r}}{r}. \quad (9.36)$$

All three potentials have a p state with the correct ionization potential of xenon and behave as $-1/r$ at large distances r . However, they have different short-range contributions. For simplicity, a cw field is used, but the distributions are focal-volume-averaged (assuming a peak intensity of $I_{\text{peak}} = 7 \times 10^{13} \text{ W/cm}^2$). The averaged PMDs have a pronounced maximum in the vicinity of the polarization axis for all three potentials. Hence, we again determine the maximum's position in p_z -direction for each p_x by a Gaussian fit.

The nondipole shifts of the central maximum are shown in Fig. 9.16(a). The distinct energy dependence of the DCS and, hence, the modified weighting of the long and short orbits lead to different nondipole shifts as a function of p_x for the used potentials. For the potential (9.36), the PMD is mostly dominated by the long trajectory and the nondipole shift roughly follows the prediction of the backreflection model for the long orbit. On the other hand, for the GSZ potential, both long and short trajectories have a similar weight between $p_x \gtrsim 1 \text{ a.u.}$ and the classical cutoff such that a broad minimum in the nondipole shift appears. The focal-averaged LFA results are in qualitative agreement with the TDSE results for a fixed intensity presented in Ref. [500].

¹⁴Qualitatively, this simple picture is also correct when considering the DCS for the Tong-Lin potential.

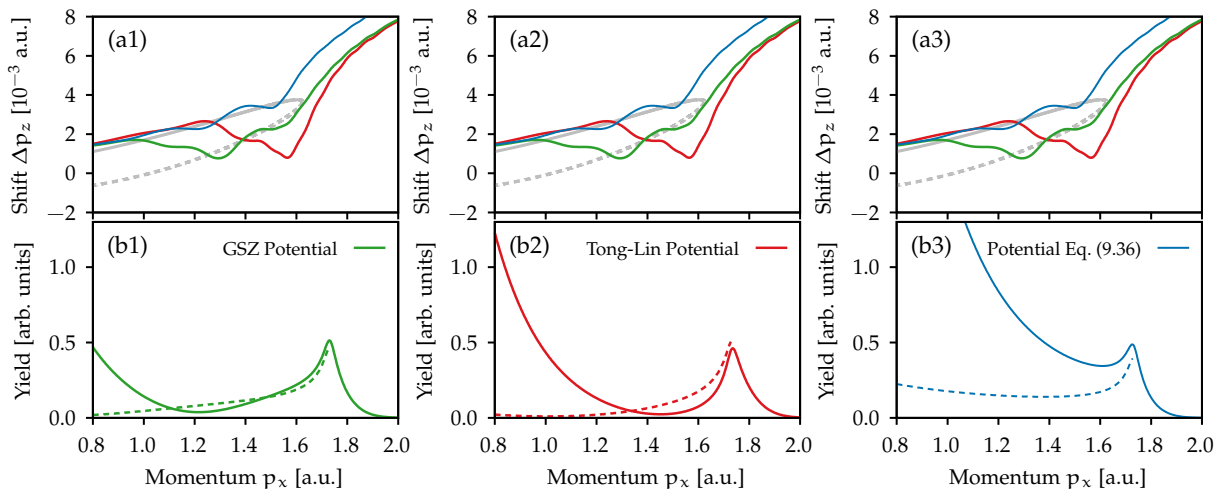


Figure 9.16: (a) Dependence of the nondipole shift of the central maximum on the single-active-electron potential used to model xenon. For better comparison, all three panels show the same results from focal-averaged LFA calculations in 2D for a cw field assuming a peak intensity of 7×10^{13} W/cm². (b) Probabilities of the individual long and short quantum orbits (solid and dashed lines) at $p_z = 0$ for a fixed intensity of 6×10^{13} W/cm² as in Fig. 9.15(b).

A prerequisite for the simple interpretation given above is that the shape of the PMD (in the vicinity of the polarization axis) is dominated by the DCS and that the PMD has a pronounced maximum in p_z -direction for each p_x .¹⁵ The first condition is not fulfilled for momenta p_x above the classical high-energy cutoff (see also the argumentation for H_2^+ in Section 9.5). In addition, a meaningful separation of long and short trajectories is only possible in the plateau region sufficiently far away from the BRR structure. Furthermore, in reality, direct ionization and photoelectron holography dominates the PMD for small $p_x \lesssim 0.8$ a.u. The exact nondipole shifts are also modified, if the interference structure of long and short orbits is not fully washed out by focal-volume averaging (see for example the weak modulation of the nondipole shift for the potential (9.36) in Fig. 9.16(a)). In particular, this is critical when the DCS as a function of velocity v_{scat} changes on the same scale as the interference pattern (see for example the region around the minimum of the DCS at about $v_{\text{scat}} = 0.8$ a.u. for the Tong-Lin potential). It is beyond the scope of this work to prove that such a minimum of the DCS in combination with the interference does not influence the nondipole shift. Most of the described problems could be avoided by using a driving field with longer wavelength (see for example Ref. [42]). The increased ponderomotive potential would lead to a more extended HATI region in the PMD and a smaller momentum scale for the interference between short and long trajectories.

9.7 Conclusion

In this chapter, the nondipole modifications of high-order above-threshold ionization (HATI) were studied in linearly-polarized fields. HATI relies on the large-angle scattering of recolliding electrons. In contrast to recollision-free strong-field ionization, the electronic structure of the target strongly influences the nondipole electron dynamics and the resulting modifications of the photoelectron momentum distributions. We considered a generalization of the three-step model beyond the dipole approximation to explain the overall physical mechanisms. During a first stage of acceleration, the electron drifts in the light-propagation direction so that the corresponding velocity component of the recolliding electron is positive. Therefore, the scattering probability is not symmetric about the polarization axis. Importantly, the shape of the final photoelectron momentum distribution is mainly determined by this scattering probability represented by the target-specific field-free differential cross section. We analyzed the appearing nondipole effects for prototypical atomic as well as molecular targets: the xenon atom and the hydrogen molecular ion H_2^+ .

¹⁵This is for example not fulfilled for helium or other possible model potentials for xenon.

For the hydrogen molecular ion H_2^+ , we presented photoelectron momentum distributions from the numerical solution of the TDSE. In agreement with our earlier work on helium [187], we observed a nondipole shift of the boundary of the high-energy plateau region and a shift of interference structures resulting from long and short rescattering trajectories. These observations are both nearly independent of the target. However, the diffraction of electrons at both centers of the parent ion results in a double-slit-like molecular-interference pattern in the differential cross section. As a result, other observables such as the forward-backward asymmetry in the signal strength strongly depend on the relative direction of the molecular axis with respect to the electric field. For perpendicular alignment, the pattern has extrema roughly parallel to the polarization axis. A close inspection showed that the positions of the extrema are shifted in the light-propagation direction compared to the dipole limit. Considering the double-slit-like interference within the three-step model, the nondipole shifts of the extrema are given mainly by the total momentum gain of the electron before and after scattering. We demonstrated that, in contrast to other nondipole modifications in HATI, the shift of the molecular-interference pattern survives focal-volume averaging, opening the possibility to experimentally observe structure-dependent nondipole effects in strong-field ionization.

The high-energy photoelectron momentum distributions for xenon also exhibit a pronounced maximum near the polarization axis. This extremum is induced by a local maximum of the differential cross section of the xenon ion at a scattering angle of 180° , i.e., it is attributed to backscattered electrons. During recollision the velocity vectors of these electrons are reversed and a considerable amount of electron momentum is transferred to the ion. Hence, for those backscattered electrons, the final momenta in the light-propagation direction are significantly reduced. As a result, the three-step model predicts systematically smaller nondipole shifts of the central maximum for xenon compared to the shifts for small diatomic molecules. For a more sophisticated modeling of the photoelectron momentum distributions in the HATI region, we considered the low-frequency approximation (LFA) beyond the electric dipole approximation, i.e., we approximated the laser-assisted scattering amplitude by the field-free scattering amplitude. The corresponding quantum-orbit model allows us to take into account interference between long and short rescattering trajectories, and at the same time represents the scattering properties of the system well. We demonstrated that the nondipole shifts of the central maximum from LFA are in excellent agreement with the experimental results for xenon [500]. The short and long rescattering trajectories are generally deflected differently in the light-propagation direction. By considering several ionic potentials, we found that this enables the control of the nondipole shift through the relative weighting of these trajectories. Importantly, in this study on xenon, we considered the position of the central maximum. Since other targets such as helium do not show a backscattering maximum, this choice is not always possible (see also our previous work [187]).

In the future, a direct comparison of the nondipole shifts for atoms and molecules would be illuminating. To this end, the well-known combination of molecular nitrogen N_2 and argon atoms with approximately the same ionization potential could be used [36]. Even though both targets exhibit a pronounced maximum of the momentum distribution in the vicinity of the polarization axis, we expect different nondipole shifts for the atomic and molecular case.

In general, nondipole effects in the high-energy region are amplified with increasing laser intensity or wavelength. With the further development of mid-infrared high-power lasers to perform laser-induced electron diffraction experiments such as in Ref. [42], the consideration of nondipole effects in the interpretation of experimental data will be indispensable. For example, if the molecular-interference pattern is used to determine bond lengths in molecules and probe the nuclear dynamics, the neglect of nondipole corrections can lead to errors in the reconstructed lengths that have similar size as today's experimental accuracy [40, 42]. Here, we laid the foundation to avoid such systematic errors in the future.

Chapter 10

Strong-Field Photoelectron Holography Beyond the Dipole Approximation

10.1 Introduction

Strong-field photoelectron holography experiments are commonly performed with linearly-polarized infrared or even mid-infrared light sources [208] (see also Chapter 3 for an introduction). However, longer wavelengths enable higher kinetic energies of the light-driven electrons such that nondipole effects become already prominent at moderate light intensities. For example, Ludwig *et al.* [152] used a 3.4 μm light source to observe effects beyond the electric dipole approximation in linearly-polarized fields at a moderate intensity on the order of $5 \times 10^{13} \text{ W/cm}^2$. Nevertheless, strong-field photoelectron holography is usually studied in the dipole approximation. To close this gap, this chapter provides a theoretical investigation of the nondipole modifications of the holographic pattern.

In recollision-free ionization, the transfer of linear momentum from the light field to the electrons results in a forward shift of the photoelectron momentum distribution (see Chapter 8 for a discussion). In contrast, the first experiments on nondipole effects with linearly-polarized light at 3.4 μm central wavelength revealed a shift of the momentum distribution for the low-energy electrons against the light-propagation direction [152]. Later, a similar observation was also made at 800 nm wavelength [51, 508]. TDSE simulation beyond the dipole approximation confirmed these experimental findings [153, 154, 508]. By scanning the ellipticity of the driving field, Maurer *et al.* attributed the backward shift to a sharp ridge of rescattered electrons [157]. Based on classical-trajectory Monte Carlo (CTMC) simulations, the unexpected backward shift was explained by the interplay between the electron-ion interaction and the magnetic-field-induced motion of the liberated electrons [152, 509]. The shift of the low-energy electrons was also investigated in CTMC simulations which include the nondipole effects on both ions and photoelectrons [155] as well as semiclassical Coulomb-corrected strong-field approximation calculations [156].

The TDSE simulations [153] and the classical simulations [155, 156] reveal that the shift is not uniform, i.e., it depends on the momentum component along the polarization axis. As introduced in Section 3.4, Coulomb focusing in 3D results in an enhanced signal in the vicinity of the polarization axis, reflected as a caustic in classical simulations [77, 78]. The shift of the caustic along the light-propagation direction was analyzed in a classical analytical model, showing that the displacement is negative for low-energy electrons and becomes positive for higher energies [510]. However, the appearance of a caustic indicates the breakdown of the semiclassical approximation [158, 256], i.e., any classical model becomes questionable. For regularization of the nonphysical behavior, the interference of the manifold of focused electron trajectories needs to be considered properly, recently done in a glory-rescattering model in the dipole approximation [158, 511].

In linearly-polarized fields, photoelectron holography patterns resulting from the superposition of a “signal” wave that is scattered upon return to the parent ion and a nonscattered “reference” wave are very prominent in the photoelectron momentum distributions [28, 74, 239]. Qualitatively, modifications of the interference fringes due to nondipole effects were already observed by Chelkowski *et al.* [153, 512]. Classically, these were attributed to changes of the direct and rescattering electron trajectories by the laser magnetic field. However, from a fundamental point of view, the holographic pattern is formed by interference and, thus, determined by the phase difference between the interfering paths (see also Chapter 3). In general, the variations of the kinematics of the trajectories and of their associated phases can differ.

In this chapter, we extend the semiclassical modeling beyond the electric dipole approximation to account for the interference in a trajectory-based description (see also the models in the dipole approximation in Refs. [121, 122] and in Section 3.3). Considering a nondipole correction of the phase associated with each trajectory, the model is able to explain the shift of the holographic fingers in 2D. An analytical simple man’s model beyond the dipole approximations is derived by neglecting the ionic potential during the acceleration stages of the electron trajectories, providing a deeper intuitive understanding of the physical processes. In 3D, Coulomb focusing prevents the interpretation of the momentum distribution in the vicinity of the central maximum by means of a two-path-interference picture. Therefore, we analyze the interplay between Coulomb focusing and nondipole effects by extending the glory-rescattering model [158].

This study was inspired by our joint work with the group of Reinhard Dörner in Frankfurt, especially Alexander Hartung. The first part of this chapter is based on the resulting publication [51]. Most results of the second part of this chapter are already published in Ref. [245]. Shortly after our publications, a joint experimental and theoretical work also discussed the nondipole modification of photoelectron holography [513]. Their findings are in agreement with the theoretical study presented in this chapter.

10.2 Anatomy of nondipole effects in photoelectron holography

Nondipole effects in recollision-free ionization were analyzed in Chapter 8. For pure linearly-polarized fields, the nondipole shift of the lateral distribution in the light-propagation direction p_z can be analytically estimated in the adiabatic limit as [151, 471, 472]

$$p_z^{\max}(p_x, p_y) = \frac{p_x^2}{2c} + \frac{1}{3c} \left(I_p + \frac{p_y^2}{2} \right) + \mathcal{O}(\gamma^2). \quad (10.1)$$

The result depends quadratically on the momentum p_x along the polarization direction and also on the third direction p_y . However, in contrast to the recollision-free ionization geometries described in Chapter 8, the liberated electrons may be driven back to the parent ion in linearly-polarized fields. The appearing scattering processes vastly modify the dynamics (see also Chapter 3 for an introduction in the dipole approximation).

In a recent experiment, Hartung *et al.* [51] considered strong-field ionization of argon by femtosecond laser pulses with 800 nm central wavelength. For each momentum p_x , the nondipole shift of the peak position of the momentum distribution in p_z -direction was analyzed. As expected, the post-ionization Coulomb interaction between parent ion and photoelectron influences the displacement of the PMD shown in Fig. 10.1(a) compared to the recollision-free SFA estimate. The aim of this section is to present theoretical results from the numerical solution of the TDSE in 3D for the conditions in Ref. [51]. These results will underline the need for a proper theoretical description of nondipole effects in photoelectron holography.

Computational details for argon

The photoelectron momentum distributions are calculated numerically in the single-active-electron approximation by using the Fourier split-operator technique on Cartesian grids (see Appendix A.2.2).

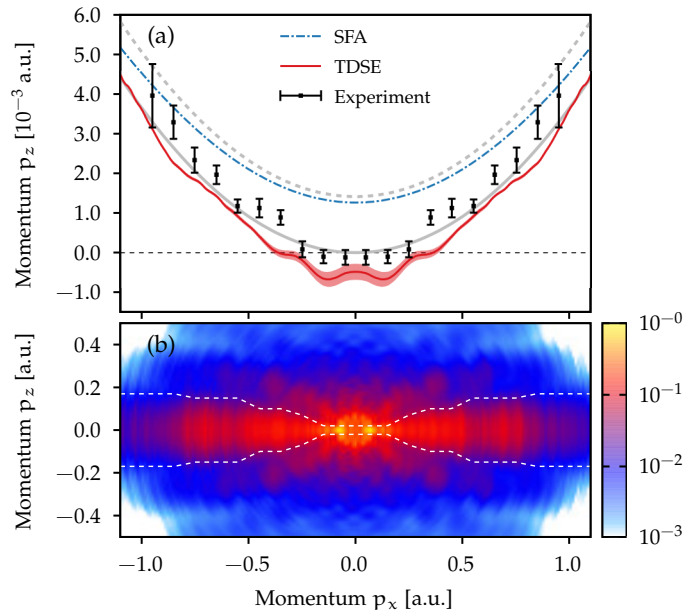


Figure 10.1: Nondipole effects for ionization of argon by linearly-polarized laser pulses at 800 nm central wavelength and a peak intensity of 1.1×10^{14} W/cm². (a) Shift of the central lobe extracted by using a Gaussian fit: experimental result provided by Hartung *et al.* [51] (black dots), focal-volume-averaged result obtained from the numerical solution of the 3D TDSE (red line) and result from the SFA in the saddle-point approximation (blue line). Additionally, the heuristic estimate $\Delta p_z = p_x^2 / (2c)$ (gray solid line) and the adiabatic limit (10.1) of the SFA (gray dashed line) are shown. The errors of the TDSE simulation are estimated as explained in the main text. (b) For visual orientation, the projection of the PMD from TDSE onto the p_x - p_z -plane is presented. The white dashed lines indicate the fit range to extract the shifts of panel (a). Figure is adapted from Hartung *et al.* [51].

Analogous to Chapter 7, a plane-wave laser pulse is considered and the natural gauge (introduced in Section 2.2) is used such that the theory covers the dynamics within the electric quadrupole and magnetic dipole approximations.

The linearly-polarized laser pulses are modeled using a \cos^2 envelope for the electric field with a full duration of ten optical cycles as in Ref. [51]. Here, a central frequency of $\omega = 0.0569$ a.u. corresponding to ≈ 800 nm wavelength is used. In order to mimic the focal-volume distribution, we follow the scheme introduced in Appendix A.2.4 and assume a peak intensity of $I_{\text{peak}} = 1.1 \times 10^{14}$ W/cm². To this end, the PMDs of 15 calculation with intensities ranging from 0.4×10^{14} W/cm² to 1.1×10^{14} W/cm² are averaged. A pseudopotential for the 3p state with a cutoff radius $r_{\text{cl}} = 1.5$ a.u. based on the Tong-Lin potential is used to model the argon atom (see Appendix A.2.3). Only ionization of the p_x orbital aligned along the polarization axis is considered.

The inner wave function is represented on a Cartesian grid with an extension of 269 a.u. and spacings of $\Delta x = 0.35$ a.u. in all directions. The momentum distribution is calculated from the outer grid after propagating the wave function for four additional cycles after the end of the pulse (resolution $\Delta p_x = \Delta p_y = 0.0116$ a.u. and $\Delta p_z = 0.0088$ a.u.). To avoid artifacts of ATI rings, the PMDs are averaged over slices of $\Delta p_x = 0.1$ a.u. in p_x -direction. The 3D PMDs are projected onto the p_x - p_z -plane (as shown in Fig. 10.1(b)). For each momentum p_x , the position of the lateral maximum is obtained from a Gaussian fit to the central region. To only select the central maximum (analogous to the experiment), the fit range depends on p_x and it is indicated by white dashed lines in Fig. 10.1(b). We find that the positions of the maximum obtained for projection or for a slice at $p_y = 0$ through the PMD differ only slightly.

For very low energies, rich structures appear in the PMDs and, in addition, Rydberg states cause some problems in the simulations based on a two-grid scheme. In order to check the stability of the simulations and of the extraction procedure, various additional simulations in two dimensions with different position and momentum grids were performed. Furthermore, we also considered remaining “continuum electrons” on the inner grid by means of a projection on plane-wave states. We estimate the error for the maximum’s position by using the maximal difference between 2D results with very high resolution and calculations with the same grid parameters as in 3D. For sufficiently high momenta

($|p_x| \gtrsim 0.3$ a.u.), the nondipole shifts are very stable with respect to the numerical procedure. However, at low energies, only qualitative accuracy is reached in these 3D simulations.

Results

Figure 10.1(a) shows both the positions of the central maximum of the lateral distribution of the experiment along with the results from TDSE. Overall the TDSE simulations reproduces the findings of the experiment well.¹ For small momenta, rich structures are visible in the photoelectron momentum distributions. Soft recollisions result in a bunching of electrons [83–86, 118], reflected as low-energy structures in the PMDs [81–84] (here for $|p_x| \lesssim 0.2$ a.u.). In this low-energy region, as introduced above, peak positions are shifted against the light-propagation direction (see for example Refs. [152, 157, 509]). In an intuitive picture, the magnetic part of the Lorentz force first pushes the low-energy electron slightly forward [475]. However, in a swing-by-process, the electron returns to the parent ion with an offset in the light-propagation direction such that the electron-ion interaction slingshots the electron into the backward direction. For $|p_x| \gtrsim 0.2$ a.u., a holographic pattern is visible in the PMD along the polarization (see Chapter 3 for an introduction). Here, the maximum's position is determined by the position of the central fringe. The nondipole shift from TDSE is systematically smaller compared to the recollision-free SFA result and it approaches the heuristic parabolic estimate $p_x^2/(2c)$ close to classical cutoff for “direct” ionization (here at ≈ 1 a.u.).

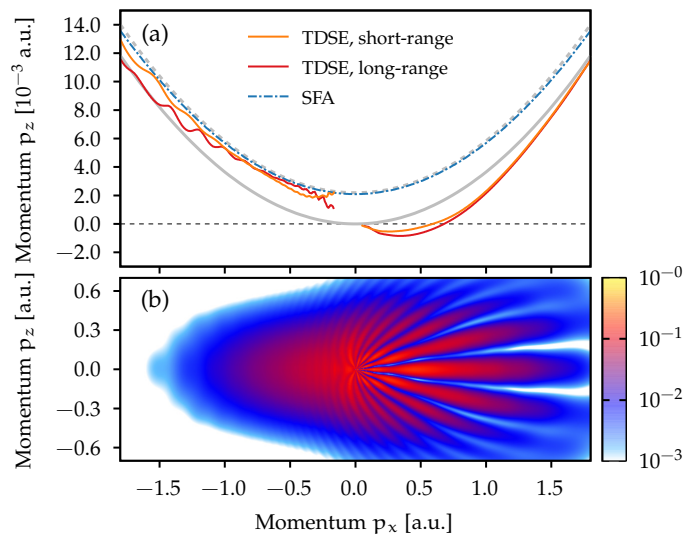


Figure 10.2: Comparison of the nondipole effects for recollision-free ionization (dominates for $p_x < 0$) and for photoelectron holography (dominates for $p_x > 0$). (a) Shift of the central lobe of the lateral distribution calculated by a Gaussian fit with a range of $|p_z| < 0.1$ a.u. for $p_x < 0$ and of $|p_z| < 0.02$ a.u. for $p_x > 0$. Shown are focal-volume-averaged results for ionization of helium modeled by a short-range potential (9.11) or a long-range potential (10.2) in 2D in two-cycle laser pulses of Eq. 10.3 with a \cos^4 envelope, 800 nm wavelength and a peak intensity of $I_{\text{peak}} = 8.0 \times 10^{14}$ W/cm². Additionally, results from the SFA in the saddle-point approximation (blue line), the adiabatic limit (10.1) of the SFA (gray dashed line) and the heuristic estimate $\Delta p_z = p_x^2/(2c)$ (gray solid line) are shown. (b) Focal-volume-averaged PMD for the long-range potential.

When considering the dynamics in 2D or short-range potentials in 3D, Coulomb focusing is absent and, hence, no ridge structure appears in classical simulations (see also Section 3.4). Figure 10.2(a) shows the nondipole shifts of the central maximum from focal-volume-averaged PMDs for ionization of 2D helium modeled by either a short-range potential (9.11) or a long-range potential (10.2). Details on the numerical simulations are given in the next section. For illustrative purposes, a very short two-cycle laser pulse is used. Nonscattered electrons dominate the main part of distribution for $p_x < 0$ and, thus, the shift of the lateral distribution is approximately given by the recollision-free SFA result. For momenta $p_x \lesssim -1.3$ a.u. close to the classical cutoff, we believe that the deviations visible for the long-range potential are caused by other types of electron scattering [205]. For $p_x > 0$, a pronounced pattern

¹It is conspicuous that the experimental values are systematically shifted up by $\approx 5 \times 10^{-4}$ a.u. compared to the TDSE results.

of holographic fringes is visible (see the distribution in Fig. 10.2(b)). In 2D, the constructive interference between forward-scattered trajectories departing in the same quarter cycle of the electric field “shapes” the central holographic finger out of the classical distribution (see also Section 3.4.1). Importantly, we find nearly the same momentum-dependent nondipole shift of the central fringe for the long-range and short-range potentials. Hence, in contrast to recent studies [153, 156, 509], this observation suggests that the classical (interference-free) probability cannot provide a complete and consistent view on the momentum-dependent shift in the lateral distribution for linearly-polarized fields.

10.2.1 Computational details for helium

In order to simplify the numerical TDSE simulations and the interpretation of the results, we will use helium as the target atom in the remaining part of the chapter. Many of the simulations are performed in reduced dimension (2D) where the target is modeled by the following potential

$$V_{2D}(r) = -\frac{e^{-0.575r} + 1}{\sqrt{r^2 + 0.75}}, \quad (10.2)$$

which reproduces the ionization potential of the helium atom $I_p \approx 0.9$ a.u. For more realistic 3D simulations, a pseudopotential for the 1s state of helium with a cutoff radius $r_{cl} = 1.5$ a.u. based on the Tong-Lin potential is used (see Appendix A.2.3). The linearly-polarized laser pulses of n_p cycles duration are chosen as

$$\mathbf{A}(\eta) = -\frac{E_0}{\omega} \sin(\omega\eta) \cos^k\left(\frac{\omega\eta}{2n_p}\right) \mathbf{e}_x \quad (10.3)$$

with central frequency of $\omega = 0.0569$ a.u. corresponding to ≈ 800 nm wavelength. The exponent k is either two or four and an intensity of $I = 7.5 \times 10^{14}$ W/cm² is used for most simulations.

As described above, the TDSE is solved numerically by means of the split-operator method on Cartesian grids. In 2D, the inner grid has a size of 819 a.u. in each direction with spacings of $\Delta x = 0.2$ a.u. A time step of $\Delta t = 0.01$ a.u. is used. The PMDs in 2D have a resolution $\Delta p_x = 0.0038$ a.u. and $\Delta p_z = 0.0019$ a.u. In 3D, the size of the inner grid is 358 a.u. in each direction with spacings of $\Delta x = 0.35$ a.u. A time step of $\Delta t = 0.02$ a.u. is used. We only consider slices at $p_y = 0$ through the 3D PMDs with a resolution of $\Delta p_x = \Delta p_z = 0.0044$ a.u. To increase the quality of the PMDs at low energies, we add up coherently the momentum-space amplitude of the outer grid and the continuum part that is still present on the inner grid (at the end of the propagation). To approximate the latter one, the localized bound states are removed from the inner wave function using a mask function and the remaining part of this wave function is projected on eikonal states as described in Appendix A.2.2.

10.3 Semiclassical model beyond the electric dipole approximation

A semiclassical treatment of the quantum mechanics offers the possibility to interpret the electron’s dynamics on the basis of classical physics. To model photoelectron holography beyond the electric dipole approximation, we basically follow the semiclassical model introduced in Chapter 3, but include nondipole corrections.² In the spirit of the two-step model of Section 2.1.1, the electron’s motion is split in two stages: In the first step, the initially-bound electron is released. Here, we neglect the ionic potential V so that this step is described within the SFA beyond the dipole approximation. In the subsequent acceleration of the freed electron, the semiclassical approximation of Feynman’s path integral is used to model the dynamics such that the Lorentz force of the electromagnetic field as well as the Coulomb attraction are included in a nonperturbative manner. We use the minimal coupling Hamiltonian (2.20) in Coulomb gauge ($H = \frac{1}{2}(\hat{\mathbf{p}} + \mathbf{A}(\eta))^2 + V(\mathbf{r})$) that governs the dynamics in a potential V and a plane-wave laser pulse represented by a vector potential $\mathbf{A}(\mathbf{r}, t) = \mathbf{A}(\eta)$ with $\eta = t - z/c$.

²Chronologically, the model presented in Chapter 10 was developed before the model in the dipole approximation of Chapter 3. Hence, certain details in the actual implementation are different.

Formally, the probability amplitude can be expressed using a Dyson representation as in Eq. (3.2). First, the system evolves in its initial state. At a time t' , the electron is “kicked” by the electromagnetic field and subsequently it interacts with the ionic core and the laser field. Hence, the mixed position-momentum-space propagator $\langle \mathbf{p} | U(t_f, t') | \tilde{\mathbf{r}} \rangle$ appears in the integral. As introduced in Section 3.3.1, the propagator is evaluated in a semiclassical approximation based on Feynman’s path integral. To this end, we consider the classical trajectories with positions $\mathbf{r}_{cl}(t)$ and canonical momenta $\mathbf{k}_{cl}(t)$ that fulfill the boundary conditions: $\mathbf{r}_{cl}(t') = \tilde{\mathbf{r}}$ and $\mathbf{k}_{cl}(t_f) = \mathbf{p}$. These classical trajectories follow the classical Hamilton’s equations of motion (EOM) (3.6) including both electric- and magnetic-field contributions:

$$\begin{aligned} \dot{\mathbf{k}}_{cl}(t) &= -\nabla_{\mathbf{r}} V(\mathbf{r}_{cl}(t)) - \frac{\mathbf{e}_z}{c} \mathbf{E} \left(t - \frac{z_{cl}(t)}{c} \right) \cdot \dot{\mathbf{r}}_{cl}(t), \\ \dot{\mathbf{r}}_{cl}(t) &= \mathbf{k}_{cl}(t) + \mathbf{A} \left(t - \frac{z_{cl}(t)}{c} \right). \end{aligned} \quad (10.4)$$

These EOM are equivalent to Newton’s equation of motion that include the Coulomb attraction and the well-known Lorentz force. In principle, for every times t' and for every initial position $\tilde{\mathbf{r}}$, we would have to determine the trajectories that are deflected to a given final momentum \mathbf{p} . However, for simplification, we again introduce a relation between the auxiliary momenta $\tilde{\mathbf{p}}'$ and the initial positions $\tilde{\mathbf{r}}$ of the classical trajectories and we only select a finite number of ionization times t' .

To this end, we follow the ideas introduced in Section 3.3.2. In the spirit of complex-time quantum-orbit models, we use the two-pronged integration path of Fig. 2.5 in the complex time. The acceleration of the liberated electron from the release time $t'_r = \text{Re}(t'_s)$ up to the final time t_f under the influence of the combined laser and Coulomb fields is approximated by real-valued trajectories. In contrast, during under-the-barrier motion associated with the contour from the complex-valued saddle-point time t'_s down to the real axis ($t'_s \rightarrow \text{Re}(t'_s)$) the potential V is neglected, i.e., the dynamics is effectively treated like in the strong-field approximation. Hence, to first order of $1/c$, the equations of motion (10.4) can be solved analytically for the release step (see for example Section 8.3.1). The canonical momentum in Coulomb gauge can be written to first order in $1/c$ as

$$\mathbf{k}_{cl}(t) = \tilde{\mathbf{p}}' + \frac{\mathbf{e}_z}{c} \left(\tilde{\mathbf{p}}' \cdot \mathbf{A}(t) + \frac{1}{2} \mathbf{A}^2(t) \right). \quad (10.5)$$

Here, the canonical momentum $\tilde{\mathbf{p}}'$ in the natural gauge of Section 2.2.2 is conserved and would be equal to the final momentum, if the potential would also be neglected in the acceleration step.

We use the momentum $\tilde{\mathbf{p}}'$ to parameterize the initial conditions of the trajectories. Analogous to previous approaches in the dipole approximation (see for example Ref. [118]), for a given $\tilde{\mathbf{p}}'$, the integration constants at time t'_r are fixed by the conditions $\text{Im}(\mathbf{r}_{cl}(t'_r)) = 0$ and $\text{Re}(\mathbf{r}_{cl}(t'_s)) = 0$.³ Under these assumptions, the tunnel-exit position \mathbf{r}_0 at the release time t'_r is given by (to first order in $1/c$)⁴

$$\mathbf{r}_0 = \text{Re} \left(\left(1 + \frac{\tilde{p}'_z}{c} \right) \alpha(t'_r, t'_s) + \frac{(t'_s - t'_r) \tilde{p}'_z}{c} \mathbf{A}(t'_s) \right) + \frac{\mathbf{e}_z}{c} \text{Re} \left(\tilde{\mathbf{p}}' \cdot \alpha(t'_r, t'_s) + \frac{1}{2} \alpha_2(t'_r, t'_s) \right) \quad (10.6)$$

with α and α_2 of Eq. (2.11). The corresponding initial velocity at t'_r reads (to first order in $1/c$)

$$\mathbf{v}_0 = \mathbf{v}(\tilde{\mathbf{p}}', t'_r) = \tilde{\mathbf{p}}' + \mathbf{A}(t'_r) + \frac{\mathbf{e}_z}{c} \left(\tilde{\mathbf{p}}' \cdot \mathbf{A}(t'_r) + \frac{1}{2} \mathbf{A}^2(t'_r) \right) \quad (10.7)$$

with the vector \mathbf{v} defined in Eq. (2.31). For each $\tilde{\mathbf{p}}'$, the complex-valued time t'_s is defined by the potential-free saddle-point equation (to first order in $1/c$)

$$\frac{\mathbf{v}^2(\tilde{\mathbf{p}}', t'_s)}{2} = \frac{1}{2} \left(\tilde{\mathbf{p}}' + \mathbf{A}(t'_s) + \frac{\mathbf{e}_z}{c} \left(\tilde{\mathbf{p}}' \cdot \mathbf{A}(t'_s) + \frac{1}{2} \mathbf{A}^2(t'_s) \right) \right)^2 = -I_p. \quad (10.8)$$

Equation (10.8) has the same form as Eq. (8.12) in the plain nondipole SFA. However, for $V \neq 0$, the auxiliary variable $\tilde{\mathbf{p}}'$ is in general not equal to the final momentum \mathbf{p} .

³The choice $\text{Im}(\mathbf{r}_{cl}(t'_r)) = 0$ helps to avoid problems with branch cuts (see for example Refs. [205, 206]).

⁴This is only one possible choice. For example, in a more recent work [479], other initial conditions were used.

The action phase associated with each orbit can also be divided into a complex-valued part corresponding to the under-the-barrier motion and a real-valued part corresponding to the acceleration step. Using the EOMs (10.4) and Eq. (10.5), the semiclassical action of Eq. (3.4) can be simplified for the potential-free under-the-barrier part:

$$\begin{aligned}
S_{\downarrow}^0 &= - \int_{t'_s}^{t'_r} dt [H(\mathbf{r}_{cl}(t), \mathbf{k}_{cl}(t), t) + \mathbf{r}_{cl}(t) \cdot \dot{\mathbf{k}}_{cl}(t)] \\
&= - \int_{t'_s}^{t'_r} dt \left[\frac{1}{2} (\mathbf{k}_{cl}(t) + \mathbf{A}(t))^2 + \frac{z_{cl}(t)}{c} \mathbf{E}(t) \cdot \dot{\mathbf{r}}_{cl}(t) + \mathbf{r}_{cl}(t) \cdot \dot{\mathbf{k}}_{cl}(t) \right] + \mathcal{O}\left(\frac{1}{c^2}\right) \\
&= - \int_{t'_s}^{t'_r} dt \frac{1}{2} (\mathbf{k}_{cl}(t) + \mathbf{A}(t))^2 + \mathcal{O}\left(\frac{1}{c^2}\right) = - \int_{t'_s}^{t'_r} dt \frac{1}{2} \mathbf{v}^2(\tilde{\mathbf{p}}', t) + \mathcal{O}\left(\frac{1}{c^2}\right).
\end{aligned} \tag{10.9}$$

The phase (3.4) associated with the acceleration step can also be rewritten using the EOMs (10.4)

$$S_{\rightarrow} = - \int_{t'_r}^{t_f} dt \left[\frac{1}{2} \dot{\mathbf{r}}_{cl}^2(t) + V(\mathbf{r}_{cl}(t)) - \mathbf{r}_{cl}(t) \cdot \nabla V(\mathbf{r}_{cl}(t)) - \mathbf{z}_{cl}(t) \cdot (\dot{\mathbf{r}}_{cl}(t) \times \mathbf{B}(t - z_{cl}(t)/c)) \right]. \tag{10.10}$$

This phase includes both the Coulomb potential and the nondipole effects in a nonperturbative manner.⁵ In the limit of vanishing potential $V = 0$, the correct action (2.33) of the Volkov states, i.e., the action entering the nondipole SFA, is recovered to first order of $1/c$. To this end, the last term of Eq. (10.10) proportional to the magnetic part of the Lorentz force is important. This term is not present in the previously-developed CCSFA beyond dipole approximation [156].

In the model, preexponential parts of the amplitude related to the release step are neglected. For each trajectory, the associated ionization probability is determined by the imaginary part $\text{Im}(S_{\downarrow}^0 + I_p t'_s)$. Thus, the model includes the nondipole shift of the initial-velocity distribution in the light-propagation direction, attributed the under-the-barrier magnetic-field effects [150, 151] (see also Section 8.2.4). Empirically, we find the observables discussed below are only weakly influenced by the nondipole corrections of the tunnel exit (10.6). In contrast, the additional nondipole part of phase as well as the modifications of the initial-velocity distribution are essential for a quantitative modeling of the probability distributions.

For an explicit calculation of the probability amplitude for a final momentum \mathbf{p} , we follow the steps:

- Solve the nondipole saddle-point equation (10.8) for each auxiliary momentum $\tilde{\mathbf{p}}'$ to obtain the corresponding saddle-point times $t'_s = t'_r + it'_i$. Establish a connection between $\tilde{\mathbf{p}}'$ and the initial conditions for the trajectories of the acceleration step, i.e., determine for each $\tilde{\mathbf{p}}'$ the corresponding tunnel-exit position \mathbf{r}_0 of Eq. (10.6) and initial velocity \mathbf{v}_0 of Eq. (10.7).
- Solve the inversion problem, i.e., find all auxiliary momenta $\tilde{\mathbf{p}}'$ that are mapped by the classical dynamics to the given final momentum \mathbf{p} . Here, we only consider the most important types of trajectories. Thus, in contrast to the model of Chapter 3, we directly tackle the inversion problem by using a combination of the multi-dimensional Newton method and the conjugate-gradient method.
- Calculate the ingredients of the probability amplitude for each solution $\tilde{\mathbf{p}}'_\mu$ of the inversion problem. To determine the phase S_{\rightarrow} of Eq. (10.10), we add an equation to the system of differential equations for the EOMs. The Jacobian $J(t_f)$ of Eq. (3.10) is numerically approximated by considering the variation of the final momenta \mathbf{p} with the auxiliary momentum $\tilde{\mathbf{p}}'$ for a fixed release time t'_r and a fixed exit point⁶

$$J(t_f) \approx \det \left[\frac{\Delta \mathbf{p}}{\Delta \tilde{\mathbf{p}}'} \right]. \tag{10.11}$$

For the different branches of trajectories, we use the same Maslov indices ν as in the dipole approximation (see Chapter 3).

⁵Equation (10.10) does not use a $1/c$ expansion.

⁶The PMDs are only weakly modified and the conclusions of this chapter are untouched, if the exit point and the time t'_r are also varied with the momentum $\tilde{\mathbf{p}}'$ according to Eqs. (10.6) and (10.8).

- Evaluate the transition amplitude for a given \mathbf{p} by using the ingredients for the trajectories

$$M(\mathbf{p}) \approx \sum_{\mu} \frac{e^{-i\nu_{\mu} \frac{\pi}{2}}}{\sqrt{|J_{\mu}(t_f)|}} e^{i(S_{\rightarrow, \mu} + S_{\downarrow, \mu}^0 + I_{\mathbf{p}}(t'_{s, \mu} - t_{\Lambda}))}, \quad (10.12)$$

where μ labels all possible initial momenta $\tilde{\mathbf{p}}'_{\mu}$ that are solutions of the inversion problem.

10.4 Simple man's model beyond the dipole approximation

The model introduced in Section 10.3 includes both nondipole effects and effects of the long-range potentials. However, for a qualitative interpretation of certain aspects of photoelectron holography, a simpler Coulomb-free semiclassical model is sufficient. To this end, we roughly follow the ideas presented in Refs. [28, 239], but include leading-order nondipole effects. The holographic pattern is modeled as the interference of a nonscattered reference wave packet and a scattered signal wave packet. The dynamics of the electron wave packets is treated analogous to the simple man's model introduced in Chapter 9 for high-order above-threshold ionization. This allows for an analytical description of the influence of nondipole effects on the interference pattern.

Tunnel ionization launches electrons at each possible release time t_0 with initial velocities $\mathbf{v}_0 \perp \mathbf{E}(t_0)$ (see Eq. (2.47)). The subsequent potential-free motion of the electrons in the electromagnetic field can be described classically. To first order in $1/c$, the canonical momentum $\tilde{\mathbf{p}}'$ in natural gauge can be expressed in terms of the initial velocity \mathbf{v}_0 as (see Eq. (10.7))

$$\tilde{\mathbf{p}}' = -\mathbf{A}(t_0) + \frac{\mathbf{A}^2(t_0)}{2c} \mathbf{e}_z + \mathbf{v}_0. \quad (10.13)$$

The reference wave packet does not feel the Coulomb force of the parent ion so that the final momentum \mathbf{p} is equal to the auxiliary momentum $\tilde{\mathbf{p}}'$. Hence, Equation (10.13) defines the mapping of the final momentum \mathbf{p} to the release time t_0^{ref} and the initial velocity $\mathbf{v}_0^{\text{ref}}$. To first order in $1/c$, the associated semiclassical phase is given by (see Eqs. (10.9) and (10.10))⁷

$$S_{\text{ref}} = - \int_{t_0^{\text{ref}}}^{t_f} dt \frac{\mathbf{v}^2(\mathbf{p}, t)}{2}, \quad (10.14)$$

where \mathbf{v} is the auxiliary velocity of Eq. (2.31). For certain ionization times, the electrons are driven back to the vicinity of the ionic core and may scatter off such that a signal wave packet is created. For an exact return to its initial position, the electron has to start with an initial velocity (see Eq. (9.6))

$$\mathbf{v}_{0,z} = - \frac{1}{2c(t_c - t_0^{\text{sig}})} \int_{t_0^{\text{sig}}}^{t_c} d\tau (\mathbf{A}(\tau) - \mathbf{A}(t_0^{\text{sig}}))^2. \quad (10.15)$$

This is caused by the drift motion in the light-propagation direction induced by the laser magnetic field. The return time t_c is determined by the motion along the polarization direction: $x(t_0^{\text{sig}}) = x(t_c)$. During the scattering, the direction of the electron's velocity and, hence, its associated auxiliary momentum is usually changed (see Section 9.3). After the scattering, the electron is again accelerated by the electromagnetic field. Hence, its outgoing velocity is mapped to the final momentum \mathbf{p} . Neglecting the phase change associated with the scattering process, the phase for the signal electron reads

$$S_{\text{sig}} = - \int_{t_0^{\text{sig}}}^{t_c} dt \frac{\mathbf{v}^2(\tilde{\mathbf{p}}', t)}{2} - \int_{t_c}^{t_f} dt \frac{\mathbf{v}^2(\mathbf{p}, t)}{2}. \quad (10.16)$$

For a given final momentum \mathbf{p} , the interference is determined by the acquired phase difference between the reference path and the signal path

$$\Delta S = \int_{t_0^{\text{ref}}}^{t_c} dt \frac{\mathbf{v}^2(\mathbf{p}, t)}{2} - \int_{t_0^{\text{sig}}}^{t_c} dt \frac{\mathbf{v}^2(\tilde{\mathbf{p}}', t)}{2}. \quad (10.17)$$

⁷The phase has the same form as the continuum part of the SFA action (2.41).

As described in Section 3.4.1, the superposition of signal and reference trajectories starting in the same quarter cycle of the field induces the holographic fingers. For final momenta close to the polarization axis, their release times (t_0^{sig} and t_0^{ref}) are quite similar and can be approximated by the values from the dipole approximation.

The condition for constructive interference in Eq. (10.17), $\Delta S = 2\pi n$ with $n \in \mathbb{N}_0$, defines the positions of the holographic fingers. Here, the central holographic finger corresponds to forward scattering of the signal trajectory [239] such that we find $\tilde{\mathbf{p}}' = \mathbf{p}$. Since reference and signal trajectories are then equivalent, their phase difference of Eq. (10.17) is zero. The position of the central finger is determined by Eqs. (10.13) and (10.15) for the signal trajectory

$$\begin{aligned} p_z^{\text{central}} &= \frac{\mathbf{A}^2(t_0^{\text{sig}})}{2c} + v_{0,z} = -\frac{1}{c} \frac{1}{t_c - t_0^{\text{sig}}} \int_{t_0^{\text{sig}}}^{t_c} dt \left(-\mathbf{A}(t_0^{\text{sig}}) \cdot \mathbf{A}(t) + \frac{1}{2} \mathbf{A}^2(t) \right) \\ &= -\frac{1}{c} \frac{1}{t_c - t_0^{\text{ref}}} \int_{t_0^{\text{ref}}}^{t_c} dt \left(\mathbf{p} \cdot \mathbf{A}(t) + \frac{1}{2} \mathbf{A}^2(t) \right). \end{aligned} \quad (10.18)$$

In the last line, we used that $p_x = -A_x(t_0^{\text{sig}})$ and that the release times of the signal and the reference trajectory are equal. Interestingly, the obtained position of the central interference fringe coincides with the position of the classical caustic in 3D derived in Refs. [157, 510].

To estimate the nondipole shift of the higher-order fringes, we restrict ourselves to the p_x - p_z -plane. Similar to Refs. [74, 239] in the dipole approximation, we find that the z -component of the first term of Eq. (10.17) dominates the phase difference. Thus, the phase difference can be approximated as

$$\Delta S \approx \int_{t_0^{\text{ref}}}^{t_c} dt \left[\frac{p_z^2}{2} + \frac{p_z}{c} \left(\mathbf{p} \cdot \mathbf{A}(t) + \frac{1}{2} \mathbf{A}^2(t) \right) \right]. \quad (10.19)$$

In the dipole approximation, the positions of the extrema are given by [234]

$$p_z^{\text{dip}} = \pm \sqrt{\frac{4\pi n}{t_c - t_0^{\text{ref}}}}. \quad (10.20)$$

Since we are only interested in the first-order nondipole corrections Δp_z , the positions are written as $p_z = p_z^{\text{dip}} + \Delta p_z$ and the phase difference (10.19) is expanded in Δp_z . To first order in $1/c$, the resulting equation can be solved analytically for the shift

$$\Delta p_z \approx -\frac{1}{c} \frac{1}{t_c - t_0^{\text{ref}}} \int_{t_0^{\text{ref}}}^{t_c} dt \left(\mathbf{p} \cdot \mathbf{A}(t) + \frac{1}{2} \mathbf{A}^2(t) \right). \quad (10.21)$$

Close to the polarization axis, the whole holographic interference pattern is uniformly displaced for fixed p_x , i.e., the central fringe as well as all higher-order fringes approximately experience the same shift. In agreement with the TDSE results presented in Section 10.2, the nondipole offset depends on the momentum p_x in polarization direction.

10.5 Results and discussion

10.5.1 The central holographic fringe without Coulomb focusing

When considering the electron dynamics in 2D, Coulomb focusing is absent and the central holographic finger is created by two-path interference between one nonscattered trajectory and one forward scattered trajectory. For simplicity, we first choose very short two-cycle pulses (as used in Fig. 10.2) such that the light-driven electrons can only undergo a single forward scattering. The PMDs from the numerical solution of the TDSE in 2D are used to extract the shifts of the central holographic fringe. To this end, the distributions are first averaged over an interval $\Delta p_x = 0.1$ a.u. Afterwards, for each p_x , a Gaussian fit to the central region with $|p_z| < 0.02$ a.u. is used to calculate the peak position in p_z -direction. We

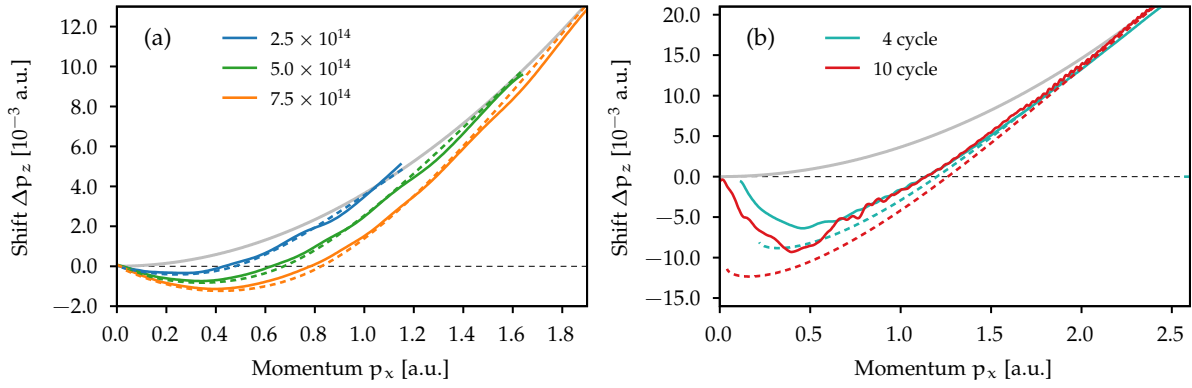


Figure 10.3: Shift of the central holographic fringe for ionization of helium extracted from 2D TDSE simulations (solid lines) and the estimate (10.21) of the simple man's model (dashed lines). (a) Results for short two-cycle \cos^4 pulses at various intensities given in the legend in W/cm^2 . (b) Results for two durations of \cos^2 pulses. The results of panel (b) are obtained summing up the PMDs for intensities 7×10^{14} , 7.5×10^{14} and 8×10^{14} W/cm^2 . To guide the eye, the gray thick line indicates the heuristic estimate $p_x^2/(2c)$. Figure is adapted from Brennecke *et al.* [245].

find that the nondipole shifts from TDSE are in perfect agreement with the simple man's estimate (10.21) (see the results for three different intensities in Fig. 10.3(a)). Close to the classical cutoff, the excursion times $t_c - t_0^{\text{sig}} \approx t_c - t_0^{\text{ref}}$ of the electrons approach zero in the simple man's model. Hence, the initial velocity \mathbf{v}_0 of Eq. (10.15) also vanishes so that the nondipole shift is solely determined by the "second" stage of acceleration by the electromagnetic field. In this limit, Equation (10.21) simplifies to the heuristic parabolic estimate $\Delta p_z \approx A^2(t_0^{\text{ref}})/(2c) \approx p_x^2/(2c)$ with $p_x \approx -A_x(t_0^{\text{ref}})$.

In agreement with the TDSE simulations in Ref. [153], the central holographic fringe is shifted in backward direction ($\Delta p_z < 0$) for small momenta p_x . For the two-cycle waveform, signal electrons corresponding to small final momenta p_x scatter after the end of the pulse and their excursion times $t_c - t_0^{\text{sig}}$ become large. Thus, according to Eq. (10.21), the shift of the simple man's model vanishes in the limit $p_x \rightarrow 0$. The simple man's results for different pulse lengths are shown in Fig. 10.3. For long laser pulses, the simple man's model predicts a shift $\Delta p_z \propto -U_p/c$ at $p_x = 0$. Since these low-energy electrons usually dominate the peak position of the lateral momentum distributions, the simple man's model qualitatively explains the linear scaling of the backward shift with the laser intensity as observed in Ref. [153] for the solution of the 2D TDSE. For four-cycle or ten-cycle pulses, the simple man's model still works well for large momenta. However, at low energies, the position of the central maximum in TDSE is less shifted to negative p_z compared to the simple man's estimate (see Fig. 10.3(b)). Here, in order to avoid the influence of intracycle interference on the extracted maximum's shift, the PMDs from TDSE corresponding to intensities 7.0×10^{14} , 7.5×10^{14} and 8.0×10^{14} W/cm^2 were averaged.

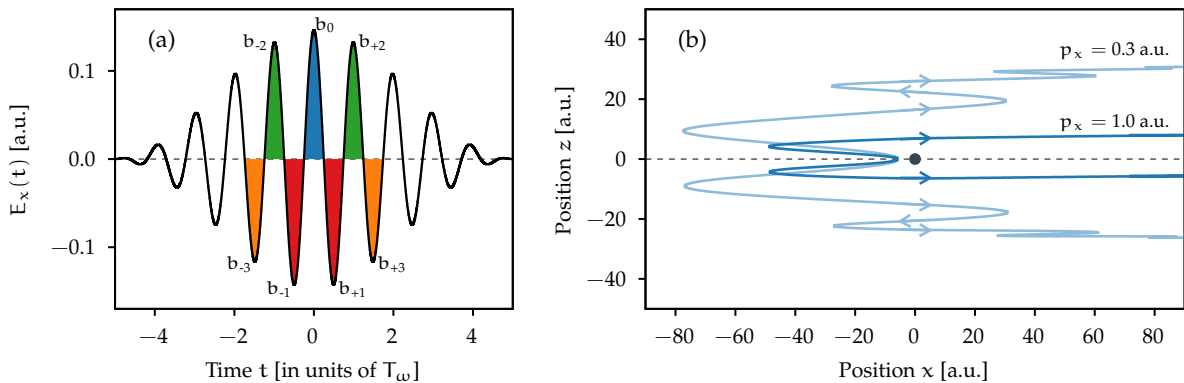


Figure 10.4: (a) Electric field of a ten-cycle \cos^2 pulse at an intensity of 7.5×10^{14} W/cm^2 with color-marked half cycles. (b) Illustration of trajectories leading to photoelectron holography on the polarization axis at $p_z = 0$. For large $p_x \gtrsim 0.45$ a.u., the electrons only pass by the ionic core for a single time. In contrast, for small $p_x \lesssim 0.45$ a.u., the electrons pass by the ionic core multiple times. Figure is adapted from Brennecke *et al.* [245].

To resolve this difference between the modeling and the TDSE results, the interplay between electromagnetic field and long-range electron-ion interaction needs to be included. For this purpose, we focus on the ten-cycle pulse and we only study the half plane with $p_x > 0$. We apply the semiclassical model developed in Section 10.3 where the potential is approximated as a bare Coulomb potential $V(r) = -1/r$, but the correct ionization potential of helium $I_p \approx 0.9$ a.u. is used. The ionization probability (represented by $\exp[-2\text{Im}(S_{\downarrow}^0 + I_p t_s')]$) depends strongly on the electric-field strength (see also Eq. (2.3)). Thus, only trajectories starting in the vicinity of the peak of the pulse envelope are taken into account (see the color-marked branches in Fig. 10.4(a)).

As described in the simple man's model of Section 2.1.1, for final momenta with $p_x > 0$, release times in branches $b_{\pm 1}$ and $b_{\pm 3}$ do not undergo rescattering and, hence, create a contribution of nonscattered electrons. On the other hand, for $p_x > 0$, the trajectories of branches b_0 and $b_{\pm 2}$ depart in descending quarter cycles of the electric-field strength. Hence, the electrons are first accelerated away, but are afterwards driven back to the parent ion and scatter off. For photoelectron holography close to the polarization axis, we restrict ourselves to forward-scattered trajectories. In each color-marked branch b_0 and $b_{\pm 2}$, two distinct trajectories depart that lead to the same final momentum \mathbf{p} . As discussed in Chapter 3, one of the trajectories passes the ion with $z > 0$ and the other with $z < 0$ (see Fig. 10.4(b)). Their interference leads to the finger-like holographic pattern. In contrast to the simple man's model, for momenta close to the polarization axis, both interfering trajectories have a similar shape in a long-range potential, just on the opposite sides of the polarization axis. Qualitatively, the correct number of fringes of the TDSE result and also their positions are well reproduced by the model, if only the trajectories starting in the central branch b_0 are considered (see Fig. 10.5). The inclusion of the branches $b_{\pm 1}$ of nonscattered electrons improves the modulation depth of the interference pattern (see also Fig. 1(e) of Ref. [245]). For $|p_x| \gtrsim 0.45$ a.u., the PMDs are only weakly modified, if more branches are added. However, the consideration of additional branches leads to more complicated interference structure at low energies.

The nondipole shifts of the central fringe extracted from the semiclassical model are in perfect agreement with the TDSE results (see Fig. 10.6(a)). In contrast, an adaptation of the earlier proposed CCSFA beyond dipole approximation [156] cannot quantitatively reproduce the TDSE findings. The overestimated magnitude of the nondipole shift is mainly attributed to the different phase used in CCSFA that is obtained from the phase of Eq. (10.10) by omitting the terms $-\mathbf{r}_{cl}(t) \cdot \nabla V(\mathbf{r}_{cl}(t))$ and $-\mathbf{z}_{cl}(t) \cdot (\dot{\mathbf{r}}_{cl}(t) \times \mathbf{B}(t - z_{cl}(t)/c))$ in the integral. For a quantitative modeling of the maximum's shift, both terms are important. Neglecting the interference of the trajectories, the semiclassical simulation reduces to a classical-trajectory Monte Carlo (CTMC) simulation in 2D. The resulting CTMC distribution has a much too broad central maximum and its peak position cannot fully reproduce the TDSE result. Thus, we find that the position of the central lobe in 2D cannot be entirely understood by considering only the kinematics of the classical trajectories (as it was done in Refs. [153, 156]).

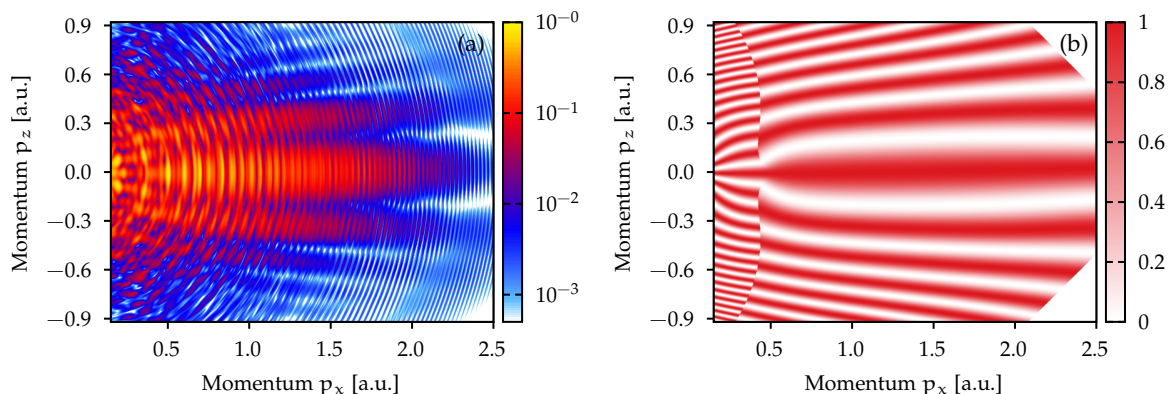


Figure 10.5: (a) Photoelectron momentum distribution for ionization of helium by ten-cycle \cos^2 pulses obtained by 2D TDSE simulations. For the result, the PMDs for intensities 7.0×10^{14} , 7.5×10^{14} and 8.0×10^{14} W/cm² are averaged. (b) Interference pattern of holography trajectories starting in branch b_0 , i.e., we show $\cos^2(\Delta S/2)$ with their phase difference ΔS in 2D based on the semiclassical model. Figure is adapted from Brennecke *et al.* [245].

The central fringe can already be modeled by only considering the two trajectories starting in the branch b_0 . Their interference pattern, $w \propto |\exp(iS_1) + \exp(iS_2)|^2 = 4 \cos^2(\Delta S/2)$, defined by the phase difference ΔS is shown in Fig. 10.5(b). In contrast to the simple man's model, the phase difference ΔS in a long-range potential varies linearly with p_z around the position of the maximum. Hence, for each p_x , ΔS has a first-order zero crossing which we call the point of constructive interference (POCI). The POCI mostly determines the position of the central lobe in the PMD (see Fig. 10.6(b)). For large p_x , the trajectories only pass by the ionic core for a single time such that the POCI and the simple man's estimate are in very good agreement. At low energies, however, there are trajectories that pass by the ionic core multiple times [85, 86, 235] (see for example the trajectories in Fig. 10.4(b) for $p_x = 0.3$ a.u.).⁸ At the boundary between a single pass-by and multiple pass-bys, the electrons undergo soft recollisions [83–86, 118], leading to low-energy structures in the PMDs [81–84]. The positions of the low-energy structures can be estimated as $p_x \approx \frac{E_0}{\omega} \frac{1}{\pi(n+1/2)}$ with $n \in \mathbb{N}$ [86]. For the laser parameters at hand, $p_x \approx 0.53$ a.u. for $n = 1$. Hence, at this boundary, the topology of the trajectories change what is reflected as a discontinuity in the phase difference at $p_x \approx 0.45$ a.u. (see Fig. 10.5(b)). Even though the low-energy structures are only barely visible in the PMD from TDSE, the interference pattern and, especially, the width of the fringes change around $p_x \approx 0.45$ a.u. As expected, multiple pass-bys present at low energies also modify the nondipole dynamics [510]. In agreement with the investigation of the Coulomb-focused caustic in Ref. [510], the magnitude of the nondipole shift of the central fringe decreases at small p_x for both TDSE and semiclassical simulations. In the semiclassical model, multiple pass-bys change the phases associated with each trajectory and, thus, the POCI, explaining the difference compared to the simple man's model (which only considers a single forward scattering event).

The width of the central interference fringe is quite small at low energies such that the POCI fully specifies the maximum's position of the semiclassical PMD. In contrast, a small difference between nondipole shift of the semiclassical PMD and the POCI is present at intermediate p_x . The difference is mostly caused by nonscattered electrons starting in branches $b_{\pm 1}$. Since the lateral distribution for recollision-free ionization is shifted in forward direction (see Eq. (10.1)), the maximum of the complete distribution in the semiclassical simulation is slightly displaced towards larger p_z compared to the POCI.

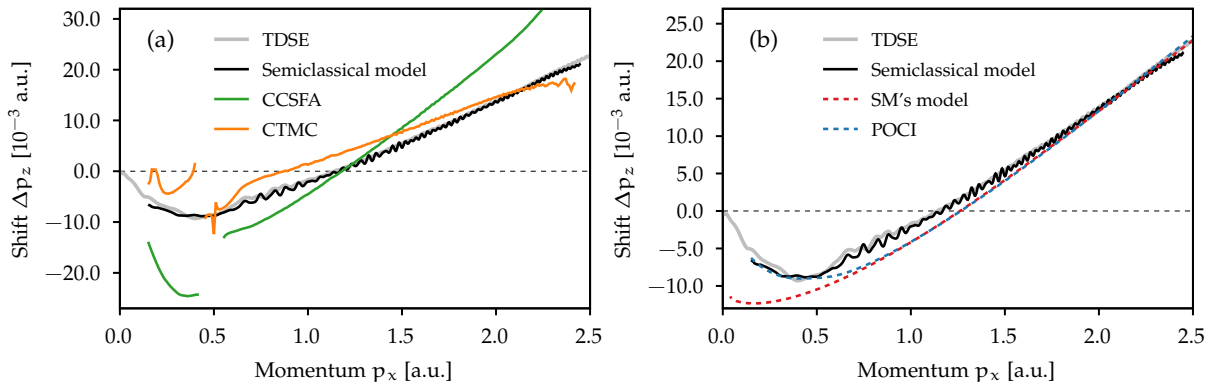


Figure 10.6: Comparison of the shift of the central maximum in 2D obtained by different levels of theory for the same conditions as in Fig. 10.5(a). The peak positions extracted from 2D TDSE simulations are shown as gray solid lines. The maximum's position of the semiclassical model in 2D including the branches b_0 and $b_{\pm 1}$ is indicated as black solid line. Additionally, in panel (a), the maximum's position of the CTMC distribution (orange line) and the CCSFA result (green line) are shown. In panel (b), the blue dashed line shows the point of constructive interference (POCI) for the two trajectories starting in branch b_0 and the red dashed line indicates the estimate of the simple man's model given by Eq. (10.21). Figure is adapted from Brennecke *et al.* [245].

10.5.2 Higher-order holographic fringes

For large lateral momenta $|p_z|$ where higher-order holographic fringes appear, the two interfering trajectories of branch b_0 are quite distinct even in the semiclassical model. One trajectory makes a wide turn

⁸Strikingly speaking, trajectories with a single pass-by are also deflected to low energies and, hence, the interference structures visible in the PMD from TDSE are very complex.

around the ion and it is only weakly perturbed by the ionic potential. In contrast, the other trajectory is driven back to the vicinity of the parent ion and it is strongly deflected during scattering (see also Section 3.4.1). Hence, a clear separation into signal and reference trajectories as in the simple man's model is appropriate.

To calculate the position of the higher-order interference fringes for the PMDs from TDSE simulations or from semiclassical simulations, the distributions are first averaged over an interval $\Delta p_x = 0.1$ a.u. Afterwards, for each interference fringe, we determine its position in p_z -direction at each p_x by means of Gaussian fit in the region around that respective maximum. For a given order of interference maxima, we quantify the nondipole shift by taking the average value

$$\Delta p_z(p_x) = \frac{p_z^+ + p_z^-}{2}, \quad (10.22)$$

where p_z^+ and p_z^- are the positions of one maximum in forward direction and one in backward direction. To further reduce the influence of ATI rings, the extracted shifts as a function of p_x are again smoothed by averaging over intervals $\Delta p_x = 0.1$ a.u. The shifts of the first- and second-order maxima from 2D TDSE calculations and from the semiclassical model are in very good agreement (see Fig. 10.7(a)). Even though the absolute positions of the holographic fringes are not correctly predicted by the simple man's model of Eq. (10.20) (see also Refs. [122, 234]), the nondipole shifts of the higher-order fringes are well reproduced by Eq. (10.21). Hence, the modification of the holographic pattern can be mostly attributed to the phase of the signal wave packet picked up in the electromagnetic field between liberation and return. For a given p_x , the shifts of the holographic fringes are indeed nearly independent of the fringe order and approximately follows the position of the central maximum. Interestingly, the higher-order fringes are also displaced backwards for momenta $p_x \gtrsim 1.3$ a.u.

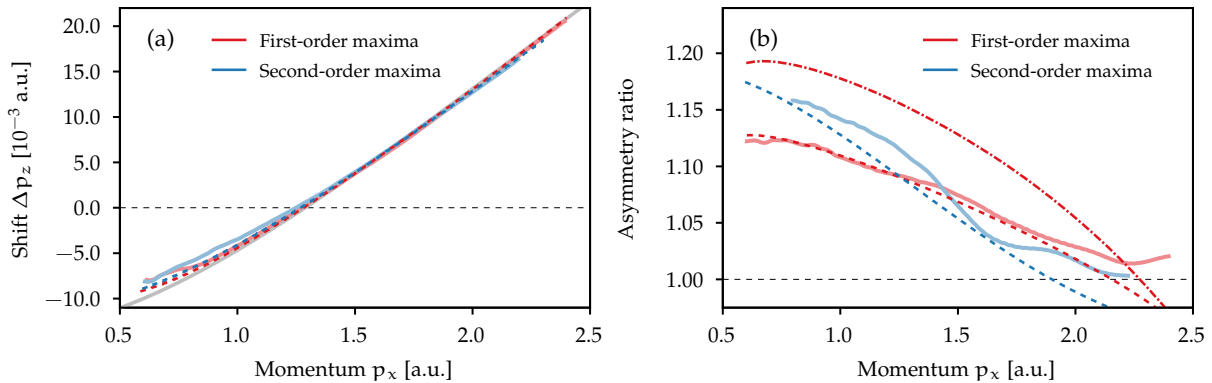


Figure 10.7: (a) Shift of the holographic fringes and (b) forward-backward asymmetry quantified as the ratio of the signal strengths for the first-order (red lines) and second-order (blue lines) maxima: TDSE results in 2D (pale thick lines) and results from the semiclassical model including only trajectories starting in branch b_0 (dashed lines). In panel (a), the simple man's model of Eq. (10.21) is also shown as gray thick line. In panel (b), a semiclassical simulation using the Jacobian in Eq. (10.12) instead of its square root is additionally presented (dashed-dotted line). Figure is adapted from Brennecke *et al.* [245].

According to Eq. (10.21), the shift of the interference fringes increases quadratically with the electric-field strength E_0 and the wavelength λ . However, as predicted by Eq. (10.20) and further discussed in Section 3.4.1, the spacings of the fringes decrease with increasing excursion times of electrons and, thus, with increasing wavelength [234]. As a result, the fringe spacings and their nondipole displacement are on the same order of magnitude for mid-infrared laser fields that are often used in today's experiments. As an example, a PMD for ionization of helium by laser pulses with 3400 nm wavelength and an intensity of 1.0×10^{14} W/cm² (as used in Refs. [152, 435]) is shown in Fig. 10.8(a). Due to the fringe structure, the normalized difference ND offers an alternative representation to observe signatures of nondipole effects in strong-field ionization. This quantity well-known from photoelectron circular dichroism studies is defined as

$$ND = \frac{w(p_x, p_z) - w(p_x, -p_z)}{w(p_x, p_z) + w(p_x, -p_z)}. \quad (10.23)$$

In the dipole approximation, the distributions are forward-backward symmetric and the normalized difference vanishes. However, beyond the dipole approximation, the normalized difference nearly reaches the extreme values of ± 1 for small and large p_x (see Fig. 10.8(b)). Around $p_x \approx 1.3$ a.u., the nondipole shift of the interference pattern is approximately zero and, hence, the normalized difference nearly vanishes.

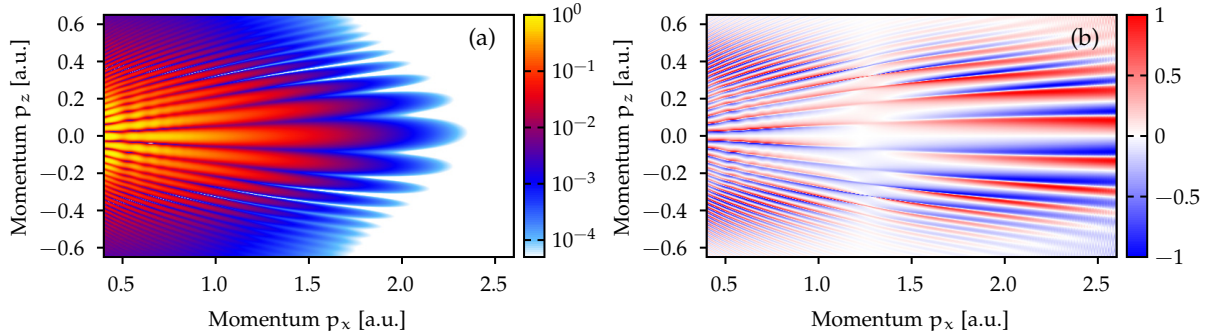


Figure 10.8: Nondipole effects in photoelectron holography for mid-infrared fields. (a) Photoelectron momentum distributions for ionization of helium by two-cycle \cos^4 pulses with 3400 nm wavelength and 1.0×10^{14} W/cm² intensity from TDSE in 2D. (b) Corresponding normalized difference of Eq. (10.23). Figure is adapted from Brennecke *et al.* [245].

The holographic fringes are not only shifted, but their relative emission strength is also modified by nondipole effects. To quantify the forward-back asymmetry for each p_x , the ratio of the signal of one holographic interference maximum in forward and the corresponding one in backward direction is used (analogous to Section 9.3). The ratios from 2D simulations are again smoothed and shown in Fig. 10.7(b) as a function of p_x . The ratios larger one indicate stronger emission in forward than in backward direction. Asymmetries as large as 1.15 are reached for small p_x at the second-order maximum. We find that the semiclassical model already reproduces well the TDSE results for the first and second-order maxima if the two dominating trajectories departing in branch b_0 are only considered. The inclusion of nonscattered electrons of branches $b_{\pm 1}$ only improves minorly the results for the second-order maximum (not shown).

In contrast to the HATI process discussed in Chapter 9, forward scattering in long-range potentials leading to holography cannot be interpreted as a single hard scattering event [208]. Hence, the asymmetry is influenced by various ingredients. In the semiclassical model, the Jacobian J somehow represents the “cross section” of the scattering process. By artificially using the Jacobian instead of its square root in Eq. (10.12), we show that this property of the scattering process is important for a quantitative modeling of the asymmetry (see the dashed-dotted line in Fig. 10.7(b)). Additionally, the distribution of initial velocities has a decisive influence. The asymmetry ratios decrease by 0.03 for the first-order holographic maxima (not shown), if the initial distribution from the dipole approximation is used in the semiclassical model. Hence, even though the influence of the combined laser and Coulomb fields during the continuum motion mainly determines the photoelectron holography signal, the distributions of initial velocities and, thus, under-the-barrier nondipole effects [151] still leave an imprint on the final momentum distributions.

10.5.3 The central holographic fringe including Coulomb focusing

In two dimensions, the holographic pattern can be described as two-path interference. For large lateral momenta p_{\perp} , this simple picture is still applicable in 3D. Near the polarization axis, however, Coulomb focusing leads to a breakdown of the semiclassical approximation such that the physics underlying the central holographic fringe is modified. In the dipole approximation, a one-dimensional manifold of classical trajectories with the same magnitude of their transverse initial velocities is mapped to the same final momentum on the polarization plane, inducing an axial singularity (see Section 3.4 for a detailed discussion). In contrast to the semiclassical model, in slices through the photoelectron momentum distributions from TDSE simulations in 3D only maxima of finite signal strength appear close to

the polarization axis, i.e., no nonphysical divergence is present (see Figure 10.9(b)). In this section, we will study Coulomb focusing beyond the electric dipole approximation and work out an approximate renormalization of the divergent signal in the semiclassical model.

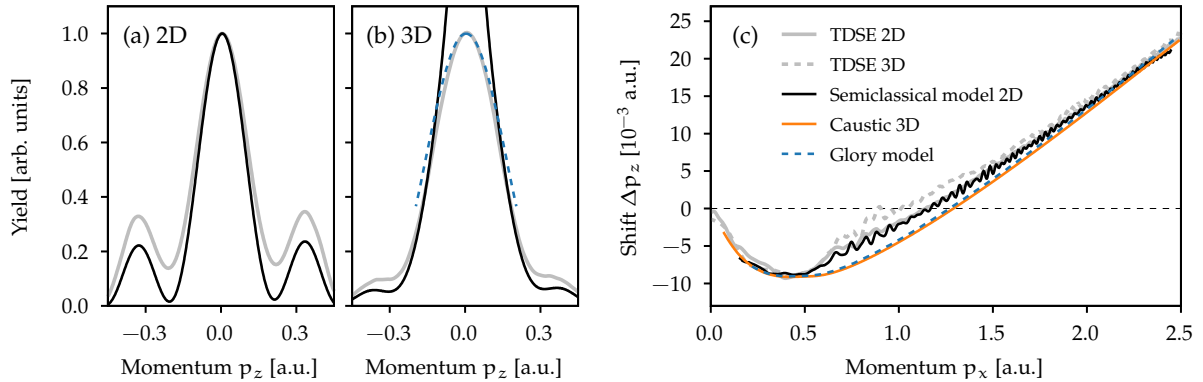


Figure 10.9: 1D slices through the PMDs at $p_x = 1.5$ a.u. in 2D (panel a) and in 3D (panel b) under the same conditions as in Fig. 10.5: TDSE result (gray line), semiclassical model of Eq. (10.12) including only trajectories starting in branch b_0 (black line) and glory model of Eq. (10.34) (blue dashed line). The distributions are normalized to a maximum signal of one. (c) Nondipole shift of the central maximum shown for different levels of theory as in Fig. 10.6. The center p_z^{cusp} of the caustic in 3D is shown as orange line and the maximum's position of the glory model is shown as blue dashed line (see main text). Figure is adapted from Brennecke *et al.* [245].

Caustic structure

In the semiclassical simulations beyond the dipole approximation in 3D, the probability amplitude also diverges what is related to zeros of the Jacobian $J(t_f)$ in Eq. (10.12). As introduced in Section 3.3.1, a vanishing Jacobian $J(t_f)$ for a given trajectory indicates that there is at least one direction \mathbf{d} such that infinitesimal changes of the initial momenta $\vec{p} \rightarrow \vec{p} + \epsilon \mathbf{d}$ leave the corresponding final momentum \mathbf{p} invariant to first order of ϵ . Thus, a plethora of initial momenta is deflected to approximately the same momentum \mathbf{p} , i.e., focusing occurs. This motivates to define a (momentum-space) caustic as the set of final momenta \mathbf{p} with vanishing Jacobian $J(t_f)$ for the trajectories starting in branch b_0 . The nondipole modifications of caustic were already discussed by Maurer *et al.* and Daněk *et al.* [157, 509].

To regularize the singularities in the semiclassical simulations, it is important to study the structure of the caustic as well as the underlying classical trajectories. To this end, we determine the caustic with very high resolution, i.e., we determine all lateral momenta $\{p_y, p_z\}$ with vanishing Jacobian $J(t_f)$ for each momentum p_x . A slice at fixed p_x through the resulting structure is shown in Fig. 10.10(a). In contrast to the dipole approximation where the caustic at fixed p_x consists of only one point at $p_\perp = 0$, a complicated one-dimensional manifold in the space of transverse momenta is visible beyond the dipole approximation. We find that the size of this structure is proportional to $1/c^2$. Importantly, the caustic's center p_z^{cusp} in the light-propagation direction changes as a function of the momentum p_x [157, 509] (see Figs. 10.9(c) and 10.10(b)). This shift along the propagation direction of the light is much larger compared to the lateral width. Thus, although strictly speaking the type of the caustic is changed (compared to the dipole approximation), we neglect the finite size of the caustic and treat it like an axial singularity.

For a better understanding, we now consider the trajectories that end up on the caustic. For fixed final p_x , these trajectories approximately correspond to the same release time and in the space of initial transverse velocities they belong to a circle of nonzero radius [155] (see Figs. 10.10(c) and (d)). In a very simple picture, the nondipole deviation of the electron's motion can be described as follows [510]. Compared to a potential-free motion, the momentum change during Coulomb focusing can be modeled by a single scattering event. For the same momentum changes during scattering as in the dipole approximation, the electrons must have the same impact parameters. Thus, to compensate the magnetically induced drift motion before scattering, the electrons need to start with a small velocity against the light-propagation direction (analogous to Eq. (10.7) in the simple man's model). Using these assumptions,

the position of the classical caustic can be described analytically [510] and coincides with the position of the central holographic fringe derived in the simple man's model (see Eq. (10.21)). This simplified result suggests that the position of the caustic (or to phrase it otherwise the focal point) and the point of constructive interference between the electron trajectories coincide. We will use this important observation to regularize the probability amplitude.

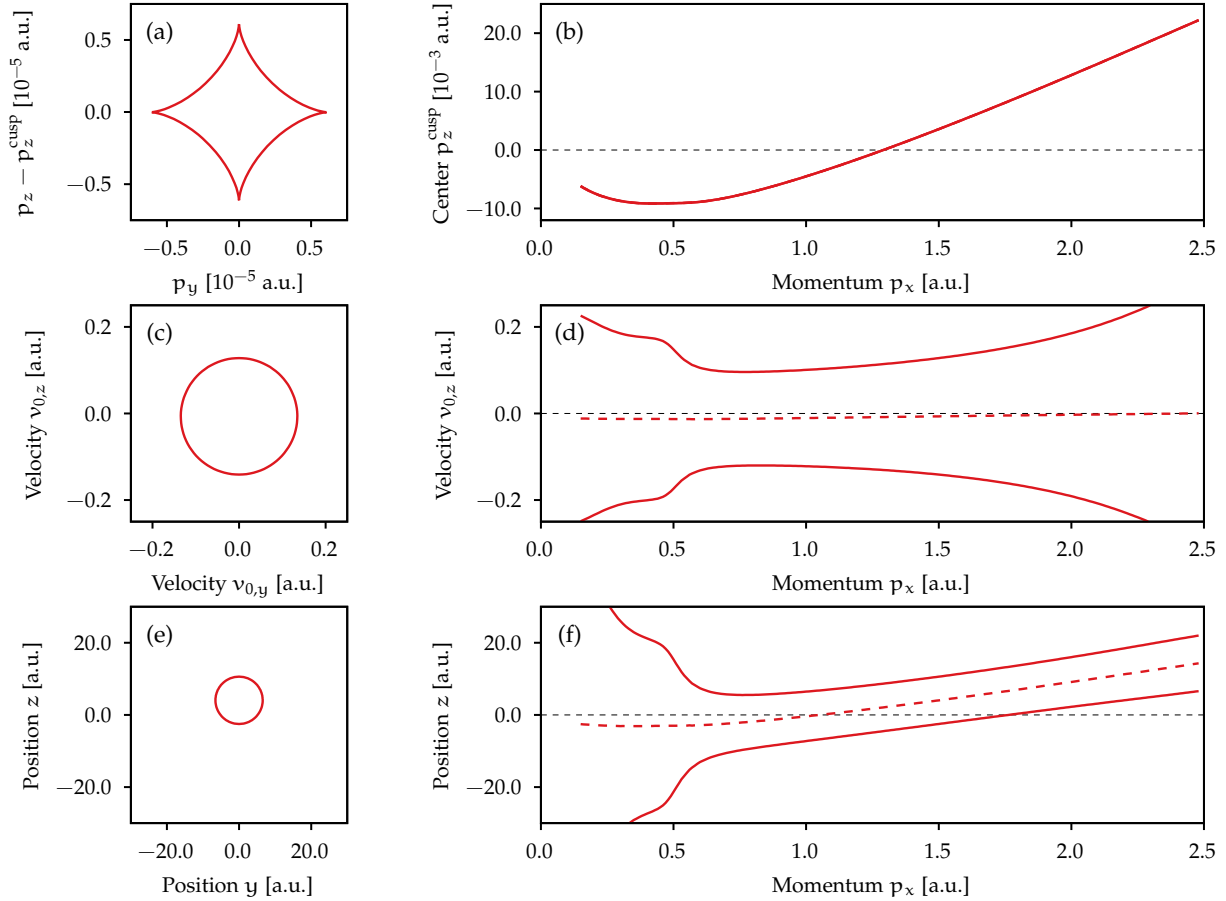


Figure 10.10: Geometry of the momentum-space caustic present in 3D semiclassical simulations and represented as the two-dimensional manifold of points with vanishing Jacobian $J(t_f)$. (a) Slice at fixed $p_x = 1.5$ a.u. through the caustic and (b) center p_z^{cusp} of the caustic. For all trajectories ending up on the caustic, the initial velocities \mathbf{v}_0 and the final positions \mathbf{r} at the end of the laser pulse are determined. For fixed final $p_x = 1.5$ a.u., the corresponding initial velocities and final positions are shown in panels (c) and (e). In addition, slices through these structures at fixed $v_{0,y} = 0$ or $y = 0$ are shown as a function of p_x in panels (d) and (f). The dashed lines indicate the centers for each p_x . Figure is adapted from Brennecke *et al.* [245].

Regularization based on the position-space description

To this end, we consider the semiclassical approximation of the propagator $\langle \mathbf{p} | U(t_f, t') | \tilde{\mathbf{r}} \rangle$ which is at the heart of the semiclassical model of Section 10.3. The semiclassical propagator is obtained from a path integral formulation by applying a stationary-phase approximation (as described in Section 3.3.1). Importantly, this is only possible, if the classical trajectories for the given boundary conditions are well separated [229]. Hence, a vanishing Jacobian $J(t_f)$ and the appearance of caustics indicate the breakdown of the semiclassical approximation for the chosen representation of the propagator [263, 511]. Importantly, a caustic is usually not related to a trajectory itself but to the representation of the propagator [229], i.e., when using another representation finite signal can be obtained. This can be motivated as follows [229]. For a fixed time t_f , we define a manifold in the \mathbf{r} - \mathbf{p} -phase space of all final positions $\mathbf{r}_{\text{cl}}(t_f)$ and final momenta $\mathbf{k}_{\text{cl}}(t_f)$ of classical trajectories starting at time t' at the position $\tilde{\mathbf{r}}$ with arbitrary initial momenta $\tilde{\mathbf{p}}$. If the (momentum-space) Jacobian $J(t_f)$ of Eq. (10.11) vanishes at some point on the manifold, the final momenta \mathbf{p} are not “good” coordinates for a chart of the manifold in the relevant region. However, other coordinates as the final positions \mathbf{r} may well parameterize a chart in this region.

The basic idea to regularize the propagator $\langle \mathbf{p} | \mathbf{U}(t_f, t') | \tilde{\mathbf{r}} \rangle$ in a certain region of final momenta is to use the semiclassical approximation for another representation of the propagator that should be regular in the corresponding region [229]. Here, instead of directly evaluating the amplitude $M(\mathbf{p})$ in the semiclassical approximation, we first calculate the position representation $M(\mathbf{r})$ of the released electron wave packet at a time t_f . The momentum-space amplitude is afterwards calculated by Fourier transformation

$$M(\mathbf{p}) = \frac{1}{(2\pi)^{3/2}} \int d\mathbf{r} M(\mathbf{r}) e^{-i\mathbf{p}\cdot\mathbf{r}}. \quad (10.24)$$

This regularization procedure was recently applied to Coulomb focusing in the dipole approximation [158]. There, it has been argued that the laser-induced rescattering process can be treated similar to glory scattering [514, 515]. Here, we extend this regularization beyond the dipole approximation.

For the semiclassical treatment of $M(\mathbf{r})$, the same initial conditions and associated probabilities are used for the real-valued trajectories during continuum motion as in the model of Section 10.3. A semiclassical treatment of the propagator $\langle \mathbf{r} | \mathbf{U}(t_f, t') | \tilde{\mathbf{r}} \rangle$ in position space can be found in the textbook [256]. To evaluate the position-space amplitude $M(\mathbf{r})$, all classical trajectories leading to a given final position \mathbf{r} at time t_f need to be determined. Analogous to the momentum-space representation, we identify two relevant trajectories for each position \mathbf{r} that start in the half cycle b_0 and that form the holographic pattern.⁹ For final $y > 0$ and small z , one trajectory passes the parent ion in the range $y > 0$ and the other in the range $y < 0$. Using the position-space amplitude $M(\mathbf{r})$ in the semiclassical approximation for a single branch of trajectories, we approximate the corresponding momentum-space amplitude as (up to an overall phase)

$$M(\mathbf{p}) \approx \frac{1}{(2\pi i)^{3/2}} \int d\mathbf{r} |M_{\text{ion}}| \left| \det \left[\frac{\partial \mathbf{r}(t_f)}{\partial \tilde{\mathbf{p}}} \right] \right|^{-1/2} e^{i(\text{Re}(S_{\downarrow}^0) + I_p(t'_r - t_{\Lambda}) + S_{\rightarrow} + (\mathbf{k}_{\text{cl}}(t_f) - \mathbf{p}) \cdot \mathbf{r})}. \quad (10.25)$$

Here, compared to the momentum-space phase S_{\rightarrow} of Eq. (10.10) used earlier, an additional phase term $(\mathbf{k}_{\text{cl}}(t_f) - \mathbf{p}) \cdot \mathbf{r}$ appears in the position-space description (see for example Ref. [122]). We neglected Maslov's phase and introduced the ionization amplitude $|M_{\text{ion}}| = |\exp(i(S_{\downarrow}^0 + I_p t'_s))|$. To check the accuracy of Eq. (10.25), we calculated the amplitude in 2D by numerical integration and found perfect agreement with the result of the semiclassical model (10.12) (not shown).

However, for an analytical description, simplifications of Eq. (10.25) are needed. If the saddle-point method (see Section 2.3.1) would be applied to the position integral in Eq. (10.25), the amplitude (10.12) of the semiclassical model would be retrieved [229] and, hence, a caustic close to the polarization axis would appear again. However, importantly, the Coulomb focusing mainly ‘‘acts’’ in the lateral directions. Thus, in order to avoid nonphysical behavior, we only apply the saddle-point method to the x -integration (polarization direction). The associated saddle-point equation is given by $p_x \approx \partial_x(S_{\rightarrow} + \mathbf{k}_{\text{cl}}(t_f) \cdot \mathbf{r})$. Importantly, in Eq. (10.10), S_{\rightarrow} is a function of the final momentum \mathbf{p} . When using the chain rule and $\mathbf{r}_{\text{cl}}(t_f) = -\nabla_{\mathbf{p}} S_{\rightarrow}$, one finds $p_x \approx k_{\text{cl},x}(t_f)$ [229]. Hence, in the trajectory simulations, we now need to determine all trajectories ending up at time t_f with a given momentum p_x and given lateral positions y and z . After the SPA, Equation (10.25) can be approximated as (up to an overall phase)

$$M(\mathbf{p}) \approx \frac{1}{2\pi i} \int dy dz P(p_x, y, z) e^{i(\text{Re}(S_{\downarrow}^0) + I_p(t'_r - t_{\Lambda}) + S_{\rightarrow} + (\mathbf{k}_{\text{cl},y}(t_f) - p_y)y + (\mathbf{k}_{\text{cl},z}(t_f) - p_z)z)}. \quad (10.26)$$

We introduced the preexponential factor

$$P(p_x, y, z) = |M_{\text{ion}}| \left| \det \left[\frac{\partial (\mathbf{k}_x(t_f), y(t_f), z(t_f))}{\partial \tilde{\mathbf{p}}} \right] \right|^{-1/2}, \quad (10.27)$$

where mixed-space determinant can be calculated numerically (similar to the Jacobian J). The remaining integrals over the lateral positions need to be considered more carefully. To this end, we analyze the properties of the integrand.

⁹Strictly speaking, there is also a caustic region in the position-space amplitude where this simple picture breaks down (see the discussion below).

We are only interested in an approximation for momenta around the momentum-space caustic. For fixed p_x and a given time t_f , we first consider the final positions of the trajectories that belong to the momentum-space caustic (see Fig. 10.10(e)). The final positions form approximately a circle with nonzero radius $r_{p_x}^0$ and with its center being displaced in the light-propagation direction to $z_{p_x}^0$. A slice at $y = 0$ through this circle is shown as a function of p_x in Fig. 10.10(f). To simplify the integration in Eq. (10.26), it is advantageous to shift the origin of the coordinate system for each fixed p_x to the center of the circle $z_{p_x}^0$ and introduce polar coordinates (r, ϕ) with

$$y = r \sin(\phi) = y', \quad z = z_{p_x}^0 + r \cos(\phi) = z_{p_x}^0 + z'. \quad (10.28)$$

In the next step, the phase in Eq. (10.26) is considered. We already found that both the central fringe in the TDSE simulation and the classical caustic are displaced to finite momenta p_z in the light-propagation direction. This motivates us to introduce a new set of final momenta

$$p_y = p'_y, \quad p_z = p'_z + \delta p_z. \quad (10.29)$$

The unknown δp_z depends on the fixed final p_x and will be determined later. In addition, we define a modified phase

$$\tilde{S}(p_x, r, \phi) = \text{Re}(S_{\downarrow}^0) + I_p(t'_r - t_{\lambda}) + S_{\rightarrow} + k_{cl,y}(t_f)y + k_{cl,z}(t_f)z - \delta p_z z' \quad (10.30)$$

such that the associated momentum fields p'_y and p'_z are approximately given as the derivatives¹⁰ of \tilde{S}

$$p'_y \approx \partial \tilde{S} / \partial y' \quad \text{and} \quad p'_z \approx \partial \tilde{S} / \partial z'. \quad (10.31)$$

Using these definitions, we rewrite Eq. (10.26) as

$$M(\mathbf{p}) = \frac{1}{2\pi i} e^{-ip_z z_{p_x}^0} \int dr r \int d\phi P(p_x, r, \phi) e^{i\tilde{S}(p_x, r, \phi)} e^{-i(p'_y y' + p'_z z')}. \quad (10.32)$$

Here, we use also the new coordinates for the preexponential factor $P(p_x, r, \phi)$ of Eq. (10.27).

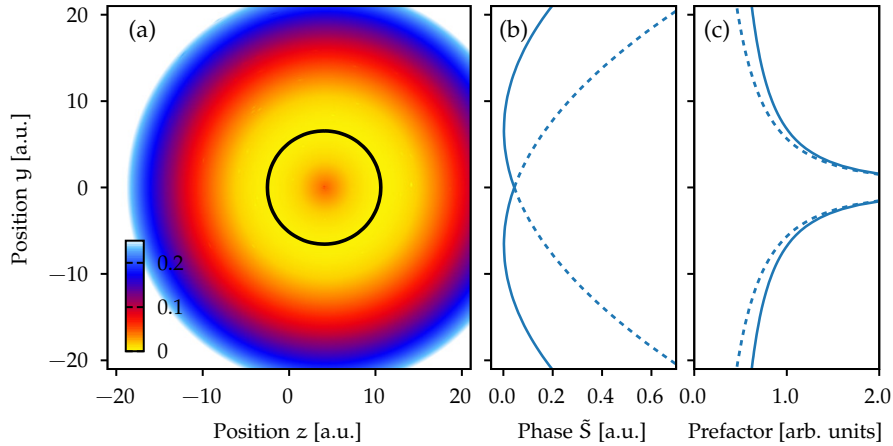


Figure 10.11: (a) Transformed phase \tilde{S} of Eq. (10.30) for fixed δp_z at the end of the laser pulse as function of final positions y and z at fixed $p_x = 1.5$ a.u. (see main text). \tilde{S} is shifted to zero at the minimum. The black line indicates the positions of trajectories with vanishing momentum-space Jacobian $J(t_f)$ and approximately marks the circle of minimal phase. (b) Slice through the phase map \tilde{S} at fixed $z = z_{p_x}^0$. The solid line corresponds to the branch shown in panel (a) whereas the dashed line shows the other branch that is important for the formation of holographic interference. (c) Corresponding prefactor P of Eq. (10.27) for the two branches shown in panel (b). Figure is adapted from Brennecke *et al.* [245].

¹⁰The relation would be exact [229], if we had not assumed a correlation for the initial conditions.

The idea of glory scattering

For photoelectron holography, there are two relevant branches of trajectories. Their phases \tilde{S} and the preexponential factor P are shown in Figs. 10.11(b) and (c) for fixed $z' = 0$, respectively. Here, small lateral momenta $p'_\perp = \sqrt{p_y'^2 + p_z'^2}$ are only studied which are mostly determined by the vicinity of the minimum of \tilde{S} (see also Eq. (10.31)). This motivates us to take only the branch with a minimum of \tilde{S} into account (blue solid line in Fig. 10.11(b)).

In the dipole approximation, the prefactor P as well as the phase \tilde{S} are rotationally symmetric and, thus, independent of ϕ such that the ϕ -integration in Eq. (10.32) can be analytically performed [158]. The idea is now to choose the parameter δp_z in a way that this is also possible beyond the dipole approximation. To this end, for each p_x , the constant δp_z is fixed by minimizing the variation of the phase \tilde{S} on the circle $r = r_{p_x}^0$ of vanishing Jacobian.¹¹ The resulting phase \tilde{S} is shown in Fig. 10.11(a) for $p_x = 1.5$ a.u. The special choice of δp_z ensures that the phase \tilde{S} is indeed approximately constant for fixed r in the vicinity of the minimum of \tilde{S} , i.e., \tilde{S} is approximately a rotationally symmetric in the y' - z' -plane. In the relevant region, the preexponential factor P also depends only weakly on the angle ϕ . Hence, similar to the dipole approximation, the ϕ -integration reduces to an integration of the plane-wave factor in Eq. (10.32) and the result is proportional to the zeroth-order Bessel-function $J_0(rp'_\perp)$.

For small p'_\perp , the remaining r -integration is approximated by means of the saddle-point method. In this special case, the saddle-point equation is also known as the glory condition. It defines the impact parameter r_g [158, 515]

$$\left. \frac{\partial \tilde{S}(p_x, r)}{\partial r} \right|_{r=r_g} = 0, \quad (10.33)$$

where the phase \tilde{S} has a minimum (see Fig. 10.11(b)). We find that the impact parameter r_g is approximately the same as the radius $r_{p_x}^0$ corresponding to vanishing Jacobian $J(t_f)$. Thus, r_g depends on the momentum p_x (see also Fig. 10.10(f)). In the vicinity of the central maximum of the PMD in 3D, the probability amplitude is approximated as (up to an overall phase factor)¹²

$$M(\mathbf{p}) \approx e^{-ip_z z_{p_x}^0} r_g P(p_x, r_g) J_0 \left(r_g \sqrt{p_y^2 + (p_z - \delta p_z)^2} \right) \sqrt{\frac{2\pi}{\partial_r^2 \tilde{S}(p_x, r_g)}} e^{i\tilde{S}(p_x, r_g)}. \quad (10.34)$$

Similar to the dipole approximation [158], the result can be interpreted as the constructive interference of an infinite number of Coulomb-focused semiclassical paths with glory impact parameter r_g that give rise to a Bessel-type interference pattern with a pronounced maximum located at δp_z . In Fig. 10.9(b), the result of Eq. (10.34) is compared to the TDSE result in 3D for a 1D slice through the PMD at $p_y = 0$ and $p_x = 1.5$ a.u. Here, the same normalization is used for the glory model and the semiclassical model. We find that the overall shape of the central maximum is well reproduced by the glory model. However, for larger lateral momenta, the glory approximation breaks down and the model of Section 10.3 should be used.

As described above, the simplification of the ϕ -integration was only possible by fixing the parameter δp_z for each p_x individually. Interestingly, we find that the position p_z^{cusp} of the caustic of the (momentum-space-based) semiclassical model and the maximum's position δp_z of the glory model only hardly differ (see Fig. 10.9(c)). For comparison, the maximum's position is also extracted from a slice at fixed $p_y = 0$ through PMD obtained by the numerical solution of the TDSE in 3D (see the gray dashed line). Similar to the 2D situation, all levels of theory perfectly agree for momenta lower than $p_x \approx 0.45$ a.u. However, for higher momenta, deviations between the model results and the TDSE result are visible. In this region, the slight asymmetry in the preexponential factor (neglected in the glory model) and the effect caused by nonscattered electrons from branches $b_{\pm 1}$ influence the maximum's position. In 3D compared to 2D, Coulomb focusing leads to an increased relative weight of the trajectories

¹¹The remaining phase variation at constant $r = r_{p_x}^0$ is smaller than 10^{-3} for all considered p_x .

¹²Strictly speaking, the prefactor P is singular in the vicinity of $r = 0$, but the factor r in the integral of Eq. (10.32) strongly damps the integrand in this region. In addition, for larger lateral momenta p'_\perp , the other branch of trajectories needs to be considered in the formation of the holographic pattern.

of branch b_0 compared to the nonscattered trajectories of branches $b_{\pm 1}$. However, at the same time, the central maximum is broader in 3D and, hence, more easily perturbed by the mentioned influences.

10.6 Conclusion

In this chapter, strong-field photoelectron holography in linearly-polarized fields was studied beyond the electric dipole approximation. To this end, photoelectron momentum distributions from the numerical solution of the TDSE including leading-order nondipole corrections were first presented. In agreement with previous works [153, 156], we observed a nonuniform displacement of the holographic pattern along the light-propagation direction, i.e., the shift depends on the momentum component p_x along the polarization axis. The fringes are shifted backward for low and forward for high momenta p_x . Astonishingly, when considering only the dynamics in reduced dimensionality (2D) or using short-range potentials, we found nearly the same nondipole shifts of the holographic pattern as in 3D simulations for long-range potentials.

To model photoelectron holography, the superposition of the signal and reference electron wave packets needs to be considered. It turned out that the nondipole modification of their phase difference is crucial to describe the interference. We derived an analytical Coulomb-free model based on the three-step picture which is able to qualitatively explain the nondipole shifts of the fringes. The displacement increases as a function of the intensity and the wavelength of the laser. Hence, especially for mid-infrared light sources, the nondipole shift is on the same momentum scale as the fringe spacing, resulting in high contrast of the normalized forward-backward difference. We can already conclude that in this range of laser parameters nondipole effects must be included for a faithful description.

We extended the semiclassical model of Chapter 3 beyond the electric dipole approximation to describe the nondipole modifications of the interference pattern in the presence of a long-range Coulomb potential. This trajectory-based description treats the influence of the electromagnetic field and Coulomb effects on the same footing, thus covering also (multiple) soft recollisions of the electrons. Compared to models in the dipole approximation [121, 122], the semiclassical phase associated with each electron trajectory contains an additional term. The correct phase from the strong-field approximation is only retrieved in the Coulomb-free situation if this term is included. Furthermore, the term is important for the full agreement of the semiclassical model with the numerical TDSE simulations in 2D. We can conclude that the semiclassical model allows a quantitative investigation of the interplay between nondipole effects and the Coulomb effects for interference structures in strong-field ionization. The trajectory-based description may allow in the future a simple study of other geometries of the laser field, e.g., for different ellipticities or two-color fields. This is especially interesting for strong-field ionization in mid-infrared fields (such as those used in Refs. [152, 157, 435, 513]), where the numerical TDSE simulations are quite challenging. In our model, we used tunnel-exit positions including nondipole modifications (see also Ref. [479]). In future work, it could be interesting to study its influence on interference patterns. To this end, an analysis of the HASE interferometer of Chapter 6 as a function of the momentum in the light-propagation direction could be promising.

The simple two-path-interference picture of holography breaks down in the vicinity of the polarization axis for systems in full dimensionality (3D). There, Coulomb focusing causes an enhancement of the yield in the TDSE simulations and induces a caustic in semiclassical simulations. We investigated the nondipole modifications of the geometry of the caustic and of the underlying classical trajectories. This enabled us to regularize the nonphysical divergence by extending the glory-rescattering approach [158] beyond the dipole approximation. The glory approach explains the enhancement and the broadening of the central holographic maximum and it allows the description of the nondipole shift of this maximum without invoking any (nonphysical) divergent structures.

Chapter 11

Summary and Conclusion

Strong-field physics offers the promise to investigate the quantum dynamics of atoms and molecules with attosecond time resolution and angstrom spatial resolution. To reach this longstanding goal, novel schemes need to be developed and existing approaches need to be tested. From a theoretical point of view, the basis for such innovations is an in-depth understanding and a faithful modeling of the underlying physical phenomena. Contributing to this development, this thesis provides a theoretical study and an explanation of selected aspects of strong-field ionization.

Simulations of the time-dependent Schrödinger equation (TDSE) for one electron interacting with an external electromagnetic field in the presence of the ionic potential formed the foundation of our investigations by providing “numerically-exact” reference solutions. We mainly considered the final photoelectron momentum distributions. Various observables were compared to experimental measurements, kindly provided by several researchers. The occurring phenomena were interpreted intuitively using simplified models. To this end, we developed and refined several approaches that are either based on the strong-field approximation or rely on a trajectory-based description of the electron dynamics within a semiclassical approximation. In particular, the second part of this work considered a theoretical description of strong-field ionization beyond the electric dipole approximation.

Several combinations of ionizing targets and external electromagnetic fields were studied. This enabled us to investigate processes that show the electron’s particle character—as in the acceleration of the released electron by the electromagnetic field and the appearance of recollisions—as well as the electron’s wave character—as in tunnel ionization, focusing, interference, and diffraction. The aspects studied in the main chapters can be summarized as follows.

In Chapter 3, we studied the focusing of electron waves in strong-field ionization. Coulomb focusing caused by the interplay between the external electromagnetic field and the electron-ion attraction acts similar to a lens in optics and forces scattered electron wave packets through focal points. In agreement with Gouy’s phase anomaly for light waves, the phases of the electron wave packets change when passing through focal points. We demonstrated that these additional phases become observable when considering interference between different kinds of electron waves such as in photoelectron holography or intracycle interference. The phase anomaly does not only appear in linear polarization but also in other waveforms that give rise to rescattering. As a result, the focal-point structure of a system influences decisively the formation of interference structures in photoelectron momentum distributions. For a quantitative interpretation, we refined the trajectory-based semiclassical description of strong-field ionization. There, the focusing effects of electron waves are encoded in a prefactor of the exponentiated action. Its proper inclusion is crucial for the excellent agreement of our model with TDSE results.

In Chapter 4, we demonstrated the control of electron wave packets at the continuum threshold by means of near-single-cycle terahertz pulses. The wave packets are prepared by multiphoton absorption in a femtosecond laser pulse and they comprise both low-energy continuum and Rydberg contributions. The precise timing of the laser pulse on the scale of an optical cycle of the terahertz field enabled us to

switch between various regimes of dynamics that were imaged by the photoelectron momentum distributions. We identified regions of recollision-free motion where the momentum distributions encode information on the energy distribution and the angular structure of the prepared wave packet. In addition, various recollision phenomena were observed and intuitively explained by means of a classical trajectory model. These effects, such as Coulomb focusing, photoelectron holography, or large-angle scattering, are reminiscent of well-known strong-field processes, but in terahertz fields, they occur on much larger time and length scales. Furthermore, we considered the yield of zero-energy electrons and, especially, the influence of a tail of the terahertz pulse on their dynamics.

In Chapter 5, we applied the attoclock scheme to study recollision-free strong-field ionization in two-dimensional fields. The Coulomb force on the outgoing electrons modifies the photoelectron momentum distributions. We found that the resulting attoclock offset depends on the lateral electron momentum, i.e., on which slice of the momentum distribution is analyzed. Within a trajectory-based modeling, this momentum-dependent attoclock offset is sensitive to the exit position at the instant of tunneling. For close-to-circularly-polarized fields, the attoclock angles are also strongly influenced by the shape of the released wave packet and by a nonadiabatic decrease of the tunnel-exit position. To avoid these complications, a bicircular laser pulse was applied, resembling linear polarization around the time of peak field strength. In this quasilinear setup, we investigated the adiabatic limit of strong-field ionization. We compared TDSE simulations and various models to reveal their weaknesses. To explore the initial-velocity dependence of the tunnel-barrier width, a momentum-space-based implementation of the classical backpropagation method was considered as an improvement to the previously-used real-space-based backpropagation.

In Chapter 6, we investigated the influence of the molecular structure on the electron wave packet created by recollision-free strong-field ionization of the hydrogen molecule H_2 . In contrast to most earlier works, the phase of the momentum-space wave function was considered, carrying spatial information on the electron wave packet. We extracted the phase from TDSE simulations and found a spatial offset of the electron's birth position after tunneling, which depends on the electron's emission direction relative to the molecular axis. For circular polarization, the modulation of the position offsets is influenced strongly by nonadiabaticity and depends weakly on the long-range part of the molecular potential. In experiments, the phase information is only accessible by interferometric approaches as recently suggested in Ref. [69]. Based on the strong-field approximation, we refined this interferometric scheme and retrieved position offsets from numerical TDSE experiments for short-range and long-range potentials. The excellent agreement of the results from the interferometric approach and the theoretically-accessible phase is an important benchmark, demonstrating that the orbital imprint on the spatial structure of the emitted electrons is experimentally accessible.

In Chapter 7, we studied the structure of (nonresonant) above-threshold ionization rings beyond the electric dipole approximation. In the dipole approximation, the multiphoton generalization of Einstein's photoeffect law predicts kinetic electron energies that are independent of the electron's emission direction. Beyond the dipole approximation, however, we confirmed a displacement of the ATI rings in TDSE simulations. The rings are shifted against the light-propagation direction, i.e., opposite to the radiation pressure. We identified a nondipole modification of the ac Stark effect for electron continuum states as the reason.

In Chapter 8, we explored nondipole effects in recollision-free and interference-free strong-field ionization. Whereas previous works mostly focused on the total average momentum transfer in the light-propagation direction, we found that the momentum transfer depends in general on the momentum component of the electron in the polarization plane. Studying this differential observable allowed us to reveal the microscopic mechanisms of nondipole effects and to identify their imprint on measurable photoelectron momentum distributions. First, we theoretically investigated the attoclock protocol to time resolve the momentum transfer on a subcycle time scale [435] and to consider the interplay between Coulomb and nondipole effects. Furthermore, the classical backpropagation approach was applied to

disentangle nondipole effects during tunnel ionization and the subsequent continuum motion. A classical description of the continuum propagation allowed us to separate the imprint of magnetic-field effects from those due to the spatially-dependent electric field on the photoelectron momentum distributions. TDSE results for a quasilinear field and a circularly-polarized field confirmed these findings.

In Chapter 9, we focused on beyond-dipole modifications of high-order above-threshold ionization. This process relies on large-angle scattering of recolliding electrons such that the nondipole effects observed in the photoelectron momentum distributions are highly target sensitive. As prototypical atomic and molecular targets, we studied xenon and the hydrogen molecular ion H_2^+ . For H_2^+ , the nondipole modifications of the molecular-interference pattern depend on the molecular orientation relative to the polarization axis. The high-energy photoelectron momentum distributions for xenon and H_2^+ at perpendicular alignment show a pronounced maximum close to the polarization axis. While the peak positions in the light-propagation direction are displaced for both targets, the magnitude of the shift is different for atoms and molecules. For an intuitive interpretation, we presented a three-step model, including an accurate description of the rescattering step using a target-specific differential scattering cross section. For xenon, the shift is related to backscattering electrons that transfer a considerable amount of their momentum to the ion during recollision. In contrast, the maximum in H_2^+ arises from the molecular interference and the nondipole shift is determined by the total momentum gain of the electron before and after scattering.

In Chapter 10, we investigated the nondipole modifications of the interference pattern in strong-field photoelectron holography. TDSE simulations revealed that the nonuniform displacement of the interference fringes in the light-propagation direction is nearly independent of the considered dimensionality and the details of the ionic potential. We explained these beyond-dipole shifts qualitatively by an intuitive Coulomb-free two-path-interference model. For an interpretation in the presence of the long-range Coulomb potential, we extended our semiclassical model beyond the dipole approximation. To reach quantitative accuracy compared to TDSE simulations, it is not sufficient to consider only the nondipole modifications of the classical trajectories, but instead a nondipole contribution to the semiclassical phase must be accounted for. Furthermore, Coulomb focusing in 3D leads to a changed physical mechanism for the formation of the central holographic maximum, requiring a beyond-dipole regularization procedure based on the concept of glory scattering. For mid-infrared laser fields, our results showed that the displacement of the interference fringes is in the same order as the fringe spacing and, thus, must be taken into account for a faithful interpretation.

In this thesis, a variety of experimental observations in strong-field ionization were theoretically reproduced and explained. For example, we considered the influence of focal-point phases on the fringe positions in photoelectron holography, provided a theoretical benchmark for the attoclock offsets for nonadiabatic ionization of atomic hydrogen, and investigated several signatures of nondipole effects. Furthermore, we revealed interesting phenomena which were later experimentally observed, such as the nondipole modifications in high-order above-threshold ionization or the linear dependence of the nondipole shift on the initial electron velocity in recollision-free strong-field ionization. Even though the foundations of strong-field physics were already laid 30 years ago, there are various unexplored aspects in the interaction of intense laser pulses with different types of matter. At the end of each chapter, specific ideas for future research were given. In general, interesting directions are for sure the applications of more complex tailored laser fields, the investigation of the rich dynamics in molecules, and the study of entanglement between electronic and nuclear degrees of freedom on an ultrafast timescale.

Appendix A

Methods

A.1 Introduction to scattering theory

In this thesis, phenomena in strong-field ionization are discussed. However, we often face one of the following two situations:

- (a) A light pulse of finite duration induces ionization. After the end of the pulse at time t_r , the motion of the created electron wave packet is only governed by the field-free Hamiltonian $H_0 = K + V(\mathbf{r})$ with $K = \frac{1}{2}\hat{\mathbf{p}}^2$. However, the experimentally-accessible photoelectron momentum distribution needs to be evaluated at large times $t \rightarrow \infty$. Hence, in principle, the out-spreading electron wave packet must be covered up to large distances.
- (b) A light pulse creates an electron wave packet that is driven back to the parent ion and may rescatter. Under certain circumstances, we can treat this as a light-field-free scattering process and are interested in the distribution of the scattered electrons.

In this section, we introduce certain aspects of scattering theory (based on the book [516]) that are used to simplify the treatment of both scenarios. To keep the discussion simple, we first assume a short-range potential.¹

For a proper state $|\psi\rangle$ at time $t = 0$, the time evolution under the field-free Hamiltonian H_0 is given by the time-evolution operator $U_0(t) = e^{-iH_0 t}$. Suppose that the orbit $U_0(t)|\psi\rangle$ describes the time evolution in some scattering experiment. After the collision, the wave packet is localized far away from the scattering center and behaves like a free wave packet. We have

$$U_0(t)|\psi\rangle \xrightarrow[t \rightarrow \infty]{} e^{-iKt}|\psi_{\text{out}}\rangle \quad (\text{A.1})$$

for some vector $|\psi_{\text{out}}\rangle$ that is called out asymptote of the actual state $|\psi\rangle$. Similarly, an in asymptote $|\psi_{\text{in}}\rangle$ can be defined by considering early times $t \rightarrow -\infty$. Each vector $|\psi_{\text{out}}\rangle \in \mathcal{H}$ is an out asymptote of some actual orbit with a state $|\psi\rangle$ at $t = 0$ and the same applies for in asymptotes. It is possible to define so-called Møller operators Ω_{\pm} as follows

$$\begin{aligned} |\psi\rangle &= \lim_{t \rightarrow +\infty} U_0^\dagger(t) e^{-iKt} |\psi_{\text{out}}\rangle = \Omega_- |\psi_{\text{out}}\rangle, \\ |\psi'\rangle &= \lim_{t \rightarrow -\infty} U_0^\dagger(t) e^{-iKt} |\psi_{\text{in}}\rangle = \Omega_+ |\psi_{\text{in}}\rangle. \end{aligned} \quad (\text{A.2})$$

Due to the appearance of bound states, not every $|\psi\rangle \in \mathcal{H}$ defines an orbit that has in and out asymptotes. Instead, the image $\mathcal{C} = \{\Omega_{\pm}|\psi\rangle, |\psi\rangle \in \mathcal{H}\}$ of the Møller operators is orthogonal to the subspace of bound \mathcal{B} states and can be identified with the continuum states. Both spaces span the whole Hilbert space $\mathcal{H} = \mathcal{C} \oplus \mathcal{B}$. For a state $|\psi\rangle$ in the continuum \mathcal{C} , the out asymptote is given by

$$|\psi_{\text{out}}\rangle = \Omega_-^\dagger |\psi\rangle = \Omega_-^\dagger \Omega_+ |\psi_{\text{in}}\rangle. \quad (\text{A.3})$$

¹More precisely, the potential should fulfill $V(\mathbf{r}) = \mathcal{O}(r^{-3})$ for $r \rightarrow \infty$ and $V(\mathbf{r}) = \mathcal{O}(r^{-3/2})$ for $r \rightarrow 0$.

For the further analysis, it is useful to introduce (improper) stationary scattering states

$$|\mathbf{k}^{(\pm)}\rangle = \Omega_{\pm}|\mathbf{k}\rangle \quad \text{with plane-wave states } |\mathbf{k}\rangle. \quad (\text{A.4})$$

Using Eqs. (A.3) and (A.4), the expansion of an out asymptote can be written as

$$\langle \mathbf{k}|\psi_{\text{out}}\rangle = \langle \mathbf{k}|\Omega_{-}^{\dagger}|\psi\rangle = \langle \mathbf{k}^{(-)}|\psi\rangle. \quad (\text{A.5})$$

Hence, the out asymptote $|\psi_{\text{out}}\rangle$ has the same expansion in terms of plane waves $|\mathbf{k}\rangle$ as the corresponding state $|\psi\rangle$ at time $t = 0$ in terms of the scattering states $|\mathbf{k}^{(-)}\rangle$. In the simulation of electron momentum distributions (see Section 2.2), we need to determine these expansion coefficients of the out asymptote. Equation (A.5) allows us to calculate these coefficients based on the knowledge of the state $|\psi\rangle$ at finite time. The question remains how to determine the stationary scattering states explicitly.

The stationary scattering states are orthogonal to each other, $\langle \mathbf{p}^{(\pm)}|\mathbf{k}^{(\pm)}\rangle = \delta(\mathbf{p}-\mathbf{k})$, and form a basis of the continuum \mathcal{C} . They fulfill the time-independent Schrödinger equation

$$H_0|\mathbf{k}^{(\pm)}\rangle = E_{\mathbf{k}}|\mathbf{k}^{(\pm)}\rangle \quad \text{with } E_{\mathbf{k}} = \mathbf{k}^2/2. \quad (\text{A.6})$$

It can be shown that the stationary scattering states also be expressed as

$$\begin{aligned} |\mathbf{k}^{(\pm)}\rangle &= |\mathbf{k}\rangle + G_0(E_{\mathbf{k}} \pm i0)V|\mathbf{k}\rangle \\ &= |\mathbf{k}\rangle + G_{\mathbf{K}}(E_{\mathbf{k}} \pm i0)V|\mathbf{k}^{(\pm)}\rangle, \end{aligned} \quad (\text{A.7})$$

with the Green's operators defined by

$$G_0(z) = (z - H_0)^{-1} \quad \text{and} \quad G_{\mathbf{K}}(z) = (z - \mathbf{K})^{-1}. \quad (\text{A.8})$$

Equation (A.7) can be used to derive the asymptotic form of the wave function $\psi_{\mathbf{k}}^{(\pm)}(\mathbf{r}) = \langle \mathbf{r}|\mathbf{k}^{(\pm)}\rangle$ at large distances r (in 3D)

$$\psi_{\mathbf{k}}^{(\pm)}(\mathbf{r}) = \langle \mathbf{r}|\mathbf{k}^{(\pm)}\rangle \xrightarrow{r \rightarrow \infty} \frac{1}{(2\pi)^{3/2}} \left[e^{i\mathbf{k}\cdot\mathbf{r}} - (2\pi)^2 \langle \pm \mathbf{k}\hat{\mathbf{r}}|V|\mathbf{k}^{(\pm)}\rangle \frac{e^{\pm i\mathbf{k}\mathbf{r}}}{r} \right]. \quad (\text{A.9})$$

The asymptotic form of the wave function $\psi_{\mathbf{k}}^{(+)}(\mathbf{r}) = \langle \mathbf{r}|\mathbf{k}^{(+)}\rangle$ is an ‘‘incident’’ plane wave plus a spherically spreading scattered wave. Hence, $\langle \mathbf{r}|\mathbf{k}^{(+)}\rangle$ is often interpreted as an infinite steady beam of particles scattering off V . In the context of potential scattering, it is useful to define a scattering amplitude

$$f(\mathbf{k}' \leftarrow \mathbf{k}) = -(2\pi)^2 \langle \mathbf{k}'|V|\mathbf{k}^{(+)}\rangle \quad (\text{A.10})$$

that is related to the elastic scattering differential cross section (DCS) by

$$\sigma(\mathbf{k}' \leftarrow \mathbf{k}) = |f(\mathbf{k}' \leftarrow \mathbf{k})|^2. \quad (\text{A.11})$$

In strong-field ionization, we usually deal with neutral systems of electrons and ions. Hence, for positively-charged ions, the potentials V covering the electron-ion interaction are long range, i.e., V behaves at large distances r like a Coulomb potential $-Z/r$. Hence, the potential influences the outgoing electron even if it is far away. As a result, the concept of in and out asymptotes cannot be applied and the rigorous mathematical description is complicated. Luckily, we are only interested in some asymptotic quantities such as the momenta or energies. In this case, a weaker asymptotic condition than Eq. (A.1) can be formulated and many of the results are still valid, if the plane waves are replaced by Coulomb states. Here, we will only summarize the equations that are important for this thesis. For a bare Coulomb potential $V_{\mathbf{C}}(r) = -\frac{Z}{r}$, stationary scattering states $\psi_{\mathbf{C},\mathbf{k}}^{(+)}(\mathbf{r})$ can be defined that need to fulfill the time-independent Schrödinger equation (A.6) and behave asymptotically as

$$\psi_{\mathbf{C},\mathbf{k}}^{(+)}(\mathbf{r}) \xrightarrow{r \rightarrow \hat{\mathbf{k}}\cdot\mathbf{r} \rightarrow \infty} \frac{1}{(2\pi)^{3/2}} \left[e^{i[\mathbf{k}\cdot\mathbf{r} + \eta \ln(kr - \mathbf{k}\cdot\mathbf{r})]} + f_{\mathbf{C}}(\mathbf{k}\hat{\mathbf{r}} \leftarrow \mathbf{k}) \frac{e^{i[kr - \eta \ln(2kr)]}}{r} \right] \quad (\text{A.12})$$

with the Sommerfeld parameter $\eta = -Z/k$. Introducing the scattering angle $\theta = \angle(\mathbf{k}, \mathbf{k}')$, the Coulomb scattering amplitude is given by

$$f_C(\mathbf{k}' \leftarrow \mathbf{k}) = \frac{2Z}{q^2} e^{2i\sigma_0(k)} e^{-i\eta \ln(\sin^2(\theta/2))} = -\frac{\eta}{2k \sin^2(\theta/2)} e^{2i\sigma_0(k)} e^{-i\eta \ln(\sin^2(\theta/2))} \quad (\text{A.13})$$

with $\mathbf{q} = \mathbf{k} - \mathbf{k}'$ and the Coulomb phase shifts defined by $\sigma_l(k) = \arg \Gamma(l + 1 + i\eta)$. In general, we consider potentials of the following form

$$V(\mathbf{r}) = V_S(\mathbf{r}) - \frac{Z}{r}, \quad (\text{A.14})$$

where V_S is a short-range part. In this case, an additional amplitude f_{SC} appears that is related to the additional scattering at the short-range part V_S of the potential in the presence of the long-range potential $-Z/r$. Similar to Eq. (A.11), the DCS can be written as

$$\sigma(\mathbf{k}' \leftarrow \mathbf{k}) = |f_C(\mathbf{k}' \leftarrow \mathbf{k}) + f_{SC}(\mathbf{k}' \leftarrow \mathbf{k})|^2. \quad (\text{A.15})$$

The following section describes the procedure for an explicit calculation of f_{SC} and is based on Ref. [496].

A.1.1 Calculation of scattering states for rotationally-symmetric systems

For rotationally-symmetric potentials $V(\mathbf{r}) = V(r)$, the calculation of stationary scattering states is particularly simple. We consider potentials of the form (A.14) such that in the limit of vanishing asymptotic charge $Z \rightarrow 0$ the results for a short-range potential can be retrieved. The scattering states can be expanded in terms of spherical harmonics $Y_l^m(\theta, \phi)$ (see for example Ref. [517])

$$\psi_{\mathbf{k}}^{(\pm)}(\mathbf{r}) = \sqrt{\frac{2}{\pi}} \frac{1}{kr} \sum_{l,m} i^l e^{\pm i[\sigma_l(k) + \delta_l(k)]} R_{l,k}(r) Y_l^m(\hat{\mathbf{r}}) Y_l^{m*}(\hat{\mathbf{k}}) \quad (\text{A.16})$$

with real-valued radial functions $R_{l,k}(r)$. Since $\psi_{\mathbf{k}}^{(\pm)}$ fulfills the time-independent Schrödinger equation (A.6), the corresponding $R_{l,k}(r)$ have to satisfy the radial Schrödinger equation

$$\left(-\frac{1}{2} \frac{d^2}{dr^2} + \frac{l(l+1)}{2r^2} + V(r) - \frac{k^2}{2} \right) R_{l,k}(r) = 0. \quad (\text{A.17})$$

This ordinary differential equation can be numerically integrated using Numerov's method. The radial functions can be written at large distances as

$$R_{l,k}(r) = AF_l(kr) + BG_l(kr) \xrightarrow{r \rightarrow \infty} \sin \left(kr - \frac{\pi}{2}l + \sigma_l(k) + \delta_l(k) - \eta \ln(2kr) \right). \quad (\text{A.18})$$

Here, we introduced the regular and irregular Coulomb wave functions (F_l and G_l). This equation can be used to extract the phase δ_l by considering $\tan(\delta_l(k)) = B/A$. The phase δ_l is related to the additional phase shift caused by the short-range deviation of the potential from a pure Coulomb potential $-Z/r$. The phases $\sigma_l(k)$ and $\delta_l(k)$ influence many properties of the scattering process such as the scattering states (A.16), Wigner time delays or scattering amplitudes. For example, the short-range part of the scattering amplitude reads

$$f_{SC}(k, \theta) = \frac{1}{k} \sum_{l=0}^{\infty} (2l+1) e^{2i\sigma_l(k)} e^{i\delta_l(k)} \sin \delta_l(k) P_l(\cos \theta) \quad (\text{A.19})$$

with the Legendre polynomials P_l . For a given momentum k , the phase shift $\delta_l(k)$ converges usually to zero as a function of l and, hence, the summation in Eq. (A.19) can be truncated at some finite l_{\max} .

A.2 Numerical solution of the time-dependent Schrödinger equation

The time-dependent Schrödinger equation (2.17) determines the time evolution of a quantum-mechanical system from its initial state $|\psi_0\rangle$ at a time t_A to its final state $|\psi(t_f)\rangle$ at a time t_f . Formally, the solution can be expressed by means of the unitary time-evolution operator U

$$|\psi(t_f)\rangle = U(t_f, t_A)|\psi_0\rangle. \quad (\text{A.20})$$

However, for a time-dependent Hamiltonian $H(t)$, the time-evolution operator is generally not analytically known. One way to tackle this problem is to divide the whole time window from t_A to t_f in small time slices $[t_n, t_{n+1}]$ of length Δt . The full time evolution can be written as a time-ordered product of short-time propagators

$$|\psi(t_f)\rangle = \mathcal{T} \left(\prod_n U_n \right) |\psi_0\rangle \quad (\text{A.21})$$

with the time-ordering operator \mathcal{T} . For sufficiently short intervals, the Hamiltonian can be approximated as time-independent operator $H^{(n)} = H(t_n + \Delta t/2)$ on each interval. Thus, the corresponding short-time propagator is approximately given by

$$U_n = U(t_{n+1}, t_n) \approx \exp(-iH^{(n)}\Delta t). \quad (\text{A.22})$$

The explicit application of the short-time propagator to a given state is by no means trivial. To this end, different schemes were used successfully in strong-field physics such as the split-operator methods [518, 519], the Crank-Nicolson algorithm [520], the second-order differencing scheme [521], the Chebyshev method [522] or the Lanczos method [523].

In this work, two approaches based on the split-operator technique are used. The idea is to split the Hamiltonian as $H^{(n)} = H_1 + H_2$ and approximate the short-time propagator by using a Trotter-Suzuki decomposition as

$$U_n \approx e^{-iH^{(n)}\Delta t} = e^{-iH_1 \frac{\Delta t}{2}} e^{-iH_2 \Delta t} e^{-iH_1 \frac{\Delta t}{2}} + i \frac{\Delta t^3}{24} [H_1 + 2H_2, [H_1, H_2]] + \mathcal{O}(\Delta t^4). \quad (\text{A.23})$$

For an efficient propagation scheme, the splitting must be done in a way that there are representations of the state such that the exponentials can be easily applied and that the conversions between the representations can be efficiently implemented. These aspects are linked to the discretization schemes used to represent the electronic state such as representations on numerical grids or expansions in basis sets. A complication in strong-field physics is that usually both the bound states and the continuum must be described properly. Hence, for the simulation of photoelectron momentum distributions, the discretization scheme has to satisfy two requirements: (i) close to the ionic core a high spatial resolution is required and (ii) the spreading photoelectron wave packet needs to be covered (at least till the end of the laser pulse). We use two different schemes to deal with these problems: (i) The *generalized pseudospectral method in spherical coordinates* is based on a pseudospectral decomposition of the field-free Hamiltonian. To this end, the angular dependence of the wave function is expanded in spherical harmonics and the radial coordinate is discretized on a nonuniform grid. (ii) The *Cartesian split-operator method* is based on a representation of the wave function on Cartesian grids and on efficient implementations of the Fourier transformations to switch between position and momentum-space representations.

A.2.1 Generalized pseudospectral method in spherical coordinates

The method was originally developed to calculate the HHG signal in linearly-polarized fields [519]. Recently, it was extended to two-dimensional waveforms and to simulate photoelectron momentum distributions [524, 525]. Here, however, we present a modified implementation that is especially well suited to calculate photoelectron momentum distributions at low energies and to describe the dynamics in moderately-strong light fields. To this end, we consider the system in the dipole approximation and

use the length gauge with an interaction Hamiltonian $H_I = \mathbf{r} \cdot \mathbf{E}(t)$. In addition, we restrict ourselves to rotationally-symmetric potentials $V(r)$. Hence, the main idea is to use the field-free Hamiltonian $H_0 = \hat{\mathbf{p}}^2/2 + V(r)$ as one operator in the splitting of Eq. (A.23) and to apply the corresponding short-time propagator by means of a spectral decomposition of H_0 .

Pseudospectral decomposition

The pseudospectral decomposition of the field-free Hamiltonian H_0 is at the heart of this method. To this end, the eigenstates of the Hamiltonian H_0 are expanded in spherical harmonics Y_l^m

$$\phi_{n,l,m}(\mathbf{r}) = \frac{\chi_{n,l}(r)}{r} Y_l^m(\theta, \phi) \quad (\text{A.24})$$

with $l = 0, 1, 2, \dots, N_l$ and $|m| \leq l$. The radial functions $\chi_{n,l}$ need to fulfill

$$\left[-\frac{1}{2} \frac{d^2}{dr^2} + \frac{l(l+1)}{2r^2} + V(r) \right] \chi_{n,l}(r) = E_{n,l} \chi_{n,l}(r) \quad (\text{A.25})$$

with eigenenergies $E_{n,l}$. We will discretize the radial coordinate r in a box with extension r_{\max} . Then, the boundary conditions are given by $\chi_{n,l}(0) = \chi_{n,l}(r_{\max}) = 0$. The latter condition is artificial, but does not influence the results as long as the extension r_{\max} is sufficiently large. However, this condition ensures that the spectrum is discrete and, hence, the states can be labeled by an integer n .

To deal with the different requirements on the representation of the radial coordinate at small and large distances, the interval $[0, r_{\max}]$ is mapped to the finite domain $[-1, 1]$ using the function $r(x)$ (which is specified later). In order to restore a symmetric eigenvalue problem, the radial wave functions are transformed to

$$\zeta_{n,l}(x) = \sqrt{r'(x)} \chi_{n,l}(r(x)) \quad \text{with } r'(x) = \frac{dr}{dx} \text{ and } x \in [-1, 1]. \quad (\text{A.26})$$

The Legendre pseudospectral method is applied for discretization of the functions $\zeta(x)$ (see Ref. [526] for an introduction). To this end, the wave functions are approximated by a finite number of Legendre polynomials $P_j(x)$, i.e., $\zeta(x) \approx \zeta^{(N_r)}(x) = \sum_{j=0}^{N_r+1} a_j P_j(x)$ with expansion coefficients a_j . The collocation points are defined by the Legendre-Lobatto grid

$$\{x_j : (1 - x_j^2) P'_{N_r+1}(x_j) = 0\} \quad \text{with } j = 0, 1, 2, \dots, N_r + 1, \quad (\text{A.27})$$

where P'_{N_r+1} is the derivative of the $(N_r + 1)$ -th order Legendre function. Then the approximation $\zeta^{(N_r)}$ is exact at these collocation points x_j , i.e., $\zeta(x_j) = \zeta^{(N_r)}(x_j)$. The function $\zeta^{(N_r)}(x)$ can be entirely represented by the values at collocation points

$$\zeta^{(N_r)}(x) = \sum_{j=0}^{N_r+1} g_j(x) \zeta(x_j)$$

with some cardinal functions g_j that are defined in Ref. [526]. Inserting Eqs. (A.26) and (A.2.1) in the eigenvalue equation (A.25) and using the boundary condition $\zeta(x_0) = \zeta(x_{N_r+1}) = 0$, the eigenvalue problem reduces to the following discretized form

$$\sum_{j=1}^{N_r} \left[-\frac{1}{2} \frac{1}{r'(x_i)} (D_2)_{i,j} \frac{1}{r'(x_j)} + \frac{l(l+1)}{2r^2(x_i)} \delta_{i,j} + V(r(x_i)) \delta_{i,j} \right] \zeta_{n,l}(x_j) = E_{n,l} \zeta_{n,l}(x_i) \quad (\text{A.28})$$

with $i = 1, 2, \dots, N_r$. The derivatives of g_j determine the representation of the second derivative

$$(D_2)_{i,j} = \begin{cases} -\frac{(N_r+1)(N_r+2)}{3(1-x_i^2)} & , i = j \\ -\frac{2}{(x_i - x_j)^2} & , i \neq j. \end{cases} \quad (\text{A.29})$$

Hence, for each quantum number l , a pseudoeigenbasis is computed via diagonalization of an $N_r \times N_r$ matrix. This provides the eigenenergies $E_{n,l}$ as well as the values of the wave functions at the collocation points. The pseudoeigenbasis represents both bound states and continuum states. One of the bound states serves usually as initial state of the time propagation.

Propagation scheme

Starting point of the time evolution is an initial position-space wave function that is discretized on a grid in spherical coordinates, i.e., represented by a tuple of complex-valued numbers $\psi_{j,\lambda,\mu} = \psi(r(x_j), \theta_\lambda, \phi_\mu)$. The radial mesh points $r(x_j)$ were defined above. Additionally, we choose the azimuth angles as

$$\phi_\mu = \frac{2\pi\mu}{2N_l + 1} \quad \text{with } \mu = 0, 1, 2, \dots, 2N_l \quad (\text{A.30})$$

and polar angles as

$$\theta_\lambda = \frac{\pi\lambda}{N_l} \quad \text{with } \lambda = 0, 1, 2, \dots, N_l. \quad (\text{A.31})$$

The forward propagation of one time step, i.e., the application of the short-time propagator (A.23) with the interaction operator $H_I = H_I = \mathbf{r} \cdot \mathbf{E}(t)$ and the field-free Hamiltonian $H_2 = H_0 = \hat{\mathbf{p}}^2/2 + V(r)$, is based on a successive application of the three exponentials:

1. Apply the exponential of the interaction operator in length gauge by multiplication

$$\psi_{j,\lambda,\mu}^{(1)} = \exp\left(-i \mathbf{r}(r(x_j), \theta_\lambda, \phi_\mu) \cdot \mathbf{E}(t) \frac{\Delta t}{2}\right) \psi_{j,\lambda,\mu} \quad \text{for each } j, \lambda, \mu. \quad (\text{A.32})$$

This has a numerical complexity $\sim N_r N_l^2$.

2. Consider the decomposition in terms of spherical harmonics

$$\psi_{j,\lambda,\mu}^{(1)} = \sum_{l,m} \frac{\rho_{l,m}^{(1)}(x_j)}{r(x_j) \sqrt{r'(x_j)}} Y_l^m(\theta_\lambda, \phi_\mu), \quad (\text{A.33})$$

i.e., determine the expansion coefficients $\rho_{l,m}^{(1)}(x_j)$ (for each j). This is efficiently possible by using a spherical harmonic transform (SHT)² and has a numerical complexity $\sim N_r N_l^3$.

3. Apply the field-free time evolution by using the spectral decomposition introduced above. The time-evolved expansion coefficients can be calculated as

$$\rho_{l,m}^{(2)}(x_j) = \sum_{i=1}^{N_r} (S_l)_{j,i} \rho_{l,m}^{(1)}(x_i) \quad \text{for each } j, l, m. \quad (\text{A.34})$$

The (time-independent) symmetric matrix S_l is given by

$$(S_l)_{j,i} = \sum_{n=1}^{N_r} \zeta_{n,l}(x_j) \zeta_{n,l}(x_i) e^{-i\Delta t E_{n,l}} \quad \text{for each } l. \quad (\text{A.35})$$

The evaluation of Eq. (A.34) is the slowest step in the simulation with a complexity $\sim N_r^2 N_l^2$.³ When the initial state has defined quantum numbers (l, m) , the dipole selection rules can be used to identify the nonvanishing expansion coefficients and to simplify the calculation.

4. Use a spherical harmonic synthesis

$$\psi_{j,\lambda,\mu}^{(2)} = \sum_{l,m} \frac{\rho_{l,m}^{(2)}(x_j)}{r(x_j) \sqrt{r'(x_j)}} Y_l^m(\theta_\lambda, \phi_\mu) \quad (\text{A.36})$$

to regain the coordinate representation. This has also a numerical complexity $\sim N_r N_l^3$.

5. Apply the exponential of the interaction operator as in step 1.

²We use the open-source implementation by Schaeffer [527].

³For an efficient implementation of the matrix-vector multiplications, we use the ZSPMV routine of the Intel MKL library.

A major disadvantage of the used length gauge compared to the velocity gauge is that states with much higher angular momenta are populated in strong laser pulses [528]. Note that the spherical harmonics are eigenstates of \mathbf{L}^2 and L_z with the angular momentum operator $\mathbf{L} = \mathbf{r} \times \hat{\mathbf{p}}$ and $\hat{\mathbf{p}}$ being the canonical momentum in the used gauge [528]. Thus, its values may differ for simulations in length and velocity gauge. Usually, the computational capabilities limit the maximal orbital angular momentum included in a simulation and, thus, put restrictions on the accessible range of intensities, wavelengths and pulse durations.

Calculation of electron momentum distributions

After the end of the pulse, the contributions of deeply-bound states are removed from the state $|\psi(t_f)\rangle$ via projection

$$|\tilde{\psi}(t_f)\rangle = \prod_{E_{n,l} < \tilde{E}} (1 - |\phi_{n,l,m}\rangle\langle\phi_{n,l,m}|) |\psi(t_f)\rangle, \quad (\text{A.37})$$

where we used the eigenstates (A.24) of field-free Hamiltonian. Usually, the constant \tilde{E} is arbitrarily chosen as $\tilde{E} = -0.03$ a.u. To determine electron momentum distributions $w(\mathbf{p}) = |M(\mathbf{p})|^2$, the probability amplitude (2.19) must be evaluated

$$M(\mathbf{p}) = \langle \mathbf{p}^{(-)} | \tilde{\psi}(t_f) \rangle \quad (\text{A.38})$$

with the field-free stationary scattering states $|\mathbf{p}^{(-)}\rangle$ introduced in Section A.1. For the considered rotationally-symmetric potentials, the scattering wave functions have the form of Eq. (A.16) and the final wave function can also be expanded in spherical harmonics

$$\tilde{\psi}(t_f, \mathbf{r}) = \sum_{l,m} \frac{\tilde{R}_{l,m}(r)}{r} Y_l^m(\theta, \phi). \quad (\text{A.39})$$

We define the following matrix elements

$$\alpha_{l,m}(\mathbf{p}) = \sqrt{\frac{2}{\pi}} \frac{1}{p} (-i)^l e^{i[\sigma_l(\mathbf{p}) + \delta_l(\mathbf{p})]} \langle \mathbf{R}_{l,p} | \tilde{R}_{l,m} \rangle_r \quad (\text{A.40})$$

for the radial wave functions $R_{l,p}$ introduced in Section A.1.1. The probability amplitude M is then given by a spherical harmonic synthesis

$$M(\mathbf{p}) = \sum_{l,m} \alpha_{l,m}(\mathbf{p}) Y_l^m(\hat{\mathbf{p}}). \quad (\text{A.41})$$

An important observable is the electron energy spectrum which can be evaluated as

$$w(E) = \sqrt{2E} \sum_{l,m} |\alpha_{l,m}(\sqrt{2E})|^2. \quad (\text{A.42})$$

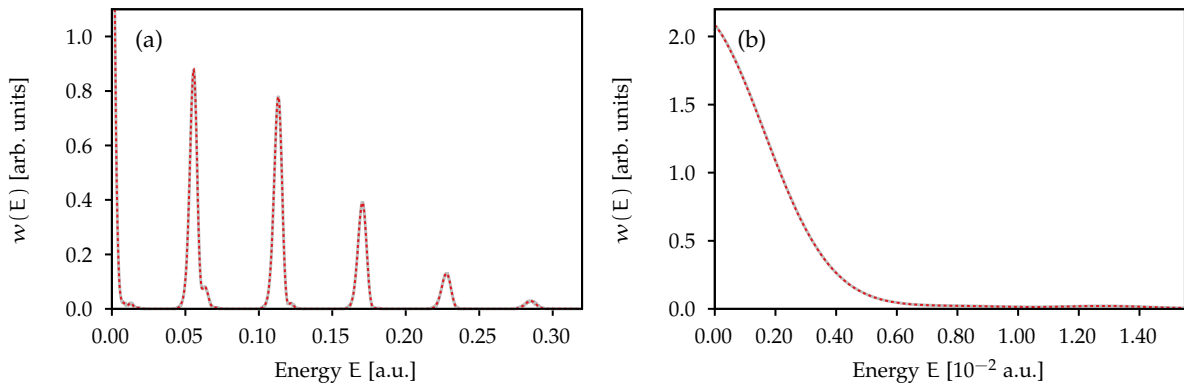


Figure A.1: Energy spectrum for multiphoton ionization of xenon atoms by linearly-polarized laser pulses for the same parameters as in Fig. 4.2 (795 nm wavelength, \cos^2 envelope of 26 optical cycles duration, 7×10^{12} W/cm²): (a) full energy range and (b) magnification of the low-energy region. The result of Eq. (A.42) based on scattering states is shown as gray line and the result obtained by population analysis using the pseudoeigenbasis is shown as red dashed line (see main text).

In order to test the calculation of scattering states, we consider multiphoton ionization of xenon as in Chapter 4 and analyze the energy spectra (see Fig. A.1). In addition to Eq. (A.42) based on the scattering states of Section A.1.1, we alternatively determine the energy spectrum by analyzing the populations of the eigenstates in the pseudospectral method and by using the density of states approximated for each l as $D(E_{n,l}) = 2/(E_{n+1,l} - E_{n-1,l})$. The results of both methods are in perfect agreement with each other (see Fig. A.1).

Mapping of the radial coordinate

In strong-field physics the appearing length, momentum and time scales pose a challenge for the discretization of the radial coordinate. Close to the ionic core (here termed region I), the ionic potential varies strongly, i.e., the deeply-bound states are localized here and hard scattering of continuum electrons may take place. To represent the wave functions properly, dense grids with a spacing $\Delta r \ll 1$ a.u. are usually required. However, when going outside, the strength of the potential decreases and disturbs the electronic motion less. Hence, at large distances (here termed region III), only the variation of the wave function with a certain maximal momentum p_{\max} must be resolved properly. At the same time, the grid extension r_{\max} must be sufficiently large to cover the relevant part of the photoelectron wave packet till the end of the light pulse.

Nonuniform grids are used here to meet these challenges. In the pseudospectral method the mapping $r(x)$ can be adjusted to tailor the numerical grid on which the radial coordinate is represented. Two different kind of mappings are used in this thesis. Similar to earlier works [270, 524], a mapping can be defined by

$$r(x) = L \frac{1+x}{(1-x + (2L/r_{\max})^{1/\beta})^\beta} \quad (\text{A.43})$$

with parameters L and β . However, especially for the simulation in THz fields of Chapter 4, the different regions have to be sampled more efficiently. To this end, the space is divided in three parts

$$r(x) = \begin{cases} \frac{1+x}{1+x_0} r_{\text{center}} & , -1 \leq x < x_0 \text{ (region I)} \\ p_{\text{inter}}(x) & , x_0 \leq x \leq x_1 \text{ (region II)} \\ r_{\text{out}} + \frac{\arccos(-x) - \arccos(-x_1)}{\pi - \arccos(-x_1)} (r_{\text{max}} - r_{\text{out}}) & , x_1 < x \leq 1 \text{ (region III)}. \end{cases} \quad (\text{A.44})$$

Here, $p_{\text{inter}}(x)$ is a polynomial of degree 5. This choice ensures a high density of points around the core (region I) and an approximately uniform grid at large distances (region III). The parameters r_{center} and r_{out} determine the extension of region I and the beginning of region III, respectively. The parameters x_0 and x_1 control the number of points in the different regions. For the choice of the parameters used in

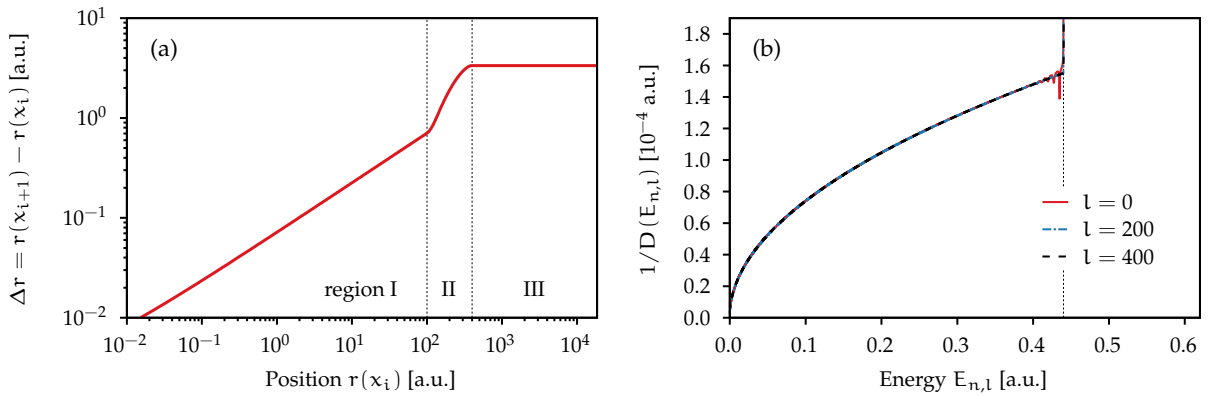


Figure A.2: (a) Local position spacing Δr as a function of the radial distance r for the grid of Eq. (A.44) used to simulate the dynamics in THz fields ($r_{\max} = 19000$ a.u., $r_{\text{center}} = 100$ a.u., $r_{\text{out}} = 400$ a.u., $x_0 = -0.989$, $x_1 = -0.973$, $N_r = 6000$). (b) Inverse density of states versus energy E for a Coulomb potential $V(r) = -1/r$ and three values of angular momentum l indicated in the legend. The dotted line indicates an estimate $E_{\max} = \frac{\pi^2}{2\Delta r_{\max}^2}$ for the highest represented energy, where the inverse density of states strongly increases.

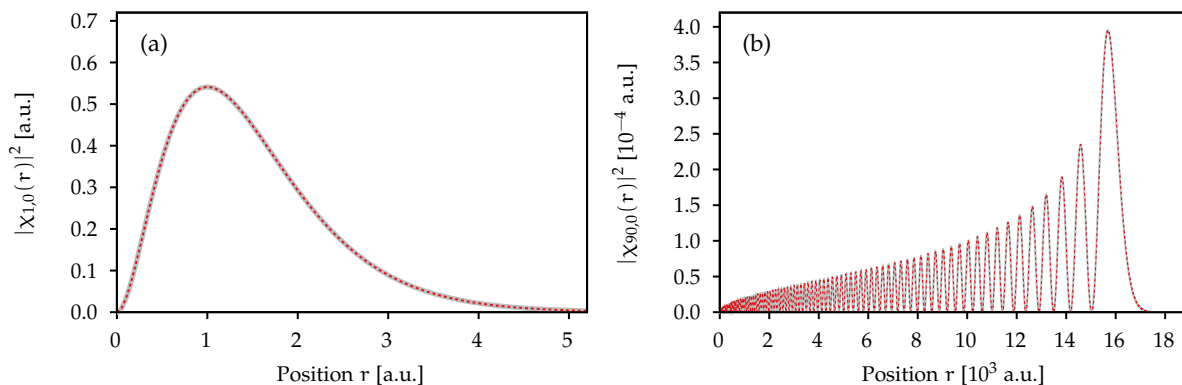


Figure A.3: Radial wave function of the hydrogen atom: (a) ground state ($n = 1, l = 0$) and (b) selected Rydberg state ($n = 90, l = 0$). The gray thick lines indicate the results of the pseudospectral method for the mapping $r(x)$ shown in Fig. A.2 and the red dotted lines are the analytical solutions.

Chapter 4, the local grid spacing Δr as a function of the distance r is shown in Fig. A.2(a). Here, Δr is determined by the mapping $r(x)$ and the nonuniform collocation points x_i .

The highest energy of continuum electrons that can be accurately represented on the grid is restricted by the largest grid spacing Δr_{\max} . Using the Nyquist–Shannon sampling theorem, we can estimate $E_{\max} = \frac{\pi^2}{2\Delta r_{\max}^2}$. To monitor the accuracy of the representation of states, the density of states in the pseudospectral method can be considered. An example of the inverse density of states $1/D(E_{n,l})$ is shown in Fig. A.2(b) for three selected values of the angular momentum l . For energies below E_{\max} , the results are proportional to \sqrt{E} . However, for energies above E_{\max} , the continuum is not described well.

To consider the representation of bound states, the ground state ($n = 0, l = 0$) as well as a Rydberg state ($n = 90, l = 0$) are shown in Fig. A.3 for the hydrogen atom. The results of the pseudospectral method are in perfect agreement with the analytical wave functions. The bound state with highest energy E_{\max}^B that can be accurately represented on the grid is mostly determined by the extension r_{\max} . A rough estimate $E_{\max}^B = -Z/r_{\max}$ can be obtained by considering the classical turning point of a bound electron. For the grid with $r_{\max} = 19000$ a.u. used in Fig. A.2, we estimate $E_{\max}^B \approx -5.2 \times 10^{-5}$ a.u. corresponding to $n \approx 98$ what is in good agreement with the numerical findings.

A.2.2 Cartesian split-operator method

In this method the short-time propagator of Eq. (A.23) is used for the following splitting of the Hamiltonian $H = H_1 + H_2 = H_r(t) + H_p(t)$ with a position-dependent part $H_1 = H_r(t)$ and a momentum-dependent part $H_2 = H_p(t)$ [447, 518]. The electronic wave function is represented on equally-spaced Cartesian grids. The exponentials in the short-time propagator (A.23) can be successively applied, because they are either multiplication operators in position space or in momentum space. Fast Fourier transformations are applied to efficiently change between position-space and momentum-space representations.⁴ Thus, in D dimensions and with N points per dimension, the numerical complexity is given by $\sim N^D \log(N^D)$. Even though this split-operator method is by far not the most efficient approach to solve the TDSE, it is easy to implement and very versatile. For example, arbitrary shapes of the light field and ionic potentials without symmetries such as for complex molecules can be treated. More detailed descriptions of this well-established method can be found in Refs. [159, 161, 201].

In simulations of the TDSE beyond the dipole approximation, we consider the unitary-transformed Hamiltonian of Eq. (2.29) which reduces to the common velocity gauge in the dipole approximation ($1/c \rightarrow 0$). In three-dimensional simulations, even the numerical calculation of the exponentials at each time step is expensive. However, since the momentum-dependent part has the following form

$$H_p(t) = \frac{1}{2} \left(\hat{\mathbf{p}} + \mathbf{A}(t) + \frac{\mathbf{e}_z}{c} \left(\hat{\mathbf{p}} \cdot \mathbf{A}(t) + \frac{1}{2} \mathbf{A}^2(t) \right) \right)^2 = \sum_{i,j=1}^D b_{i,j}(t) \hat{p}_i \hat{p}_j + \sum_i d_i(t) \hat{p}_i + e(t) \quad (\text{A.45})$$

⁴We use the open-source FFTW library which is parallelized via OpenMP or Intel MKL.

with some time-dependent functions $b_{i,j}(t)$, $d_i(t)$ and $e(t)$, the exponentials can be written as products of exponentials that contain at most two momentum components

$$\exp(-i\Delta t H_p(t)) = \left(\prod_{i,j=1}^D \exp(-i\Delta t b_{i,j}(t) \hat{p}_i \hat{p}_j) \right) \left(\prod_{i=1}^D \exp(-i\Delta t d_i(t) \hat{p}_i) \right) (\exp(-i\Delta t e(t))). \quad (\text{A.46})$$

This procedure decreases the computed number of exponentials from $\sim N^D$ to $\sim D^2 N^2$. When nondipole corrections are included, the position-dependent part $H_r(t)$ is also time dependent, but no simple separation can be applied due to the appearing potential. However, we are only interested in the first-order nondipole corrections in $1/c$. Thus, the shifted potential is expanded as

$$H_r(t) = V\left(\mathbf{r} - \frac{z}{c}\mathbf{A}(t)\right) \approx V(\mathbf{r}) - \frac{z}{c}\mathbf{A}(t) \cdot \nabla V(\mathbf{r}). \quad (\text{A.47})$$

The time-independent part $V(\mathbf{r})$ is fully considered via an exponential short-time propagator that must be calculated only once. In contrast, the small nondipole correction is implemented via a Crank-Nicolson propagator, i.e.,

$$\exp(-i\Delta t H_r(t)) \approx \exp(-i\Delta t V(\mathbf{r})) \frac{1 + i\frac{\Delta t}{2} \frac{z}{c} \mathbf{A}(t) \cdot \nabla V(\mathbf{r})}{1 - i\frac{\Delta t}{2} \frac{z}{c} \mathbf{A}(t) \cdot \nabla V(\mathbf{r})}. \quad (\text{A.48})$$

For the evaluation of the second term, a number of multiplications proportional to N^D is needed in each time step.

The major problem of Cartesian grids is that for given number of grid points N per dimension (that is typically limited by the available numerical capacities) and for a given spacing Δx (that must be sufficiently small to resolve the structures close to the ionic core) the spatial extension of the grid is fixed: $L = N\Delta x$. Thus, in order to keep the outgoing electron wave packet confined to the simulation volume till the end of the light pulse, a huge number of points per dimension is required.

Single-grid simulations

In one or two spatial dimensions and for short laser pulses, our numerical capabilities allow to choose a large grid which is enough to contain the wave function till the end of the pulse. Then, the TDSE is simply solved till the end of the light pulse as described above. Afterwards, the contribution of the initial state is removed (similar to Eq. (A.37)). Additionally, a mask function is applied to remove the region around the origin ($r < 30$ a.u.) that contains contributions of localized bound states, resulting in a state $|\tilde{\Psi}(t_f)\rangle$. To calculate electron momentum distributions $w(\mathbf{p}) = |M(\mathbf{p})|^2$, we use an eikonal approximation for the scattering states

$$\psi_{\mathbf{p}}^{(E)}(\mathbf{r}) = \frac{1}{(2\pi)^{D/2}} \exp\left[i\mathbf{p} \cdot \mathbf{r} + i \int_0^\infty d\zeta V(\mathbf{r} + \mathbf{p}\zeta)\right]. \quad (\text{A.49})$$

To calculate the integral in Eq. (A.49), we divide the potential in a long-range Coulomb part $-Z/r$ and a short range part $V_S(r)$ as in Eq. (A.14). The integral for the short-range part is calculated numerically, whereas the result for a Coulomb potential can be given in closed form

$$\int_0^\infty d\zeta \frac{-Z}{\sqrt{(\mathbf{r} + \mathbf{p}\zeta)^2}} = \frac{Z}{p} \ln(\mathbf{p} \cdot \mathbf{r} + p r), \quad (\text{A.50})$$

where the divergent position-independent contribution of the upper limit is omitted. The probability amplitude $M(\mathbf{p}) \approx \langle \psi_{\mathbf{p}}^{(E)} | \tilde{\Psi}(t_f) \rangle$ is calculated by numerical integration. This single-grid approach incorporates the effect of the long-range potential on the outgoing electrons in eikonal approximation and, hence, allows for a good quality of electron momentum distributions at low energies.

Two-grid simulations

For long laser pulses or simulations in 3D, the brute-force numerical approach on a single grid is not possible. In order to simulate electron momentum distributions more efficiently, we follow a scheme

where an inner space around the ionic core and an asymptotic outer space are treated differently [15]. The main idea is to neglect the variation of the ionic potential in the outer part such that the corresponding Hamiltonian is diagonal in momentum representation and, thus, we do not need to access the position information in the outer space.

Formally, the scheme can be described as follows. The electronic state is separated in an inner part $|\psi_{\text{in}}(t)\rangle$ and an outer part $|\psi_{\text{out}}(t)\rangle$, i.e., the full state is $|\psi(t)\rangle = |\psi_{\text{in}}(t)\rangle + |\psi_{\text{out}}(t)\rangle$. We introduce an absorbing potential V_A that introduces probability transfer from the inner part to the outer part. To this end, the Schrödinger equation (2.17) is written in two separate equations

$$i\frac{\partial}{\partial t}|\psi_{\text{in}}(t)\rangle = H(t)|\psi_{\text{in}}(t)\rangle - iV_A|\psi_{\text{in}}(t)\rangle \quad (\text{A.51})$$

for the inner part and

$$i\frac{\partial}{\partial t}|\psi_{\text{out}}(t)\rangle = H(t)|\psi_{\text{out}}(t)\rangle + iV_A|\psi_{\text{in}}(t)\rangle \quad (\text{A.52})$$

for the outer part, respectively. For the whole state $|\psi(t)\rangle$, the terms with absorbing potential cancel each other and the common Schrödinger equation (2.17) is retrieved. The initial states are usually located close to the ionic core, i.e., the initial conditions are chosen as $|\psi_{\text{in}}(t_A)\rangle = |\psi(t_A)\rangle$ and $|\psi_{\text{out}}(t_A)\rangle = 0$. Equation (A.51) for the inner part can be solved using the split-operator method on Cartesian grids as described above.

The absorbing potential should fulfill two requirements: (i) It should not disturb the dynamics at small distances. (ii) It should provide for efficient absorption and negligible reflection of outgoing electron wave packets. In this work, we use a fourth-order polynomial as absorbing potential [161]

$$V_A(r) = \begin{cases} 0 & , r < r_A \\ \alpha(r - r_A)^4 & , r \geq r_A \end{cases} \quad \text{with} \quad \alpha = \frac{(4+1)p_{\text{max}}}{2(\Delta r_A)^{4+1}} (-\log \epsilon). \quad (\text{A.53})$$

The absorbing potential starts at a radial distance r_A and over a distance of Δr_A (typically chosen between 30 a.u. and 50 a.u.) outgoing wave packets with momenta specified by p_{max} are efficiently damped. The parameter ϵ controls the possible transmission and is usually chosen as $\epsilon = 10^{-10}$. The absorbing potential ensures that the inner wave function $\psi_{\text{in}}(r) = \langle \mathbf{r} | \psi_{\text{in}} \rangle$ approximately vanishes at distances $r > r_A + \Delta r_A$ for all times t . Hence, the inner state can be represented on a Cartesian grid with extension $L = 2(r_A + \Delta r_A)$. A schematic illustration of the setup is shown in Fig. A.4.

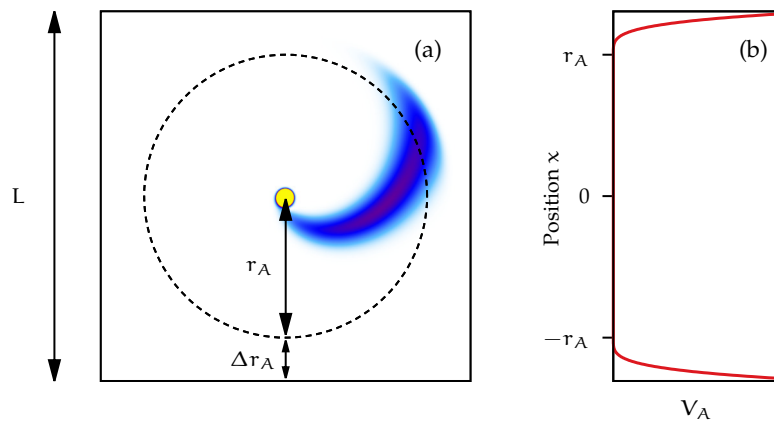


Figure A.4: (a) Sketch of the inner grid in a two-grid simulation. Shown is a snapshot of the position-space probability distribution in the presence of a laser pulse, illustrating the absorption of outgoing electron flux. (b) Slice at $y = 0$ through the corresponding absorbing potential V_A .

For the outer state $|\psi_{\text{out}}(t)\rangle$, the last term $iV_A|\psi_{\text{in}}(t)\rangle$ in Eq. (A.52) acts as a source term. Up to this point no approximation has been made. In principle, Equation (A.52) could also be solved numerically. In this case, however, the two-grid scheme would be even less efficient than single-grid simulations. The calculations can be simplified, if we assume that (i) the potential V is constant for distances $r \geq r_A$

and (ii) the outer wave function vanishes at distances $r < r_A$. Then, the explicit solution for the time evolution of $|\psi_{\text{out}}(t)\rangle$ is given by [161]

$$|\psi_{\text{out}}(t)\rangle = -i \int_{t_A}^t dt' U_F(t, t') e^{-iV(r_A)(t-t')} iV_A |\psi_{\text{in}}(t')\rangle \quad (\text{A.54})$$

with the Volkov propagator U_F of Eq. (2.34). Condition (ii) is in good approximation fulfilled for recollision-free ionization. In contrast, in field shapes allowing for recollisions such as linearly-polarized mid-infrared fields, outer parts can be driven back and, hence, Equation (A.54) is only an approximation.

In natural gauge of Section 2.2.2, the momentum-space representation of the outer state has the form

$$\begin{aligned} \tilde{\psi}_{\text{out}}(\mathbf{p}, t) &= \langle \mathbf{p} | \psi_{\text{out}}(t) \rangle \\ &= \int_{t_A}^t dt' e^{-i(\frac{1}{2} \int_{t'}^t d\zeta v^2(\mathbf{p}, \zeta) + V(r_A)(t-t'))} J(\mathbf{p}, t') \end{aligned} \quad (\text{A.55})$$

with a source term

$$J(\mathbf{p}, t') = \frac{1}{(2\pi)^{D/2}} \int d\mathbf{r} e^{-i\mathbf{p}\cdot\mathbf{r}} V_A(\mathbf{r}) \psi_{\text{in}}(\mathbf{r}, t'). \quad (\text{A.56})$$

In practice, the time integral in Eq. (A.55) is evaluated on-the-fly during the numerical propagation of the inner part (see Eq. (A.51)). The propagation of one time step Δt is given by

$$\tilde{\psi}_{\text{out}}(\mathbf{p}, t + \Delta t) \approx e^{-i(\frac{1}{2}v^2(\mathbf{p}, t + \Delta t/2) + V(r_A))\Delta t} \tilde{\psi}_{\text{out}}(\mathbf{p}, t) + \Delta t J(\mathbf{p}, t + \Delta t). \quad (\text{A.57})$$

The source term (A.56) is efficiently calculated using a Fast Fourier transformation on Cartesian grids. An advantage of the scheme is that the position representation of the outer state is not required. In addition, the grid in momentum space can be independently chosen. By default, the same grid as for the inner state is used. However, especially in 3D simulations, it is advantageous to calculate additional slices with high resolution [529].

For very long simulation times, all continuum electrons have left the inner region and the probability amplitude for electrons with asymptotic momentum \mathbf{p} is simply given by the momentum-space wave function $\tilde{\psi}_{\text{out}}(\mathbf{p}, t \rightarrow \infty)$ of the outer state. However, for finite final times t_f , only electrons with momenta $p_{\text{min}} = r_A/t_f$ have classically reached the absorber region. To extract the remaining photoelectrons from the inner state at a finite time t_f , it can be beneficial to use a projection on eikonal states as described for the single-grid scheme.

In solution of the TDSE beyond the dipole approximation, we considered a $1/c$ -expansion of the Hamiltonian (see Eq. (2.24)). However, in principle, in multi-cycle laser pulses as used in Chapter 7 retardation effects could accumulate. Here, we give a brief sketch how to estimate the importance of these higher-order effects by using the two-grid scheme. Up to Eq. (A.54) no explicit form of the Hamiltonian has been used. The inner part is restricted to a length scale of $r_A + \Delta r_A$. Hence, if $r_A + \Delta r_A \ll \lambda$, retardation effects can be neglected and it is appropriate to approximate the Hamiltonian in $1/c$. However, in the outer part, the released electron wave packets travel large distances. Thus, a $1/c$ approximation seems at first questionable and instead the Hamiltonian of Eq. (2.20) should be considered. In the two-grid scheme, this changes only the Volkov propagator U_F in Eq. (A.54). For the Hamiltonian (2.20) with $V = 0$, a construction of this “full” propagator was given in Ref. [190]. Importantly, the “full” solution depends on the light-cone coordinate $\eta = t - z/c$ whereas the solution of Eq. (2.34) depends on the time t . Hence, at large distances z , both solutions will differ when the light pulse is present. However, after the end of this pulse (when the electron momentum distributions are evaluated), this problem is cured. We find that, for $p_z \ll c$ and sufficiently small $r_A + \Delta r_A$, the “full” propagator results only in an additional function $G(\mathbf{p}, t' - z/c)$ in Eq. (A.56) compared to the $1/c$ expansion. For selected laser conditions, we explicitly calculated G as introduced in Ref. [190] and found much smaller higher-order corrections than the nondipole corrections that are already included in the Hamiltonian of Eq. (2.24). Hence, we expect that when the electron does not interact with an ionic potential over large distances (in the order of the wavelength), the higher-order corrections due to retardation effects can be neglected.

Calculation of eigenstates states

Typically, the electronic system starts out in an energy eigenstate before the light pulse arrives. In such a situation, the initial states should be stationary in the absence of external fields, i.e., this means that the states should only change by a purely time-dependent phase factor. Thus, for vanishing electric-field strength, there should not be any outgoing electron flux which could spoil an actual electron momentum distribution. This is in particular important for simulations of regions in the momentum distributions with low probability such as the high-energy rescattering region.

One frequently-used approach to determine the initial states is to propagate an (almost) arbitrary state $|\psi_{\text{trial}}\rangle$ in imaginary time. Since the trial state can be expanded in terms of eigenstates $|n\rangle$ of the field-free Hamiltonian H_0

$$|\psi_{\text{trial}}\rangle = \sum_n c_n |n\rangle \quad \text{with } H_0 |n\rangle = E_n |n\rangle, \quad (\text{A.58})$$

the imaginary time propagation is given by

$$e^{-\tau H_0} |\psi_{\text{trial}}\rangle = \sum_n c_n e^{-\tau E_n} |n\rangle. \quad (\text{A.59})$$

Hence, the contributions of the different eigenstates are suppressed according to their energy eigenvalue E_n . For large times τ , the eigenstate with the lowest energy⁵ dominates the expansion in Eq. (A.59). By repeating iteratively this approach, excited states can be found in the orthogonal complement of the known bound states with lower or equal energy. Usually, an implementation is based on the repeated application of the short-time propagator (with an imaginary time step $\Delta t = -i\Delta\tau$).

However, as pointed out in Ref. [530] for the Fourier split-operator method, the eigenstates of the Hamiltonian H_0 and also the states resulting from imaginary-time propagation are not exactly stationary under numerical real-time propagation based on the approximated short-time propagator of Eq. (A.23). To circumvent this difficulty, the eigenstates of the approximated real-time short-time propagator (A.23) with nonzero time step Δt can be used as initial states of the subsequent real-time propagation in the presence of the field [530]. To this end, the power method can be applied with the operator $e^{-i\Delta t H_0} + i\mathbf{1}$, i.e., this operator is repeatedly applied to the trial state. Here, $\mathbf{1}$ is the identity operator. The resulting ‘‘eigenstates’’ depend on the used time step Δt . They are different from the eigenstates of H_0 which are only retrieved in the limit of a vanishing time step $\Delta t \rightarrow 0$. For nonzero time steps Δt , we found that the results of time-dependent simulations with initial states chosen as eigenstates of the short-time propagator resemble the limit of vanishing time step best. In the actual implementation, we first prepare roughly an initial state by using the imaginary-time propagation. Afterwards, this result is refined by means of the power method with the operator $e^{-i\Delta t H_0} + i\mathbf{1}$.

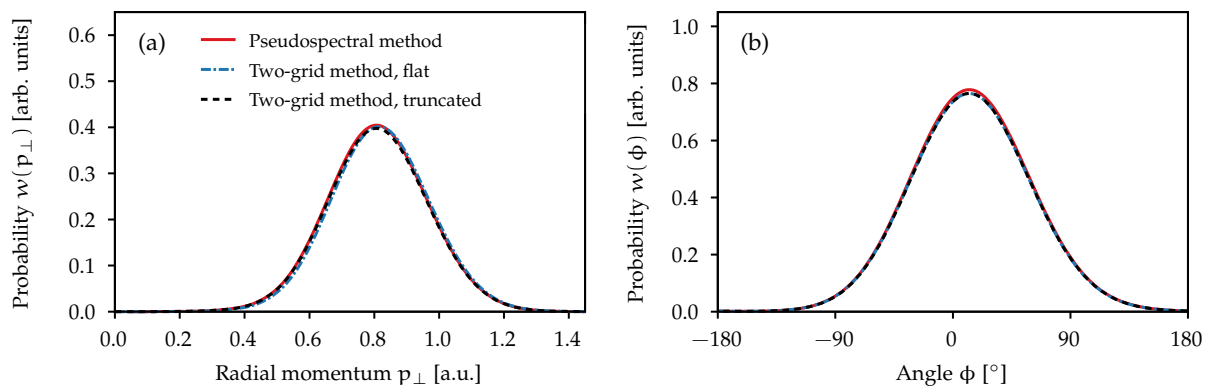


Figure A.5: (a) Radial momentum distribution in the polarization plane and (b) corresponding angular distribution for hydrogen ionized by short circularly-polarized laser pulses (800 nm central wavelength, 1×10^{14} W/cm² intensity, \cos^2 envelope of two cycles duration). The lines correspond to results from different schemes for the numerical solution of the TDSE (see main text).

⁵It is important that the corresponding coefficient c_0 is nonzero.

Comparison of results from different propagation schemes

To test the propagation schemes, we consider the circularly-polarized attoclock setup of Chapter 5 and performed simulations based on the pseudospectral method (see Section A.2.1) and the Fourier split-operator method on two Cartesian grids (see Section A.2.2). The result of the pseudospectral method is stable against changes of the numerical parameters and, thus, serves as a benchmark. For the Fourier split-operator method, we choose common numerical parameters with an inner grid spanning 409.6 a.u. in each dimension, a spacing of $\Delta x = 0.4$ a.u. and a time step of 0.03 a.u. Except for a slightly too small yield, the angular distributions are in perfect agreement with the benchmark results (see Fig. A.5(b)). We performed two simulations using the Fourier split-operator method. The same radius $r_A = 150$ a.u. was used in both cases, but the ionic potential was treated differently at large distances:

- For the “flat” choice, the variation of the potential is considered at distances $r \leq r_A$, but the potential is set to a constant $V(r_A) < 0$ for $r > r_A$. Hence, the deceleration of the electron wave packet by the Coulomb tail is neglected, introducing an error of about $\Delta E = -Z/r_A$ in the final electron kinetic energy. As a result, the radial momentum distribution in Fig. A.5(a) is centered at slightly too large momenta.
- For the “truncated” choice, the true potential is turned off using a \sin^2 function at a short distance before the absorber starts. Hence, in principle, the wave packet is decelerated. However, depending on the exact laser field, we find that the field-induced motion can change the direction of the electrons at distances $r > r_A$ such that the deceleration happens effectively in a wrong direction.

These effects are also visible in electron momentum distribution from a bicircular attoclock configuration as introduced in Section 5.3 (Fig. A.6). However, for common choices of the absorber distance r_A , we find that the “truncation” of the potential artificially deforms the shape of the outgoing wave packets. Hence, numerical errors in highly-differential observables such as the momentum-dependent attoclock shift are enhanced. For selected laser conditions, we verified that this error vanishes with increasing distance r_A . Overall, depending on the concrete physical observable and laser parameters under study, it can be advantageous to either use the “flat” or the “truncated” choice of the potential.

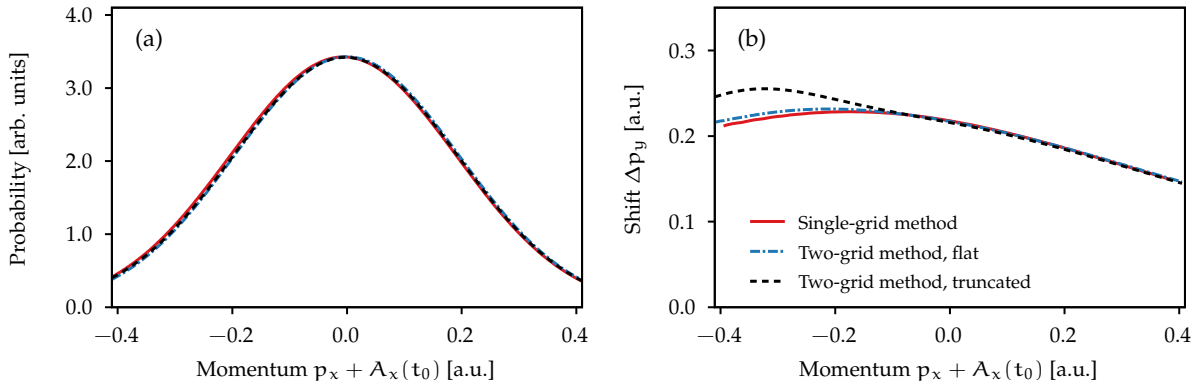


Figure A.6: (a) Slice through the photoelectron momentum distribution (at $p_y = 0$) and (b) momentum-dependent attoclock shift as a function of $p_x + A_x(0)$ for ionization of 2D helium in a bicircular attoclock configuration with 4×10^{14} W/cm² intensity and 800 nm effective wavelength (see Section 5.3). The shown results are calculated using the single-grid method or the two-grid method. In the latter cases, a distance of $r_A = 150$ a.u. is used. For the “truncated” choice, the potential is damped out over a distance of 50 a.u. before the absorber starts.

A.2.3 Choice of the potential

The effective potential used in single-active-electron simulations describes the interaction of the active electron with the nuclei (or nucleus for an atom) as well as an averaged effect of other electrons in multielectron systems. In strong-field physics, two basic requirements on the potential are that (i) the correct ionization energy of the real electronic system is retrieved and (ii) the correct behavior of the

	Z	α_1	α_2	α_3	α_4	α_5	α_6	I_p
H	1.0	0.000	0.000	0.000	0.000	0.000	0.000	0.500
He	1.0	1.231	0.662	-1.325	1.236	-0.231	0.480	0.904
Ne	1.0	8.069	2.148	-3.570	1.986	0.931	0.602	0.793
Ar	1.0	16.039	2.007	-25.543	4.525	0.961	0.443	0.580
Xe	1.0	51.356	2.112	-99.927	3.737	1.644	0.431	0.445

Table A.1: Parameters for the Tong-Lin potential (A.60) reprinted from [326].

potential is resembled for large distances r . In addition, depending on the studied physical processes, other potential-dependent quantities such as the eigenenergies of excited states or the field-free differential cross section for electron scattering can be important. For atoms, a common choice is the Tong-Lin potential

$$V(r) = -\frac{Z + \alpha_1 e^{-\alpha_2 r} + \alpha_3 r e^{-\alpha_4 r} + \alpha_5 e^{-\alpha_6 r}}{r} \quad (\text{A.60})$$

that is obtained by approximation of the single-particle potentials from density functional theory [531]. The charge Z determines the behavior $-Z/r$ at large distances r whereas the potential reduces to $-Z_{\text{core}}/r$ at small distances r with the core charge $Z_{\text{core}} = Z + \alpha_1 + \alpha_5$. The parameters for atoms used in this thesis are reprinted in Table A.1.

The singularity at $r \rightarrow 0$ of the potential causes difficulties in the numerical solution of the TDSE with the Fourier split-operator method and, hence, should be avoided. Similar to Ref. [161], we convert the potential into a pseudopotential as described in Ref. [532]. The pseudopotential matches the original potential at distances larger than a cutoff radius r_{cl} , but it is approximated by polynomials at shorter distances. To this end, a bound state $\phi_{n,l,m}(\mathbf{r}) = R_{n,l}(r)Y_l^m(\theta, \phi)$ is selected whose binding energy $E_{n,l}$ shall be exactly retrieved in the pseudopotential. For the pseudopotential, a modified radial part of this wave function is then defined as

$$R_{n,l}^{\text{PP}}(r) = \begin{cases} R_{n,l}(r) & , r > r_{cl} \\ r^l \exp(p_{n,l}(r)) & , r \leq r_{cl} \end{cases} \quad (\text{A.61})$$

with a polynomial

$$p_{n,l}(r) = c_0 + c_2 r^2 + c_4 r^4 + c_6 r^6 + c_8 r^8 + c_{10} r^{10} + c_{12} r^{12}. \quad (\text{A.62})$$

The coefficients are determined by the conditions that (i) the norm of the wave function is conserved, (ii) the curvature of the screened pseudopotential at the origin vanishes and (iii) the pseudo wave function is continuous up to the fourth derivative at r_{cl} . The assumption that the constructed wave function $R_{n,l}^{\text{PP}}(r)$ should be an eigenstate of the pseudopotential $V_{n,l}^{\text{PP}}(r)$ with the correct eigenenergy $E_{n,l}$ fully determines this potential. Hence, using the pseudo wave function (A.61) and the radial Schrödinger equation (A.25), the potential is derived

$$V_{n,l}^{\text{PP}}(r) = \begin{cases} V(r) & , r > r_{cl} \\ E_{n,l} + \frac{l+1}{r} p'_{n,l}(r) + \frac{p''_{n,l}(r) + (p'_{n,l}(r))^2}{2} & , r \leq r_{cl}. \end{cases} \quad (\text{A.63})$$

By construction the pseudopotentials depend on the selected state and the cutoff radius r_{cl} . The coefficients of the potentials are given in Table A.2 for the targets used in this thesis. Unfortunately, with the coefficients presented in Ref. [161], the fourth-order derivatives of the radial functions and, hence, the second-order derivatives of the potentials were not continuous. Except for the simulations on xenon discussed in Chapter 8, the coefficients of Ref. [161] are used throughout this thesis. For completeness, the corrected coefficients are shown in Table A.2. For light targets such as helium and neon, the differences in the coefficients can be neglected. For heavier targets such as argon and xenon, we only considered recollision-free ionization and, hence, expect negligible modifications of the observables for the corrected coefficients.

	state	r_{c1}	c_2	c_4	c_6	c_8	c_{10}	c_{12}	comments
H	1s	1.5	$-7.262 \cdot 10^{-1}$	$-1.055 \cdot 10^{-1}$	$2.862 \cdot 10^{-1}$	$-1.549 \cdot 10^{-1}$	$3.722 \cdot 10^{-2}$	$-3.444 \cdot 10^{-3}$	
He	1s	1.5	$-1.227 \cdot 10^{+0}$	$-3.013 \cdot 10^{-1}$	$6.555 \cdot 10^{-1}$	$-3.498 \cdot 10^{-1}$	$8.376 \cdot 10^{-2}$	$-7.736 \cdot 10^{-3}$	from [161]
He	1s	1.5	$-1.229 \cdot 10^{+0}$	$-3.021 \cdot 10^{-1}$	$6.597 \cdot 10^{-1}$	$-3.533 \cdot 10^{-1}$	$8.487 \cdot 10^{-2}$	$-7.864 \cdot 10^{-3}$	
Ne	2p	1.5	$-2.129 \cdot 10^{+0}$	$-6.473 \cdot 10^{-1}$	$1.336 \cdot 10^{+0}$	$-7.055 \cdot 10^{-1}$	$1.676 \cdot 10^{-1}$	$-1.537 \cdot 10^{-2}$	from [161]
Ne	2p	1.5	$-2.138 \cdot 10^{+0}$	$-6.533 \cdot 10^{-1}$	$1.359 \cdot 10^{+0}$	$-7.233 \cdot 10^{-1}$	$1.731 \cdot 10^{-1}$	$-1.599 \cdot 10^{-2}$	
Ar	3p	1.5	$-5.270 \cdot 10^{-1}$	$-3.967 \cdot 10^{-2}$	$-5.400 \cdot 10^{-2}$	$5.302 \cdot 10^{-2}$	$-1.520 \cdot 10^{-2}$	$1.503 \cdot 10^{-3}$	from [161]
Ar	3p	1.5	$-5.030 \cdot 10^{-1}$	$-3.614 \cdot 10^{-2}$	$-8.000 \cdot 10^{-2}$	$7.164 \cdot 10^{-2}$	$-2.063 \cdot 10^{-2}$	$2.088 \cdot 10^{-3}$	
Xe	5p	2.0	$1.423 \cdot 10^{-1}$	$-2.893 \cdot 10^{-3}$	$-6.711 \cdot 10^{-2}$	$2.238 \cdot 10^{-2}$	$-2.970 \cdot 10^{-3}$	$1.467 \cdot 10^{-4}$	from [161]
Xe	5p	2.0	$1.712 \cdot 10^{-1}$	$-4.185 \cdot 10^{-3}$	$-7.401 \cdot 10^{-2}$	$2.538 \cdot 10^{-2}$	$-3.472 \cdot 10^{-3}$	$1.774 \cdot 10^{-4}$	

Table A.2: Relevant parameters for the pseudopotential of Eq. (A.63) calculated based on the indicated states. The coefficients obtained in Ref. [161] are reprinted.

We consider the Coulomb potential for hydrogen and the Tong-Lin potential for xenon as examples. The original potentials and their corresponding pseudopotentials are shown in Fig. A.7(a). The radial wave functions for the 1s state in hydrogen and the 5p state in xenon as well as the corresponding pseudo wave functions are depicted in Fig. A.7(b). For hydrogen, both functions have the same overall shape. In contrast, we use a cutoff radius r_{c1} larger than the outermost node of the radial wave function for xenon, resulting in a pseudo wave function without nodes. By construction, both wave functions agree for distances larger than the cutoff radius. Hence, for nonresonant recollision-free strong-field ionization, the correct physical properties are reproduced by the pseudopotentials. To illustrate this, we consider the attoclock offset angles as well as the ionization probabilities for strong-field ionization of hydrogen by short circularly-polarized laser pulses as discussed in Chapter 5. For a fixed wavelength of 800 nm, the results are shown as a function of the intensity in Fig. A.8. For all intensities, reaching from the high-intensity region dominated tunneling down to nonadiabatic ionization in weaker fields, the results for the Coulomb potential and the pseudopotential are in perfect agreement. Even for the lowest considered intensity of 0.14×10^{14} W/cm², the attoclock angles differ by less than 0.2°.

A.2.4 Focal-volume averaging

In a typical strong-field experiment, a laser beam is focused onto a gas target. Hence, the field strength experienced by the electrons depends on the position of the target atom in the laser focus. Usually, the length scale of intensity change over the focus is much larger than the distance traveled by the photoelectrons during their propagation in subpicosecond laser pulses. Hence, on a microscopic scale, the laser beam can be approximated as a plane wave with spatially constant intensity. The intensity volume effect can then be considered by averaging the observables over the different intensities contained in the focus (see for example Ref. [533]).

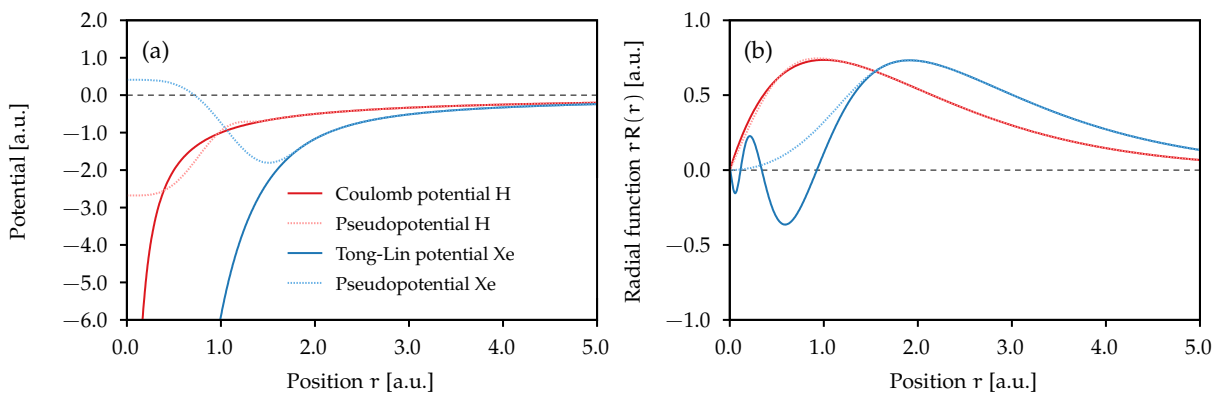


Figure A.7: (a) Coulomb potential for hydrogen and Tong-Lin potential for xenon and corresponding pseudopotentials with cutoff radii $r_{c1} = 1.5$ a.u. and $r_{c1} = 2.0$ a.u., respectively. (b) Radial wave functions $\chi(r) = rR(r)$ for the 1s state in hydrogen and the 5p state in xenon as well as their corresponding pseudo wave functions.

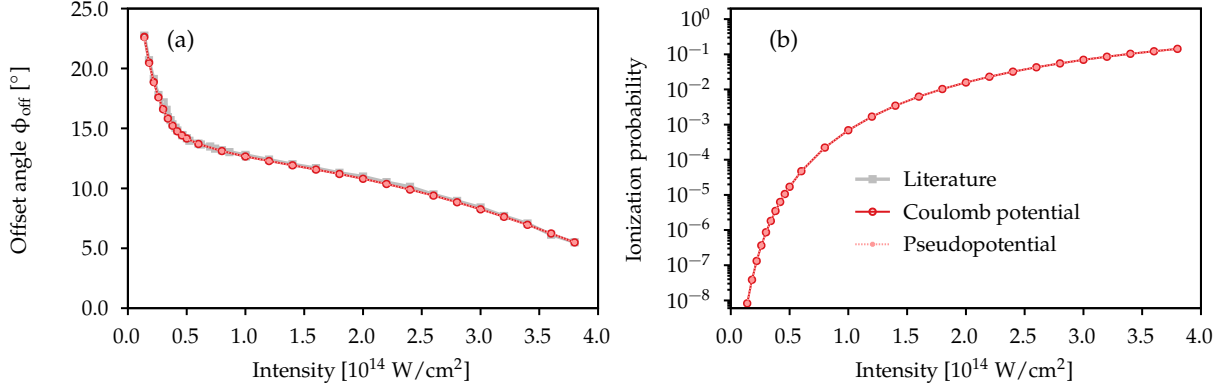


Figure A.8: (a) Offset angles and (b) total ionization probability as a function of the intensity for ionization of hydrogen in a circular attoclock configuration based on a two-cycle circularly-polarized laser pulse (800 nm central wavelength) similar to Fig. 5.1(b). The TDSE results for a bare Coulomb potential $-1/r$ and for the corresponding pseudopotential with cutoff radius $r_{c1} = 1.5$ a.u. are calculated using the pseudospectral method. For comparison, the results of Ref. [352] as well as the set of results labeled H2 in Ref. [213] are reprinted in panel (a) (gray points).

A photoelectron momentum distribution at a given laser intensity I is denoted as $w(\mathbf{p}; I)$. For a given spatial peak intensity I_{peak} , the focal-volume-averaged distribution is then given by

$$w_{\text{av}}(\mathbf{p}) = \int_0^{I_{\text{peak}}} w(\mathbf{p}; I) \left[-\frac{\partial V(I_{\text{peak}}, I)}{\partial I} \right] dI. \quad (\text{A.64})$$

Here, $V(I_{\text{peak}}, I)$ is the cumulated volume function, defined as the spatial volume in the laser focus occupied by intensities between I and I_{peak} . For a Gaussian focus in 3D, the cumulated volume function can be written analytically as (up to a multiplicative factor)

$$V(I_{\text{peak}}, I) \propto \frac{4}{3} \left[\frac{I_{\text{peak}}}{I} - 1 \right]^{1/2} + \frac{2}{9} \left[\frac{I_{\text{peak}}}{I} - 1 \right]^{3/2} - \frac{4}{3} \arctan \left[\frac{I_{\text{peak}}}{I} - 1 \right]^{1/2} \quad (\text{A.65})$$

and, thus, the weight in Eq. (A.64) reads [534]

$$-\frac{\partial V(I_{\text{peak}}, I)}{\partial I} \propto \sqrt{I_{\text{peak}} - I} [2I + I_{\text{peak}}] \frac{1}{I^{5/2}}. \quad (\text{A.66})$$

A.3 Strong-field approximation beyond the dipole approximation

The strong-field approximation offers a simplified description of recollision-free strong-field ionization. This can help to understand qualitatively the underlying physical mechanism. The aim of this section is to derive an analytical expression for the released electron wave packet based on strong-field approximation beyond the dipole approximation. To this end, the results from SFA in saddle-point approximation are expanded in powers of the Keldysh parameter γ . We consider only direct ionization as introduced in Section 2.3 and an initial 1s state of the electron. All equations are only consistent to first order in $1/c$.

The probability amplitude of Eq. (2.40) in length gauge is evaluated in saddle-point approximation (see Section 2.3.1). For each final momentum \mathbf{p} , only a single saddle-point time $t'_s = t'_r + it'_i$ is considered. The corresponding saddle-point equation reads

$$\frac{1}{2} \left[\mathbf{p} + \mathbf{A}(t'_s) + \frac{\mathbf{e}_z}{c} \left(\mathbf{p} \cdot \mathbf{A}(t'_s) + \frac{1}{2} \mathbf{A}^2(t'_s) \right) \right]^2 + I_p = 0. \quad (\text{A.67})$$

Under these assumptions, the photoelectron momentum distribution has the following form

$$w_{\text{SFA}}(\mathbf{p}) \propto \frac{1}{|\dot{\mathbf{S}}_{\text{SFA}}(\mathbf{p}, t'_s)|^\alpha} e^{-2\text{Im}S_{\text{SFA}}(\mathbf{p}, t'_s)} \quad (\text{A.68})$$

with the nondipole action of Eq. (2.41) given by

$$S_{\text{SFA}}(\mathbf{p}, t') = - \int_{t'}^{t_f} dt \frac{1}{2} \left[\mathbf{p} + \mathbf{A}(t) + \frac{\mathbf{e}_z}{c} \left(\mathbf{p} \cdot \mathbf{A}(t) + \frac{1}{2} \mathbf{A}^2(t) \right) \right]^2 + I_p(t' - t_A). \quad (\text{A.69})$$

The power α depends on the chosen gauge. Following the recipe in Ref. [194] to treat the pole in the matrix element, we have $\alpha = 1 + Z/\sqrt{2I_p}$ in length gauge (2.26) with Z being the asymptotic charge.

The initial probability distribution at the tunnel exit can be extracted based on the classical back-propagation method (introduced in Section 5.2.4). To this end, the asymptotic phase-space distribution is classically propagated back in time until the time t'_r is reached for each trajectory.⁶ In this potential-free setting, the classical mapping between the initial velocities \mathbf{v}_0 at the tunnel-exit position and the final momenta \mathbf{p} is given by (see Eqs. (8.2) and (8.3))

$$\mathbf{v}_0 = \mathbf{p} + \mathbf{A}(t'_r) + \frac{\mathbf{e}_z}{2c} [(\mathbf{p} + \mathbf{A}(t'_r))^2 - \mathbf{p}^2] = \mathbf{p} + \mathbf{A}(t'_r) + \frac{\mathbf{e}_z}{2c} [\mathbf{v}_0^2 - \mathbf{p}^2]. \quad (\text{A.70})$$

In addition, the relation between the times t'_r and the momenta \mathbf{p} is defined by the saddle-point equation (A.67). Hence, a mapping between the final momenta \mathbf{p} and the initial coordinates is established: $(t'_r, v_{0,\perp}, v_{0,z}) = \mathbf{D}(\mathbf{p})$. The probability distribution of the initial coordinates $(t'_r, v_{0,\perp}, v_{0,z})$ is defined as (see Eq. (5.16))

$$w_{\text{ini}}(t'_r, v_{0,\perp}, v_{0,z}) = \frac{w_{\text{SFA}}(\mathbf{p})}{|\det \mathbf{D}'(\mathbf{p})|}. \quad (\text{A.71})$$

Here, we introduced the Jacobi matrix \mathbf{D}' of the mapping \mathbf{D} with respect to \mathbf{p} . The distribution of Eq. (A.71) can be used to calculate observables at the tunnel exit such as the average $\langle v_{0,z} \rangle(t'_r, v_{0,\perp})$ of the initial velocity in the light-propagation direction as a function of the release time t'_r and the velocity component in the polarization plane $v_{0,\perp}$ (see Eq. (8.15)).

A.3.1 Adiabatic expansion of the saddle-point times

It is advantageous to measure the different quantities in the natural scales of strong-field ionization (see Section 2.1). Two different time scales appear: (i) the Keldysh time $\sqrt{2I_p}/E_0$ for a characteristic field strength E_0 and (ii) an optical cycle of the laser field $T_\omega = 2\pi/\omega$. Their ratio indicates the ionization regime and is usually represented by the dimensionless Keldysh parameter $\gamma = \sqrt{2I_p}\omega/E_0$. Here, we use the same system of units as in Ref. [161].⁷ Real times are measured in units of the inverse frequency ($t'_r = \tilde{t}'_r/\omega$), but imaginary times in units of the Keldysh time ($t'_i = \sqrt{2I_p}/E_0 \tilde{t}'_i$). A dimensionless velocity is defined as $\mathbf{v} = \sqrt{2I_p} \tilde{\mathbf{v}}$. If we denote the n th derivative of the electric field as $\mathbf{E}^{(n)}(t)$, we write $\mathbf{E}^{(n)}(t) = E_0 \omega^n \tilde{\mathbf{E}}^{(n)}(t)$. Following the ideas in Refs. [161, 209–211, 535], we derive a simplification of the SFA expressions close to the adiabatic limit.

To this end, we expand the vector potential around the real part t'_r of the saddle-point time [536]

$$\mathbf{A}(t'_r + i\tau) = \mathbf{A}(t'_r) - \sqrt{2I_p} \sum_{n=1}^{\infty} \frac{\gamma^{n-1} \tilde{\mathbf{E}}^{(n-1)}(t'_r)}{n!} (i\tilde{\tau})^n \quad \text{for } \tau \in \mathbb{R}. \quad (\text{A.72})$$

In the sum, we expressed the various quantities in the new system of units. Hence, an expansion in imaginary time can also be viewed as an expansion in the Keldysh parameter γ . This opens the possibility to derive expressions for different observables in the adiabatic limit ($\gamma \rightarrow 0$), and to include successively leading-order nonadiabatic corrections in γ . For simplicity, we omit the argument t'_r of the fields. In addition, we define an auxiliary velocity

$$\tilde{\mathbf{w}} = \tilde{\mathbf{v}}_0 + \frac{1}{2} \gamma \tilde{\mathbf{E}}' \tilde{t}'_i{}^2. \quad (\text{A.73})$$

⁶Here, we identify the release time t_0 with the real part t'_r of the saddle-point time.

⁷Note that the used time and velocity scales differ by a factor of two compared to Section 5.3.1. In addition, we use $\tilde{\mathbf{E}} = \mathbf{E}'$.

Even though this has no direct physical meaning, it simplifies the calculations. Inserting the expansion (A.72) in the saddle-point equation (A.67) and keeping only terms up to first order in γ (and to first order in $1/c$), we find

$$1 + \tilde{\mathbf{w}}^2 - \tilde{t}'_i \tilde{\mathbf{E}}^2 \left(1 + \frac{w_z}{c}\right) + \frac{w_z}{c} \gamma \tilde{t}'_i \tilde{\mathbf{w}} \cdot \tilde{\mathbf{E}}' - 2i \tilde{t}'_i \tilde{\mathbf{w}} \cdot \tilde{\mathbf{E}} \left(1 + \frac{w_z}{c}\right) \approx 0. \quad (\text{A.74})$$

Separation into real part and imaginary part, the saddle-points have to fulfill

$$\tilde{\mathbf{w}} \cdot \tilde{\mathbf{E}} = 0 \quad (\text{A.75})$$

as well as

$$\tilde{t}'_i = \sqrt{\frac{1 + \tilde{\mathbf{w}}^2}{\left(1 + \frac{w_z}{c}\right) \tilde{\mathbf{E}}^2 - \gamma \frac{w_z}{c} \tilde{\mathbf{w}} \cdot \tilde{\mathbf{E}}'}} \approx \sqrt{\frac{1 + \tilde{\mathbf{w}}^2}{\left(1 + \frac{w_z}{c}\right) \tilde{\mathbf{E}}^2}} \left(1 + \frac{1}{2} \gamma \frac{w_z}{c} \frac{\tilde{\mathbf{w}} \cdot \tilde{\mathbf{E}}'}{\tilde{\mathbf{E}}^2}\right). \quad (\text{A.76})$$

For a given real part \tilde{t}'_r of the saddle-point time, Equation (A.75) selects all possible auxiliary momenta $\tilde{\mathbf{w}}$. For each possible $\tilde{\mathbf{w}}$, the corresponding imaginary part of the saddle-point time is then given by Eq. (A.76). To reconstruct the associated physical initial velocity $\tilde{\mathbf{v}}_0$, Equation (A.73) is used.

Implicitly, the expansion contains higher-order terms in the Keldysh parameter γ . However, the solutions are only correct to first order in γ . In the adiabatic limit $\gamma \rightarrow 0$, the auxiliary velocity $\tilde{\mathbf{w}}$ approaches the initial velocity \mathbf{v}_0 and the saddle-point solutions are defined by

$$\mathbf{v}_0 \cdot \mathbf{E}(t'_r) = 0, \quad t'_i = \sqrt{\frac{\mathbf{v}_0^2 + 2I_p}{\left(1 + \frac{v_{0,z}}{c}\right) \mathbf{E}^2(t'_r)}}. \quad (\text{A.77})$$

The first equation is the well-known condition for the initial velocity in adiabatic tunneling (see Eq. (2.47)). It is unaffected by the nondipole corrections.

A.3.2 Adiabatic expansion of the wave packet

The ionization probability in Eq. (A.68) is dominated by the imaginary part of the action (A.69). To derive an approximation for $\text{Im}S_{\text{SFA}}$, we measure the imaginary part of the action in $(2I_p)^{3/2}/E_0$, i.e., $\text{Im}S_{\text{SFA}} = (2I_p)^{3/2}/E_0 \text{Im}\tilde{S}_{\text{SFA}}$. The imaginary part of the action is then approximately evaluated by inserting the expansion of Eq. (A.72) into Eq. (A.69). Keeping only terms to first order in the Keldysh parameter γ and in $1/c$, we find

$$\begin{aligned} 2\text{Im}\tilde{S}_{\text{SFA}} &= \tilde{t}'_i + \frac{E_0}{(2I_p)^{3/2}} \text{Re} \int_0^{\tilde{t}'_i} d\tau \left[\mathbf{p} + \mathbf{A}(t'_r + i\tau) + \frac{\mathbf{e}_z}{c} \left(\mathbf{p} \cdot \mathbf{A}(t'_r + i\tau) + \frac{1}{2} \mathbf{A}^2(t'_r + i\tau) \right) \right]^2 \\ &= \tilde{t}'_i + \int_0^{\tilde{t}'_i} d\tilde{\tau} \left(\tilde{\mathbf{v}}_0^2 - \left(1 + \frac{v_{0,z}}{c}\right) [\tilde{\mathbf{E}}^2 - \gamma \tilde{\mathbf{v}}_0 \cdot \tilde{\mathbf{E}}'] \tilde{\tau}^2 \right) + \mathcal{O}\left(\gamma^2, \frac{1}{c^2}\right) \\ &= \left[1 + \tilde{\mathbf{v}}_0^2\right] \tilde{t}'_i - \frac{1}{3} \left(1 + \frac{v_{0,z}}{c}\right) [\tilde{\mathbf{E}}^2 - \gamma \tilde{\mathbf{v}}_0 \cdot \tilde{\mathbf{E}}'] \tilde{t}'_i{}^3 + \mathcal{O}\left(\gamma^2, \frac{1}{c^2}\right). \end{aligned} \quad (\text{A.78})$$

This expression is then evaluated at the approximate saddle-point times of Eq. (A.76). Since we are only interested in the first-order nonadiabatic corrections, the relation (A.73) between $\tilde{\mathbf{w}}$ and $\tilde{\mathbf{v}}_0$ can be used to eliminate $\tilde{\mathbf{w}}$. The imaginary part of the action is approximated as

$$2\text{Im}\tilde{S}_{\text{SFA}} = \frac{2}{3} \frac{[1 + \tilde{\mathbf{v}}_0^2]^{3/2}}{\sqrt{\left(1 + \frac{v_{0,z}}{c}\right) [\tilde{\mathbf{E}}^2 - \gamma \tilde{\mathbf{v}}_0 \cdot \tilde{\mathbf{E}}']}} + \mathcal{O}\left(\gamma^2, \frac{1}{c^2}\right). \quad (\text{A.79})$$

To be consistent, the result is expanded to first-order in γ and expressed again in atomic units

$$\begin{aligned} 2\text{Im}S_{\text{SFA}} &= \frac{2}{3} \frac{[2I_p + \mathbf{v}_0^2]^{3/2}}{\sqrt{\left(1 + \frac{v_{0,z}}{c}\right) \mathbf{E}^2}} \left(1 + \frac{1}{2} \frac{\mathbf{v}_0 \cdot \tilde{\mathbf{E}}}{\mathbf{E}^2}\right) + \mathcal{O}\left(\gamma^2, \frac{1}{c^2}\right) \\ &= \frac{2}{3} \frac{[2I_p + v_{0,\perp}^2 + (v_{0,z} - \frac{1}{3c} [I_p + \mathbf{v}_0^2/2])^2]^{3/2}}{\sqrt{\mathbf{E}^2}} \left(1 + \frac{1}{2} \frac{\mathbf{v}_0 \cdot \tilde{\mathbf{E}}}{\mathbf{E}^2}\right) + \mathcal{O}\left(\gamma^2, \frac{1}{c^2}\right). \end{aligned} \quad (\text{A.80})$$

Typically, it is a good approximation to neglect the prefactor in the momentum distribution in Eq. (A.68). Its influence on nondipole observables was discussed in Ref. [474].

The final momentum distribution and the initial probability distribution differ by the Jacobian in Eq. (A.71). In the approximation shown in Eq. (A.77), the real part t'_r of the saddle-point time and also $v_{0,\perp}$ are independent of the moment p_z in the light-propagation direction. According to Eq. (A.70), we find $\partial v_{0,z}/\partial p_z = 1$ to first order in $1/c$. Hence, the Jacobian in Eq. (A.71) can be written as

$$\det \mathbf{D}'(\mathbf{p}) = \det \begin{pmatrix} \frac{\partial t'_r}{\partial p_x} & \frac{\partial v_{0,\perp}}{\partial p_x} & \frac{\partial v_{0,z}}{\partial p_x} \\ \frac{\partial t'_r}{\partial p_y} & \frac{\partial v_{0,\perp}}{\partial p_y} & \frac{\partial v_{0,z}}{\partial p_y} \\ 0 & 0 & 1 \end{pmatrix} = \det \begin{pmatrix} \frac{\partial t'_r}{\partial p_x} & \frac{\partial v_{0,\perp}}{\partial p_x} \\ \frac{\partial t'_r}{\partial p_y} & \frac{\partial v_{0,\perp}}{\partial p_y} \end{pmatrix} \quad (\text{A.81})$$

and it does not depend on p_z . For further simplification, we neglect its influence on the initial probability distribution. The wave packet at the tunnel exit is then given by Eq. (8.16) (for small $v_{0,z}$).

A.4 Analytic approximations for tunnel-exit positions

A.4.1 Adiabatic expansion of the tunnel-exit position in the SFA

For an initial $1s$ state, the tunnel-exit position from classical backpropagation with SFA input coincides with the common SFA tunnel-exit position in the dipole approximation (see Section 5.2.4)

$$\mathbf{r}_0 = \text{Re} \left(\int_{t'_s}^{t'_r} d\tau (\mathbf{p} + \mathbf{A}(\tau)) \right), \quad (\text{A.82})$$

where t'_s is the complex-valued saddle-point time and t'_r is its real part. To derive an approximation for \mathbf{r}_0 , we define a scaled position $\tilde{\mathbf{r}}_0 = 2I_p/E_0 \tilde{\mathbf{r}}_0$. Inserting the expansion of the vector potential (A.72) in Eq. (A.82) and keeping only first-order terms in γ , we find

$$\tilde{\mathbf{r}}_0 = \frac{E_0}{2I_p} \text{Im} \left(\int_0^{t'_i} d\tau \mathbf{A}(t'_r + i\tau) \right) = \text{Im} \left(\int_0^{\tilde{t}'_i} d\tilde{\tau} (-i\tilde{\tau} \tilde{\mathbf{E}}) \right) + \mathcal{O}(\gamma^2) = -\frac{1}{2} \tilde{\mathbf{E}} \tilde{t}'_i{}^2 + \mathcal{O}(\gamma^2). \quad (\text{A.83})$$

This expression is then evaluated at the approximate saddle-point times of Eq. (A.76). Since we are only interested in the first-order nonadiabatic corrections, the relation (A.73) between $\tilde{\mathbf{w}}$ and $\tilde{\mathbf{v}}_0$ can be used to eliminate $\tilde{\mathbf{w}}$. To first order in γ , the tunnel-exit position becomes

$$\tilde{\mathbf{r}}_0 = -\frac{1 + \tilde{\mathbf{v}}_0^2}{2\tilde{\mathbf{E}}^2} \left(1 + \gamma \frac{\tilde{\mathbf{v}}_0 \cdot \tilde{\mathbf{E}}'}{\tilde{\mathbf{E}}^2} \right) \tilde{\mathbf{E}} + \mathcal{O}(\gamma^2), \quad (\text{A.84})$$

where the possible ionization times t'_r and initial velocities $\tilde{\mathbf{v}}_0$ are selected by Eq. (A.75). Expressing the results in atomic units results in Eq. (5.25) of the main text. In linear polarization, the first-order nonadiabatic correction for the exit position vanishes, because $\tilde{\mathbf{E}}' \parallel \tilde{\mathbf{E}} \perp \tilde{\mathbf{v}}_0$. In contrast, for circular polarization, it is $\tilde{\mathbf{E}}' \perp \tilde{\mathbf{E}} \perp \tilde{\mathbf{v}}_0$ and the first-order nonadiabatic correction is present.

A.4.2 Tunnel-exit positions from the analytical R-matrix theory

The ARM theory offers a systematic approach to include the binding potential V as a first-order correction to the strong-field approximation (see Section 2.5). This allows us to derive a correction of the SFA tunnel-exit positions induced by a long-range Coulomb potential. To this end, we apply the classical backpropagation method (see Section 5.2.4) to the electron wave packets from ARM theory. Hence, the aim is to determine initial position \mathbf{r}_0 for a fixed release time (here denoted as \tilde{t}) and a given initial velocity $\mathbf{v}_0 = v_{0,\perp} \mathbf{e}_\perp + v_{0,z} \mathbf{e}_z$.

When the binding potential is neglected, the ARM theory results in the same tunnel exit as the SFA approach (see Section 5.2.4). Thus, to zeroth order in V , the tunnel-exit position is given by

$$\mathbf{r}_{00} = \text{Re} \left(\int_{t'_{s0}}^{\tilde{t}} d\tau (\mathbf{p}_0 + \mathbf{A}(\tau)) \right). \quad (\text{A.85})$$

The auxiliary momentum \mathbf{p}_0 is defined in a way that the velocity criterion in classical backpropagation, $\mathbf{E}(\tilde{t}) \cdot (\mathbf{p}_0 + \mathbf{A}(\tilde{t})) = 0$, is fulfilled and that the correct initial velocity $\mathbf{v}_0 = \mathbf{p}_0 + \mathbf{A}(\tilde{t})$ is obtained. The corresponding saddle-point time is determined by

$$\frac{1}{2} (\mathbf{p}_0 + \mathbf{A}(t'_{s0}))^2 = -I_p. \quad (\text{A.86})$$

In this potential-free scenario (and considering the velocity gauge), the momentum \mathbf{p}_0 is conserved during the classical time evolution and the zeroth-order trajectory is given by

$$\mathbf{r}^{(0)}(t) = \text{Re} \left(\int_{t'_{s0}}^t d\tau (\mathbf{p}_0 + \mathbf{A}(\tau)) \right). \quad (\text{A.87})$$

The long-range Coulomb attraction modifies the dynamics such that the momentum changes over time. To determine its influence on the classical dynamics during the backpropagation, we consider the Coulomb force as a perturbation. In a backpropagation simulation, the trajectories start at the final time t_f with a momentum \mathbf{p} at a position \mathbf{r}_f . In order to still fulfill the velocity criterion at the fixed release time \tilde{t} , the final momentum \mathbf{p} needs to be chosen as $\mathbf{p} = \mathbf{p}_0 + \Delta\mathbf{p}$ with the correction

$$\Delta\mathbf{p} = \int_{t_f}^{\tilde{t}} dt' \nabla V(\mathbf{r}^{(0)}(t')). \quad (\text{A.88})$$

The tunnel-exit position is then determined by classical propagation backwards in time. To first order in the potential, it is given by

$$\mathbf{r}_{01} = \mathbf{r}_f + \int_{t_f}^{\tilde{t}} dt' (\mathbf{p}_0 + \mathbf{A}(t')) + \Delta\mathbf{p}(\tilde{t} - t_f) - \int_{t_f}^{\tilde{t}} dt'' \int_{t_f}^{t''} dt' \nabla V(\mathbf{r}^{(0)}(t')) \quad (\text{A.89})$$

In the backpropagation method, the final position \mathbf{r}_f is determined by the negative phase gradient of the momentum-space wave packet (see Eq. (5.14)). Using the ARM action of Eq. (2.59), this position can be estimated as

$$\begin{aligned} \mathbf{r}_f = -\nabla_{\mathbf{p}} \text{Re} S_{\text{ARM}}(\mathbf{p}) = & \text{Re} \left(\int_{t'_s}^{t_f} d\tau (\mathbf{p} + \mathbf{A}(\tau)) \right) + \text{Re} \left(\int_{t'_k}^{t_f} d\tau \nabla_{\mathbf{r}} V(\mathbf{r}_L(\tau; \mathbf{p}, t'_s)) (\tau - t'_s) \right) \\ & + \text{Re} \left(-\nabla_{\mathbf{p}} t_s \left[V(\mathbf{r}_L(t'_k; \mathbf{p}, t'_s)) + (\mathbf{p} + \mathbf{A}(t'_s)) \int_{t'_k}^{t_f} d\tau \nabla_{\mathbf{r}} V(\mathbf{r}_L(\tau; \mathbf{p}, t'_s)) \right] \right) \end{aligned} \quad (\text{A.90})$$

with the ARM orbit \mathbf{r}_L of Eq. (2.56). We express the final momentum \mathbf{p} by the potential-free momentum \mathbf{p}_0 and the momentum correction $\Delta\mathbf{p}$. Hence, to first order in the potential, the tunnel-exit position (from backpropagation) can be written as $\mathbf{r}_0 = \mathbf{r}_{00} + \Delta\mathbf{r}_0$ with the potential-free result \mathbf{r}_{00} of Eq. (A.85) and the correction

$$\begin{aligned} \Delta\mathbf{r}_0 = & \Delta\mathbf{p}(\tilde{t} - t'_{r0}) - \int_{t_f}^{\tilde{t}} dt'' \int_{t_f}^{t''} dt' \nabla V(\mathbf{r}^{(0)}(t')) - \text{Re} \left((\mathbf{p}_0 + \mathbf{A}(t'_{s0})) (\Delta\mathbf{p} \cdot \nabla_{\mathbf{p}} t'_{s0}) \right) \\ & + \text{Re} \left(\int_{t'_{k0}}^{t_f} d\tau \nabla_{\mathbf{r}} V(\mathbf{r}_L(\tau; \mathbf{p}_0, t'_{s0})) (\tau - t'_{s0}) \right) \\ & + \text{Re} \left(-\nabla_{\mathbf{p}} t'_{s0} \left[V(\mathbf{r}_L(t'_{k0}; \mathbf{p}_0, t'_{s0})) + (\mathbf{p}_0 + \mathbf{A}(t'_{s0})) \int_{t'_{k0}}^{t_f} d\tau \nabla_{\mathbf{r}} V(\mathbf{r}_L(\tau; \mathbf{p}_0, t'_{s0})) \right] \right). \end{aligned} \quad (\text{A.91})$$

The first term is an artifact of the chosen velocity criterion in backpropagation. In the cases considered in this work, the times \tilde{t} and $\text{Re} t'_{s0}$ agree and the term vanishes. The second term is related to the position offset picked up during the classical motion backwards in time. The third term is caused by the difference of the final momentum \mathbf{p} (where the phase gradient is calculated in backpropagation) compared to the initial momentum \mathbf{p}_0 . The last terms are the corrections of the final positions due to the ionic potential.

A.5 Low-frequency approximation beyond the dipole approximation

In Section 9.4, the rescattering amplitude in strong-field ionization is studied. In this context, the laser-assisted scattering amplitude appears [497]

$$R_{\mathbf{k},\mathbf{m}}(t, t') = \langle \psi_{\mathbf{k}}^F(t) | V U(t, t') | \psi_{\mathbf{m}}^F(t') \rangle \quad (\text{A.92})$$

with Volkov states $|\psi_{\mathbf{m}}^F(\tau)\rangle$ of Eq. (2.32) in generalized length gauge of Eq. (2.26). The low-frequency approximation (LFA) [495] is an approximation to this laser-assisted scattering amplitude. Here, we follow the derivation in Ref. [497] and include leading-order nondipole corrections. To this end, it is convenient to introduce the retarded Green's operator G with $U(t, t'') = iG(t, t'')$ for $t > t''$ and $G(t, t'') = 0$ for $t < t''$. By using a Dyson representation, the laser-assisted scattering amplitude can be written as

$$R_{\mathbf{k},\mathbf{m}}(t, t') = \langle \psi_{\mathbf{k}}^F(t) | V | \psi_{\mathbf{m}}^F(t) \rangle + \int_{t'}^{\infty} dt'' \langle \psi_{\mathbf{k}}^F(t) | V G(t, t'') V | \psi_{\mathbf{m}}^F(t'') \rangle. \quad (\text{A.93})$$

In first Born approximation (1BA) only the first term is included. To consider corrections of the second term, the Green's operator is studied. This operator satisfies the equation

$$\left[i \frac{\partial}{\partial t} - H(t) \right] G(t, t'') = \delta(t - t''). \quad (\text{A.94})$$

For an approximation, we parameterize the two times by means of the collision time $t = t_1$ and the time interval $t - t'' = t_2$, i.e., $t = t_1$ and $t'' = t_1 - t_2$. Using the chain rule and Eq. (A.94), the reparameterized operator $\hat{G}(t_1, t_2) = G(t_1, t_1 - t_2)$ has to fulfill

$$\left[i \frac{\partial}{\partial t_1} + i \frac{\partial}{\partial t_2} - H(t_1) \right] \hat{G}(t_1, t_2) = \delta(t_2). \quad (\text{A.95})$$

In order to approximate this Green's operator in a series of the light frequency ω , it is advantageous to study the "Fourier-transformed" operator $\tilde{G}(t_1, z)$ that is implicitly defined by

$$\hat{G}(t_1, t_2) = \frac{1}{2\pi} \int dE \tilde{G}(t_1, z) e^{-izt_2} \quad (\text{A.96})$$

with $z = E + i0$. Using $\delta(t_2) = \frac{1}{2\pi} \int dE e^{-izt_2}$, Eq. (A.95) can be written as

$$\int dE \left(\left[i \frac{\partial}{\partial t_1} + z - H(t_1) \right] \tilde{G}(t_1, z) - 1 \right) e^{-izt_2} = 0. \quad (\text{A.97})$$

Hence, it follows

$$\left[i \frac{\partial}{\partial t_1} + z - H(t_1) \right] \tilde{G}(t_1, z) = 1. \quad (\text{A.98})$$

This is an exact expression and it is the same as Eq. (27) in Ref. [497]. However, we are only interested in the time evolution in the special situation defined in Eq. (A.93). We apply a unitary transformations that somehow accounts for "the potential-free" dynamics in the electromagnetic field:

$$\tilde{U} = \hat{U} e^{-i(S_F(\mathbf{m}, t_1) + E t_1)} \quad \text{with} \quad \hat{U} = e^{-i\chi_U(t_1)} e^{-i\mathbf{A}(t_1) \cdot \mathbf{r}} \quad (\text{A.99})$$

with the action S_F defined in Eq. (2.33) and the generating operator $\chi_U(t_1) = \frac{z}{c} (\hat{\mathbf{p}} \cdot \mathbf{A}(t_1) + \frac{1}{2} \mathbf{A}^2(t_1))$. We can rewrite Eq. (A.98) as

$$\begin{aligned} 1 &= \tilde{U}^\dagger \tilde{U} \left[z - H(t_1) + i \frac{\partial}{\partial t_1} \right] \tilde{U}^\dagger \tilde{U} \tilde{G}(t_1, z) \\ &= \tilde{U}^\dagger \left[z - E + \tilde{E}(\mathbf{m}, t_1) - \hat{U} H(t_1) \hat{U}^\dagger + i \hat{U} \left(\frac{\partial}{\partial t_1} \hat{U}^\dagger \right) + i \frac{\partial}{\partial t_1} \right] \tilde{U} \tilde{G}(t_1, z) \end{aligned} \quad (\text{A.100})$$

with the "kinetic energy" of the light-driven electron

$$\tilde{E}(\mathbf{m}, t) = \frac{\mathbf{v}^2(\mathbf{m}, t)}{2}. \quad (\text{A.101})$$

The unitary transformation \hat{U} transforms the generalized length gauge to the natural gauge introduced in Section 2.2.2. Hence, we find

$$i\hat{U} \left(\frac{\partial}{\partial t_1} \hat{U}^\dagger \right) - \hat{U}H(t_1)\hat{U}^\dagger = -\hat{U}H_0\hat{U}^\dagger, \quad (\text{A.102})$$

where H_0 is the field-free Hamiltonian. Thus, Equation (A.100) can be expressed as

$$\begin{aligned} 1 &= \tilde{U}^\dagger \left[+i0 + \tilde{E}(\mathbf{m}, t_1) - \hat{U}H_0\hat{U}^\dagger + i\frac{\partial}{\partial t_1} \right] \tilde{U} \tilde{G}(t_1, z) \\ &= \tilde{U}^\dagger \left[\hat{U}G_0^{-1}(\tilde{E}(\mathbf{m}, t_1) + i0)\hat{U}^\dagger + i\frac{\partial}{\partial t_1} \right] \tilde{U} \tilde{G}(t_1, z) \end{aligned} \quad (\text{A.103})$$

with the field-free Green's operator defined in Eq. (A.8).

In the first term in brackets, the dependence on the time t_1 appears solely through the vector potential \mathbf{A} . Hence, it is advantageous to measure time in units of $1/\omega$ for a characteristic frequency ω of the electromagnetic field, i.e., we define $\tau = \omega t_1$. In addition, we define the operator (see Ref. [497])

$$\Gamma(\tau) = \hat{U}G_0(\tilde{E}(\mathbf{m}, \tau/\omega) + i0)\hat{U}^\dagger. \quad (\text{A.104})$$

Equation (A.103) can be rephrased as

$$1 = \tilde{U}^\dagger \left[\Gamma^{-1}(\tau) + i\omega\frac{\partial}{\partial \tau} \right] \tilde{U} \tilde{G}(t_1, z). \quad (\text{A.105})$$

This equation can be solved by expanding \tilde{G} in terms of the frequency ω and determining the full solution iteratively. The low-frequency approximation considers only the zeroth-order term of this series, i.e., the Fourier-transformed Green's operator is approximated as $\tilde{G}^{\text{LFA}}(t_1, z) = G_0(\tilde{E}(\mathbf{m}, t_1) + i0)$. The time-dependent Green's operator of Eq. (A.96) reduces to

$$\hat{G}^{\text{LFA}}(t_1, t_2) = \frac{1}{2\pi} \int dE \tilde{G}^{\text{LFA}}(t_1, z) e^{-izt_2} = G_0(\tilde{E}(\mathbf{m}, t_1) + i0)\delta(t_2), \quad (\text{A.106})$$

where a Fourier representation of the Delta distribution is used. Transforming back to the times t and t'' , we find the result $G^{\text{LFA}}(t, t'') = G_0(\tilde{E}(\mathbf{m}, t) + i0)\delta(t - t'')$. Thus, as expected, the LFA neglects the light-field-induced change of the electron's velocity during the scattering process. Inserting this approximation in Eq. (A.93) (similar to Ref. [497]), the Delta distribution resolves the time integral and the laser-assisted scattering amplitude is given by

$$\begin{aligned} R_{\mathbf{k}, \mathbf{m}}^{\text{LFA}}(t, t') &= \langle \psi_{\mathbf{k}}^{\text{F}}(t) | V | \psi_{\mathbf{m}}^{\text{F}}(t) \rangle + \langle \psi_{\mathbf{k}}^{\text{F}}(t) | V G_0(\tilde{E}(\mathbf{m}, t) + i0) V | \psi_{\mathbf{m}}^{\text{F}}(t) \rangle \\ &= \langle \psi_{\mathbf{k}}^{\text{F}}(t) | V + V G_0(\tilde{E}(\mathbf{m}, t) + i0) V | \psi_{\mathbf{m}}^{\text{F}}(t) \rangle. \end{aligned} \quad (\text{A.107})$$

This result is equal to Eq. (9.17) of the main text.

On the first glance, the derived approximation seems arbitrary due to the choice of the transformation \tilde{U} . However, a strength of the presented derivation is that it could be extended to estimate leading-order errors in the expansion of Eq. (A.105). In the context of laser-assisted potential scattering such an error estimation was performed (see for example Refs. [537, 538]) and the relevant parameters that limit the applicability of LFA were identified.⁸ In Ref. [539] the same conditions were given for the HATI process in the dipole approximation. When replacing the quantities in the dipole approximation by the generalized quantities beyond the dipole approximation, the expressions in our derivation have the same form as in Ref. [497]. Hence, we are confident that the same range of applicability can be expected for LFA beyond the dipole approximation.

⁸For high intensities (with $|\mathbf{m}| < A_0$), the relevant parameter is given by ω/U_p whereas the relevant parameter is given by $(\omega/E_m)(A_0/|\mathbf{m}|)$ for low intensities (with $|\mathbf{m}| > A_0$) [539].

Bibliography

- [1] A. Einstein, "Über einen die Erzeugung und Verwandlung des Lichtes betreffenden heuristischen Gesichtspunkt," *Ann. Phys.* **322**, 132–148 (1905).
- [2] M. Göppert-Mayer, "Über Elementarakte mit zwei Quantensprüngen," *Ann. Phys.* **401**, 273–294 (1931).
- [3] P. A. Franken, A. E. Hill, C. W. Peters et al., "Generation of Optical Harmonics," *Phys. Rev. Lett.* **7**, 118–119 (1961).
- [4] W. Kaiser and C. G. B. Garrett, "Two-Photon Excitation in $\text{CaF}_2: \text{Eu}^{2+}$," *Phys. Rev. Lett.* **7**, 229–231 (1961).
- [5] P. Agostini, F. Fabre, G. Mainfray et al., "Free-Free Transitions Following Six-Photon Ionization of Xenon Atoms," *Phys. Rev. Lett.* **42**, 1127 (1979).
- [6] D. Strickland and G. Mourou, "Compression of amplified chirped optical pulses," *Opt. Commun.* **56**, 219–221 (1985).
- [7] T. F. Gallagher, "Above-Threshold Ionization in Low-Frequency Limit," *Phys. Rev. Lett.* **61**, 2304 (1988).
- [8] P. B. Corkum, N. H. Burnett and F. Brunel, "Above-Threshold Ionization in the Long-Wavelength Limit," *Phys. Rev. Lett.* **62**, 1259 (1989).
- [9] J. L. Krause, K. J. Schafer and K. C. Kulander, "High-Order Harmonic Generation from Atoms and Ions in the High Intensity Regime," *Phys. Rev. Lett.* **68**, 3535 (1992).
- [10] P. B. Corkum, "Plasma Perspective on Strong Field Multiphoton Ionization," *Phys. Rev. Lett.* **71**, 1994 (1993).
- [11] A. McPherson, G. Gibson, H. Jara et al., "Studies of multiphoton production of vacuum-ultraviolet radiation in the rare gases," *J. Opt. Soc. Am. B* **4**, 595 (1987).
- [12] M. Ferray, A. L'Huillier, X. F. Li et al., "Multiple-harmonic conversion of 1064 nm radiation in rare gases," *J. Phys. B* **21**, L31 (1988).
- [13] D. N. Fittinghoff, P. R. Bolton, B. Chang et al., "Observation of Nonsequential Double Ionization of Helium with Optical Tunneling," *Phys. Rev. Lett.* **69**, 2642 (1992).
- [14] T. Weber, H. Giessen, M. Weckenbrock et al., "Correlated electron emission in multiphoton double ionization," *Nature* **405**, 658–661 (2000).
- [15] M. Lein, E. K. U. Gross and V. Engel, "Intense-Field Double Ionization of Helium: Identifying the Mechanism," *Phys. Rev. Lett.* **85**, 4707 (2000).
- [16] G. G. Paulus, W. Nicklich, H. Xu et al., "Plateau in above Threshold Ionization Spectra," *Phys. Rev. Lett.* **72**, 2851 (1994).

- [17] G. G. Paulus, W. Becker, W. Nicklich et al., "Rescattering effects in above-threshold ionization: A classical model," *J. Phys. B* **27**, L703 (1994).
- [18] M. Lewenstein, K. C. Kulander, K. J. Schafer et al., "Rings in above-threshold ionization: A quasi-classical analysis," *Phys. Rev. A* **51**, 1495–1507 (1995).
- [19] P. B. Corkum and F. Krausz, "Attosecond science," *Nat. Phys.* **3**, 381–387 (2007).
- [20] F. Krausz and M. Ivanov, "Attosecond physics," *Rev. Mod. Phys.* **81**, 163 (2009).
- [21] F. Calegari, G. Sansone, S. Stagira et al., "Advances in attosecond science," *J. Phys. B* **49**, 062001 (2016).
- [22] M. Lein, "Molecular imaging using recolliding electrons," *J. Phys. B* **40**, R135 (2007).
- [23] J. Itatani, J. Levesque, D. Zeidler et al., "Tomographic imaging of molecular orbitals," *Nature* **432**, 867 (2004).
- [24] S. Baker, J. S. Robinson, C. A. Haworth et al., "Probing Proton Dynamics in Molecules on an Attosecond Time Scale," *Science* **312**, 424 (2006).
- [25] O. Smirnova, Y. Mairesse, S. Patchkovskii et al., "High harmonic interferometry of multi-electron dynamics in molecules," *Nature* **460**, 972 (2009).
- [26] P. M. Kraus, B. Mignolet, D. Baykusheva et al., "Measurement and laser control of attosecond charge migration in ionized iodoacetylene," *Science* **350**, 790 (2015).
- [27] P. Peng, C. Marceau and D. M. Villeneuve, "Attosecond imaging of molecules using high harmonic spectroscopy," *Nat. Rev. Phys.* **1**, 144–155 (2019).
- [28] X.-B. Bian and A. D. Bandrauk, "Attosecond Time-Resolved Imaging of Molecular Structure by Photoelectron Holography," *Phys. Rev. Lett.* **108**, 263003 (2012).
- [29] M. Meckel, A. Staudte, S. Patchkovskii et al., "Signatures of the continuum electron phase in molecular strong-field photoelectron holography," *Nat. Phys.* **10**, 594 (2014).
- [30] M. Haertelt, X.-B. Bian, M. Spanner et al., "Probing Molecular Dynamics by Laser-Induced Backscattering Holography," *Phys. Rev. Lett.* **116**, 133001 (2016).
- [31] S. G. Walt, N. Bhargava Ram, M. Atala et al., "Dynamics of valence-shell electrons and nuclei probed by strong-field holography and rescattering," *Nat. Commun.* **8**, 15651 – (2017).
- [32] M. He, Y. Li, Y. Zhou et al., "Direct Visualization of Valence Electron Motion Using Strong-Field Photoelectron Holography," *Phys. Rev. Lett.* **120**, 133204 (2018).
- [33] T. Zuo, A. D. Bandrauk and P. B. Corkum, "Laser-induced electron diffraction: A new tool for probing ultrafast molecular dynamics," *Chem. Phys. Lett.* **259**, 313 (1996).
- [34] M. Lein, J. P. Marangos and P. L. Knight, "Electron diffraction in above-threshold ionization of molecules," *Phys. Rev. A* **66**, 051404 (2002).
- [35] M. Spanner, O. Smirnova, P. B. Corkum et al., "Reading diffraction images in strong field ionization of diatomic molecules," *J. Phys. B* **37**, L243 (2004).
- [36] T. Morishita, A.-T. Le, Z. Chen et al., "Accurate Retrieval of Structural Information from Laser-Induced Photoelectron and High-Order Harmonic Spectra by Few-Cycle Laser Pulses," *Phys. Rev. Lett.* **100**, 013903 (2008).

- [37] M. Okunishi, T. Morishita, G. Prümper et al., "Experimental Retrieval of Target Structure Information from Laser-Induced Rescattered Photoelectron Momentum Distributions," *Phys. Rev. Lett.* **100**, 143001 (2008).
- [38] D. Ray, B. Ulrich, I. Bocharova et al., "Large-Angle Electron Diffraction Structure in Laser-Induced Rescattering from Rare Gases," *Phys. Rev. Lett.* **100**, 143002 (2008).
- [39] M. Okunishi, R. Itaya, K. Shimada et al., "Two-Source Double-Slit Interference in Angle-Resolved High-Energy Above-Threshold Ionization Spectra of Diatoms," *Phys. Rev. Lett.* **103**, 043001 (2009).
- [40] C. I. Blaga, J. Xu, A. D. DiChiara et al., "Imaging ultrafast molecular dynamics with laser-induced electron diffraction," *Nature* **483**, 194 (2012).
- [41] M. Meckel, D. Comtois, D. Zeidler et al., "Laser-Induced Electron Tunneling and Diffraction," *Science* **320**, 1478 (2008).
- [42] M. G. Pullen, B. Wolter, A.-T. Le et al., "Imaging an aligned polyatomic molecule with laser-induced electron diffraction," *Nat. Commun.* **6**, 7262 (2015).
- [43] A. T. J. B. Eppink and D. H. Parker, "Velocity map imaging of ions and electrons using electrostatic lenses: Application in photoelectron and photofragment ion imaging of molecular oxygen," *Rev. Sci. Instrum.* **68**, 3477 (1997).
- [44] C. Bordas, F. Paulig, H. Helm et al., "Photoelectron imaging spectrometry: Principle and inversion method," *Rev. Sci. Instrum.* **67**, 2257 (1996).
- [45] M. J. J. Vrakking, "An iterative procedure for the inversion of two-dimensional ion/photoelectron imaging experiments," *Rev. Sci. Instrum.* **72**, 4084 (2001).
- [46] M. Wollenhaupt, M. Krug, J. Köhler et al., "Three-dimensional tomographic reconstruction of ultrashort free electron wave packets," *Appl. Phys. B* **95**, 647 (2009).
- [47] C. Smeenk, L. Arissian, A. Staudte et al., "Momentum space tomographic imaging of photoelectrons," *J. Phys. B* **42**, 185402 (2009).
- [48] R. Dörner, V. Mergel, O. Jagutzki et al., "Cold target recoil ion momentum spectroscopy: A 'momentum microscope' to view atomic collision dynamics," *Phys. Rep.* **330**, 95 – 192 (2000).
- [49] O. Jagutzki, A. Cerezo, A. Czasch et al., "Multiple hit readout of a microchannel plate detector with a three-layer delay-line anode," *IEEE Trans. Nucl. Sci.* **49**, 2477 (2002).
- [50] J. Ullrich, R. Moshhammer, A. Dorn et al., "Recoil-ion and electron momentum spectroscopy: Reaction-microscopes," *Rep. Prog. Phys.* **66**, 1463 (2003).
- [51] A. Hartung, S. Eckart, S. Brennecke et al., "Magnetic fields alter strong-field ionization," *Nat. Phys.* **15**, 1222 (2019).
- [52] P. Eckle, M. Smolarski, P. Schlup et al., "Attosecond angular streaking," *Nat. Phys.* **4**, 565 (2008).
- [53] P. Eckle, A. N. Pfeiffer, C. Cirelli et al., "Attosecond Ionization and Tunneling Delay Time Measurements in Helium," *Science* **322**, 1525 (2008).
- [54] A. N. Pfeiffer, C. Cirelli, M. Smolarski et al., "Attoclock reveals natural coordinates of the laser-induced tunnelling current flow in atoms," *Nat. Phys.* **8**, 76 (2012).
- [55] A. S. Kheifets, "The attoclock and the tunneling time debate," *J. Phys. B* **53**, 072001 (2020).
- [56] C. Hofmann, A. S. Landsman and U. Keller, "Attoclock revisited on electron tunnelling time," *J. Mod. Opt.* **66**, 1052 (2019).

- [57] X. M. Tong, Z. X. Zhao and C. D. Lin, "Theory of molecular tunneling ionization," *Phys. Rev. A* **66**, 033402 (2002).
- [58] G. Lagmago Kamta and A. D. Bandrauk, "Imaging electron molecular orbitals via ionization by intense femtosecond pulses," *Phys. Rev. A* **74**, 033415 (2006).
- [59] A. Staudte, S. Patchkovskii, D. Pavičić et al., "Angular Tunneling Ionization Probability of Fixed-in-Space H₂ Molecules in Intense Laser Pulses," *Phys. Rev. Lett.* **102**, 033004 (2009).
- [60] X. Zhu, Q. Zhang, W. Hong et al., "Molecular orbital imaging via above-threshold ionization with circularly polarized pulses," *Opt. Express* **19**, 13722–13731 (2011).
- [61] M. Spanner, S. Gräfe, S. Chelkowski et al., "Coulomb asymmetry and sub-cycle electron dynamics in multiphoton multiple ionization of H₂," *J. Phys. B* **45**, 194011 (2012).
- [62] E. P. Wigner, "Lower Limit for the Energy Derivative of the Scattering Phase Shift," *Phys. Rev.* **98**, 145 (1955).
- [63] J. Itatani, F. Quéré, G. L. Yudin et al., "Attosecond Streak Camera," *Phys. Rev. Lett.* **88**, 173903 (2002).
- [64] M. Schultze, M. Fieß, N. Karpowicz et al., "Delay in Photoemission," *Science* **328**, 1658 (2010).
- [65] P. M. Paul, E. S. Toma, P. Breger et al., "Observation of a Train of Attosecond Pulses from High Harmonic Generation," *Science* **292**, 1689 (2001).
- [66] K. Klünder, J. M. Dahlström, M. Gisselbrecht et al., "Probing Single-Photon Ionization on the Attosecond Time Scale," *Phys. Rev. Lett.* **106**, 143002 (2011).
- [67] M. Huppert, I. Jordan, D. Baykusheva et al., "Attosecond Delays in Molecular Photoionization," *Phys. Rev. Lett.* **117**, 093001 (2016).
- [68] J. Vos, L. Cattaneo, S. Patchkovskii et al., "Orientation-dependent stereo Wigner time delay and electron localization in a small molecule," *Science* **360**, 1326 (2018).
- [69] S. Eckart, "Holographic angular streaking of electrons and the Wigner time delay," *Phys. Rev. Res.* **2**, 033248 (2020).
- [70] F. Schell, T. Bredtmann, C. P. Schulz et al., "Molecular orbital imprint in laser-driven electron recollision," *Sci. Adv.* **4**, 8148 (2018).
- [71] F. Lindner, M. G. Schätzel, H. Walther et al., "Attosecond Double-Slit Experiment," *Phys. Rev. Lett.* **95**, 040401 (2005).
- [72] D. G. Arbó, E. Persson and J. Burgdörfer, "Time double-slit interferences in strong-field tunneling ionization," *Phys. Rev. A* **74**, 063407 (2006).
- [73] R. Gopal, K. Simeonidis, R. Moshhammer et al., "Three-Dimensional Momentum Imaging of Electron Wave Packet Interference in Few-Cycle Laser Pulses," *Phys. Rev. Lett.* **103**, 053001 (2009).
- [74] Y. Huismans, A. Rouzée, A. Gijsbertsen et al., "Time-Resolved Holography with Photoelectrons," *Science* **331**, 61 (2011).
- [75] P. A. Korneev, S. V. Popruzhenko, S. P. Goreslavski et al., "Interference Carpets in Above-Threshold Ionization: From the Coulomb-Free to the Coulomb-Dominated Regime," *Phys. Rev. Lett.* **108**, 223601 (2012).
- [76] X. Xie, S. Roither, D. Kartashov et al., "Attosecond Probe of Valence-Electron Wave Packets by Subcycle Sculpted Laser Fields," *Phys. Rev. Lett.* **108**, 193004 (2012).

- [77] T. Brabec, M. Y. Ivanov and P. B. Corkum, "Coulomb focusing in intense field atomic processes," *Phys. Rev. A* **54**, R2551 (1996).
- [78] D. Comtois, D. Zeidler, H. Pépin et al., "Observation of Coulomb focusing in tunnelling ionization of noble gases," *J. Phys. B* **38**, 1923 (2005).
- [79] A. Rudenko, K. Zrost, T. Ergler et al., "Coulomb singularity in the transverse momentum distribution for strong-field single ionization," *J. Phys. B* **38**, L191 (2005).
- [80] L. G. Gouy, "Sur une propriété nouvelle des ondes lumineuses," *C. R. Acad. Sci. Paris* **110**, 1251 (1890).
- [81] R. Moshhammer, J. Ullrich, B. Feuerstein et al., "Rescattering of Ultralow-Energy Electrons for Single Ionization of Ne in the Tunneling Regime," *Phys. Rev. Lett.* **91**, 113002 (2003).
- [82] C. I. Blaga, F. Catoire, P. Colosimo et al., "Strong-field photoionization revisited," *Nat. Phys.* **5**, 335 (2009).
- [83] W. Quan, Z. Lin, M. Wu et al., "Classical Aspects in Above-Threshold Ionization with a Midinfrared Strong Laser Field," *Phys. Rev. Lett.* **103**, 093001 (2009).
- [84] C. Y. Wu, Y. D. Yang, Y. Q. Liu et al., "Characteristic Spectrum of Very Low-Energy Photoelectron from Above-Threshold Ionization in the Tunneling Regime," *Phys. Rev. Lett.* **109**, 043001 (2012).
- [85] C. Liu and K. Z. Hatsagortsyan, "Origin of Unexpected Low Energy Structure in Photoelectron Spectra Induced by Midinfrared Strong Laser Fields," *Phys. Rev. Lett.* **105**, 113003 (2010).
- [86] A. Kästner, U. Saalman and J. M. Rost, "Electron-Energy Bunching in Laser-Driven Soft Recollisions," *Phys. Rev. Lett.* **108**, 033201 (2012).
- [87] G. G. Paulus, W. Becker and H. Walther, "Classical rescattering effects in two-color above-threshold ionization," *Phys. Rev. A* **52**, 4043 (1995).
- [88] M. Kitzler and M. Lezius, "Spatial Control of Recollision Wave Packets with Attosecond Precision," *Phys. Rev. Lett.* **95**, 253001 (2005).
- [89] D. Ray, Z. Chen, S. De et al., "Momentum spectra of electrons rescattered from rare-gas targets following their extraction by one- and two-color femtosecond laser pulses," *Phys. Rev. A* **83**, 013410 (2011).
- [90] X. Xie, S. Roither, S. Gräfe et al., "Probing the influence of the Coulomb field on atomic ionization by sculpted two-color laser fields," *New J. Phys.* **15**, 043050 (2013).
- [91] L. Zhang, X. Xie, S. Roither et al., "Subcycle Control of Electron-Electron Correlation in Double Ionization," *Phys. Rev. Lett.* **112**, 193002 (2014).
- [92] M. Richter, M. Kunitski, M. Schöffler et al., "Streaking Temporal Double-Slit Interference by an Orthogonal Two-Color Laser Field," *Phys. Rev. Lett.* **114**, 143001 (2015).
- [93] D. Würzler, N. Eicke, M. Möller et al., "Velocity map imaging of scattering dynamics in orthogonal two-color fields," *J. Phys. B* **51**, 015001 (2018).
- [94] P. Johnsson, R. López-Martens, S. Kazamias et al., "Attosecond Electron Wave Packet Dynamics in Strong Laser Fields," *Phys. Rev. Lett.* **95**, 013001 (2005).
- [95] P. Johnsson, J. Mauritsson, T. Remetter et al., "Attosecond Control of Ionization by Wave-Packet Interference," *Phys. Rev. Lett.* **99**, 233001 (2007).
- [96] J. Mauritsson, P. Johnsson, E. Mansten et al., "Coherent Electron Scattering Captured by an Attosecond Quantum Stroboscope," *Phys. Rev. Lett.* **100**, 073003 (2008).

- [97] P. Ranitovic, X. M. Tong, B. Gramkow et al., "IR-assisted ionization of helium by attosecond extreme ultraviolet radiation," *New J. Phys.* **12**, 013008 (2010).
- [98] J. Mauritsson, T. Remetter, M. Swoboda et al., "Attosecond Electron Spectroscopy Using a Novel Interferometric Pump-Probe Technique," *Phys. Rev. Lett.* **105**, 053001 (2010).
- [99] M.-H. Xu, L.-Y. Peng, Z. Zhang et al., "Attosecond Streaking in the Low-Energy Region as a Probe of Rescattering," *Phys. Rev. Lett.* **107**, 183001 (2011).
- [100] M. Kübel, Z. Dube, A. Y. Naumov et al., "Streak Camera for Strong-Field Ionization," *Phys. Rev. Lett.* **119**, 183201 (2017).
- [101] C. Raman, C. W. S. Conover, C. I. Sukenik et al., "Ionization of Rydberg Wave Packets by Subpicosecond, Half-Cycle Electromagnetic Pulses," *Phys. Rev. Lett.* **76**, 2436–2439 (1996).
- [102] R. R. Jones, "Creating and Probing Electronic Wave Packets Using Half-Cycle Pulses," *Phys. Rev. Lett.* **76**, 3927–3930 (1996).
- [103] T. J. Bensity, M. B. Campbell and R. R. Jones, "Half-Cycle Pulse Assisted Electron-Ion Recombination," *Phys. Rev. Lett.* **81**, 3112–3115 (1998).
- [104] R. R. Jones, D. You and P. H. Bucksbaum, "Ionization of Rydberg atoms by subpicosecond half-cycle electromagnetic pulses," *Phys. Rev. Lett.* **70**, 1236–1239 (1993).
- [105] S. Li and R. R. Jones, "Ionization of Excited Atoms by Intense Single-Cycle THz Pulses," *Phys. Rev. Lett.* **112**, 143006 (2014).
- [106] L. V. Keldysh, "Ionization in the Field of a Strong Electromagnetic Wave," *Sov. Phys. JETP* **20**, 1307 (1965).
- [107] F. H. M. Faisal, "Collision of electrons with laser photons in a background potential," *J. Phys. B* **6**, L312 (1973).
- [108] H. R. Reiss, "Effect of an intense electromagnetic field on a weakly bound system," *Phys. Rev. A* **22**, 1786 (1980).
- [109] M. Lewenstein, P. Balcou, M. Y. Ivanov et al., "Theory of high-harmonic generation by low-frequency laser fields," *Phys. Rev. A* **49**, 2117 (1994).
- [110] P. Salières, B. Carré, L. L. Déroff et al., "Feynman's Path-Integral Approach for Intense-Laser-Atom Interactions," *Science* **292**, 902 (2001).
- [111] D. B. Milošević, G. G. Paulus, D. Bauer et al., "Above-threshold ionization by few-cycle pulses," *J. Phys. B* **39**, R203 (2006).
- [112] O. Smirnova and M. Ivanov, "Multielectron high harmonic generation: Simple man on a complex plane," in *Attosecond and XUV Physics* (John Wiley & Sons, Ltd, 2014) Chap. 7, pp. 201–256.
- [113] L. Torlina and O. Smirnova, "Time-dependent analytical R-matrix approach for strong-field dynamics. I. one-electron systems," *Phys. Rev. A* **86**, 043408 (2012).
- [114] J. Kaushal and O. Smirnova, "Nonadiabatic Coulomb effects in strong-field ionization in circularly polarized laser fields," *Phys. Rev. A* **88**, 013421 (2013).
- [115] M. V. Berry and K. E. Mount, "Semiclassical approximations in wave mechanics," *Rep. Prog. Phys.* **35**, 315 (1972).
- [116] S. V. Popruzhenko, G. G. Paulus and D. Bauer, "Coulomb-corrected quantum trajectories in strong-field ionization," *Phys. Rev. A* **77**, 053409 (2008).

- [117] S. V. Popruzhenko and D. Bauer, "Strong field approximation for systems with Coulomb interaction," *J. Mod. Opt.* **55**, 2573 (2008).
- [118] T.-M. Yan, S. V. Popruzhenko, M. J. J. Vrakking et al., "Low-Energy Structures in Strong Field Ionization Revealed by Quantum Orbits," *Phys. Rev. Lett.* **105**, 253002 (2010).
- [119] T.-M. Yan and D. Bauer, "Sub-barrier Coulomb effects on the interference pattern in tunneling-ionization photoelectron spectra," *Phys. Rev. A* **86**, 053403 (2012).
- [120] M. Li, J.-W. Geng, H. Liu et al., "Classical-Quantum Correspondence for Above-Threshold Ionization," *Phys. Rev. Lett.* **112**, 113002 (2014).
- [121] X.-Y. Lai, C. Poli, H. Schomerus et al., "Influence of the Coulomb potential on above-threshold ionization: A quantum-orbit analysis beyond the strong-field approximation," *Phys. Rev. A* **92**, 043407 (2015).
- [122] N. I. Shvetsov-Shilovski, M. Lein, L. B. Madsen et al., "Semiclassical two-step model for strong-field ionization," *Phys. Rev. A* **94**, 013415 (2016).
- [123] M. Lein, "Attosecond Probing of Vibrational Dynamics with High-Harmonic Generation," *Phys. Rev. Lett.* **94**, 053004 (2005).
- [124] P. Wustelt, F. Oppermann, L. Yue et al., "Heteronuclear Limit of Strong-Field Ionization: Fragmentation of HeH^+ by Intense Ultrashort Laser Pulses," *Phys. Rev. Lett.* **121**, 073203 (2018).
- [125] A. D. Shiner, B. E. Schmidt, C. Trallero-Herrero et al., "Probing collective multi-electron dynamics in xenon with high-harmonic spectroscopy," *Nat. Phys.* **7**, 464–467 (2011).
- [126] V. P. Majety and A. Scrinzi, "Dynamic Exchange in the Strong Field Ionization of Molecules," *Phys. Rev. Lett.* **115**, 103002 (2015).
- [127] F. Wilken and D. Bauer, "Adiabatic Approximation of the Correlation Function in the Density-Functional Treatment of Ionization Processes," *Phys. Rev. Lett.* **97**, 203001 (2006).
- [128] F. Wilken and D. Bauer, "Momentum distributions in time-dependent density-functional theory: Product-phase approximation for nonsequential double ionization in strong laser fields," *Phys. Rev. A* **76**, 023409 (2007).
- [129] L. Greenman, P. J. Ho, S. Pabst et al., "Implementation of the time-dependent configuration-interaction singles method for atomic strong-field processes," *Phys. Rev. A* **82**, 023406 (2010).
- [130] D. Hochstuhl and M. Bonitz, "Time-dependent restricted-active-space configuration-interaction method for the photoionization of many-electron atoms," *Phys. Rev. A* **86**, 053424 (2012).
- [131] H. Miyagi and L. B. Madsen, "Time-dependent restricted-active-space self-consistent-field theory for laser-driven many-electron dynamics," *Phys. Rev. A* **87**, 062511 (2013).
- [132] S. Bauch, L. K. Sørensen and L. B. Madsen, "Time-dependent generalized-active-space configuration-interaction approach to photoionization dynamics of atoms and molecules," *Phys. Rev. A* **90**, 062508 (2014).
- [133] V. P. Majety, A. Zielinski and A. Scrinzi, "Photoionization of few electron systems: A hybrid coupled channels approach," *New J. Phys.* **17**, 063002 (2015).
- [134] A. H. Compton, "A quantum theory of the scattering of X-rays by light elements," *Phys. Rev.* **21**, 483–502 (1923).
- [135] J. H. Poynting, "Radiation in the solar system: Its effect on temperature and its pressure on small bodies," *Proc. R. Soc. Lond.* **72**, 265–266 (1904).

- [136] H. P. Robertson and H. N. Russell, "Dynamical Effects of Radiation in the Solar System," *Mon. Not. R. Astron. Soc.* **97**, 423–437 (1937).
- [137] T. Esirkepov, M. Borghesi, S. V. Bulanov et al., "Highly Efficient Relativistic-Ion Generation in the Laser-Piston Regime," *Phys. Rev. Lett.* **92**, 175003 (2004).
- [138] A. Ashkin, "Acceleration and Trapping of Particles by Radiation Pressure," *Phys. Rev. Lett.* **24**, 156–159 (1970).
- [139] A. Ashkin and J. M. Dziedzic, "Optical trapping and manipulation of viruses and bacteria," *Science* **235**, 1517–1520 (1987).
- [140] D. J. Wineland, R. E. Drullinger and F. L. Walls, "Radiation-Pressure Cooling of Bound Resonant Absorbers," *Phys. Rev. Lett.* **40**, 1639–1642 (1978).
- [141] A. Aspect, E. Arimondo, R. Kaiser et al., "Laser Cooling below the One-Photon Recoil Energy by Velocity-Selective Coherent Population Trapping," *Phys. Rev. Lett.* **61**, 826–829 (1988).
- [142] W. D. Phillips, "Nobel lecture: Laser cooling and trapping of neutral atoms," *Rev. Mod. Phys.* **70**, 721–741 (1998).
- [143] S. Gigan, H. R. Böhm, M. Paternostro et al., "Self-cooling of a micromirror by radiation pressure," *Nature* **444**, 67–70 (2006).
- [144] H. R. Reiss, "Limits on Tunneling Theories of Strong-Field Ionization," *Phys. Rev. Lett.* **101**, 043002 (2008).
- [145] H. R. Reiss, "The tunnelling model of laser-induced ionization and its failure at low frequencies," *J. Phys. B* **47**, 204006 (2014).
- [146] C. T. L. Smeenk, L. Arissian, B. Zhou et al., "Partitioning of the Linear Photon Momentum in Multiphoton Ionization," *Phys. Rev. Lett.* **106**, 193002 (2011).
- [147] H. R. Reiss, "Relativistic strong-field photoionization," *J. Opt. Soc. Am. B* **7**, 574–586 (1990).
- [148] A. S. Titi and G. W. F. Drake, "Quantum theory of longitudinal momentum transfer in above-threshold ionization," *Phys. Rev. A* **85**, 041404 (2012).
- [149] H. R. Reiss, "Relativistic effects in nonrelativistic ionization," *Phys. Rev. A* **87**, 033421 (2013).
- [150] S. Chelkowski, A. D. Bandrauk and P. B. Corkum, "Photon Momentum Sharing between an Electron and an Ion in Photoionization: From One-Photon (Photoelectric Effect) to Multiphoton Absorption," *Phys. Rev. Lett.* **113**, 263005 (2014).
- [151] M. Klaiber, E. Yakaboylu, H. Bauke et al., "Under-the-Barrier Dynamics in Laser-Induced Relativistic Tunneling," *Phys. Rev. Lett.* **110**, 153004 (2013).
- [152] A. Ludwig, J. Maurer, B. W. Mayer et al., "Breakdown of the Dipole Approximation in Strong-Field Ionization," *Phys. Rev. Lett.* **113**, 243001 (2014).
- [153] S. Chelkowski, A. Bandrauk and P. Corkum, "Photon-momentum transfer in multiphoton ionization and in time-resolved holography with photoelectrons," *Phys. Rev. A* **92**, 051401 (2015).
- [154] I. A. Ivanov, J. Dubau and K. T. Kim, "Nondipole effects in strong-field ionization," *Phys. Rev. A* **94**, 033405 (2016).
- [155] J. F. Tao, Q. Z. Xia, J. Cai et al., "Coulomb rescattering in nondipole interaction of atoms with intense laser fields," *Phys. Rev. A* **95**, 011402 (2017).

- [156] T. Keil and D. Bauer, "Coulomb-corrected strong-field quantum trajectories beyond dipole approximation," *J. Phys. B* **50**, 194002 (2017).
- [157] J. Maurer, B. Willenberg, J. Daněk et al., "Probing the ionization wave packet and recollision dynamics with an elliptically polarized strong laser field in the nondipole regime," *Phys. Rev. A* **97**, 013404 (2018).
- [158] Q. Z. Xia, J. F. Tao, J. Cai et al., "Quantum Interference of Glory Rescattering in Strong-Field Atomic Ionization," *Phys. Rev. Lett.* **121**, 143201 (2018).
- [159] J. Henkel, *Phenomena in Strong-Field Interaction with Atoms and Molecules* (Verlag Dr. Hut, Munich, 2015).
- [160] S. Brennecke, *Quantum Dynamics of Atoms in Strong Fields with Tailored Polarization* (Leibniz University, Hanover, 2018).
- [161] N. Eicke, *Momentum distributions from bichromatic ionization of atoms and molecules* (Leibniz University, Hanover, 2020).
- [162] S. V. Popruzhenko, "Keldysh theory of strong field ionization: History, applications, difficulties and perspectives," *J. Phys. B* **47**, 204001 (2014).
- [163] M. Klaiber, K. Z. Hatsagortsyan and C. H. Keitel, "Tunneling Dynamics in Multiphoton Ionization and Attoclock Calibration," *Phys. Rev. Lett.* **114**, 083001 (2015).
- [164] M. Klaiber and J. S. Briggs, "Crossover from tunneling to multiphoton ionization of atoms," *Phys. Rev. A* **94**, 053405 (2016).
- [165] A. M. Perelomov, V. S. Popov and M. V. Terent'ev, "Ionization of Atoms in an Alternating Electric Field," *Sov. Phys. JETP* **23**, 924 (1966).
- [166] A. M. Perelomov, V. S. Popov and M. V. Terent'ev, "Ionization of Atoms in an Alternating Electric Field: II," *Sov. Phys. JETP* **24**, 207 (1967).
- [167] M. V. Ammosov, N. B. Delone and V. P. Krainov, "Tunnel ionization of complex atoms and of atomic ions in an alternating electromagnetic field," *Sov. Phys. JETP* **64**, 1191 (1986).
- [168] N. B. Delone and V. P. Krainov, "Energy and angular electron spectra for the tunnel ionization of atoms by strong low-frequency radiation," *J. Opt. Soc. Am. B* **8**, 1207–1211 (1991).
- [169] S. Augst, D. D. Meyerhofer, D. Strickland et al., "Laser ionization of noble gases by coulomb-barrier suppression," *J. Opt. Soc. Am. B* **8**, 858–867 (1991).
- [170] S. Eckart, K. Fehre, N. Eicke et al., "Direct Experimental Access to the Nonadiabatic Initial Momentum Offset upon Tunnel Ionization," *Phys. Rev. Lett.* **121**, 163202 (2018).
- [171] A. Szöke, "Interpretation of electron spectra obtained from multiphoton ionisation of atoms in strong fields," *J. Phys. B* **18**, L427–L432 (1985).
- [172] R. R. Freeman, P. H. Bucksbaum, H. Milchberg et al., "Above-Threshold Ionization With Subpicosecond Laser Pulses," *Phys. Rev. Lett.* **59**, 1092–1095 (1987).
- [173] P. H. Bucksbaum, R. R. Freeman, M. Bashkansky et al., "Role of the ponderomotive potential in above-threshold ionization," *J. Opt. Soc. Am. B* **4**, 760–764 (1987).
- [174] J. W. Cooper, "Photoelectron-angular-distribution parameters for rare-gas subshells," *Phys. Rev. A* **47**, 1841–1851 (1993).
- [175] A. Sommerfeld and G. Schur, "Über den Photoeffekt in der K-Schale der Atome, insbesondere über die Voreilung der Photoelektronen," *Ann. Phys.* **396**, 409–432 (1930).

- [176] S. Grundmann, M. Kircher, I. Vela-Perez et al., "Observation of Photoion Backward Emission in Photoionization of He and N₂," *Phys. Rev. Lett.* **124**, 233201 (2020).
- [177] J. N. Bardsley, B. M. Penetrante and M. H. Mittleman, "Relativistic dynamics of electrons in intense laser fields," *Phys. Rev. A* **40**, 3823–3835 (1989).
- [178] A. Di Piazza, C. Müller, K. Z. Hatsagortsyan et al., "Extremely high-intensity laser interactions with fundamental quantum systems," *Rev. Mod. Phys.* **84**, 1177–1228 (2012).
- [179] A. Staudte, D. Pavičić, S. Chelkowski et al., "Attosecond Strobing of Two-Surface Population Dynamics in Dissociating H₂⁺," *Phys. Rev. Lett.* **98**, 073003 (2007).
- [180] E. S. Smyth, J. S. Parker and K. Taylor, "Numerical integration of the time-dependent Schrödinger equation for laser-driven helium," *Comput. Phys. Commun.* **114**, 1–14 (1998).
- [181] A. Zielinski, V. P. Majety and A. Scrinzi, "Double photoelectron momentum spectra of helium at infrared wavelength," *Phys. Rev. A* **93**, 023406 (2016).
- [182] V. P. Majety and A. Scrinzi, "Absence of electron correlation effects in the Helium attoclock setting," *J. Mod. Opt.* **64**, 1026 (2017).
- [183] D. Bauer, "Two-dimensional, two-electron model atom in a laser pulse: Exact treatment, single-active-electron analysis, time-dependent density-functional theory, classical calculations, and non-sequential ionization," *Phys. Rev. A* **56**, 3028 (1997).
- [184] C. Yu and L. B. Madsen, "Above-threshold ionization of helium in the long-wavelength regime: Examining the single-active-electron approximation and the two-electron strong-field approximation," *Phys. Rev. A* **95**, 063407 (2017).
- [185] D. Cricchio, E. Fiordilino and K. Z. Hatsagortsyan, "Momentum partition between constituents of exotic atoms during laser-induced tunneling ionization," *Phys. Rev. A* **92**, 023408 (2015).
- [186] N. J. Kylstra, R. M. Potvliege and C. J. Joachain, "Photon emission by ions interacting with short intense laser pulses: Beyond the dipole approximation," *J. Phys. B* **34**, L55 (2001).
- [187] S. Brennecke and M. Lein, "High-order above-threshold ionization beyond the electric dipole approximation," *J. Phys. B* **51**, 094005 (2018).
- [188] M. D. Feit and J. A. Fleck Jr., "Solution of the Schrödinger equation by a spectral method ii: Vibrational energy levels of triatomic molecules," *J. Chem. Phys.* **78**, 301–308 (1983).
- [189] M. W. Walser, C. H. Keitel, A. Scrinzi et al., "High Harmonic Generation Beyond the Electric Dipole Approximation," *Phys. Rev. Lett.* **85**, 5082–5085 (2000).
- [190] P.-L. He, D. Lao and F. He, "Strong Field Theories beyond Dipole Approximations in Nonrelativistic Regimes," *Phys. Rev. Lett.* **118**, 163203 (2017).
- [191] M. Y. Ivanov, M. Spanner and O. Smirnova, "Anatomy of strong field ionization," *J. Mod. Opt.* **52**, 165 (2005).
- [192] M. Klaiber, K. Hatsagortsyan and C. Keitel, "Above-threshold ionization beyond the dipole approximation," *Phys. Rev. A* **71**, 033408 (2005).
- [193] L. B. Madsen, "Gauge invariance in the interaction between atoms and few-cycle laser pulses," *Phys. Rev. A* **65**, 053417 (2002).
- [194] G. F. Gribakin and M. Y. Kuchiev, "Multiphoton detachment of electrons from negative ions," *Phys. Rev. A* **55**, 3760 (1997).

- [195] D. Bauer, D. B. Milošević and W. Becker, “Strong-field approximation for intense-laser–atom processes: The choice of gauge,” *Phys. Rev. A* **72**, 023415 (2005).
- [196] T. K. Kjeldsen and L. B. Madsen, “Strong-field ionization of N_2 : Length and velocity gauge strong-field approximation and tunnelling theory,” *J. Phys. B* **37**, 2033–2044 (2004).
- [197] A. Lohr, M. Kleber, R. Kopold et al., “Above-threshold ionization in the tunneling regime,” *Phys. Rev. A* **55**, R4003 (1997).
- [198] A. Galstyan, O. Chuluunbaatar, A. Hamido et al., “Reformulation of the strong-field approximation for light-matter interactions,” *Phys. Rev. A* **93**, 023422 (2016).
- [199] W. Becker, F. Grasbon, R. Kopold et al., “Above-Threshold Ionization: From Classical Features to Quantum Effects,” *Adv. At. Mol. Opt.* **48**, 35 (2002).
- [200] R. Kopold, *Atomare Ionisationsdynamik in starken Laserfeldern* (Technische Universität München, Munich, 2001).
- [201] I. Petersen, *Photoelectron Momentum Distributions from Recollision-Free Strong-Field Ionization of Atoms and Molecules* (Verlag Dr. Hut, Munich, 2014).
- [202] R. Kopold, D. B. Milošević and W. Becker, “Rescattering Processes for Elliptical Polarization: A Quantum Trajectory Analysis,” *Phys. Rev. Lett.* **84**, 3831–3834 (2000).
- [203] G. G. Paulus, F. Zacher, H. Walther et al., “Above-Threshold Ionization by an Elliptically Polarized Field: Quantum Tunneling Interferences and Classical Dodging,” *Phys. Rev. Lett.* **80**, 484–487 (1998).
- [204] C. Figueira de Morisson Faria, H. Schomerus and W. Becker, “High-order above-threshold ionization: The uniform approximation and the effect of the binding potential,” *Phys. Rev. A* **66**, 043413 (2002).
- [205] T. Keil, S. V. Popruzhenko and D. Bauer, “Laser-Driven Recollisions under the Coulomb Barrier,” *Phys. Rev. Lett.* **117**, 243003 (2016).
- [206] E. Pisanty and M. Ivanov, “Slalom in complex time: Emergence of low-energy structures in tunnel ionization via complex-time contours,” *Phys. Rev. A* **93**, 043408 (2016).
- [207] A. S. Maxwell, S. V. Popruzhenko and C. F. de M. Faria, “Treating branch cuts in quantum trajectory models for photoelectron holography,” *Phys. Rev. A* **98**, 063423 (2018).
- [208] C. F. de Morisson Faria and A. S. Maxwell, “It is all about phases: Ultrafast holographic photoelectron imaging,” *Rep. Prog. Phys.* **83**, 034401 (2020).
- [209] S. P. Goreslavskii and S. V. Popruzhenko, “Differential photoelectron distributions in a strong elliptically polarized low-frequency laser field,” *J. Exp. Theor. Phys.* **83**, 661–669 (1996).
- [210] S. P. Goreslavski, G. G. Paulus, S. V. Popruzhenko et al., “Coulomb Asymmetry in Above-Threshold Ionization,” *Phys. Rev. Lett.* **93**, 233002 (2004).
- [211] H. Ni, N. Eicke, C. Ruiz et al., “Tunneling criteria and a nonadiabatic term for strong-field ionization,” *Phys. Rev. A* **98**, 013411 (2018).
- [212] L. Torlina, F. Morales, H. G. Muller et al., “Ab initio verification of the analytical R-matrix theory for strong field ionization,” *J. Phys. B* **47**, 204021 (2014).
- [213] L. Torlina, F. Morales, J. Kaushal et al., “Interpreting attoclock measurements of tunnelling times,” *Nat. Phys.* **11**, 503 (2015).

- [214] O. Smirnova, M. Spanner and M. Ivanov, "Coulomb and polarization effects in sub-cycle dynamics of strong-field ionization," *J. Phys. B* **39**, S307 (2006).
- [215] O. Smirnova, M. Spanner and M. Ivanov, "Analytical solutions for strong field-driven atomic and molecular one- and two-electron continua and applications to strong-field problems," *Phys. Rev. A* **77**, 033407 (2008).
- [216] F. Gittes and C. F. Schmidt, "Interference model for back-focal-plane displacement detection in optical tweezers," *Opt. Lett.* **23**, 7–9 (1998).
- [217] A. B. Ruffin, J. V. Rudd, J. F. Whitaker et al., "Direct Observation of the Gouy Phase Shift with Single-Cycle Terahertz Pulses," *Phys. Rev. Lett.* **83**, 3410–3413 (1999).
- [218] F. Lindner, G. G. Paulus, H. Walther et al., "Gouy Phase Shift for Few-Cycle Laser Pulses," *Phys. Rev. Lett.* **92**, 113001 (2004).
- [219] P. Balcou, P. Salières, A. L'Huillier et al., "Generalized phase-matching conditions for high harmonics: The role of field-gradient forces," *Phys. Rev. A* **55**, 3204–3210 (1997).
- [220] N. C. R. Holme, B. C. Daly, M. T. Myaing et al., "Gouy phase shift of single-cycle picosecond acoustic pulses," *Appl. Phys. Lett.* **83**, 392–394 (2003).
- [221] C. R. Carpenter, "Gouy phase advance with microwaves," *Am. J. Phys.* **27**, 98–100 (1959).
- [222] T. Feurer, N. S. Stoyanov, D. W. Ward et al., "Direct Visualization of the Gouy Phase by Focusing Phonon Polaritons," *Phys. Rev. Lett.* **88**, 257402 (2002).
- [223] I. G. da Paz, P. L. Saldanha, M. C. Nemes et al., "Experimental proposal for measuring the Gouy phase of matter waves," *New J. Phys.* **13**, 125005 (2011).
- [224] G. Guzzinati, P. Schattschneider, K. Y. Bliokh et al., "Observation of the Larmor and Gouy Rotations with Electron Vortex Beams," *Phys. Rev. Lett.* **110**, 093601 (2013).
- [225] T. C. Petersen, D. M. Paganin, M. Weyland et al., "Measurement of the Gouy phase anomaly for electron waves," *Phys. Rev. A* **88**, 043803 (2013).
- [226] R. W. Boyd, "Intuitive explanation of the phase anomaly of focused light beams," *J. Opt. Soc. Am.* **70**, 877–880 (1980).
- [227] P. Hariharan and P. A. Robinson, "The Gouy phase shift as a geometrical quantum effect," *J. Mod. Opt.* **43**, 219–221 (1996).
- [228] S. Feng and H. G. Winful, "Physical origin of the Gouy phase shift," *Opt. Lett.* **26**, 485–487 (2001).
- [229] R. G. Littlejohn, "The Van Vleck Formula, Maslov Theory, and Phase Space Geometry," *J. Stat. Phys.* **68**, 7–50 (1992).
- [230] K. Takatsuka, "Dynamics and quantization of Hamiltonian chaos: Density of states in phase-space semiclassical mechanics," *Phys. Rev. A* **45**, 4326–4339 (1992).
- [231] S. Takahashi and K. Takatsuka, "Geometrical evaluation of the Maslov index," *Phys. Rev. A* **69**, 022110 (2004).
- [232] R. W. McGowan, R. A. Cheville and D. Grischkowsky, "Direct observation of the Gouy phase shift in THz impulse ranging," *Appl. Phys. Lett.* **76**, 670–672 (2000).
- [233] D. G. Arbó, K. L. Ishikawa, K. Schiessl et al., "Intracycle and intercycle interferences in above-threshold ionization: The time grating," *Phys. Rev. A* **81**, 021403 (2010).

- [234] Y. Huismans, A. Gijbetsen, A. S. Smolkowska et al., “Scaling Laws for Photoelectron Holography in the Midinfrared Wavelength Regime,” *Phys. Rev. Lett.* **109**, 013002 (2012).
- [235] D. D. Hickstein, P. Ranitovic, S. Witte et al., “Direct Visualization of Laser-Driven Electron Multiple Scattering and Tunneling Distance in Strong-Field Ionization,” *Phys. Rev. Lett.* **109**, 073004 (2012).
- [236] M. Möller, F. Meyer, A. M. Saylor et al., “Off-axis low-energy structures in above-threshold ionization,” *Phys. Rev. A* **90**, 023412 (2014).
- [237] A. S. Maxwell, C. F. d. M. Faria, X. Lai et al., “Spiral-like holographic structures: Unwinding interference carpets of Coulomb-distorted orbits in strong-field ionization,” *Phys. Rev. A* **102**, 033111 (2020).
- [238] D. Gabor, *Nobel Lectures, Physics* (World Scientific, Singapore, 1992) pp. 1971–1980.
- [239] X.-B. Bian, Y. Huismans, O. Smirnova et al., “Subcycle interference dynamics of time-resolved photoelectron holography with midinfrared laser pulses,” *Phys. Rev. A* **84**, 043420 (2011).
- [240] M.-M. Liu, M. Li, C. Wu et al., “Phase Structure of Strong-Field Tunneling Wave Packets from Molecules,” *Phys. Rev. Lett.* **116**, 163004 (2016).
- [241] H. Kang, A. S. Maxwell, D. Trabert et al., “Holographic detection of parity in atomic and molecular orbitals,” *Phys. Rev. A* **102**, 013109 (2020).
- [242] M. Li, H. Xie, W. Cao et al., “Photoelectron Holographic Interferometry to Probe the Longitudinal Momentum Offset at the Tunnel Exit,” *Phys. Rev. Lett.* **122**, 183202 (2019).
- [243] D. G. Arbó, S. Yoshida, E. Persson et al., “Interference Oscillations in the Angular Distribution of Laser-Ionized Electrons near Ionization Threshold,” *Phys. Rev. Lett.* **96**, 143003 (2006).
- [244] S. D. López and D. G. Arbó, “Holographic interference in atomic photoionization from a semiclassical standpoint,” *Phys. Rev. A* **100**, 023419 (2019).
- [245] S. Brennecke and M. Lein, “Strong-field photoelectron holography beyond the electric dipole approximation: A semiclassical analysis,” *Phys. Rev. A* **100**, 023413 (2019).
- [246] S. Levit and U. Smilansky, “The Hamiltonian path integrals and the uniform semiclassical approximations for the propagator,” *Ann. Phys.* **108**, 165 – 197 (1977).
- [247] S. Levit, K. Möhring, U. Smilansky et al., “Focal points and the phase of the semiclassical propagator,” *Ann. Phys.* **114**, 223 – 242 (1978).
- [248] S. Brennecke, N. Eicke and M. Lein, “Gouy’s Phase Anomaly in Electron Waves Produced by Strong-Field Ionization,” *Phys. Rev. Lett.* **124**, 153202 (2020).
- [249] G. G. Paulus, F. Grasbon, H. Walther et al., “Absolute-phase phenomena in photoionization with few-cycle laser pulses,” *Nature* **414**, 182 (2001).
- [250] A. Baltuška, T. Udem, M. Uiberacker et al., “Attosecond control of electronic processes by intense light fields,” *Nature* **421**, 611 (2003).
- [251] G. G. Paulus, F. Lindner, H. Walther et al., “Measurement of the Phase of Few-Cycle Laser Pulses,” *Phys. Rev. Lett.* **91**, 253004 (2003).
- [252] H. Geiseler, N. Ishii, K. Kaneshima et al., “High-energy half-cycle cutoffs in high harmonic and rescattered electron spectra using waveform-controlled few-cycle infrared pulses,” *J. Phys. B* **47**, 204011 (2014).
- [253] M. W. Walser and T. Brabec, “Semiclassical path integral theory of strong-laser-field physics,” *J. Phys. B* **36**, 3025–3030 (2003).

- [254] M. Spanner, "Strong Field Tunnel Ionization by Real-Valued Classical Trajectories," *Phys. Rev. Lett.* **90**, 233005 (2003).
- [255] F. Grossmann, *Theoretical Femtosecond Physics*, Springer Series on Atomic, Optical, and Plasma Physics (Springer Berlin Heidelberg, Berlin, Heidelberg, 2008).
- [256] H. Kleinert, *Path Integrals in Quantum Mechanics, Statistics, Polymer Physics, and Financial Markets*, EBL-Schweitzer (World Scientific, 2009).
- [257] K. G. Kay, "Semiclassical propagation for multidimensional systems by an initial value method," *J. Chem. Phys.* **101**, 2250–2260 (1994).
- [258] M. Morse, *Variational Analysis*, New York (Wiley, 1973).
- [259] A. M. Perelomov and V. S. Popov, "Ionization of Atoms in an Alternating Electric Field: III," *Sov. Phys. JETP* **25**, 336 (1967).
- [260] C. Z. Bisgaard and L. B. Madsen, "Tunneling ionization of atoms," *Am. J. Phys.* **72**, 249 (2004).
- [261] V. S. Popov, "Tunnel and multiphoton ionization of atoms and ions in a strong laser field (Keldysh theory)," *Phys.-Uspekhi* **47**, 855 (2004).
- [262] A. S. Landsman and U. Keller, "Attosecond science and the tunnelling time problem," *Phys. Rep.* **547**, 1 (2015).
- [263] G. Dangelmayr and W. Veit, "Semiclassical approximation of path integrals on and near caustics in terms of catastrophes," *Ann. Phys.* **118**, 108 – 138 (1979).
- [264] A. S. Maxwell, A. Al-Jawahiry, T. Das et al., "Coulomb-corrected quantum interference in above-threshold ionization: Working towards multitrajectory electron holography," *Phys. Rev. A* **96**, 023420 (2017).
- [265] A. S. Maxwell, A. Al-Jawahiry, X. Y. Lai et al., "Analytic quantum-interference conditions in Coulomb corrected photoelectron holography," *J. Phys. B* **51**, 044004 (2018).
- [266] L. Zhang, X. Xie, S. Roither et al., "Laser-sub-cycle two-dimensional electron-momentum mapping using orthogonal two-color fields," *Phys. Rev. A* **90**, 061401 (2014).
- [267] H. Eichmann, A. Egbert, S. Nolte et al., "Polarization-dependent high-order two-color mixing," *Phys. Rev. A* **51**, R3414 (1995).
- [268] A. Fleischer, O. Kfir, T. Diskin et al., "Spin angular momentum and tunable polarization in high-harmonic generation," *Nat. Photonics* **8**, 543 (2014).
- [269] O. Kfir, P. Grychtol, E. Turgut et al., "Generation of bright phase-matched circularly-polarized extreme ultraviolet high harmonics," *Nat. Photonics* **9**, 99 (2015).
- [270] D. Baykusheva, S. Brennecke, M. Lein et al., "Signatures of Electronic Structure in Bicircular High-Harmonic Spectroscopy," *Phys. Rev. Lett.* **119**, 203201 (2017).
- [271] C. A. Mancuso, D. D. Hickstein, P. Grychtol et al., "Strong-field ionization with two-color circularly polarized laser fields," *Phys. Rev. A* **91**, 031402 (2015).
- [272] E. Hasović, W. Becker and D. B. Milošević, "Electron rescattering in a bicircular laser field," *Opt. Express* **24**, 6413 (2016).
- [273] D. B. Milošević and W. Becker, "Improved strong-field approximation and quantum-orbit theory: Application to ionization by a bicircular laser field," *Phys. Rev. A* **93**, 063418 (2016).

- [274] D. B. Milošević, "Possibility of introducing spin into attoscience with spin-polarized electrons produced by a bichromatic circularly polarized laser field," *Phys. Rev. A* **93**, 051402 (2016).
- [275] C. A. Mancuso, D. D. Hickstein, K. M. Dorney et al., "Controlling electron-ion rescattering in two-color circularly polarized femtosecond laser fields," *Phys. Rev. A* **93**, 053406 (2016).
- [276] E. Hasović, W. Becker and D. B. Milošević, "Electron Rescattering in a Bicircular Laser Field," *J. Phys. Conf. Ser.* **826**, 012009 (2017).
- [277] V.-H. Hoang, V.-H. Le, C. D. Lin et al., "Retrieval of target structure information from laser-induced photoelectrons by few-cycle bicircular laser fields," *Phys. Rev. A* **95**, 031402 (2017).
- [278] J. L. Chaloupka and D. D. Hickstein, "Dynamics of Strong-Field Double Ionization in Two-Color Counterrotating Fields," *Phys. Rev. Lett.* **116**, 143005 (2016).
- [279] S. Eckart, M. Richter, M. Kunitski et al., "Nonsequential Double Ionization by Counterrotating Circularly Polarized Two-Color Laser Fields," *Phys. Rev. Lett.* **117**, 133202 (2016).
- [280] C. A. Mancuso, K. M. Dorney, D. D. Hickstein et al., "Controlling Nonsequential Double Ionization in Two-Color Circularly Polarized Femtosecond Laser Fields," *Phys. Rev. Lett.* **117**, 133201 (2016).
- [281] S. Ben, P.-Y. Guo, X.-F. Pan et al., "Recollision induced excitation-ionization with counter-rotating two-color circularly polarized laser field," *Chem. Phys. Lett.* **679**, 38 (2017).
- [282] D. M. Reich and L. B. Madsen, "Illuminating Molecular Symmetries with Bicircular High-Order-Harmonic Generation," *Phys. Rev. Lett.* **117**, 133902 (2016).
- [283] M. Li, W.-C. Jiang, H. Xie et al., "Strong-field photoelectron holography of atoms by bicircular two-color laser pulses," *Phys. Rev. A* **97**, 023415 (2018).
- [284] S. Eckart, M. Kunitski, I. Ivanov et al., "Subcycle interference upon tunnel ionization by counter-rotating two-color fields," *Phys. Rev. A* **97**, 041402 (2018).
- [285] K. G. Kay, "Semiclassical initial value treatments of atoms and molecules," *Annu. Rev. Phys. Chem.* **56**, 255–280 (2005).
- [286] R. Conte, F. Gabas, G. Botti et al., "Semiclassical vibrational spectroscopy with Hessian databases," *J. Chem. Phys.* **150**, 244118 (2019).
- [287] S. Ray, P. Ostmann, L. Simon et al., "Dynamics of interacting bosons using the Herman–Kluk semiclassical initial value representation," *J. Phys. A*, **49**, 165303 (2016).
- [288] N. Werby, A. S. Maxwell, R. Forbes et al., "Dissecting subcycle interference in photoelectron holography," *Phys. Rev. A* **104**, 013109 (2021).
- [289] K. Doblhoff-Dier, K. I. Dimitriou, A. Staudte et al., "Classical analysis of Coulomb effects in strong-field ionization of H_2^+ by intense circularly polarized laser fields," *Phys. Rev. A* **88**, 033411 (2013).
- [290] S. M. Baumann, D. M. Kalb, L. H. MacMillan et al., "Propagation dynamics of optical vortices due to Gouy phase," *Opt. Express* **17**, 9818 (2009).
- [291] O. I. Tolstikhin and T. Morishita, "Strong-field ionization, rescattering, and target structure imaging with vortex electrons," *Phys. Rev. A* **99**, 063415 (2019).
- [292] A. S. Maxwell, G. S. J. Armstrong, M. F. Ciappina et al., "Manipulating twisted electrons in strong-field ionization," *Faraday Discuss.* **228**, 394–412 (2021).
- [293] J. Henkel, T. Witting, D. Fabris et al., "Prediction of attosecond light pulses in the VUV range in a high-order-harmonic-generation regime," *Phys. Rev. A* **87**, 043818 (2013).

- [294] M. Chini, X. Wang, Y. Cheng et al., “Coherent phase-matched VUV generation by field-controlled bound states,” *Nat. Photonics* **8**, 437–441 (2014).
- [295] S. Beaulieu, S. Camp, D. Descamps et al., “Role of Excited States In High-order Harmonic Generation,” *Phys. Rev. Lett.* **117**, 203001 (2016).
- [296] H. Yun, J. H. Mun, S. I. Hwang et al., “Coherent extreme-ultraviolet emission generated through frustrated tunnelling ionization,” *Nat. Photonics* **12**, 620–624 (2018).
- [297] M. P. de Boer and H. G. Muller, “Observation of Large Populations in Excited States After Short-Pulse Multiphoton Ionization,” *Phys. Rev. Lett.* **68**, 2747–2750 (1992).
- [298] R. R. Jones, D. W. Schumacher and P. H. Bucksbaum, “Population trapping in Kr and Xe in intense laser fields,” *Phys. Rev. A* **47**, R49–R52 (1993).
- [299] H. Zimmermann, S. Patchkovskii, M. Ivanov et al., “Unified Time and Frequency Picture of Ultrafast Atomic Excitation in Strong Laser Fields,” *Phys. Rev. Lett.* **118**, 013003 (2017).
- [300] T. Nubbemeyer, K. Gorling, A. Saenz et al., “Strong-Field Tunneling without Ionization,” *Phys. Rev. Lett.* **101**, 233001 (2008).
- [301] N. I. Shvetsov-Shilovski, S. P. Goreslavski, S. V. Popruzhenko et al., “Capture into Rydberg states and momentum distributions of ionized electrons,” *Laser Phys.* **19**, 1550–1558 (2009).
- [302] S. P. Xu, M. Q. Liu, S. L. Hu et al., “Observation of a transition in the dynamics of strong-field atomic excitation,” *Phys. Rev. A* **102**, 043104 (2020).
- [303] N. E. Tielking and R. R. Jones, “Coherent population transfer among Rydberg states by subpicosecond, half-cycle pulses,” *Phys. Rev. A* **52**, 1371–1381 (1995).
- [304] B. C. Yang and F. Robicheaux, “Field-ionization threshold and its induced ionization-window phenomenon for Rydberg atoms in a short single-cycle pulse,” *Phys. Rev. A* **90**, 063413 (2014).
- [305] B. C. Yang and F. Robicheaux, “Field ionization of Rydberg atoms in a single-cycle pulse,” *Phys. Rev. A* **91**, 043407 (2015).
- [306] E. S. Shuman, R. R. Jones and T. F. Gallagher, “Multiphoton Assisted Recombination,” *Phys. Rev. Lett.* **101**, 263001 (2008).
- [307] X. Zhang, R. R. Jones and F. Robicheaux, “Time-Dependent Electron Interactions in Double Rydberg Wave Packets,” *Phys. Rev. Lett.* **110**, 023002 (2013).
- [308] J.-W. Geng, W.-H. Xiong, X.-R. Xiao et al., “Nonadiabatic Electron Dynamics in Orthogonal Two-Color Laser Fields with Comparable Intensities,” *Phys. Rev. Lett.* **115**, 193001 (2015).
- [309] M. Drescher, M. Hentschel, R. Kienberger et al., “X-ray Pulses Approaching the Attosecond Frontier,” *Science* **291**, 1923 (2001).
- [310] E. Goulielmakis, M. Uiberacker, R. Kienberger et al., “Direct Measurement of Light Waves,” *Science* **305**, 1267 (2004).
- [311] L. Chen, C. Huang, X. Zhu et al., “Molecular photoelectron holography by an attosecond XUV pulse in a strong infrared laser field,” *Opt. Express* **22**, 20421–20431 (2014).
- [312] A. K. Kazansky, A. V. Bozhevolnov, I. P. Sazhina et al., “Attosecond near-threshold photoionization in a strong laser field,” *Phys. Rev. A* **90**, 033409 (2014).
- [313] J.-W. Geng, W.-H. Xiong, X.-R. Xiao et al., “Steering continuum electron dynamics by low-energy attosecond streaking,” *Phys. Rev. A* **94**, 023411 (2016).

- [314] X. Yu, M. Li, M. Han et al., "Controlling backward-scattering photoelectron holography by attosecond streaking," *Phys. Rev. A* **98**, 013415 (2018).
- [315] J. Liang, Y. Zhou, J. Tan et al., "Low-energy photoelectron interference structure in attosecond streaking," *Opt. Express* **27**, 37736–37752 (2019).
- [316] M. Mandrysz, M. Kübel, J. Zakrzewski et al., "Rescattering effects in streaking experiments of strong-field ionization," *Phys. Rev. A* **100**, 063410 (2019).
- [317] Q. Liu, A. Piper, D. Kiewewetter et al., "Strong field simulator: Attosecond study of strong field ionization in noble gas atoms," in *The International Conference on Ultrafast Phenomena (UP) 2022* (Optica Publishing Group, 2022).
- [318] G. Gademann, F. Kelkensberg, W. K. Siu et al., "Attosecond control of electron-ion recollision in high harmonic generation," *New J. Phys.* **13**, 033002 (2011).
- [319] D. Azoury, M. Krüger, G. Orenstein et al., "Self-probing spectroscopy of XUV photo-ionization dynamics in atoms subjected to a strong-field environment," *Nat. Commun.* **8**, 1453 (2017).
- [320] M. Ranke, *Investigation of low-energy photoelectron dynamics accelerated in terahertz light fields using a novel Velocity-Map-Imaging spectrometer* (University of Hamburg, Hamburg, 2019).
- [321] M. Ranke, S. Walther, T. Gebert et al., "Velocity map imaging spectrometer with an electric-field-matched gas capillary," *Meas. Sci. Technol.* **32**, 095901 (2021).
- [322] S. Brennecke, M. Ranke, A. Dimitriou et al., "Control of Electron Wave Packets Close to the Continuum Threshold Using Near-Single-Cycle THz Waveforms," *Phys. Rev. Lett.* **129**, 213202 (2022).
- [323] P. Kaminski, R. Wiehle, V. Renard et al., "Wavelength dependence of multiphoton ionization of xenon," *Phys. Rev. A* **70**, 053413 (2004).
- [324] X. M. Tong and C. D. Lin, "Empirical formula for static field ionization rates of atoms and molecules by lasers in the barrier-suppression regime," *J. Phys. B* **38**, 2593 (2005).
- [325] A. E. S. Green, D. L. Sellin and A. S. Zachor, "Analytic Independent-Particle Model for Atoms," *Phys. Rev.* **184**, 1 (1969).
- [326] Q. Zhang, P. Lan and P. Lu, "Empirical formula for over-barrier strong-field ionization," *Phys. Rev. A* **90**, 043410 (2014).
- [327] J. Dura, N. Camus, A. Thai et al., "Ionization with low-frequency fields in the tunneling regime," *Sci. Rep.* **3**, 2675 (2013).
- [328] B. Wolter, C. Lemell, M. Baudisch et al., "Formation of very-low-energy states crossing the ionization threshold of argon atoms in strong mid-infrared fields," *Phys. Rev. A* **90**, 063424 (2014).
- [329] E. Diesen, U. Saalman, M. Richter et al., "Dynamical Characteristics of Rydberg Electrons Released by a Weak Electric Field," *Phys. Rev. Lett.* **116**, 143006 (2016).
- [330] S. Larimian, S. Erattupuzha, C. Lemell et al., "Coincidence spectroscopy of high-lying Rydberg states produced in strong laser fields," *Phys. Rev. A* **94**, 033401 (2016).
- [331] U. Fröhling, M. Wieland, M. Gensch et al., "Single-shot terahertz-field-driven X-ray streak camera," *Nat. Photonics* **3**, 523–528 (2009).
- [332] B. Schütte, U. Fröhling, M. Wieland et al., "Electron wave packet sampling with laser-generated extreme ultraviolet and terahertz fields," *Opt. Express* **19**, 18833–18841 (2011).
- [333] B. Feuerstein and U. Thumm, "On the computation of momentum distributions within wavepacket propagation calculations," *J. Phys. B* **36**, 707 (2003).

- [334] X. Wang, J. Tian and J. H. Eberly, "Extended Virtual Detector Theory for Strong-Field Atomic Ionization," *Phys. Rev. Lett.* **110**, 243001 (2013).
- [335] X. Wang and F. Robicheaux, "Ionization from Rydberg atoms and wave packets by scaled terahertz single-cycle pulses," *Phys. Rev. A* **99**, 033418 (2019).
- [336] C. Bordas, "Classical motion of a photoelectron interacting with its ionic core: Slow photoelectron imaging," *Phys. Rev. A* **58**, 400–410 (1998).
- [337] C. Nicole, I. Sluimer, F. Rosca-Pruna et al., "Slow Photoelectron Imaging," *Phys. Rev. Lett.* **85**, 4024–4027 (2000).
- [338] S. Larimian, C. Lemell, V. Stummer et al., "Localizing high-lying Rydberg wave packets with two-color laser fields," *Phys. Rev. A* **96**, 021403(R) (2017).
- [339] P. Ge and Y. Liu, "Control of the yield of surviving Rydberg atoms in strong-field ionization with two-color laser fields," *J. Phys. B* **50**, 125001 (2017).
- [340] J. Wu, A. Vredenburg, B. Ulrich et al., "Multiple Recapture of Electrons in Multiple Ionization of the Argon Dimer by a Strong Laser Field," *Phys. Rev. Lett.* **107**, 043003 (2011).
- [341] A. von Veltheim, B. Manschwetus, W. Quan et al., "Frustrated Tunnel Ionization of Noble Gas Dimers with Rydberg-Electron Shakeoff by Electron Charge Oscillation," *Phys. Rev. Lett.* **110**, 023001 (2013).
- [342] U. S. Sainadh, H. Xu, X. Wang et al., "Attosecond angular streaking and tunnelling time in atomic hydrogen," *Nature* **568**, 75 (2019).
- [343] H. Xie, M. Li, S. Luo et al., "Energy-dependent angular shifts in the photoelectron momentum distribution for atoms in elliptically polarized laser pulses," *Phys. Rev. A* **96**, 063421 (2017).
- [344] E. Bloch, S. Larroque, S. Rozen et al., "Revealing the influence of molecular chirality on tunnel-ionization dynamics," *Phys. Rev. X* **11**, 041056 (2021).
- [345] C. Wang, X. Li, X. Liu et al., "Decoding electron tunnelling delay time by embracing wave-particle duality," (2021).
- [346] C. P. J. Martiny, M. Abu-samha and L. B. Madsen, "Counterintuitive angular shifts in the photoelectron momentum distribution for atoms in strong few-cycle circularly polarized laser pulses," *J. Phys. B* **42**, 161001 (2009).
- [347] N. I. Shvetsov-Shilovski, D. Dimitrovski and L. B. Madsen, "Ionization in elliptically polarized pulses: Multielectron polarization effects and asymmetry of photoelectron momentum distributions," *Phys. Rev. A* **85**, 023428 (2012).
- [348] I. A. Ivanov and A. S. Kheifets, "Strong-field ionization of He by elliptically polarized light in attoclock configuration," *Phys. Rev. A* **89**, 021402 (2014).
- [349] J. Liu, Y. Fu, W. Chen et al., "Offset angles of photocurrents generated in few-cycle circularly polarized laser fields," *J. Phys. B* **50**, 055602 (2017).
- [350] H. Ni, U. Saalmann and J.-M. Rost, "Tunneling Ionization Time Resolved by Backpropagation," *Phys. Rev. Lett.* **117**, 023002 (2016).
- [351] H. Ni, U. Saalmann and J.-M. Rost, "Tunneling exit characteristics from classical backpropagation of an ionized electron wave packet," *Phys. Rev. A* **97**, 013426 (2018).
- [352] A. W. Bray, S. Eckart and A. S. Kheifets, "Keldysh-Rutherford Model for the Attoclock," *Phys. Rev. Lett.* **121**, 123201 (2018).

- [353] N. Eicke and M. Lein, "Trajectory-free ionization times in strong-field ionization," *Phys. Rev. A* **97**, 031402(R) (2018).
- [354] I. Barth and O. Smirnova, "Nonadiabatic tunneling in circularly polarized laser fields: Physical picture and calculations," *Phys. Rev. A* **84**, 063415 (2011).
- [355] S. Eckart, M. Kunitski, M. Richter et al., "Ultrafast preparation and detection of ring currents in single atoms," *Nat. Phys.* **14**, 701 (2018).
- [356] J. M. Rost and U. Saalmann, "Attoclock and tunnelling time," *Nat. Photonics* **13**, 439 (2019).
- [357] D. Trabert, N. Anders, S. Brennecke et al., "Nonadiabatic Strong Field Ionization of Atomic Hydrogen," *Phys. Rev. Lett.* **127**, 273201 (2021).
- [358] J. Kaushal, F. Morales, L. Torlina et al., "Spin-orbit Larmor clock for ionization times in one-photon and strong-field regimes," *J. Phys. B* **48**, 234002 (2015).
- [359] N. Eicke and M. Lein, "Attoclock with counter-rotating bicircular laser fields," *Phys. Rev. A* **99**, 031402(R) (2019).
- [360] K. Fehre, S. Eckart, M. Kunitski et al., "Angular streaking in strong field ionization of chiral molecules," *Phys. Rev. Res.* **1**, 033045 (2019).
- [361] C. Hofmann, T. Zimmermann, A. Zielinski et al., "Non-adiabatic imprints on the electron wave packet in strong field ionization with circular polarization," *New J. Phys.* **18**, 043011 (2016).
- [362] A. N. Pfeiffer, C. Cirelli, A. S. Landsman et al., "Probing the Longitudinal Momentum Spread of the Electron Wave Packet at the Tunnel Exit," *Phys. Rev. Lett.* **109**, 083002 (2012).
- [363] C. Hofmann, A. S. Landsman, C. Cirelli et al., "Comparison of different approaches to the longitudinal momentum spread after tunnel ionization," *J. Phys. B* **46**, 125601 (2013).
- [364] A. S. Landsman, C. Hofmann, A. N. Pfeiffer et al., "Unified Approach to Probing Coulomb Effects in Tunnel Ionization for Any Ellipticity of Laser Light," *Phys. Rev. Lett.* **111**, 263001 (2013).
- [365] C. Hofmann, A. S. Landsman, A. Zielinski et al., "Interpreting electron-momentum distributions and nonadiabaticity in strong-field ionization," *Phys. Rev. A* **90**, 043406 (2014).
- [366] X. Sun, M. Li, J. Yu et al., "Calibration of the initial longitudinal momentum spread of tunneling ionization," *Phys. Rev. A* **89**, 045402 (2014).
- [367] N. Eicke, S. Brennecke and M. Lein, "Attosecond-Scale Streaking Methods for Strong-Field Ionization by Tailored Fields," *Phys. Rev. Lett.* **124**, 043202 (2020).
- [368] H. A. Bethe and E. E. Salpeter, *Quantum Mechanics of One- and Two-Electron Atoms* (Academic, New York, 1957).
- [369] S. Brennecke, S. Eckart and M. Lein, "Attoclock with bicircular laser fields as a probe of velocity-dependent tunnel-exit positions," *J. Phys. B* **54**, 164001 (2021).
- [370] V. D. Mur, S. V. Popruzhenko and V. S. Popov, "Energy and momentum spectra of photoelectrons under conditions of ionization by strong laser radiation (The case of elliptic polarization)," *Sov. Phys. JETP* **92**, 777 (2001).
- [371] R. Boge, C. Cirelli, A. S. Landsman et al., "Probing Nonadiabatic Effects in Strong-Field Tunnel Ionization," *Phys. Rev. Lett.* **111**, 103003 (2013).
- [372] M. Ohmi, O. I. Tolstikhin and T. Morishita, "Analysis of a shift of the maximum of photoelectron momentum distributions generated by intense circularly polarized pulses," *Phys. Rev. A* **92**, 043402 (2015).

- [373] M. Bashkansky, P. H. Bucksbaum and D. W. Schumacher, "Asymmetries in Above-Threshold Ionization," *Phys. Rev. Lett.* **60**, 2458–2461 (1988).
- [374] P. H. Bucksbaum, L. D. Van Woerkom, R. R. Freeman et al., "Nonresonant above-threshold ionization by circularly polarized subpicosecond pulses," *Phys. Rev. A* **41**, 4119–4122 (1990).
- [375] I. A. Ivanov and A. S. Kheifets, "Time delay in atomic photoionization with circularly polarized light," *Phys. Rev. A* **87**, 033407 (2013).
- [376] E. E. Serebryannikov and A. M. Zheltikov, "Strong-Field Photoionization as Excited-State Tunneling," *Phys. Rev. Lett.* **116**, 123901 (2016).
- [377] D. Trabert, S. Brennecke, K. Fehre et al., "Angular dependence of the Wigner time delay upon tunnel ionization of H₂," *Nat. Commun.* **12**, 1697 (2021).
- [378] I. V. Litvinyuk, K. F. Lee, P. W. Dooley et al., "Alignment-Dependent Strong Field Ionization of Molecules," *Phys. Rev. Lett.* **90**, 233003 (2003).
- [379] D. Pavičić, K. F. Lee, D. M. Rayner et al., "Direct Measurement of the Angular Dependence of Ionization for N₂, O₂, and CO₂ in Intense Laser Fields," *Phys. Rev. Lett.* **98**, 243001 (2007).
- [380] M. Odenweller, N. Takemoto, A. Vredenburg et al., "Strong Field Electron Emission from Fixed in Space H₂⁺ Ions," *Phys. Rev. Lett.* **107**, 143004 (2011).
- [381] H. Akagi, T. Otobe, A. Staudte et al., "Laser tunnel ionization from multiple orbitals in HCl," *Science* **325**, 1364–1367 (2009).
- [382] L. Holmegaard, J. L. Hansen, L. Kalkhøj et al., "Photoelectron angular distributions from strong-field ionization of oriented molecules," *Nat. Phys.* **6**, 428–432 (2010).
- [383] J. L. Hansen, H. Stapelfeldt, D. Dimitrovski et al., "Time-Resolved Photoelectron Angular Distributions from Strong-Field Ionization of Rotating Naphthalene Molecules," *Phys. Rev. Lett.* **106**, 073001 (2011).
- [384] J. L. Hansen, L. Holmegaard, L. Kalkhøj et al., "Ionization of one- and three-dimensionally-oriented asymmetric-top molecules by intense circularly polarized femtosecond laser pulses," *Phys. Rev. A* **83**, 023406 (2011).
- [385] D. Dimitrovski, M. Abu-samha, L. B. Madsen et al., "Ionization of oriented carbonyl sulfide molecules by intense circularly polarized laser pulses," *Phys. Rev. A* **83**, 023405 (2011).
- [386] I. Petersen, J. Henkel and M. Lein, "Signatures of Molecular Orbital Structure in Lateral Electron Momentum Distributions from Strong-Field Ionization," *Phys. Rev. Lett.* **114**, 103004 (2015).
- [387] M. Kübel, Z. Dube, A. Y. Naumov et al., "Spatiotemporal imaging of valence electron motion," *Nat. Commun.* **10**, 1042 (2019).
- [388] M. Kunitski, N. Eicke, P. Huber et al., "Double-slit photoelectron interference in strong-field ionization of the neon dimer," *Nat. Commun.* **10**, 1 (2019).
- [389] J. Wu, M. Magrakvelidze, L. P. H. Schmidt et al., "Understanding the role of phase in chemical bond breaking with coincidence angular streaking," *Nat. Commun.* **4**, 2177 (2013).
- [390] J. Wu, M. Meckel, L. P. H. Schmidt et al., "Probing the tunnelling site of electrons in strong field enhanced ionization of molecules," *Nat. Commun.* **3**, 1113 (2012).
- [391] V. V. Serov, A. W. Bray and A. S. Kheifets, "Numerical attoclock on atomic and molecular hydrogen," *Phys. Rev. A* **99**, 063428 (2019).

- [392] W. Quan, V. V. Serov, M. Wei et al., "Attosecond Molecular Angular Streaking with All-Ionic Fragments Detection," *Phys. Rev. Lett.* **123**, 223204 (2019).
- [393] A. Khan, D. Trabert, S. Eckart et al., "Orientation-dependent dissociative ionization of H₂ in strong elliptic laser fields: Modification of the release time through molecular orientation," *Phys. Rev. A* **101**, 023409 (2020).
- [394] J. Yan, W. Xie, M. Li et al., "Photoelectron ionization time of aligned molecules clocked by attosecond angular streaking," *Phys. Rev. A* **102**, 013117 (2020).
- [395] H. G. Muller, "Reconstruction of attosecond harmonic beating by interference of two-photon transitions," *Appl. Phys. B* **74**, s17–s21 (2002).
- [396] D. Baykusheva and H. J. Wörner, "Theory of attosecond delays in molecular photoionization," *J. Chem. Phys.* **146**, 124306 (2017).
- [397] S. Grundmann, D. Trabert, K. Fehre et al., "Zeptosecond birth time delay in molecular photoionization," *Science* **370**, 339–341 (2020).
- [398] W. Xie, J. Yan, M. Li et al., "Picometer-Resolved Photoemission Position within the Molecule by Strong-Field Photoelectron Holography," *Phys. Rev. Lett.* **127**, 263202 (2021).
- [399] Y. Zhou, J. Tan, M. Li et al., "Probing the launching position of the electron wave packet in molecule strong-field tunneling ionization," *Sci. China Phys. Mech.* **64**, 273011 (2021).
- [400] D. W. Schumacher, F. Weihe, H. G. Muller et al., "Phase Dependence of Intense Field Ionization: A Study Using Two Colors," *Phys. Rev. Lett.* **73**, 1344 (1994).
- [401] L. J. Zipp, A. Natan and P. H. Bucksbaum, "Probing electron delays in above-threshold ionization," *Optica* **1**, 361 (2014).
- [402] X. Song, G. Shi, G. Zhang et al., "Attosecond Time Delay of Retrapped Resonant Ionization," *Phys. Rev. Lett.* **121**, 103201 (2018).
- [403] Y. Feng, M. Li, S. Luo et al., "Semiclassical analysis of photoelectron interference in a synthesized two-color laser pulse," *Phys. Rev. A* **100**, 063411 (2019).
- [404] M. Han, P. Ge, Y. Shao et al., "Attoclock Photoelectron Interferometry with Two-Color Corotating Circular Fields to Probe the Phase and the Amplitude of Emitting Wave Packets," *Phys. Rev. Lett.* **120**, 073202 (2018).
- [405] P. Ge, M. Han, Y. Deng et al., "Universal Description of the Attoclock with Two-Color Corotating Circular Fields," *Phys. Rev. Lett.* **122**, 013201 (2019).
- [406] R. Murray, W.-K. Liu and M. Y. Ivanov, "Partial Fourier-transform approach to tunnel ionization: Atomic systems," *Phys. Rev. A* **81**, 023413 (2010).
- [407] R. Murray, M. Spanner, S. Patchkovskii et al., "Tunnel Ionization of Molecules and Orbital Imaging," *Phys. Rev. Lett.* **106**, 173001 (2011).
- [408] M. Liu and Y. Liu, "Application of the partial-Fourier-transform approach for tunnel ionization of molecules," *Phys. Rev. A* **93**, 043426 (2016).
- [409] M.-M. Liu and Y. Liu, "Semiclassical models for strong-field tunneling ionization of molecules," *J. Phys. B* **50**, 105602 (2017).
- [410] C. de Carvalho and H. Nussenzveig, "Time delay," *Phys. Rep.* **364**, 83–174 (2002).
- [411] L. Gallmann, I. Jordan, H. J. Wörner et al., "Photoemission and photoionization time delays and rates," *Struct. Dyn.* **4**, 061502 (2017).

- [412] J. Muth-Böhm, A. Becker and F. H. M. Faisal, "Suppressed Molecular Ionization for a Class of Diatomics in Intense Femtosecond Laser Fields," *Phys. Rev. Lett.* **85**, 2280–2283 (2000).
- [413] A. Jaroń-Becker, A. Becker and F. H. M. Faisal, "Dependence of strong-field photoelectron angular distributions on molecular orientation," *J. Phys. B* **36**, L375 (2003).
- [414] A. Jaroń-Becker, A. Becker and F. H. M. Faisal, "Ionization of N₂, O₂, and linear carbon clusters in a strong laser pulse," *Phys. Rev. A* **69**, 023410 (2004).
- [415] S. Petretti, Y. V. Vanne, A. Saenz et al., "Alignment-Dependent Ionization of N₂, O₂, and CO₂ in Intense Laser Fields," *Phys. Rev. Lett.* **104**, 223001 (2010).
- [416] S.-K. Son and S.-I. Chu, "Multielectron effects on the orientation dependence and photoelectron angular distribution of multiphoton ionization of CO₂ in strong laser fields," *Phys. Rev. A* **80**, 011403 (2009).
- [417] M. D. Śpiewanowski and L. B. Madsen, "Alignment- and orientation-dependent strong-field ionization of molecules: Field-induced orbital distortion effects," *Phys. Rev. A* **91**, 043406 (2015).
- [418] B. Zhang and M. Lein, "High-order harmonic generation from diatomic molecules in an orthogonally polarized two-color laser field," *Phys. Rev. A* **100**, 043401 (2019).
- [419] S. Eckart, D. Trabert, K. Fehre et al., "Sideband modulation by subcycle interference," *Phys. Rev. A* **102**, 043115 (2020).
- [420] M. Han, P. Ge, Y. Fang et al., "Unifying Tunneling Pictures of Strong-Field Ionization with an Improved Attoclock," *Phys. Rev. Lett.* **123**, 073201 (2019).
- [421] Z. Guo, P. Ge, Y. Fang et al., "Probing molecular frame Wigner time delay and electron wavepacket phase structure of CO molecule," *Ultrafast Science* **2022**, 9802917 (2022).
- [422] S. Skruszewicz, J. Tiggesbäumker, K.-H. Meiwes-Broer et al., "Two-Color Strong-Field Photoelectron Spectroscopy and the Phase of the Phase," *Phys. Rev. Lett.* **115**, 043001 (2015).
- [423] M. A. Almajid, M. Zabel, S. Skruszewicz et al., "Two-color phase-of-the-phase spectroscopy in the multiphoton regime," *J. Phys. B* **50**, 194001 (2017).
- [424] V. A. Tulskey, M. A. Almajid and D. Bauer, "Two-color phase-of-the-phase spectroscopy with circularly polarized laser pulses," *Phys. Rev. A* **98**, 053433 (2018).
- [425] V. A. Tulskey, B. Krebs, J. Tiggesbäumker et al., "Revealing laser-coherent electron features using phase-of-the-phase spectroscopy," *J. Phys. B* **53**, 074001 (2020).
- [426] J. Zhao and M. Lein, "Determination of Ionization and Tunneling Times in High-Order Harmonic Generation," *Phys. Rev. Lett.* **111**, 043901 (2013).
- [427] S. H. Autler and C. H. Townes, "Stark effect in rapidly varying fields," *Phys. Rev.* **100**, 703–722 (1955).
- [428] B. R. Mollow, "Power spectrum of light scattered by two-level systems," *Phys. Rev.* **188**, 1969–1975 (1969).
- [429] J. Dalibard and C. Cohen-Tannoudji, "Laser cooling below the Doppler limit by polarization gradients: Simple theoretical models," *J. Opt. Soc. Am. B* **6**, 2023–2045 (1989).
- [430] B. J. Sussman, D. Townsend, M. Y. Ivanov et al., "Dynamic Stark control of photochemical processes," *Science* **314**, 278–281 (2006).

- [431] V. Kalosha, M. Spanner, J. Herrmann et al., "Generation of Single Dispersion Precompensated 1-fs Pulses by Shaped-Pulse Optimized High-Order Stimulated Raman Scattering," *Phys. Rev. Lett.* **88**, 103901 (2002).
- [432] P. J. Bustard, B. J. Sussman and I. A. Walmsley, "Amplification of Impulsively Excited Molecular Rotational Coherence," *Phys. Rev. Lett.* **104**, 193902 (2010).
- [433] H. Stapelfeldt and T. Seideman, "Colloquium: Aligning molecules with strong laser pulses," *Rev. Mod. Phys.* **75**, 543–557 (2003).
- [434] M. D. Perry, A. Szoke and K. C. Kulander, "Resonantly Enhanced Above-Threshold Ionization of Helium," *Phys. Rev. Lett.* **63**, 1058–1061 (1989).
- [435] B. Willenberg, J. Maurer, B. W. Mayer et al., "Sub-cycle time resolution of multi-photon momentum transfer in strong-field ionization," *Nat. Commun.* **10**, 5548 (2019).
- [436] A. Hartung, S. Brennecke, K. Lin et al., "Electric Nondipole Effect in Strong-Field Ionization," *Phys. Rev. Lett.* **126**, 053202 (2021).
- [437] B. Böning, W. Paufler and S. Fritzsche, "Nondipole strong-field approximation for spatially structured laser fields," *Phys. Rev. A* **99**, 053404 (2019).
- [438] S. V. B. Jensen, M. M. Lund and L. B. Madsen, "Nondipole strong-field-approximation Hamiltonian," *Phys. Rev. A* **101**, 043408 (2020).
- [439] S. Brennecke and M. Lein, "Nondipole modification of the ac Stark effect in above-threshold ionization," *Phys. Rev. A* **104**, L021104 (2021).
- [440] M. M. Lund and L. B. Madsen, "Nondipole photoelectron momentum shifts in strong-field ionization with mid-infrared laser pulses of long duration," *J. Phys. B* **54**, 165602 (2021).
- [441] K. Lin, S. Eckart, A. Hartung et al., "Photoelectron energy peaks shift against the radiation pressure in strong-field ionization," *Sci. Adv.* **8**, 7386 (2022).
- [442] J. H. Shirley, "Solution of the Schrödinger equation with a Hamiltonian periodic in time," *Phys. Rev.* **138**, B979–B987 (1965).
- [443] H. Sambe, "Steady states and quasienergies of a quantum-mechanical system in an oscillating field," *Phys. Rev. A* **7**, 2203–2213 (1973).
- [444] N. B. Delone and V. P. Krainov, "AC Stark shift of atomic energy levels," *Phys.-Uspekhi* **42**, 669–687 (1999).
- [445] S. Chelkowski, A. D. Bandrauk and P. B. Corkum, "Photon-momentum transfer in photoionization: From few photons to many," *Phys. Rev. A* **95**, 053402 (2017).
- [446] M. Lein, E. K. U. Gross and V. Engel, "Discrete peaks in above-threshold double-ionization spectra," *Phys. Rev. A* **64**, 023406 (2001).
- [447] M. D. Feit, J. A. Fleck and A. Steiger, "Solution of the Schrödinger equation by a spectral method," *J. Comput. Phys.* **47**, 412 (1982).
- [448] F. Maulbetsch and J. S. Briggs, "Selection rules for transitions to two-electron continuum states," *J. Phys. B* **28**, 551 (1995).
- [449] K. Henrichs, S. Eckart, A. Hartung et al., "Experimental evidence for selection rules in multiphoton double ionization of helium and neon," *Phys. Rev. A* **97**, 031405 (2018).

- [450] C. I. Moore, J. P. Knauer and D. D. Meyerhofer, "Observation of the Transition from Thomson to Compton Scattering in Multiphoton Interactions with Low-Energy Electrons," *Phys. Rev. Lett.* **74**, 2439–2442 (1995).
- [451] D. D. Meyerhofer, J. P. Knauer, S. J. McNaught et al., "Observation of relativistic mass shift effects during high-intensity laser–electron interactions," *J. Opt. Soc. Am. B* **13**, 113–117 (1996).
- [452] D. S. Guo and T. Aberg, "Quantum electrodynamical approach to multiphoton ionisation in the high-intensity H field," *J. Phys. A* **21**, 4577 (1988).
- [453] H. R. Reiss, "Complete Keldysh theory and its limiting cases," *Phys. Rev. A* **42**, 1476–1486 (1990).
- [454] A. Bugacov and R. Shakeshaft, "Multiphoton transitions in a strong field: Inclusion of the photon momentum," *Phys. Rev. A* **47**, 674–685 (1993).
- [455] D. P. Crawford and H. R. Reiss, "Relativistic ionization of hydrogen by linearly polarized light," *Opt. Express* **2**, 289–297 (1998).
- [456] M. Klaiber, K. Z. Hatsagortsyan and C. H. Keitel, "Gauge-invariant relativistic strong-field approximation," *Phys. Rev. A* **73**, 053411 (2006).
- [457] M. Klaiber, K. Z. Hatsagortsyan and C. H. Keitel, "Fully relativistic laser-induced ionization and recollision processes," *Phys. Rev. A* **75**, 063413 (2007).
- [458] Y. I. Salamin, "Strong-field multiphoton ionization of hydrogen: Nondipolar asymmetry and ponderomotive scattering," *Phys. Rev. A* **56**, 4910–4917 (1997).
- [459] F. H. M. Faisal and T. Radozycki, "Three-dimensional relativistic model of a bound particle in an intense laser field," *Phys. Rev. A* **47**, 4464–4473 (1993).
- [460] V. S. Popov, V. D. Mur and B. M. Karnakov, "The imaginary-time method for relativistic problems," *J. Exp. Theor. Phys.* **66**, 229–235 (1997).
- [461] N. Milosevic, V. P. Krainov and T. Brabec, "Relativistic theory of tunnel ionization," *J. Phys. B* **35**, 3515 (2002).
- [462] V. S. Popov, B. M. Karnakov and V. D. Mur, "On the relativistic theory of tunneling," *J. Exp. Theor. Phys.* **79**, 262–267 (2004).
- [463] V. P. Krainov and S. P. Roshupkin, "Relativistic effects in the angular distribution of ejected electrons in tunneling ionization of atoms by strong electromagnetic fields," *J. Opt. Soc. Am. B* **9**, 1231–1233 (1992).
- [464] V. Krainov, "Energy distribution of relativistic electrons in the tunneling ionization of atoms by super-intense laser radiation," *Opt. Express* **2**, 268–270 (1998).
- [465] V. P. Krainov, "Energy and angular distribution of relativistic electrons in the tunnelling ionization of atoms by circularly polarized light," *J. Phys. B* **32**, 1607 (1999).
- [466] J. Ortner and V. M. Rylyuk, "Relativistic semiclassical approach in strong-field nonlinear photoionization," *Phys. Rev. A* **61**, 033403 (2000).
- [467] J. Ortner, "Relativistic photoelectron spectra in the ionization of atoms by elliptically polarized light," *J. Phys. B* **33**, 383 (2000).
- [468] H. K. Avetissian, A. G. Markossian and G. F. Mkrtchian, "Relativistic theory of the above-threshold multiphoton ionization of hydrogenlike atoms in ultrastrong laser fields," *Phys. Rev. A* **64**, 053404 (2001).

- [469] V. P. Krainov and A. V. Sofronov, "High-energy electron-energy spectra of atoms undergoing tunneling and barrier-suppression ionization by superintense linearly polarized laser radiation," *Phys. Rev. A* **69**, 015401 (2004).
- [470] J. Liu, Q. Z. Xia, J. F. Tao et al., "Coulomb effects in photon-momentum partitioning during atomic ionization by intense linearly polarized light," *Phys. Rev. A* **87**, 041403 (2013).
- [471] E. Yakaboylu, M. Klaiber, H. Bauke et al., "Relativistic features and time delay of laser-induced tunnel ionization," *Phys. Rev. A* **88**, 063421 (2013).
- [472] M. Klaiber, E. Yakaboylu and K. Z. Hatsagortsyan, "Above-threshold ionization with highly charged ions in superstrong laser fields. ii. Relativistic Coulomb-corrected strong-field approximation," *Phys. Rev. A* **87**, 023418 (2013).
- [473] A. Hartung, *Der Photonenimpuls in der Starkfeldionisation* (Johann Wolfgang Goethe-University, Frankfurt, 2019).
- [474] H. Ni, S. Brennecke, X. Gao et al., "Theory of Subcycle Linear Momentum Transfer in Strong-Field Tunneling Ionization," *Phys. Rev. Lett.* **125**, 073202 (2020).
- [475] J. Maurer and U. Keller, "Ionization in intense laser fields beyond the electric dipole approximation: Concepts, methods, achievements and future directions," *J. Phys. B* **54**, 094001 (2021).
- [476] I. Barth and O. Smirnova, "Spin-polarized electrons produced by strong-field ionization," *Phys. Rev. A* **88**, 013401 (2013).
- [477] A. Hartung, F. Morales, M. Kunitski et al., "Electron spin polarization in strong-field ionization of xenon atoms," *Nat. Photonics* **10**, 526–528 (2016).
- [478] I. Barth and M. Lein, "Numerical verification of the theory of nonadiabatic tunnel ionization in strong circularly polarized laser fields," *J. Phys. B* **47**, 204016 (2014).
- [479] L. B. Madsen, "Nondipole effects in tunneling ionization by intense laser pulses," *Phys. Rev. A* **105**, 043107 (2022).
- [480] M. Klaiber, K. Z. Hatsagortsyan and C. H. Keitel, "Subcycle time-resolved nondipole dynamics in tunneling ionization," *Phys. Rev. A* **105**, 053107 (2022).
- [481] P.-L. He, M. Klaiber, K. Z. Hatsagortsyan et al., "Nondipole coulomb sub-barrier ionization dynamics and photon momentum sharing," *Phys. Rev. A* **105**, L031102 (2022).
- [482] P.-L. He, K. Z. Hatsagortsyan and C. H. Keitel, "Nondipole Time Delay and Double-Slit Interference in Tunneling Ionization," *Phys. Rev. Lett.* **128**, 183201 (2022).
- [483] D. B. Milošević, S. Hu and W. Becker, "Quantum-mechanical model for ultrahigh-order harmonic generation in the moderately relativistic regime," *Phys. Rev. A* **63**, 011403 (2000).
- [484] C. C. Chirilă, N. J. Kylstra, R. M. Potvliege et al., "Nondipole effects in photon emission by laser-driven ions," *Phys. Rev. A* **66**, 063411 (2002).
- [485] Y. I. Salamin, S. X. Hu, K. Z. Hatsagortsyan et al., "Relativistic high-power laser-matter interactions," *Phys. Rep.* **427**, 41 – 155 (2006).
- [486] E. Pisanty, D. D. Hickstein, B. R. Galloway et al., "High harmonic interferometry of the Lorentz force in strong mid-infrared laser fields," *New J. Phys.* **20**, 053036 (2018).
- [487] M. Dammasch, M. Dörr, U. Eichmann et al., "Relativistic laser-field-drift suppression of nonsequential multiple ionization," *Phys. Rev. A* **64**, 061402 (2001).

- [488] J. Prager and C. H. Keitel, "Laser-induced nonsequential double ionization approaching the relativistic regime," *J. Phys. B* **35**, L167 (2002).
- [489] A. Emmanouilidou, T. Meltzer and P. B. Corkum, "Non-dipole recollision-gated double ionization and observable effects," *J. Phys. B* **50**, 225602 (2017).
- [490] F. Sun, X. Chen, W. Zhang et al., "Longitudinal photon-momentum transfer in strong-field double ionization of argon atoms," *Phys. Rev. A* **101**, 021402 (2020).
- [491] K. Lin, X. Chen, S. Eckart et al., "Magnetic-Field Effect as a Tool to Investigate Electron Correlation in Strong-Field Ionization," *Phys. Rev. Lett.* **128**, 113201 (2022).
- [492] J. V. de Aldana and L. Roso, "Magnetic-field effect in atomic ionization by intense laser fields," *Opt. Express* **5**, 144–148 (1999).
- [493] M. Førre, J. P. Hansen, L. Kocbach et al., "Nondipole Ionization Dynamics of Atoms in Superintense High-Frequency Attosecond Pulses," *Phys. Rev. Lett.* **97**, 043601 (2006).
- [494] W. Becker, A. Lohr and M. Kleber, "Effects of rescattering on above-threshold ionization," *J. Phys. B* **27**, L325 (1994).
- [495] N. M. Kroll and K. M. Watson, "Charged-particle scattering in the presence of a strong electromagnetic wave," *Phys. Rev. A* **8**, 804–809 (1973).
- [496] A. Čerkić, E. Hasović, D. B. Milošević et al., "High-order above-threshold ionization beyond the first-order Born approximation," *Phys. Rev. A* **79**, 033413 (2009).
- [497] D. B. Milošević, "Low-frequency approximation for above-threshold ionization by a laser pulse: Low-energy forward rescattering," *Phys. Rev. A* **90**, 063423 (2014).
- [498] Z. Chen, A.-T. Le, T. Morishita et al., "Quantitative rescattering theory for laser-induced high-energy plateau photoelectron spectra," *Phys. Rev. A* **79**, 033409 (2009).
- [499] S. Chelkowski and A. D. Bandrauk, "Photon-momentum transfer in molecular photoionization," *Phys. Rev. A* **97**, 053401 (2018).
- [500] K. Lin, S. Brennecke, H. Ni et al., "Magnetic-Field Effect in High-Order Above-Threshold Ionization," *Phys. Rev. Lett.* **128**, 023201 (2022).
- [501] S. Brennecke and M. Lein, "High-order above-threshold ionization beyond the electric dipole approximation: Dependence on the atomic and molecular structure," *Phys. Rev. A* **98**, 063414 (2018).
- [502] M. Lein, P. P. Corso, J. P. Marangos et al., "Orientation dependence of high-order harmonic generation in molecules," *Phys. Rev. A* **67**, 023819 (2003).
- [503] G. G. Paulus, F. Grasbon, A. Dreischuh et al., "Above-Threshold Ionization by an Elliptically Polarized Field: Interplay between Electronic Quantum Trajectories," *Phys. Rev. Lett.* **84**, 3791 (2000).
- [504] M. Busuladžić, A. Gazibegović-Busuladžić, D. B. Milošević et al., "Strong-field approximation for ionization of a diatomic molecule by a strong laser field. ii. The role of electron rescattering off the molecular centers," *Phys. Rev. A* **78**, 033412 (2008).
- [505] C. Jönsson, "Elektroneninterferenzen an mehreren künstlich hergestellten Feinspalten," *Z. Phys.* **161**, 454–474 (1961).
- [506] E. Hasović, A. Gazibegović-Busuladžić, M. Busuladžić et al., "High-order above-threshold ionization with few-cycle laser pulses: Molecular improved strong-field approximation vs. molecular low-frequency approximation," *Laser Phys.* **22**, 1819–1826 (2012).

- [507] J. Henkel, M. Lein and V. Engel, "Interference in above-threshold-ionization electron distributions from molecules," *Phys. Rev. A* **83**, 051401 (2011).
- [508] N. Haram, I. Ivanov, H. Xu et al., "Relativistic Nondipole Effects in Strong-Field Atomic Ionization at Moderate Intensities," *Phys. Rev. Lett.* **123**, 093201 (2019).
- [509] J. Daněk, M. Klaiber, K. Z. Hatsagortsyan et al., "Interplay between Coulomb-focusing and non-dipole effects in strong-field ionization with elliptical polarization," *J. Phys. B* **51**, 114001 (2018).
- [510] J. Daněk, K. Z. Hatsagortsyan and C. H. Keitel, "Analytical approach to Coulomb focusing in strong-field ionization. i. Nondipole effects," *Phys. Rev. A* **97**, 063409 (2018).
- [511] C. DeWitt-Morette and P. Cartier, "Physics on and near caustics," in *Functional Integration: Basics and Applications*, edited by C. DeWitt-Morette, P. Cartier and A. Folacci (Springer US, Boston, MA, 1997) pp. 51–66.
- [512] S. Chelkowski and A. D. Bandrauk, "Photon momentum transfer in photoionisation: Unexpected breakdown of the dipole approximation," *Molec. Phys.* **115**, 1971–1983 (2017).
- [513] B. Willenberg, J. Maurer, U. Keller et al., "Holographic interferences in strong-field ionization beyond the dipole approximation: The influence of the peak and focal-volume-averaged laser intensities," *Phys. Rev. A* **100**, 033417 (2019).
- [514] M. V. Berry, "Uniform approximations for glory scattering and diffraction peaks," *J. Phys. B* **2**, 381–392 (1969).
- [515] C. DeWitt-Morette and B. L. Nelson, "Glories - and other degenerate points of the action," *Phys. Rev. D* **29**, 1663–1668 (1984).
- [516] J. R. Taylor, *Scattering Theory: The Quantum Theory on Nonrelativistic Collisions*, 1st ed. (John Wiley, New York, 1972).
- [517] J. Dahlström, D. Guénot, K. Klünder et al., "Theory of attosecond delays in laser-assisted photoionization," *Chem. Phys.* **414**, 53–64 (2013), attosecond spectroscopy.
- [518] J. A. Fleck, J. R. Morris and M. D. Feit, "Time-dependent propagation of high energy laser beams through the atmosphere," *App. Phys.* **10**, 129–160 (1976).
- [519] X. M. Tong and S. Chu, "Theoretical study of multiple high-order harmonic generation by intense ultrashort pulsed laser fields: A new generalized pseudospectral time-dependent method," *Chem. Phys.* **217**, 119 – 130 (1997).
- [520] E. A. McCullough and R. E. Wyatt, "Dynamics of the collinear H+H₂ reaction. II. Energy analysis," *J. Chem. Phys.* **54**, 3592–3600 (1971).
- [521] A. Askar and A. S. Cakmak, "Explicit integration method for the time-dependent Schrödinger equation for collision problems," *J. Chem. Phys.* **68**, 2794–2798 (1978).
- [522] H. Tal-Ezer and R. Kosloff, "An accurate and efficient scheme for propagating the time-dependent Schrödinger equation," *J. Chem. Phys.* **81**, 3967–3971 (1984).
- [523] C. Lanczos, "An iteration method for the solution of the eigenvalue problem of linear differential and integral operators," *J. Res. Nat. Bur. Stand.* **45**, 255–282 (1950).
- [524] M. Murakami, O. Korobkin and M. Horbatsch, "High-harmonic generation from hydrogen atoms driven by two-color mutually orthogonal laser fields," *Phys. Rev. A* **88**, 063419 (2013).
- [525] M. Murakami and S.-I. Chu, "Photoelectron momentum distributions of the hydrogen atom driven by multicycle elliptically polarized laser pulses," *Phys. Rev. A* **93**, 023425 (2016).

- [526] J. Wang, S.-I. Chu and C. Laughlin, "Multiphoton detachment of H^- . II. Intensity-dependent photodetachment rates and threshold behavior - complex-scaling generalized pseudospectral method," *Phys. Rev. A* **50**, 3208–3215 (1994).
- [527] N. Schaeffer, "Efficient spherical harmonic transforms aimed at pseudospectral numerical simulations," *Geochem. Geophys. Geosyst.* **14**, 751–758 (2013).
- [528] E. Cormier and P. Lambropoulos, "Optimal gauge and gauge invariance in non-perturbative time-dependent calculation of above-threshold ionization," *J. Phys. B* **29**, 1667–1680 (1996).
- [529] R. Heather and H. Metiu, "An efficient procedure for calculating the evolution of the wave function by fast Fourier transform methods for systems with spatially extended wave function and localized potential," *J. Chem. Phys.* **86**, 5009–5017 (1987).
- [530] F. Oppermann, N. Eicke and M. Lein, "Real-time propagator eigenstates," *J. Phys. B* **55**, 19LT01 (2022).
- [531] X.-M. Tong and S.-I. Chu, "Density-functional theory with optimized effective potential and self-interaction correction for ground states and autoionizing resonances," *Phys. Rev. A* **55**, 3406 (1997).
- [532] N. Troullier and J. L. Martins, "Efficient pseudopotentials for plane-wave calculations," *Phys. Rev. B* **43**, 1993 (1991).
- [533] P. Wang, A. M. Sayler, K. D. Carnes et al., "Disentangling the volume effect through intensity-difference spectra: Application to laser-induced dissociation of H_2^+ ," *Opt. Lett.* **30**, 664–666 (2005).
- [534] G. N. Gibson, R. R. Freeman, T. J. McIlrath et al., "Excitation and ionization dynamics in short-pulse multiphoton ionization," *Phys. Rev. A* **49**, 3870–3874 (1994).
- [535] M. V. Frolov, N. L. Manakov, A. A. Minina et al., "Adiabatic-limit Coulomb factors for photoelectron and high-order-harmonic spectra," *Phys. Rev. A* **96**, 023406 (2017).
- [536] V. S. Popov, "Imaginary-time method in quantum mechanics and field theory," *Phys. At. Nucl.* **68**, 686 (2005).
- [537] D. B. Milošević, "On-shell and off-shell low-frequency approximations for potential scattering in a strong laser field-optical theorem and sum rule," *J. Phys. B* **28**, 1869 (1995).
- [538] D. B. Milošević, "Off-shell and on-shell low-frequency approximations for potential scattering in a strong elliptically polarized laser field," *Phys. Rev. A* **53**, 619–622 (1996).
- [539] D. B. Milošević, A. Čerkić, B. Fetić et al., "Low-frequency approximation for high-order above-threshold ionization," *Laser Phys.* **20**, 573–580 (2010).

List of Abbreviations

1BA	First Born approximation
ADK	Ammosov-Delone-Krainov (rate)
ARM	Analytical R-matrix (theory)
ATI	Above-threshold ionization
BRR	Backward rescattering ridge
CCSFA	Coulomb-corrected strong-field approximation
CEP	Carrier-envelope phase
COLTRIMS	Cold target recoil ion momentum spectroscopy
CQSFA	Coulomb quantum-orbit strong-field approximation
CTMC	Classical-trajectory Monte Carlo (simulation)
CW	Continuous wave
DCS	Differential cross section
FDM	Field-direction model
FWHM	Full width at half maximum
HASE	Holographic angular streaking of electrons
HATI	High-order above-threshold ionization
HHG	High-harmonic generation
IR	Infrared
KFR	Keldysh-Faisal-Reiss (amplitude)
LCAO	Linear combination of atomic orbitals
LFA	Low-frequency approximation
LIED	Laser-induced electron diffraction
NSDI	Nonsequential double ionization
PMD	Photoelectron momentum distribution
POCI	Point of constructive interference
PPT	Perelomov-Popov-Terent'ev
QOM	Quantum-orbit model
QTMC	Quantum-trajectory Monte Carlo (simulation)
RABBITT	Reconstruction of attosecond beating by interference of two-photon transitions
SCTS	Semiclassical two-step (model)
SFA	Strong-field approximation
SM's	Simple man's (model)
SPA	Saddle-point approximation
TCSFA	Trajectory-based Coulomb-corrected strong-field approximation
TDSE	Time-dependent Schrödinger equation

TIPIS	Tunnel ionization in parabolic coordinates with induced dipole and Stark shift
VMI	Velocity-map imaging
XUV	Extreme ultraviolet

Curriculum Vitae

Personal details

Name	Simon Brennecke
Date of birth	September 05, 1993
Place of birth	Hameln, Germany

Education

05/2018–02/2023	Doctoral studies in the group of Manfred Lein at Leibniz Universität Hannover
01/2021–07/2021	Scholarship awarded by the German Academic Exchange Service (DAAD) for an exchange to Stanford University (canceled due to COVID-19 pandemic)
10/2015–03/2018	Studies of physics at Leibniz Universität Hannover Thesis: “Quantum Dynamics of Atoms in Strong Fields with Tailored Polarization” Degree: Master of Science (M.Sc.)
09/2016–03/2017	Research project in the group of Hans Jakob Wörner at ETH Zürich, Switzerland
10/2012–11/2015	Studies of physics at Leibniz Universität Hannover Thesis: “Electron Angular Distributions from Laser-Induced Ionization of Molecules” Degree: Bachelor of Science (B.Sc.)
05/2015–03/2018	Scholarship awarded by the German Academic Scholarship Foundation
08/2004–07/2012	Viktoria-Luise Gymnasium Hameln Degree: General qualification for university entrance

List of Publications

- [S. Brennecke](#), M. Ranke, A. Dimitriou, S. Walther, M. J. Prandolini, M. Lein, and U. Fröhling, “Control of Electron Wave Packets Close to the Continuum Threshold Using Single-Cycle THz Waveforms,” *Physical Review Letters* **129**, 213202 (2022).
- K. Lin, [S. Brennecke](#), H. Ni, X. Chen, A. Hartung, D. Trabert, K. Fehre, J. Rist, X.-M. Tong, J. Burgdörfer, L. Ph. H. Schmidt, M. S. Schöffler, T. Jahnke, M. Kunitski, F. He, M. Lein, S. Eckart, and R. Dörner, “Magnetic-Field Effect in High-Order Above-Threshold Ionization,” *Physical Review Letters* **128**, 023201 (2022).
- D. Trabert, N. Anders, [S. Brennecke](#), M. S. Schöffler, T. Jahnke, L. Ph. H. Schmidt, M. Kunitski, M. Lein, R. Dörner, and S. Eckart, “Nonadiabatic Strong Field Ionization of Atomic Hydrogen,” *Physical Review Letters* **127**, 273001 (2021).
- [S. Brennecke](#), and M. Lein, “Nondipole modification of the ac Stark effect in above-threshold ionization,” *Physical Review A* **104**, L021104 (2021).
- [S. Brennecke](#), S. Eckart, and M. Lein, “Attoclock with bicircular laser fields as a probe of velocity-dependent tunnel-exit position,” *Journal of Physics B: Atomic, Molecular and Optical Physics* **54**, 164001 (2021).
- D. Trabert, [S. Brennecke](#), K. Fehre, N. Anders, A. Geyer, S. Grundmann, M. S. Schöffler, L. Ph. H. Schmidt, T. Jahnke, R. Dörner, M. Kunitski, and S. Eckart, “Angular dependence of the Wigner time delay upon tunnel ionization of H₂,” *Nature Communications* **12**, 1697 (2021).
- A. Hartung, [S. Brennecke](#), K. Lin, D. Trabert, K. Fehre, J. Rist, M. S. Schöffler, T. Jahnke, L. Ph. H. Schmidt, M. Kunitski, M. Lein, R. Dörner, and S. Eckart, “Electric Nondipole Effect in Strong-Field Ionization,” *Physical Review Letters* **126**, 053202 (2021).
- H. Ni, [S. Brennecke](#), X. Gao, P.-L. He, S. Donsa, I. Březinová, F. He, J. Wu, M. Lein, X.-M. Tong, and J. Burgdörfer, “Theory of Subcycle Linear Momentum Transfer in Strong-Field Tunneling Ionization,” *Physical Review Letters* **125**, 073202 (2020).
- S. Yue, [S. Brennecke](#), H. Du, and M. Lein, “Probing dynamical symmetries by bicircular high-harmonic spectroscopy beyond the Born-Oppenheimer approximation,” *Physical Review A* **101**, 053438 (2020).
- [S. Brennecke](#), N. Eicke, and M. Lein, “Gouy’s Phase Anomaly in Electron Waves Produced by Strong-Field Ionization,” *Physical Review Letters* **124**, 153202 (2020).
- M. Kircher, F. Trinter, S. Grundmann, I. Vela-Perez, [S. Brennecke](#), N. Eicke, J. Rist, S. Eckart, S. Houamer, O. Chuluunbaatar, Y. V. Popov, I. P. Volobuev, K. Bagschik, M. N. Piancastelli, M. Lein, T. Jahnke, M. S. Schöffler, and R. Dörner, “Kinematically Complete Experimental Study of Compton Scattering at Helium Atoms near the Threshold,” *Nature Physics* **16**, 756 (2020).
- N. Eicke, [S. Brennecke](#), and M. Lein, “Attosecond-Scale Streaking Methods for Strong-Field Ionization by Tailored Fields,” *Physical Review Letters* **124**, 043202 (2020).

- A. Hartung, S. Eckart, S. Brennecke, J. Rist, D. Trabert, K. Fehre, M. Richter, H. Sann, S. Zeller, K. Henrichs, G. Kastirke, J. Hoehl, A. Kalinin, M. S. Schöffler, T. Jahnke, L. Ph. H. Schmidt, M. Lein, M. Kunitski, and R. Dörner, "Magnetic fields alter strong-field ionization," *Nature Physics* **15**, 1222 (2019).
- S. Brennecke, and M. Lein, "Strong-field photoelectron holography beyond the electric dipole approximation: a semiclassical analysis," *Physical Review A* **100**, 023413 (2019).
- S. Brennecke, and M. Lein, "High-order above-threshold ionization beyond the electric dipole approximation: Dependence on the atomic and molecular structure," *Physical Review A* **98**, 063414 (2018).
- S. Brennecke, and M. Lein, "High-order above-threshold ionization beyond the electric dipole approximation," *Journal of Physics B: Atomic, Molecular and Optical Physics* **51**, 094005 (2018).
- D. Baykusheva, S. Brennecke, M. Lein, and H. J. Wörner, "Signatures of Electronic Structure in Bircircular High-harmonic Spectroscopy," *Physical Review Letters* **119**, 203201 (2017).